Geophysical Monograph Series

177 **Ocean Modeling in an Eddying Regime** *Matthew Hecht and Hiroyasu Hasumi (Eds.)*
178 **Magma to Microbe: Modeling Hydrothermal Processes at Oceanic Spreading Centers** *Robert P. Lowell, Jeffrey S. Seewald, Anna Metaxas, and Michael R. Perfit (Eds.)*
179 **Active Tectonics and Seismic Potential of Alaska** *Jeffrey T. Freymueller, Peter J. Haeussler, Robert L. Wesson, and Göran Ekström (Eds.)*
180 **Arctic Sea Ice Decline: Observations, Projections, Mechanisms, and Implications** *Eric T. DeWeaver, Cecilia M. Bitz, and L.-Bruno Tremblay (Eds.)*
181 **Midlatitude Ionospheric Dynamics and Disturbances** *Paul M. Kintner, Jr., Anthea J. Coster, Tim Fuller-Rowell, Anthony J. Mannucci, Michael Mendillo, and Roderick Heelis (Eds.)*
182 **The Stromboli Volcano: An Integrated Study of the 2002–2003 Eruption** *Sonia Calvari, Salvatore Inguaggiato, Giuseppe Puglisi, Maurizio Ripepe, and Mauro Rosi (Eds.)*
183 **Carbon Sequestration and Its Role in the Global Carbon Cycle** *Brian J. McPherson and Eric T. Sundquist (Eds.)*
184 **Carbon Cycling in Northern Peatlands** *Andrew J. Baird, Lisa R. Belyea, Xavier Comas, A. S. Reeve, and Lee D. Slater (Eds.)*
185 **Indian Ocean Biogeochemical Processes and Ecological Variability** *Jerry D. Wiggert, Raleigh R. Hood, S. Wajih A. Naqvi, Kenneth H. Brink, and Sharon L. Smith (Eds.)*
186 **Amazonia and Global Change** *Michael Keller, Mercedes Bustamante, John Gash, and Pedro Silva Dias (Eds.)*
187 **Surface Ocean–Lower Atmosphere Processes** *Corinne Le Quèrè and Eric S. Saltzman (Eds.)*
188 **Diversity of Hydrothermal Systems on Slow Spreading Ocean Ridges** *Peter A. Rona, Colin W. Devey, Jérôme Dyment, and Bramley J. Murton (Eds.)*
189 **Climate Dynamics: Why Does Climate Vary?** *De-Zheng Sun and Frank Bryan (Eds.)*
190 **The Stratosphere: Dynamics, Transport, and Chemistry** *L. M. Polvani, A. H. Sobel, and D. W. Waugh (Eds.)*
191 **Rainfall: State of the Science** *Firat Y. Testik and Mekonnen Gebremichael (Eds.)*
192 **Antarctic Subglacial Aquatic Environments** *Martin J. Siegert, Mahlon C. Kennicut II, and Robert A. Bindschadler*
193 **Abrupt Climate Change: Mechanisms, Patterns, and Impacts** *Harunur Rashid, Leonid Polyak, and Ellen Mosley-Thompson (Eds.)*
194 **Stream Restoration in Dynamic Fluvial Systems: Scientific Approaches, Analyses, and Tools** *Andrew Simon, Sean J. Bennett, and Janine M. Castro (Eds.)*
195 **Monitoring and Modeling the Deepwater Horizon Oil Spill: A Record-Breaking Enterprise** *Yonggang Liu, Amy MacFadyen, Zhen-Gang Ji, and Robert H. Weisberg (Eds.)*
196 **Extreme Events and Natural Hazards: The Complexity Perspective** *A. Surjalal Sharma, Armin Bunde, Vijay P. Dimri, and Daniel N. Baker (Eds.)*
197 **Auroral Phenomenology and Magnetospheric Processes: Earth and Other Planets** *Andreas Keiling, Eric Donovan, Fran Bagenal, and Tomas Karlsson (Eds.)*
198 **Climates, Landscapes, and Civilizations** *Liviu Giosan, Dorian Q. Fuller, Kathleen Nicoll, Rowan K. Flad, and Peter D. Clift (Eds.)*
199 **Dynamics of the Earth's Radiation Belts and Inner Magnetosphere** *Danny Summers, Ian R. Mann, Daniel N. Baker, and Michael Schulz (Eds.)*
200 **Lagrangian Modeling of the Atmosphere** *John Lin (Ed.)*
201 **Modeling the Ionosphere-Thermosphere** *Jospeh D. Huba, Robert W. Schunk, and George V Khazanov (Eds.)*
202 **The Mediterranean Sea: Temporal Variability and Spatial Patterns** *Gian Luca Eusebi Borzelli, Miroslav Gačić, Piero Lionello, and Paola Malanotte-Rizzoli (Eds.)*
203 **Future Earth - Advancing Civic Understanding of the Anthropocene** *Diana Dalbotten, Gillian Roehrig, and Patrick Hamilton (Eds.)*
204 **The Galápagos: A Natural Laboratory for the Earth Sciences** *Karen S. Harpp, Eric Mittelstaedt, Noémi d'Ozouville, and David W. Graham (Eds.)*
205 **Modeling Atmospheric and Oceanic Flows: Insights from Laboratory Experiments and Numerical Simulations** *Thomas von Larcher and Paul D. Williams (Eds.)*
206 **Remote Sensing of the Terrestrial Water Cycle** *Venkat Lakshmi (Eds.)*
207 **Magnetotails in the Solar System** *Andreas Keiling, Caitríona Jackman and Peter Delamere (Eds.)*
208 **Hawaiian Volcanoes: From Source to Surface** *Rebecca Carey, Valerie Cayol, Michael Poland, and Dominique Weis (Eds.)*
209 **Sea Ice: Physics, Mechanics, and Remote Sensing** *Mohammed Shokr and Nirmal Sinha (Eds.)*
210 **Fluid Dynamics in Complex Fractured-Porous Systems** *Boris Faybishenko, Sally M. Benson, and John E. Gale (Eds.)*
211 **Subduction Dynamics: From Mantle Flow to Mega Disasters** *Gabriele Morra, David A. Yuen, Scott King, Sang Mook Lee, and Seth Stein (Eds.)*
212 **The Early Earth: Accretion and Differentiation** *James Badro and Michael Walter (Eds.)*
213 **Extreme Events** *Mario Chavez, Michael Ghil, and Jaime Urrutia Fucugauchi (Eds.)*
214 **Global Vegetation Dynamics** *Dominique Bachelet and David Turner (Eds.)*
215 **Auroral Dynamics and Space Weather** *Yongliang Zhang and Larry Paxton (Eds.)*
216 **Low-Frequency Waves in Space Plasmas** *Andreas Keiling, Dong-Hun Lee, and Valery M. Nakariakov (Eds.)*
217 **Deep Earth** *Hidenori Terasaki and rebecca Fischer (Eds.)*
218 **Integrated Imaging of the Earth** *Max Moorkamp, Peter Lelièvre, Niklas Linde, and Amir Khan (Eds.)*
219 **Plate Boundaries and Natural Hazards** *Joao Duarte and Wouter Schellart (Eds.)*

Geophysical Monograph 220

# Ionospheric Space Weather

## *Longitude and Hemispheric Dependences and Lower Atmosphere Forcing*

**Timothy Fuller-Rowell**
**Endawoke Yizengaw**
**Patricia H. Doherty**
**Sunanda Basu**
***Editors***

This Work is a copublication between the American Geophysical Union and John Wiley and Sons, Inc.

AGU
American Geophysical Union

WILEY

This Work is a copublication between the American Geophysical Union and John Wiley & Sons, Inc.

**Published under the aegis of the AGU Publications Committee**

Brooks Hanson, Director of Publications
Robert van der Hilst, Chair, Publications Committee



Published by John Wiley & Sons, Inc., Hoboken, New Jersey
Published simultaneously in Canada



*Library of Congress Cataloging-in-Publication Data is available.*

ISBN: 978-1-118-92920-9

Cover images: Front Cover: Figure shows images of ionospheric irregularities over Africa as seen in airglow depletions. The dark patches within the brighter equatorial "arcs," on either side of the geomagnetic equator (dotted curved line), indicate where communication signals would be lost (figure courtesy of Larry Paxton, Applied Physics Laboratory). Back cover: (left) Ground-based instrument coverage in Africa seven years ago and (right) the current ground-based instrumentation in Africa.

Printed in the United States of America

10 9 8 7 6 5 4 3 2 1

# CONTENTS

# CONTRIBUTORS

**Gebregiorgis Abraha**
Department of Physics, Addis Ababa University
Addis Ababa, Ethiopia;
Department of Physics
Mekele University
Mekele, Ethiopia

**Rasaq A. Adeniji-Adele**
Department of Physics
Lagos State University
Ojo, Lagos, Nigeria

**Andrew O. Akala**
Department of Physics
University of Lagos
Akoka, Lagos, Nigeria

**David Anderson**
Cooperative Institute for Research in
Environmental Sciences (CIRES)
University of Colorado at Boulder
Boulder, Colorado, USA; *and*
Space Weather Prediction Center (SWPC)
National Oceanic and Atmospheric
Administration (NOAA)
Boulder, Colorado, USA

**Joseph Baker**
Bradley Department of Electrical and
Computer Engineering
Virginia Tech
Blacksburg, Virginia, USA

**Athanasios Boudouridis**
Center for Space Plasma Physics
Space Science Institute
Boulder, Colorado, USA

**Dalia Burešová**
Department of Aeronomy
Institute of Atmospheric Physics
Academy of Sciences of the Czech Republic (ASCR)
Prague, Czech Republic

**Brett A. Carter**
Institute for Scientific Research
Boston College
Chestnut Hill, Massachusetts, USA

**Peter Chi**
Department of Earth and Space Sciences
University of California, Los Angeles
Los Angeles, California, USA

**Anthea J. Coster**
Haystack Observatory
Massachusetts Institute of Technology
Westford, Massachusetts, USA

**Baylie Damtie**
Department of Physics
Washera Geospace and Radar Science
Laboratory
Bahir Dar University
Bahir Dar, Ethiopia

**Vafi Doumbia**
Laboratoire de Physique de l'Atmosphère
Université Félix Houphouët-Boigny
Abadji Kouté, Abidjan, Côte d'Ivoire

**Florence M. D'ujanga**
Department of Physics
Makerere University
Kampala, Uganda

**Francis G. Eparvier**
Laboratory for Atmospheric and Space Physics
University of Colorado at Boulder
Boulder, Colorado,
USA

**Philip J. Erickson**
Haystack Observatory
Massachusetts Institute of Technology
Westford, Massachusetts, USA

**Tzu-Wei Fang**
Cooperative Institute for Research in
Environmental Sciences (CIRES)
University of Colorado at Boulder
Boulder, Colorado, USA; *and*
Space Weather Prediction Center (SWPC)
National Oceanic and Atmospheric
Administration (NOAA)
Boulder, Colorado, USA

**Daniel J. Fisher**
Department of Electrical and Computer Engineering
University of Illinois at Urbana-Champaign
Urbana, Illinois, USA

**Olanike O. Folarin**
Ionospheric & Space Physics Laboratory
Department of Physics
University of Lagos, Akoka, Nigeria

**John C. Foster**
Haystack Observatory
Massachusetts Institute of Technology
Westford, Massachusetts, USA

**Timothy J. Fuller-Rowell**
Cooperative Institute for Research in Environmental Sciences (CIRES)
University of Colorado at Boulder
Boulder, Colorado, USA; *and*
Space Weather Prediction Center (SWPC)
National Oceanic and Atmospheric Administration (NOAA)
Boulder, Colorado, USA

**Oswald Didier Franck Grodji**
Laboratoire de Physique de l'Atmosphère
Université Félix Houphouët-Boigny
Abadji Kouté, Abidjan, Côte d'Ivoire

**Roderick A. Heelis**
William Hanson Center for Space Sciences
University of Texas at Dallas
Richardson, Texas, USA

**Klemens Hocke**
Institute of Applied Physics
University of Bern
Bern, Switzerland

**Peter Hoffmann**
Leibniz Institute of Atmospheric Physics
Rostock University
Kühlungsborn, Germany

**Mohammed Mainul Hoque**
Institute of Communications and Navigation
German Aerospace Center (DLR)
Neustrelitz, Germany

**Joseph D. Huba**
Plasma Physics Division
Naval Research Laboratory
Washington, D.C., USA

**Enerst E. Iheonu**
Department of Physics
Lagos State University
Ojo, Lagos, Nigeria

**Norbert Jakowski**
Institute of Communications and Navigation
German Aerospace Center (DLR)
Neustrelitz, Germany

**Gebreab Kidanu**
Department of Physics, Addis Ababa University
Addis Ababa, Ethiopia; *and*
University of Texas at Dallas
Dallas/Fort Worth, Texas, USA

**Jan Laštovička**
Department of Aeronomy
Institute of Atmospheric Physics
Academy of Sciences of the Czech Republic (ASCR)
Prague, Czech Republic

**Jonathan J. Makela**
Department of Electrical and Computer Engineering
University of Illinois at Urbana-Champaign
Urbana, Illinois, USA

**James P. Mason**
Laboratory for Atmospheric and Space Physics
University of Colorado at Boulder
Boulder, Colorado, USA

**Vivien Matthias**
Leibniz Institute of Atmospheric Physics
Rostock University
Kühlungsborn, Germany

**Gizaw Mengistu Tsidu**
Department of Physics, Addis Ababa University, Addis Ababa, Ethiopia; Karlsruhe Institute of Technology (KIT), Institute for Meteorology and Climate Research (IMK-ASF), Karlsruhe, Germany; *and*
Department of Earth and Environmental Sciences, Botswana International University of Science and Technology (BIUST)
Palapye, Botswana

**John W. Meriwether**
Department of Physics and Astronomy
Clemson University
Clemson, South Carolina, USA

**Mark B. Moldwin**
Atmospheric, Oceanic, and Space Science (AOSS)
University of Michigan
Ann Arbor, Michigan, USA

**Chigomezyo M. Ngwira**
Department of Physics
Catholic University of America
Washington, D.C., USA; *and*
Space Weather Laboratory
NASA Goddard Space Flight Center
Greenbelt, Maryland, USA

**Melessew Nigussie**
Department of Physics
Washera Geospace and Radar Science Laboratory
Bahir Dar University
Bahir Dar, Ethiopia

**Aghogho Ogwala**
Department of Physics
Lagos State University
Ojo, Lagos, Nigeria

**Eugene O. Onori**
Department of Physics
Lagos State University
Ojo, Lagos, Nigeria

**Phillip Opio**
Department of Physics
Makerere University
Kampala, Uganda

**Edgardo E. Pacheco**
Instituto Geofísico del Perú
Jicamarca Radio Observatory, Lima
Lima, Peru

**A. Babatunde Rabiu**
Center for Atmospheric Research (CAR)
National Space Research and Development Agency
Anyigba, Nigeria

**Sandro M. Radicella**
Telecommunication/ICT for Development Laboratory
Abdu Salam International Center for Theoretical Physics (ICTP)
Trieste, Italy

**J. Michael Ruohoniemi**
Bradley Department of Electrical and Computer Engineering
Virginia Tech
Blacksburg, Virginia, USA

**Ludger Scherliess**
Center for Atmospheric and Space Sciences
Utah State University
Logan, Utah, USA

**Robert Sheehan**
Institute for Scientific Research
Boston College
Newton, Massachusetts, USA

**Emmanuel O. Somoye**
Department of Physics
Lagos State University
Ojo, Lagos, Nigeria

**Simone Studer**
Institute of Applied Physics
University of Bern
Bern, Switzerland

**Evan G. Thomas**
Bradley Department of Electrical and Computer Engineering
Virginia Tech
Blacksburg, Virginia, USA

**Justin S. Tsu**
Atmospheric, Oceanic, and Space Science (AOSS)
University of Michigan
Ann Arbor, Michigan, USA

**Francis Twinomugisha**
Department of Physics
Makerere University
Kampala, Uganda

**Teiji Uozumi**
International Center for Space Weather Science and Education (ICSWSE)
Kyushu University
Fukuoka, Japan

**Cesar E. Valladares**
Institute for Scientific Research
Boston College
Newton, Massachusetts, USA

**Houjun Wang**
Cooperative Institute for Research in Environmental Sciences (CIRES)
University of Colorado at Boulder
Boulder, Colorado, USA; *and*
Space Weather Prediction Center (SWPC)
National Oceanic and Atmospheric Administration (NOAA)
Boulder, Colorado, USA

**James M. Weygand**
Institute of Geophysics and Planetary Physics
University of California, Los Angeles
Los Angeles, California, USA

**Thomas N. Woods**
Laboratory for Atmospheric and Space Physics
University of Colorado at Boulder
Boulder, Colorado, USA

**Endawoke Yizengaw**
Institute for Scientific Research
Boston College
Chestnut Hill, Massachusetts, USA

**Akimasa Yoshikawa**
Earth and Planetary Sciences
Kyushu University
Fukuoka, Japan;
International Center for Space Weather Science and Education (ICSWSE)
Kyushu University
Fukuoka, Japan

**Eftyhia Zesta**
Heliophysics Science Division
NASA Goddard Space Flight Center
Greenbelt, Maryland, USA

# PREFACE

This monograph is the outcome of an American Geophysical Union (AGU) Chapman Conference, "Longitude and Hemispheric Dependence of Space Weather," held in Addis Ababa, Ethiopia, in 2012. The meeting was the culmination of a series of space science meetings and summer schools held in Africa over the past 8 yr. Five years earlier, in 2007, a space science meeting was held in the same city as part of the International Heliophysical Year (IHY). IHY was an effort to reinvigorate the international collaboration in geophysics under the umbrella of the United Nations, a tradition that began 50 yr earlier with the International Geophysical Year (IGY). Subsequent meetings were held in Zambia in 2009. IHY was superseded by the International Space Weather Initiative (ISWI), again under the umbrella of the United Nations. In recognition of the unprecedented achievement of the space science development in Africa, AGU held a prestigious International Chapman Conference in Africa, the first of its kind in the space sciences. One of the highlights of the meeting was formally establishing the African Geophysical Society (AGS).

Although much progress has been made in the study of ionospheric space weather in the last decade, many gaps remain in our global understanding of some of the fundamental processes. For instance, the global electrodynamics that governs the formation of equatorial ionospheric irregularities, which is of practical importance impacting satellite communication and navigation, is still not well understood, hindered by uneven distribution of ground-based instruments. Questions remain, such as, are ionospheric space weather effects the same over the American, African, and Asian longitude sectors, or are they different, and if so why? Observations from instruments on board LEO satellites (e.g., the Communications/Navigation Outage Forecast System C/NOFS), indicate that there is, in fact, strong longitude dependence. Ionospheric irregularities for some reason appear to be more prevalent over the African continent, but it is unclear why. The front cover of this monograph shows images of equatorial plasma bubbles in the ionosphere over Africa obtained from the GUVI instrument on the TIMED satellite using airglow emissions at 135.6 nm (courtesy of Larry Paxton, JHU-APL). The regions of depleted airglow within the brighter equatorial "arcs" are the regions where satellite signals would be scintillated and communication could be lost. Addressing the reason for the longitudinal differences was one of the foci of the Chapman Conference.

One of the reasons for the barrier to understanding some of these longitude dependences is the uneven distribution of ground-based instruments worldwide. Space-based observations, such as C/NOFS, contribute a lot, but there is no substitute for the extended continuous observations from the ground. An obvious step forward in addressing some of the questions on continental and longitude scales was to improve ground-based observations over Africa, an extensive region with a dearth of observations. The Chapman Conference and other meetings held in Africa were a means of focusing attention on an extensive geographic region where observations were critically needed to address some of the fundamental questions of the physical processes driving the ionosphere locally and globally.

The concerted effort over the past 8 yr to try to develop the observational infrastructure has resulted in the situation depicted on the back cover of this monograph. The comparison of ground-based distribution of space science instrumentations (including GNSS receivers, magnetometers, ionosondes, and radars) over Africa in 2007 (left panel) with 2012 (right panel), shows the significant change. There are now many more ground-based ionospheric electron-content observations from GNSS receivers, and plasma drifts estimation from magnetometer observations, that can tackle some of the outstanding scientific questions.

The Chapman Conference was an ideal opportunity to hear about some of these new observations over Africa, which are starting to confirm that the occurrence of ionospheric irregularities are indeed more frequent and stronger in this longitude sector. One possibility that emerged as the cause is the very symmetric shape of the geomagnetic equator over African longitudes, compared with the American sector where it is very distorted with steep tilts in declination and offsets compared with the geographic equator. Another possibility is the size of the landmass in Africa, which has the longest section of the geomagnetic equator over land.

In addition to highlighting the longitude dependence, the meeting explored the impact of the lower atmosphere on space weather. When the Sun is active and a large solar flare or geomagnetic storm is in progress, the Sun is certainly dominant. However, a lot of the day-to-day variability in near-Earth space weather, and some of the longitude dependence, is driven by tropospheric weather and the changing synoptic weather patterns. This may be one of the reasons the African continent experiences

different space weather phenomena. It is clear that "tropospheric" weather and lower atmosphere dynamics have a definite, clear, and coherent impact on space weather in the ionosphere. This means that regular terrestrial weather, such as the strength of tropical convection, which is known to have large ocean/land differences, may be producing very different background conditions in the upper atmosphere and ionosphere. The Chapman Conference brought African and international scientists together to discuss these issues.

Waves and tides originating in the low atmosphere and propagating upward into the upper atmosphere and ionosphere were important topics of discussion and are part of this monograph. The waves from the lower atmosphere impacting space weather include gravity waves (GW), migrating and nonmigrating tidal waves, and planetary waves (PW). The tropospheric origin of GWs with periods of about 20 min up to several hours and vertical wavelengths of about 100–300 km can propagate rapidly toward higher altitudes and modulate ionospheric electrodynamics and density distributions. Secondary GWs, which may be generated in the lower thermosphere, have higher phase speeds and larger spatial scales. They are able to penetrate well into ionospheric altitudes and may initiate the growth of ionospheric irregularities, generated by the Rayleigh-Taylor instability. The ionospheric irregularities are often referred to as equatorial plasma bubbles (EPBs). Ionospheric modeling of centimeter- to kilometer-scale low-latitude ionospheric irregularities suggests that poleward neutral winds tend to stabilize the ionospheric plasma, whereas equatorward winds tend to destabilize. It was also reported at the meeting that the zonal wind is responsible for the formation of the longitudinal wavenumber-4 structures, which have been observed at all universal times. The geomagnetic declination also contributes significantly to the growth of plasma bubbles.

Another important space-weather impact is geomagnetically induced currents in electrical distribution systems and pipelines. The focus is normally on middle and high latitudes where the ionospheric currents are expected to be the strongest. Observations reported at the Chapman Conference and in this monograph show that the equatorial electrojet (EEJ) as well as storm sudden commencement (SSC) currents can give rise to rapid changes in the horizontal component of Earth's magnetic field ($dB_H/dt$), with values of hundreds of nT/min during storm periods, which is comparable to the March 1989 auroral electrojet of 500 nT/min. These large geomagnetic responses to the EEJ current can cause large induced currents (GICs) and hence damage power plants located near the magnetic equator. The other perception is that power grids are of smaller scale and less well developed at low latitudes, implying GICs would have less of an impact in the region. However, recent economic development data show that countries under the EEJ region are some of the fastest growing economies in the world and are developing large-scale power transmission systems, which can be easily exposed to power failures during large geomagnetic or space weather disturbances.

The Chapman Conference was successful in all aspects. Collaborations were established, and, more important, students were exposed to the field of space science and had opportunities to have one-on-one discussions with established international scientists. International Chapman Conferences such as this make a valuable contribution to worldwide scientific research and outreach programs.

To develop space science research infrastructure within Africa, space science educational infrastructure also needs to be developed to support the long-term operation and use of the science instrumentation. One way to address this concern is to increase and facilitate a strong interaction between scientists from developed countries and African young professors and postgraduate students. In response to these needs, several other international workshops/conferences and summer schools have already been conducted across the African continent.

With the increasing reliance on technology, the impact of space weather on engineered systems will certainly increase unless suitable protective measures are taken. Understanding the physics behind space weather and improving the forecasting is a major objective of the space-science community. It is well recognized that many space-weather impacts, especially on communications systems, arise from structures in the ionosphere. The equatorial ionosphere in particular is one of the most complex and is host to numerous instabilities and interactions, with many unresolved questions regarding its dynamics and variability. Radio waves, either transmitted through the ionosphere for satellite communication and navigation or reflected off the ionosphere for high-frequency (HF) and radar applications, are all impacted by ionospheric variability and structure. Ionospheric irregularities, or plasma bubbles, occurring at low latitudes are one such source of interference. These irregularities cause scintillations on satellite-radio transmissions resulting in information loss in communications, as well as degradation in positioning and navigation used in aviation and maritime industries.

The compilation of papers in this monograph covers various aspects of the physics of the system, and the mechanisms that control ionospheric space weather, in a combination of tutorial-like and focused articles that will be of value to the upper atmosphere scientific community in general and to the ongoing global magnetosphere-ionosphere-thermosphere (MIT) modeling effort in particular. A number of articles from each science theme describe details of the physics behind each phenomenon that help to solve the complexity of the MIT system.

Since the monograph is an outcome of the research presented at this first international space science Chapman Conference held in Africa, it has further provided an opportunity and motivation to the African scientists to communicate their research results with the international community using the volume as a vehicle. In addition, the meeting and this conference volume will greatly enhance the space-science education and research interest in the African continent and around the world.

*Ionospheric Space Weather* includes articles from six science themes that were discussed at the Chapman Conference in 2012. These include:

- Hemispherical dependence of magnetospheric energy injection and the thermosphere-ionosphere response
- Longitude and hemispheric dependence of storm-enhanced densities (SED)
- Response of the thermosphere and ionosphere to variability in solar radiation
- Longitude spatial structure in total electron content and electrodynamics
- Temporal response to lower-atmosphere disturbances
- Ionospheric irregularities and scintillation

*Ionospheric Space Weather: Longitude and Hemispheric Dependences and Lower Atmosphere Forcing* will be useful to both active researchers and advanced graduate students in the fields of physics, geophysics, and engineering, especially those who are keen to acquire a global understanding of ionospheric phenomena, including observational information from all longitude sectors across the globe.

The editors would also like to take this opportunity to thank the many people that devoted their time to carefully reviewing the manuscripts for this volume. We would also like to thank Karen O'Loughlin for checking all the manuscripts for internal consistency and for ensuring completeness of the index.

**Timothy Fuller-Rowell**
**Endawoke Yizengaw**
**Patricia H. Doherty**
**Sunanda Basu**

# Part I
# Hemispherical Dependence of Magnetospheric Energy Injection and the Thermosphere-Ionosphere Response

# 1

# Interhemispheric Asymmetries in Magnetospheric Energy Input

**Eftyhia Zesta,[1] Athanasios Boudouridis,[2] James M. Weygand,[3] Endawoke Yizengaw,[4] Mark B. Moldwin,[5] and Peter Chi[6]**

## ABSTRACT

Energy transfer from the solar wind to the magnetosphere-ionosphere-thermosphere system occurs via multiple routes with coupling efficiency depending on the Interplanetary Magnetic Field (IMF), solar wind, and the magnetosphere prior state. The energy is not always released in the two hemispheres symmetrically. Ultra low frequency (ULF) waves are the natural perturbations of the magnetosphere and the plasma in it, thus constituting an excellent diagnostic of how energy is transported throughout this complex system. We explore the question of how energy is deposited asymmetrically in the two hemispheres by studying (1) asymmetries of auroral currents and (2) asymmetries in ULF wave power at magnetically conjugate locations. We also construct a Southern Hemisphere auroral electrojet (AE) index and compare it with the standard AE index. We find that while in general the north and south electrojet indices correlate well, significant asymmetries occur frequently, primarily in the local midnight region. We also find that at low latitudes and midlatitudes the north-to-south wave-power ratio exhibits clear annual variation with a systematic offset: the Northern Hemisphere always has stronger power than the Southern Hemisphere. This systematic asymmetry is also seen in the ionospheric total electron content (TEC), implying a close link.

**Key Points:**
Interhemispheric asymmetries in ULF wave power and total electron content
A southern auroral electrojet index and comparison with the standard AE index
Interhemispheric asymmetries between northern and southern auroral electrojet indices

**Key Terms:** equatorial ionosphere, equatorial electrojet (EEJ), ground-induced currents (GIC)

[1]*Heliophysics Science Division, NASA Goddard Space Flight Center, Greenbelt, Maryland, USA*
[2]*Center for Space Plasma Physics, Space Science Institute, Boulder, Colorado, USA*
[3]*Institute of Geophysics and Planetary Physics, University of California, Los Angeles, Los Angeles, California, USA*
[4]*Institute for Scientific Research, Boston College, Chestnut Hill, Massachusetts, USA*
[5]*Atmospheric, Oceanic, and Space Science (AOSS), University of Michigan, Ann Arbor, Michigan, USA*
[6]*Department of Earth and Space Sciences, University of California, Los Angeles, Los Angeles, California, USA*

## 1.1. INTRODUCTION

It is generally assumed that most of the dynamic geospace phenomena, like magnetic storms and substorms, develop in unison in both Northern and Southern Hemispheres, typically starting in the polar regions. High-latitude geomagnetic field lines carry a load of field-aligned currents (FACs) and electromagnetic waves directly from the magnetopause, where the heavy coupling from the solar wind to the magnetosphere occurs, down to the ionosphere and thermosphere, depositing energy in the form

*Ionospheric Space Weather: Longitude and Hemispheric Dependences and Lower Atmosphere Forcing, Geophysical Monograph 220*, First Edition. Edited by Timothy Fuller-Rowell, Endawoke Yizengaw, Patricia H. Doherty, and Sunanda Basu.

of Poynting flux that heats both the ionosphere and neutral atmosphere. A part of the solar-wind energy gets processed in the magnetotail first, and is ultimately deposited in the ionosphere via both currents and electromagnetic waves, but also particle precipitation that can form bright auroras. Another part of the solar-wind energy is stored in the inner magnetosphere and couples to the mid-latitude and low-latitude ionosphere through electric fields, waves, and particle precipitation. During equinox, it is generally assumed that the load of currents and waves is approximately symmetric into the north and south polar ionospheres, but becomes quite asymmetric when either of the poles is tilted toward the Sun during the solstices [e.g., *Wu et al.*, 1991]. At those times, the uneven solar EUV illumination becomes a controlling factor for the asymmetric ionospheric conductivity in the two polar regions, leading to large asymmetries in the electrodynamic coupling with the magnetosphere and the amount of heating that is transferred to the neutrals.

While seasonal effects are strong drivers of interhemispheric asymmetries, other factors, such as the dipole tilt with respect to the rotation axis, the Interplanetary Magnetic Field (IMF) orientation, local magnetic field structures, and even atmospheric dynamics, can and do play a significant role in the strong interhemispheric asymmetries that are observed at all latitudes. For example, *Knipp et al.* [2000] showed significant difference in the amount of energy input, both from Joule heating and precipitation, in the two hemispheres during an 11-hr interval in May 1999. *Knipp et al.* argued that the large asymmetries were due to both the Northern Hemisphere sunward tilt and to the IMF orientation.

The tilt and offset of the dipolar part of the Earth's magnetic field places the polar caps at different geographic latitudes resulting in lower geomagnetic latitudes seeing 24 hr darkness in the Southern Hemisphere in the Americas longitude sector than in the Northern Hemisphere during northern summer, further exacerbating conductivity and electrodynamic asymmetries. *Cnossen and Richmond* [2012] demonstrated via modeling that the tilt angle of the geomagnetic dipole is a strong controlling factor in the distribution of Joule heating in the high latitudes and in the neutral temperature and winds. *Förster and Cnossen* [2013] took this work further to demonstrate, again via modeling, the effect the nondipolar components of the Earth's magnetic field have in interhemispheric asymmetries. They found that while the effect in the large-scale plasma convection was rather small, the effect on the neutral winds was substantial.

It is a common assumption, particularly in simulations, that auroral activity, brightenings, and dynamics in the Northern and Southern hemispheres are a mirror image of each other, based on the assumption that the magnetospheric processes are similarly mapped down to the two polar regions, and the source particles are evenly distributed along the same field lines to the two ionospheres. While seasonal differences have been statistically reported [e.g., *Newell et al.*, 1996; *Liou et al.*, 2001], the global patterns of precipitation are typically assumed symmetric in the two hemispheres.

The substorm phenomenon is perhaps the most common and dramatic nightside auroral intensification. All of today's models of substorms are based mostly on Northern Hemisphere observations and assume conjugacy between hemispheres. Studies of the conjugacy (or not) of substorm onset and its dynamics have primarily relied on ground or aircraft imagers and magnetometers located at conjugate points [e.g., *Belon et al.*, 1969; *Stenbaek-Nielsen et al.*, 1972, 1973; *Hajkowicz*, 2006; *Motoba et al.*, 2014]. Studies based on older instrumentation and limited cases found good conjugacy between of the auroras for both quiet and active conditions [e.g., *Belon et al.*, 1969; *Stenbaek-Nielsen et al.*, 1972], but new studies with more sophisticated instrumentation and longer statistical studies have begun to demonstrate interhemispheric asymmetries in larger and smaller scale size structures [e.g., *Hajkowicz*, 2006; *Laundal and Østgaard*, 2009; *Motoba et al.*, 2014; *Weygand et al.*, 2014a]. Fewer studies were able to use satellite auroral imagery on few fortuitous conjunctions [*Ostgaard et al.*, 2004, 2007; *Frank and Sigwarth*, 2003; *Sato et al.*, 2012]. Many of these studies have reported significant asymmetries, both in the location and timing of the substorm onset [e.g., *Morioka et al.*, 2011; *Sato et al.*, 1998; *Weygand et al.*, 2014b]. *Kivelson et al.* [1996] and *Ostgaard et al.* [2004, 2007] found that the north-south displacement of the onset systematically depends on the IMF $B_y$ sign and magnitude.

*Frank and Sigwarth* [2003] presented the first simultaneous satellite observations of a substorm onset (observed by Polar VIS camera at both hemispheres simultaneously). They found a 1–2 min delay in the occurrence of the onset between the two hemispheres and that traditional mapping would place the source of the onset from the two hemispheres on significantly different locations on the tail. Clearly, our understanding of how tail dynamics couple down to the ionosphere is incomplete.

While there are many works looking at the asymmetries of substorm auroral dynamics, there are limited studies that demonstrate asymmetric auroral features and energy input for less active periods. *Shi et al.* [2012] showed that the cusp location moved asymmetrically between the two hemispheres while the dipole tilt angle increased, resulting at the cusp forming at different latitudes at the two hemispheres. *Fillingim et al.* [2005] used coincidental observations from IMAGE FUV and Polar UVI and observed significant asymmetries in the structure of the afternoon aurora, which they attributed to IMF $B_y$ effects. *Stubbs et al.* [2005] looked at the relative location

of the complete auroral oval from simultaneous IMAGE and Polar observations from both hemispheres and found that not only IMF $B_y$, but also $B_x$, affect the displacement of the oval in the two hemispheres. *Motoba et al.* [2012] recently analyzed detailed observations of auroral beads from conjugate all-sky auroral imagers that occurred ~15 min before a substorm onset. They found that the beads developed simultaneously and with great similarity in the two hemispheres.

There is evidence that the auroral electrojets exhibit seasonal asymmetries [*Wu et al.*, 1991], although most studies depend on spatially limited magnetometer chains, or individual conjugate pairs of magnetometers. *Wu et al.* [1991] reported that the substorm westward electrojet flows at higher latitudes in the winter hemisphere than in the summer hemisphere by as much as 4°. The interhemispheric asymmetries of the auroral electrojets are likely a direct result of the interhemispheric asymmetries in field-aligned currents (FACs). Theoretical studies have predicted that conductivity differences between the winter and summer hemispheres will create a set of interhemispheric FACs (IHCs) [*Benkevich et al.*, 2000]. The IHCs flow from one hemisphere to the other along highly conductive magnetic field lines connecting the two conjugate auroral zones and have the effect of redistributing the ionospheric currents in the two hemispheres with significantly different conductivities. Although IHCs have been modeled from first principles [*Benkevich et al.*, 2000; *Lyatskaya et al.*, 2014a; 2014b], they have yet to be observed, primarily due to lack of the necessary observations, that is, coincidental observations of FACs from both hemispheres on the same local time sector. Our lack of conjugate observations on the global scale has clearly limited our understanding of dynamic phenomena like substorms.

This is where more recent data assembly techniques like AMPERE [*Anderson et al.*, 2002] and SuperMAG [*Gjerloev*, 2012] can help break through the prior observational limitation. The Active Magnetosphere and Planetary Electrodynamics Response Experiment (AMPERE) Science Data Center is a facility that uses magnetometer data from the 66 IRIDIUM satellites and sophisticated algorithms to provide the global FAC patterns every 10 min [*Anderson et al.*, 2002]. SuperMAG [*Gjerloev*, 2012] is a worldwide collaboration of ground magnetometer chains that operate more than 300 magnetometers and provides easy access to validated ground magnetic field perturbations in the same coordinate system and identical time resolution with a common baseline removal approach. Products like the global equivalent ionospheric currents are also provided. It is now possible to support large-scale interhemispheric studies.

Here we focus on two specific topics. First, in Section 1.2, we discuss interhemispheric asymmetries of the auroral electrojets as a means of understanding how dynamic phenomena develop differently in the two hemispheres. Then, in Section 1.3, we discuss interhemispheric asymmetries of the power of ultra low frequency (ULF) waves at low latitudes and midlatitudes and see what the role of the ionosphere is in such asymmetries. We end with a brief summary.

## 1.2. ASYMMETRIES IN HIGH-LATITUDE DYNAMICS AND THE AURORAL CURRENTS

The auroral elecrojet (AE) index (*Davis and Sugiura*, 1966) is traditionally calculated from a set of 10–13 ground magnetometer stations located around the typical northern auroral oval location (between 60° and 70° geomagnetic latitude). There is no Southern Hemisphere AE index because there is not sufficient station coverage from the southern auroral oval. The AE index is used as the most common indicator of global geomagnetic activity and it is well correlated with the strength of the auroral electrojets and also with auroral activity. It is typically used for identifying the occurrence, onset, and strength of a substorm. Considering the evidence for significant differences in both the location and timing of the auroral substorm onset and dynamics, it follows that the AE index should exhibit similar asymmetries.

Efforts to calculate a southern AE index are few, given the limited landmass availability at the appropriate latitudes in the Southern Hemisphere. *Maclennan et al.* [1991] used 22 available ground magnetometer stations from Antarctica to calculate a southern AE (SAE) index for 7 days in June 1982 and compare it with the northern World Data Center (WDC) AE. They found that the WDC AE was consistently stronger than the SAE index, which was likely due to seasonal effects. The *Maclennan et al.* [1991] study, however, included stations within a wide latitude range, from 50° to 90° magnetic, thus almost certainly including stations that at any moment were not within the auroral oval. Similarly, *Saroso et al.* [1992] compared the WDC AE with a southern polar cap index SAE, derived from four evenly spaced Antarctic magnetometer stations. The comparison results from this study are inconclusive, mostly because the southern stations were at higher magnetic latitude than the AE stations.

### 1.2.1. AE Interhemispheric Asymmetries

Recently, *Weygand and Zesta* [2008] conducted a study similar to that of *Maclennan et al.* [1991] and created an SAE index for comparison with the World Data Center (WDC) AE index for 7 days in December 2005. *Weygand and Zesta* [2008] used all seven available Southern Hemisphere stations at magnetic latitudes between −60° and −71°, so that both northern and southern stations

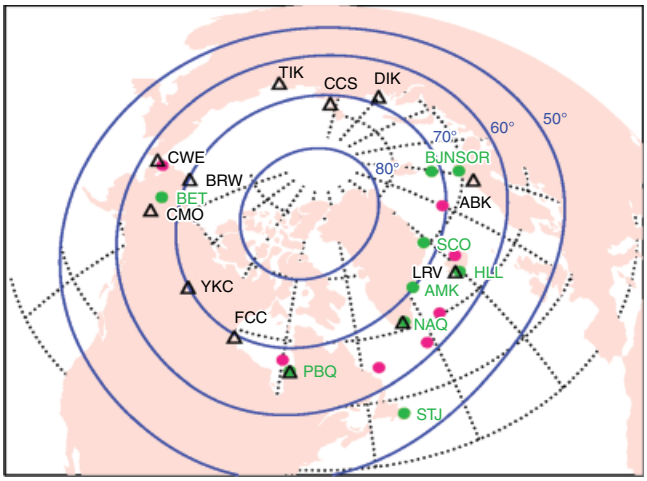


**Figure 1.1** Map of northern and southern stations used for NAE and SAE calculations in *Weygand and Zesta* [2008]. In magenta are the north conjugate locations of the 7 southern stations for SAE, in green are the 9 northern stations for NAE, and the black triangles are the 12 standard AE stations.

were within the same topological region of the magnetosphere at the same time.

Figure 1.1 is a reproduction of Figure 2 from *Weygand and Zesta* [2008] and displays the location and distribution of all the Northern and Southern (projected to the north) hemisphere stations used for their study. The black triangles depict the standard AE stations, magenta solid circles are the north conjugate locations for the seven southern stations, as projected by the International Geomagnetic Reference Field (IGRF) model, and the green solid circles are northern stations selected for being as near conjugate as possible to the seven southern stations and are used to produce a northern AE (NAE) index conjugate to SAE. Black dotted lines are lines of geographic latitude and longitude and the solid blue lines are lines of constant geomagnetic latitude, calculated from Altitude Adjusted Corrected Geomagnetic Coordinate model [*Baker and Wing*, 1989]. The southern stations MAW, SYO, SNA, NVL, HBA, and WSD provide closely spaced coverage of a good portion of the auroral zone while MCQ station is farther away leaving a gap between WSD and MCQ and an even bigger gap from MCQ to MAW. The lack of similar coverage from the seven southern stations and the WDC AE stations is why *Weygand and Zesta* [2008] also created the conjugate NAE index from nine northern stations. There are more northern magnetometer stations than southern stations because exact conjugate stations are not always available. So, where necessary, data from the northern magnetometers that "surround" the conjugate southern station location are averaged together. For example, the conjugate signature for HBA (magenta circle immediately to the right of PBQ) is produced by averaging the data from NAQ, STJ, and PBQ. All the details of the different stations used and their coordinates are given in the original paper.

Figure 1.2 is reproduced from Figures 4 and 9 of *Weygand and Zesta* [2008] and shows the calculated indices for 10 December 2005 (an active day) on the top, and for 8 December 2005 (a quiet day) on the bottom. For each day, the AU, AL, and AE indices for the southern (SAE/AU/AL), conjugate Northern Hemisphere data (NAE/AU/AL), and the WDC indices are shown. The Northern Hemisphere indices are given in the top panels as solid black lines, and the Southern Hemisphere indices are shown in the bottom panels, also in solid black lines. The gray lines in the top panels are the WDC quick look indices that can stand in place of the standard AE, AU, and AL indices. In Figure 1.2a, only the first 12 hr of the day are available for 10 December 2005. There is good agreement between the northern indices and the WDC indices for the substorm just after 0600 UT visible in both NAE and AE. The correlation coefficient between AE and NAE is 0.86, which implies that activity is happening in local times where there is good coverage from southern stations (since the conjugate locations to the southern index are reproducing well the standard AE index) and the large gaps in coverage are not affecting this particular day. However, there is less agreement between the NAE and SAE indices, with a correlation coefficient of 0.69, which implies some real asymmetries between the Northern and Southern Hemispheres. The NAE and AE have clearly greater magnitude perturbations than the southern index, even though the event occurs during northern winter (low conductivity) and southern summer (high conductivity), when we expect stronger ionospheric currents in the Southern Hemisphere. The evidence therefore indicates the existence of significant asymmetries between the Northern and Southern hemisphere auroral electrojets, seemingly unrelated to seasonal variations and strong enough to overcome the expected seasonal asymmetries.

Figure 1.2b shows the northern and southern indices in the same format as in the previous event for a quiet day, 8 December 2005, and therefore the magnitude of the indices is significantly smaller. The black bar in each panel indicates the period of time when there is no station coverage in the local midnight sector for either SAE or NAE. For this event, there are significant differences between NAE and AE, particularly between 18 and 24 UT. In fact, the SAE index correlates much better with AE at that period of time, picking up the substorm activity at ~20 UT that is totally missed by NAE. Even for this very quiet day, there is strong evidence for interhemispheric asymmetries, likely due to IMF $B_y$.

It is likely that the interhemispheric currents, which have been theoretically postulated [*Benkevich et al.*, 2000; *Lyatskaya et al.*, 2014a, 2014b], contribute greatly to the

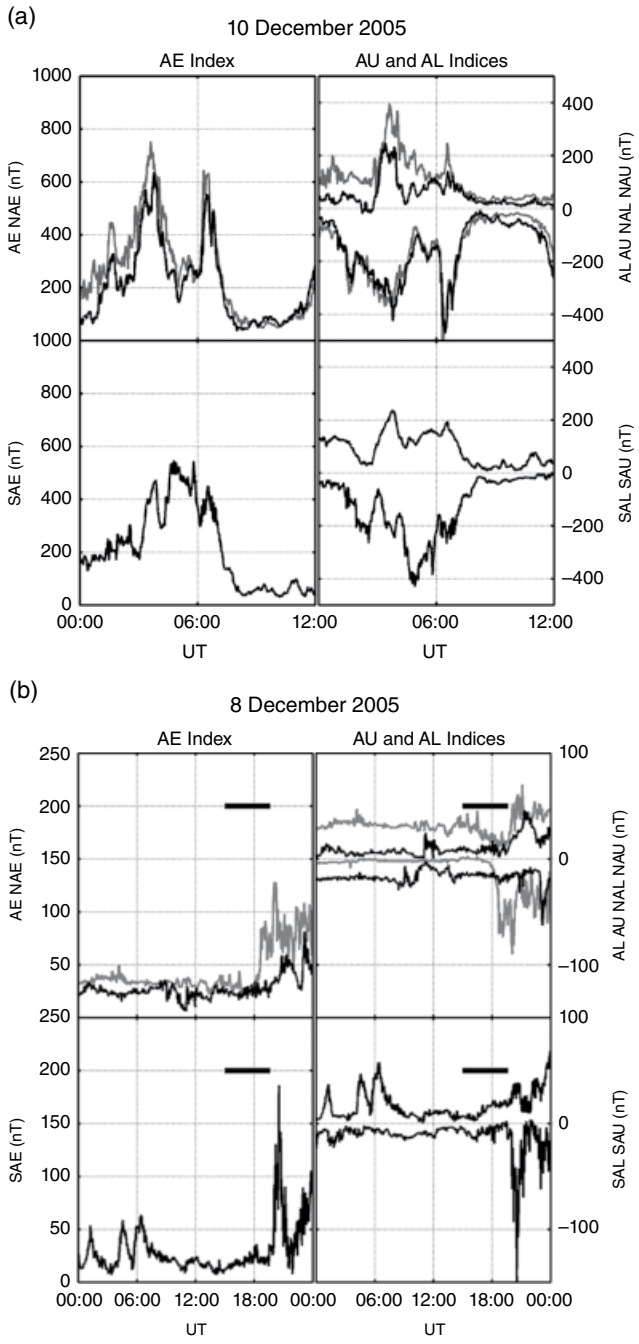


**Figure 1.2** AE, NAE, and SAE calculations for (a) the active day on 10 December 2005, and (b) the quiet day on 8 December 2005. The black lines in top and bottom panels are the NAE/NAU/NAL and SAE/SAU/SAL indices, respectively, while the gray lines on the top panels are the standard AE/AU/AL indices.

observed asymmetries. *Weygand and Zesta* [2008] showed that the maximum north-south magnitude differences in the ground magnetic perturbations are seen in the local midnight region and are likely due to interhemispheric asymmetries of the nightside westward electroject. By extension, they suggested that when the local midnight region is well covered by stations in Antarctica, then the NAE can reasonably represent the WDC AE and then differences between NAE and SAE reasonably represent interhemispheric asymmetries in the auroral electrojets. This now opens the way for significant advancement in interhemispheric studies and in the effects of such asymmetries in global simulations.

*Weygand et al.* [2014a] expanded on the work of *Weygand and Zesta* [2008] by conducting a large statistical study on the correlation between the SAE, NAE, and AE indices. *Weygand et al.* [2014a] used the most complete, to date, database of Southern Hemisphere auroral magnetometers from 2005 to 2010 and were able to calculate the NAE and SAE indices simultaneously for a total of 274 days. (The individual NAE and SAE indices were available for a significantly greater number of days in each case.). The station distribution used in *Weygand et al.* [2014a] is very similar to that of Figure 1.1 with some small changes.

Figures 1.3a and b are reproduced from Figures 10 and 12 of *Weygand et al.* [2014a] and demonstrate some fundamental statistical properties for the northern and southern indices, based on the 274 days of available observations. Figure 1.3a shows histograms of the daily correlation between the SAE and NAE indices (top panel) and their mean daily differences (bottom panel). The correlation distribution peaks at 0.8, but the mean of the distribution is 0.65 with a maximum of 0.98 and a minimum of −0.2. This implies that, statistically, Northern and Southern Hemispheres electrojets are well correlated in terms of the timing of their dynamic changes. However, since the distribution is widely spread, there are often times of significant interhemispheric asymmetries. *Weygand et al.* [2014a] showed that the highest correlations occur during spring and to a lesser degree at fall, while the lowest correlations occur during northern winter and summer, when the two hemispheres are very asymmetrically illuminated, so there is an observed seasonal effect. The low correlation values in the top panel of Figure 1.3a correspond to quiet geomagnetic activity, as was also shown by *Weygand and Zesta* [2008], because the linear correlation of a nearly flat line (no activity) with another flat line is nearly zero by definition. This is demonstrated more clearly in Figure 1.3b where the mean daily correlation coefficients between SAE-NAE and SAE-AE are plotted with respect to the daily mean of the SAE index on the top and bottom panels, respectively. The black dots are the individual daily means and the gray squares are means of SAE index bins for a bin size of 50 nT. The gray bars are the standard deviation of the means for each bin. The gray line is drawn as visual aid for the data trends. Low correlation coefficients are only associated with very low geomagnetic activity, while higher correlations exist for both quiet and active days. Highly active days have only higher correlation coefficients, >0.5.

The persistent magnitude difference between SAE and NAE indices demonstrated in Figure 1.3a, bottom panel,

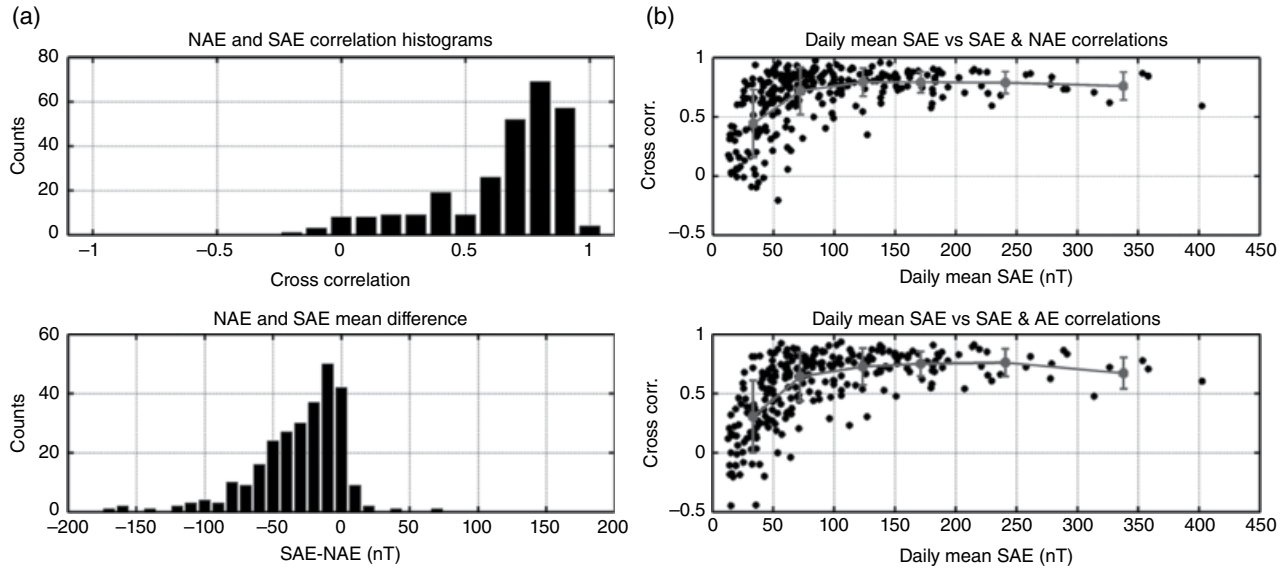


**Figure 1.3** (a) Histograms of the SAE-NAE daily correlations (top) and of the SAE-NAE mean daily differences (bottom); (b) daily mean SAE-NAE correlation (top) and SAE-AE correlations (bottom) with respect to the daily mean SAE [from *Weygand et al.*, 2014a].

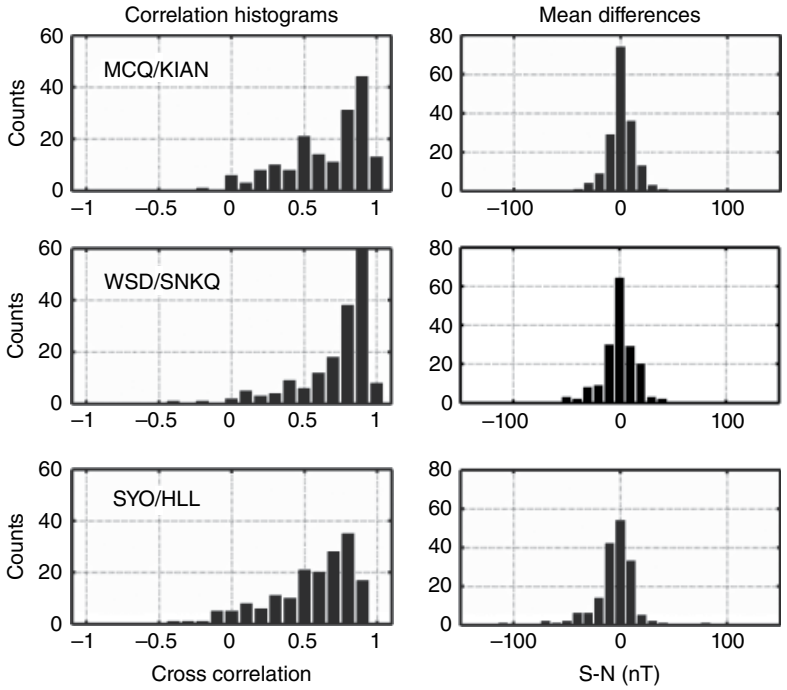


**Figure 1.4** (Left) Histograms of the correlations between closely conjugate south-north pairs of stations MCQ-KIAN, WSD-SNKQ, and SYO-HLL, and (right) histograms of the difference between the *H* component for each pair of stations.

with SAE on average smaller than NAE was reported also by *Maclennan et al.* [1991] and seems to indicate that the northern auroral electrojets are consistently stronger than the southern auroral electrojets. Since this is not a physically intuitive result, *Weygand et al*. [2014a] explored this matter further by isolating north-south pairs of stations included in the SAE and NAE calculations with good and poor conjugacy.

Figure 1.4 is a reproduction of Figure 14 from *Weygand et al.* [2014a] and shows, on the left column, histograms of the daily correlation of the *H* magnetic field component for station pairs MCQ-KIAN, WSD-SNKQ, and SYO-HLL,

where the first part of each pair is a southern station and the second is the northern station. On the right column of Figure 1.4, the daily mean differences are shown for the same three pairs of stations. The correlation plots for all three pairs are very similar to the SAE-NAE correlation histogram shown in Figure 1.3a (top panel), with the correlations peaking at 0.9. However, the daily mean histograms for the three pairs in Figure 1.4 are significantly different from the SAE-NAE daily mean in Figure 1.3a, bottom panel. The mean daily difference for the three conjugate pairs is centered at 0 nT. Even though there is a spread to the distribution and there are clearly times with large interhemispheric asymmetries, the histograms of Figure 1.4, right column, seems to indicate that there is no systematic asymmetry between the north and south electrojets. The distributions of Figure 1.4 were produced with daily averaged values of north-south amplitude differences and for all different conditions. In Figure 1.5, we plot histogram distributions of the amplitude differences for the same three pairs of closely conjugate stations, but for 1 min averaged differences observed only in the local midnight region, ±3 hr around 00 MLT. The differences between north and south responses to the electrojet for low Kp are similar to those in Figure 1.4, namely centered around 0 and denoting no obvious systematic asymmetry between Northern and Southern Hemispheres. The histograms for high Kp values, however, show that for two of the three pairs, MCQ/KIAN and SYO/HLL, the peak is negative, indicating persistent stronger amplitudes at the northern stations. The third pair, WSD/SNKQ, has stations located in significantly different geographic latitudes.

The electrojet indices (AE, SAE, or NAE) are sensitive to the global DP2 current system, namely the global-scale two-cell convection pattern [*Nishida*, 1968], but are also most strongly sensitive to the nightside westward electrojet that is typically the result of substorm or other strong activity, known as the DP1 current system [*Nishida*, 1968]. One then would expect most of the interhemispheric asymmetries in the north and south indices to also be strongly sensitive to the nightside westward electrojet.

Figure 1.6 is a reproduction of Figure 17 from *Weygand et al.* [2014a] and demonstrates exactly this point. Figure 1.6 shows a superposed epoch analysis of the SAE-NAE differences on the top panel, and the difference in the *H* component between the south and north stations of the closely conjugate pairs that were discussed in Figure 1.4 and from all available data in the bottom three panels. For each pair of stations, the black line is the median and the two gray curves are the upper and lower quartiles of the distribution. The open circle in each panel indicates local midnight and the solid circle indicates local noon for that pair of stations. While the median curve varies minimally, it is clear from the quartile curves that the largest differences between the north and south stations of the pair occur around local midnight and are therefore associated with the nightside westward electrojet. We therefore propose that for times when there is good coverage of the local midnight region from the

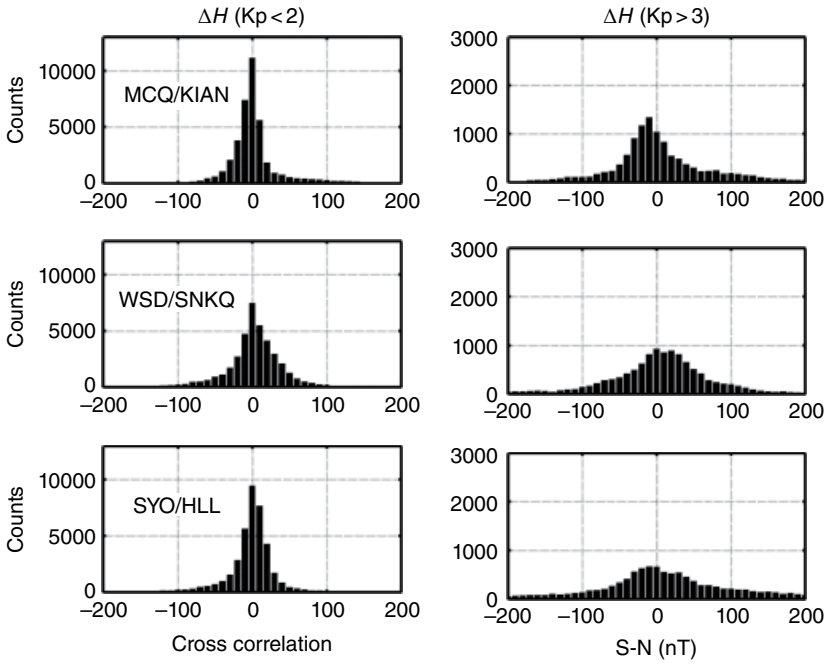


**Figure 1.5** Histograms of the *H* component differences for the same three pairs of closely conjugate stations as in Figure 1.4. On the left are the histograms for low geomagnetic activity (Kp < 2) and on the right are the histograms for high geomagnetic activity (Kp > 3).

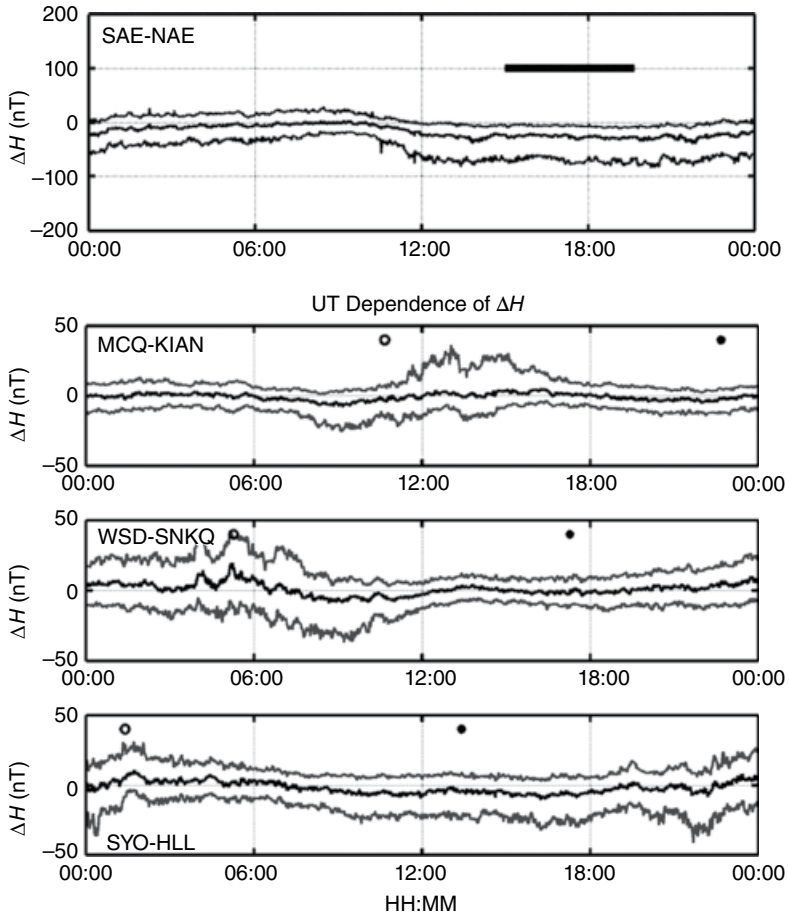


**Figure 1.6** (Top panel) Superposed epoch UT dependence of the SAE-NAE differences, solid line. The lighter shade lines are the upper and lower quartiles of the distribution. (Panels 2–4) Superposed epoch of the difference in the *H* component for the same three closely conjugate pairs of ground magnetometer stations of Figure 1.4. The station pairs are given on the left side of the panel; the open circles indicate local midnight for each station, and the filled circles indicate local noon. Upper and lower distribution quartiles are shown in lighter shade lines around the main distribution.

Southern Hemisphere, the SAE can be used as the equivalent Southern Hemisphere Auroral Electrojet index.

Most important, Figure 1.6, in combination with the histograms of Figure 1.5, gives an insight into possible reasons for the systematic asymmetry between SAE and NAE from Figure 1.3a. The negative SAE-NAE distribution peak is manifested in the 12–24 UT period, which engulfs the time period when no southern stations are in near local midnight (indicated by the horizontal bar), where most of the amplitude and differences in SAE and NAE originate. The longitudinal distribution of stations is clearly a contributor to the observed systematic asymmetry between SAE and NAE. The UT differences of the *H* component for the three pairs in Figure 1.6 demonstrate another important point. While the daily averaged differences may be centered at 0 (Fig. 1.4), the distributions can be systematically positive or negative during the day. This and the systematic differences for higher geomagnetic activity in Figure 1.5 indicate that the SAE/NAE systematic asymmetry is not due just to the longitudinal gaps in the Southern Hemisphere, but also to other factors like the geographic differences between station pairs, interhemispheric currents, or activity levels.

While the precise causes of the observed north-south asymmetry in SAE and NAE remain unclear, the spread of the histogram distributions in Figures 1.4 and 1.5 demonstrate the significant interhemispheric asymmetries that habitually occur.

### 1.2.2. The Effect of Solar Wind and IMF on the Interhemispheric Asymmetries

We now look at the role the solar wind and IMF may play in the observed interhemispheric asymmetries as evidenced by the calculated SAE and NAE indices.

Specifically, we examine how different solar-wind parameters affect the correlation between the SAE and NAE indices.

For the solar-wind study, we recalculated cross correlation coefficients between the three AE indices (standard AE, NAE, and SAE) at a much faster cadence than was used in the *Weygand et al.* [2014a] work. We used our complete database, which amounts to 274 days, from December 2005 to August 2010, when all three indices are available. The cross correlation coefficients are estimated every 10 min with a correlation window of 2 hr around each point in time. The solar-wind and IMF quantities are taken from ACE data and are propagated to 17 $R_E$ using the Weimer technique [*Weimer et al.*, 2003; *Weimer*, 2004]. In order to include propagation to the ionosphere and effects of preconditioning of the magnetosphere by previous solar wind and IMF values, we introduce two additional time constants: delay time, $T_d$, for the propagation to the ionosphere from 17 $R_E$, and preconditioning time, $T_p$, for averaging the solar wind and IMF data before each point. For $T_d$ we use 10 min as an average propagation window from 17 $R_E$ upstream to the ionosphere. For $T_p$ we use 20 min and that is the time period beyond the 10 min ($T_d$) for which we average the SW parameters to get a sense of preconditioning. Therefore, each index correlation is assigned solar wind and IMF values by shifting the propagated ACE data by $T_d$ minutes, and then averaging the solar-wind data for $T_p$ minutes before that. With all the correlation coefficients calculated, a statistical study of the effects of solar wind and IMF conditions on the electrojet index correlations can be performed. While a more complete and focused manuscript is in preparation, we show here some key results of this new work. Specifically, we examine the effect of IMF $B_y$, IMF $B_z$, and solar-wind dynamic pressure, $P_{sw}$ on the north-south index correlations.

Figure 1.7 shows the magnitude of the AE/SAE and NAE/SAE correlations as a function of IMF $B_z$ and $P_{sw}$. The IMF and dynamic pressure data accompanying the correlation coefficients are binned at 1 nT and 0.25 nPa bins. In each bin, we plot the percentage of high-correlation coefficients ($R > 0.7$) that occur during the bin conditions. The "percentage of correlations" quantity was chosen over the average bin correlation coefficient because it shows the IMF and dynamic pressure dependence more clearly. It is clear that both the AE/SAE (left) and NAE/SAE (right) plots suggest strong dependence of the north/south correlations on IMF $B_z$ and $P_{sw}$. The percentage of high coefficients is higher for southward IMF, and for steady IMF it increases with dynamic pressure. In other words, the more southward the IMF and the higher the dynamic pressure, the better correlated the north-south electrojets are, while more northward IMF and low dynamic pressure are more statistically likely to produce asymmetrical north and south electrojets. We should caution here that high correlations between north and south indices do not exclude high differences in amplitude between north and south, and future work will address all these issues. Both IMF $B_z$ and high dynamic pressure can be strong drivers of geomagnetic activity, relocating magnetospheric population boundaries, enhancing large-scale field-aligned currents, enhancing convection in the magnetosphere and ionosphere, as well as ionospheric currents. Under strongly driven conditions, both SAE and NAE (or AE) would be characterized by distinct enhancements well correlated in time,

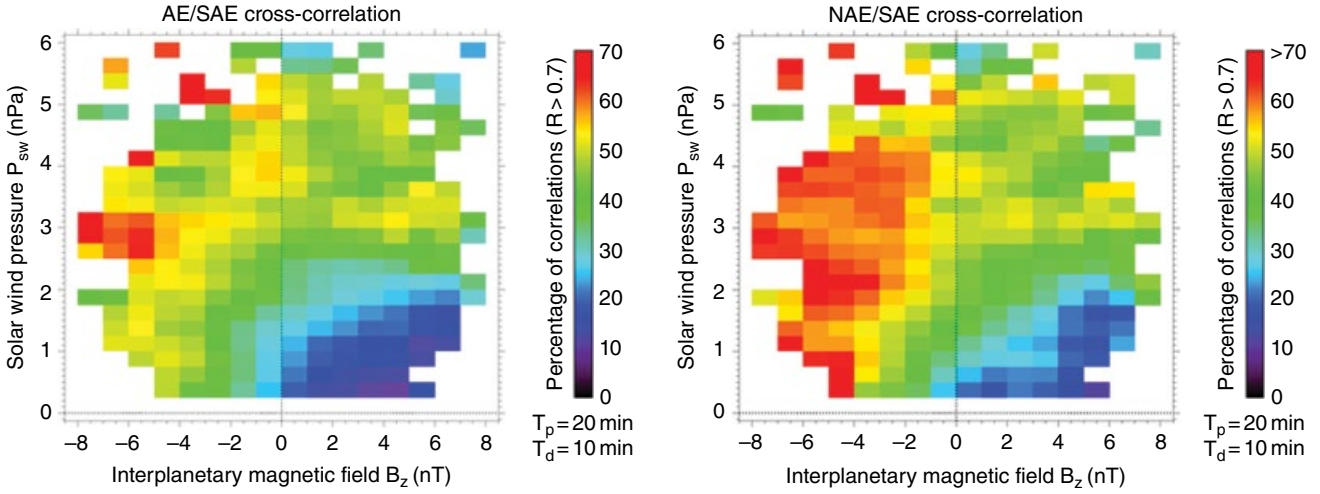


**Figure 1.7** (Left) AE/SAE and (right) NAE/SAE correlation results as a function of ACE IMF $B_z$ and solar wind dynamic pressure.

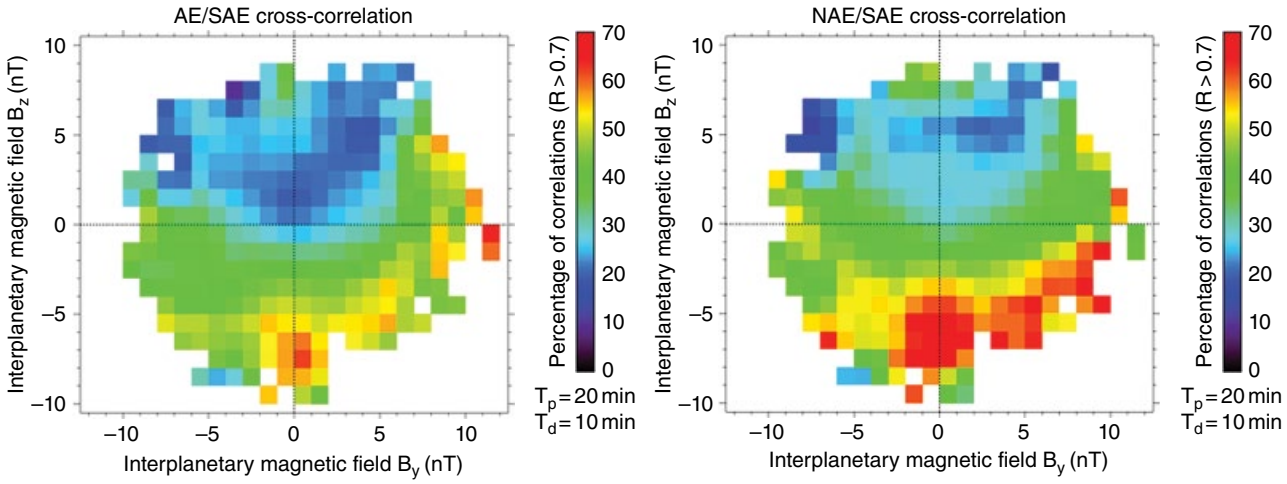


**Figure 1.8** (Left) AE/SAE and (right) NAE/SAE correlation results as a function of ACE IMF $B_y$ and $B_z$.

leading to high correlation coefficients even though their amplitude differences may not be necessarily small.

Figure 1.8 shows the dependence of the percentage of high correlations on the concurrent IMF $B_y$ and $B_z$ components. The IMF $B_z$ dependence is again clear. In addition, high correlation coefficients appear for high absolute values of IMF $B_y$, even when the IMF is northward. Furthermore, high correlations seem to be present when the IMF is purely northward but with high magnitude; however, it is unclear if this is a real dependence or result of low statistics at these high northward IMF values. An asymmetry for positive and negative IMF $B_y$ is also evident, mostly for southward IMF. We see stronger correlations for positive IMF $B_y$ than for negative IMF $B_y$.

## 1.3. ULF WAVE POWER ASYMMETRIES

Ultra low frequency waves are the lowest frequency magnetohydrodynamic (MHD) waves generated in the magnetosphere in response to solar-wind drivers and internal dynamic processes. They are an excellent diagnostic tool that can determine and track the energy flow from the solar wind and through the different magnetospheric regions. They also provide a good way of understanding how magnetospheric processes couple down to the ionosphere and thermosphere. For example, *Yizengaw et al.* [2013] demonstrated that during a solar-wind high speed stream (HSS) event, upstream oscillations directly drove ULF waves globally within the magnetosphere, which also penetrated to the ionosphere at all latitudes and down to the equator where they drove similar oscillation in the equatorial electrojet and the measured ionospheric total electron content (TEC).

### 1.3.1. Prior Studies

Conjugate studies of ULF waves can additionally provide information on how the flow of energy from the solar wind is distributed to the two hemispheres, but unfortunately such prior studies are few and far between.

Most of the conjugate studies on ULF pulsations have been done at high latitudes and the cusp. *Ables et al.* [2000] and *Liu et al.* [2003] studied resonant Pc5 waves with high conjugacy to determine IMF dependencies, *Matthews et al.* [1996] used both ground magnetometers and radar observations to study the conjugate wave response to a solar-wind shock impact, and *Posch et al.* [1999] looked at conjugate asymmetries of broadband (0–50 mHz) waves.

Conjugate wave studies from lower latitudes are just as uncommon as high-latitude studies. A series of publications looked at various aspects of conjugacy in Pc4-5 waves near L = 4, using magnetometer data from Siple station in Antarctica and a set of three near conjugate stations from the north. *Lanzerotti et al.* [1973] and *Surkan and Lanzerotti* [1974] looked at the conjugate wave power at quiet and disturbed conditions, respectively, during the 1971 December solstice. They found that during quiet days the ratio of south to north wave power was ~1, but for disturbed days the wave power was much stronger in the southern station, which is opposite to what we are reporting here, but they examined higher latitudes. *Feng et al.* [1995] studied conjugate Pc3-4 pulsations at low latitude, L = 1.2, and while they did not report on the relative wave power between the north and south stations, they found evidence that the observed waves were due to resonances and their daily occurrence pattern is controlled by their source and propagation characteristics.

*Obana et al.* [2005] studied the north-south asymmetry of Pc3-5 waves at higher latitudes with a pair of conjugate stations at L = 5.4. While the latitude of the conjugate observations is much higher than the low-latitude and midlatitude station pairs we are including in our study, the *Obana et al.* [2005] work is the only other work that directly looks at the wave-power ratio between the two hemispheres. They found a seasonal variation in the north vs. south power ratio and also found that the power in the northern station is always higher than at the southern stations throughout the year, as we report here. They named that the "positive effect." They considered ionospheric conductivity effects as the source for the observed seasonal asymmetries and differences in the magnitude of the background magnetic field to explain the positive effect. We provide more detailed comparisons in the section below.

### 1.3.2. Low Latitude and Midlatitude ULF Wave-Power Asymmetries

We performed a conjugate study of ULF wave power along the Americas meridian and we present here some key representative results. We utilized stations from three magnetometer chains: the South American Meridional B-field Array (SAMBA) [*Boudouridis and Zesta*, 2007], a chain of 12 magnetometers along Chile and in Antarctica, covering mostly low latitudes and midlatitudes, the Magnetometers along the Eastern Atlantic Seaboard for Undergraduate Research and Education (MEASURE) [*Berube et al.*, 2003], which has several stations along the East Coast of the United States, some of them being directly conjugate with SAMBA stations, and the Midcontinent Magnetoseismic Chain (McMAC) [*Chi et al.*, 2013], which extends the CARISMA (Canadian Array for Realtime Investigations of Magnetic Activity) Churchill line of magnetometers southward to Mexico at low latitudes. The McMAC meridian is approximately 2 hr of MLT separated by the average meridian of the MEASURE and SAMBA chains.

Figure 1.9 is a map of the magnetometer locations set in the Southern Hemisphere with the three Northern Hemisphere stations that we used projected to their magnetic conjugate points, using the appropriate epoch IGRF model. The dotted lines are lines of geographic latitude 10° apart, and geographic longitude 20° apart. The blue lines are lines of constant geomagnetic latitude from −10° to −60°. The southern SAMBA stations of PAC, OHI, and PAL are denoted as blue solid circles, while the northern stations of FIT and APL from MEASURE, and AMER from McMAC are red solid circles. FIT and PAC are approximately at L = 1.7, while the remaining stations are approximately at L = 2.3.

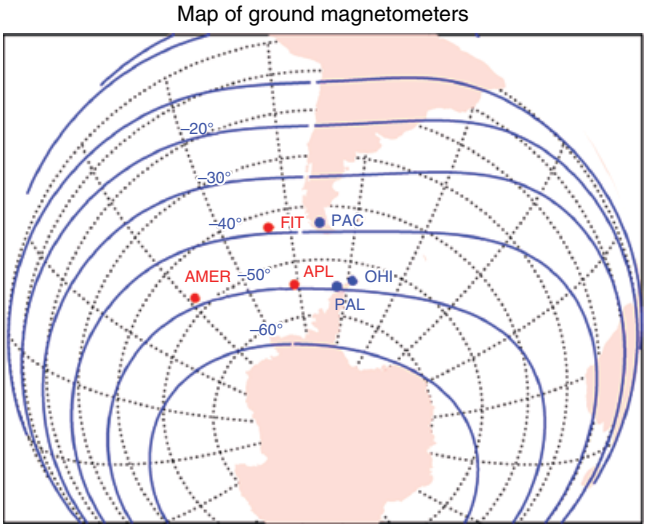


**Figure 1.9** Map showing the southern and northern conjugate stations that were used for studying the north-south asymmetries of ULF wave power. In blue are the southern SAMBA stations, while in red are the conjugate projections of the northern MEASURE and McMAC stations.

For our comparisons of interhemispheric wave power and its seasonal and annual variations, we calculate the total daily power separately in the Pc3 (20–100 mHz) and Pc4-5 (2–20 mHz) bands for each station. The daily power calculation includes only the dayside, approximately 0630–1730 MLT, for each station. Pc3–Pc5 waves typically have different sources on the dayside and nightside and are regularly present and stronger on the dayside, resulting primarily from upstream sources and solar wind magnetosphere interactions [e.g., *Yumoto*, 1985; *Troitskaya and Bolshakova*, 1988]. Our station pairs are conjugate in latitude but can be separated in MLT by as little as a half hour, in the case of the FIT-PAC pair, or as much as 3 hr, in the case of the AMER-OHI pair. Since this is a statistical study with only daily values of dayside wave power, any instantaneous MLT differences between our conjugate pairs of stations do not influence our conclusions. We calculate the daily total power from the dynamic spectrum analysis from summed 1 min bins. We calculate the total power in all frequency bins every 1 min with a 10-min Fourier window centered on the minute of calculation. We continue moving our 10-min window to the subsequent slot until the full dayside period is covered and the total daily power is the sum of the power values of all the individual 1-min bins. We do this at each station and for the two frequency regimes, Pc3 and Pc4-5.

Figure 1.10 shows the results for the PAC-FIT pair of stations at L = 1.7 and for year 2005. The top panel shows the daily power for the north station FIT in red and for the south station PAC in blue. The bottom panel shows the ratio of the north to south station power (FIT-PAC).

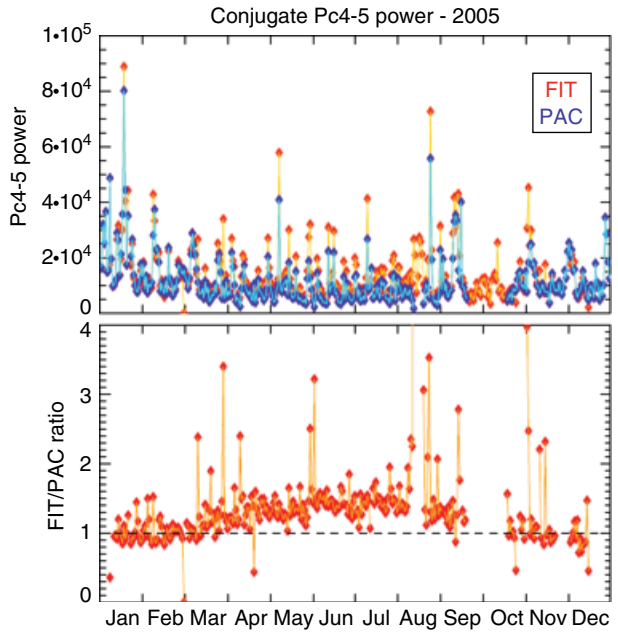


**Figure 1.10** Conjugate Pc4-5 power at L = 1.7 for the FIT-PAC pair and for year 2005. The wave power for the north station FIT (red) and south station PAC (blue) is shown in the top panel, while the north-to-south power ratio is shown in the bottom panel.

A clear seasonal/annual variation is seen in the FIT-PAC ratio, with the ratio maximizing at June solstice (more illumination of the Northern Hemisphere) and minimizing at December solstice (less illumination of the Northern Hemisphere), which is intuitively expected by the ionospheric illumination patterns of the north and south hemispheres during the solstices. Most interesting, the December minimum of the FIT-PAC ratio is ~1, indicating similar wave power in the two hemispheres during December solstice, while the ratio maximum is ~1.5, indicating much stronger wave power in the north during June solstice. In short, there seems to be a Northern Hemisphere bias, in addition to the annual seasonal variation of wave power, with the northern station having consistently higher power than the southern station throughout the year.

This pattern observed in Figure 1.10 is consistent for both Pc3 and Pc4-5 bands and at both low-latitude (L = 1.7) and midlatitude (L = 2.3) conjugate stations. Figure 1.11 shows the daily Pc4-5 wave-power values for FIT on top and PAC on the bottom for year 2005 with polynomial fitted lines to demonstrate the annual variation of the data. We found that the best fit was a second order polynomial of the form $ax^2 + bx + c$, and it is shown

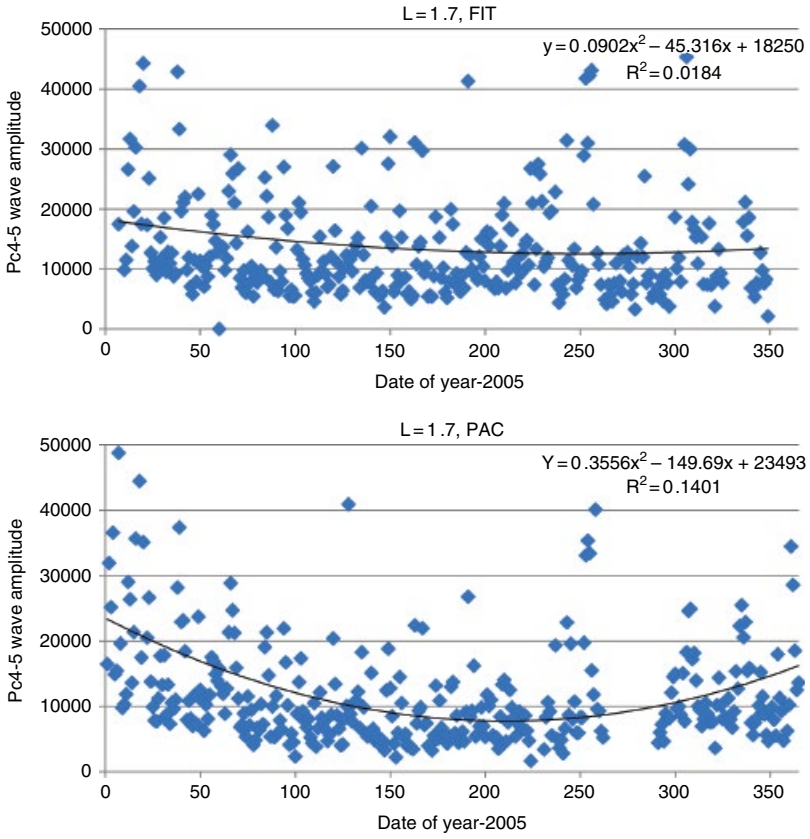


**Figure 1.11** Annual distribution of the FIT and PAC daily wave power for 2005 and with second-order polynomial fits to demonstrate any seasonal trends.

as a solid black line with the equation and $R^2$ value on the figure. While the $R^2$ is poor for both stations, it does seem to fit well the general shape of the bulk of points in each panel. Our results then are indicative of the situation of the two hemispheres during periods of lower to moderate geomagnetic activity. The northern line fit is rather flat, while the southern line fit has a clear curvature with high amplitudes around the December solstice. PAC has a higher *a* coefficient value, which leads to the curved shape and $R^2$ values demonstrating a stronger correlation. The shape of this regression line is a driver for the shape of the power ratio plots seen in Figure 1.10. It is the south decreasing around the June solstice and not the north increasing that drives the shape of the power ratio. Second, the northern station line is shifted up throughout the year, which causes the power ratio to remain above 1. The interesting conclusion from this analysis seems to be that the northern station exhibits only very weak annual or seasonal variation (if at all) while the southern station shows significant seasonal variation, which in turn determines the ratio of the north-south ratio.

Our result of a power ratio above 1 for all seasons is in agreement with *Obana et al.* [2005] but the explanation is not. *Obana et al.* explain the "positive effect" as a result of the stronger background magnetic field in the Northern Hemisphere with respect to that in the Southern Hemisphere. This explanation is consistent with the background fields for the conjugate pair FIT-PAC at L = 1.7. However, the background fields at our conjugate pair at L = 2.3, AMER-OHI, are similar, and there is still a north-to-south ratio greater than 1 for all seasons. We believe that our explanation outlined in Figure 1.11 better describes all our observations, since the annual wave-power trends for AMER and OHI are very similar to those shown in Figure 1.11.

### 1.3.3. The Role of the Ionosphere and Thermosphere

Ground magnetometer perturbations are an integrated response to all currents within the sensor's field of view (typically of radius equal to the distance of the current that impacts the magnetometer, ~120 km for ionospheric currents). Inhomogeneous ionospheric conductivity can modulate and influence the characteristics of ULF waves as they are coupled from the magnetosphere down to the ionosphere [*Hughes and Southwood*, 1976; *Pilipenko et al.*, 2000; *Alperovic and Fedorov*, 2007]. The assumption is that the wave electric field will map similarly to both ionospheric footpoints and the resulting field will be a combination of reflected and absorbed components, which depend strongly on the local height-integrated ionospheric conductivity. While it is true that the amount of wave power that penetrates the ionosphere and the amount reflected depend on the conductivity and the Hall to Pedersen ratio, ground magnetometers remotely respond primarily to Hall currents. For the same wave *E* field, you get more fluctuation currents, and therefore higher ground perturbations, when you have higher integrated conductivity. Therefore, one would intuitively expect stronger wave power in the more illuminated ionosphere. The variations we show in Figure 1.11 are consistent with this interpretation when considering the geographic latitude of FIT and PAC. FIT is at geographic latitude of 28° and remains well illuminated throughout the year, therefore not exhibiting strong seasonal variation. PAC, on the other hand, is at geographic latitude of −53.2° and shows higher wave power around December solstice, when its ionosphere is better illuminated. *Obana et al.* [2005] looked at the Pc3-5 north-to-south wave-power ratios at L = 5.4. They found, in agreement with our results, that the Northern Hemisphere has stronger power throughout the year. However, in contrast with our results, they found that the seasonal variation of the power ratio has a peak in December solstice and minimum at June solstice. They suggest that the higher northern conductivity during June solstice actually blocks the transmission of MHD waves from the magnetosphere to ionosphere. This is clearly not true for our conjugate pairs at L = 1.7, where the power ratio peaks in June and has a minimum in December-January.

We, therefore, examine measurements of the total electron content (TEC), as measured by ground GPS receivers at the two conjugate locations, to examine whether a similar asymmetry pattern as that seen in the wave power is also observed in the ionospheric content. The TEC observed on the ground is dominated by the ionospheric electron density (the plasmaspheric density being significantly smaller) and is therefore a reasonable proxy of the ionospheric content and conductivity at that location. We used data from GPS receivers co-located or in close proximity with our magnetometer stations.

Figure 1.12 shows, in the top panel, the TEC of the north (red) and south (blue) GPS receivers close to the locations of the FIT and PAC magnetometer stations. The ratio of the northern to southern TEC is plotted in the bottom panel for the year 2003. The northern station shows unambiguously higher TEC throughout the year and the north-south ratio remains above 1.0 similar to the Pc4-5 wave-power ratio in Figure 1.10. In contrast to the wave-power ratio, the TEC ratio exhibits a semiannual variation with peaks at the two solstices and dips at the two equinoxes. It is interesting that the absolute TECs at both northern and southern GPS stations has the opposite semiannual variation, namely they peak at the equinoxes and dip at the solstices. In other words, while there is more ionosphere at both hemispheres during equinoxes, the conductivity is more equitably distributed in the two hemispheres. During the solstices, the ionosphere is thinner at both hemispheres in comparison with their respective equinox content, but the Northern Hemisphere has significantly more content irrespective of whether it is the June or December solstice.

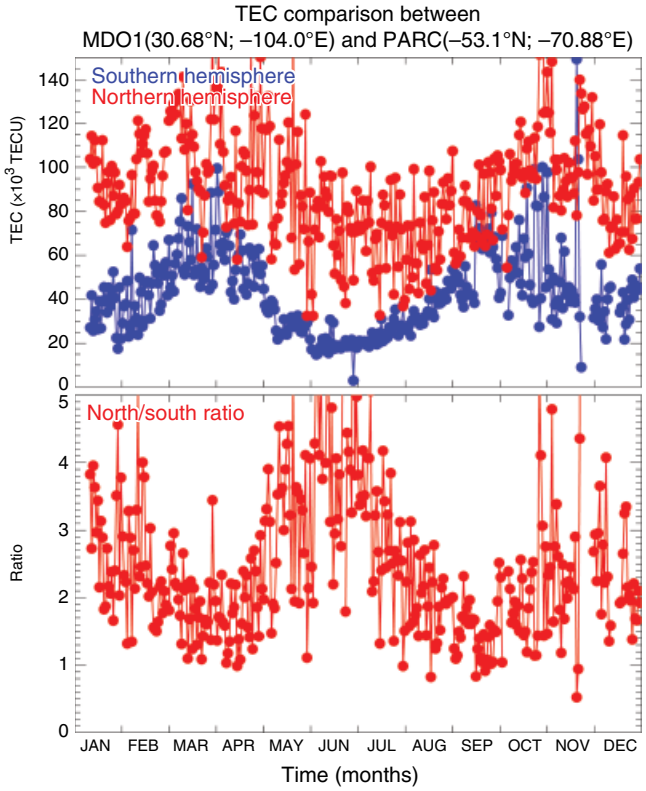


**Figure 1.12** (Top panel) Annual distribution of daily TEC at conjugate locations at L = 1.7, close to the FIT and PAC magnetometer sites; (bottom panel) the north to south TEC ratio.

This semiannual TEC variation has been reported before by *Lee et al.* [2010] and *Bagiya et al.* [2009], who used individual GPS receivers in Taiwan and India, respectively, to study the diurnal and seasonal variation of TEC at low latitudes. Both studies found a clear semiannual variation in TEC with peaks at the equinoxes, in exact agreement with our results. It has also been recently reported and examined as global TEC climatology by *Liu et al.* [2009] and *Lean et al.* [2011]. The north-south asymmetries of TEC were examined by *Mendillo et al.* [2005] in terms of global asymmetries. Their Figure 2 clearly shows the north to south asymmetric pattern at low latitudes and midlatitudes in agreement with our observation. We offer, for the first time, similar north to south asymmetries for both ULF wave power and TEC and suggest a link between the two.

Figure 1.13 shows in each column from top to bottom the north-to-south wave-power ratio for Pc3 waves, for Pc4-5 waves, and the TEC north-to-south ratio for years 2006 (left) and 2007 (right) at L = 2.3 for the station pair AMER-OHI. Similar to the results at L = 1.7 (Fig. 1.10), here we again see a clear seasonal variation in the Pc3 and Pc4-5 ratios, which peaks in northern summer and minimizes in northern winter. The ratio never drops below 1 throughout the year for either frequency band, indicating that there is a strong offset toward the Northern Hemisphere and a systematic asymmetry in addition to the seasonal variation. The offset is stronger for the

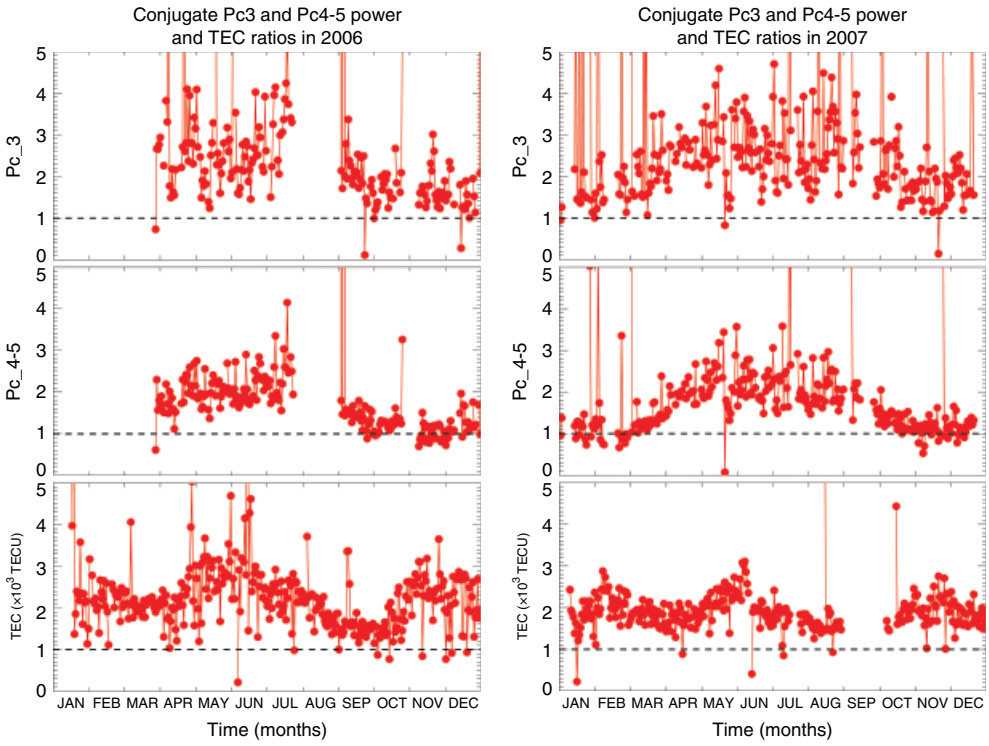


**Figure 1.13** From top to bottom, north to south power ratio for Pc3 waves, Pc4-5 waves, and for TEC, at L = 2.3 for years 2006 (left) and 2007 (right).

higher frequency waves (for Pc3). The TEC ratio also shows a clear bias toward the Northern Hemisphere (ratio >1 throughout the year), and it is even stronger than the one exhibited by the waves. In addition to the northern bias, the TEC ratio exhibits a clear semiannual variation that peaks at the two solstices and minimizes at the equinoxes.

Note that the annual variation of the waves and the semiannual variation of TEC is much more pronounced at the midlatitude L = 2.3, than it was at low latitude of L = 1.7 (compare Figs. 1.13 and 1.10). Furthermore, our results only partly agree with the results of *Obana et al.* [2005], who conducted a similar study but at a higher latitude of L = 5.4. Although *Obana et al.* [2005] found a similar northern bias in their analysis (their north-to-south power ratio was also always >1), the seasonal variation at their latitude was exactly opposite to the one we report in Figures 1.9 and 1.10. Specifically, they found that the wave-power ratio maximized at northern winter and minimized at northern summer. *Obana et al.* [2005] interpreted their observed seasonal variation as a likely result from inductive shielding of the waves by a highly conducting ionosphere: lower wave power in the summer beneath the higher conductive ionosphere than at winter, according to the shielding theory by *Yoshiwaka et al.* [2002]. However, the results shown in *Obana et al.* [2005] show seasonal variation on the ratio of the north-to-south amplitudes not on the north or south amplitudes themselves, so without knowing the seasonal variation of the wave amplitudes themselves, it is unclear how the inductive shielding theory of *Yoshiwaka et al.* [2002] would apply. In our dataset, there is no clear evidence for ionospheric shielding either, although more detailed analysis will be in a future work.

Perhaps the most intriguing result is the consistent northern bias that we found in both low latitudes and midlatitudes in the Americas meridian, that *Obana et al.* [2005] also found in the Asian meridian, and that the bias is even stronger in the TEC than it is in the ULF wave power. There are similar results in *Titheridge and Buonsanto* [1983] and *Su et al.* [1998] who both studied the annual variations of the low-latitude topside ionosphere from satellite and ground observations. Both of the *Titheridge and Buonsanto* [1983] and *Su et al.* [1998] studies found that the TEC and topside density values, respectively, are higher during the December solstice than during the June solstice, and they were able to show that the chemistry and dynamics of the neutral species have a significant effect in shaping the observed asymmetries.

*Titheridge and Buonsanto* [1983] looked at TEC from two near-conjugate pairs of ground stations for a period of 3 yr and also found a persistent higher amplitude of TEC in the Northern Hemisphere than in the Southern Hemisphere. *Su et al.* [1998] used observations from the low-inclination Hinotori satellite to look primarily at longitudinal patterns of the electron density, but also saw similar north-south TEC asymmetries, which they attributed to neutral winds. While they were not able to explain this, both studies suggested some type of trans-equatorial neutral wind could be the cause of the asymmetries. We suggest that there is potentially a strong connection between neutral, plasma, and wave properties. Future work should clarify whether such north-south asymmetries occur at all longitudes and latitudes and illuminate their physical sources.

In summary, the ULF wave power shows a clear interhemispheric asymmetry with stronger power always in the northern conjugate station. This north-south asymmetry is stronger at midlatitudes than at low latitudes (higher ratios at L = 2.3 than at L = 1.7) and it is stronger for the higher frequency waves (higher ratios for Pc3 waves). The ionospheric TEC exhibits the same interhemispheric asymmetry, implying that the state of the ionosphere affects and partly causes the observed wave interhemispheric asymmetry. It is unclear why the TEC ratio has a biannual variation while the wave power only exhibits annual variation and needs to be further investigated in future work.

## 1.4. SUMMARY

We explore pathways for energy input into the ionosphere-thermosphere system and asymmetries between the Northern and Southern Hemispheres. Seasonal effects are strong drivers of interhemispheric asymmetries, the uneven illumination of the two hemispheres resulting in asymmetric ionospheric conductivities and therefore asymmetric current distribution in the two hemispheres. Additional factors may also contribute significantly to the asymmetric energy input into the two hemispheres as prior studies have reported. Factors like the Earth's dipole tilt with respect to the rotation axis, the IMF orientation, local magnetic field structures, and even atmospheric dynamics. We review several of these factors and their effects. We focus on asymmetries of auroral dynamics, particularly substorms, for which there is considerable prior work defining their onset and dynamics in the two hemispheres. Similar asymmetries should be expected in the auroral electrojets that are well correlated with the auroral dynamics.

We calculate a Southern Hemisphere auroral electrojet index, SAE, from all available southern auroral stations and compare it with a conjugate northern auroral electrojet index, NAE, and with the standard AE index. We look at both case studies and a large statistical study of the correlations and difference between SAE, NAE, and AE. We found that, in general, SAE correlates well with AE and even better with NAE and that correlation is better under strong southward IMF and/or strong solar-wind dynamic

pressure. Strong interhemispheric asymmetries occur often and are likely the result of IMF $B_y$ or interhemispheric currents. Differences in the amplitude of the electrojet indices between the two hemispheres are strongest in the local midnight and are the result of the nightside westward electrojet.

We look at the power of ULF waves in two bands, Pc3 (20–100 mHz), and Pc4-5 (2–20 mHz) and study the power in pairs of conjugate stations at low latitudes, L = 1.7, and midlatitudes, L = 2.3, in the Americas meridian. We calculate the daily wave power in the two frequency bands and then calculate the north-to-south daily power ratio. We find that the ULF wave power shows a clear interhemispheric asymmetry with stronger power always in the northern conjugate station. This north-south asymmetry is stronger at midlatitudes than at low latitudes (higher ratios at L = 2.3 than at L = 1.7), and it is stronger for the higher frequency waves (higher ratios for Pc3 waves). The ionospheric TEC exhibits similar interhemispheric asymmetry, namely higher TEC all year round in the Northern Hemisphere, implying that the state of the ionosphere affects and partly causes the observed wave interhemispheric asymmetry. We believe that the link between the ULF wave power and TEC are in the north-south asymmetry, but the seasonal-annual variation of the ULF power and TEC are different and the result of different processes.

## ACKNOWLEDGMENTS

This work was supported by NSF grant ATM-0100902, NSF grant OPP-ANT-1043621, AFOSR grant LRIR #10RV07COR, NASA LWS (NNX10AQ53G) and Geospace Science programs (NNX07AM22G and NNX09AR84G), and AFOSR YIP grant (FA9550-10-1-0096). We would also like to thank GIMA (Geophysical Institute Magnetometer Array) for the data from the BET station; the THEMIS team for the data from SNKQ and KIAN; DMI (Danish Meteorological Institute) for data from AMK, NAQ, and SCO; BAS (British Antarctic Survey) for data from the HBA and M78-337 stations; Science Institute, University of Iceland, for the data from LVR; Geoscience Australia for data from MCQ and MAW; INTERMAGNET (International Real-time Magnetic Observatory) for data from PBQ; Oleg Troshichev for the data from NVL station; Pieter Stoker for data from the SNA magnetometer; IMAGE (International Monitor for Auroral Geomagnetic Effects) for the data from SOR and BJN; the WDC for Aurora in National Institute of Polar Research in Japan for data from the HLL and SYO stations; and the WDC for geomagnetism, Kyoto, for the standard AE index data.

## REFERENCES

Ables, S. T., B. J. Fraser, J. V. Olson, and R. J. Morris (2000), Conjugate ULF field line resonances at cusp latitudes, *Advances in Space Res.*, *26*(1), 125–130; ISSN 0273-1177; http://dx.doi.org/10.1016/S0273-1177(99)01038-8.

Alperovich, L. S., and E. N. Fedorov (2007), *Hydromagnetic Waves in the Magnetosphere and the Ionosphere*, vol. 353, Astrophysics and Space Science Library, XXIV.

Anderson, B. J., K. Takahashi, T. Kamei, C. L. Waters, and B. A. Toth (2002), Birkeland current system key parameters derived from Iridium observations: Method and initial validation results, *J. Geophys. Res.*, *107*(A6); doi:10.1029/2001JA000080.

Bagiya, M. S., H. P. Joshi, K. N. Iyer, M. Aggarwal, S. Ravindram, and B. M. Pathan (2009), TEC variations during low solar activity period (2005–2007) near the Equatorial Ionospheric Anomaly Crest region in India, *Ann. Geophysicae*, *27*, 1047–1057; doi:10.5194/angeo-27-1047-2009.

Baker, K. B., and S. Wing (1989), A new magnetic coordinate system for conjugate studies at high latitudes, *J. Geophys. Res.*, *94*(A7), 9139–9143; doi:10.1029/JA094iA07p09139.

Belon, A. E., J. E. Maggs, T. N. Davis, K. B. Mather, N. W. Glass, and G. F. Hughes (1969), Conjugacy of visual auroras during magnetically quiet periods, *J. Geophys. Res.*, *74*, 1–28; doi:10.1029/JA074i001p00001.

Benkevich, L., W. Lyatsky, and L. L. Cogger (2000), Field-aligned currents between the conjugate hemispheres, *J. Geophys. Res.*, *105*, 27727–27737; doi:10.1029/2000JA900095.

Berube, D., M. B. Moldwin, and J. M. Weygand (2003), An automated method for the detection of field line resonance frequencies using ground magnetometer techniques, *J. Geophys. Res.*, *108*, 1348; doi:10.1029/2002JA009737, A9.

Boudouridis, A., and E. Zesta (2007), Comparison of Fourier and wavelet techniques in the determination of geomagnetic field line resonances, *J. Geophys. Res.*, *112*, A08205; doi:10.1029/2006JA011922.

Chi, P. J., et al. (2013), Sounding of the plasmasphere by Midcontinent Magnetoseismic Chain (McMAC) magnetometers, *J. Geophys. Res. Space Phys.*, *118*, 3077–3086; doi:10.1002/jgra.50274.

Cnossen, I., and A. D. Richmond (2012), How changes in the tilt angle of the geomagnetic dipole affect the coupled magnetosphere-ionosphere-thermosphere system, *J. Geophys. Res.*, *117*, A10317; doi:10.1029/2012JA018056.

Davis, T. N., and M. Sugiura (1966), Auroral electrojet index AE and its universal time variations, *J. Geophys. Res.*, *71*, 785–801.

Feng, Q., B. J. Fraser, F. W. Menk, C. W. S. Ziesolleck, O. Saka, and T. Kitamura (1995), Pc3-4 geomagnetic pulsations observed at very low latitude conjugate stations, *J. Geophys. Res.*, *100*(A10), 19287–19298; doi:10.1029/94JA01260 .

Fillingim, M. O., G. K Parks, H. U. Frey, T. J. Immel, and S. B. Mende (2005), Hemispheric asymmetry of the afternoon electron aurora, *Geophys. Res. Lett.*, *32*, L03113; doi:10.1029/2004GL021635.

Förster, M., and I. Cnossen (2013), Upper atmosphere differences between northern and southern high latitudes: The role of magnetic field asymmetry, *J. Geophys. Res. Space Phys.*, *118*, 5951–5966; doi:10.1002/jgra.50554.

Frank, L. A., and j. B. Sigwarth (2003), Simultaneous images of the northern and southern auroras from the polar spacecraft: An auroral substorm, *J. Geophys. Res.*, *108*, 8015; doi:10.1029/2002JA009356.

Gjerloev, J. W. (2012), The SuperMAG data processing technique, *J. Geophys. Res.*, *117*, A09213; doi:10.1029/2012JA017683.

Hajkowicz, L. A. (2006), Magnetoconjugate phenomena in Alaska and Macquarie Is., Australia in 2003: Position of the global maximum iso-aurorae, *Ann. Geophysicae*, *24*, 2611–2617; doi:10.5194/angeo-24-2611-2006.

Hughes, W. J., and D. J. Southwood (1976), An illustration of modification of geomagnetic pulsation structure by the ionosphere, *J. Geophys. Res.*, *81*, 3241–3247; doi:10.1029/JA081i019p03241.

Kivelson, M. G., K. K. Khurana, R. J. Walker, L. Kepko, and D. Xu (1996), Flux ropes, interhemispheric conjugacy, and magnetospheric current closure, *J. Geophys. Res.*, *101*, 27,341–27,350; doi:10.1029/96JA02220.

Knipp, D. J., C.-H. Lin, B. A. Emery, J. M. Ruohoniemi, F. J. Rich, and D. S. Evans (2000), Hemispheric asymmetries in ionospheric electrodynamics during the solar wind void of 11 May 1999, *Geophys. Res. Lett.*, *27*, 4013; doi:10.1029/2000GL003801.

Lanzerotti, L. J., and M. F. Robbins (1973), ULF geomagnetic power near $L$ = 4: 1. Quiet day power spectra at conjugate points during December Solstice, *J. Geophys. Res.*, *78*(19), 3816–3827; doi:10.1029/JA078i019p03816.

Laundal, K. M., and N. Ostgaard (2009), Asymmetric auroral intensities in the Earth's Northern and Southern hemispheres, *Nature*, *460*, 491–193; doi:10.1038/nature08154.

Lean, J. L., R. R. Meier, J. M. Picone, and J. T. Emmert (2011), Ionospheric total electron content: Global and hemispheric climatology, *J. Geophys. Res.*, *116*, A10318; doi:10.1029/2011JA016567.

Lee, C. C., Y. J. Chuo, F. D. Chu (2010), Climatology of total electron content near the dip equator under geomagnetic quiet-conditions, *J. Atmos. Solar Terr. Phys.*, *72*(2–3), February, 207–212; http://dx.doi.org/10.1016/j.jastp.2009.11.011.

Liou, K., P. T. Newell, C.-I. Meng, M. Brittnacher, and G. Parks (2001), Seasonal effects on auroral particle acceleration and precipitation, *J. Geophys. Res.*, *106*, 5531–5542; doi:10.1029/1999JA000391.

Liu, L., W. Wan, B. Ning, and M. -L. Zhang (2009), Climatology of the mean total electron content derived from GPS global ionospheric maps, *J. Geophys. Res.*, *114*, A0630; doi:10.1029/2009JA014244.

Liu, Y. H., B. J. Fraser, R. Y. Liu, and P. V. Ponomarenko (2003), Conjugate phase studies of ULF waves in the Pc5 band near thecusp, *J. Geophys. Res.*, *108*, 1274; doi:10.1029/2002JA009336.

Lyatskaya, S., W. Lyatsky, and G. V. Khazanov (2014a), Effect of interhemispheric field-aligned currents on the Region 1 currents, *Geophys. Res. Lett.*, *41*, 3731–3737; doi:10.1002/2014GL060413.

Lyatskaya, S., G. V. Khazanov, and E. Zesta (2014b), Interhemispheric field-aligned currents: Simulation results, *J. Geophys. Res.*; doi:10.1002/2013JA019558.

Maclennan, C. G., L. J. Lanzerotti, S. -I. Akasofu, A. N. Zaitzev, P. J. Wilkinson, A. Wolfe, and V. Popov (1991), Comparison of "electrojet" indices from the Northern and Southern hemispheres, *J. Geophys. Res.*, *96*, 267–264; doi:10.1029/90JA01366.

Mendillo, M., C.-L. Huang, X. Pi, H. Rishbeth, R. Meier (2005), The global ionospheric asymmetry in total electron content, *J. Atmos. Solar Terr. Phys.*, *67*(15), 1377–1387; http://dx.doi.org/10.1016/j.jastp.2005.06.021.

Morioka, A., et al. (2011), On the simultaneity of substorm onset between two hemispheres, *J. Geophys. Res.*, *116*, A04211; doi:10.1029/2010JA016174.

Matthews, D. L., J. M. Ruohoniemi, J. R. Dudeney, C. F. Farrugia, L. J. Lanzerotti, and E. Friis-Christensen (1996), Conjugate cusp-region ULF pulsation responses to the solar wind event of 23 May 1989, *J. Geophys. Res.*, *101*(A4), 7829–7841; doi:10.1029/95JA03470.

Motoba T., K. Hosokawa, A. Kadokura, and N. Sato, Magnetic conjugacy of northern and southern auroral beads, *Geophys. Res. Lett.*, *39*, L08108; doi:10.1029/2012GL051599, 2012.

Motoba, T., K. Hosokawa, N. Sato, A. Kadokura, and G. Bjornsson (2010), Varying interplanetary magnetic field By effects on interhemispheric conjugate auroral features during a weak substorm, *J. Geophys. Res.*, *115*, A09210; doi:10.1029/2010JA015369.

Motoba, T., S. Ohtani, A. Kadokura, and J. Gjerloev (2014), Interrelationship between preonset auroral and magnetic signatures at a geomagnetically conjugate Iceland-Syowa pair, *J. Geophys. Res. Space Phys.*, *119*; doi:10.1002/2013JA019512.

Newell, P. T., C.-I. Meng, and K. M. Lyons (1996), Suppression of discrete aurorae by sunlight, *Nature 381*, 766–767; doi:10.1038/381766a0.

Nishida, A. (1968), Geomagnetic DP-2 fluctuations and associated magnetospheric phenomena, *J. Geophys. Res.*, *13*, 1795; doi:10.1029/JA073i005p01795.

Obana, Y., A. Yoshikawa, J. V. Olson, R. J. Morris, B. J. Fraser, and K. Yumoto (2005), North-south asymmetry of the amplitude of high-latitude Pc3-5 pulsations: Observations at conjugate stations, *J. Geophys. Res.*, *110*, A10214; doi:10.1029/2003JA010242 .

Østgaard, N., N. A. Tsyganenko, S. B. Mende, H. U. Frey, T. J. Immel, M. Fillingim, L. A. Frank, and J. B. Sigwarth (2005), Observations and model predictions of substorm auroral asymmetries in the conjugate hemispheres, *Geophys. Res. Lett.*, *32*, L05111; doi:10.1029/2004GL022166.

Østgaard, N., S. B. Mende, H. U. Frey, J. B. Sigwarth, A. Åsnes, J. M. Weygand (2007), Auroral conjugacy studies based on global imaging, *J. Atmos. Solar Terr. Phys.*, *69*, 249–255; doi:10.1016/j.jastp.2006.05.026.

Østgaard, N., S. B. Mende, H. U. Frey, T. J. Immel, L. A. Frank, J. B. Sigwarth, T. J. Stubbs (2004), Interplanetary magnetic field control of the location of substorm onset and auroral features in the conjugate hemisphere, *J. Geophys. Res.*, *109*, A07204; doi: 10.1029/2003J010370.

Pilipenko, V., M. Vellante, and E. Fedorov (2000), Distortion of the ULF wave spatial structure upon transmission through the ionosphere, *J. Geophys. Res.*, *105*, 21225–21236; doi;10.1029/2000JA900063.

Posch, J. L., M. J. Engebretson, A. T. Weatherwax, D. L. Detrick, W. J. Hughes, and C. G. Maclennan (1999), Characteristics of broadband ULF magnetic pulsations at conjugate cusp latitude stations, *J. Geophys. Res.*, *104*(A1), 311–331; doi:10.1029/98JA02722.

Saroso, S. M. Sugiura, T. Iyemori, T. Araki, and T. Kamei (1992), Derivation of polar cap AE indices, *Proc. NIPR Symp. Upper Atmos. Phys.*, *5*, 35–45.

Sato, N., A. Kadokura, T. Motoba, K. Hosokawa, G. Bjornsson, and T. Saemundsson (2012), Ground-based aurora conjugacy and dynamic tracing of geomagnetic conjugate points, 91–98, in *Auroral Phenomenology and Magnetospheric Processes: Earth and Other Planets*, AGU Geophys. Monogr. Ser., vol. 197, edited by A. Keiling et al., Washington, DC: doi:10.1029/2011GM001154, 2012.

Sato, N., T. Nagaoka, K. Hashimoto, and T. Saemundsson (1998), Conjugacy of isolated auroral arcs and nonconjugate auroral breakups, *J. Geophys. Res.*, *103*, 11,641–11,652; doi:10.1029/-98JA00461.

Shi, J., J. Guo, M. Dunlop, M., T. Zhang, Z. Liu, E. Lucek, A. Fazakerley, H. Rème, and I. Dandouras (2012), Interhemispheric asymmetry of dependence of the cusp location on dipole tilt during northward IMF conditions, *Ann. Geophys.*, *30*, 21–26; doi:10.5194/angeo-30-21-2012.

Stenbaek-Nielsen, H. C., T. N. Davis, and N. W. Glass (1972), Relative motion of auroral conjugate points during substorms, *J. Geophys. Res.*, *77*, 1844–1858; doi:10.1029/JA077i010p01844.

Stenbaek-Nielsen, H. C., T. N. Wescott, T. N., Davis, and R. W. Peterson (1973), Auroral intensity differences at conjugate points, *J. Geophys. Res.*, *78*, 659–671; doi:10.1029/JA078i004p00659.

Stubbs, T. J., R. R. Vondrak, N. Østgaard, J. B. Sigwarth, and L. A. Frank (2005), Simultaneous observations of the auroral oval in both hemispheres under varying conditions, *Geophys. Res. Lett.*, *32*, L03103; doi:10.1029/2004GL021199.

Su, Y. Z., G. J. Bailey, and K. -I. Oyama (1998), Annual and seasonal variations in the low-latitude topside ionosphere, *Ann. Geophysicae*, *16*(8), 974–985; doi:10.1007/s00585-998-0974-0.

Surkan, A. J., and L. J. Lanzerotti (1974), ULF geomagnetic power near L = 4 3. Statistical study of power spectra in conjugate areas during December solstice, *J. Geophys. Res.*, *79*(16), 2403–2412; doi:10.1029/JA079i016p02403.

Titheridge, J. E., and M. J. Buonsanto (1983), Annual variations in the electron content and height of the F layer in the Northern and Southern hemispheres, related to neutral composition, *J. Atmos. Solar Terr. Phys.*, *45*(10), 683–696; http://dx.doi.org/10.1016/S0021-9169(83)80027-0.

Troitskaya, V. A., and O. V. Bolshakova (1988), Diagnostics of the magnetosphere using multipoint measurements of ULF-waves, *Advances in Space Res.*, *8*(9–10), 413–425; http://dx.doi.org/10.1016/0273-1177(88)90155-X.

Weimer, D. R. (2004), Correction to "Predicting interplanetary magnetic field (IMF) propagation delay times using the minimum variance technique," *J. Geophys. Res.*, *109*, A12104; doi:10.1029/2004JA010691.

Weimer, D. R., D. M. Ober, N. C. Maynard, M. R. Collier, D. J. McComas, N. F. Ness, C. W. Smith, and J. Watermann (2003), Predicting interplanetary magnetic field (IMF) propagation delay times using the minimum variance technique, *J. Geophys. Res.*, *108*, 1026; doi:10.1029/2002JA009405.

Weygand, J. M., and E. Zesta (2008), Comparison of auroral electrojet indices in the Northern and Southern hemispheres, *J. Geophys. Res.*, *113*, A08202; doi:10.1029/2008JA013055.

Weygand, J. M., E. Zesta, and O. Troshichev (2014a), Auroral electrojet indices in the Northern and Southern hemispheres: A statistical comparison, *J. Geophys. Res. Space Phys.*, *119*, 4819–4840; doi:10.1002/2013JA019377.

Weygand, J. M., E. Zesta, R. L. McPherron, and T. -S. Hsu (2014), *The Differences in Onset Time of Conjugate Substorms, the American Geophysical Union Fall Conference*, San Francisco, CA, December 2014, *EOS Trans.*, 95, 2014b.

Wu, Q., T. J. Rosenberg, L. J. Lanzerotti, C. G. Maclennan, and A. Wolfe (1991), Seasonal and diurnal variations of the latitude of the westward auroral electrojet in the nightside polar cap, *J. Geophys. Res.*, *96*(A2), 1409–1419; doi:10.1029/90JA02379.

Yizengaw, E., E. Zesta, C. M. Biouele, M. B. Moldwin, A. Boudouridis, B. Damtie, A. Mebrahtu, F. Anad, R. F. Pfaff, and M. Hartinger (2013), Observations of ULF wave related equatorial electrojet and density fluctuations, *J. Atmos. Solar Terr. Phys.*; doi:10.1016/j.jastp.2013.03.015.

Yoshikawa, A., Y. Obana, M. Shinohara, M. Itonaga, and K. Yumoto (2002), Hall-induced inductive shielding effect on magnetic pulsations, *Geophys. Res. Lett.*, *29*(8), 1266; doi:10.1029/2001GL013610.

Yumoto, K. (1985), Low-frequency upstream wave as a probable source of low-latitude Pc3-4 magnetic pulsations, *Planet. Space Sci.*, *33*(2), 239–249; doi:10.1016/0032-0633(85)90133-3.

# 2

# Simultaneity and Asymmetry in the Occurrence of Counterequatorial Electrojet along African Longitudes

**A. Babatunde Rabiu,[1] Olanike O. Folarin,[2] Teiji Uozumi,[3] and Akimasa Yoshikawa[3,4]**

## ABSTRACT

The simultaneity and asymmetry in the occurrence of counterequatorial electrojet (CEJ) along African longitudes was investigated. We utilized 1 min interval data of the horizontal geomagnetic field intensity recorded from January to December 2009 (mean sunspot number = 3.1), by network of the Magnetic Data Acquisition System installed at Ilorin ILR (4.68°E, 8.50°N; dip latitude, 1.82°S), Addis Ababa AAB (38.77°E, 9.04°N; dip latitude, 0.18°N), Lagos (3.43°E, 6.48°N; dip latitude 3.04°S), and Nairobi (36.48°E, 1.16°S; dip latitude 10.65°S). In this work, Asymmetry-1 on any particular day is defined as the scenario when there is occurrence of morning CEJ along the west (ILR) between 06:00 LT and 11:00 LT with no simultaneous morning occurrence along the east (Addis AAB), but afternoon occurrence. Asymmetry-2 refers to the occurrence of CEJ in the afternoon between 13:00 LT and 18:00 LT at ILR with no simultaneous afternoon occurrence, but morning occurrence at AAB on same day. Most frequent simultaneous occurrence of CEJ at both equatorial stations was in the morning (77%). Asymmetry-2 (41.3%) is more prevalent than Asymmetry-1 (4.9%). The longitudinal variability in the local time of occurrence of CEJ along these longitudes is attributed to the differences in meridional currents and some other phenomena.

**Key Points:**
Most frequent and simultaneous occurrence of CEJ was found on days of morning CEJ
The occurrence of morning simultaneity of CEJ was maximum during the June solstice.
There is a seasonal variability of the mechanisms responsible for the occurrence of CEJ.

**Key Terms:** counterequatorial electrojet, ionospheric currents, simultaneity, asymmetry

[1]*Center for Atmospheric Research (CAR), National Space Research and Development Agency, Anyigba, Nigeria*

[2]*Ionospheric & Space Physics Laboratory, Department of Physics, University of Lagos, Akoka, Nigeria*

[3]*International Center for Space Weather Science and Education (ICSWSE), Kyushu University, Fukuoka, Japan*

[4]*Earth and Planetary Sciences, Kyushu University, Fukuoka, Japan*

## 2.1. INTRODUCTION

The discovery of the transient variation in the Earth's magnetic field in 1722 by Graham sparked off the study of geomagnetic field variation [*Graham*, 1724]. *Stewart* [1882] proposed that the most probable seat of the solar action that produces this geomagnetic variations is the upper atmosphere and the source is the electric current in

*Ionospheric Space Weather: Longitude and Hemispheric Dependences and Lower Atmosphere Forcing, Geophysical Monograph 220*, First Edition. Edited by Timothy Fuller-Rowell, Endawoke Yizengaw, Patricia H. Doherty, and Sunanda Basu.

that region. *Alex and Jadhav* [2007] reported that the daily variation in the magnetic field at the Earth's surface during the geomagnetic quiet condition is known to be generated by solar heating, which results in tidal winds in the *E* region of the ionosphere, where the magnitude of conductivity is appreciable.

In the equatorial regions, the normal quiet daily (*Sq*) variation of the geomagnetic field shows a strong enhancement, which has been attributed to a narrow electric current sheet flowing eastward along the magnetic dip equator, termed the equatorial electrojet (EEJ) [*Egedal*, 1947 and 1948; *Chapman*, 1951]. Its associated magnetic fields are only observed in a zone approximately 3° on either side of the magnetic dip equator.

In 1962, the reversal in the direction of the normal northward directed field of the horizontal component was noticed around midday hours at Addis Ababa, an equatorial station [*Gouin*, 1962]. This reversal was observed as a negative depression in the daily variation of the horizontal component (*H*) of the geomagnetic field below the night level and was named "counter equatorial electrojet" [*Gouin*, 1962]. This current is similar to the electrojet but flows in the reverse direction. Just like the EEJ, this current flows within ±3° of the dip equator in the ionospheric *E* region.

*Gouin and Mayaud* [1967], *Mayaud* [1977], *Onwumechili and Akasofu* [1972] and *Onwumechili* [1997] explained the negative depression of the regular *H* field to be the effect of a westward electric current flowing on a very quiet day within a narrow band, centered on the dip equator. Similar occurrences in the diurnal variation in the *H* component were later observed at other equatorial stations: Ibadan [*Onwumechilli*, 1963], Zaria [*Hutton and Oyinloye*, 1970], and Trivandrum [*Sastry and Jayakar*, 1972], among others.

*Rastogi and Patel* [1975] showed that the reversal of an equatorial electrojet current is associated with the northward turning of the interplanetary magnetic field. From a detailed simulation study, *Hanuise et al.* [1983] explained the possible reversal of the east-west electric field during this counterequatorial electrojet (CEJ) event as due to an abnormal combination of global-scale tidal wind modes.

*Kane* [1973] and *Rastogi* [1974] examined the cases of various counterelectrojet events at different longitudes, and they pointed out that the depressions of the *H* field at these longitudes are varying in nature and discussed the feature of limited longitudinal extent. *Alex and Mukherjee* [2001] compared CEJ events at the two equatorial stations, Trivandrum and Addis Ababa (40° apart in longitude), and concluded that there are some differences in CEJ events when observed in different longitudinal sectors.

This present study, concentrates, for the first time, on the simultaneity and asymmetry in the occurrence of counterequatorial electrojet events during geomagnetic quiet conditions along the West and East African longitudes, respectively, with the aim to understand the pattern of occurrence of CEJ and its diurnal distribution along these longitudes. The recent installation of Magnetic Data Acquisition System (MAGDAS) magnetometers along the African longitudes has made this study a possibility.

## 2.2. DATA PROCESSING TECHNIQUE

One-minute interval data of the horizontal geomagnetic field intensity *H* obtained from the MAGDAS magnetometers installed along the African longitudes, and managed by the International Center for Space Weather Science and Education formerly known as Space Environmental Research Center (SERC), Kyushu University, Japan, were used for this study. The data is composed of 1-yr data (January to December 2009) from the network of four geomagnetic observatories located along the east and west of the African longitudes, respectively: Addis Ababa (Ethiopia: 38.77°E, 9.04°N; dip latitude, 0.18°N) and Nairobi (Kenya: 36.48°E, 1.16°S; dip latitude 10.65°S), Ilorin (Nigeria: 4.68°E, 8.50°N; dip latitude, 1.82°S), and Lagos (Nigeria: 3.43°E, 6.48°N; dip latitude 3.04°S). Table 2.1, gives the coordinates of the stations, and Figure 2.1 shows the distribution of the observatories on the map of Africa. Both Ilorin and Addis Ababa are located within the equatorial electrojet belt, which lies around ±3° latitude of the magnetic equator, while Lagos and Nairobi are outside the electrojet belt.

Only data obtained on the international quiet days are engaged in this research, since the EEJ is a quiet condition phenomenon. The Ap index was used to check the measure of disturbance in the ionosphere. ILR and LAG are 1 hr

**Table 2.1** Geomagnetic Observatories and Their Coordinates

| | | Geomagnetic coordinates | | Geographic coordinates | |
|---|---|---|---|---|---|
| Geomagnetic observatories | Code | Longitude (°) | Latitude (°) | Longitude (°E) | Latitude (°N) |
| Ilorin | ILR | 76.80 | –1.82 | 4.68 | 8.50 |
| Lagos | LAG | 75.33 | –3.04 | 3.43 | 6.48 |
| Addis Ababa | AAB | 110.47 | 0.18 | 38.77 | 9.04 |
| Nairobi | NAB | 108.18 | –10.65 | 36.48 | –1.16 |

ahead of the GMT, while AAB and NAB are 3 hr ahead. So the concept of local time (LT) was used throughout the analysis.

The solar quiet daily variation *Sq* in horizontal field (*H*) at the stations was estimated following the methods described by *Rabiu et al.* [2007a]. The analytical methods involved in the estimation of *Sq* are the daily baseline, midnight departures, and correction for noncyclic variation.

The daily baseline is obtained from the four hourly values (23, 24, 1, 2 hr LT) of the horizontal geomagnetic field component flanking the local midnight. The time series data in hours of the value of $H_t$ were considered, where ($t = 1, 2, 3, \ldots, 24$). The daily baseline value ($H_o$) for the geomagnetic element *H* of the data was then determined by finding the average of the 4 hr flanking the local midnight, and it is given as

$$H_0 = \frac{1}{4}\left(H_{23} + H_{24} + H_1 + H_2\right) \tag{2.1}$$

where $H_1$, $H_2$, $H_{23}$, $H_{24}$ are the hourly values of *H* at 1, 2, 23, and 24 hr local time, respectively.

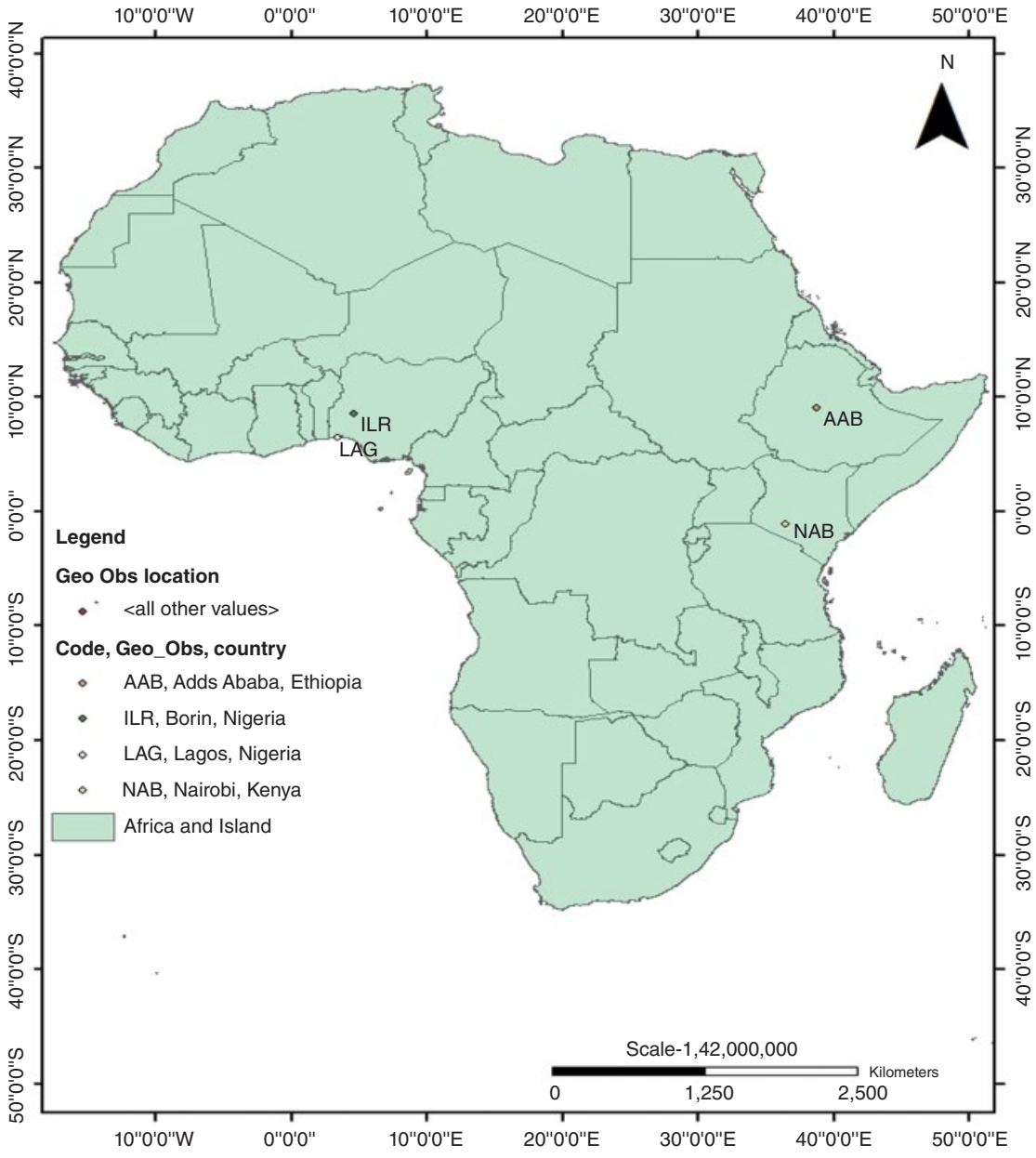


**Figure 2.1** The distribution of the geomagnetic observatories used for the study.

The hourly departures of $H$ from midnight baseline values are obtained by subtracting the midnight baseline values (which were calculated in Equation [2.1]) for a particular day from the hourly values for that particular day.

Thus for $t$ hour LT:

$$dH = H_t - H_0 \tag{2.2}$$

where $t$ is the local time ranging from 1 to 24 hr and $H_t$ is the hourly value of geomagnetic element $H$. Hence, $dH$ gives the measure of the hourly amplitude of variation of the horizontal component of the Earth's magnetic field $H$.

The hourly departure is further corrected for noncyclic variation, a phenomenon in which the value at 1 LT is different from the value at 24 LT [*Vestine*, 1947; *Rabiu*, 2000]. This is done by making linear adjustments in the values of the daily hourly departures of $dH$. The noncyclic index is given as

$$\Delta_c = \frac{dH_1 - dH_{24}}{23} \tag{2.3}$$

The linearly adjusted values at these hours are $dH_1 + 0\Delta_c$; $dH_2 + 1\Delta_c$; $dH_3 + 2\Delta_c$, …, $dH_{23} + 22\Delta_c$; $dH_{24} + 23\Delta_c$. The hourly departures corrected for noncyclic variation give the solar quiet daily variation in $H$, $Sq$ ($H_t$), such that

$$Sq(H_t) = dH_t + (t-1)\Delta_c \tag{2.4}$$

where $t$ is the local time ranging from 1 to 24 hr. Estimation of $Sq$ and thus EEJ using the above method is detailed in *Rabiu et al.* [2007a,b].

### 2.2.1. Estimation of Counterequatorial Electrojet

Hourly $Sq$ obtained at Lagos (a nonelectrojet) station was subtracted from the corresponding $Sq$ at Ilorin (an electrojet) station to obtain the EEJ along the western longitude, $EEJ_w$. Similarly, hourly $Sq$ at Nairobi (a nonelectrojet) station was subtracted from the corresponding $Sq$ at Addis Ababa (an electrojet) station to obtain the EEJ along the eastern longitude, $EEJ_e$. In other words

$$EEJ_w^t = Sq_{ILR}^t - Sq_{LAG}^t \tag{2.5}$$

$$EEJ_e^t = Sq_{AAB}^t - Sq_{NAB}^t \tag{2.6}$$

where,

$Sq_{ILR}^t = Sq$ at $LT$ time $t$ at $ILR$

$Sq_{LAG}^t = Sq$ at $LT$ time $t$ at $LAG$

$Sq_{AAB}^t = Sq$ at $LT$ time $t$ at $AAB$

$Sq_{NAB}^t = Sq$ at $LT$ time $t$ at $NAB$

$EEJ_w^t = EEJ$ along the Western longitude, and

$EEJ_e^t = EEJ$ along the Eastern longitude

CEJ is said to occur when EEJ reverses and changes direction in daytime [*Fambitakoye et al.*, 1973; *Rastogi*, 1974]. Therefore, CEJ is identified at any time $t$ in daytime when EEJ at that particular time is negative. That is,

$$CEJ^t = \left(EEJ^t < 0\right) \tag{2.7}$$

Daytime is actually considered as the sunshine dispensation. And so we focused the study on local time of 06:00–18:00 LT hr. This is a common approach to the study of equatorial electrojet and its counterelectrojet as found in the works of *Ezema et al.* [1996], *Onwumechili* [1997], *Alex and Mukherjee* [2001], and *Yizengaw et al.* [2014].

### 2.2.2. Simultaneity and Asymmetry

When the two equatorial stations are synchronized on local time (LT) basis, then we consider the concurrent time regimes at Ilorin ILR and Addis Ababa AAB as simultaneous. For example 06:00–11:00 LT is considered as morning time; and so occurrence of CEJ between 06:00 and 11:00 LT at any of the stations is considered as morning occurrence and referred to as morning CEJ (MCEJ). In this work, simultaneity is defined as the concurrent occurrence of morning CEJ or afternoon CEJ (ACEJ) on the same day at both stations. Therefore, when we have simultaneous occurrence of CEJ at both stations in the morning period (06:00–11:00 LT), we refer to this as morning simultaneity. Afternoon simultaneity refers to simultaneous occurrence of CEJ at both stations in the afternoon period (13:00–18:00 LT).

Asymmetry-1 (Asym-1) on any particular day is defined as the scenario when there is occurrence of morning CEJ along the west (Ilorin ILR) between 06:00 LT and 11:00 LT with no simultaneous morning occurrence along the east (Addis Ababa AAB), but afternoon occurrence. On the other hand, Asymmetry-2 (Asym-2) refers to the occurrence of afternoon CEJ between 13:00 LT and 18:00 LT at ILR with no simultaneous afternoon occurrence, but morning occurrence at AAB on the same day.

On the whole, 57 days were analyzed since these are the days where we had data for both stations for accurate comparison. Table 2.2 shows the number of days in which data were available in each month.

## 2.3. RESULTS AND OBSERVATIONS

### 2.3.1. Diurnal Distribution of EEJ

The contour plots shown in Figure 2.2 reflect the variation of the eastward equatorial electrojet as a function of days against local time during the quiet days of the year 2009, along the West and East African longitudes, respectively, from the hours of 6:00 to 18:00 LT.

These plots clearly show the diurnal distribution of EEJ along the West and East African longitudes, respectively. It is seen that this diurnal variation displays minimum magnitude in the early morning hours, attains a maximum positive value around noon, while in the afternoon it varies slowly, and gradually subsides at dusk. *Doumouya et al.* [1998] confirmed this pattern of variation mainly near the magnetic equator, and such variation had earlier been attributed to ionospheric augmentation by solar activity in consistency with the atmospheric dynamo theory [*Onwumechili and Ezema*, 1977; *Rabiu et al.*, 2009]. This further confirms that there is a difference in the ionospheric dynamics prevailing during the rising of the electrojet in the morning and its decay in the afternoon [*Rabiu et al.*, 2007b].

The $\Delta H$ profile sometimes reversed during morning and afternoon hours [e.g., *Fambitakoye*, 1976; *Onwumechili*, 1997; *Doumouya et al.*, 1998]. It has also been reported to show a complete reversal during the noon time [*Mayaud*, 1977; *Marriott et al.*, 1979; *Rastogi*, 1994]. Considering Figures 2.2a and b, two distinct areas are observed on the contour maps: the positive field and the negative field. The positive field represents the EEJ, while the negative field at dawn and dusk time is a manifestation of CEJ, which indicates the reversal of the $H$ field.

Figure 2.3 shows a typical CEJ day on 2 March 2009 at Addis Ababa. The negative field values of EEJ found both in the morning and afternoon, at hours 07:00 –10:00 LT and 15:00–17:00 LT, are a manifestation of CEJ. Such negative field was also reported by *Gouin* [1962], *Rastogi and Patel* [1975], *Fambitakoye and Mayaud* [1976], *Mayaud* [1977], *Marriott et al.* [1979], and *Rastogi and Yumoto* [2006]. *Doumouya et al.* [1998] also observed the manifestation of two distinct areas of the $\Delta H$ component in their results and concluded that these

**Table 2.2** Distributions of Days Used in This Work

| Month | Days of availability of data |
|---|---|
| January | 8 |
| February | 10 |
| March | 4 |
| April | 7 |
| May | 9 |
| June | 2 |
| July | 9 |
| August | 8 |

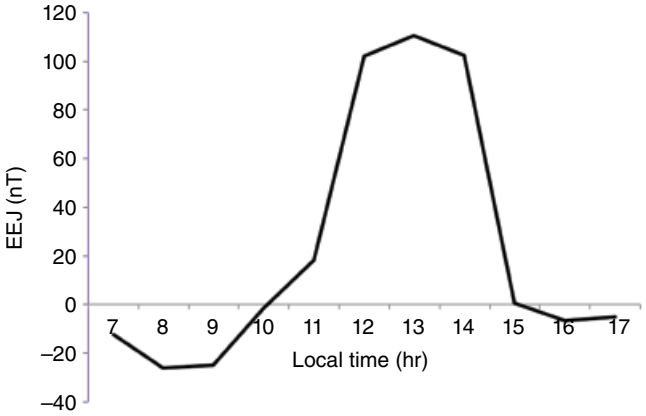


**Figure 2.3** A typical diurnal variation of the equatorial electrojet (EEJ) on 2 March 2009 at Addis Ababa showing morning and afternoon counterequatorial electrojet (CEJ). (The negative field values of EEJ found in both the morning and afternoon at hours 07:00–10:00 LT and 15:00–17:00 LT show manifestation of CEJ.)

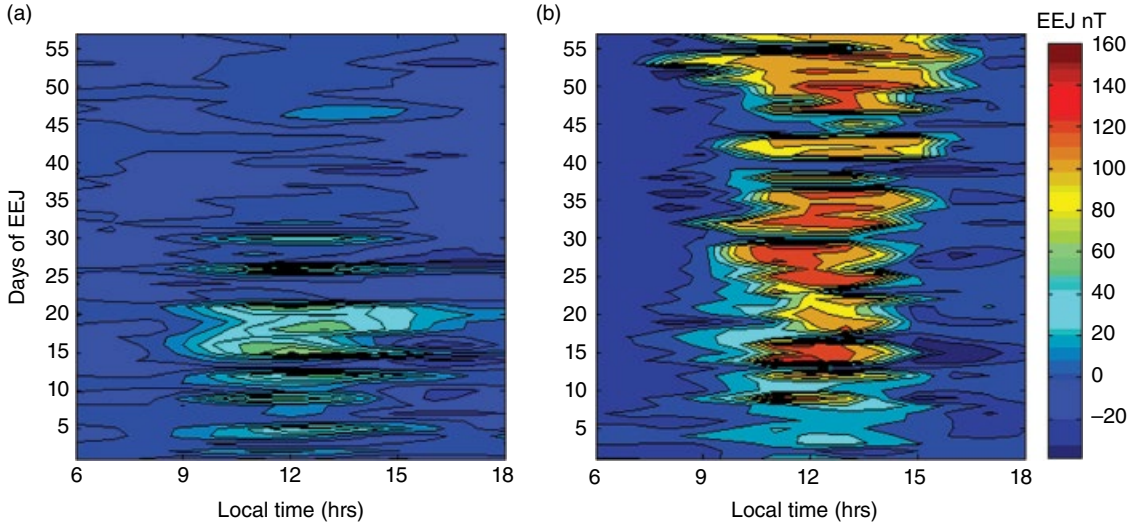


**Figure 2.2** Diurnal variation of equatorial electrojet (EEJ) for consistency with Figure 2.3 along the (a) West African and (b) East African longitudes, respectively.

additional zones are the obvious signature of a reversed current with respect to EEJ, known as the counterequatorial electrojet (CEJ).

The CEJ field for Addis Ababa (AAB), which represents the East African longitude, peaks from 06:00 LT and terminates around 10:00 LT and then later increases from 13:00 LT until it gets to its peak around 17:00 LT. It is clear from Figure 2.2b that CEJ is a dawn and dusk phenomenon. This is in agreement with the reviews of *Mayaud* [1977], *Marriot et al.* [1979], and *Stening* [1992].

The same trend was observed at Ilorin (ILR), which represents the West African longitude, except that the CEJ field at this station extends from 6:00 LT to 18:00 LT. This indicates the occurrence of CEJ around local noon along the West African longitude, which is a rare phenomenon as reported by *Onwumechili* [1997]. This local noon occurrence of CEJ is absolutely absent in the east. This depicts that, on some days, local time differences do exist between the CEJ occurrence along the East and West African longitudes, respectively. The difference in the local time of occurrence of CEJ from one longitude to another is attributed to differences in meridional currents across different longitudes. The direction of meridional current varies significantly with longitude and, possibly, with the local time and season [*Rastogi and Yumoto*, 2006].

### 2.3.2. Simultaneity in the Occurrence of CEJ

The simultaneity in the occurrence of counterequatorial electrojet was chosen based on the day of concurrent occurrence of CEJ at AAB as well as ILR from 06:00 to 11:00 LT in the morning and 13:00 to 18:00 LT in the afternoon hours, respectively. Figure 2.4 shows that the morning simultaneity of CEJ during the year 2009 occurred every day of the months of May and June (100%). February, March, and April have 80%, 71.4%, and 85.7%, while July and August have 66.7% and 77.8%, respectively. The least occurrence was found in January with a percentage of 50. The inequality in the occurrence of the morning simultaneity of EEJ across the months suggests the longitudinal variability of thermospheric winds even on magnetic quiet days as mentioned by *Vichare and Richmond* [2005]. Earlier on, *Hagan and Forbes* [2002, 2003] reported that the thermospheric winds that drive the ionospheric dynamo could have longitudinal variations due to atmospheric solar tides that are not sun synchronous.

For the afternoon simultaneity of the occurrence of CEJ at both longitudes, Figure 2.5 shows that there was no afternoon simultaneity in March; June has the maximum occurrence of 100%, January and February have 50%, while the rest of the months (April, May, July, and August) are relatively below 50%.

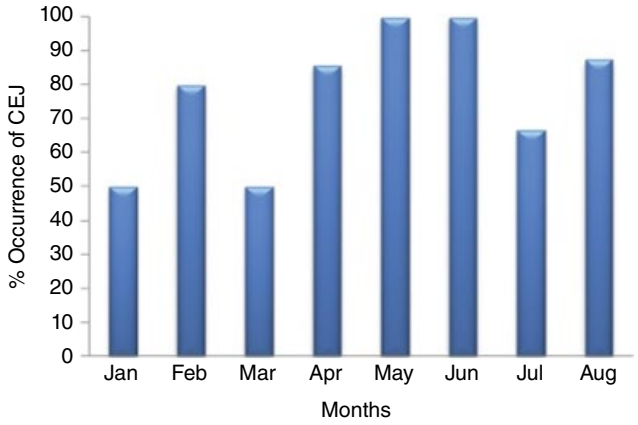


**Figure 2.4** Morning simultaneity of occurrence of counterequatorial electrojet (CEJ) at AAB and ILR.

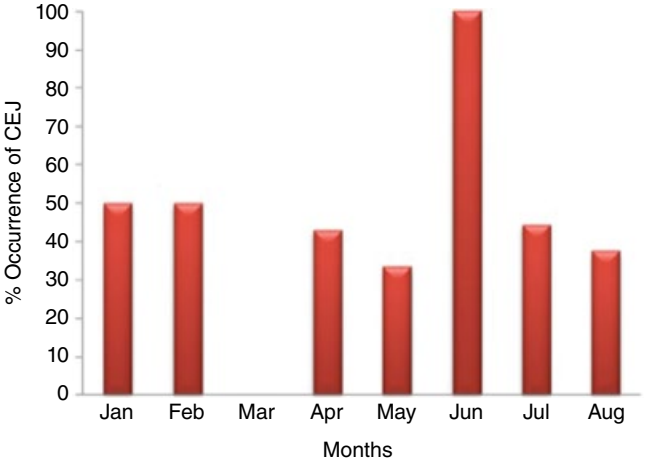


**Figure 2.5** Afternoon simultaneity of occurrence of counterequatorial electrojet (CEJ) at AAB and ILR.

On the whole, the total percentage occurrence of morning simultaneity of CEJ is 77.2% while that of the afternoon simultaneity of CEJ is 42.1%. Hence, the greater occurrence frequency of CEJ simultaneity along the East and West African longitudes was found on days of morning counterequatorial electrojet.

### 2.3.3. Asymmetry in the Occurrence of CEJ

Figure 2.6 shows the percentage morning-afternoon asymmetry (Asym-1) of the occurrence of CEJ for all the months in the year 2009. The percentage Asym-1 in the occurrence of CEJ for all the available months is 0%, except for the months of January, February, and April, which are 12.5%, 10%, and 14.3%, respectively. The maximum percentage frequency of occurrence was in April, having a value of 14.3%, while there was no occurrence in March, May, June, July, or August.

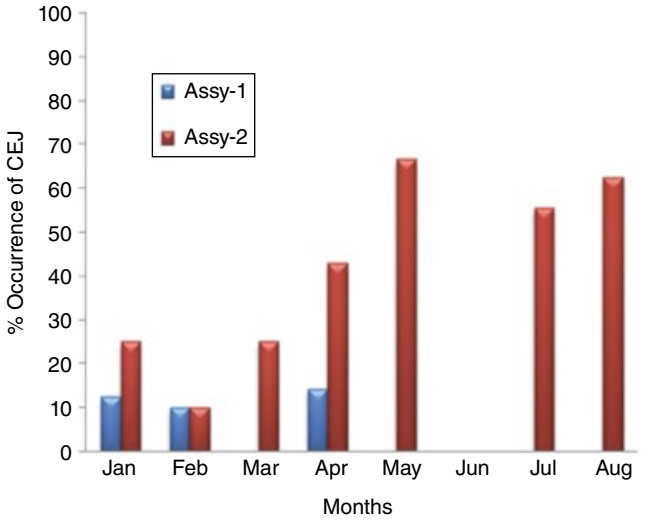


**Figure 2.6** Asymmetry of occurrence of counterequatorial electrojet (CEJ) at AAB and ILR.

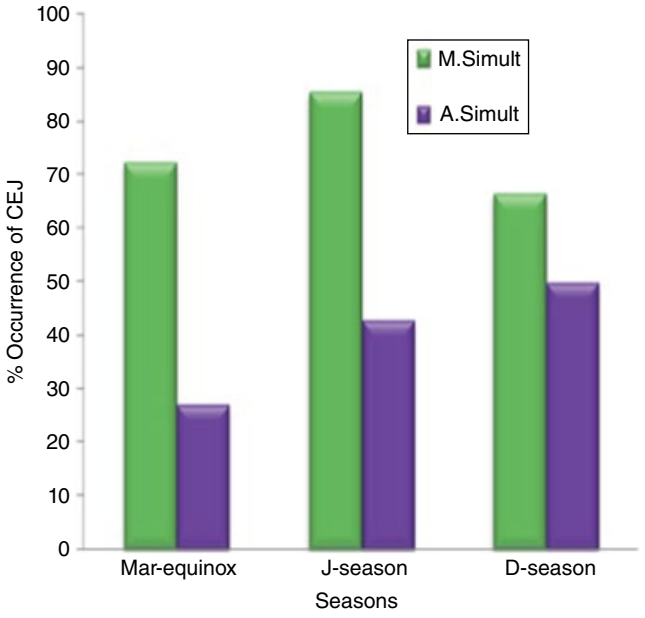


**Figure 2.7** Seasonal simultaneity of occurrence of counter-equatorial electrojet (CEJ) for the March equinox, and the June and December solstices. Green is the morning simultaneity, while purple is the afternoon.

Asymmetry-2 events were chosen based on days of afternoon CEJ at ILR with no afternoon occurrence at AAB but morning CEJ occurrence. Figure 2.5 also displays the result of the percentage Asym-2 in the occurrence of CEJ for each month of the year 2009. The percentage frequency of Asym-2 occurrence varies from one month to the other. It is about 25% in January as well as in March; 10%, 42.9%, 66.7%, 0%, 55.6%, and 62.5% for the months of February, April, May, June, July, and August, respectively. The month of May has the maximum percentage occurrence with a value of 66.7%, while there was no occurrence at all in June.

### 2.3.4. Seasonal Distribution in the Percentage Occurrence of CEJ

The seasonal distributions of CEJ are analyzed as shown in Figure 2.7. In general, the percentage morning simultaneity of CEJ over the year 2009 occurred on about 72.7 per cent of days during the March equinox, about 85.7 per cent of days during the June solstice, and only on 66.7 per cent of days during the December solstice.

For the afternoon simultaneity, CEJ occurred on about 27.3 per cent of days during the March equinox, 42.9 per cent of days during the June solstice, and 50 per cent of days during the December solstice. Figure 2.7 displays the statistical representation of the seasonal distribution of the occurrence of both morning and afternoon simultaneity of counterequatorial electrojet in each season of the year 2009 at ILR and AAB. It is evident that seasonal distribution of the percentage occurrence of morning simultaneity of CEJ is maximum at both stations during the June solstice (85.7%) and minimum during the

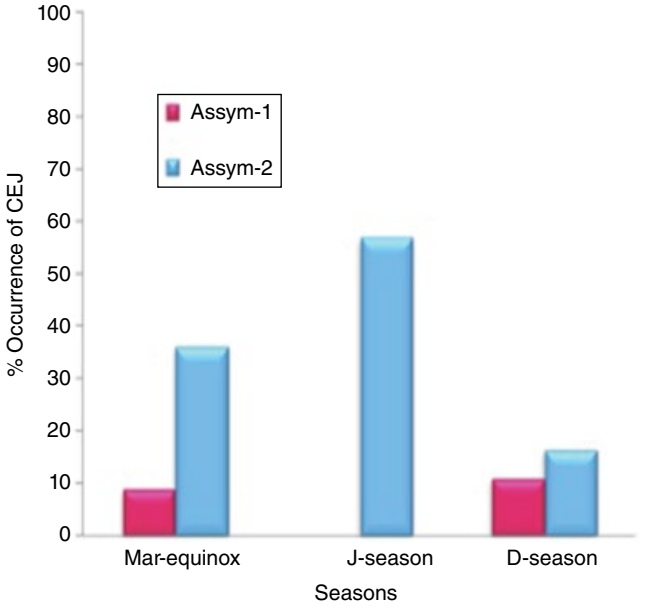


**Figure 2.8** Seasonal asymmetry of occurrence of counterequatorial electrojet (CEJ) for both the East (AAB) and West (ILR) African longitudes. While the March equinox and the December solstice show asymmetry-1, the June solstice does not.

December solstice at 66.7%, while the percentage occurrence of afternoon simultaneity is maximum during the December solstice at 50% but minimum during the March equinox at 47.3%.

### 2.3.5. Asymmetry of the Occurrence of CEJ

The seasonal distributions of the percentage asymmetry of the occurrence of CEJ at each season for the year under study appear in Figure 2.8. On the whole, the percentage occurrence of morning-afternoon asymmetry (Asym-1) of CEJ over the year 2009 during March equinox was 9.1% and 11.1% during the December solstice, while there was no occurrence of Asym-1 during the June solstice for both the East (AAB) and West (ILR) African longitudes. Therefore, Asym-1 is maximum during the December solstice.

For the afternoon-morning asymmetry (Asym-2), the percentage occurrence of CEJ over the year 2009 for each season is about 36.4% in March equinox, 57.1% during the June solstice, and only 16.7% during the December solstice. It is clearly seen that occurrence of Asym-2 CEJ at both longitudes is maximum during the June solstice (57.1%) and minimum during the December solstice (16.7%). The frequency of occurrence of Asym-2 of CEJ in the East and West African longitudes is clearly shown to be greater than the Asym-1 occurrence, for all the seasons.

## 2.4. DISCUSSION

Many researchers have established that the strength of the equatorial electrojet is controlled by the eastward electric field, neutral winds, longitudinal gradients of the electric fields, and ionospheric conductivities [*Ananda Rao*, 1976; *Gagnepain et al.*, 1976; *Ananda Rao et al.*, 1977; *Bhargava and Sastri*, 1977; *Woodman et al.*, 1977; *Crochet et al.*, 1977; *Raghavarao and Anandarao*, 1980, 1987; *Kane and Trivedi*, 1981; *Alex et al.*, 1986; *Deminov et al.*, 1988; *Benkova et al.*, 1990; *Patil et al.*, 1990a and 1990b; *Rangarajan and Rastogi*, 1993; *Onwumechili*, 1997; *Alex and Mukherjee*, 2001; *Vichare and Richmond*, 2005; and *Yizengaw et al.*, 2014]. *Stening* [1977] emphasized that the EEJ current and the *Sq* current are driven mainly by the electric fields that originate in the global wind dynamo and its associated day-to-day variations resulting in the variability of equatorial electrojet along with that of the *Sq* current system.

The concurrent occurrences in the MCEJ (Fig. 2.3) are established at both stations, as also observed by *Mayaud* [1977] and *Alex and Mukherjee* [2001]. The greater occurrence frequency of CEJ simultaneity along the East and West African longitudes was found on days of MCEJ. This result is at variance with the work of *Alex and Mukherjee* [2001], who found most frequent days of simultaneity of CEJ at Addis Ababa and Trivandrum to be in the afternoon hours.

Our work recorded lesser concurrent occurrence of afternoon CEJ than concurrent morning CEJ. *Rastogi* [1973] suggested the possibility that the ACEJ can be fairly localized in nature and may not occur concurrently at two stations even if they are separated only by 2–3 hr longitude. *Kane* [1973] reported such cases to be due to short-lived equatorial wind typhoons at ionospheric heights. *Rastogi* [1974] showed that the occurrence of the morning and ACEJ events is correlated with the time of maximum effect of the lunar semidiurnal magnetic variation.

*Ananda Rao* [1976] and *Ananda Rao et al.* [1977] investigated the effects of horizontal wind shears and the effects of vertical winds on CEJs. The limited longitudinal extent of the phenomenon of occurrence of CEJ at both stations in the afternoon hours could necessarily be attributed to the influence of local winds confined to a narrow longitude zone. The asymmetry characteristics demonstrated by CEJ occurrence may be attributed to theoretical findings of earlier researchers on localized wind dynamo, vertical local winds, and neutral wind shears [*Raghava Rao and Ananda Rao*, 1980; *Kane and Trivedi*, 1981; *Rangarajan and Rastogi*, 1993], but need to be subjected to further study to understand adequately the reason for this occurrence pattern.

The seasonal distribution of simultaneity and asymmetry of CEJ occurrence shows a maximum during the June solstice and agreed with the solstitial maximum in CEJ occurrence observed in the Brazilian sector by *Denardini et al.* [2009]. The counterelectrojet is known to be more frequent during solar minimum solstice months [*Mayaud*, 1977]. *Ezema et al.* [1996], in consistency with *Marriot et al.* [1979], reported that occurrences of morning and afternoon CEJ in the Indian sector in 1986 are more frequent during the June solstice than in the other seasons. It should be noted that the seasonal distribution of the occurrences of CEJ at different time regimes implies a seasonal variability of the mechanisms responsible for the occurrence of CEJ. Such causative mechanisms linked to seasonal variabilities affecting the seasonal distribution of occurrence of CEJ include any of the following or their combination: height-varying local winds capable of causing the reversal in the current system [*Richmond*, 1973], gravity wave-associated vertical winds [*Raghavarao and Anandarao*, 1980], global-scale tidal winds with appropriate phase combination [*Forbes and Lindzen*, 1976; *Marriott et al.*, 1979; *Forbes*, 1981; *Singh and Cole*, 1987; *Stening*, 1989; *Somayajulu et al.*, 1993], high-latitude stratospheric warming events [*Stening et al.*, 1996, *Vineeth et al.*, 2009], daytime vertically driven downward electric field (negative Ez) [*Onwumechili*, 1997], and semidiurnal tide [*Gurubaran*, 2002, *Sridharan et al.*, 2002, 2009].

## 2.5. CONCLUSION

1. The maximum occurrence of morning simultaneity (100%) of CEJ was observed in the months of May and June; while the least occurrence was in January with 50%.

The afternoon simultaneity of CEJ has maximum occurrence in June (100%), while there was no occurrence in March.

2. The maximum percentage frequency of Asymmetry-1 occurrence of CEJ was observed in April having a value of 14.3%, while there was no occurrence in March, May, June, July, or August, respectively. The month of May has the maximum percentage Asym-2 with a value of 66.7%, while there was no occurrence at all in June.

3. Most frequent and simultaneous occurrence of CEJ at both equatorial stations was found on days of morning counterequatorial electrojet (77.2%). The occurrence of Asym-2 is much more prevalent at both longitudes (31.5%) than Asym-1 (5.3%).

4. The occurrences of morning simultaneity of CEJ and Asym-2 CEJ are maximum during the June solstice season and minimum during the December solstice, respectively. The afternoon simultaneity of CEJ is maximum during the December solstice and minimum during the March equinox, while Asym-1 is maximum during the December solstice and has no occurrence during the June solstice.

5. Seasonal distribution of the occurrences of CEJ at different time regimes implies a seasonal variability of the mechanisms responsible for the occurrence of CEJ.

## ACKNOWLEDGMENTS

The Magnetic Data Acquisition System (MAGDAS) data used for this paper were obtained from the International Center for Space Weather Science and Education (ICSWSE), Kyushu University, Fukuoka, Japan. This work was supported by Japan Society for the Promotion of Science (JSPS) JSPS KAKENHI Grant Number 268022. The MAGDAS/CPMN group at International Center for Space Weather Science and Education (ICSWSE), Kyushu University, Japan, and all hosts of the MAGDAS facilities at the stations whose data were engaged in this research.

## REFERENCES

Alex, S., and M. M. Jadhav (2007), Day-to-day variability in the occurrence characteristics of Sq focus during d-months and its association with diurnal changes in the declination component, *Earth Planets Space*, *59*(12), 1197–1203; doi:10.1186/BF03352067.

Alex, S., and S. Mukherjee (2001), Local time dependence of the equatorial counter electrojet effect in a narrow longitudinal belt, *Earth Planets Space*, *53*(12), 1151–1161; doi:10.1186/BF03352410.

Alex, S., A. R. Patil, and R. G. Rastogi (1986), Equatorial counter electrojet, solution of some dilemma, *Ind. J. Radio Space Phys.*, *15*, 114–118.

Ananda Rao, B. G. (1976), Effects of gravity wave winds and wind shears on equatorial electrojet, *Geophys. Res. Lett.*, *3*, 545–547; doi:10.1029/GL003i009p00545.

Ananda Rao, B. G., R. Ragahava Rao, and C. Raghava Reddi (1977), Electric fields by gravity wave winds in the equatorial electrojet, *J. Geophys. Res.*, *82*, 1513.

Benkova, N. P., M. G. Deminov, A. T. Karpachev, N. A. Kochenova, Y. V. Kusnerevsky, V. V. Migulin, S. A. Pulinets, and M. D. Fligel (1990), Longitude features shown by topside sounder data and their importance in ionospheric mapping, *Adv. Space Res.*, *10*, (8)57–(8)66; doi:10.1016/0273-1177(90)90186-4.

Bhargava, B. N., and N. S. Sastri, (1977), A comparison of days with and without occurrence of counter electrojet afternoon events in the Indian region, *Ann. Geophys.*, *33*, 329–333.

Chapman S. (1951), The equatorial electrojet as detected from the abnormal electric current distribution above Huancayo, Peru and elsewhere, *Arch. Meteorol. Geophys. Bioclimatol. Serv.*, *A4*, 368–390; doi:10.1007/BF02246814.

Crochet, M., C. Hanuise, and P. Broche (1979), HF radar studies of two-stream instability during an equatorial counter electrojet, *J. Geophys. Res.*, *84*, 5223–5233; doi:10.1029/JA084iA09p05223.

Deminov, M. G., N. A. Kochenova, and I. S. Sitnov (1988), Longitudinal electric-field variations in the daytime equatorial ionosphere, *Geomagnet. Aeronom.*, *28*, 71–75.

Denardini C. M., M. A. Abdu, H. C. Aveiro, L. C. A. Resende, P. D. S. C. Almeida, E. P. A. Olivio, J. H. A. Sobral, and C. M. Wrasse (2009), Counter electrojet features in the Brazilian sector, simultaneous observation by radar, digital sounder and magnetometers, *Ann. Geophys.*, *27*, 1593–1603; doi:10.5194/angeo-27-1593-2009.

Doumouya V., J. Vassal, Y. Cohen, O. Fambitakoye, and M. Menvielle (1998), Equatorial electrojet at African lLongitudes: First result from magnetic measurements, *Ann. Geophys. 16*, 658–676; doi:10.1007/s00585-998-0658-9.

Egedal, J. (1947), The magnetic diurnal variation of the horizontal force near the magnetic equator, *Terr. Magn. Atmos. Electr.*, *52*, 449–451; doi:10.1029/TE052i004p00449.

Egedal, J. (1948), Daily variation of the horizontal magnetic force at the geomagnetic equator, *Nature*, *161*, 443–449.

Ezema, P. O., C. A. Onwumechili, and S. O. Oko (1996), Geomagnetically quiet day ionospheric currents over the Indian sector-III. Counter equatorial electrojet currents, *J. Atmos. Terr. Phys.*, *58*, 565–571; doi:10.1016/0021-9169(95)00057-7.

Fambitakoye, O., and P. N. Mayaud (1976a), Equatorial electrojet and regular daily variation $S_R$–II: The centre of equatorial electrojet, *J. Atmos. Terr. Phys.*, *38*, 19–26; doi:10.1016/0021-9169(76)90189-6.

Fambitakoye, O., R. G. Rastogi, J. Tabbagh, and P. Vila (1973), Counter electrojet and Esq disappearance, *J. Atmos. Terr. Phys.*, *35*, 1119–1126; doi:10.1016/0021-9169(73)90009-3.

Forbes, J. M. (1981), The equatorial electrojet, *Rev. Geophys. Space Phys.*, *19*, 469–504; doi:10.1029/RG019i003p00469.

Forbes, J. M., and R. S. Lindzen (1976), Atmospheric solar tides and their electrodynamic effects–II. The equatorial electrojet, *J. Atmos. Terr. Phys.*, *38*, 911–920; doi:10.1016/0021-9169(76)90074-X.

Gagnepain, J., M. Crochet, and A. D. Richmond (1976), Theory of longitudinal gradients in the equatorial electrojet, *J. Atmos. Terr. Phys.*, *38*, 279–286; doi:10.1016/0021-9169(76)90094-5.

Gouin, P. (1962), Reversal of the magnetic daily variations at Addis Ababa, *Nature*, *139*, 1145–1146; doi:10.1038/1931145a0.

Gouin, P., and P. N. Mayaud (1967), A propos de l'existence possible d'un contre-électrojet aux latitudes, magnétiques équatoriales, *Ann. Géophys.*, *23*(1), 41–47.

Graham, G. (1724), An account of observations made of the variation of the horizontal needle at London, in the later part of the year 1722 and beginning of 1723. *Philosophical Transaction Royal Society, London, A*, *32*.

Gurubaran, S. (2002), The equatorial counter electrojet: Part of a worldwide current system? *Geophys. Res. Lett.*, *29*(9), 1337; doi:10.1029/2001GL014519.

Hagan, M. E., and J. M. Forbes (2002), Migrating and nonmigrating diurnal tides in the middle and upper atmosphere excited by tropospheric latent heat release, *J. Geophys. Res.*, *107*(D24), 475; doi :10.1029/2001JD001236.

Hagan, M. E., and J. M. Forbes (2003), Migrating and nonmigrating semi-diurnal tides in the upper atmosphere excited by tropospheric latent heat release, *J. Geophys. Res.*, *108*(A2), 1062; doi:10.1029/2002JA009466.

Hanuise, C., C. Mazaudier, P. Vila, M. Blanc, and M. Crochet (1983), Global dynamo simulation of ionospheric currents and their connection with the equatorial electrojet and counter electrojet: A case study, *J. Geophys. Res.*, *88*, 253–270; doi:10.1029/JA088iA01p00253.

Hutton, R., and J. O. Oyinloye (1970), The counter electrojet in Nigeria, *Ann. Geophys.*, *26*, 921–926.

Kane, R. P. (1973), Longitudinal extent of the counter electrojet, *Physical Research Laboratory, Report AER*, 73–78, Ahmedabad.

Kane, R. P., and N. B. Trivedi (1981), Confinement of equatorial counter electrojet to restricted longitudes, *J. Geomag. Geoelectr.*, *33*, 379–382; doi:10.5636/jgg.33.379.

Marriott, R. T., Richmond, A. D., and S. V. Venkateswaran (1979), The quiet time equatorial electrojet and counter-electrojet, *J. Geomag. Geoelect.*, *31*, 311–340; doi:10.5636/jgg.31.311.

Mayaud P. N. (1977), The equatorial counter electrojet: A review of its geomagnetic aspects, *J. Atmos. Terr. Phys.*, *39*, 1055–1070; doi:10.1016/0021-9169(77)90014-9.

Onwumechill, A. (1963), Lunar effects on the diurnal variation of the geomagnetic horizontal field near the magnetic equator, *J. Atmos. Terr. Phys.*, *25*, 55–70; doi:10.1016/0021-9169(63)90115-6.

Onwumechili A., and S. I. Akasofu (1972), On the abnormal depression of Sq(H) under the equatorial electrojet in the afternoon, *J. Geomag. Geoelect.*, *24*, 161–173; doi:10.5636/jgg.24.161.

Onwumechili, C. A. (1997), *The Equatorial Electrojet*, Gordon and Breach Science Publishers, The Netherlands, 627 pp.

Onwumechili, C. A., and P. O. Ezema (1977), On course of the geomagnetic daily variation in low latitudes, *J. Atoms. Terr. Phys.*, *39*, 1079–1086; doi:10.1016/0021-9169(77)90016-2.

Patil, A. R., D. R. K. Rao, and R. G. Rastogi (1990a), Equatorial electrojet strength in the Indian and American sectors; Part I, during low solar activity, *J. Geomagn. Geoelectr.*, *42*, 801–811; doi:10.5636/jgg.42.801.

Patil, A. R., D. R. K. Rao, and R. G. Rastogi (1990b), Equatorial electrojet strength in the Indian and American sectors; Part II, During high solar activity, *J. Geomag. Geoelect.*, *42*, 813–823.

Rabiu A. B. (2000), Geomagnetic Field Variation at Mid-Latitudes, Ph.D. Thesis, University of Nigeria, Nsukka.

Rabiu A. B., A. I. Mamukuyomi, and E. O. Joshua (2007a), Variability of equatorial ionosphere inferred from geomagnetic field measurements, *Bull. Astron. Soc. India*, *35*, 607–618.

Rabiu A. B., N. Nagarajan, and K. Saratchandra (2007b), Rising and Decay Rates of Solar Quiet Daily Variation and Electrojet at Equatorial Region, *Online Journal of Earth Sciences*, *1*, 85–92; http://medwelljournals.com/abstract/?doi=ojesci.2007.85.92.

Rabiu, A. B., I. A. Adimula, K. Yumoto, J. O. Adeniyi, G. Maeda (2009), Preliminary results from the magnetic field measurements using MAGDAS at Ilorin, Nigeria, *Earth, Moon, and Planets*, *104*, 173; doi:10.1007/s11038-008-9290-7.

Raghvarao, R., and B. G. Anandarao (1980), Vertical winds as a plausible cause for equatorial counter electrojet, *Geophys. Res. Lett.*, *7*, 357–360; doi:10.1029/GL007i005p00357.

Raghavarao, R., and B. G. Anandarao (1987), Equatorial electrojet and counter electrojet, *Ind. J. Radio Space Phys., 16,* 54–75.

Rangarajan, G. K. and R. G. Rastogi (1993), Longitudinal difference in magnetic field variations associated with quiet day counter electrojet, *J. Geomag. Geoelectr.*, *45*, 649–656; doi:10.5636/jgg.45.649.

Rastogi, R. G. (1973), Equatorial sporadic E and the electric field, *J. Atmos. Terr. Phys.*, *35*, 367–371; doi:10.1016/0021-9169(73)90103-7.

Rastogi, R. G. (1974), Westward equatorial electrojet during daytime hours, *J. Geophys. Res.*, *79*, 1503–1512; doi:10.1029/JA079i010p01503.

Rastogi, R. G. (1994), Ionospheric current system associated with equatorial counter electrojet, *J. Geophys. Res.*, *99*(A7), 13209–13217; doi:10.1029/93JA03028.

Rastogi R. G., and K. Yumoto (2006), Equatorial electrojet in the East Brazil anomaly region, *Earth Planets and Space*, *58*, 103–106; doi:10.1186/BF03352682.

Rastogi, R. G., and V. L. Patel (1975), Effect of interplanetary magnetic field on ionosphere over the magnetic equator, *Proc. Ind. Acad. Sci.*, *82*(4), 121–141; doi: 10.1007/BF03046722.

Richmond, A. D. (1973), Equatorial electrojet. I. Development of model including winds and instabilities, *J. Atmos. Terr. Phys.*, *35*, 1083–1103; doi:10.1016/0021-9169(73)90007-X.

Sastry, N. S., and R. W. Jayakar (1972), Afternoon depression in horizontal component of the geomagnetic field at Trivandrum, *Ann. Geophys.*, *28*(3), 589–591.

Singh, A., and K. D. Cole (1987), A numerical model of the ionospheric dynamo–III, Electric current at equatorial and low latitudes, *J. Atmos. Terr. Phys.*, *49*, 539–547; doi:10.1016/0021-9169(87)90069-9.

Somayajulu, V. V., L. Cherian, K. Rajeev, G. Ramkumar, and C. Raghava Reddy (1993), Mean winds and tidal components

during counter electrojet events, *Geophys. Res. Lett.*, *20*, 1443–1446; doi:10.1029/93GL00088.

Sridharan, S., S. Gurubaran, and R. Rajaram (2002), Structural changes in the tidal components in mesospheric winds as observed by the MF radar during afternoon counter electrojet events, *J. Atmos. Solar Terr. Phys.*, *64*, 1455–1463; doi:10.1016/S1364-6826(02)00109-8.

Sridharan, S., S. Sathishkumar, and S. Gurubaran (2009), Variabilities of mesospheric tides and equatorial electrojet strength during major stratospheric warming events, *Ann. Geophys.*, *27*, 4125–4130; doi:10.5194/angeo-27-4125-2009.

Stening, R. J. (1977), Analysis of contributions to Ionospheric dynamo currents from e.m.f.'s at different latitudes, *Planet. Space Sci.*, *25*, 587–594; doi:10.1016/0032-0633(77)90065-4.

Stening, R. J. (1989), A calculation of ionospheric currents due to semidiurnal asymmetric tides, *J. Geophys. Res.*, *94*, 1525–1531.

Stening R. J. (1992), The enigma of the counter electrojet and lunar tidal influences in the equatorial region, *Adv. Space Res. 12*, 623–632; doi:10.1016/0273-1177(92)90036-W.

Stening, R. J., C. E. Meek, and A. H. Manson (1996), Upper atmospheric wind systems during reverse equatorial electrojet events, *Geophys. Res. Lett.*, *23*, 3243–3246; doi:10.1029/96GL02611.

Stewart, B. (1882), Terrestrial magnetism, in *Encyclopaedia Britannica*, 9th ed.

Vestine E. (1947), *The Geomagnetic Field, its Description and Analysis*, Carnegie Institute, Washington Publ., *580*.

Vichare, G., and A. D. Richmond (2005), Simulation study of the longitudinal variation of evening vertical ionospheric drifts at the magnetic equator during equinox, *J. Geophys. Res.*, *110*, A05304; doi:10.1029/2004JA010720.

Vineeth, C., T. Kumar Pant, and R. Sridharan (2009), Equatorial counter electrojets and polar stratospheric sudden warmings: A classical example of high latitude-low latitude coupling? *Ann. Geophys.*, *27*, 3147–3153; doi:10.5194/angeo-27-3147-2009.

Woodman, R. F., R. G. Rastogi, and C. Calderon (1977), Solar cycle effects on the electric fields in the equatorial ionosphere, *J. Geophys. Res.*, *82*(32), 5257–5260; doi:10.1029/JA082i032p05257.

Yizengaw, E., M. B. Moldwin, C. Zesta, C. M. Biouele, B. Damtie, A. Mebrahtu, A. B. Rabiu, and R. Stoneback (2014), The longitudinal variability of equatorial electrojet and vertical drift velocity in the African and American sectors, *Ann. Geophys.*, *32*, 231–238; doi:10.5194/angeo-32-231-2014.

# 3

# Stormtime Equatorial Electrojet Ground-Induced Currents: Increasing Power Grid Space Weather Impacts at Equatorial Latitudes

**Mark B. Moldwin and Justin S. Tsu**

## ABSTRACT

Auroral electroject ground-induced currents (GIC) are well-known space weather effects in the auroral zones and midlatitudes. The equatorial electrojet (EEJ) gives rise to large ground magnetic perturbations within a few degrees of the geomagnetic equator. As electrification and transnational power grids develop in regions below the EEJ in South America, Africa, India, and Southeast Asia, space-weather GIC impacts should become more prevalent. This study estimates GIC perturbations due to geomagnetic stormtime EEJ intensifications and discusses their potential role in enhanced space-weather power grid impacts in rapidly economically growing equatorial countries.

**Key Points:**
The equatorial electrojet (EEJ) can impact power grids through ground-induced currents (GIC).
Equatorial nations are economically growing fast and developing transnational power grids.
The development of these new power grids makes these countries increasingly susceptible to space weather impacts.

**Key Terms:** ground-induced currents (GIC), equatorial electrojet (EEJ), power grid

## 3.1. INTRODUCTION

Ground-induced currents (GIC) are well-known space-weather hazards to power grid systems in high latitudes and midlatitudes and are mainly driven by large auroral electroject (AEJ) intensifications during large geomagnetic storms and substorms [e.g., *Pirjola*, 2002; *Kappenman*, 2004; *Moldwin*, 2008; *Fiori et al.*, 2014]. Since the largest geomagnetic perturbations (dB/dt) occur due to the AEJ, GICs have generally been a concern for high latitudes and for large geomagnetic storms in which the auroral oval (and hence the AEJ) move equatorward to midlatitudes. The magnetopause current and the ring current during large geomagnetic storms also can generate a large magnetic perturbation due to the sudden storm commencement (SSC) and the main phase that could also drive GIC in midlatitudes and low latitudes [e.g., *Kappenman*, 2003; 2006, *Liu et al.*, 2009], but generally the SSC amplitude is smaller (100 s of nT changes over minutes) compared to large substorm perturbations (which can reach over 1000 nT change over minutes). Because of this, "conventional wisdom" holds that for "low-latitude regions…GICs should be small and harmless as a rule" [*Trivedi et al.*, 2007].

A similar east-west current system to the AEJ exists under the geomagnetic equator and is called the equatorial electrojet (EEJ) [e.g., *Amory-Mazaudier et al.*, 2005] and gives rise to normally small dB/dt signatures that are constrained to a narrow latitudinal belt around the

*Atmospheric, Oceanic, and Space Science (AOSS), University of Michigan, Ann Arbor, Michigan, USA*

*Ionospheric Space Weather: Longitude and Hemispheric Dependences and Lower Atmosphere Forcing, Geophysical Monograph 220*, First Edition. Edited by Timothy Fuller-Rowell, Endawoke Yizengaw, Patricia H. Doherty, and Sunanda Basu.

geomagnetic equator. The current (and associated electric field) system gives rise to a vertical $\mathbf{E} \times \mathbf{B}$ drift that leads to a variety of space-weather impacts such as satellite radio scintillation and large off the equator density peaks (Appleton anomaly) that can impact GPS signals [e.g., *Stening*, 2005], but generally have not been considered with regard to GIC until recently [e.g., *Ngwira et al.*, 2013]. In general, the EEJ gives rise to small dB/dt [e.g., *Ducruix et al.*, 1977]. However, during geomagnetic storms, the prompt penetration (PP) electric field can result in large EEJ intensifications [e.g., *Ngwira et al.*, 2013].

In addition to generally having smaller geomagnetic perturbations at low latitudes, GICs have not been a concern traditionally because the power-grid infrastructure at low latitudes (equatorial South America, Africa, and Asia) has been less developed than at midlatitudes (Europe, Japan, USA). However, over the last few decades, these equatorial region countries have had some of the fastest growing economies [*IMF*, 2014] and the development of transnational power grids that now leaves their economies and technological infrastructure susceptible to space-weather hazards. In addition to these expanding and interconnected grids in countries directly beneath the EEJ, there are a number of "super-grid" proposals that would connect low-latitude and equatorial power sources to population centers on different continents (e.g., connecting solar powered generation stations in the Sahara to Europe) that in some cases span the EEJ [e.g., *Lloyd's*, 2010].

This brief chapter examines the magnitude of geomagnetic perturbations under the equatorial electrojet and describes the growth of power-grid infrastructure in Brazil, Africa, India, and southeast Asia to demonstrate that space-weather GICs are now global concerns. Many high-latitude and midlatitude countries have developed mitigation strategies to respond to space-weather power grid impacts [e.g., *Kappenman*, 2010; *Arajarvi et al.*, 2011] that equatorial nations should also consider.

## 3.2. GROUND-INDUCED CURRENTS AND THE EQUATORIAL ELECTROJET

Ground-induced currents can flow into the power grid and cause transformer failure (see excellent overview of GIC by *Kappenman* [2007]). Often the geomagnetic perturbation (dB/dt or dH/dt, the horizontal component of the geomagnetic field) is used as a proxy for the strength of the GIC in power transmission lines [e.g., *Ngwira et al.*, 2013]. The currents due to geomagnetic storms (including sudden storm commencement and main phase responses of the magnetopause and ring current as well as intensifications of the EEJ) can give rise to large dB/dt signatures at low latitudes.

The equatorial electroject is confined to a narrow (few degree) region around the geomagnetic dip equator that is characterized by large amplitude magnetic perturbations [see Fig. 3.1 and the review by *Abdu*, 1997]. These perturbations can couple within the conductive layer of the Earth's surface to induce currents (GIC) [e.g., *Rastogi*, 2004]. Figure 3.2 shows the horizontal magnetogram for an EEJ station (Guam) during a geomagnetic storm. The amplitude of the dH/dt is approximately 100 nT/min.

*Ngwira et al.* [2013] measured the size of the GIC as a function of latitude and found that the largest values are associated with the auroral electrojet and rapidly decrease in strength with decreasing latitude, but that the EEJ gives rise to an order of magnitude increase compared to the surrounding low-latitude regions. The typical dB/dt amplitudes of the 12 storms in this study under the EEJ are similar to those shown in Figure 3.2. In contrast, *Kuvshinov et al.* [2007] found that EEJ contributed insignificantly to induced effects except along coastlines, pointing out the important role that ground conductivity plays in determining the size of the GIC. Note that most of the countries that are beneath the EEJ have their major population centers (and hence power transmission lines) along the coast.

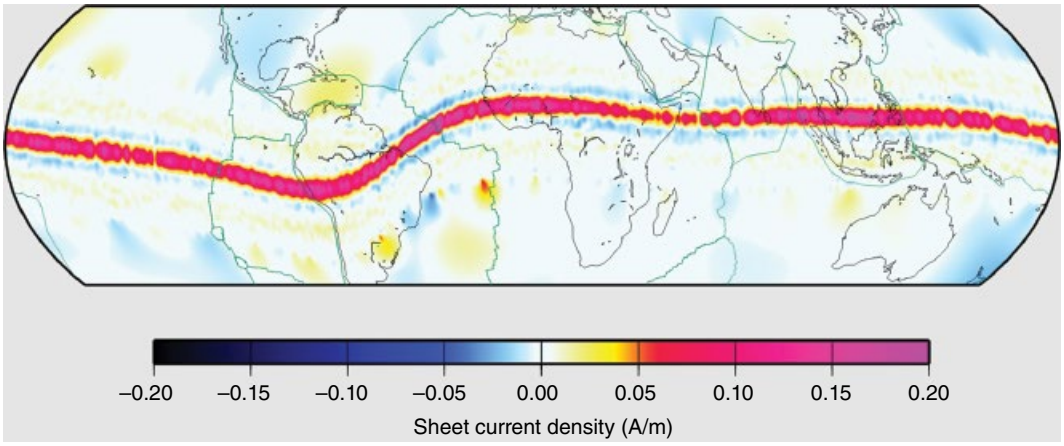


**Figure 3.1** Map of the equatorial electrojet (EEJ) current density as inferred by the CHAMP satellite [from *Lühr et al.*, 2004].

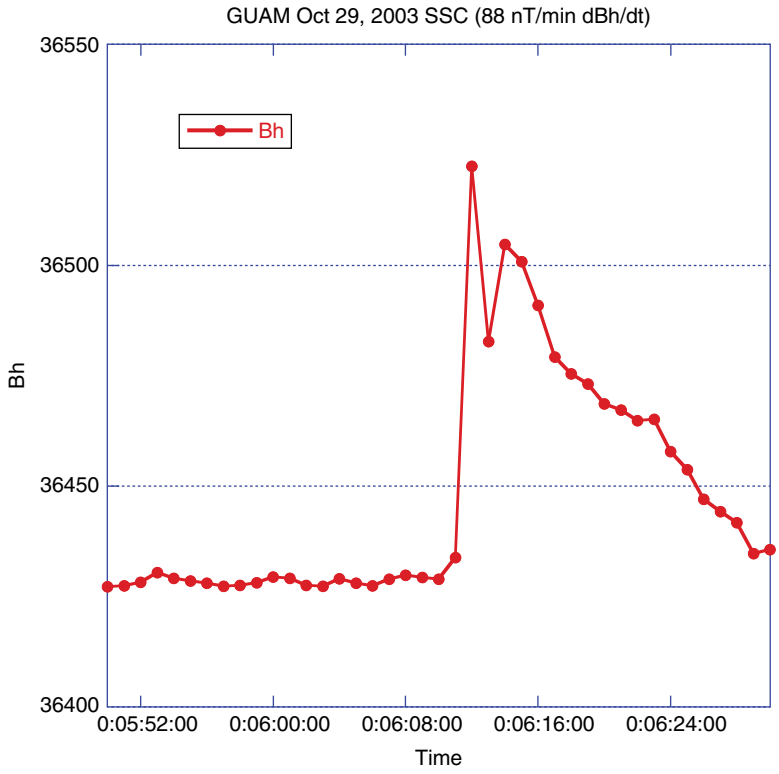


**Figure 3.2** Magnetogram of the horizontal magnetic field observed at Guam during an SSC for the 29 October 2003 geomagnetic storm.

## 3.3. EQUATORIAL COUNTRY ECONOMIC GROWTH AND DEVELOPMENT OF TRANSNATIONAL POWER GRIDS

Some of the fastest growing economies in the world post-2008 recession are the so-called BRICS countries (Brazil, Russia, India, China, and South Africa) [e.g., *Mallick and Sousa*, 2013]. Brazil and India are directly under the equatorial electrojet and have rapidly growing electric infrastructure. Other fast growing economies include those in SE Asia (Vietnam, Malaysia, Indonesia) and sub-Saharan Africa (particularly Nigeria). All of these regions have been developing transnational power grid distribution systems. This chapter examines the power transmission grids of Brazil, sub-Saharan Africa, India, and Southeast Asia.

### 3.3.1. Brazil

Brazil is the fifth largest country in the world in terms of size (8,515,767 km$^2$, about the same size of Europe) and population (202,680,000 www.ibge.gov.br/apps/populacao/projecao/) and is the world's seventh largest economy. The geomagnetic equator and equatorial electrojet runs directly above the north-central part of the country. To increase the reliability of the power system, Brazil has been developing a large power transmission network connecting the different regions of the country (Fig. 3.3). This transmission grid spans the physical size of Europe and connects hydroelectric generation plants in the Amazon basin to population centers on the coast.

### 3.3.2. Africa

Sub-Saharan Africa is the fastest growing region of the world in terms of population [*PRB*, 2013] and the economy of the region has been growing and is forecast to continue to have steady growth [*IMF*, 2013]. Access to electricity is one of the significant issues hindering public health and economic development [e.g., *Kanagawa and Nakata*, 2008]. With over two out of three people (nearly 600 million) without regular access to electricity [*USAID*, 2014], significant investment in the power infrastructure of the region is ongoing, with the development of hydroelectric, conventional, and off-grid initiatives. The major investments have developed or are developing transnational or extensive national distribution networks. Figure 3.4 (from *Szabó et al.* [2011]) shows some of the existing transnational high-voltage power grids in Sub-Saharan Africa. Note the high-concentration of power lines in West Africa and Ethiopia, both directly under the equatorial electrojet.

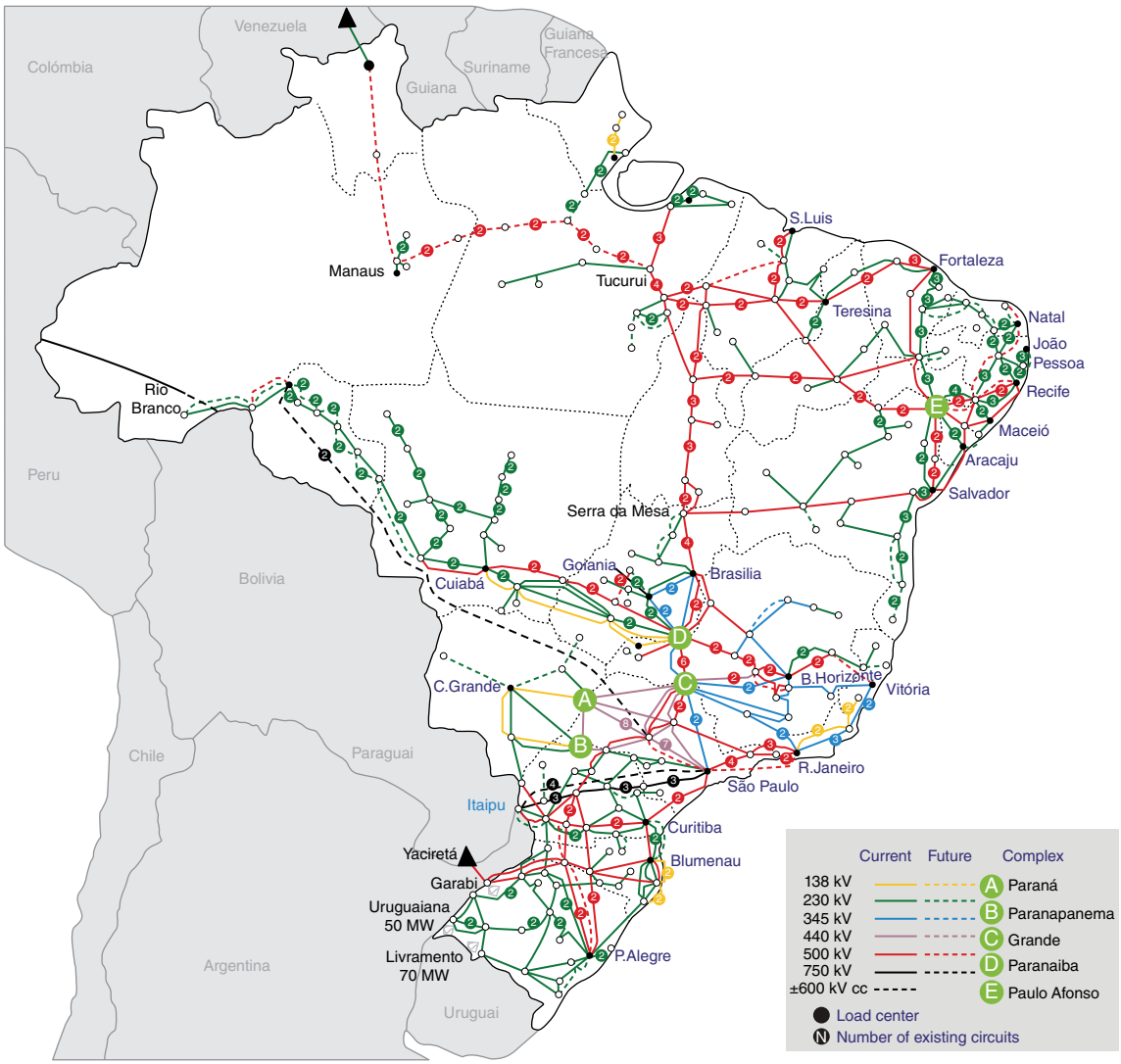


**Figure 3.3** Brazilian power transmission grid as of 2013 (from Electric System National Operator [ONS]).

### 3.3.3. India

India has one of the largest populations and dynamic economies in the world [*IMF*, 2014]. In 2012, India also experienced the world's largest power outages in terms of population impacted [e.g., *Zhang et al.*, 2013]. Due to the impact on economic growth of poor power-grid infrastructure, significant development of the power transmission grid has been undertaken in the last few years culminating in the completion of a truly national grid in 2013 [*Bashkar et al.*, 2014]. This initiative interconnected the different regional grids into a national grid (see Fig. 3.5). Even before the complete integration of the grid, the susceptibility of the grid to cascading failures was clearly highlighted in the 2012 outages that impacted over 600 million people [e.g., *Yardley and Harris*, 2012]. Since southern India lies directly beneath the geomagnetic equator, GIC due to the EEJ is one more potential worry for the Indian power distribution network.

### 3.3.4. Southeast Asia

Southeast Asia is home to some of the fastest growing economies in the world as well as unevenly distributed energy resources. To help alleviate a significant power generation and energy demand imbalance, 10 countries in the Association of South East Asian Nations (ASEAN), which includes Brunei Darussalam, the Kingdom of Cambodia, the Republic of Indonesia, the Lao People's Democratic Republic, Malaysia, the Union of Myanmar, the Republic of the Philippines, the Republic of Singapore, the Kingdom of Thailand, and the Socialist Republic of Viet Nam signed an agreement in 1997 to create the ASEAN Power Grid (APG) with the goal of

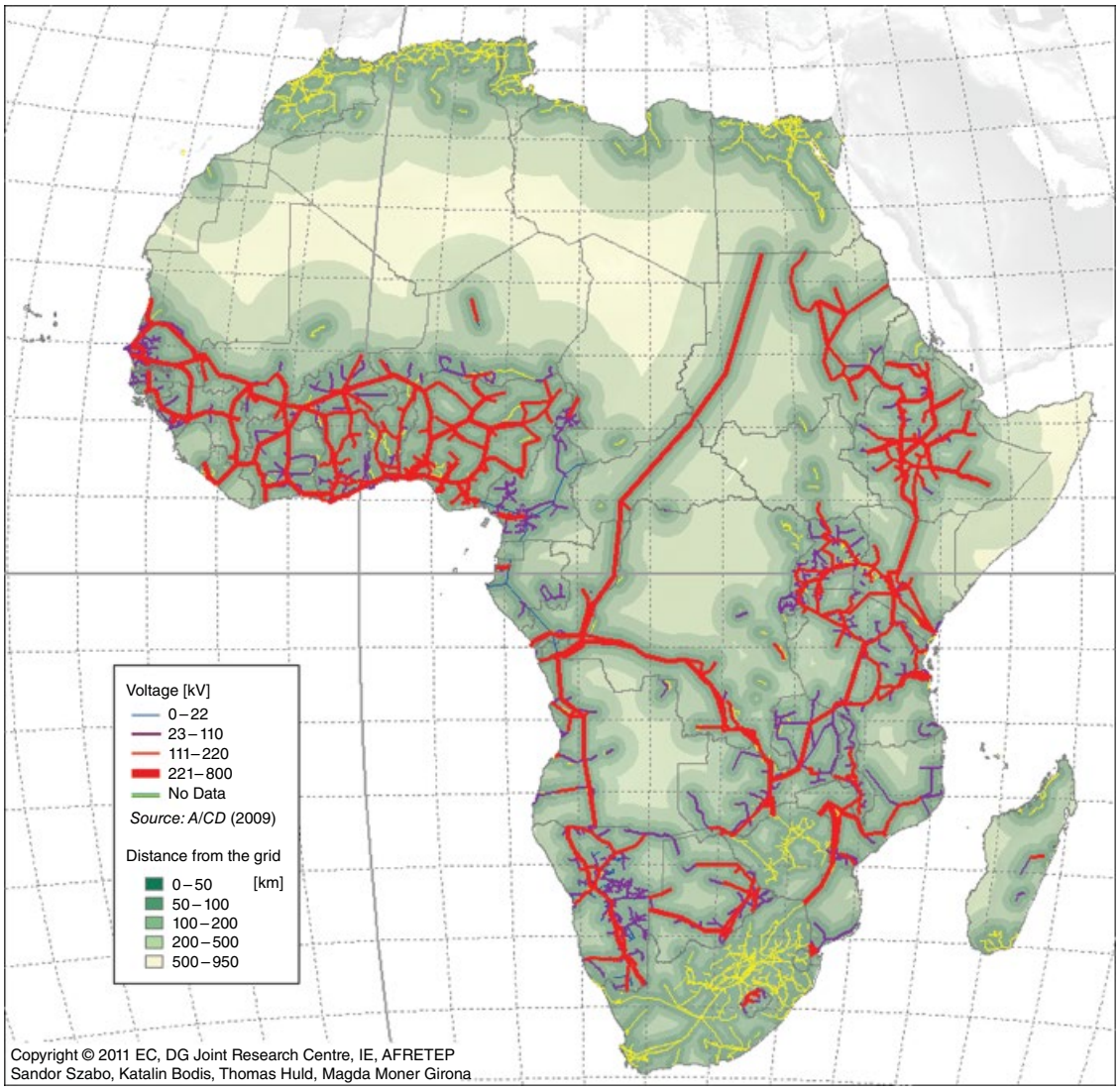


**Figure 3.4** The existing electric power grid in sub-Saharan Africa showing the dense interconnections in West and East Africa under the EEJ [from *Szabó et al.,* 2011].

creating a transnational power grid [*ASEAN MOU*, 1997]. The APG, which essentially interconnects the different national grids, lies directly under the equatorial electrojet and creates a distribution network spanning thousands of kilometers and servicing hundreds of million of people (see Fig. 3.6).

## 3.4. DISCUSSION AND CONCLUSIONS

GICs have been extensively studied for decades, but the realization of potential impacts on low latitudes is normally discussed in the context of geomagnetic storm current signatures such as SSC [e.g., *Kappenman*, 2003]. The EEJ has been extensively studied for decades, but the realization of its impact on GICs has only recently been discussed [e.g., *Ngwira et al.*, 2013]. The main reason for the lack of urgency of EEJ and GIC studies is that the power transmission grid under the EEJ has been significantly less developed than at midlatitudes. The growth of geomagnetic equatorial nations' economies, and the subsequent growth of transnational power grids, now makes this region's power grids susceptible to GIC-related space-weather impacts.

We now know that the stormtime equatorial electrojet can drive relatively large amplitude geomagnetic-induced currents in power grids under the geomagnetic equator (especially in coastal regions) in Brazil, West and East Central Africa, India, and SE Asia. Regional power-grid operators should recognize that GIC impacts are not only important at high latitudes, but potentially could impact hundreds of millions of people at low latitudes. Though GIC signatures under the EEJ are on average

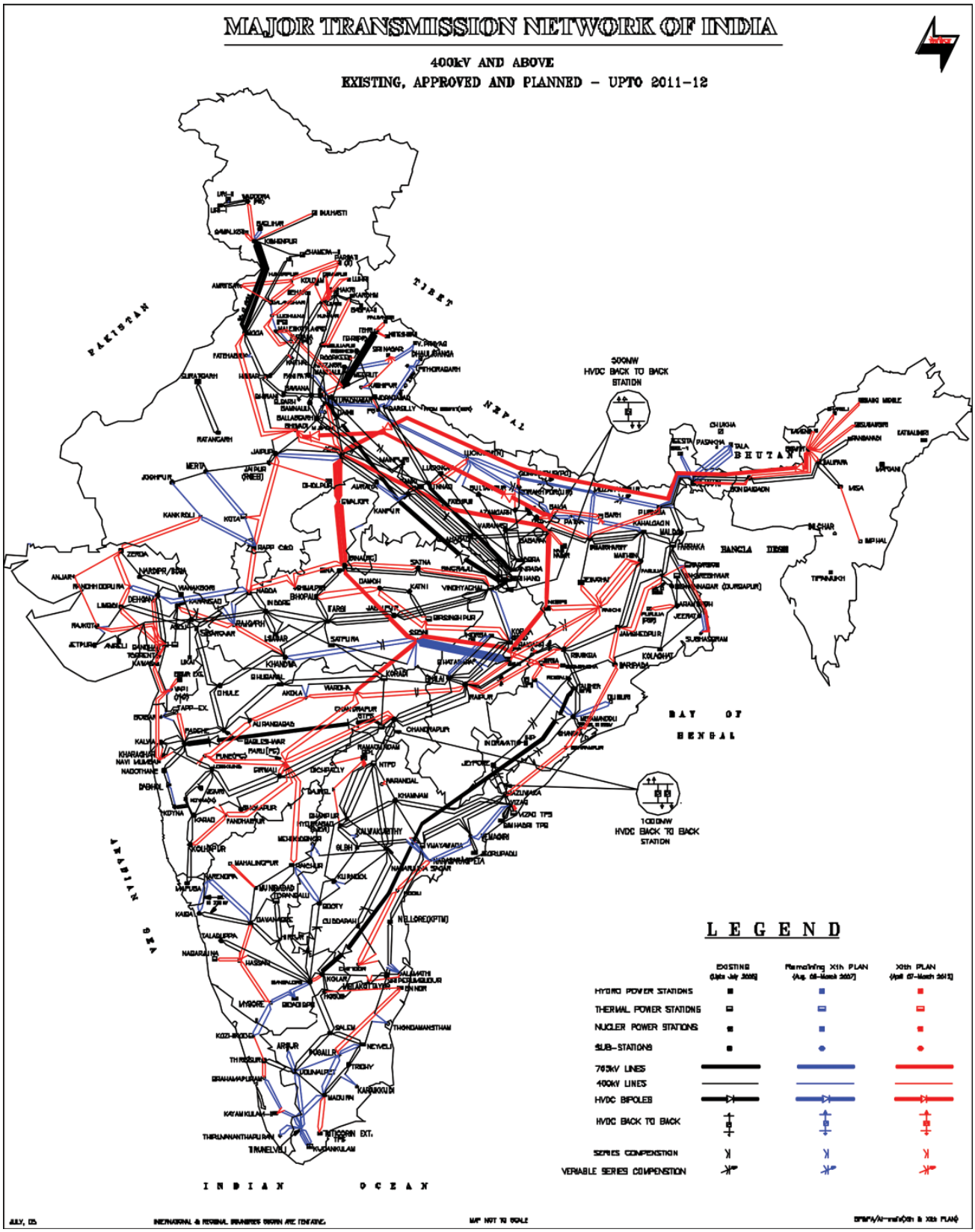


**Figure 3.5** The power grid of India, which in 2013 underwent interconnection across the different regions making for a truly national grid.

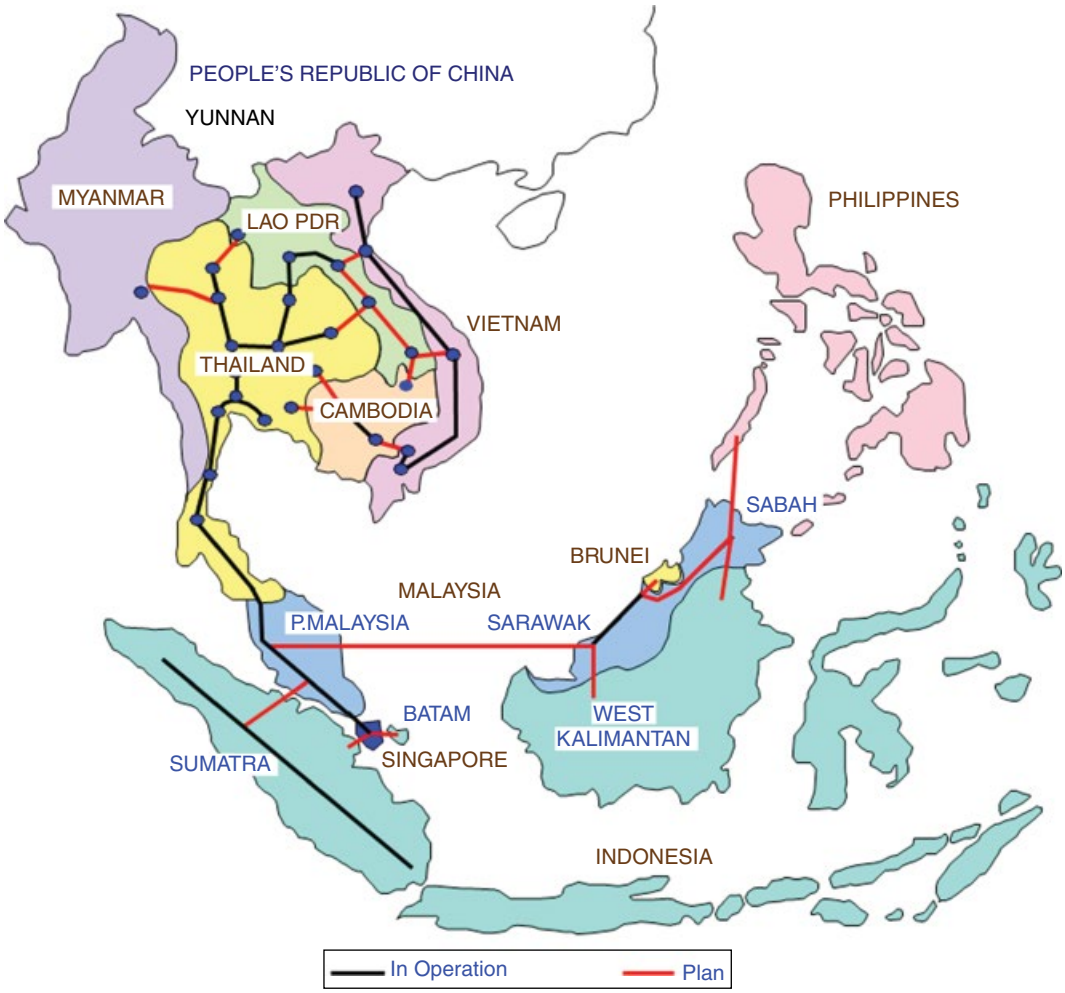


**Figure 3.6** The ASEAN Power Grid interconnection project is developing interconnects between national grid systems throughout Southeast Asia.

smaller than AEJ signatures at high latitudes, the combination of SSC, main phase, and EEJ signatures can be significant. More important, the growth of the equatorial regions' economies and the subsequent development of large national and transnational power-transmission grids make space-weather GIC impacts more likely.

## ACKNOWLEDGMENTS

This work was partially supported by a NASA LWS grant (NNX10AQ53G).

## REFERENCES

Abdu, M. A. (1997), Major phenomena of the equatorial ionosphere-thermosphere system under disturbed conditions, *J. Atmos. Solar Terr. Phys.*, *59*(13), 1505–1519; doi:10.1016/S1364-6826(96)00152-6.

Amory-Mazaudier, C., A. Kobea, P. Vila, A. Achy-Séka, E. Blanc, K. Boka, J. Bouvet, J-F. Cécile, Y. Cohen, J. -J. Curto, M. Dukhan, V. Doumouya, O. Fambitakoye, T. Farges, C. Goutelard, E. Guisso, R. Hanbaba, E. Houngninou, E. Kone, P. Lassudrie-Duchesne, C. Lathuillere, Y. Leroux, M. Menvielle, E. Obrou, M. Petitdidier, S. O. Ogunade, C. A. Onwumechili, D. Rees, E. Sambou, M. Sow, and J. Vassal (2005), On equatorial geophysics studies: A review on the IGRGEA results during the last decade, *J. Atmos. Solar Terr. Phys.*, *67*(4), 301–313; doi:10.1016/j.jastp.2004.10.001.

Arajärvi, E., R. Pirjola, and A. Viljanen (2011), Effects of neutral point reactors and series capacitors on geomagnetically induced currents in a high-voltage electric power transmission system, *Space Weather*, *9*, S11005; doi:10.1029/2011SW000715.

ASEAN (1997), Memorandum of Understanding, 1997, http://www.asean.org/communities/asean-economic-community/item/memorandum-of-understanding-on-the-asean-power-grid (accessed 13 June 2014).

Bhaskar, U., A. Raj, A. Ramanathan (2014), India now one nation, one grid, *LiveMint*, January 1; http://www.livemint.com/Politics/jIOljqqvinQqqngk7BYLZP/Southern-transmission-line-connected-to-National-Grid.html (accessed 23 June 2014).

Ducruix, J., V. Courtillot, and J. L. Le Mouël (1977), On the induction effects associated with the equatorial electrojet, *J. Geophys. Res.*, *82*(2), 335–351; doi:10.1029/JB082i002p00335.

Fiori, R. A. D., D. H. Boteler, and D. M. Gillies (2014), Assessment of GIC risk due to geomagnetic sudden commencements and identification of the current systems responsible, *Space Weather*, *12*, 76–91; doi:10.1002/2013SW000967.

International Monetary Fund (2013), Sub-Saharan Africa: Keeping the pace, regional economic outlook, https://www.imf.org/external/pubs/ft/reo/2013/afr/eng/sreo1013.pdf (accessed 13 June 2014).

International Monetary Fund (2014), World Economic Outlook Database, http://www.imf.org/external/pubs/ft/weo/2014/01/weodata/index.aspx (accessed 23 June 2014).

Kanagawa, M., and T. Nakata (2008), Assessment of access to electricity and the socio-economic impacts in rural areas of developing countries, *Energy Policy*, *36*(6), 2016–2029; doi:10.1016/j.enpol.2008.01.041.

Kappenman, J. (2010), Low-frequency protection concepts for the electric power grid: Geomagnetically induced current (GIC) and E3 HEMP mitigation, *Rep. Meta-R-322*, Metatech Corp., Goleta, California.

Kappenman, J. G. (2003), Storm sudden commencement events and the associated geomagnetically induced current risks to ground-based systems at low-latitude and midlatitude locations, *Space Weather*, *1*(3), 1016; doi:10.1029/2003SW000009.

Kappenman, J. G. (2004), Space weather and the vulnerability of electric power grids, 257–286, in *Effects of Space Weather on Technology Infrastructure*, edited by I. A. Eaglis, Kluwer Acad, Dordrecht, Netherlands.

Kappenman, J. G. (2006), Great geomagnetic storms and extreme impulsive geomagnetic field disturbance events: An analysis of observational evidence including the great storm of May 1921, *Adv. Space Res.*, *38*(2), 188–199; doi:10.1016/j.asr.2005.08.055.

Kappenman, J. G. (2007), Geomagnetic disturbances and impacts upon power system operation, 1–22, in *The Electric Power Engineering Handbook*, 2nd ed., edited by L. L. Grigsby, CRC Press, Boca Raton, Florida.

Kuvshinov, A., C. Manoj, N. Olsen, and T. Sabaka (2007), On induction effects of geomagnetic daily variations from equatorial electrojet and solar quiet sources at low and middle latitudes, *J. Geophys. Res.*, *112*, B10102; doi:10.1029/2007JB004955.

Liu, C. -M., L. -G. Liu, R. Pirjola, and Z. -Z. Wang (2009), Calculation of geomagnetically induced currents in mid to low-latitude power grids based on the plane wave method: A preliminary case study, *Space Weather*, *7*, S04005; doi:10.1029/2008SW000439.

Lloyd's 360° Risk Insight (2010), Space weather: Its impact on Earth and implications for business.

Lühr, H., S. Maus, and M. Rother (2004), Noon-time equatorial electrojet: Its spatial features as determined by the CHAMP satellite, *J. Geophys. Res.*, *109*, A01306; doi:10.1029/2002JA009656.

Mallick, S. K., and R. M. Sousa (2013), Commodity prices, inflationary pressures, and monetary policy: Evidence from BRICS economies, *Open Econ. Rev.*, *24*, 677–694; doi:10.1007/s11079-012-9261-5.

Moldwin, M. B. (2008), *An Introduction to Space Weather*, Cambridge University Press.

Ngwira, C. M., A. Pulkkinen, F. D. Wilder, and G. Crowley (2013), Extended study of extreme geoelectric field event scenarios for geomagnetically induced current applications, *Space Weather*, *11*, 121–131; doi:10.1002/swe.20021.

Pirjola, R. (2002), Review on the calculation of surface electric and magnetic fields and of geomagnetically induced currents in ground-based technological systems, *Surv. Geophys.*, *23*(1), 71–90; doi:10.1023/A:1014816009303.

Population Reference Bureau (2013), http://www.prb.org/Publications/Datasheets/2013/2013-world-population-data-sheet/data-sheet.aspx (accessed 13 June 2014).

Rastogi, R. G. (2004), Electromagnetic induction by the equatorial electrojet, *Geophys. J. Int.*, *158*(1), 16–31; doi:10.1111/j.1365-246X.2004.02128.x.

Stening, R. J. (2003), Space weather in the equatorial ionosphere, *Space Sci. Rev.*, *107*, 263–271.

Szabó, S., K. Bódis, T. Huld, and M. Moner-Girona (2011), Energy solutions in rural Africa: Mapping electrification costs of distributed solar and diesel generation versus grid extension, *Environ. Res. Lett.*, *6* (July-September) 034002; doi:10.1088/1748-9326/6/3/034002.

Trivedi, N. B., et al. (2007), Geomagnetically induced currents in an electric power transmission system at low latitudes in Brazil: A case study, *Space Weather*, *5*, S04004; doi:10.1029/2006SW000282.

USAID (2014), Power Africa (2014), http://www.usaid.gov/powerafrica (accessed 13 June 2014).

Yardley J., and G. Harris (2012), Second day of power failures cripple large swaths of India, *NY Times*, *31* July 2012, http://www.nytimes.com/2012/08/01/world/asia/power-outages-hit-600-million-in-india.html (accessed 23 June 2014).

Zhang, G. D., Z. Li, B. Zhang, and W. A. Halang (2013), Understanding the cascading failures in Indian power grids with complex networks theory, *Physica A-Statistical Mechanics and Its Applications*, *392*; doi: 10.1016/j.physa.2013.03.003.

# 4

# Differences in Midlatitude Ionospheric Response to Magnetic Disturbances at Northern and Southern Hemispheres and Anomalous Response During the Last Extreme Solar Minimum

**Dalia Burešová and Jan Laštovička**


## ABSTRACT

In order to give users reliable information/warning of changing space weather conditions that may affect a diverse range of technological systems, thoroughgoing knowledge of disturbed ionosphere behavior and its solar activity, local time, seasonal, latitudinal/longitudinal dependence, as well as possible hemispherical asymmetries are needed. Here investigations of differences in ionospheric effects are based on data obtained at different magnetic latitudes and longitudes of both hemispheres. Variability of main ionospheric parameters ($f_oF_2$ and $h_mF_2$), obtained for Euro-African and American sectors for geomagnetic storms of different intensity, which occurred within solar cycles 23 and 24, is analyzed. Ionospheric response to weak geomagnetic storms during the declining phase of the 23rd solar cycle and deep 23/24 solar minimum is found to be comparable with or even slightly stronger than that of strong storms under higher solar activity conditions, which might be partly related to specific impact of different drivers of geomagnetic activity. Hemispheric asymmetry of ionospheric response at middle latitudes, on average, is not a dominant and/or strong feature. The asymmetry in individual events may be well pronounced both in $f_oF_2$ and $h_mF_2$, but mostly it seems to be an impact of other factors like seasonal variation, magnetic coordinates, or local time.



**Key Points:**
Midlatitude ionospheric response to magnetic storms is analyzed
Effects of weak magnetic storm during solar minimum could be considerable
Possible hemispheric asymmetry is studied.

**Key Terms:** ionospheric storms, midlatitude, hemispheric asymmetry, solar minimum 23/24


## 4.1. INTRODUCTION

*Prölss* [2008] described ionospheric storm as a large-scale perturbation of electron density caused by a strongly enhanced dissipation of solar wind energy in the space environment of the Earth. It is well-known fact that ionospheric storms are nearly always associated with magnetic storms. *Webb* [1995] pointed out that, on average, the distribution of magnetic storms over the solar activity cycle exhibits two peaks of different solar and heliospheric sources. Generally speaking, a peak near solar maximum is associated with coronal mass ejections (CMEs) and a later peak during declining phase is mostly attributed to corotating stream interaction regions (CIRs). The occurrence rate of interplanetary coronal mass ejections (ICMEs) is

*Department of Aeronomy, Institute of Atmospheric Physics, Academy of Sciences of the Czech Republic (ASCR), Prague, Czech Republic*

*Ionospheric Space Weather: Longitude and Hemispheric Dependences and Lower Atmosphere Forcing, Geophysical Monograph 220*, First Edition. Edited by Timothy Fuller-Rowell, Endawoke Yizengaw, Patricia H. Doherty, and Sunanda Basu.

shown to follow the sunspot cycle, while strong CIRs are predominant during the declining phase [*Kamide*, 2001]. CIRs arise from interactions at the boundaries between streamers (slow wind) and coronal holes (fast winds). If the *Z*-component of the IMF in the fast wind is southward, the passing of a CIR is a signal of upcoming enhanced magnetic activity. *Tsurutani et al.* [2006] and *Koskinen* [2011] pointed out that the occurrence of CIR-related storms has a strong 27-day periodicity, as the storm driver in most cases is the fast wind, which originates from the coronal holes. The large coronal holes are the most stable regions of the corona (the cause of the recurrence) and extend to low solar latitudes during the declining phase of the solar cycle. The same holes return toward the direction of the Earth with about 27-day periodicity in accordance with rotation of the Sun. Thus the recurrent storms occur predominantly during the declining phase with 27-day period (e.g., 65 such events for the prolonged declining phase and solar minimum of the last solar cycle). Differences between ICME-driven and CIR-related storms are listed in *Borovsky and Denton* [2006] and discussed by *Kamide* [2001], *Turner et al.* [2009], *Knipp et al.* [2011] and *Koskinen* [2011].

Magnetic storms create complicated changes in the complex morphology of the electric fields, temperature, winds, and composition and affect all ionospheric parameters. The main feature of the stormy ionosphere is a great degree of irregular variability, which persists from several hours to days. A storm classification scheme based on a total of 1085 magnetic storms was introduced by *Loewe and Prölss* [1997] and represents five different storm classes. According to this scheme, class 1 storms are weak storms with a minimum $D_{st}$ index between −30 and 50 nT, while class 5 magnetic storms are so-called superstorms with a minimum $D_{st}$ index of less than −350 nT. There is a broadly accepted opinion in the scientific community that only large magnetic storms (with $D_{st}$ index less than –100 nT) induce a global ionospheric storm.

Many years of continuous studies of magnetic storm effects on the ionosphere gave a typical course of the *F*-region response at middle latitudes as described by *Prölss* [1995] and summarized by *Rishbeth and Field* [1997] with an initial phase with enhanced peak electron density lasting a few hours after the start of the magnetic storm. The subsequent main phase with electron-density depletion usually lasts a day or more. A recovery phase of the storm could last from several hours to several days. However, there are also storms having only positive (particularly in winter) or only negative (particularly in summer) phase. Strong dynamic effects (heating and winds) occur during the initial phase, leading to fluctuations of the $F_2$-layer height. Most of extra ionization is usually produced at heights below the $F_2$-layer, and the $F_2$-layer ionization is not greatly enhanced. However, during some storms, the topside ionospheric electron content is much more enhanced than the bottomside electron content [*Zhao et al.*, 2012]. The electron concentration at heights near the $F_2$-layer maximum could be more sensitive to changes of neutral composition, temperature and horizontal winds, whereas effects of electrodynamics affect strongly higher altitudes (~400–800 km) [*Danilov*, 2013].

In today's ionospheric disturbance scenario based on intimate coupling between thermospheric and ionospheric storms, changes in the neutral gas composition are particularly responsible for ionization decrease at middle latitudes, while electron density enhancement is predominantly caused by thermospheric winds and traveling atmospheric disturbances [TADs; *Prölss*, 2004]. Electric fields play an important role in magnetic storm effects on the ionosphere at low and high latitudes. Observations at middle latitudes showed that both a significant density decrease as well as an anomalous electron density increase can occur over the course of a magnetic storm [*Burešová et al.*, 2007]. Also, the existence of occasions when significant magnetic disturbances were not accompanied by ionospheric disturbances, or vice versa, has been observed [*Field et al.*, 1998; *Li et al.*, 2012].

As for review papers, more recent representative examples include the following studies. *Buonsanto* [1999] and *Danilov* [2013] described ionospheric storms in the $F_2$ region, *Mendillo* [2006] reviewed ionospheric storms in terms of total electron content (TEC) behavior, *Burns et al*. [2007] gave an analysis of ionosphere and thermosphere response to CMEs.

The ionosphere reacts to magnetic storms over regions extending from poles to equator. Observations and modeling results during the last few decades gave notice of the seasonal, latitudinal, longitudinal, and local time dependence of ionospheric response to magnetic storm-induced disturbances. *Kintner et al*. [2008] pointed out that the most dramatic changes in the state of the ionosphere occur not at high or equatorial latitudes, but at middle latitudes, where TEC can change by factors of 3 to 10 over the duration of magnetic storms.

According to *Prölss* [2008], storm-induced changes in the maximum ionization density are somewhat larger than those in the TEC, on average by about 20%. *Prölss* [1993] attempted to explain the local-time variation of ionospheric storms at middle latitudes using a model that is based on a close coupling between thermospheric and ionospheric disturbance effects. The author pointed out that daytime positive storms are attributed to traveling atmospheric-ionospheric disturbances and subsequent changes in the global-wind circulation, while negative storm effects are attributed to neutral gas composition changes, which are advected toward middle latitudes during nighttime and which subsequently rotate into the day sector. Changes in wind system during geomagnetic storms play a very important role in the positive ionospheric effects also at lower middle and low latitudes, and in further development of the equatorial ionization

anomaly (EIA), as it was corroborated, for example, by *Balan et al.* [2010].

There are a couple of reasons why we might expect some differences in behavior of the Southern Hemisphere (SH) and Northern Hemisphere (NH) ionosphere. It is known that magnetic-field strength is not the same and this may generate differences in auroral intensity between the two hemispheres [*Stanbaek-Nielsen et al.*, 1973]. There is also a large asymmetry in the interhemispheric distribution of various electrodynamic parameters, in addition to seasonal changes in UV irradiance, the ionosphere undergoes a variation caused by the offset between the geomagnetic and geographic poles, which is higher at SH compared with NH [*Lukianova et al.*, 2008]. Field-aligned currents (FACs) are partially controlled by IMF $B_y$ and season, and indicate differences in the interhemispheric current density and total current in summer and winter hemispheres [*Lukianova et al.*, 2012].

Therefore, we may expect somewhat different response of the southern and northern ionosphere to geomagnetic storms. *Astafyeva* [2009] observed a north-south asymmetry in the dayside ionospheric response to an intense geomagnetic storm with the use of data of Jason-1, TOPEX, CHAMP, and SAC-C satellites. *Sahai et al.* [2009] observed an asymmetry in the positive-negative ionospheric storm phases in the American sector for strong geomagnetic storms of early November 2004. *Mendillo and Narvaez* [2010] used $N_mF_2$ from ionosonde stations Wallops Island (NH) and Hobart (SH). They found only subtle differences linked to possible presence of hemispheric asymmetries governed by the non-mirror-image of geomagnetic morphology in each hemisphere. *Wang et al.* [2010] investigated ionospheric responses to the initial phases of three geomagnetic storms. They observed a north-south asymmetry in the positive response as the northern hemispheric response appeared to be more pronounced. *de Abreu et al.* [2010] studied the asymmetry of *F*-region response to an intense geomagnetic storm of September 2002 in the American sector. Their main finding is a strong hemispheric asymmetry in the recovery phase of the storm. *Mansilla and Zossi* [2013] studied ionospheric response to a geomagnetic storm of 3 August 2010 in three longitudinal sectors and they found a clear hemispheric asymmetry. The asymmetry of ionospheric response to individual geomagnetic storms was also studied by *Blagoveschensky et al.* [2003], *Sahai et al.* [2005], and *Karpachev et al.* [2007]. A hemispheric asymmetry was found in the equatorial ionization anomaly based on CHAMP and GRACE data [*Xiong et al.*, 2013]. The authors pointed out that the electron density and the magnetic latitudes of the EIA crests are almost symmetric about the dip equator during the equinoxes, while during solstice seasons clear interhemispheric asymmetry has been observed. It was also concluded that due to the varying latitudinal distances between magnetic and geographic equator, significant longitudinal variations could be expected. *Zakharenkova et al.* [2014] used ionosonde data from Juliusruh and Hobart; they observed significantly larger winter anomaly in $N_mF_2$ at NH compared with SH. *Prikryl et al.* [2013] reported significantly higher occurrence frequency of ionospheric scintillations in southern than northern polar cap and cusp. Polar patches also occur more frequently on the SH [*Noja et al.*, 2013]. Cross-polar neutral wind and ion drift velocities are higher on NH [*Förster and Cnossen*, 2013]. This all illustrates general differences in the southern and northern ionosphere, particularly but not only at high latitudes.

In general, all these studies indicate that the ionospheric storm effects reveal some hemispheric asymmetry, but this has not been investigated enough. Investigations have been only case studies.

We studied the hemispheric asymmetry of the *F*-region ionospheric response to magnetic storms at middle latitudes of the European-African and American sector. The European-African sector has one advantage compared to the American or East Asian-Australian sector: the difference between geographic and geomagnetic latitudes, which generally contributes to hemispheric asymmetry, is small in the European-African sector. Moreover, this sector is not affected by the South Atlantic/Brazilian magnetic anomaly. Thus, it is more suitable for studying "pure" hemispheric asymmetry.

The prolonged declining phase and last very deep solar activity minimum, particularly years 2008–2009, displayed to some extent unexpected behavior of the thermosphere and ionosphere. *Solomon et al.* [2010] analyzed the extremely low thermospheric neutral densities in the solar minimum year 2008 compared to 1996 and concluded that the decrease of the solar EUV flux by 13%–15% (SOHO and TIMED observations) can account for this decrease of thermospheric density. *Deng et al*. [2012] took into account also the decrease of geomagnetic energy. Their simulations with TIE-GCM model indicate that for the density decrease, about 75% was caused by EUV and 25% by the geomagnetic energy decrease. This would reduce the 1996–2008 EUV difference to some 10%–12%. *Laštovička* [2013] estimated the EUV decrease to be about 10% based on various data. *Solomon et al.* [2013] estimated a global average $N_mF_2$ decline between solar minima 1996 and 2008–2009 by ~15%. A 10% reduction of solar EUV played the largest role in causing the ionospheric change, with a minor contribution from lower geomagnetic activity and a very small additional effect from anthropogenic increase in $CO_2$.

*Sunda et al*. [2013] observed surprisingly strong effects of moderate geomagnetic storms of 20 November 2007, 9 March 2008, 11 October 2008, and 29 July 2009 in the total electron content (TEC) over India. *Burešová et al.* [2014] observed the same in $F_2$-region parameters in

middle latitudes of the European-African sector during minor magnetic storms, both under extremely low solar activity conditions in 2007–2009. Therefore, we will pay special attention to investigations of possible hemispheric differences in the response of the ionosphere to magnetic storms also under extremely low solar activity conditions, particularly because in the next few solar cycles, we can expect similar very low solar activity minima not observed before during the era of ionospheric measurements.

## 4.2. EFFECTS OF STRONG-TO-SEVERE MAGNETIC STORMS

Numerous investigations during the last several decades demonstrated the complex nature of the ionospheric response to magnetic storm-induced disturbances associated with the interplay of several physical processes.

Simulation of ionospheric and thermospheric response to the January 1997 geomagnetic storm carried out by *Lu et al.* [2001] using the thermosphere-ionosphere-electrodynamics general circulation model (TIE-GCM) and subsequent comparison of the simulation results with observations showed evident longitudinal, latitudinal, and UT dependences. While North America experienced a negative storm phase, a strong positive effect was observed for the Central American region as well as for western Europe and Russia.

Analysis of the observations obtained for the 15 May 2005 event was also aimed at evaluating hemispheric dependence on ionospheric reaction. The intense magnetic storm developed as a consequence of a fast halo CME that originated from an eruption of solar active region AR 10759. It was associated with a long-duration M8 class X-ray flare with peak emission at about 5:00 p.m. UT on 13 May. It is necessary to emphasize the transient south and northward turning of the Interplanetary Magnetic Field (IMF) $B_z$ component. According to the data obtained from the Advanced Composition Explorer (ACE) Science Center (http://www.srl.caltech.edu/ACE/ASC/), the $B_z$ turned steeply southward and reached its lowest value of −33 nT at about 6:00 a.m. UT of 15 May, then it turned northward. At 10:00 a.m., the positive value of 20.5 nT was recorded by ACE spacecraft (Fig. 4.1a). Storm Sudden Commencement (SSC) peaked at 2:39 a.m. UT and was followed by rapid decrease of $D_{st}$ index with the minimum of −247 nT at about 9:00 a.m. UT and more than 100 hours recovery phase. This event reached Kp = 9. Also high AE values indicated strong auroral disturbances.

The very long-term enhancement of AE during this storm, as seen in Figure 4.1a, may indicate long-term heating of the auroral regions and extension of the thermosphere. Figure 4.1b represents digisonde observations for six locations. Five of them are European ionospheric stations, and one, Grahamstown, is located at the south of the African continent. It is necessary to mention that all ionosonde data used in the study have been manually checked. Solid lines are for daily observations of $f_oF_2$, while dashed lines give 27-day running means centered on storm culminations day. It is evident from the figure that at the European higher-middle latitudes, negative storm effects prevailed. El Arenosillo station recorded significant positive effects, particularly during 16 May. Athens showed positive effect already at storm culmination day and the next day of storm recovery phase. Similar positive effect on $f_oF_2$ with two distinct well separated peaks at the storm culmination day has been obtained by *Galav et al.* [2014] for Northern Hemisphere lower-middle latitude station Alma-Aty (geomagnetic coordinates: 34.33°N; 152.99°E).

The observed first positive peak could be attributed to the prompt penetration of the electric field caused by the sudden southward turning of IMF $B_z$, and the second increase in plasma density, which was also superposed by wavelike modulations, most probably was caused by the storm-induced winds. *Galav et al.* [2014] pointed out that enhanced plasma density observed during the daytime at midlatitudes was found to be locally produced, and not transported from the equatorial ionization anomaly region because the time of enhanced plasma density at midlatitude is earlier than that observed at low latitudes.

Ionospheric response during the storm maximum day observed above the Southern Hemisphere lower-middle latitude station Grahamstown was negative and very weak. On 16 May, significant positive effect was recorded followed by moderate decrease of $f_oF_2$ for the next few days of the storm-recovery phase. *Ngwira et al.* [2012] reported for this storm over South Africa a positive effect in TEC and a dissimilar $f_oF_2$ response (similar to that observed by us). They suggested this dissimilarity was likely to be due to the westward electric field and equatorward neutral wind competing effects.

During the storm main phase, the night side GPS observations from the midlatitude Canadian station ALGO [*Galav et al.* 2014] showed moderate to large TEC fluctuations and short-duration depletions that occurred in a narrow latitude zone. The observed TEC behavior authors attributed to the combined effect of storm-induced equatorward movement of the middle latitude ionospheric trough due to the expansion of auroral oval and the storm-time enhanced density.

The course of $f_oF_2$ recorded for the same storm period and for several ionospheric stations along the American sector is given in Figure 4.1c. In general, changes in the daily course of $f_oF_2$ were similar for all selected North America stations. The ionospheric effect during the storm maximum day was negative. Except Point Arguello, positive effect has been observed at the next storm day.

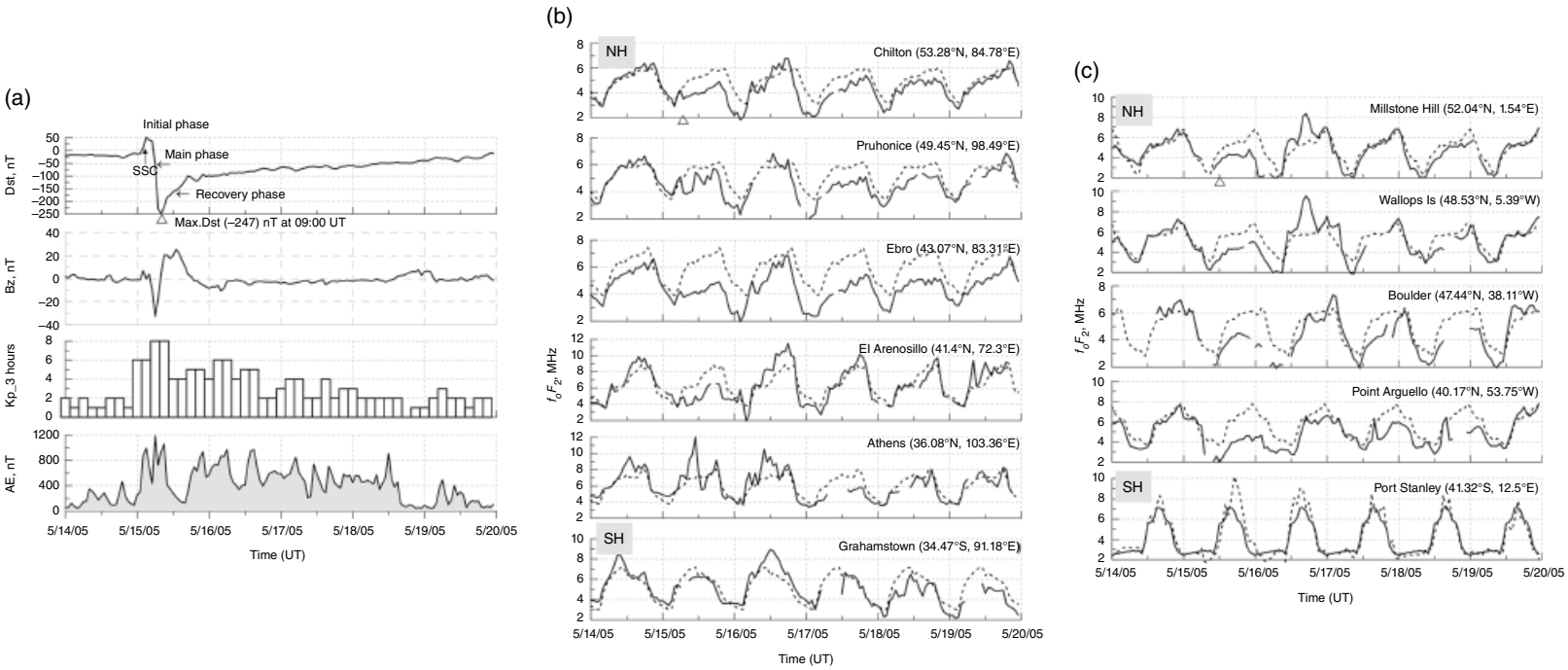


**Figure 4.1** Magnetic storm of May 2005: (a) the panels give courses of solar and geomagnetic indices for the analyzed storm period; (b) panels in the middle represent changes in $f_oF_2$ for selected NH and SH middle latitude ionospheric stations in the Euro-African sector (solid line is for daily $f_oF_2$, while dashed lines give 27-day running mean); (c) right side panels are for selected American sector stations.

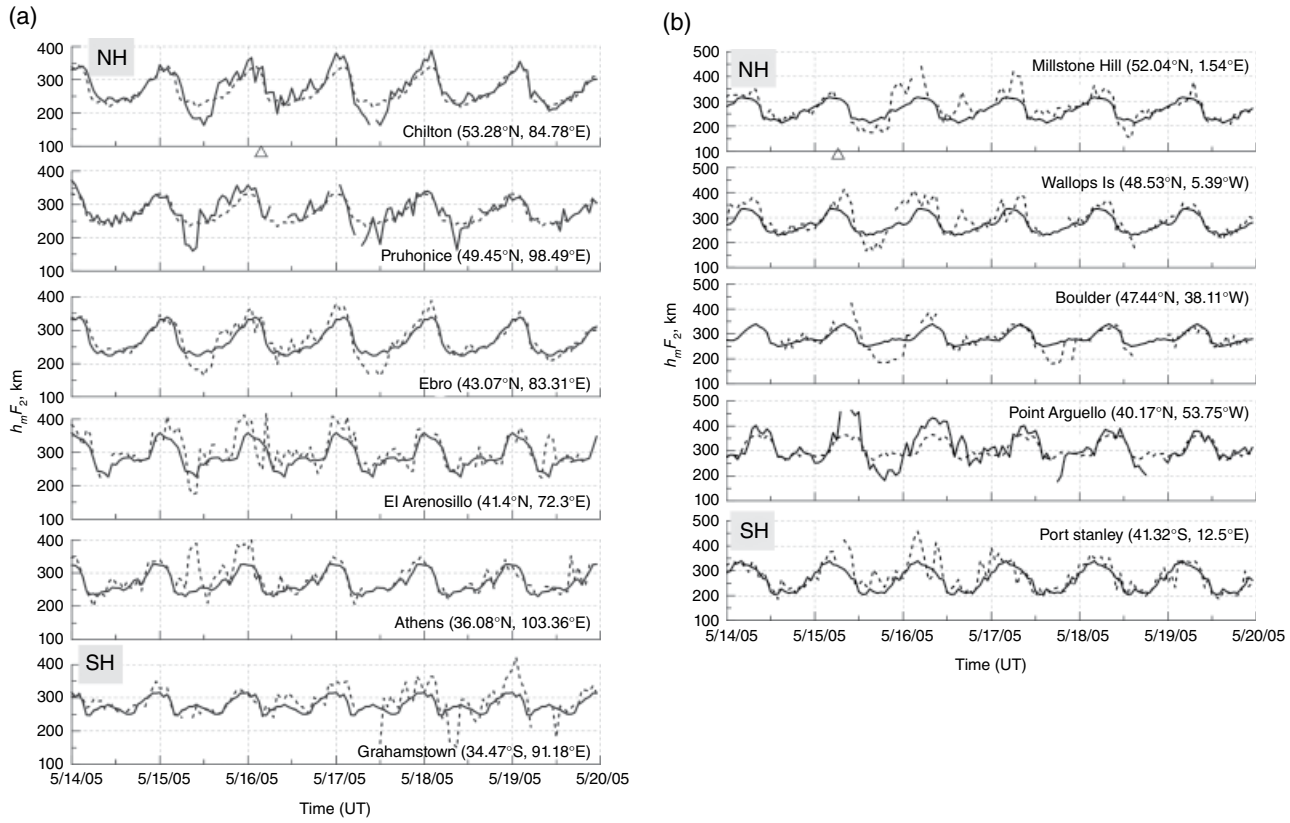


**Figure 4.2** Magnetic storm of May 2005: (a) left side panels give courses of daily $h_mF_2$ (solid line) and their 27-day mean values (dashed line) for the entire analyzed storm period for the European-African sector; (b) the same for the American sector.

In contrast to Northern Hemisphere stations, Port Stanley showed mostly positive effect for the entire analyzed storm period. On storm maximum day, negative effect on $f_oF_2$ was observed above European and North American higher-middle and middle latitudes followed by alternation of electron density enhancement and/or decrease of different magnitude during the recovery phase. As mentioned earlier, European lower-middle latitude station Athens displayed significant positive effect on storm culmination day, which is different from what was observed at Southern Hemisphere lower-middle latitude station Grahamstown. Different effects obtained for Grahamstown and Port Stanley could be impacted by different latitude and longitude.

When comparing May 2005 magnetic storm effects on $F_2$ peak height $h_mF_2$ obtained for NH and SH ionospheric stations (Fig. 4.2), it is necessary to point out that except Athens all European stations showed steep decrease of $h_mF_2$, which coincides with the decrease of $D_{st}$ index. Another similar decrease was observed for Chilton, Pruhonice, and Ebro during the recovery phase on 17 May. Above Athens, mostly positive effect on $h_mF_2$ prevailed. In contrast to European stations, the South African station Grahamstown recorded no effect during the storm initial and main phases (Fig. 4.2a). Significant negative and positive differences against mean values have been observed for the recovery phase on 17–19 May. Increase and subsequent decrease in $F_2$-layer peak height during the storm culmination day and alternation of positive and negative effect within recovery phase was observed for North American stations. In contrast to Grahamstown, South American station Port Stanley displayed positive deviations on 15–16 May, and no significant deviations from the mean values were observed for the rest of the recovery phase (Fig. 4.2b).

The CME that hit Earth's magnetic field on 24 October 2011 at approximately 18:00 UT originated from an unstable magnetic filament, which erupted around 01:00 UT two days earlier. The impact caused a strong compression of Earth's magnetic field allowing solar wind to penetrate all the way down to geosynchronous orbit for a very brief period around 19:00 UT and triggered off a strong magnetic storm, which culminated at 01:00 UT on 25 October when $D_{st}$ index decreased to −132 nT (Fig. 4.3a). The highest observed value of Kp index was 7. The aurora was seen around the world including in over 30 US states.

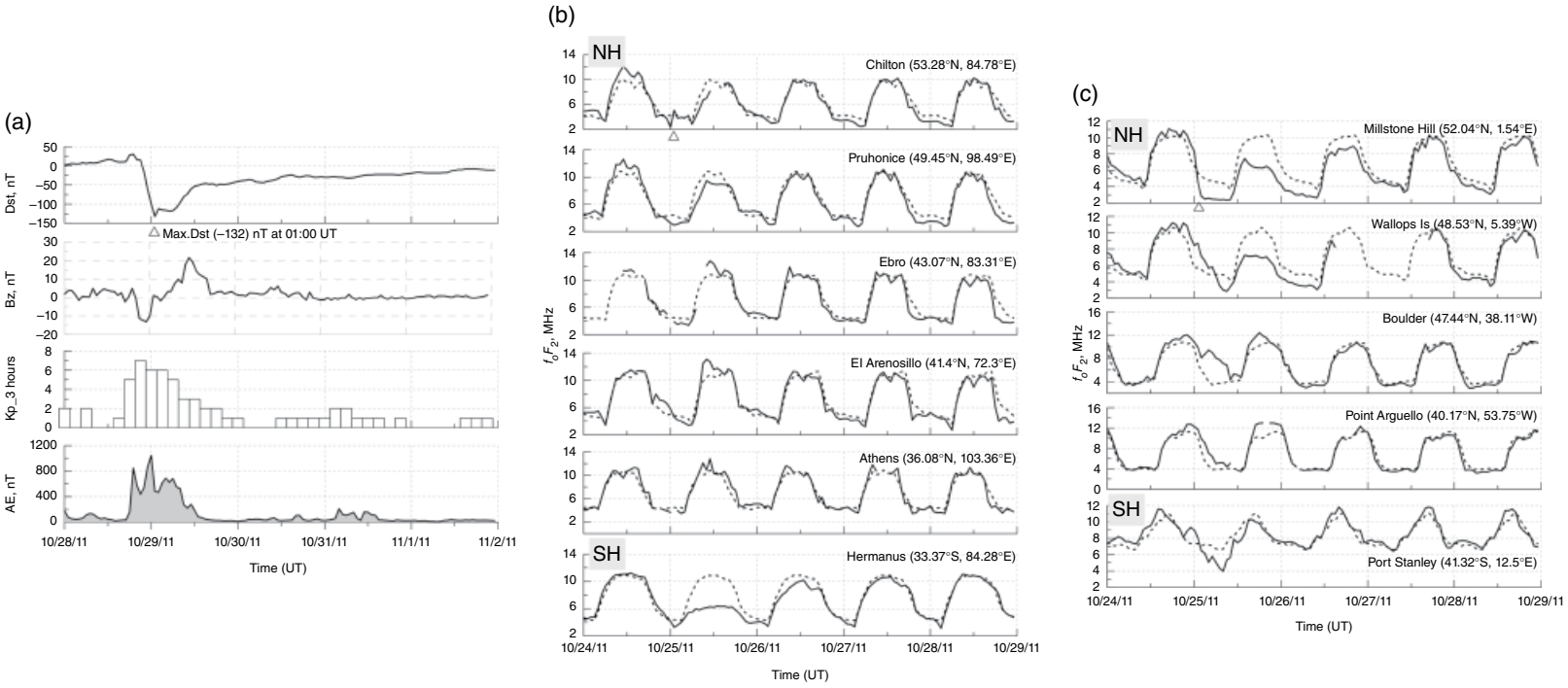


**Figure 4.3** Magnetic storm of October 2011: (a) the panels give courses of solar and geomagnetic indices for the analyzed storm period; (b) panels in the middle represent changes in $f_oF_2$ for selected NH and SH middle latitude ionospheric stations in the Euro-African sector (solid line is for daily $f_oF_2$, while dashed lines give 27-day running mean); (c) right side panels are for selected American sector stations.

Analysis of digisonde data showed different ionospheric response above single NH and SH locations. Figure 4.3b represents the results obtained for European-African middle latitudes, while Figure 4.3c is for the American sector. In general, all European stations involved in the analysis indicated moderate changes in the regular daily course of $f_oF_2$. At higher-middle latitude stations Chilton and Pruhonice, a slight increase of $f_oF_2$ values was observed on 24 October followed by a moderate decrease during the storm culmination day, while lower-middle latitude stations Ebro, El Arenosillo, and Athens showed mild negative response in the early morning hours replaced by slight positive effect on October 25th. The most significant negative effect was observed for SH ionospheric station Hermanus at storm maximum day, which was partially recovered during the next day.

At the North American stations Millstone Hill and Wallops Island, strong negative effect was recorded at 25 October. Lower-middle latitude stations Boulder and Point Arguello at the same time underwent only positive changes on $f_oF_2$. The most significant effect was observed for Boulder. Similar to Hermanus, the SH ionospheric station Port Stanley showed negative effect during the storm maximum day, which was alternated by moderate positive effects on 26 October.

Ionospheric disturbances, which occurred within the period of 30 September to 3 October 2012 was a consequence of a strong magnetic storm with minimum $D_{st}$ index of −143 nT, recorded at 3:00 a.m. UT on 1 October (Fig. 4.4a). According to the NOAA Space Weather Prediction Center (NOAA/SWPC) alert, the event was caused by the 28 September CME, which impacted Earth's magnetic field at 10:20 p.m. UT on 30 September. No large coronal holes were observed on the Earth side of the Sun. A weak interplanetary shock wave hit Earth at 10:20 a.m. UT followed by a stronger CME strike at approximately 10:20 p.m. UT. The magnetic storm developed in two steps during the main phase. The maximum value Kp 7 was reached on 1 October at 03:00 a.m. UT.

Figures 4.4b and c show ionospheric reaction through European-African and American middle latitudes, respectively. Five European stations involved in the analysis show moderate enhancement of $f_oF_2$ values at 29–30 September and subsequent decrease against mean values during the storm maximum day, which was higher at higher-middle latitude. Similar behavior of $f_oF_2$ has been observed for North American ionospheric stations, except Austin, where the positive effect was significantly higher. Two South African middle-latitude stations Grahamstown and Hermanus displayed very moderate ionospheric effect for the entire storm period with some reduced $f_oF_2$ values during morning hours of 1 October. Moderate changes in $f_oF_2$ have been observed also for the South America ionospheric station Port Stanley. On 30 September, positive effect prevailed and in general no effect was recorded for the storm culmination day.

Maximum and minimum deviations of $f_oF_2$ and $h_mF_2$ from their 27-day running mean for the analyzed October 2011 and 2012 magnetic storm culmination day and for several selected NH and SH stations are presented in Table 4.1. The deviations are expressed in percentage ($\delta f_oF_2 = [f_oF_{2\,daily} - f_oF_{2mean}/f_oF_{2\mathrm{mean}}] \times 100\%$). When evaluating magnetic-storm effects on regular ionospheric behavior, it is necessary to take into account findings by *Rishbeth and Mendillo* [2001] that the broad average of percentage standard deviation of the $F_2$-layer peak electron density from its monthly median is 20% by day and 33% at night. The analysis of digisonde data for the October 2011 and 2012 magnetic storms indicates that, in general, differences in ionospheric response were largest across North American lower-middle latitudes with some evidence of hemispheric asymmetry.

## 4.3. IONOSPHERIC DISTURBANCES UNDER EXTREMELY LOW SOLAR ACTIVITY CONDITIONS

*Kilpua et al.* [2014] investigated interplanetary conditions during the long declining phase of the 23rd solar activity cycle through the rising phase of cycle 24. The authors concluded that it was weak southward IMF and the lack of strong ICMEs that led to particularly weak ring current activity. On the other hand, the prolonged quiet period in the magnetosphere offered a possibility to investigate how different sources of solar activity and different types of solar wind affect magnetosphere-ionosphere coupling processes.

The period of the last extremely long declining phase of the 23rd solar cycle and deep solar minimum (2007–2009) did not exhibit strong magnetic storms (with $D_{st} < -100$ nT), and the number of moderate events ($-50$ nT $< D_{st} < -100$ nT) decreased (five events in 2007; four events in 2008; one event in 2009) until 2010, when it increased again (seven events). Nevertheless, there were numerous cases observed of minor magnetic disturbances ($D_{st} > -50$ nT) with the unexpectedly substantial ionospheric response across both hemispheres.

*Burešová et al.* [2014] analyzed ionospheric variability during 4–9 January (minimum $D_{st}$ −31 nT) and 24–28 November 2008 (minimum $D_{st}$ −12 nT) weak magnetic disturbances. Similar positive effect on $f_oF_2$ was observed for both Pruhonice and Grahamstown stations regardless of different seasons (winter in the NH and summer in the SH). Significant enhancement of $f_oF_2$ was observed during 5 January and later in the early morning hours of the next day (storm main phase). The difference between observations and the 27-day running mean reached about

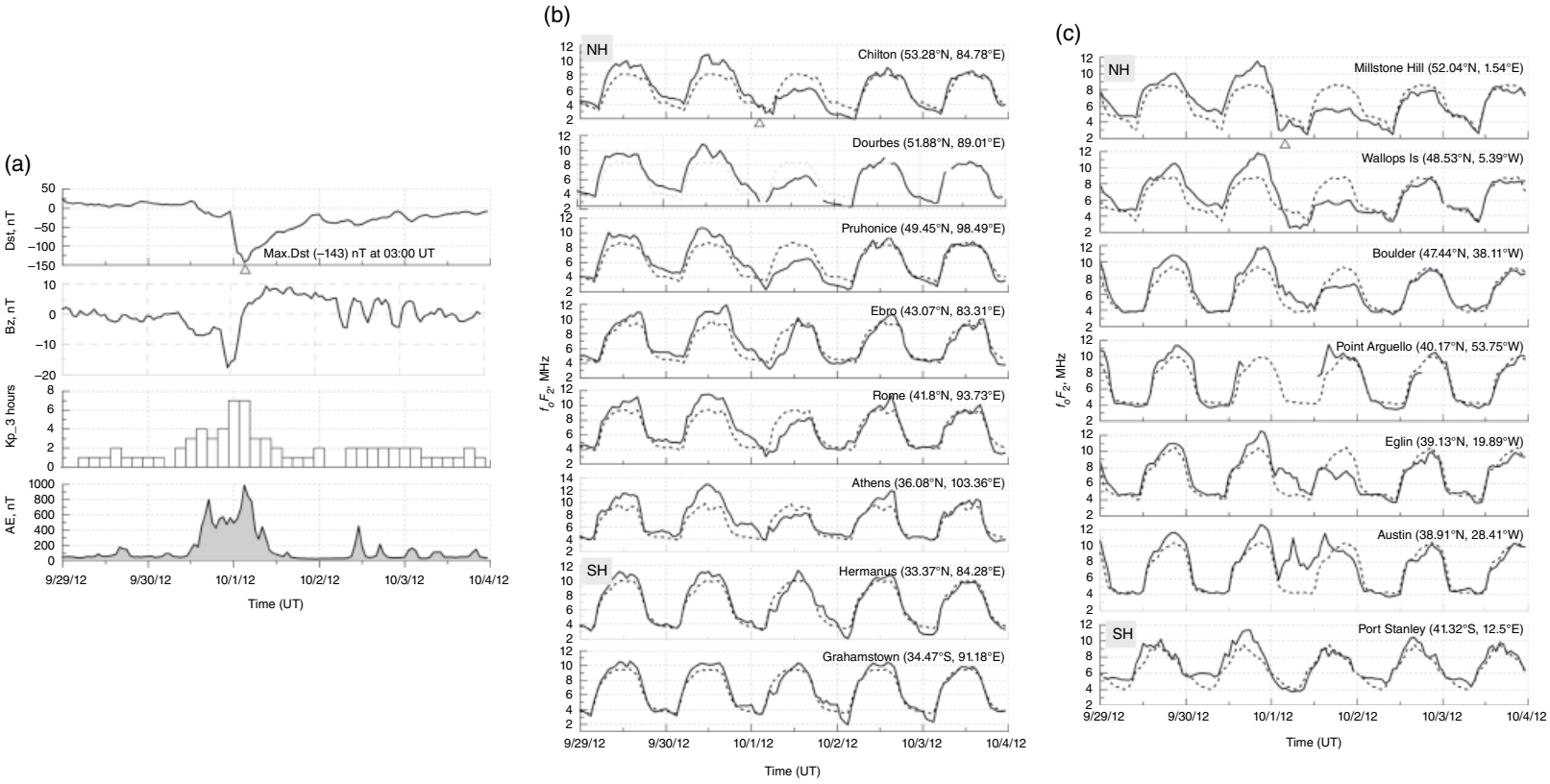


**Figure 4.4** Magnetic storm of September-October 2012: (a) the panels give courses of solar and geomagnetic indices for the analyzed storm period; (b) panels in the middle represent changes in $f_oF_2$ for selected NH and SH middle latitude ionospheric stations in the Euro-African sector (solid line is for daily $f_oF_2$, while dashed lines give 27-day running mean); (c) right side panels are for selected American sector stations.

**Table 4.1** Ionospheric Effect for Selected Northern Hemisphere (NH) and Southern Hemisphere (SH) Stations as It Was Observed for October 2011 and October 2012 Magnetic Storm Culmination Day

| Ionospheric stations | | 25 October 2011 Maximum and minimum differences against 27-day running mean in percentage | | 1 October 2012 Maximum and minimum differences against 27-day running mean in percentage | |
|---|---|---|---|---|---|
| NH | | $f_oF_2$ | $h_mF_2$ | $f_oF_2$ | $h_mF_2$ |
| | Chilton | 20,2 | 57 | 18,8 | 32,6 |
| | (53.28°N, 84.78°E) | –44,1 | –1,2 | –38,6 | 1,6 |
| | Pruhonice | 17,4 | 38,2 | 28,7 | 38,4 |
| | (49.45°N, 98.49°E) | –32,4 | –1,7 | –39,9 | 0,2 |
| | Ebro | 18,5 | 59,9 | 30,8 | 68,2 |
| | (43.07°N, 83.31°E) | 22,5 | –0,3 | –37,8 | 0 |
| | Athens | 35,8 | 42,9 | 57,5 | 36,7 |
| | (36.08°N, 103.36°E) | –22,3 | –9 | –30,3 | –1,5 |
| | Millstone Hill | 25,3 | 33,6 | 12,8 | 31,5 |
| | (52.04°N, 1.54°E) | –49,5 | –2,1 | –39,8 | –7,1 |
| | Wallops Island | 52,6 | 42,1 | 45,2 | 35,3 |
| | (48.53°N, 5.39°W) | –38,4 | –0,8 | –45 | –5,6 |
| | Boulder | 160,9 | 41,7 | 49 | 38,4 |
| | (47.44°N, 38.11°W) | –6,9 | –17,1 | –26,7 | –5,4 |
| | Point Arguello | 67,4 | 22,7 | 78,8 | 14,3 |
| | (40.17°N, 53.75°W) | –9,2 | –17,6 | –3,7 | –3,7 |
| SH | Hermanus | –6,5 | 24,6 | 38,5 | 30,6 |
| | (33.37°S, 84.28°E) | –43,6 | –6,8 | –28,5 | –9,9 |
| | Port Stanley | 22 | –33,6 | 7,6 | 40,7 |
| | (41.32°S, 12.5°E) | –41 | 12,6 | –19,8 | –4,8 |

*Note*: Maximum and minimum deviation of $f_oF_2$ from the 27-day running mean is expressed in percentage ($\delta f_oF_2 = [f_oF_{2daily} – f_oF_{2mean}/f_oF_{2mean}]$ x 100%). Stations are listed with geomagnetic coordinates.

100% at Pruhonice and about 80% at Grahamstown. The ionospheric disturbance continued with moderate negative effect on 6–7 January, which was less significant for Pruhonice.

The $F_2$-layer peak height $h_mF_2$ has undergone more distinct changes within the storm recovery phase. Values of $h_mF_2$ were significantly higher during the night of 8 and 9 January at Pruhonice. Grahamstown showed a not so clear course of $h_mF_2$. The data indicated some decrease during 6 and 7 January and also some positive effect within the rest of the analyzed period. A considerable enhancement of electron density has been observed also for Millstone Hill and Port Stanley (American sector). For Millstone Hill the $f_oF_2$ values were increased particularly during 5–7 January, while at Port Stanley we observed rather positive effects at the beginning of the analyzed period, then an enhancement and decrease of $f_oF_2$ alternated. Similarly to Pruhonice, there was no significant effect on $h_mF_2$ observed at 4–6 January for Millstone Hill station. A significant increase in the peak altitude above Millstone Hill occurred during the recovery phase, whereas Port Stanley exhibited predominantly positive effect on $h_mF_2$ starting from the storm main phase. The storm-time $f_oF_2$ and $h_mF_2$ behavior above Millstone Hill was similar to this observed for Pruhonice. Port Stanley showed positive and negative effects on $f_oF_2$ and mainly positive effect on peak height. In comparison with the effects observed at Grahamstown, Port Stanley showed rather different behavior.

The minor storm of November 2008 started at about the midnight of the 25th. Similar to the above discussed January 2008 event both Pruhonice and Grahamstown ionospheric stations recorded significant increase of $f_oF_2$ at 25 November. Contrary to Grahamstown, for the rest of the analyzed stormy period mainly positive effect on $f_oF_2$ dominated over Pruhonice and no significant changes have been observed in $h_mF_2$. Grahamstown recorded decrease in $f_oF_2$ at 26–27 November and both positive and negative effects on $h_mF_2$ during the storm main and recovery phases. Above Millstone Hill a positive effect on $f_oF_2$ (up to 40%) prevailed during the storm main phase on 25 November and dominated for the entire analyzed period. The observation is similar to the ionospheric response obtained for Pruhonice. The largest electron density enhancement (~50%) has been observed at the local night/morning of 27 November (the storm recovery phase). When comparing changes in $h_mF_2$, data obtained for Millstone Hill shows significant short-duration

increase of the $F_2$-layer peak height mainly during local morning hours of 25–26 November, while for Pruhonice no such significant departure from mean values was observed. Observations at Port Stanley indicated decrease in both $f_oF_2$ and $h_mF_2$ parameters during the storm main phase and some positive effects of slightly higher magnitude during the subsequent recovery phase.

We processed data for 45 minor-to moderate events, which occurred within the period 2007–2009 (11 summer storms, 13 equinoxes, 21 winter storms) to obtain some statistical information on the magnitude of the ionospheric effects. Summarized results for Pruhonice and Grahamstown are shown in Figure 4.5. At Pruhonice for a considerable number of analyzed events (20), the observed range of maximum positive effects was $30\% < \delta < 80\%$. For three events, we found positive deviations larger than 80%, while no such large negative effects were observed. Negative deviations mostly occurred in the range of 20%–30% or less than 20%. When comparing a magnitude of the storm-time $f_oF_2$ and $h_mF_2$ deviations from their 27-day means expressed in percentage, we found the storm effect on $f_oF_2$ in general to be higher. For instance, the $h_mF_2$ deviations obtained for 36 events (2008–2009) over Pruhonice were in the frame of ±40% [*Burešová et al.*, 2014].

To assess hemispherical dependence, we analyzed the same 45 events using Grahamstown ionosonde data (for one summer event and one winter event there were no data available). The results for Grahamstown (Fig. 4.5, bottom panels) show similar statistical picture for $f_oF_2$: most of the maximum positive deviations are in the range of $30\% < \delta < 80\%$, while the maximum negative effects mostly are not higher than 20%–30% or less than 20%. Observed differences in ionospheric response could be caused by different seasons at both locations, that is, by a higher number of boreal winter storms than austral winter storms.

Figure 4.6 illustrates the size of the effects on $f_oF_2$ observed during magnetic storms of different magnitude under different solar activity conditions. When comparing the effects of strong magnetic storms of May 2005 and October 2012 (left side panels of Fig. 4.6) with the effects of the minor events described above, it is necessary to point out that changes of $f_oF_2$ observed during the analyzed minor magnetic disturbances of January and November 2008 (right side panels of Fig. 4.6) were comparable and at some locations and on average even larger than those, induced by strong magnetic storms under higher solar activity conditions. This high ionospheric efficiency of weak geomagnetic storms in the deep solar minimum may perhaps be partly related to the different character of geomagnetic activity and its sources in solar minimum.

Figure 4.7 shows the range of departures of $f_oF_2$ from the corresponding 27-day running means for the strong storm of September-October 2012 (left side panels) and for the minor storm of January 2008 (right side panels) during different storm phases as it was recorded at the selected ionospheric stations. The positive effect on $f_oF_2$ prevailed during the main phase of January 2008, and positive deviations were larger also during the recovery phase, while for the September-October 2012 storm, the only positive effect has been observed mainly above lower-middle latitudes. During the beginning of the recovery phase (under still disturbed conditions – $D_{st} < -50$ nT) for most of the selected locations, negative deviations have been observed. During the next part of the recovery phase ($D_{st} > -50$ nT), all stations involved in the analysis recorded both positive and negative effects. The positive effects for this phase, in general, were lower compared with the observations for the recovery phase of the January 2008 storm. Similar analysis has been done by *Burešová et al.* [2014] for $h_mF_2$. In general, for both events, the positive effect was found to be higher, and magnitude of the deviations was larger within the recovery phase. As for possible hemispheric asymmetry in response to geomagnetic storms, Figures 4.6 and 4.7 show that if there is any asymmetry, it is not a pronounced feature of ionospheric behavior.

## 4.4. DISCUSSIONS AND CONCLUSIONS

We studied ionospheric behavior above Northern and Southern Hemispheres during intense and minor CMEs- and CIRs-driven geomagnetic disturbances, which occurred through the 23rd and 24th solar cycles with special focus on prolonged declining phase/deep solar minimum of the last solar cycle. Nowadays, it is very well known that a combination of different factors produces a complex picture, which is different from a simple type-casting of expected storm effects on the ionosphere depending on day time, season, latitude/longitude including also simple interhemispheric mirroring.

However, as it was mentioned by *Lukianova et al.* [2008], it is necessary to take into account a large asymmetry in the interhemispheric distribution of various electrodynamic parameters, as an impact of, for example, asymmetry in ionospheric conductance produced by solar UV radiation, seasonal changes in UV illumination, or variation caused by the offset between geographic and geomagnetic poles.

*Ridley* [2007] and *Lukianova et al.* [2008] showed that the ionospheric conductance changes the properties of the plasma convection and affects the field-aligned currents (FAC) connecting the magnetosphere and ionosphere. The authors also pointed out that the IMF $B_y$ component affects electrodynamics in the magnetosphere, so that a voltage appears between the two magnetospheric lobes. Thus, we can expect a radial electric field and

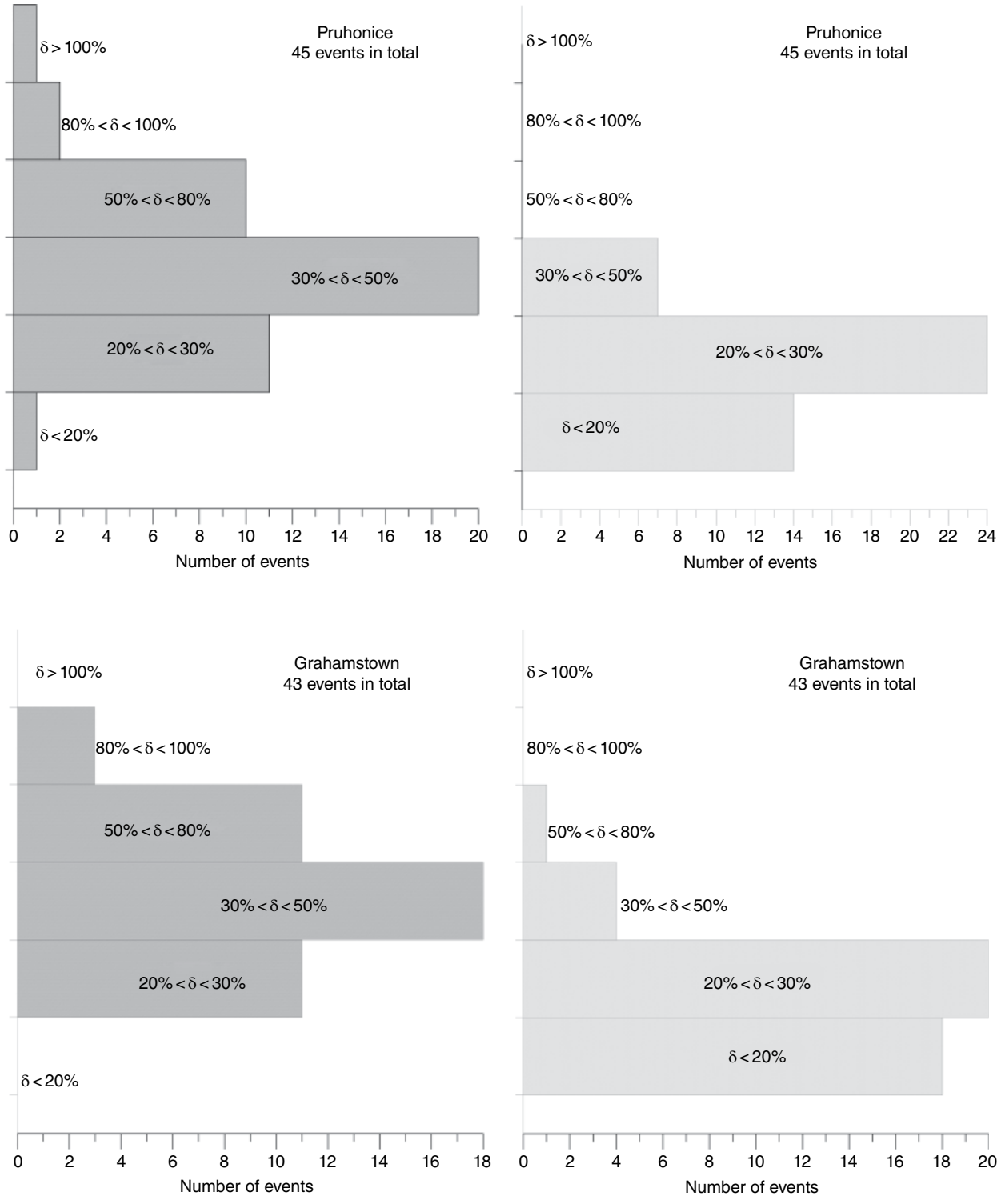


**Figure 4.5** Summary of ranges of maximum effects on $f_oF_2$ as it was observed over Pruhonice (top panels) and Grahamstown (bottom panels) for 45 and 43 minor magnetic storms, respectively, which occurred during extremely low solar activity period of 2007–2009. Left side bar charts represent ranges of maximum positive deviations of $f_oF_2$ from its 27-day mean, while right side bar charts are for negative effects.

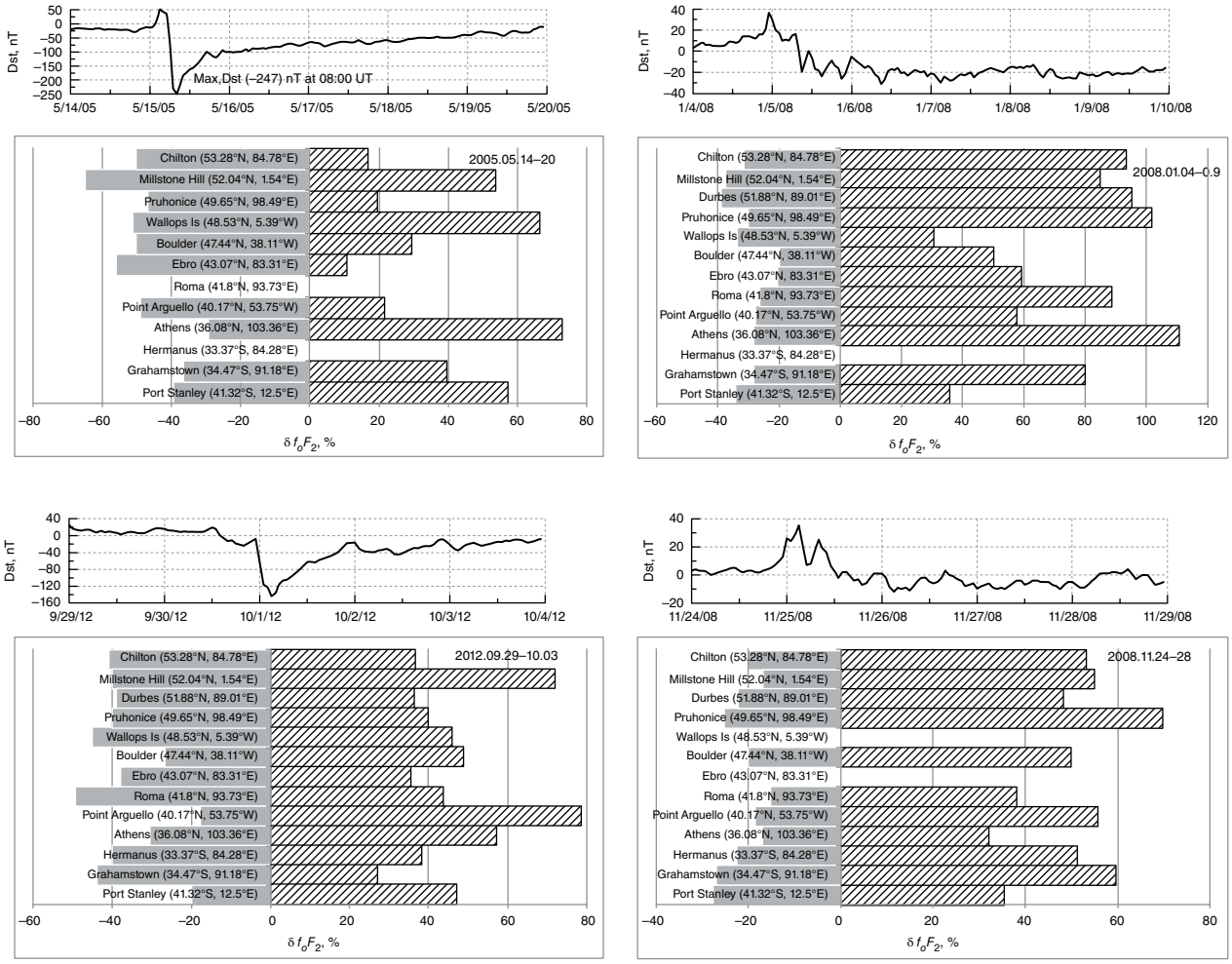


**Figure 4.6** Comparison of the effects of strong magnetic storms of May 2005 and October 2012 (left side panels) on $f_oF_2$ with those of the minor magnetic storms of January and November 2008 (right side panels), as it was observed above several ionospheric stations (geomagnetic coordinates), ranked according to geomagnetic latitude. Plots above each chart bar give course of hourly $D_{st}$ index for the analyzed period (time is in UT). Grey parts of the columns in the bar charts mean values of the peak negative deviation in percentage from the 27-day mean recorded within entire analyzed storm period, whereas those parts with diagonal lines represent the peak positive effect.

azimuthal plasma flow around the poles, which are oppositely directed in the Northern and Southern hemispheres. The magnitude of this effect seems to be depended on the sign of the IMF $B_z$ component.

Penetration of the electric field to regions of closed geomagnetic field lines may be quite significant too, causing a mutual electrodynamic influence of the opposite hemispheres [*Lukianova et al.*, 2008]. When evaluating observed ionospheric behavior under magnetic storm conditions of different magnitude, our results show that, in general, both positive and negative long- and short-lasting departures of $f_oF_2$ and $h_mF_2$ from their 27-day running means took place in all seasons and studied locations for all strong-to-intense and minor events involved in the analysis. This is well illustrated by ionospheric data obtained for the May 2005 magnetic storm (e.g., Fig. 4.1).

The course of $f_oF_2$ above Grahamstown was similar to those recorded for Chilton or Pruhonice with mostly negative effect during the storm maximum day and with an enhancement in electron density during the following day (for Grahamstown it was more significant), whereas, in contrast to Northern American stations above Port Stanley, a distinct positive effect prevailed within the entire storm period. The differences in the behavior of $f_oF_2$ could be affected by local time and magnetic coordinates.

As for $h_mF_2$, a similar course was observed for all American Sector stations. On the other hand, during the

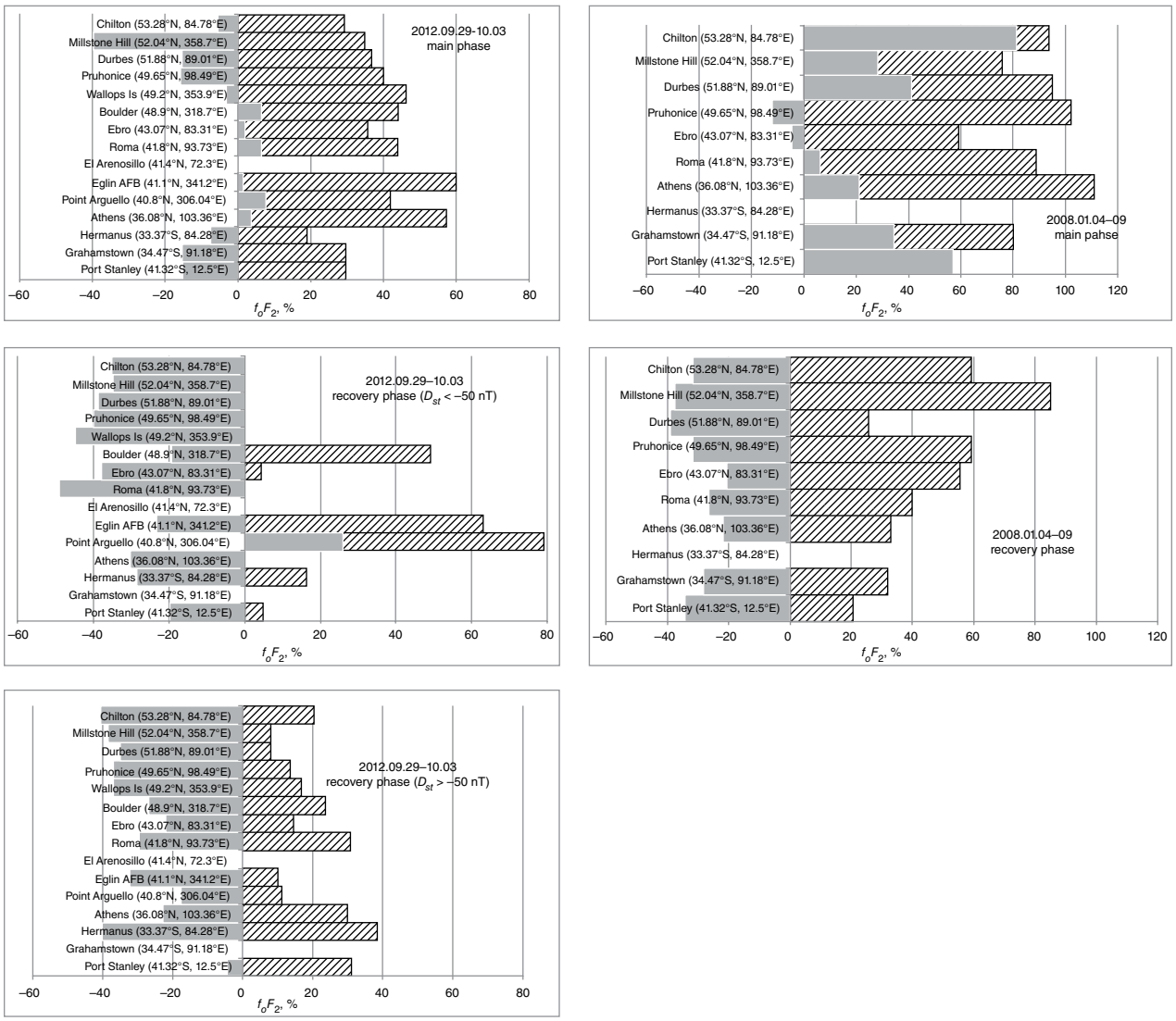


**Figure 4.7** Range of the effects on $f_oF_2$, as it was observed for strong magnetic storm of September-November 2012 (panels on the left side) and minor magnetic storm of January 2008 (panels on the right side) above selected ionospheric stations (geomagnetic coordinates). Grey color parts of the columns in the bar charts mean values of the peak negative deviation in percentage from the 27-day means, whereas those parts with diagonal lines represent the peak positive effect.

October 2011 magnetic storm, the effect on the regular $f_oF_2$ variation recorded at Port Stanley was similar to that obtained for Millstone Hill (e.g., Fig. 4.3). In the case of the September-October 2012 event, all NH and SH stations, in general, displayed similar ionospheric response. Above SH stations, the response was of smaller magnitude. *Lu et al.* [2001] pointed out that the coexistence of both positive and negative storm phases is a result of the complex dynamical and chemical interactions between charged particles and neutral gases.

Several recent publications [e.g., *Araujo-Pradere et al.*, 2011; *Cander and Haralambous*, 2011; *Liu et al.*, 2012; *Verkhoglyadova et al.*, 2013; *Zakharenkova et al.*, 2013; *Surenda Sunda et al.*, 2013; *Burešová et al.*, 2014] and the presented results show that it is necessary to draw the attention of the ionospheric community to surprisingly large effects of minor magnetic storms on the regular behavior of the $F_2$-layer, which occurred during the prolonged declining phase of solar cycle 23 and particularly during the unusually deep solar minimum of the cycles 23/24.

As was mentioned in the Introduction, the occurrence rate of interplanetary coronal mass ejections (ICMEs) is shown to follow the sunspot cycle, while strong CIRs are predominant during the declining phase [*Kamide*, 2001].

It was shown by *Kamide* [2001] that CIR-related magnetic storms are weak to moderate. *Burns et al.* [2012] studied effects of CIR/HSS storms, which occurred during March and April 2008. One of their conclusions was that while CIRs are the most important factor affecting the thermosphere-ionosphere response, the level and duration of the continuing forcing during the HSS is also important. The continued forcing, apart from other effects, leads to enhanced neutral densities and NO cooling for a couple of days after the end of the CIR phase. CIRs at 1 AU are not accompanied by a shock wave, but before their leading edge, the solar wind particle concentration is substantially enhanced. The solar wind with substantially enhanced particle concentration suppresses the magnetosphere, which results in a remarkable increase of the positive $D_{st}$. When this solar wind particle enhancement terminates, $D_{st}$ switches over to negative values. Typically, $B_z$ fluctuates, AE and Kp is increasing but effect in $D_{st}$ is relatively small with the positive phase of $D_{st}$ often larger than the negative one, as it often happened in 2007–2009 [*Burešová et al.*, 2014]. Under higher (normal) geomagnetic/solar activity conditions, the negative phase dominates in the $D_{st}$ storm behavior as a rule. *Koskinen* [2011] pointed out that although $D_{st}$ remains smaller, the fast streams with southward IMF may last much longer and, consequently CIR-related storms are of longer duration. Thus, the cumulative effects of the fast wind-driven storms could be more severe than the effects of ICME events with large peak $D_{st}$.

*Astafyeva and Heki* [2011] analyzed variation of total electron content (TEC) within the time period of April to September 2008, when five large earthquakes occurred around the Japanese Islands. The authors analyzed TEC mainly in order to identify possible atmospheric peculiarities/earthquake precursors before selected events of 7 May, 13 June, 19 July, 23 July, and 11 September of 2008. Nevertheless, they observed positive regional dayside VTEC anomalies (~20%–25%) corresponding to variations of solar flux and interplanetary magnetic field parameters on 23 and 30 April, 2 and 19 May, and, 15–16 June, 12 July, 10 August, and 4 September 2008.

As a possible cause of the observed VTEC enhancement, appearance of strong dawn-to-dusk electric field, triggered by reconnection between intensive southward IMF $B_z$ and the Earth's magnetic field, was considered. The dawn-to-dusk electric field usually moves the equatorial *F*-region plasma upward and enhances the fountain effect. This is valid within the EIA along with displacements of the EIA crests to ±30° of magnetic latitude.

In our study, we focused mainly on middle latitudes and on ionospheric effects of minor magnetic disturbances. The disturbed days with observed TEC enhancement over Japan, mentioned by *Astafyeava and Heki* [2011] are also within the periods we have involved in our analysis. For instance, on 15–16 June for Pruhonice (higher middle latitudes), we obtained nighttime enhancement of $f_oF_2$ against 27-day running mean (~25%), for 12 July the enhancement was ~20%, while on 10 August and 4 September, we observed negative deviation of ~25%–30%, which is opposite to that recorded above Japan. Results of *Verkhoglyadova et al*. [2013] also showed distinct low- and midlatitude VTEC response to HSSs: an enhancement up to 33 TECU (annual average of ~20 TECU) near local noon in 2008. Iin 2009, the authors found the maximum response to HSSs of ~30 TECU with a slightly lower average value than in 2008.

As it is seen from Figure 4.5, a majority of significant effects on $f_oF_2$ (>40%) observed at Pruhonice and Grahamstown under extreme solar minimum conditions are positive. At middle latitudes, there are known short- and long-duration electron density enhancements. The long-duration positive disturbances could be attributed to two mechanisms: downwelling of neutral atomic oxygen and uplifting of the *F*-layer due to neutral winds. Both mechanisms rely on the large-scale changes in thermospheric circulation caused by heating in the auroral zone. Changes in the thermospheric circulation could cause downwelling of the neutral species through constant pressure surface at low-middle latitude equatorward of the composition disturbance zone, increasing the density of the oxygen relative to molecular nitrogen ($N_2$) and molecular oxygen ($O_2$). This will result in an enhancement of the electron concentration.

The origin of positive ionospheric storms is not yet well understood, with several mechanism having been proposed to explain their origin without arriving at a generally accepted explanation. For positive ionospheric storm effects, the increase in electron density is preceded by a significant increase in the height of the $F_2$ region. The neutral composition, advection (the transfer of heat or matter by the flow of a fluid horizontally in the atmosphere) of high-density plasma, equatorward winds, and eastward-directed electric field mechanisms are all important and will contribute to positive ionospheric storm effects. But the neutral composition and advection of high-density plasma do not explain the observed increase in layer altitude. However, the equatorward winds and eastward-directed electric field mechanisms are based on an increase in layer altitude [*Prölss*, 2008; *Ngwira et al.*, 2012].

The results of the extensive analysis of ionospheric storm-time behavior indicate high ionospheric efficiency of weak geomagnetic storms in terms of $D_{st}$, which take place at 2007–2009 (declining phase and deep solar minimum of the solar cycle 23/24). These storms are characterized by higher positive (early phase) than

negative (later phase) excursion of $D_{st}$. The $f_oF_2$ response is found to be comparable to or even larger than the response to strong geomagnetic storms under medium to high solar activity conditions, as it is illustrated by Figure 4.6. The observed ionospheric effects are most probably related to dominant CIR/HSS origin of geomagnetic perturbations. The results are in accordance with the findings reported by *Koskinen* [2011] and *Chen et al.* [2012].

Further investigations are needed to clarify the explanation of the magnitude of increase of ionospheric response under extreme solar minimum conditions. One contributing effect might be the wind response to weak storms confined to latitudes higher than those of analyzed ionospheric stations. In other words, heating in high-latitude thermosphere results in enhanced transport of atomic oxygen, which could increase $f_oF_2$, but the air with more molecular ions is transported to these latitudes in a very limited amount, which could result in only a weak negative phase of ionospheric storm.

Another interesting finding is the occurrence of occasional large deviations from climatological (undisturbed) values of $f_oF_2$ during the recovery phase of geomagnetic storms, when the ionosphere in general returns to undisturbed state. These excursions of $f_oF_2$ values may give even larger deviations from "ground" state than $f_oF_2$ during the main phase of the geomagnetic storm, as shown by Figure 4.7. Occurrence of such large $f_oF_2$ excursions is still not clear. A possible explanation could be longer duration of CIR-related storms. *Knipp et al.* [1998] analyzed satellite and ground-based data obtained for the entire period of the 8-day-long CIR-related storm of November 1993. The authors found that the total Joule heating was at about $13.7 \times 10^{16}$ J. It was 60% of the total dissipation and about 25% of it took place during the first 24 hours after the storm onset.

As for possible hemispheric asymmetry, on average the asymmetry of ionospheric response to geomagnetic storms at middle latitudes is not a dominant and/or strong feature. The asymmetry in individual events may be well pronounced both in $f_oF_2$ and $h_mF_2$ (see, e.g., Figs. 4.1–4.4) but mostly it is an impact of other factors like seasonal variation of ionospheric response, intensity of geomagnetic storm, difference between geographic and geomagnetic coordinates, and so on.

In conclusion, it is necessary to say that there still remains the open question of the strongest player(s) in the ionospheric reaction to magnetic storm-induced disturbances. When investigating NH-SH asymmetry, further studies and larger statistical analyses are necessary to consider the significance of latitudinal/longitudinal, seasonal, local time, and solar activity dependence of the magnetosphere-thermosphere-ionosphere coupling.

## ACKNOWLEDGMENTS

This work has been supported by the Grant P209/12/2440 of the Grant Agency of the Czech Republic. The authors also thank data centers (mainly Digital Ionogram Database of the UMLCAR, WDC1, Chilton, and WDC for Geomagnetism, Kyoto) and ionospheric observatories for supplying them with data.

## REFERENCES

Araujo-Pradere, E. A., R. Redmon, M. Fedrizzi, R. Viereck, and T. J. Fuller-Rowell (2011), Some characteristics of the ionospheric behavior during the solar cycle 23–24 minimum, *Solar Phys.*, *274*, 439–456; doi: 10.1007/s11207-011-9728-3.

Astafyeva, E. I. (2009), Dayside ionospheric uplift during strong geomagnetic storms as detected by the CHAMP, SAC-C, TOPEX, and Jason-1 satellites, *Adv. Space Res.*, *43*, 1749–1756, doi: 10.1016/j.jasr.2008.09.036.

Astafyeva, E., and K. Heki (2011), Vertical TEC over seismically active region during low solar activity, *J. Atmos. Solar-Terr. Phys.*, *73*, 1643–1652, doi:10.1016/j.jastp.2011.02.020.

Balan, N., K. Shiokawa, Y. Otsuka, T. Kikuchi, D. Vijaya Lekshmi, S. Kawamura, M. Yamamoto, and G. J. Bailey (2010), A physical mechanism of positive ionospheric storms at low latitudes and midlatitudes, *J. Geophys. Res.*, *115*, A02304; doi:10.1029/2009JA014515.

Blagoveschensky, D. V., O. M. Pirog, N. M. Polekh, and L. V. Chistyakova (2003), Mid-latitude effects of the May 15, 1997 magnetic storm, *J. Atmos. Solar Terr. Phys.*, *65*, 203–210; doi: 10.1016/S1364-6826(02)00227-4.

Borovsky, J. E., and M. H. Denton (2006), Differences between CME-driven storms and CIR-driven storms, *J. Geophys. Res.*, *114*; doi: 10.1029/2005JA014058.

Buonsanto, M. J. (1999), Ionospheric storms: A review, *Space Sci. Rev*., *88*, 563–60; doi:10.1023/A:1005107532631.

Burešová, D., J. Laštovička, and G. De Franceschi (2007), Manifestation of strong geomagnetic storms in the ionosphere above Europe, 185–202, in *Space Weather Research toward Applications in Europe*, edited by J. Lilensten, Springer, Dordrecht.

Burešová, D., J. Laštovička, P. Hejda, and J. Bochnicek (2014), Ionospheric disturbances under low solar activity conditions, *Adv. Space Res*., *54*, 185–196; doi.org/10.1016/j.asr.2014.04.007.

Burns, A. G., S. C. Solomon, W. Wang, and T. L. Killeen (2007), The ionospheric and thermospheric response to CMEs: Challenges and successes, *J. Atmos. Solar- Terr. Phys.*, 69, 77–85, doi:10.1016/j.jastp.2006.06.010.

Burns, A. G., S. C. Solomon, L. Qian, W. Wang, B. A. Emery, M. Wiltberger, and D. R. Weimer (2012), The effect of corotating interaction region/high speed stream storms on the thermosphere and ionosphere during the last solar minimum, *J. Atmos. Solar Terr. Phys.*, *83*, 79–87; doi:10.1016/j.jastp.2012.02.006.

Cander, L. R., and H. Haralambous (2011), On the importance of total electron content enhancements during the extreme solar minimum, *Adv. Space Res.*, *47*, 304–311; doi:10.1016/j.asr.2010.08.026.

Chen, G.-M., J. Xu, W. Wang, J. Lei, and A. G. Burns (2012), A comparison of the effects of CIR- and CME-induced geomagnetic activity on thermospheric densities and spacecraft orbits: Case studies, *J. Geophys. Res.*, *117*, A08315; doi: 10.1029/2012JA017782.

Danilov, A. D. (2013), Ionospheric F-region response to geomagnetic disturbances, *Adv. Space Res*., *52*(3). 343–366; doi:10.1016/S1364-6826(00)00175-9.

de Abreu, A. J., P. R. Fagundes, Y. Sahai, R. de Jesus, J. A. Bittencourt, C. Brunini, M. Gnede, V. G. Pillat, W. L. C. Lima, J. R. Abalde, and A. A. Pimenta (2010), Hemispheric asymmetries in the ionospheric response observed in the American sector during an intense geomagnetic storm, *J. Geophys. Res.*, *115*, A12312; doi: 10.1029/2010JA015661.

Deng, Y., Y. Huang, S. Solomon, L. Qian, D. Knipp, D. R.Weimer, and J.-S. Wang (2012), Anomalously low geomagnetic energy inputs during 2008 solar minimum, *J. Geophys. Res.*, *117*, A09307; doi:10.1029/2012JA018039.

Field, P. R., H. Rishbeth, R. J. Moffet, D. W. Idenden, T. J. Fuller-Rowell, G. H. Millward, and A. D. Aylward (1998), Modelling composition changes in F-layer storms, *J. Atmos. Solar Terr. Phys.*, *60*(5), 523–543; doi: 10.1016/S1364-6826(97)00074-6.

Förster, M., and I. Cnossen (2013), Upper atmosphere differences between northern and southern high latitudes: The role of magnetic field asymmetry, *J. Geophys. Res. Space Phys.*, *118*(9), 5951–5966; doi: 10.1002/jgra.50554.

Galav, P., S. S. Rao, S. Sharma, G. Gordiyenko, and R. Pandey (2014), Ionospheric response to the geomagnetic storm of 15 May 2005 over mid latitudes in the day and night sector simultaneously, *J. Geophys. Res.: Space Phys.*, *119*(6), 5020–5031; doi: 10.1002/2013JA019679.

Kamide, Y. (2001), Geomagnetic storms as a dominant component of space weather: classic picture and recent issues, 43–77, in *Space Storms and Space Weather Hazards*, edited by I. A. Daglis, Series II: Mathematics, Physics and Chemistry, vol. 38, Kluwer Academic Publishers, Netherlands.

Karpachev, A. T., L. Z. Biktash, and T. Maruyama (2007), The high-latitude ionosphere structure on 22 March, 1979, magnetic storm from multi-satellite and ground-based observations, *Adv. Space Res.*, *40*, 1852–1857; doi: 10.1016/j.asr.2007.04.088.

Kilpua, E. K. J., J. G. Luhmann, L. K. Jian, C. T. Russell, and Y. Li (2014), Why have geomagnetic storms been so weak during the recent solar minimum and the rising phase of cycle 24? *J. Atmos. Solar Terr. Phys.*, *107*, 12–19, doi:10.1016/j.jastp.2013.11.001.

Kintner Jr., P. M., A. J. Coster, T. Fuller-Rowell, A. J. Mannucci, M. Mendillo, and R. Heelis (2008), Midlatitude ionospheric dynamics and disturbances: Introduction, 1–7, in *Middle Ionospheric Dynamics and Disturbances*, edited by P. M. Kintner Jr., A. J. Coster, T. Fuller-Rowell, A. J. Mannucci, M. Mendillo, and R. Heelis, *Geophysical Monograph Series, vol. 181,* American Geophysical Union, Washington, DC.

Knipp, D., S. Eriksson, L. Kilcommons, G. Crowley, J. Lei, M. Hairston, and K. Drake (2011), Extreme Poyting flux in the day-side thermosphere: Examples and statistics, *Geophys. Res. Lett.*, *38*, L16102; doi: 10.1029/2011GL048302.

Knipp, D. J., B. A. Emery, M. Engebretson, X. Li, A. H. McAllister, T. Mukai, S. Kokubun, G. D. Reeves, D. Evans, T. Obara, X. Pi, T. Rosenberg, A. Weatherwax, M. G. McHarg, F. Chun, K. Mosely, M. Codrescu, L. Lanzerotti, F. J. Rich, J. Sharber, and P. Wilkinson (1998), An overview of the early November 1993 geomagnetic storm, *Geophys. Res. Lett.*, *38*(103), 26,197–26,220; doi:10.1029/98JA00762.

Koskinen, H. E. J. (2011), *Physics of Space Storms: From the Solar Surface to the Earth*, Springer-Verlag, Berlin Heidelberg.

Laštovička, J. (2013), Are trends in total electron content (TEC) really positive? *J. Geophys. Res. Space Phys.*, *118*, 3831–3835; doi: 10.1002/jgra.50261.

Li, Z., F. Wei, X. Feng, J. Guo, B. A. Emery, and X. Zhao (2012), Large ionospheric disturbances during minor geomagnetic storm on June 23, 2000, *Ann. Geophys.*, *55*(2), 253–263; doi: 10.4401/ag-5409.

Liu L., J. Yang, H. Le, Y. Chen, W. Wan, and C. -C. Lee (2012), Comparative study of the equatorial ionosphere over Jicamarca during recent two solar minima, *J. Geophys. Res.*, *117*, A01315; doi:10.1029/2011JA017215.

Loewe, C. A., and G. W. Prölss (1997), Classification and mean behavior of magnetic storms, *J. Geophys. Res.*, *102*, 14,209–14,213; doi:10.1029/96JA04020.

Lu, G., A. D. Richmond, R. G. Roble, and B. A. Emery (2001), Coexistence of ionospheric positive and negative storm phases under northern winter conditions: A case study, *J. Geophys. Res.*, *106*, NOA11, 24,493–24,504; doi:10.1029/2001JA000003.

Lukianova, R., C. Hanuise, and F. Christiansen (2008), Asymmetric distribution of the ionospheric electric potential in the opposite hemispheres as inferred from the SuperDARN observations and FAC-based convection model, *J. Atmos. Terr. Phys.*, *70*, 2324–2335; doi:10.1016/j.jastp.2008.05.015.

Lukianova, R., Yu, A. Kozlovskii, and F. Christiansen (2012), Field-aligned currents in the winter and summer hemispheres caused by IMF By, *Geomag. Aeron.*, *52*(3), 300–308; doi:10.1134/S0016793212020089.

Mansilla, G. A., and M. M. Zossi (2013), Ionospheric response to the 3 August 2010 geomagnetic storm at mid and mid-high latitudes, *Adv. Space Res.*, *51*(1), 50–60; doi: 10.1016/j.asr.2012.09.001.

Mendillo, M. (2006), Storms in the ionosphere: Patterns and processes for total electron content, *Rev. Geophys.*, *44*, RG4001; doi:10.1029/2005RG000193.

Mendillo, M., and C. Narvaez (2010), Ionospheric storms at geophysically equivalent sites. Part 2: Local time storm patterns for sub-auroral ionospheres, *Ann. Geophys.*, *28*(7), 1449–1462; doi: 10.5194/angeo-28-1449-2010.

Ngwira, C. M., L. -A. McKinnell, P. J. Cilliers, and E. Yizengaw (2012), An investigation of ionospheric disturbances over South Africa during the magnetic storm on 15 May 2005, *Adv. Space Res.*, *49*(2), 327–335; doi:10.1016/j.asr.2011.09.035

Noja, M., C. Stolle, J. Park, and H. Lühr (2013), Long-term analysis of ionospheric polar patches based on CHAMP TEC data, *Radio Sci.*, *48*(3), 289–301; doi: 10.1002/rds.20033.

Prikryl, P., Y. Zhang, Y. Ebihara, et al. (2013), An interhemispheric comparisons of GPS phase scintillation with auroral emission observed at the South Pole and from DMSP satellite, *Ann. Geophys.*, *56*, R0216; doi:10.4401/ag-6227.

Prölss, G. W. (1993), On explaining the local time variation of ionospheric storm effects, *Ann. Geophys.*, *11*(1), 1–9.

Prölss, G. W. (1995), Ionospheric F-region storms, 195–248, in *Handbook of Atmospheric Electrodynamics*, vol. 2, edited by H. Volland, CRC Press, Boca Raton, Florida.

Prölss, G. W. (2004), *Physics of the Earth's Space Environment*, Springer-Verlag, Berlin Heidelberg, Germany.

Prölss, G. W. (2008), Ionospheric storms at mid-latitude: A short review, 9–24, in *Middle Ionospheric Dynamics and Disturbances*, edited by P. M. Kintner Jr., A. J. Coster, T. Fuller-Rowell, A. J. Mannucci, M. Mendillo, and R. Heelis, *Geophysical Monograph Series*, *vol. 181*, American Geophysical Union, Washington, DC.

Ridley, A. J. (2007), Effects of seasonal changes in the ionospheric conductance on magnetospheric field-aligned currents, *Geophys. Res. Lett.*, *34*, L05101; doi:10.1029/2006GL028444.

Rishbeth, H., and M. Mendillo (2001), Patterns of F2-layer variability, *J. Atmos. Terr. Phys.*, *63*, 1661–1680; doi:10.1016/S1364-6826(01)00036-0.

Rishbeth, H., and P. R. Field (1997), Latitude and solar-cycle patterns in the response of the ionosphere F2-layer to geomagnetic activity, *Adv. Space Res.*, *20*(9), 1689–1692; doi:10.1016/S0273-1177(97)00573-5.

Sahai, Y., et al. (2005), Effects of the major geomagnetic storms of October 2003 on the equatorial and low-latitude F-region in two longitudinal sectors, *J. Geophys. Res.*, *110*, A12S91; doi: 10.1029/2004JA010999.

Sahai, Y., et al. (2009), Effects observed in the Latin American sector ionospheric F region during the intense geomagnetic disturbances in the early part of November 2004, *J. Geophys. Res.*, *114*, A00A19; doi: 10.1029/2007JA013007.

Solomon, S. C., L. Qian, and A. G. Burns (2013), The anomalous ionosphere between solar cycles 23 and 24, *J. Geophys. Res. Space Physics*, *118*(10), 6524–6535; doi: 10.102/jgra.50561.

Solomon, S. C., T. N. Woods, L. V. Didkovski, J. T. Emmert, and L. Qian (2010), Anomalously low solar extreme-ultraviolet irradiance and thermospheric density during solar minimum, *Geophys. Res. Lett.*, *37*, L16103; doi: 10.1029/2010GL044468.

Surendra Sunda, B. M. Vyas, and P. V. Khekale (2013), Storm time spatial variations in TEC during moderate geomagnetic storms in extremely low solar activity conditions (2007–2009) over Indian region, *Adv. Space Res.*, *52*, 158–176; doi:10.1016/j.asr.2013.03.006.

Tsurutani, B. T., R. L. McPherron, W. D. Gonzalez, G. Lu, N. Gopalswamy, and F. L. Guarnieri (2006), Magnetic storms caused by corotating solar wind streams, 1–17, in *Geophysical Monograph Series*, vol. 167, American Geophysical Union, Washington, DC.

Turner, N. E., W. D. Cramer, S. K. Earles, and B. A. Emery (2009), Geoefficiency and energy partitioning in CIR-driven and CME-driven storms, *J. Atmos. Solar Terr. Phys.*, *71*, 1023–1031; doi:10.1016/j.jastp.2009.02.005.

Verkhoglyadova, O. P., B. T. Tsurutani, A. J. Mannucci, M. G. Mlynczak, L. A. Hunt, and T. Runge (2013), Variability of ionospheric TEC during solar and geomagnetic minima (2008–2009): External hig speed stream drivers, *Ann. Geophys.*, *31*, 263–276; doi:10.5194/angeo-31-263-2013.

Wang, W., J. Lei, A. G. Burns, S. C. Solomon, M. Wiltberger, J. Xu, Y. Zhang, L. Paxton, and A. Coster (2010), Ionospheric response to the initial phase of geomagnetic storms: Common features (Review), *J. Geophys. Res.*, *115*(7*)*; doi: 10.1029/2009JA014461.

Webb, D. F. (1995), Solar and geomagnetic disturbances during the declining phase of recent solar cycle, *Adv. Space Res.*, *16*(9), 57–69; doi:10.1016/0273-1177(95)00315-6.

Xiong, C., H. Lühr, and S. Y. Ma (2013), The magnitude and inter-hemispheric asymmetry of equatorial ionization anomaly based on CHAMP and GRACE observations, *J. Atmos. Solar Terr. Phys.*, 105–106, 160–169; doi:10.1016/j.jastp.2013.09.010.

Zakharenkova, I. E., I. V. Cherniak, A. Krankowski, and I. I. Shagimuratov (2013), Analysis of electron content variations over Japan during solar minimum: Observations and modeling, *Adv. Space Res.*, *52*, 1827–1836; doi:10.1016/j.asr.2012.09.043.

Zakharenkova, I. E., I. V. Cherniak, A. Krankowski, and I. I. Shagimuratov (2014), Cross-hemisphere comparisonof mid-latitude ionospheric variability during 1996–2009: Juliusruh vs. Hobart, *Adv. Space Res.*, *53*(2), 175–189; doi:10.1016/j.asr.2013.10.027.

Zhao, B., W. Wan, J. Lei, Y. Wei, Y. Sahai, and B. Reinisch (2012), Positive ionospheric storm effects at Latin America longitude during the superstorm of 20–22 November 2003, revisit, *Ann. Geophys.*, *30*, 831–840; doi:10.5194/angeo-30-831-2012.

# Part II
# Longitude Dependence of Storm-Enhanced Densities (SEDs)

# 5

# Longitude and Hemispheric Dependencies in Storm-Enhanced Density

**Roderick A. Heelis**

## ABSTRACT

Various observations of storm-enhanced density (SED) show that this phenomenon is associated with high levels of magnetic activity for which the global ionospheric dynamics are changed. SED itself has large spatial scales extending for many hours around local noon and occupying a region that may extend 15° or 20° in latitude equatorward of the auroral zone. In addition to the large spatial SED feature, there also exists a SED plume that extends from the base of the broad SED toward higher latitudes near local noon. Complete descriptions of these features in the Northern and Southern hemispheres are hampered by inadequate measurements. However, some observations suggest that while the dynamics of the features may be approximately the same, their magnitude is dependent on hemisphere, longitude, and season. Here we review the observed features of SED and SED plumes and pursue a model for their development that predicts longitudinal, seasonal, and hemispheric asymmetries that may be revealed in further observations.

**Key Points:**
Density dependent on storm-time dynamics.
Longitude and seasonal dependencies.

**Key Terms:** ionospheric density enhancement, total electron content

## 5.1. INTRODUCTION

During magnetic storms, the ionospheric density near and above the *F* peak shows both increases and decreases that are related to the storm phase and local time. A recent review given by *Mendillo* [2006] describes both increases in the ionospheric density across the dayside during the storm main phase and decreases in the nightside at later epochs of the storm. The advent of global images of the ionosphere provided by total electron content (TEC) measurements from GPS satellites [*Mannucci et al.*, 1998] has provided an additional perspective on the storm-time response of the ionosphere. Among the many features in such images are increases in the dayside TEC equatorward of the auroral zone that are linked to storm-enhanced density (SED) originally identified by *Foster* [1993]. Since the original identification of SED, extensive studies utilizing GPS images of global TEC variations have revealed more details of its features and many coincident storm-time variations that are linked through the continuity of the system [*Foster et al.*, 2004; *Immel et al.*, 2005; *Foster et al.*, 2007]. Here we briefly describe the major features of SED and its longitudinal and hemispheric dependencies in the context of storm-time variations in neutral and plasma motions in the ionosphere and magnetosphere-ionosphere coupling.

*William Hanson Center for Space Sciences, University of Texas at Dallas, Richardson, Texas, USA*

*Ionospheric Space Weather: Longitude and Hemispheric Dependences and Lower Atmosphere Forcing, Geophysical Monograph 220*, First Edition. Edited by Timothy Fuller-Rowell, Endawoke Yizengaw, Patricia H. Doherty, and Sunanda Basu.

## 5.2. PLASMA DENSITY AND TEC VARIATIONS

SED was first identified in storm-time variations in the plasma density observed near the equatorial edge of the auroral zone [*Foster*, 1993]. During the storm main phase, the plasma density above the *F* peak is seen to increase equatorward of the auroral zone at nearly all local times across the noon sector and into the evening side. The enhanced plasma density is also seen to project poleward into a so-called SED plume that extends in a longitudinally confined region from the base of the SED toward the cusp region near local noon. More recently, this daytime enhancement in the plasma density and the existence of a connected plume of enhanced density extending toward the cusp, has been dramatically illustrated in a number of images of the spatial distribution of TEC obtained from GPS satellite signals.

Figure 5.1, taken from the work of *Coster and Skone* [2009], shows examples of SED and SED plumes observed in the European and American sectors. In both examples, the high TEC identified as SED is seen to extend across the dayside as previously described, while the plume appears as a continuous, longitudinally narrow extension of enhanced TEC that leaves the base of the SED region and extends to higher latitudes near local noon. We use the labels SED and SED plume to distinguish the midlatitude feature that extends across the dayside from the spatially confined feature that extends toward, and sometimes into, the cusp. In the American sector, plumes are generally seen in the postnoon hours and extend to higher latitudes and earlier local times during large storms. However, there are also reports of SED plumes observed in the prenoon hours *Yizengaw et al.* [2006] and in the case shown here, assuming the SED plume observed in the European sector is connected to the midlatitude SED near 60° longitude, it too emerges from the prenoon hours.

A detailed examination of the latitude distribution of the plasma density or the TEC shows that across the afternoon sector the SED feature most frequently lies at the poleward edge of enhancements that can be identified with the equatorial anomaly [*Mannucci et al.*, 2005; *Heelis and Coley*, 2007]. Figure 5.2 reproduces a figure from the measurements of topside TEC described by *Mannucci et al.* [2005] where storm-time enhancements in the TEC associated with the equatorial anomaly can be seen clearly in the postnoon sector around 1300 local time in the American longitude sector. But also present are enhancements in TEC that appear as shoulders in the latitude distribution near 50° magnetic in the north and near 45° magnetic in the south. These features are identified as SED.

Figure 5.3 shows profiles of the topside ionospheric density near 800 km altitude, taken during a storm time and prior to the storm, observed just before 1800 local time. During quiet times, signatures of the equatorial anomaly are normally absent in the topside at this local time. However, enhanced upward plasma drifts at the equator, which are associated with the storm, produce the anomaly feature at higher altitudes. More important, a plasma density enhancement poleward of the anomaly features can be identified as SED. In this case, these

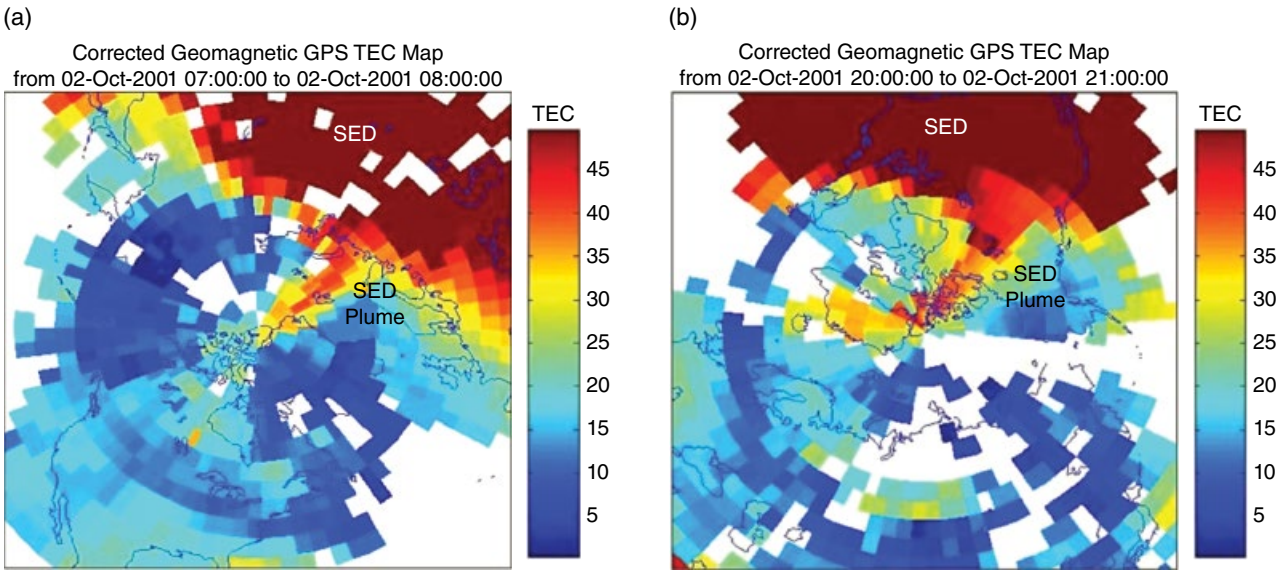


**Figure 5.1** The global distribution of TEC derived from ground-based receivers shows the storm-time SED in dark red across the dayside and a TEC plume that extends toward the pole. TEC plumes are observed in the European (left panel) and the American (right panel) longitude sectors [reproduced from *Coster and Skone*, 2008].

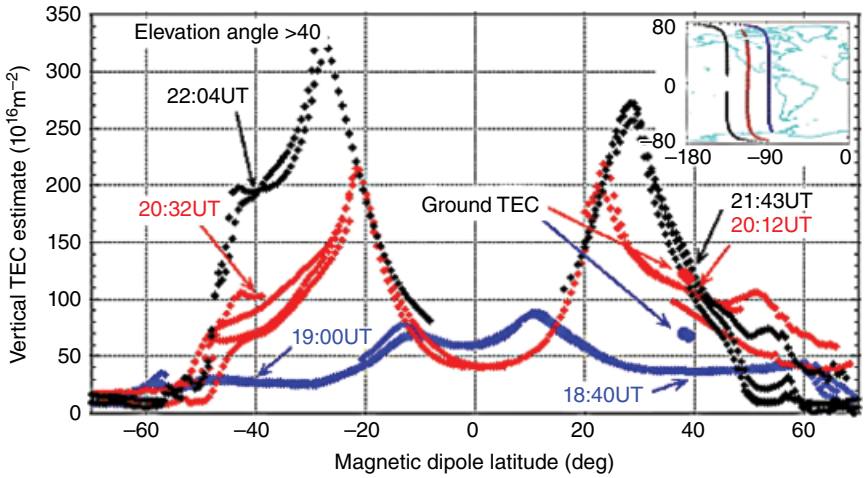


**Figure 5.2** TEC above about 400 km shows storm-time signatures of equatorial anomaly peaks near 30° and SED shoulders beyond 40° magnetic latitude [reproduced from *Mannucci et al.*, 2005].

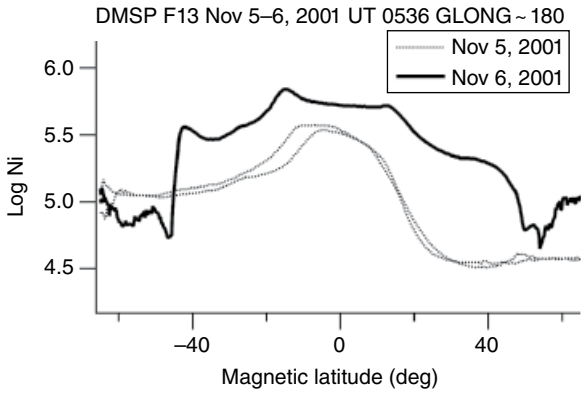


**Figure 5.3** DMSP measurements of local plasma density near 800 km show the usual quiet time variation with latitude (dotted curve) and a storm-time variation that displays a signature of the equatorial anomaly peaks near 20° and SED shoulders near 40° magnetic latitude.

prominent SED signatures are observed in the longitude region around 180°. However, observations of TEC enhancements identified as SED have also been observed in the European sector [*Coster et al.*, 2007] and by *Maruyama* [2006] near 150° longitude at local times just after dusk.

Thus, it appears that the mechanisms responsible for the enhanced anomaly and SED may not be restricted to a particular longitude, even though a longitude dependence in their magnitude may exist. Indeed, *Coster et al.* [2007] show that TEC enhancements identified as SED show a minimum in the longitude sector near 50° and a maximum in the longitude sector near 270° corresponding approximately to the geographic latitude (cf. solar zenith angle) of the SED base.

*Immel and Mannucci* [2013] describe fractional changes in TEC as a function of latitude, longitude, and universal time. Their statistical analysis, while perhaps aliased by storm phase and season, also indicates that storm-time enhancements in TEC are organized by longitude and local time with the most prominent increases in the South American sector. This sector also shows the widest latitudinal distribution of TEC perturbations that might be associated with the presence of SED in the Northern Hemisphere. The percentage change in TEC from nominal quiet time values is rarely examined in detail. However, *Immel and Mannucci* [2013] also report that the largest percentage changes occur in the American sector.

The ionospheric plasma density is largely organized by the magnetic field and solar zenith angle. If the plasma is in diffusive equilibrium, then the plasma density also depends upon the divergence in the horizontal flux in an inertial reference frame. Electrodynamic transport processes associated with the production of SED will of course be magnetically conjugate. However, the corotation velocity and the solar zenith angle can be different at conjugate locations. Thus, we might expect conjugate features such as the equatorial anomaly peaks and SED to differ in spatial configuration and magnitude. We have seen previously that across the entire dayside, the plasma number density and the TEC associated with the equatorial anomaly are enhanced during a storm time.

Whether this enhancement can be called SED is not clear but this feature is clearly a conjugate effect resulting from a so-called super fountain [*Tsurutani et al.*, 2004]. We will discuss the plasma drift feature responsible for this phenomenon in more detail in the following section. The more easily identified SED feature, which appears at middle latitudes, lies poleward of the equatorial anomaly

and rather precise studies of these features by *Foster and Coster* [2007] and *Foster and Rideout* [2007] show convincingly that the poleward edges of the midlatitude SED are magnetically conjugate and remain so even after they are produced and subsequently corotate into the evening. The finding of conjugate features is also consistent with the observation that SED appears just equatorward of the auroral zone [*Heelis and Coley*, 2007] where the magnetic flux lines are almost dipolar. It is important to emphasize that the TEC features that we identify as SED are widely distributed in longitude and thus their conjugate appearance may not indicate more than the fact that similar energy dissipation and convective features exist in each hemisphere during a storm. In addition to hemispheric asymmetries in magnitude produced by solar zenith angle, the action of neutral winds, which also depend on solar zenith angle, geographic latitude, and the magnitude and location of the storm-time energy inputs to the high latitude ionosphere, may also be a factor. To my knowledge, no systematic study of these effects has yet been conducted.

The SED plume is a feature that extends from the middle latitude SED itself toward higher latitudes and toward the noon hours. It is much more restricted in latitude and longitude than the midlatitude SED feature itself, which extends across the dayside at all longitudes. Establishing the conjugate nature of the SED plume is more complicated due to its relatively small spatial extent and the absence of measurements in the right place at the right time. Nevertheless, *Foster and Rideout* [2007] also provide some evidence for observations of SED plumes at conjugate locations, suggesting that their formation is associated with plasma convective effects.

## 5.3. PLASMA CONVECTION ASSOCIATED WITH SED

SED is a storm-time phenomenon that is necessarily accompanied by storm-time changes in the plasma convection, the neutral atmosphere composition, and neutral winds. Before discussing how these changes may be causally related to SED, it is useful to describe the features themselves in simple terms that will build a framework for establishing the connections between the various phenomena.

The onset of a magnetic storm is associated with significant increases in the electric potential difference applied across the magnetosphere. We expect that during large storms, when SED phenomena are most prominent, the magnetopause is eroded as it moves closer to the Earth, and the ionospheric polar cap, identified as the region of open magnetic flux, increases in area. The increased region-1 currents, associated with the change in the solar-wind driver, are not immediately accommodated by currents in the inner magnetosphere and thus a significant fraction of the current closes through the plasmasphere [*Jaggi and Wolf*, 1973]. As a result the two-cell ionospheric convection pattern, usually confined to high latitudes, expands to occupy more of the plasmasphere. This results in a broadly sinusoidal pattern of vertical and zonal perturbation plasma drifts at low and middle latitudes sometimes referred to as penetration fields. Vertical drift perturbations are upward during the day and downward and night with extrema at noon and midnight, while zonal drifts are westward in the postnoon sector and eastward in the prenoon sector, with extrema at dusk and dawn. As the storm progresses, this pattern of perturbation plasma drifts changes due to modifications in the neutral wind and its resulting dynamo action [*Scherliess and Fejer*, 1997].

In addition, the demands of current generation in the magnetosphere and closure in the ionosphere produce two additional convective features associated with penetration fields. First, the gradient in ionospheric conductance between the plasmasphere and the auroral zone produces a so-called subauroral polarization stream (SAPS) that is manifest as enhanced westward flows across the evening and afternoon sectors [*Foster and Vo*, 2002]. Second, the gradient in ionospheric conductance across the dusk terminator leads to enhanced upward vertical drifts at middle and low latitudes across dusk [*Huba et al.*, 2005]. We note that a seasonal and longitude maximum in this feature may appear in the South American sector since the enhanced upward plasma drifts across dusk will depend on the magnitude of the local time gradient in the integrated conductance of the ionosphere.

*Heelis and Coley* [2007] and *Tsurutani et al.* [2004] show that enhanced upward plasma drifts at the equator produce a widening of the equatorial anomaly. But this feature is spatially separated from midlatitude SED, which appears as a poleward shoulder to the anomaly enhancement. More recently, a multiinstrument study of SED by *Zou et al.* [2013] also attributes the equatorward expansion of the high-latitude convection pattern to the appearance of SED.

If an expansion, or penetration, of the high-latitude convection pattern is an essential feature of the midlatitude SED then certainly it is formed as previously corotating plasma becomes entrained in the convection. In the prenoon hours this means that corotating plasma moving toward the sun will be entrained in poleward moving plasma that moves to higher latitudes. In the postnoon and evening sectors this means that plasma previously corotating away from the Sun is entrained in poleward and sunward flow.

*Foster et al.* [2007] show that in the Northern Hemisphere, across the evening sector where SAPS are

prominent, the enhanced westward flows appear at the poleward edge of the midlatitude SED. They also relate these convective features to the erosion of the plasmasphere in the equatorial plane, which is reported in more detail by *Foster et al.* [2014]. In such instances, the poleward edge of the midlatitude SED marks a region of rapid sunward flow, but the local time over which such rapid flows persist at the poleward edge of the SED is not well known. In fact a description of the plasma motions within a SED feature remains a significant challenge, perhaps in part because the storm-time flow perturbations that are required to produce the bulk of the midlatitude SED feature are small and differ significantly over the range of local times and storm-time epochs for which SED are observed.

It is important to recognize that across the dayside the ionospheric plasma is continually being produced, lost, and transported during the storm evolution. Thus, along any given plasma trajectory, it is not appropriate to attribute a specific location to a plasma source, but more informative to establish the variations in production, loss, and transport along the trajectory that give rise to the observed distribution of plasma. This challenge is best met with sophisticated models that describe these processes.

### 5.4. MODELING SED FEATURES

From the previous discussions, it is clear that there are four main targets for modeling of SED features, which appear among other changes in the TEC that are seen during storm times. First, is the bulk of the SED feature itself, which appears at middle latitudes across the dayside ionosphere and into the evening sector. Second, is the increase in the intensity and latitudinal widening of the equatorial anomaly. Third, is the appearance of a SED plume, extending from the base of the midlatitude SED toward higher latitudes near local noon. Fourth, is the apparent longitude dependence in the appearance and magnitude of the SED and SED plume.

Following the first observational descriptions of SED, there have been many attempts to determine the most influential drivers that can produce them. The features we are describing are largely equatorward of regions of significant electron or ion precipitation but they appear at the high latitude extent of the plasmasphere where the storm-time dynamics of the system may place the magnetic flux tubes in a constant state of refilling. This is a complication that needs to be kept in mind, but to my knowledge, most models of the SED formation process at middle latitudes [e.g., *Lin et al.*, 2005] begin with a quasi steady state in which the topside plasma is in diffusive equilibrium. In this case, the TEC can only be increased by changing the photochemical production and loss rates.

The photochemical production and loss rates can be changed by changing the neutral composition. In particular, a storm-time increase in the daytime $O/N_2$ ratio will result in an increase in the local plasma density and the associated TEC. While composition changes may contribute to longer lasting positive and negative phases in storm time changes in TEC [*Mendillo*, 2006], the roles of plasma motions associated with electric fields and neutral winds have received the most attention in various models of the ionosphere and atmosphere. Of particular importance is the ability of vertical plasma drifts to raise the *F* layer to high altitudes as it is being produced and thereby reduce the column loss rate and increase the TEC.

Observations such as those by *Mannucci et al.* [2005], *Heelis and Coley* [2007], and others, strongly suggest that storm-time enhancements in TEC associated with the equatorial anomaly and those associated with the higher latitude feature called SED are spatially separate features that appear at the same time. Close to the magnetic equator the low inclination of the magnetic field significantly reduces the effectiveness of horizontal neutral winds in raising or lowering the layer and thus plasma motion perpendicular to the magnetic field is most effective in changing TEC.

The effects of enhanced vertical plasma drifts across the dayside have been effectively modeled by a number of investigators [*Tsurutani et al.*, 2004; *Lin et al.*, 2005; *Balan et al.*, 2010]. These studies reveal the action of enhanced upward drifts across the dayside is to produce a more intense and latitudinally widened equatorial anomaly in which the TEC is increased at northern and southern excursions from the magnetic equator while it is decreased at the magnetic equator. This signature of a so-called super fountain produces TEC enhancements associated with the equatorial anomaly that move to higher latitudes than seen during moderately active or quiet times. While the increase in the anomaly TEC may maximize near local noon, the maximum excursion of the anomaly can occur near dusk, where the upward drifts can be the largest. In this region at the magnetic equator, the local number density in the topside ionosphere may be severely depleted and after sunset the bottomside ionosphere residing at relatively high altitudes will be very susceptible to instabilities [*Basu et al.*, 2005].

It is well understood that plasma motions perpendicular to the magnetic field will have a vertical component at all latitudes, albeit decreasing with increasing latitude. Indeed, it has been suggested by *Heelis et al.* [2009] that the vertical component of the plasma drift perpendicular to B is sufficient to account for the observed increases in TEC at middle latitudes. However, as pointed out earlier, at certain local times the latitudinal variation in storm-time TEC shows two features, one associated with the

anomaly and another shoulder at higher latitudes. Since the vertical component of $\mathbf{E} \times \mathbf{B}$ drift and the photoionization rate both decrease with increasing latitude, a latitudinal profile with secondary maxima at middle latitudes is not easily reconciled with only plasma motion perpendicular to B. For these reasons, the action of equatorial horizontal neutral winds in the magnetic meridian is also considered. For a constant neutral wind, the effect on the vertical plasma motion will maximize at a dip angle of 45°. Such studies by *Lin et al.* [2005] and *Balan et al.* [2010] confirm that the characteristics of the latitude profile of the TEC enhancements may be reproduced with a combination of equatorward neutral winds driving plasma upward along B and upward plasma drifts perpendicular to B.

It will be illustrated later that the time constant for producing large increases in TEC is of order 1 hr. If the drivers for the TEC increase are subsequently removed, then it takes of order 1 hr for the ionosphere to return to a background state in sunlight. However, after sunset both the background and the enhancement decay at the same rate. Then, the latitudinal profile of storm-time TEC enhancements imprinted on the ionosphere during daytime can subsequently be observed after sunset when the drivers are removed and the signatures return to residence in the corotating atmosphere. Thus, the anomaly and SED features may be seen after sunset as an indicator of processes that were applied in daylight [c.f. *Maruyama*, 2006; *Lin et al.*, 2009].

Models of a SED plume, which appears attached to the base of the SED and projects toward higher latitudes near local noon, are based on the notion that the major driver is the expansion of the high-latitude convection pattern to lower latitudes. Such an expansion takes magnetic flux tubes that were previously corotating across the dayside ionosphere and entrains them on convection trajectories that move poleward toward the cusp. Figure 5.4 shows a sequence of maps of the TEC taken from a storm simulation over a period of 7 hr conducted by *David et al.* [2011]. The small black circle in each panel traces the path of a magnetic flux tube that is initially corotating with the atmosphere but becomes entrained in the convection pattern between 1700 and 1800 UT. The subsequent poleward motion of the plasma, as it is produced in sunlight, produces significant enhancements in TEC across the dayside, recognized as a SED and a characteristic SED plume that extends toward local noon. Note that in this case the convection trajectories that produce the SED plume arise from the prenoon hours as seen in the observations of *Yizengaw et al.* [2006]. However, as we will discuss later, there are various configurations of the convection pattern that can give rise to similar trajectories originating from the postnoon sector. It is important to understand that

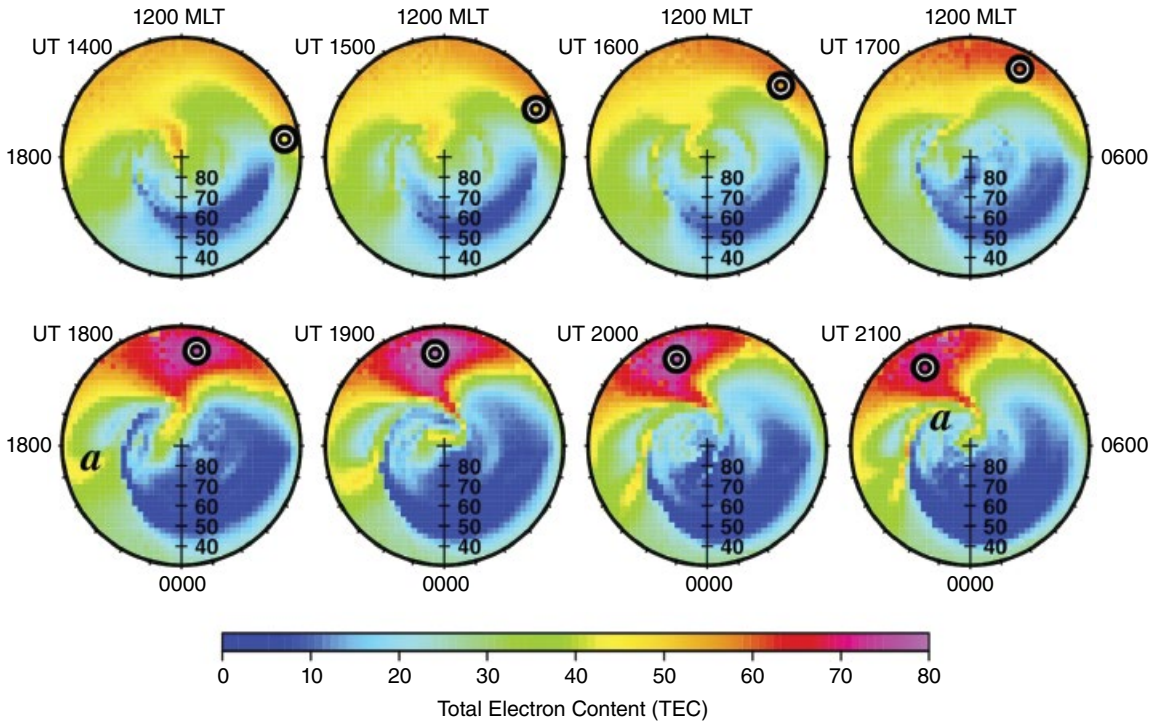


**Figure 5.4** A time series of TEC calculations shows that plasma packets subjected to an expanded convection pattern immediately display the features of SED and a ZSED plume. [reproduced from *David et al.*, 2011].

this tongue of ionization is produced in the same way as the tongue of ionization identified with convective trajectories through the cusp [*Sojka et al.*, 1994]. However, in the case of this expanded convection pattern, plasma trajectories directed toward higher latitudes, and associated with higher plasma density, first appear at lower latitudes than usual.

In this and other studies of the expanded convection pattern, the calculations are performed with the newly created convection pattern put in place instantaneously. It should be recognized that the reconfiguration of the convection pattern takes place on timescales of the order of 1 hr [*Morley and Lockwood*, 2006] and that the plasma distribution resulting from the reconfiguration itself should also be considered. An additional modeling challenge that remains concerns the apparent longitude dependence in the occurrence of the plume and the observed conjugate behavior of the plume. In this regard, the temporal evolution of the convection pattern and the universal time over which it occurs will again be important.

## 5.5. COLLECTIVE FINDINGS

Based on the observations reported and the modeling studies completed, we can assemble a brief description of the plasma flow and density that prevail during a large magnetic storm when SED is most prevalent. The constructed picture points to some dependences on hemisphere, storm epoch, season, local time, and longitude that may be testable with observations and further modeling. During a storm, the plasma density, the plasma motions, and the neutral atmosphere motions must all evolve self-consistently.

In seeking to establish the relationships between these parameters, it is necessary to rigorously establish a temporal history of the storm-time changes that occur. Excluding changes in atmospheric composition, it is well understood that changes in the TEC cannot occur without a change in the plasma motion. Thus, we must first describe the time evolution of the plasma motion and then the subsequent changes in the plasma density that would result. In this regard, the model results seem to point to a dominant process. An initial expansion of the convection pattern will produce poleward and vertically upward plasma motions across the dayside and in the presence of sunlight increases in TEC will result from the reduction in the plasma loss rate. The plasma that becomes entrained in the expanded convection pattern was previously corotating in the plasmasphere and now resides on convection trajectories that are directed poleward toward the cusp.

However, the time taken for a plasma packet to reach the cusp may be much longer than the persistence of the expanded pattern. For example, a poleward flow of $100\,ms^{-1}$ will require over 3 hr to advance a plasma packet 10° in latitude. Similarly, a zonal flow of $300\,ms^{-1}$ will require over 2.5 hr to advance a plasma packet by 3 hr in local time near 60° latitude. By contrast, the timescale to locally increase the plasma density, due to a poleward motion of $100\,ms^{-1}$, is less than 1 hr, as can be seen in the calculations by *David et al.* [2011]. Increases in the plasma-flow speed decrease the transport time but also decrease the residence time of the plasma in sunlight. Thus, both local transport and production contribute to the enhancement of TEC.

We note that in the region between 0600 and 0900 local time and between 1500 and 1800 local time, the poleward component of the high-latitude convective flow takes place at less favorable solar zenith angles than the region across local noon. Thus, the corresponding increase in TEC will decrease at local times/longitudes away from local noon. Upward motions induced by equatorial neutral winds will be determined to a large extent by the local time dependence of the energy input at high latitudes, but for a uniform input across the dayside, we might expect equatorial winds to be more effective across dawn and dusk when they do not directly oppose the day-to-night circulation generated by solar heating. There seems to be little doubt that the combination of poleward and upward plasma drifts and equatorward winds in a sunlit ionosphere is responsible for the observed increases in midlatitude TEC that are termed SED. However, since the drifts and winds are likely dependent on local time and storm-time epoch, a decomposition of these contributions for specific events would be required to assess their relative contributions.

The SED features we have described all arise from the combined effects of vertical plasma motion and sunlight conditions. We have seen that the formation of SED across the dayside at middle latitudes may well involve both the convective motion of the plasma and storm-induced equatorward neutral winds. Even though the important convective motion is that in the inertial frame, we may expect the convective features associated with SED to be almost conjugate with differences less than a fraction of the corotation speed. However, given the existence of significant hemispheric differences in equatorward winds and solar zenith angle at magnetically conjugate points, it is not clear that the magnitude of SED features themselves should be conjugate.

For the purpose of illustration, we will assume that significant vertical motions are imposed near 45° magnetic latitude. In the Northern Hemisphere, the offset between the magnetic and geographic poles is about 8° and thus, even in the winter (with a 23° tilt in the geographic pole), this region would reside in sunlight and thus we expect a SED to appear. For a given vertical plasma drift, the

seasonal and longitude dependence of the solar zenith angle at this location would determine the magnitude of the SED feature. By contrast for winter conditions in the Southern Hemisphere when the offset between the geomagnetic and geographic poles is about 25°, vertical plasma motions at 45° magnetic latitude would take place in darkness, and thus a SED feature would not appear. This produces a testable hypothesis that the appearance and magnitude of SED features at a given magnetic latitude will be seasonally and longitudinally dependent in both hemispheres, and that SED will be significantly less likely in the Southern Hemisphere during local winter when the southern pole is directed away from the sun.

Concerning the configuration of so-called SED plumes, there appear to be three considerations. One is the displacement of the magnetic pole and the geographic pole. Another is the history of the solar zenith angle along the trajectory. Finally, one must consider the time spent on a given convective path. Throughout this discussion we have appealed to the convective motion of the plasma as it is being produced in sunlight as the key contributor to SED. We have also referenced models that produce so-called SED plumes observed in the neighborhood of local noon by the same process. Concerning the SED-plume formation in the ionosphere, it is important to appreciate the convection trajectories that could give rise to this feature.

Figure 5.5 shows the typical addition of a symmetric high-latitude convection pattern with the corotating plasma. In this schematic representation, four open-flow trajectories are shown in red and black after an instantaneous expansion of the convection pattern to lower latitudes, such that the flow between the dashed and solid circles shown in blue, which was previously corotating, is now entrained in the high-latitude convection pattern. The dashed and solid black circles show nominal locations for the convection reversal (or polar cap) boundary before and after the expansion. The black and red flow trajectories are illustrative of those that have significant poleward components at the lowest latitudes in a region equatorward of the heavy orange line where the solar zenith angle is relatively small. The poleward motions in sunlight produce the widely distributed midlatitude TEC enhancement called SED. On the two red trajectories are also shown small heavy segments where the solar zenith angle is larger, but where significant poleward convective motions can give rise to the SED plume that appears in model calculations. The magnitude of the TEC enhancements along these trajectories decreases with increasing solar zenith angle and increasing magnetic dip angle and is thus rapidly attenuated with increasing latitude.

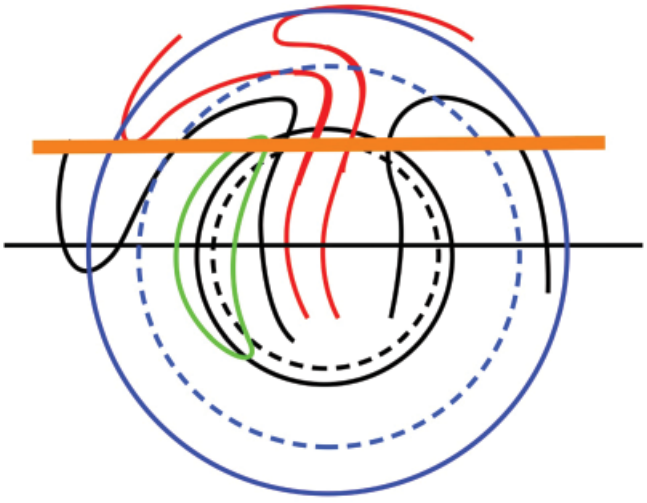

**Figure 5.5** Instantaneous plasma flow trajectories identify regions in black and red that entrain previously corotating plasma into the high-latitude convection pattern and regions (heavy red lines) with substantial poleward flows at the smallest solar zenith angles required to produce a SED plume. The green trajectory represents typical convection through the auroral zone. The orange bar represents the ionization production terminator.

Note that the detailed configuration of the convection pattern can produce these trajectories that emanate from the prenoon or postnoon hours. However, they are always among the shortest convection trajectories that entrain corotating plasma into the convection pattern. Thus, a plume may be created on a timescale that is comparable to, or shorter than, the timescale over which changes in the convection trajectories occur. It is important to emphasize that each of these open trajectories in the morning and afternoon sides, represent an erosion of the plasmasphere, but not all are related to the plasmaspheric erosion tail observed near dusk in the equatorial plane [*Grebowsky*, 1970; *Goldstein et al.*, 2003]. They are however, directly associated with a plasmaspheric bulge across the dayside [*Foster et al.*, 2002; *Goldstein et al.*, 2004]. During extreme events, the appearance of SED and SED plumes allows the connection between some plasma convection paths in the ionosphere with those in the magnetosphere [*Foster et al.*, 2002, 2014]. However, it is important to recognize that erosion of the plasmasphere and transport of this plasma to the magnetopause occur all the time in response to changes in the interplanetary medium. Only during extreme events, when the longitude and solar zenith angle conditions are favorable, do signatures of some of the erosion paths appear in contours of enhanced density in the ionosphere that may be identified as SED features.

Finally, we note that the poleward edge of the main SED feature usually exhibits a sharp latitudinal boundary, at least across the afternoon and evening sectors. Such a significant gradient in the plasma density is usually produced by different plasma convective paths and we attribute this boundary to that between plasma that is entrained into the

convection pattern from lower latitudes from that entrained in the pattern from higher latitudes as shown by the closed green flow trajectory. We note that rapid subauroral plasma flows (SAPS) are also a storm-time phenomenon that is observed at the poleward edge of SEDs observed in the afternoon and evening hours. They would appear to span the boundary between the closed (green) and open (black) trajectories shown here.

*Goldstein et al.* [2005] have shown that the inclusion of SAPS flows provides a better description for the observed location of the plasmapause in the evening sector and *Foster et al.* [2007] show that the SED and SAPS features do indeed overlap in this region. Rapid flows can act to enhance the plasma recombination rate [*Schunk et al.*, 1976] and further enhance a latitudinal gradient in the plasma density that is created by differing plasma-flow paths. Electrodynamic features associated with motions in the inner magnetosphere such as SAPS are certainly expected to be magnetically conjugate. However, plasma features such as SED are highly dependent on the solar zenith angle, thus producing longitude and seasonal dependencies that need not be conjugate.

## 5.6. CONCLUSIONS

A significant observation and modeling effort has been devoted to describing and understanding the formation and evolution of SED. The major characteristics of SED are well explained by the imprint of the high-latitude convection pattern inside the plasmasphere during extremely active times. However, simulations of a specific event will require a description of the global electric field and neural wind distributions in the *F* region that is not yet possible. The magnitude of the TEC enhancement in a SED plume and the location of the plume can be explained in broad terms by the expansion of the convection pattern. However, the spatial extent of the plume and its lifetime are very strong functions of longitude, season, and the temporal evolution of the convection electric field.

Presently, there is insufficient observational evidence to describe the processes at work in a specific instance and to establish any systematic contribution from winds and plasma drifts that are common to all events. If the underlying foundations for SED and SED-plume formation are correct, then there exist significant hemispheric asymmetries in the appearance and magnitude of SED features with season and longitude that could be tested with appropriate observations.

## ACKNOWLEDGMENTS

This work has benefitted greatly from exchanges with many scientists who have contributed to advancements in the field and to exchanges that took place at the Chapman Conference on this topic in Addis Ababa in 2012. I especially thank John Foster for many informative insights. This work is supported by NASA grant NNX10AT02G to the University of Texas at Dallas.

## REFERENCES

Balan, N., K. Shiokawa, Y. Otsuka, T. Kikuchi, D. Vijaya Lekshmi, S. Kawamura, M. Yamamoto, and G. J. Bailey (2010), A physical mechanism of positive ionospheric storms at low latitudes and midlatitudes, *J. Geophys. Res.*, *115*, A02304; doi:10.1029/2009JA014515.

Basu, S., S. Basu, K. M. Groves, E. MacKenzie, M. J. Keskinen, and F. J. Rich (2005), Near-simultaneous plasma structuring in the midlatitude and equatorial ionosphere during magnetic superstorms, *Geophys. Res. Lett.*, *32*, L12S05; doi:10.1029/2004GL021678.

Coster, A., and S. Skone (2009), Monitoring storm-enhanced density using IGS reference station data, *J. Geod.*, *83*, 345–351; doi: 10.1007/s00190-008-0272-3.

Coster, A. J., M. J. Colerico, J. C. Foster, W. Rideout, and F. Rich (2007), Longitude sector comparisons of storm enhanced density, *Geophys. Res. Lett.*, *34*, L18105; doi:10.1029/2007GL030682.

David, M., J. J. Sojka, R. W. Schunk, M. W. Liemohn, and A. J. Coster (2011), Dayside midlatitude ionospheric response to storm time electric fields: A case study for 7 September 2002, *J. Geophys. Res.*, *116*, A12302; doi:10.1029/2011JA016988.

Foster, J. C. (1993), Storm-time plasma transport at middle and high latitudes, *J. Geophys. Res.*, *98*, 1675; doi:10.1029/92JA02032.

Foster, J. C., and A. Coster (2007), Conjugate localized enhancements of total electron content at low latitudes in the American sector, *J. Atmos. Solar Terr. Phys.*, *69*, 1241; doi:10.1016/j/jastp.2006.09.012.

Foster, J. C., and H. B. Vo (2002), Average characteristics and activity dependence of the subauroral polarization stream, *J. Geophys. Res.*, *107*(A12), 1475; doi:10.1029/2002JA009409, 2002.

Foster, J. C., and W. Rideout (2007), Storm enhanced density: Magnetic conjugacy effects, *Ann. Geophys.*, *25*, 1791–1799; doi:10.5194/angeo-25-1791-2007.

Foster, J. C., A. J. Coster, P. J. Erickson, F. J. Rich, and B. R. Sandel (2004), Stormtime observations of the flux of plasmaspheric ions to the dayside cusp/magnetopause, *Geophys. Res. Lett.*, *31*, L08809; doi:10.1029/2004GL020082.

Foster, J. C., P. J. Erickson, A. J. Coster, J. Goldstein, and F. J. Rich (2002), Ionospheric signatures of plasmaspheric tails, *Geophys. Res. Lett.*, *29*(13); doi:10.1029/2002GL015067.

Foster, J. C., P. J. Erickson, A. J. Coster, S. Thaller, J. Tao, J. R. Wygant, and J. W. Bonnell (2014), Storm time observations of plasmasphere erosion flux in the magnetosphere and ionosphere, *Geophys. Res. Lett.*, *41*, 762–768; doi:10.1002/2013GL059124.

Foster, J. C., W. Rideout, B. Sandel, W. T. Forrester, and F. J. Rich (2007), On the relationship for SAPS to storm-enhanced density, *J. Atmos. Solar Terr. Phys.*, *69*, 303; doi:10.1016/j/jastp.2006.07.021.

Goldstein, J., and B. Sandel (2005), Inner magnetosphere Interactions: New perspectives from imaging, *Geophysical Monograph Series*, vol. 159, American Geophysical Union, Washington, DC.

Goldstein, J., B. R. Sandel, M. F. Thomsen, M. Spasojević, and P. H. Reiff (2004), Simultaneous remote sensing and in situ observations of plasmaspheric drainage plumes, *J. Geophys. Res.*, *109*, A03202; doi:10.1029/2003JA010281.

Goldstein, J., B. R. Sandel, M. R. Hairston, and P. H. Reiff (2003), Control of plasmaspheric dynamics by both convection and sub-auroral polarization stream, *Geophys. Res. Lett.*, *30*, 2243; doi:10.1029/2003GL018390.

Grebowsky, J. M. (1970), Model study of plasmapause motion, *J. Geophys. Res.*, *75*(22), 4329–4333; doi:10.1029/JA075i022p04329.

Heelis, R. A., and W. R. Coley (2007), Variations in the low- and middle-latitude topside ion concentration observed by DMSP during superstorm events, *J. Geophys. Res.*, *112*, A08310; doi:10.1029/2007JA012326.

Heelis, R. A., J. J. Sojka, M. David, and R. W. Schunk (2009), Storm time density enhancements in the middle-latitude dayside ionosphere, *J. Geophys. Res.*, *114*, A03315; doi:10.1029/2008JA013690.

Huba, J. D., G. Joyce, S. Sazykin, R. Wolf, and R. Spiro (2005), Simulation study of penetration electric field effects on the low- to mid-latitude ionosphere, *Geophys. Res. Lett.*, *32*, L23101; doi:10.1029/2005GL024162.

Immel, T. J., and A. J. Mannucci (2013), Ionospheric redistribution during geomagnetic storms, *J. Geophys. Res. Space Phys.*, *118*, 7928–7939; doi:10.1002/2013JA018919.

Immel, T. J., J. C. Foster, A. J. Coster, S. B. Mende, and H. U. Frey (2005), Global storm time plasma redistribution imaged from the ground and space, *Geophys. Res. Lett.*, *32*, L03107; doi:10.1029/2004GL021120.

Jaggi, R. K., and R. A. Wolf (1973), Self-consistent calculation of the motion of a sheet of ions in the magnetosphere, *J. Geophys. Res.*, *78*(16), 2852–2866; doi:10.1029/JA078i016p02852.

Lin, C. H., A. D. Richmond, J. Y. Liu, G. J. Bailey, and B. W. Reinisch (2009), Theoretical study of new plasma structures in the low-latitude ionosphere during a major magnetic storm, *J. Geophys. Res.*, *114*, A05303; doi:10.1029/2008JA013951.

Lin, C. H., A. D. Richmond, R. A. Heelis, G. J. Bailey, G. Lu, J. Y. Liu, H. C. Yeh, and S.-Y. Su (2005), Theoretical study of the low- and midlatitude ionospheric electron density enhancement during the October 2003 superstorm: Relative importance of the neutral wind and the electric field, *J. Geophys. Res.*, *110*, A12312; doi:10.1029/2005JA011304.

Mannucci, A. J., B. D. Wilson, D. N. Yuan, C. H. Ho, U. J. Lindqwister, and T. F. Runge (1998), A global mapping technique for GPS-derived ionospheric total electron content measurements, *Radio Sci.*, *33*, 565; doi: 10.1029/97RS02707.

Mannucci, A. J., B. T. Tsurutani, B. A. Iijima, A. Komjathy, A. Saito, W. D. Gonzalez, F. L. Guarnieri, J. U. Kozyra, and R. Skoug (2005), Dayside global ionospheric response to the major interplanetary events of October 29–30, 2003 "Halloween Storms," *Geophys. Res. Lett.*, *32*, L12S02; doi:10.1029/2004GL021467.

Maruyama, T. (2006), Extreme enhancement in total electron content after sunset on 8 November 2004 and its connection with storm enhanced density, *Geophys. Res. Lett.*, *33*, L20111; doi:10.1029/2006GL027367.

Mendillo, M. (2006), Storms in the ionosphere: Patterns and processes for total electron content, *Rev. Geophys*, *44*, RG4001; doi:10.1029/2005RG000193.

Morley, S. K., and M. Lockwood (2006), A numerical model of the ionospheric signatures of time-varying magnetic reconnection: III. Quasi-instantaneous convection responses in the Cowley-Lockwood paradigm, *Ann. Geophys.*, *24*, 961–972; doi:10.5194/angeo-24-961-2006.

Scherliess, L., and B. G. Fejer (1997), Storm time dependence of equatorial disturbance dynamo zonal electric fields, *J. Geophys. Res.*, *102*(A11), 24037–24046; doi:10.1029/97JA02165.

Schunk, R. W., P. M. Banks, and W. J. Raitt (1976), Effects of electric fields and other processes upon the nighttime high-latitude F layer, *J. Geophys. Res.*, *80*, 3271–3282; doi:10.1029/JA081i019p03271.

Sojka, J. J., M. D. Bowline, and R. W. Schunk (1994), Patches in the polar ionosphere: UT and seasonal dependence, *J. Geophys. Res.*, *99*(A8), 14959–14970; doi:10.1029/93JA03327.

Tsurutani, B., *et al.* (2004), Global dayside ionospheric uplift and enhancement associated with interplanetary electric fields, *J. Geophys. Res.*, *109*, A08302; doi:10.1029/2003JA010342.

Yizengaw, E., M. B. Moldwin, and D. A. Galvan (2006), Ionospheric signatures of a plasmaspheric plume over Europe, *Geophys. Res. Lett.*, *33*, L17103; doi:10.1029/2006GL026597.

Zou, S., A. J. Ridley, M. B. Moldwin, M. J. Nicolls, A. J. Coster, E. G. Thomas, and J. M. Ruohoniemi (2013), Multi-instrument observations of SED during 24–25 October 2011 storm: Implications for SED formation processes, *J. Geophys. Res. Space Physics*, *118*, 7798–7809; doi:10.1002/2013JA018860.

# 6

# Solar Cycle 24 Observations of Storm-Enhanced Density and the Tongue of Ionization

**Anthea J. Coster,[1] Philip J. Erickson,[1] John C. Foster,[1] Evan G. Thomas,[2] J. Michael Ruohoniemi,[2] and Joseph Baker[2]**

## ABSTRACT

Storm-enhanced density (SED) plumes form in the ionosphere and plasmasphere at midlatitudes during geomagnetically disturbed conditions. In some cases, ionospheric plasma in the storm-enhanced density (SED) plume becomes entrained in expanded polar cap convection patterns and enters the polar cap through the cusp region to form the tongue of ionization (TOI). The recent addition of several GPS receivers in the Antarctic has led to improvements in TEC spatial coverage in the Southern Hemisphere. In addition, new tools have been developed for merging Super Dual Auroral Network (SuperDARN) observations of decameter scale irregularities with GPS-derived total electron content (TEC) data. This paper will review these new merged data sets and will present a selection of SED and TOI observations from the years 2009, 2012, and 2013 during the current solar cycle 24. The particular SED/TOI observational cases presented represent characteristic longitudinal, hemispherical, and seasonal differences observed during both quiet (2009) and moderate (2012, 2013) solar-flux conditions. The denser observational coverage of GPS receivers during this current solar cycle, especially in Antarctica, allows for better comparisons of SED features in the two hemispheres, and allows conclusions to be drawn about key TEC longitude, hemisphere, and seasonal patterns.

**Key Points:**
Summary of storm enhanced density features as a function of season, hemisphere, time of day, solar cycle.

**Key Terms:** geomagnetic storms, total electron content, storm enhanced density, tongue of ionization

## 6.1. INTRODUCTION

The storm-enhanced density (SED) plume can be described as a latitudinally narrow and large amplitude total electron content (TEC) enhancement, observed in the afternoon and dusk sectors at the equatorward edge of the main ionospheric trough and the region of strong sunward convection during geomagnetically active times. This feature is to be differentiated from enhanced daytime midlatitude plasma due to storm-time uplift of the *F* region. The SED plume can be described as streaming plasma transported by storm-time electric fields in a channellike flow pattern, similar to smoke transported by winds from a chimney or smoke stack. In the same sense, the SED plume maps the ionospheric flow pattern away from its source.

The SED plume can have electron densities in the subauroral region that are greater than typical electron

[1]*Haystack Observatory, Massachusetts Institute of Technology, Westford, Massachusetts, USA*
[2]*Bradley Department of Electrical and Computer Engineering, Virginia Tech, Blacksburg, Virginia, USA*

*Ionospheric Space Weather: Longitude and Hemispheric Dependences and Lower Atmosphere Forcing, Geophysical Monograph 220*, First Edition. Edited by Timothy Fuller-Rowell, Endawoke Yizengaw, Patricia H. Doherty, and Sunanda Basu.

densities at mid and lower latitudes. Initially identified as a large-scale recurring phenomenon through Millstone Hill incoherent scatter radar observations [*Foster*, 1993], SED enhancements have been studied using ground-based TEC measurements and radars [*Vlasov et al.*, 2003; *Kelley et al.*, 2004; *Thomas et al.*, 2013], satellite data and models [*Heelis et al.*, 2009], and modeling studies [*Lin et al.*, 2005; *Lu et al.*, 2008; *David et al.*, 2011].

These studies and others have found that midlatitude SED enhancements are related to magnetosphere-ionosphere coupling in subauroral regions, likely through the effects of storm-time penetration electric fields and the expansion of the general high-latitude convection pattern into midlatitudes [*Heelis et al.*, 2009]. The region of the ionosphere under the influence of magnetospheric Region 2 closure currents and associated electric fields expands dramatically toward lower latitudes during storm times [*Heelis et al.*, 2009] and therefore storm-time electric fields play significant roles in the formation of SED plasma and SED streams.

Figure 6.1 presents a representative polar projection of global TEC at universal times associated with American longitudes in the afternoon on the duskside, and labels some of the processes involved with SED formation. First is the large storm-time increase in midlatitude plasma thought to be associated with storm-time penetration electric fields, indicated by the large area in red labeled as "SED." Part of this enhanced plasma is affected by a disturbance electric field known as the subauroral polarization stream (SAPS) [*Foster and Burke*, 2002; *Foster and Vo*, 2002]. The SAPS electric field forms in the vicinity of Region 2 magnetospheric current closure near areas of low ionospheric conductivity equatorward of auroral electron precipitation.

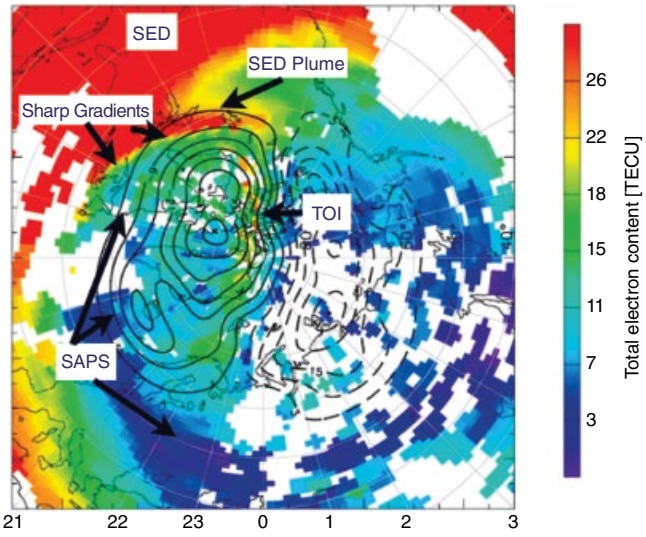


**Figure 6.1** North geomagnetic pole coordinate projection of global TEC at 19:50 UT on 17 March 2013, with 12 MLT located at the top. High-latitude convection flow contours (black solid and dashed lines) are separately estimated from HF radar observations by the SuperDARN network. The storm-enhanced density (SED) feature is the large red region centered on the postnoon sector. Near noon at about 60° magnetic invariant latitude is an SED plasma plume being pulled sunward toward noon by the edge of the dusk convection cell. The yellow and red regions forming a line across the polar cap form a patchy tongue of ionization (TOI).

In Figure 6.1, SAPS electric-field climatologies predict its location in magnetic latitude coordinates as a function of magnetic local time (MLT) in the dusk to midnight sector [*Clausen et al.*, 2012]. The arrows in Figure 6.1 labeled SAPS point to a dark blue region (and light blue region in the dusk sector) that correspond to extremely low TEC values and represent the ionospheric trough region, an area of low ionospheric conductivity. *Zheng et al.* [2008] explains that where the conductivity is low, Region 2 field-aligned currents (FACs) flow into the region and need to be closed via Pedersen currents (to maintain current continuity). These currents are directed poleward, and therefore result in a poleward electric field that is responsible for the magnetically westward flow seen with SAPS. Thus, the arrows in Figure 6.1 point to the region defined as the SAPS channel, which forms within the trough region. Furthermore, there is the well-known cause-and-effect relationship between high-speed plasma flow (i.e., SAPS) and reduced *F*-region density through the mechanism of collisional recombination [*Schunk et al.*, 1975]. The result is that the SAPS channel acts to reduce the *F* density such that the deepest part of the trough (the dark blue region) corresponds to the center of the high-speed flow (SAPS).

SAPS is characterized by a strong sunward (westward) flow channel covering a broad latitudinal region (~3–5°) in the dusk-to-dawn sector a few degrees below the auroral oval [*Foster and Vo*, 2002]. Where the SAPS electric field overlays the more poleward region of subauroral enhanced plasma, a "channel" of the SED plasma is observed to split off, and this material eventually becomes entrained in expanded convection flow to the cusp region. This SED plasma entrainment in the enhanced polar convection pattern clearly appears in Figure 6.1 as it is carried over the pole as a tongue of ionization [TOI; *Foster et al.*, 2005].

In this paper, we use TOI to mean the envelope within which enhanced ionization is observed at polar latitudes. If convection into the polar cap were a continuous process, this would be a relatively continuous tongue of somewhat uniform plasma density. In reality plasma in the TOI is found to be very patchy. The TOI can be thought of as a stream of islands of high-density plasma with electron density values larger by double or more than surrounding plasma regions. These islands have been described by many studies as polar cap patches [e.g. *Crowley*, 1996]. A simple distinction between convection

that forms continuous plasma tongues vs. patchy tongues can be found, for example, in *Lockwood and Carlson* [1992]. Their morphology has been described from satellite data [*Basu and Valladeras*, 1999] and ground-based data [*Carlson*, 2012].

The SED phenomenon is responsible for some of the largest space weather effects observed at midlatitudes [*Coster and Foster*, 2007]. For example, SED events over the continental United States have been associated with the largest TEC spatial gradients ever observed, in the range of 50 TEC units per degree [e.g., *Foster and Rideout*, 2005]. Large TEC gradients are significantly disruptive to positioning systems relying on radio wave propagation through the ionosphere through generation of large errors in range measurements. Large impacts from large TEC gradients also occur in application contexts such as satellite tracking by radar, GPS navigation, and surveying. All of these applications have a compelling need to identify the presence of SED effects and assess their expected impact on users. However, the distribution and evolution of SED is to date neither well understood nor adequately observed in a global sense, making SED effects hard to predict and mitigate [*Kintner et al.*, 2007, 2008].

This chapter will focus on SED and TOI events observed in both the Northern and Southern hemispheres during the years 2009, 2012, and 2013, periods near solar maximum of the current solar cycle 24. The year 2009 was at the beginning of the solar cycle following an extended period of unusually quiet solar-flux conditions. In 2009, the average yearly 10.7 cm radio flux was 70.6 SFU, where 1 SFU = $10^{-22}$W m$^{-2}$ Hz$^{-1}$. This solar flux value is very low, which causes SED plume amplitudes in general to be more difficult to detect. However, 2009 also had a significant increase in geomagnetic activity allowing SED events to be observable. For 2012 and 2013, years closer to the maximum of solar cycle 24, the average yearly 10.7 cm radio flux values were 120 and 123 SFU, respectively, considerably higher than 2009, but lower than in previous solar cycles.

The solar cycle 24 SED observations presented here were selected to illustrate longitudinal, hemispherical, and seasonal differences in the SED feature observed during both quiet (2009) and moderate (2013) solar-flux conditions. The denser coverage of GPS receivers during this current solar cycle, especially in Antarctica, allows for far better comparisons of SEDs in the two hemispheres than previously available. Before presenting these observations, however, we review the longitudinal, hemispherical, and seasonal differences in SEDs as understood from solar cycle 23 data, along with consideration of SED magnetic conjugate aspects. We will conclude this paper by describing new capabilities developed by merging other observations such as SuperDARN with the global GPS TEC database.

### 6.1.1. Observations from Solar Cycle 23: Longitudinal, Seasonal, Hemispherical Differences in SEDs

During solar cycle 23 (1996–2008), TEC maps derived from the global set of global navigation satellite system (GNSS) data provided a paradigm shift in the way that the Earth's ionosphere and magnetosphere were observed. Prior to GNSS TEC maps, most scientific measurements of the magnetosphere-ionosphere system were from individual observing sites or systems providing information about a region or a single point. With GNSS, by combining individual measurements from multiple receivers, high-resolution temporal and spatial TEC data became available on a global scale.

Among the first important observations made with these new TEC maps were observations of large-amplitude SED plumes across the United States [*Coster et al.*, 2001]. Then *Foster et al.* [2002] demonstrated that SED ionospheric plumes mapped directly to plasmaspheric "drainage plumes," large inner-magnetospheric plasma structures also observed in helium ion 30.4 nm EUV images with the IMAGE satellite [*Goldstein et al.*, 2003].

These observations and a number of other studies established SED plumes as important indicators of significant magnetosphere-ionosphere coupling processes during geomagnetic storms. Recently, using THEMIS to observe magnetospheric crossings, *Walsh et al.* [2014] demonstrated that the reconnecting magnetopause maps to the point in the ionosphere where the TOI is formed and where enhancements in TEC begin to stream tailward over the pole on open field lines. This important finding confirms that the formation of the TOI in the ionosphere is spatially linked to the presence of the plume and reconnection at the magnetopause.

While the initial observations of SED plumes were in the American sector, SEDs were also subsequently reported over Europe [*Yizengaw et al.*, 2006] and over Japan [*Maruyama*, 2006]. Significant longitudinal differences have also been reported. *Coster et al.* [2007] described SEDs observed almost continuously for 15–20 hr during three different 2001 storms. In each case, the SED feature appeared first over Russia, then northern Europe, and then America. In the European sector, the geomagnetic invariant latitude of the SED plume base was observed to be between 61° and 63° (geomagnetic) and at times close to local noon. In the American sector, however, the position of the base of the plume shifted from local noon toward dusk as time progressed during an event, and moved to lower latitudes (geomagnetic) while remaining at a nearly fixed longitude. The study noted that the latitudinal location of the base of the plume with respect to UT had a highly repeatable and consistent pattern. This repeatable pattern may be related

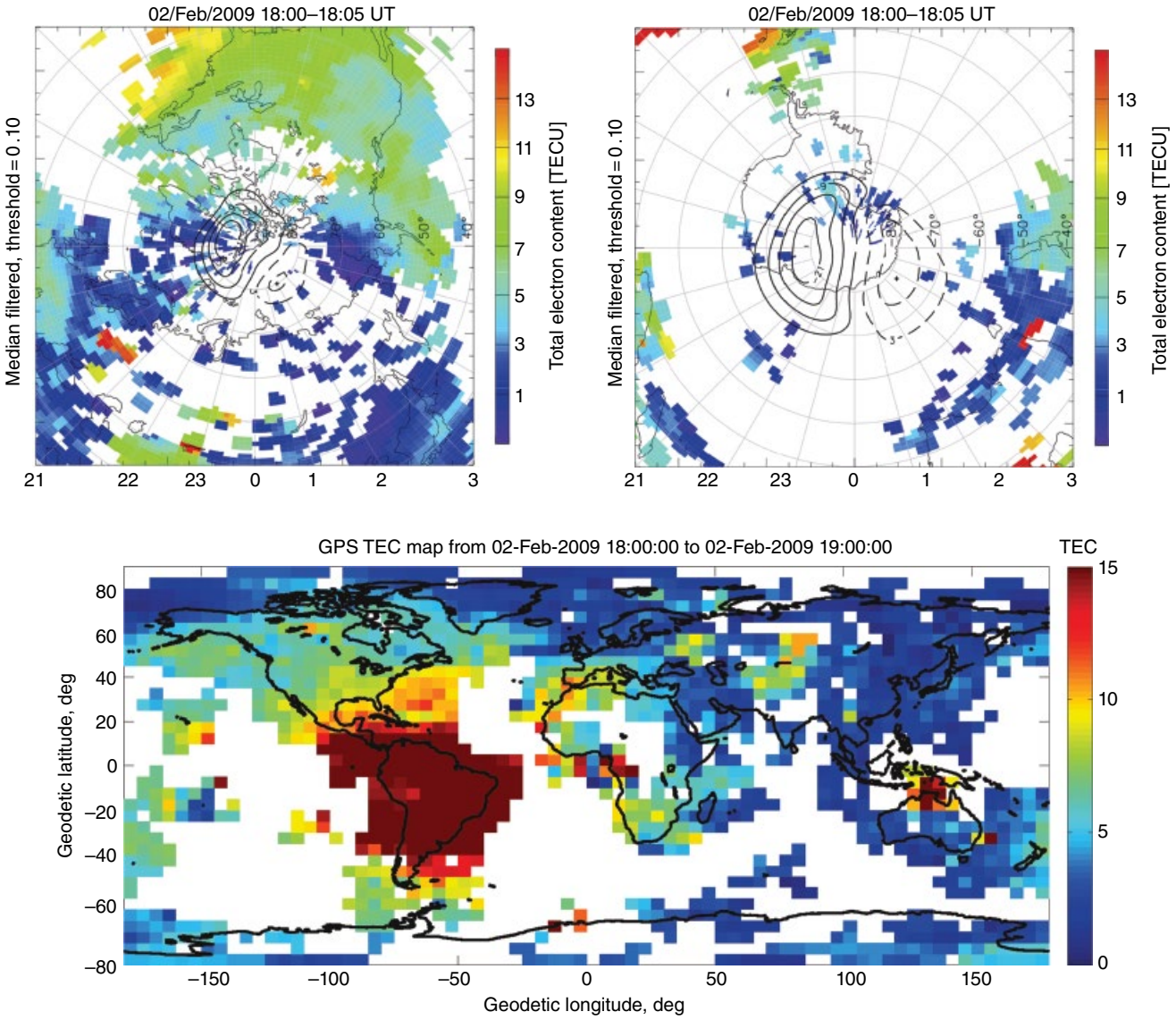


**Figure 6.2** Geomagnetically quiet day TEC on 2 February 2009. Kp = 0.0–0.3. The top plots, shown in MLT coordinates, correspond to polar views of the TEC map, the North Pole on the left, the South Pole on the right. The SuperDARN convection patterns are overlaid onto the TEC maps.

to the background magnetic field configuration over the United States. Although not mentioned in the earlier study, it is worth noting that the magnetic field has significant declination change over the continental United States. *Zhang et al.* [2011] noted the importance of the longitude of zero magnetic declination over the middle of the continental United States on TEC climatologies. The difference in magnetic declination gives rise to upward and downward ion drifts across the zero declination for a given thermospheric zonal wind direction.

Less is known about hemispherical differences in SED. In particular, with the exception of South America, there has been minimal observation to date of storm-enhanced density effects in the Southern Hemisphere. This is primarily due to the lack of publicly available GNSS data in the Southern Hemisphere, especially over the oceans. SED in the Southern Hemisphere forms primarily over the ocean south of Australia and Africa, or extends from the tip of South America across the South Pacific to Antarctica. During the last solar maximum period (1998–2003), *Yizengaw et al.* [2005] used data from 10 GPS receivers (6 GPS in Australia) from the 31 March 2001 storm to do a tomographic reconstruction of the ionosphere. That study's reconstruction reported propagating fingerlike ionization features (SED) over Australia with a 600 km height extension and a width of 300–400 km.

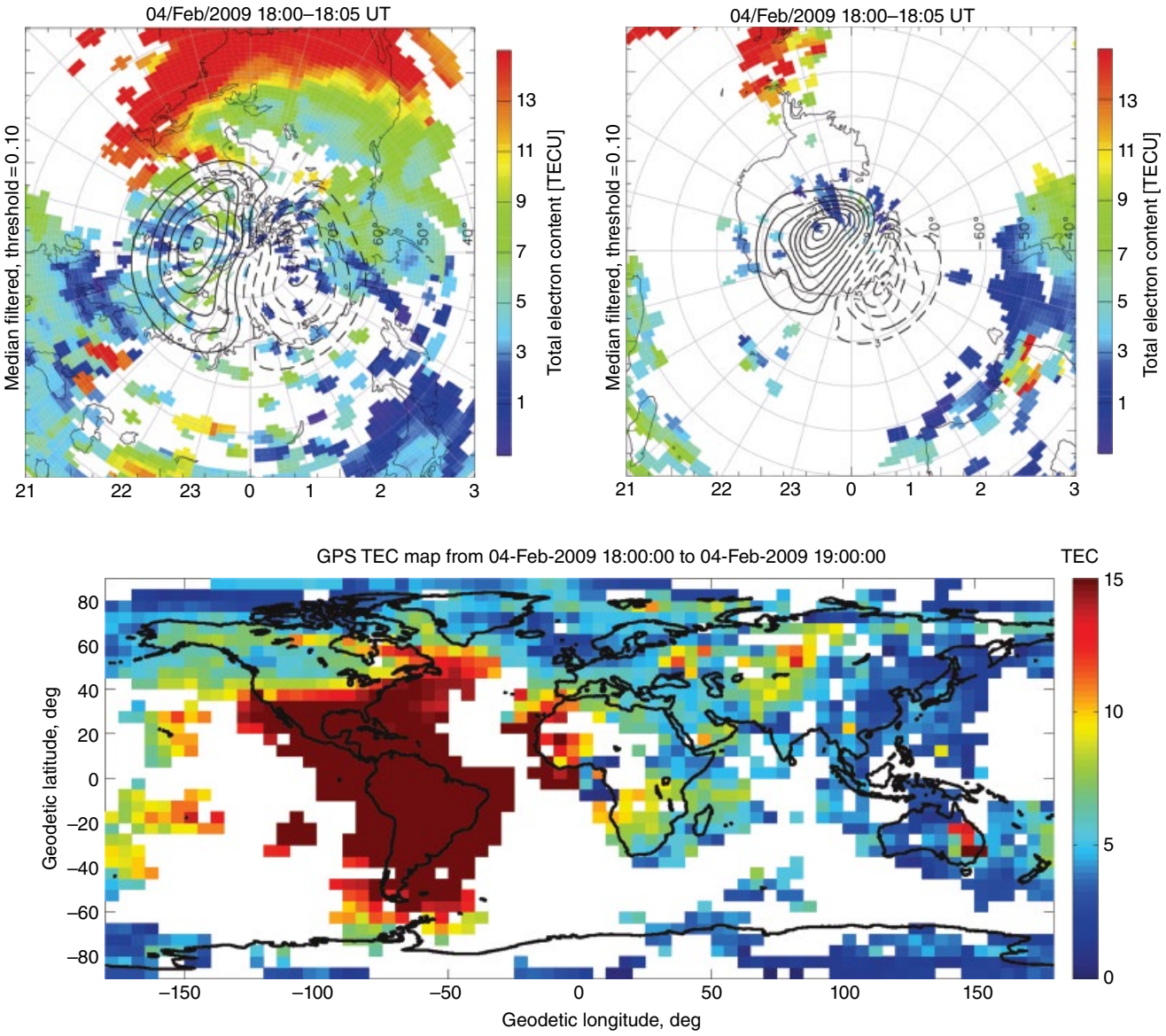


**Figure 6.3** Storm-time TEC on 4 February 2009. The Northern Hemisphere has a clearly visible TEC plume. A small enhancement of TEC is also visible in the Southern Hemisphere, especially when compared with Figure 6.2.

*Skone and Coster* [2007] describe additional SED events over Australia. In particular, on 29 October 2003, from 10:00 to 11:00 UT, large ionospheric gradients in the southeast region of Australia were observed. These large gradient regions appeared to be conjugate to an SED plume observed over Europe and Asia at the same time.

*Foster and Rideout* [2007] performed a detailed study of the magnetic conjugacy of SED for several storms. They observed that most, but not all, features of SED exhibited elements of magnetic conjugacy and appeared simultaneously in both hemispheres. For example, the entry of the SED plume into the polar cap near noon is observed in both hemispheres. They interpreted this conjugacy as an indication that storm-time electric fields are responsible for the transport of SED TEC from its source to the vicinity of the noontime cusp. The feature of SED that does not appear to be conjugate is the magnitude of TEC enhancement at the base of the SED plume. The amount of TEC enhancement appears to exhibit localized and longitude-dependent features, perhaps due to the offset of geographic and geomagnetic latitudes in the American sector [*Coster et al.*, 2007; *Foster and Coster*, 2007; *Foster and Erickson*, 2013]. *Heelis et al.* [2009] predicts that the most effective

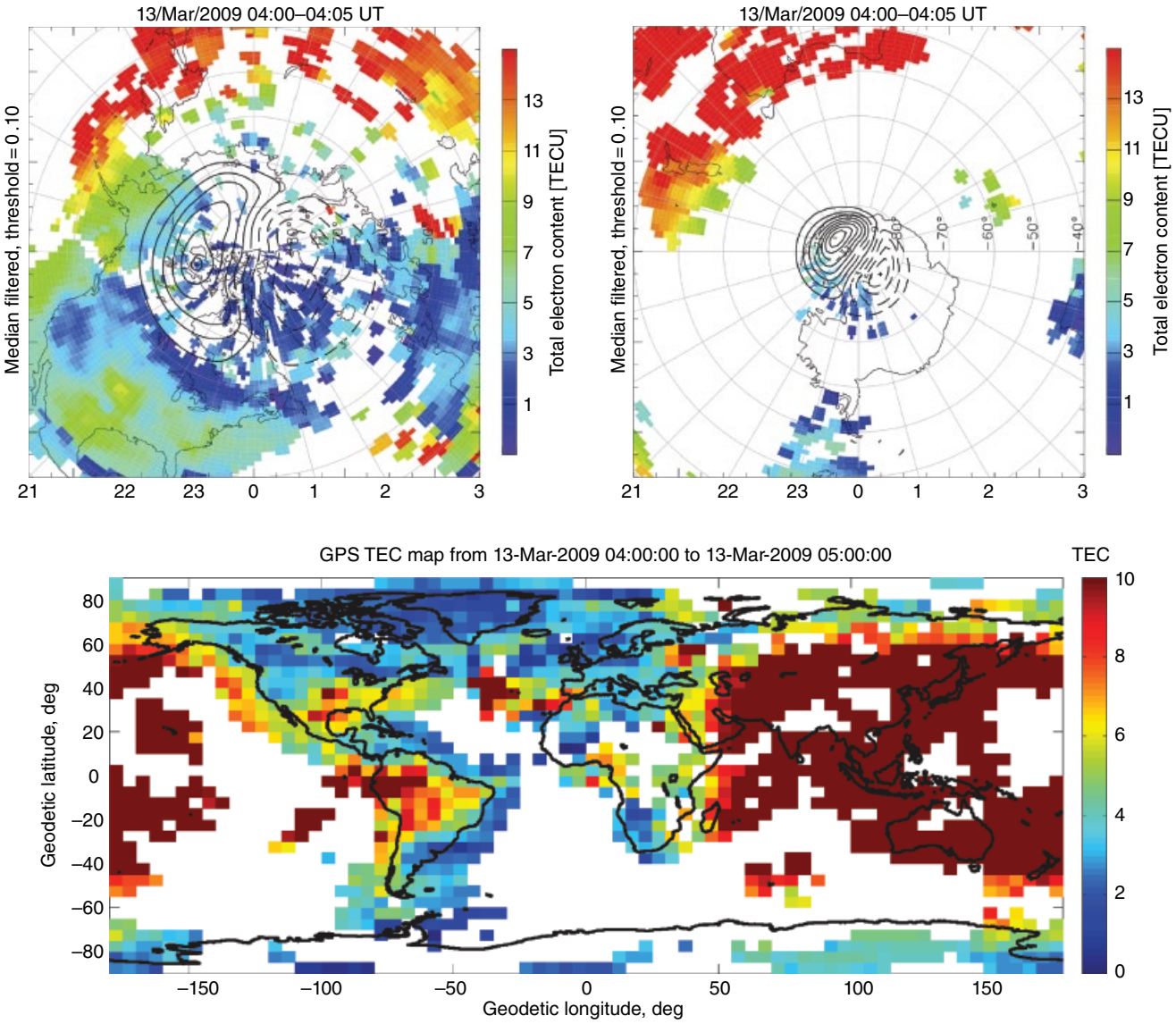


**Figure 6.4** Global TEC Map with Kp = 4 conditions on 13 March 2009 at 4:00 UT, reflecting a similar geomagnetic disturbance to that observed in Figure 6.3, although at a different longitude sector.

universal times for TEC enhancements should occur in the Northern Hemisphere near 19:00 UT and in the Southern Hemisphere near 07:00 UT. This is because enhancements should be largest when the longitude region incorporating the magnetic pole is tilted toward the dayside.

The seasonal dependence of SED plumes is still under investigation. The majority of observed SED events has occurred within the equinoctial months, with only a few notable exceptions (an important one being the very first SED event imaged, the Bastille day storm of 15 July 2000). The reason for this seasonal dependency may possibly be attributed to the pronounced seasonal variation of the occurrence rate of great geomagnetic storms [*Svalgaard et al.*, 2002; *Cliver and Crooker*, 1993]. The different wind patterns extant between the solstices and the equinoxes may also play a role. Finally, analysis of TEC data from the TOPEX/Poseidon mission [*Jee et al.*, 2004] has shown that at low and midlatitudes, the peak electron density is greater at the equinoxes than at the solstice. All of these factors, or some combination of them, may be related to the seasonal dependence observed in the formation of the SED plumes following geomagnetic disturbances.

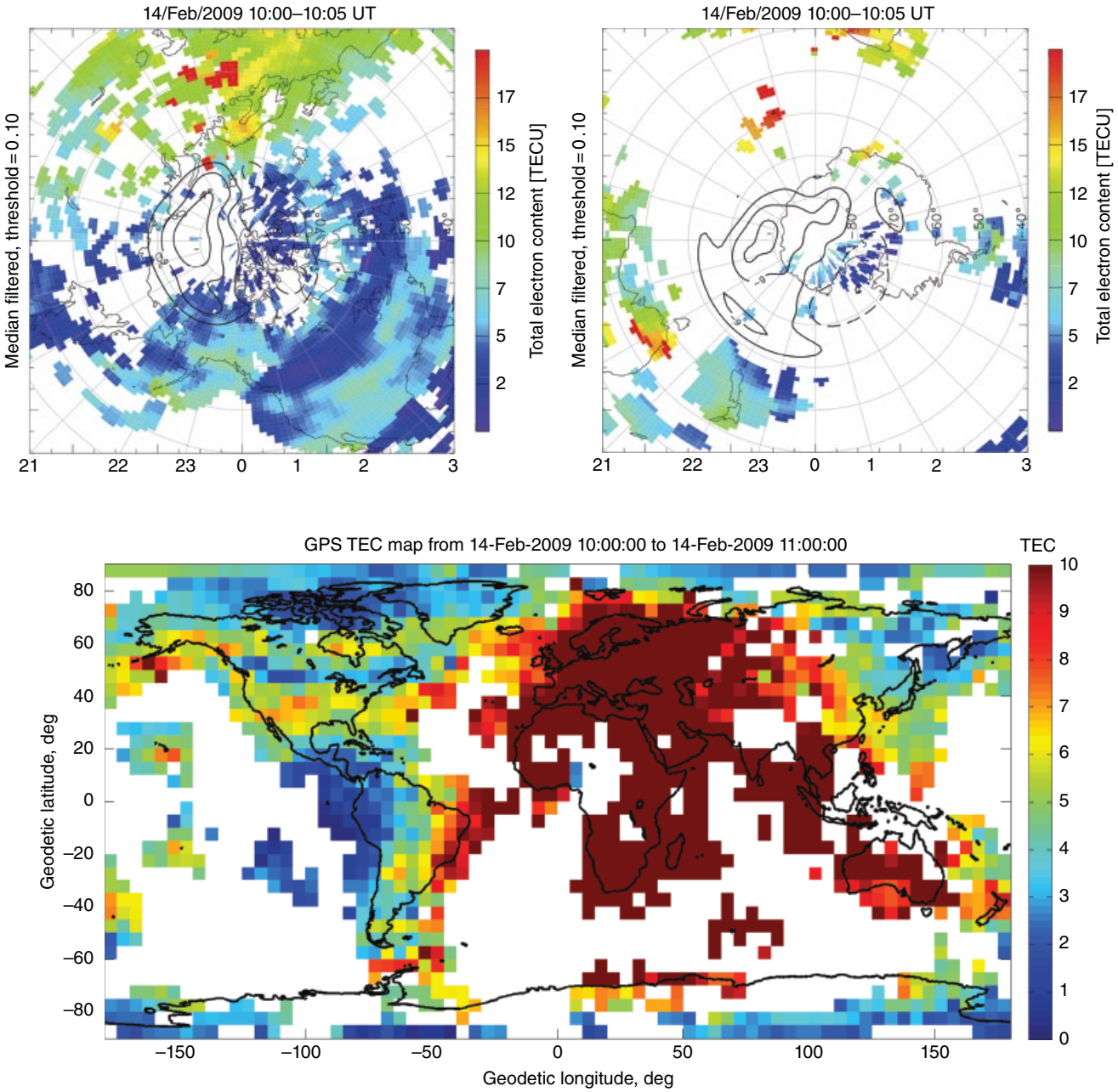


**Figure 6.5** Kp = 4 conditions on 14 February 2009 at 10:00 UT. A hint of enhanced plasma can be observed close to local noon in the Northern Hemisphere. Traces of this feature of enhanced plasma can also be observed in the Southern Hemisphere.

## 6.2. DATA AND METHODOLOGY

### 6.2.1. 2009 Observations: Low $F_{10.7}$ cm Flux Observations

The data used in this study include TEC global maps from the Madrigal database [*Rideout and Coster*, 2006]. SuperDARN HF radar observations have been used to estimate the convection pattern [*Ruohoniemi and Baker*, 1998] and have been overlaid onto the GPS TEC maps. During the solar minimum period, which continued through 2009, we show a comparison between global TEC observed for 2 days in February. The first day, 2 February 2009, shown in Figure 6.2, was geomagnetically quiet, with a Kp between 0.0 and 0.3 between 18:00 and 19:00 UT. On that day, there is no clear evidence of

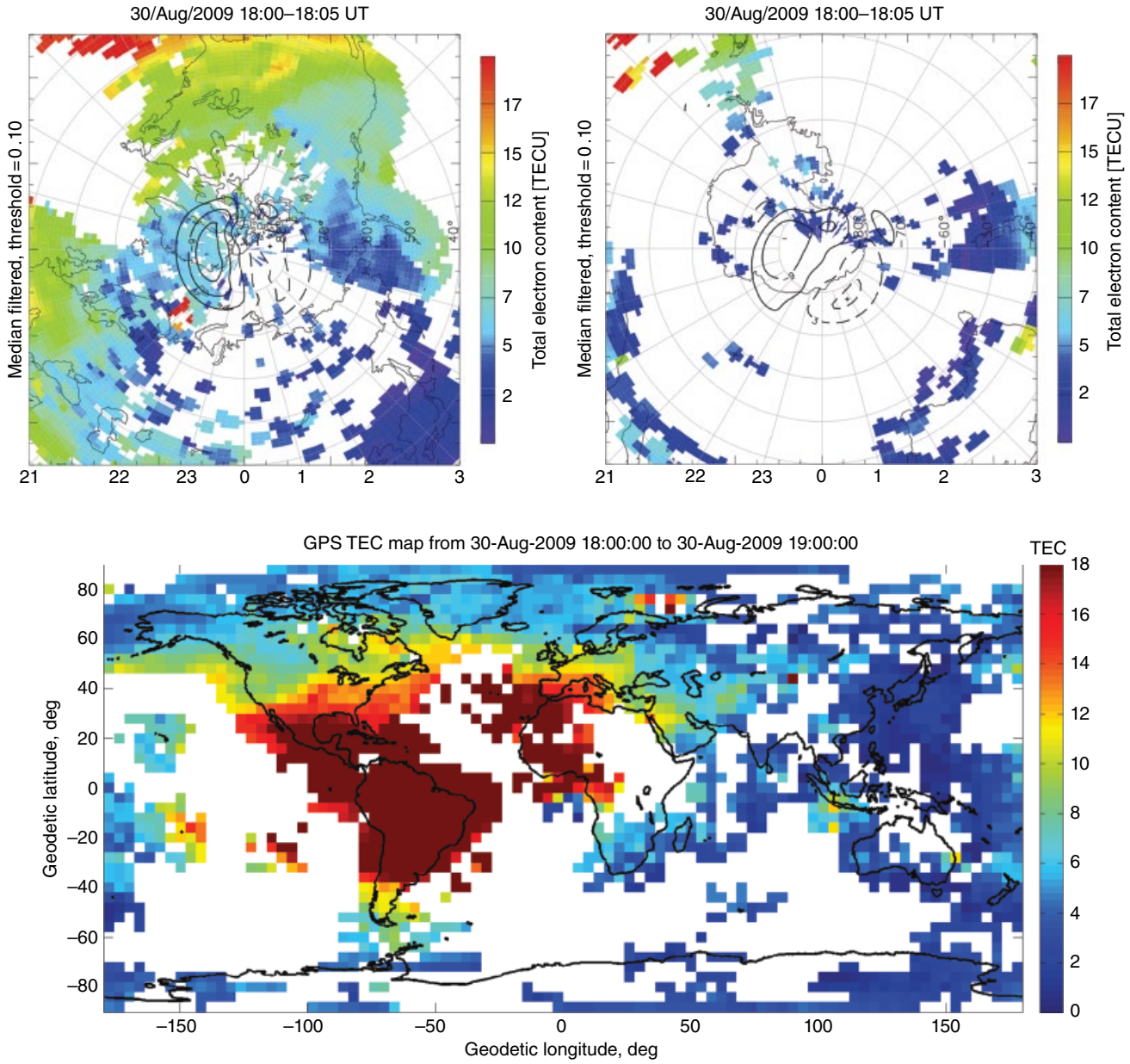


**Figure 6.6** A Kp = 4 storm on 30 August 2009 illustrating the seasonal variations of the SED plume.

a TEC plume in either hemisphere. Figure 6.2 shows polar views of TEC on the top (North Pole on left, South Pole on right) and the global TEC map below. Figures 6.3 through 6.8 all follow this format. The second day shown in Figure 6.3, 4 February 2009, was slightly disturbed with a Kp equal to 3.0 to 3.3. Figure 6.3 clearly shows an SED plume forming in the northeast of Canada, with a hint of a TOI feature as plasma sweeps across the polar region and over into Europe. A hint of an enhanced TEC region is also visible in the Southern Hemisphere, especially when compared with Figure 6.2.

Figures 6.4 and 6.5 both show TEC maps for similar Kp = 4 conditions to those observed in Figure 6.3, but at different UT time periods, and feature either the presence or absence of an SED in the different longitude regions. For example, in Figure 6.4, at 4:00 UT on 13 March 2009, there is no evidence of an SED feature, although one might expect an SED structure in China and another one over Indonesia. A possible explanation

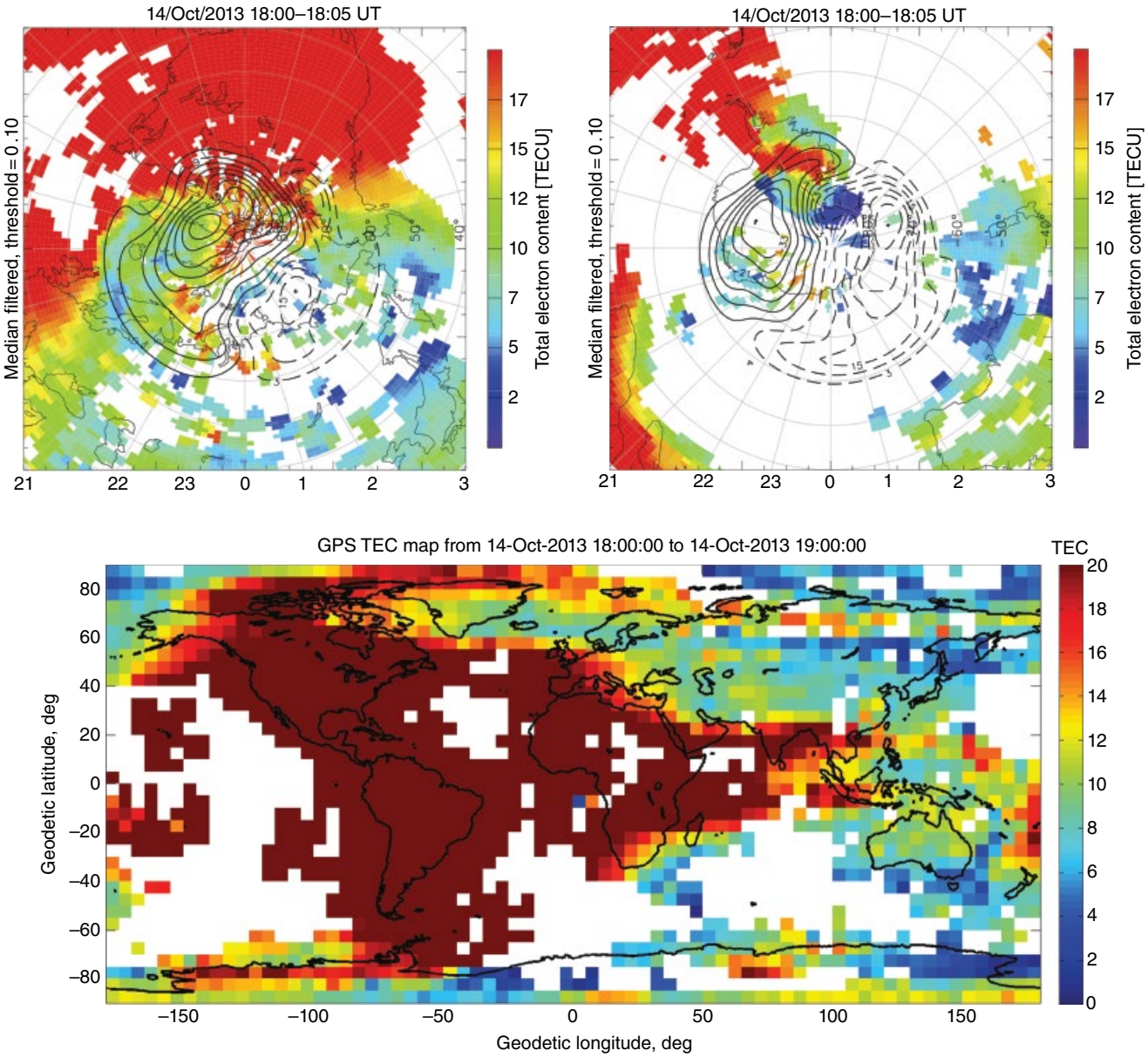


**Figure 6.7** 14 October 2013, Kp = 4 to 4.3. SED structures observed in both hemispheres between 18:00 and 19:00 UT. For this event, the SED/TOI structure appears slightly stronger in the Northern Hemisphere.

for this observation may lie in the lack of GPS coverage in these areas, masking the ability to observe SED plumes.

At 10:00 UT on 14 February 2009 (Fig. 6.5), a time corresponding to a Kp of 3.7, an enhanced region of SED plasma does appear to be starting to form very weakly over Europe. A similar enhancement, although with much poorer data coverage, can be observed in the Southern Hemisphere. In both hemispheres, one may detect the beginning of a weak plume structure.

Finally, Figure 6.6 shows a Kp = 4 storm at 18:00 UT in late August 2009, at the end of the summer solstice period. These data were selected to illustrate the seasonal differences in SED appearances. In Figure 6.6, an SED structure is weakly observed in the Northern Hemisphere and Southern Hemisphere. The shape of the SED plume in the Northern Hemisphere has similar characteristics to that observed in Figure 6.3, although it is clearly not as well defined. The Figure 6.6 data were associated with very similar geomagnetic conditions to the data shown in Figure 6.3. The 30th of August is in between the solstice and the equinox, yet only a very weak SED plume is observed on this day.

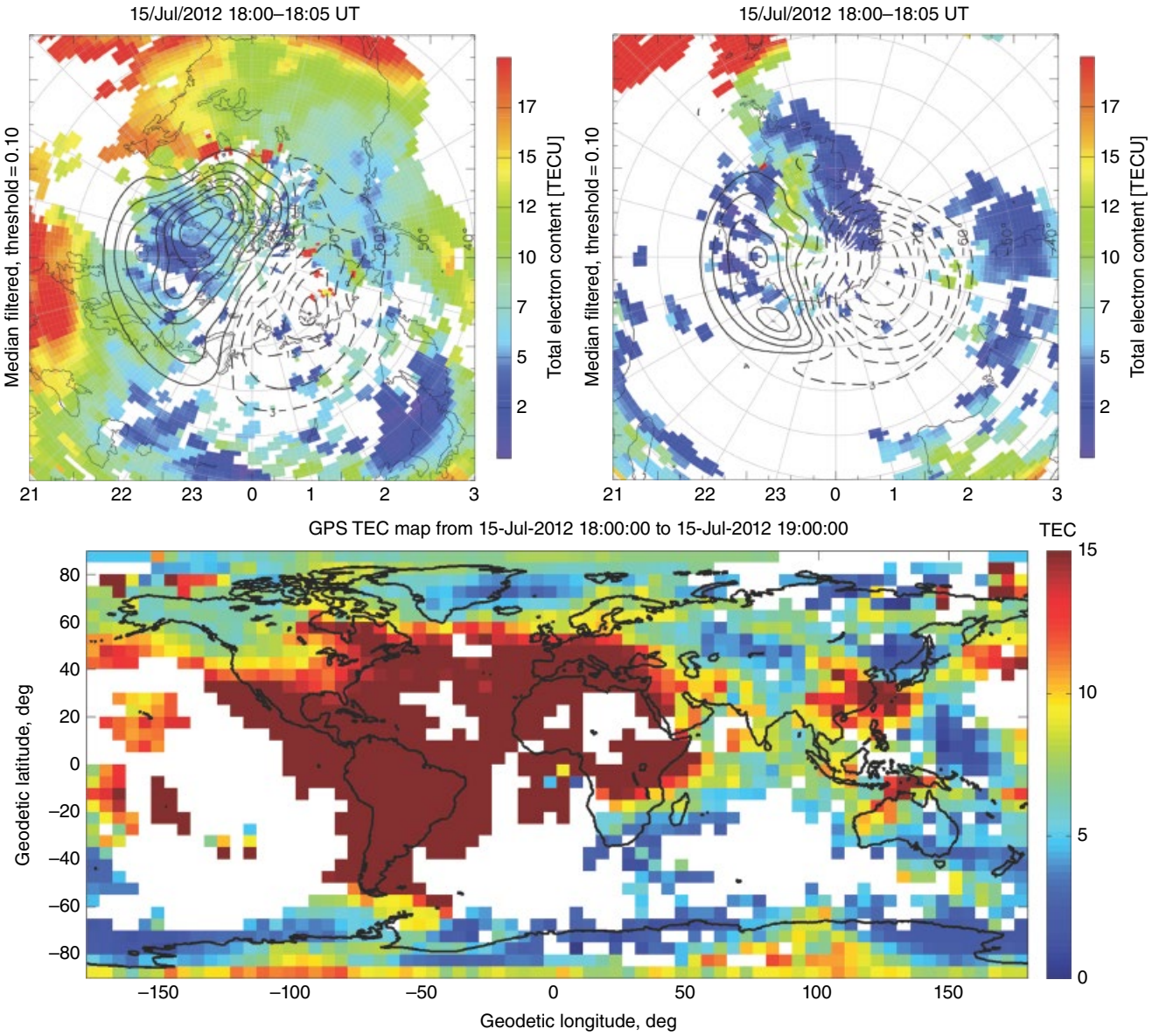


**Figure 6.8** SED structures observed in both hemispheres between 18:00 and 19:00 UT on 15 July 2012 during a Kp = 7 geomagnetic storm. For this event, the SED/TOI structure appears slightly stronger in the Northern Hemisphere.

### 6.2.2. 2012–2013 Observations: Moderate $F_{10.7}$ cm Flux Observations

The data shown in Figures 6.7, 6.8, and 6.9 are from the 2012–2013 period with characteristically high solar flux. In particular, the data in Figures 6.7 and 6.8 were selected to illustrate the same seasonal dependence observed in the SED plumes of Figures 6.3 and 6.6 during the much higher solar flux conditions in 2012 and 2013. Figure 6.7 shows a strong SED pattern in both hemispheres on 14 October 2013 at 18:00 UT. The Kp index was between 4.0 and 4.3 at 18:00 UT.

Figure 6.8 shows an SED event for a Kp = 7 event on 15 July 2012 at 18:00 UT. This time period is a considerably more geomagnetically active time than the Kp = 4 of Figure 6.7. This event was selected because an observable SED/TOI during the 2012 and 2013 solstice periods for Kp = 4 conditions could not be found. A comparison of Figure 6.7 and Figure 6.8 further illustrates that, in general, the SED plumes that do form during time periods near the equinoxes are typically stronger and more defined than those forming at or near the solstices for geomagnetic storms of equal, or even greater, strength.

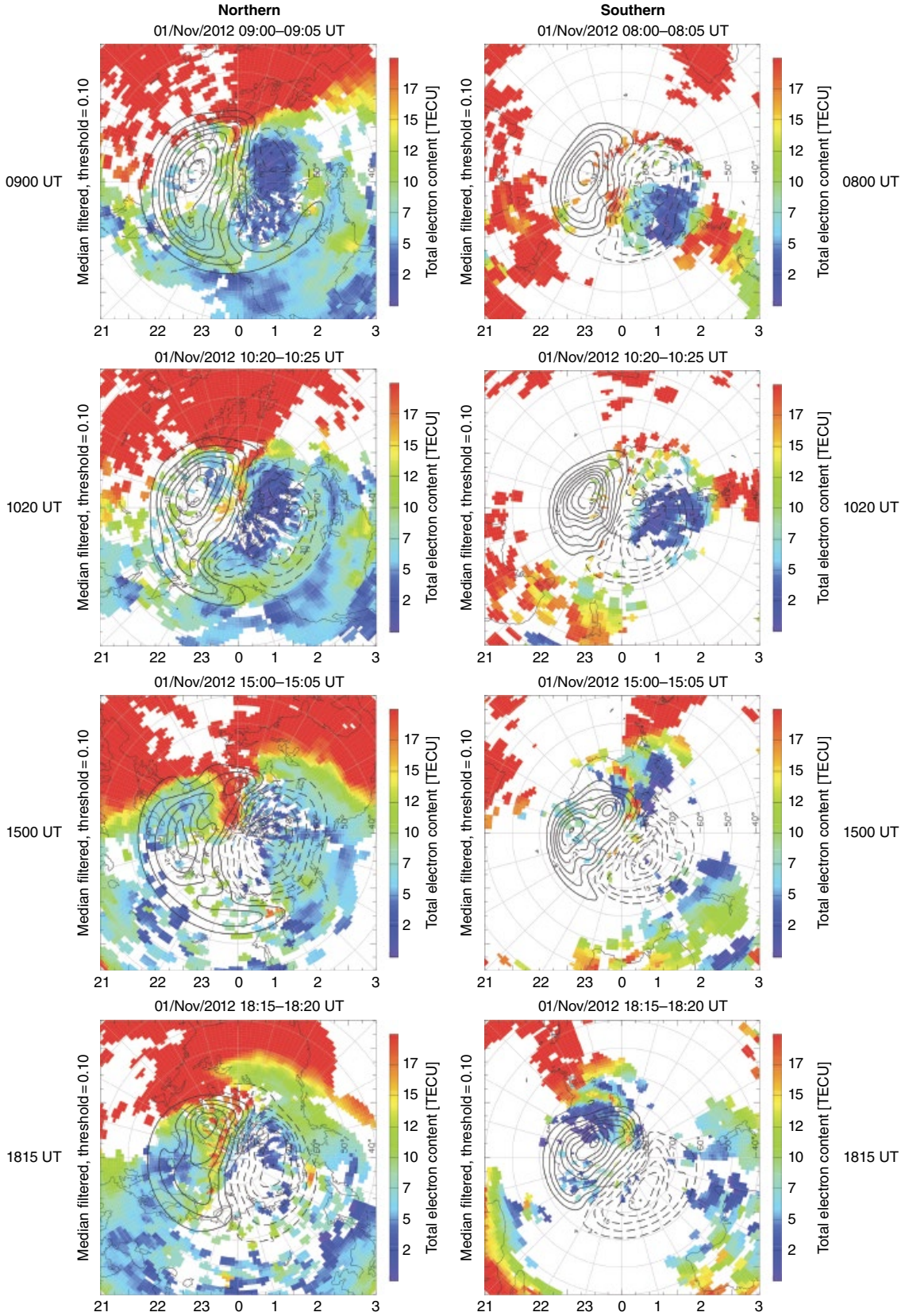


**Figure 6.9** SED/TOI observations on 01 November 2012 at multiple UT times, longitude sectors.

The observations shown in Figure 6.9 correspond to SED/TOI structures observed at multiple UT time periods on 1 November 2012. This was one of the only days we observed such a strong SED/TOI plume at various times periods throughout the day, such as at 9:00 UT, 10:20 UT, 15:00 UT, and 18:15 UT. On this day, the Kp varied from a low of 3.0 to a high of 4.7. Starting at 4:00 UT, $B_z$ turned negative and stayed there for the rest of the day. $B_x$ was positive throughout the time period. It is interesting to note that the SED plume in the Southern Hemisphere appears earlier than the one in the Northern Hemisphere, at 8:00 UT versus 9:00 UT.

## 6.3. SUMMARY

This paper presents observations of SED/TOI plumes during the solar cycle 24. The observations presented here suggest the following.

1. There is a clear seasonal dependence in SED plumes/TOI structures, including a preference for formation during or near the equinoxes. However, when SED/TOI form during the solstices, they are not as defined as during the equinoxes and may need stronger geomagnetic storm input to the geospace system in order to form.

2. SED/TOI structures appear to form at all longitude sectors, although data coverage is currently sparse over China/Indonesia. The 1 November 2012 data were unique in that they clearly showed that SED/TOI features can form in all longitude sectors. The SED/TOI structures appear to be larger in general in the American longitude sector.

3. The SED/TOI structures appear in both hemispheres, although effects appear to be stronger in the Southern Hemisphere around 8:00 UT (data coverage may limit earlier UT observations in the Southern Hemisphere) and stronger in the Northern Hemisphere around 18:00 UT, corresponding to the American sector.

## ACKNOWLEDGMENTS

We gratefully acknowledge support from NSF grant ANT-1141923 and AGS-1243058 to MIT Haystack Observatory.

## REFERENCES

Basu, S., and C. E. Valladares (1999), Global aspects of plasma structures, *J. Atmos. Sol. Terr.*, *61*, 127–139; doi:10.1016/S1364-6826(98)00122-9.

Carlson, H. C., (2012), Sharpening our thinking about polar cap ionospheric patch morphology, research, and mitigation techniques, *Radio Sci.*, *47*, RS0L21; doi:10.1029/2011RS004946.

Clausen, L. B. N., J. Baker, J. Ruohoniemi, R. Greenwald, E. Thomas, S. Shepherd, E. Talaat, W. Bristow, Y. Zheng, A. Coster, and S. Sazykin (2012), Large-scale observations of a subauroral polarization stream by midlatitude SuperDARN radars: Instantaneous longitudinal velocity variations, *J. Geophys. Res.*, *117*(A5), A05306; doi:10.1029/2011JA017232.

Cliver, E. W., and N. U. Crooker (1993), A seasonal dependence for the geoeffectiveness of eruptive solar events, *Solar Phys., June 145, I. 2*, 347–357; doi:10.1007/BF00690661.

Coster, A., and J. Foster (2007), Space weather impacts of the sub-auroral polarization stream, *Radio Sci. Bull.*, *321* (June).

Coster, A. J., J. C. Foster, P. J. Erickson, F. J. Rich (2001), Regional GPS mapping of storm enhanced density during the 15–16 July 2000 geomagnetic storm, in *Proceedings of ION GPS 2001*, 11–14 Sept. 2001, Salt Lake City, Utah, 2531–2539.

Coster, A. J., M. J. Colerico, J. C. Foster, W. Rideout, and F. Rich (2007), Longitude sector comparisons of storm enhanced density, *GRL*, *34*, L18105; doi:10.1029/2007GL030682.

Crowley, G. (1996), A critical review of ionospheric patches and blobs, *Rev. Radio Sci., 1993–1996*, 619–660, edited by W. R. Stone, pp. 619, Oxford Univ. Press, New York.

David, M., J. Sojka, R. W. Schunk, M. W. Liemohn, and A. J. Coster (2011), Dayside mid-latitude ionospheric response to storm-time electric fields: A case study for 07 September 2002, *J. Geophys. Res.*, *116*, A12302; doi:10.1029/2011JA016988.

Foster, J. C. (1993), Storm-time plasma transport at middle and high latitudes, *J. Geophys. Res.*, *98*, 1675–1689; doi:10.1029/92JA02032.

Foster, J. C., and A. J. Coster (2007), Conjugate localized enhancement of total electron content at low latitudes in the American sector, *J. Atmos. Space Terr. Phys.*, *69*, 1241–1252; doi:10.1016/j.jastp.2006.09.012.

Foster, J. C., and H. B. Vo (2002), Average characteristics and activity dependence of the subauroral polarization stream, *J. Geophys. Res.*, *107*, A12; doi:10.1029/2002JA009409.

Foster, J. C., and P. J. Erickson (2013), Ionospheric superstorms: Polarization terminator effects in the Atlantic sector, *J. Atmos. Solar Terr. Phys.*, *103*, 147–156; doi:10.1016/j.jastp.2013.04.001.

Foster, J. C., and W. J. Burke (2002), SAPS: A new categorization for sub-auroral electric fields, *EOS Transactions*, *83*, 393–394; doi:10.1029/2002EO000289.

Foster, J. C., and W. Rideout (2005), Midlatitude TEC enhancements during the October 2003 superstorm, *Geophys. Res. Lett.*, *32*, L12S04; doi:10.1029/2004GL021719.

Foster, J. C., and W. Rideout (2007), Storm enhanced density: Magnetic conjugacy effects, *Ann. Geophys.*, *25*, 1791–1799; doi:10.5194/angeo-25-1791-2007.

Foster, J. C., A. J. Coster, P. J. Erickson, J. M. Holt, F. D. Lind, W. Rideout, M. McCready, A. van Eyken, R. J. Barnes, R. A. Greenwald, and F. J. Rich (2005), Multiradar observations of the polar tongue of ionization, *J. Geophys. Res.*, *110*, A09S31; doi:10.1029/2004JA010928.

Goldstein, J., B. R. Sandel, M. R. Hairston, and P. H. Reiff (2003), Control of plasmaspheric dynamics by both

convection and sub-auroral polarization stream, *Geophys. Res. Lett.*, *30*(24), 2243; doi:10.1029/2003GL018390.

Heelis, R. A., J. J. Sojka, M. David, and R. W. Schunk (2009), Storm time density enhancements in the middle-latitude dayside ionosphere, *J. Geophys. Res.*, *114*, A03315; doi:10.1029/2008JA013690.

Jee, G., R. W. Schunk, and L. Scherliess (2004), Analysis of TEC data from the TOPEX/Poseidon mission, *J. Geophys. Res.*, *109*, A01301; doi:10.1029/2003JA010058.

Kelley, M. C., M. N. Vlasov, J. C. Foster, and A. J. Coster (2004), A quantitative explanation for the phenomenon known as storm-enhanced density, *Geophys. Res. Lett.*, *31*(19), L19809; doi:10.1029/2004GL020875.

Kintner, P., A. Coster, T. Fuller-Rowell, and A. J. Manucci (2007), Overview of midlatitude ionospheric storms, *Eos Trans. AGU*, *88*(37), 358; doi:10.1029/2007EO370002.

Kintner, P., A. Coster, T. Fuller-Rowell, A. J. Mannucci, M. Mendillo, R. Heelis, eds. (2008), *Geophysical Monograph Series*, vol. 181, American Geophysical Union, Washington, DC.

Lin, C. H., A. D. Richmond, R. A. Heelis, G. J. Bailey, G. Lu, J. Y. Liu, H. C. Yeh, and S.-Y. Su (2005), Theoretical study of the low- and midlatitude ionosphere electron density enhancement during the October 2003 superstorm: Relative importance of the neutral wind and electric field, *J. Geophys. Res.*, *110*, A12312; doi:10.1029/2005JA011304.

Lockwood, M., and Carlson, H. C. (1992), Production of polar cap electron density patches by transient magnetopause reconnection, *Geophys. Res. Lett.*, *19*, 1731–1734; doi:10.1029/92GL01993.

Lu, G., L. P. Goncharenko, A. J. Coster, A. D. Richmond, R. G. Roble, N. Aponte, and L. J. Paxton (2008), A data-model comparative study of ionospheric positive storm phase in the mid-latitude *F* region, 63–77, in *AGU Monograph on Chapman Conference: Mid-Latitude Dynamics and Disturbances*, American Geophysical Union, Washington, DC.

Maruyama, T. (2006), Extreme enhancement in total electron content after sunset on 8 November 2004 and its connection with storm enhanced density, *Geophys. Res. Lett*., *33*, L20111; doi:10.1029/2006GL027367.

Rideout, W., and A. Coster (2006), Automated GPS processing for global total electron content data, *GPS Solut.*; doi: 10.1007/s10291-006-0029-5.

Ruohoniemi, J. M., and K. B. Baker (1998), Large-scale imaging of high-latitude convection with Super Dual Auroral Radar Network HF radar observations, *J. Geophys. Res.*, *103*(A9), 20797–20811; doi:10.1029/98JA01288.

Schunk, R. W., W. J. Raitt, and P. M. Banks (1975), Effect of electric-fields on daytime high latitude E and F regions, *J. Geophys. Res.*, *80*(22), 3121–3130; doi:10.1029/JA080i022p03121.

Skone, S., and A. Coster (2007), *Investigation of Storm Enhanced Density Effects in Southern Hemisphere*, Proceedings of ION GNSS, Fort Worth, Texas.

Svalgaard, L., E. W. Clivers, and A. G. Ling (2002). The semiannual variation of great geomagnetic storms, *Geophys. Res. Lett*., *29*(16); doi:1029/2001GL014145.

Thomas, E. G., J. B. H. Baker, J. M. Ruohoniemi, L. B. N. Clausen, A. J. Coster, J. C. Foster, and P. J. Erickson (2013), Direct observations of the role of convection electric field in the formation of a polar tongue of ionization from storm enhanced density, *J. Geophys. Res. Space Phys.*, *118*, 1180–1189; doi:10.1002/jgra.50116.

Vlasov, M., M. C. Kelley, and H. Kil (2003), Analysis of ground-based and satellite observations of F-region behavior during the great magnetic storm of July 15, 2000, *J. Atmos. Solar Terr. Phys.*, *65*(11–13), 1223–1234; doi:10.1016/j.jastp.2003.08.012.

Walsh, B. M., J. C. Foster, P. J. Erickson, and D. G. Sibeck (2014), Simultaneous ground- and space-based observations of the plasmaspheric plume and reconnection, *Science*, *343*(6175), 1122–1125; doi:10.1126/science.1247212.

Yizengaw, E., M. B. Moldwin, and D. A. Galvan (2006), Ionospheric signatures of a plasamspheric plume over Europe, *J. Geophys. Res.*, *33*; doi:10.1029/2006GL026597.

Yizengaw, E., P. L. Dyson, E. A. Essex, and M. B. Moldwin, (2005), Ionosphere dynamics over the Southern Hemisphere during the 31 March 2001 severe magnetic storm using multi-instrument measurement data, *Ann. Geophys.*, *23*(3), 707–721; doi:10.5194/angeo-23-707-2005.

Zhang, S., J. C. Foster, A. J. Coster, and P. J. Erickson (2011), East-West Coast differences in total electron content over the continental US, *Geophys. Res. Lett.*, *38*, L19101; doi:10.1029/2011GL049116.

Zheng, Y., P. C. Brandt, A. T. Y. Lui, and M.-C. Fok (2008), On ionospheric trough conductance and subauroral polarization streams: Simulation results, *J. Geophys. Res.*, *113*, A04209; doi:10.1029/2007JA012532.

# 7

# A Global Ionospheric Range Error Correction Model for Single-Frequency GNSS Users

**Norbert Jakowski and Mohammed Mainul Hoque**

## ABSTRACT

The basic approach of a model of the total electron content (TEC) that has recently been developed at the German Aerospace Center (DLR) is presented and the performance is discussed in comparison with Global Navigation Satellite System (GNSS) single-frequency correction models such as the Klobuchar and the NeQuick model, in particular, for low-latitude conditions. The empirical approach describes functions on season, local time, geographic/geomagnetic location, and solar activity conditions approximated by the solar radio flux index $F_{10.7}$. The 12 coefficients are derived from global TEC data provided by the University of Berne over more than half a solar cycle (1998–2007). It has been found that both the global Neustrelitz TEC Model (NTCM-GL) and the NeQuick model show a better performance than the Klobuchar model by a factor of about two. Nevertheless, NTCM and NeQuick models deviate considerably at low latitudes indicating that modeling of the low-latitude ionosphere is a challenging task that needs further research. Since NTCM requires only 12 coefficients it is much easier to handle than NeQuick and might also be used as a single-frequency correction model for single-frequency GNSS applications, such as the Klobuchar model currently used in GPS.

**Key Points:**

The described global TEC model is better than the current GPS ionospheric correction algorithm (Klobuchar model) approximately by a factor of two.

Although the TEC model uses only 12 coefficients its performance is comparable with that of the NeQuick model used as the ionospheric correction model for Galileo.

Challenging conditions of the low latitude ionosphere require additional efforts to improve the modelling.

**Key Terms:** ionosphere, equatorial crest, model, solar activity, GNSS

## 7.1. INTRODUCTION

Transionospheric navigation and radar systems operating at single frequencies of less than 10 GHz are impacted by ionospheric refraction. Since the ionospheric delay is proportional to the total electron content (TEC) of the ionosphere along the ray path, a user-friendly TEC model is helpful in various applications. Such models are used in particular for single-frequency applications in GPS [Klobuchar model; *Klobuchar*, 1987] and Galileo (NeQuick) [*Nava et al.*, 2008] or in TEC mapping [*Jakowski et al.*, 2011a]. Here we consider the global Neustrelitz TEC Model (NTCM-GL) in comparison with independent TEC measurements and the Klobuchar and NeQuick models focusing on low-latitude characteristics.

*Institute of Communications and Navigation, German Aerospace Center (DLR), Neustrelitz, Germany*

*Ionospheric Space Weather: Longitude and Hemispheric Dependences and Lower Atmosphere Forcing, Geophysical Monograph 220*, First Edition. Edited by Timothy Fuller-Rowell, Endawoke Yizengaw, Patricia H. Doherty, and Sunanda Basu.

## 7.2. CORRECTION MODELS

### 7.2.1. Klobuchar Model

GPS offers a simple ionospheric TEC model for correcting single-frequency measurements by about 50%. The ionospheric correction algorithm (ICA) developed by *Klobuchar* [1987] provides a vertical delay at L1 frequency for a given location and local time. The daytime variation of the vertical delay is modeled by a half cosine function whose amplitude peak is fixed at 2:00 p.m. local time. During nighttime, the vertical ionospheric delay is fixed at a constant value of 5 ns (1.5 m at L1 frequency). The model approach is realized by third-order polynomials for the amplitude and the period of the half-cosine function. The eight coefficients are updated daily by the GPS master control station, uploaded to the GPS satellites and transmitted down to the users via the navigation message. For application, the vertical ionospheric errors must be converted to the slant ray path geometries of received satellites. This procedure is based on the assumption of a spherically stratified ionosphere concentrated in a thin layer at 350 km height. The simplified obliquity factor M(E) or mapping function is given by the expression:

$$M(E)_{GPS} = 1 + 16 \cdot (0.53 - E)^3 \tag{7.1}$$

where the elevation angle $E$ is defined in semicircles. It is worth notice that the COMPASS ionospheric model (CIM) is very similar to the GPS model by using a geographic reference frame for the modeling instead of a geomagnetic one [*Wu et al.*, 2013]. For the mapping function, the standard thin-shell mapping function $M(E)$, given by

$$M(E) = \frac{STEC}{VTEC} = \left(1 - \left(\frac{R_E \cos E}{R_E + h_I}\right)^2\right)^{-1/2} \tag{7.2}$$

is used. Here $R_E$ designs the Earth radius and $h_I$ stands for the height of the ionospheric layer. The achieved performance is comparable to the original Klobuchar approach, slightly better at the Northern Hemisphere and worse at the Southern Hemisphere [*Wu et al.*, 2013].

### 7.2.2. NeQuick Model

The three-dimensional electron-density model NeQuick of the ionosphere/plasmasphere systems has been developed at the International Centre for Theoretical Physics (ICTP) in Trieste, Italy, and at the University of Graz, Austria [*Hochegger et al.*, 2000; *Nava et al.*, 2008]. The spatial and temporal behavior of key parameters such as $N_mF_2$ is deduced from monthly tables of the CCIR (Comité Consultatif International des Radio communications) covering low, medium, and high solar conditions [*Jones and Gallet*, 1962]. The vertical electron-density profile is given by a sum of specific functions for the ionospheric layers $E$, $F_1$, and $F_2$ and for the plasmasphere. Since NeQuick is a three-dimensional model, the slant TEC (STEC) is computed by integrating the electron density along the ray path. No simplifying mapping function is needed. In addition to latitudinal and longitudinal dependence of these coefficients, the geomagnetic field dependence is given by the modified dipole parameter modip μ as introduced by Rawer [*Rawer*, 1963].

It is worth mentioning that NeQuick is foreseen to be used as the single-frequency correction model in the European navigation satellite system Galileo. In Galileo application, the external solar activity index is replaced by an "effective ionization level" Az, which is computed by the Galileo operation center in order to get an optimal value for the current ionization level on global scale.

### 7.2.3. NTCM-GL Model

#### *7.2.3.1. Basic Approach*

The TEC model NTCM-GL (Neustrelitz TEC Model–GLobal) described by *Jakowski et al.* [2011a] was developed for assisting calibration, mapping, and forecasting in TEC monitoring procedures [*Jakowski et al.*, 2011b]. Type and outcome of the model are comparable with the GPS or Klobuchar model. But unlike the Klobuchar model, NTCM-GL is an autonomous model covering the full solar cycle including low and high solar activity conditions. It provides a multiplicative representation of temporal and spatial variations of global VTEC for a full solar cycle according to the general expression:

$$VTEC_{NTCM-GL} = F_{LT} \cdot F_{seas} \cdot F_{mag} \cdot F_{crest} \cdot F_{sol} \tag{7.3}$$

Here the terms $F_{xx}$ describe the dependencies from local time, season, geomagnetic field, latitude, and solar activity. In addition to former mid- and high-latitude regional models developed at the German Aerospace Center (DLR) special care has been taken to describe low-latitude features such as the low-latitude crest in an effective way. To keep the number of coefficients in (7.3) as small as possible, the coefficients are fitted to the input data by an iterative nonlinear least-squares technique. Thus, it was possible to describe all the dependencies by only 12 coefficients with reasonable accuracy as will be discussed in the subsequent section.

The latitudinal dependence is described by a dipole approach of the geomagnetic latitude and a special expression for the crests at both sides of the geomagnetic equator. Equatorial anomaly associated crests are a well-known phenomenon in ionospheric physics. Location and shape have been derived from numerous ground- and

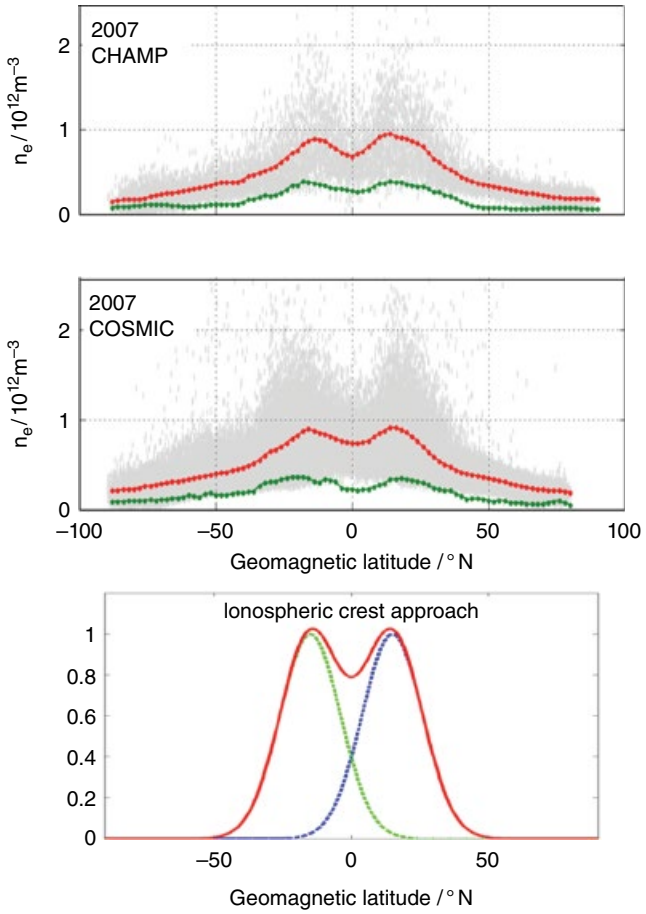


**Figure 7.1** Modelling approach for the normalized TEC (red) in the northern (blue) and the southern (green) ionospheric crest (lower panel) according to Equation (4) in relation to latitudinal profiles of the peak electron density $N_mF_2$ (red: mean $N_mF_2$, green: standard deviation) retrieved from radio occultation measurements onboard CHAMP (upper panel) and from COSMIC satellites (middle panel) in 2007 (00-24 LT).

space-based observations on a global scale. Thus, space-based radio occultation measurements obtained onboard CHAMP [*Jakowski*, 2005] and COSMIC [*Schreiner et al.*, 2007] demonstrate position and shape of both crests as shown in the upper panels of Figure 7.1.

To model the crests in an effective way, the model approach is based on the sum of two Gaussian functions located at both sides of the geomagnetic equator around ±15°N as illustrated in Figure 7.1.

The corresponding term $F_{crest}$ in (7.3) is given by:

$$F_4 = \left(1 + c_9 \exp\left(EC_1\right) + c_{10} \exp\left(EC_2\right)\right) \tag{7.4}$$

with

$$EC_1 = -\frac{\left(\varphi_m - \varphi_{c1}\right)^2}{2\sigma_{c1}^2} \tag{7.5}$$

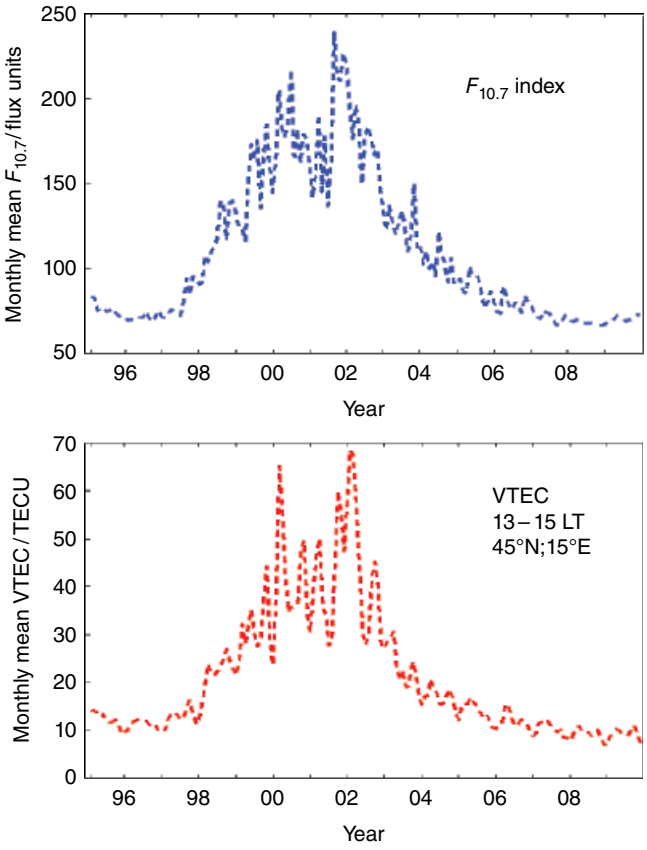


**Figure 7.2** Comparison of monthly medians of the solar radio flux $F_{10.7}$ and related TEC derived for 45°N; 15°E over solar cycle 23 from 1995–2009 at DLR.

for the northward crest and

$$EC_2 = -\frac{\left(\varphi_m - \varphi_{c2}\right)^2}{2\sigma_{c2}^2} \tag{7.6}$$

for the southward crest.

It is a well-known fact that TEC is closely related to space weather, in particular to the solar activity level as illustrated in Figure 7.2 showing TEC over mid-Europe and the associated solar radio flux during solar cycle 23. The solar radio flux measured at 10.7 cm wavelength in Ottawa ($F_{10.7}$) is a widely accepted proxy for characterizing the ionizing radiation level of the sun in the EUV wavelength range.

As found by many authors, the relationship between TEC is mostly linear if the solar radio flux doesn't exceed 200 solar flux units (sfu) with 1 sfu = $10^{-22}$ $Wcm^{-2}s^{-1}$. Accordingly, NTCM-GL utilizes the simple relationship

$$F_5 = \left(c_{11} + c_{12} F_{10.7}\right) \tag{7.7}$$

for describing the solar activity dependence of VTEC.

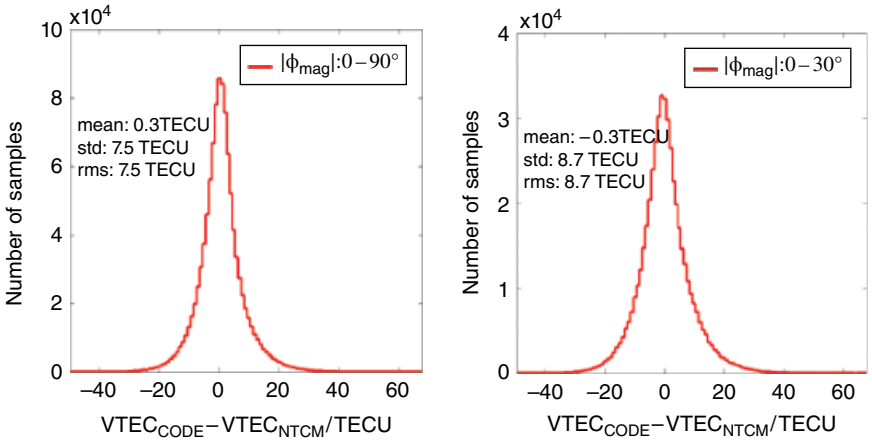


**Figure 7.3** Histogram of NTCM-GL model residuals, that is the difference of input data minus model values for all longitude ranges. Left panel includes all latitudes; right panel is restricted to low geomagnetic latitudes (0°–30°). The mean deviation, standard deviation (std), and root mean squared (rms) values of residuals are also given.

#### *7.2.3.2. Database*

As mentioned above, the model coefficients were determined by a nonlinear least-squares fitting of the 12 coefficients to the long-term VTEC data sets from the Center for Orbit Determination in Europe (CODE) at the University of Berne [*Hugentobler et al.,* 2000]. The two-hourly VTEC maps are derived at CODE from GPS data provided by the global network of the International GNSS Service (IGS) [*Dow et al.,* 2009]. The high-quality TEC data set of the first NTCM-GL approach comprises data from more than 130 IGS stations within the years 1998–2007. Thus, the TEC input data cover more than half a solar cycle. Some free parameters such as the position and the width of both crests were fixed in the fitting process because their variability is not significant for the final result. For the position $\varphi_c$ of the crests the values $\varphi_{c1} = 16°\text{N}$ and, $\varphi_{c2} = -10°\text{N}$ were used. The corresponding half widths are then given by $\sigma_{c1} = 12°$ and $\sigma_{c2} = 13°$. Due to the fixing of a few parameters like these, the nonlinear approach requires only 12 coefficients and the solar activity index $F_{10.7}$ as an external parameter to compute VTEC at any location and time on the globe.

The goodness of fit of the input data using this approach is shown in Figure 7.3. The overall fit has only a small bias of 0.3 TECU and is with RMS = 7.5 TECU quite good for global conditions at all times covering nearly a full solar cycle. It is worth mentioning that the goodness of fit with RMS = 8.7 TECU reduces at low geomagnetic latitudes (0°–30°). This is mainly due to the much higher ionization level at low latitudes as seen in Figure 7.1. In addition, a reduced accuracy of the input VTEC data at low latitudes also has to be taken into account. In particular, the simplified mapping function used for TEC mapping is a nonnegligible source of errors when estimating VTEC from low elevation Global Navigation Satellite System (GNSS) measurements of STEC [*Hoque and Jakowski*, 2013].

## 7.3. COMPARISON OF MODELS

To finally prove the quality of NTCM-GL presented here, the performance will be estimated by comparing it with independent measurements and with the corresponding outcome of other models, such as the GPS ionospheric correction model [*Klobuchar*, 1987], NeQuick [*Nava et al.*, 2008], and IRI [*Bilitza*, 2001].

Although the output term is the same as provided by the GPS model, there is a significant difference concerning the utilization of NTCM and Klobuchar models. Whereas the autonomous NTCM takes into account the strong dynamic of solar activity via the solar radio flux proxy (cf. Fig. 7.2) during a full solar cycle, the Klobuchar model requires a permanent updating of the eight coefficients via the GPS navigation message to ensure the expected model performance. To assess the low-latitude performance (−30…30°N), NTCM, Klobuchar and NeQuick models have been compared with independent TOPEX/Poseidon and Jason satellite altimetry measurements that provide VTEC up to a height of 1336 km. The comparison has been made both for low solar activity (LSA) conditions (Jason1; December 2006) and high solar activity (HSA) conditions (TOPEX/Poseidon; May 2002) as shown in Figure 7.4.

Here the upper left panel of Figure 7.4 indicates a quite good entire day performance of all three models in the low-latitude range under LSA conditions (RMS ranges from 6 to 7 TECU). It becomes worse at HSA in March 2002 (RMS ranges from 13.3 to 26.9 TECU) due to the much higher ionization level. When considering

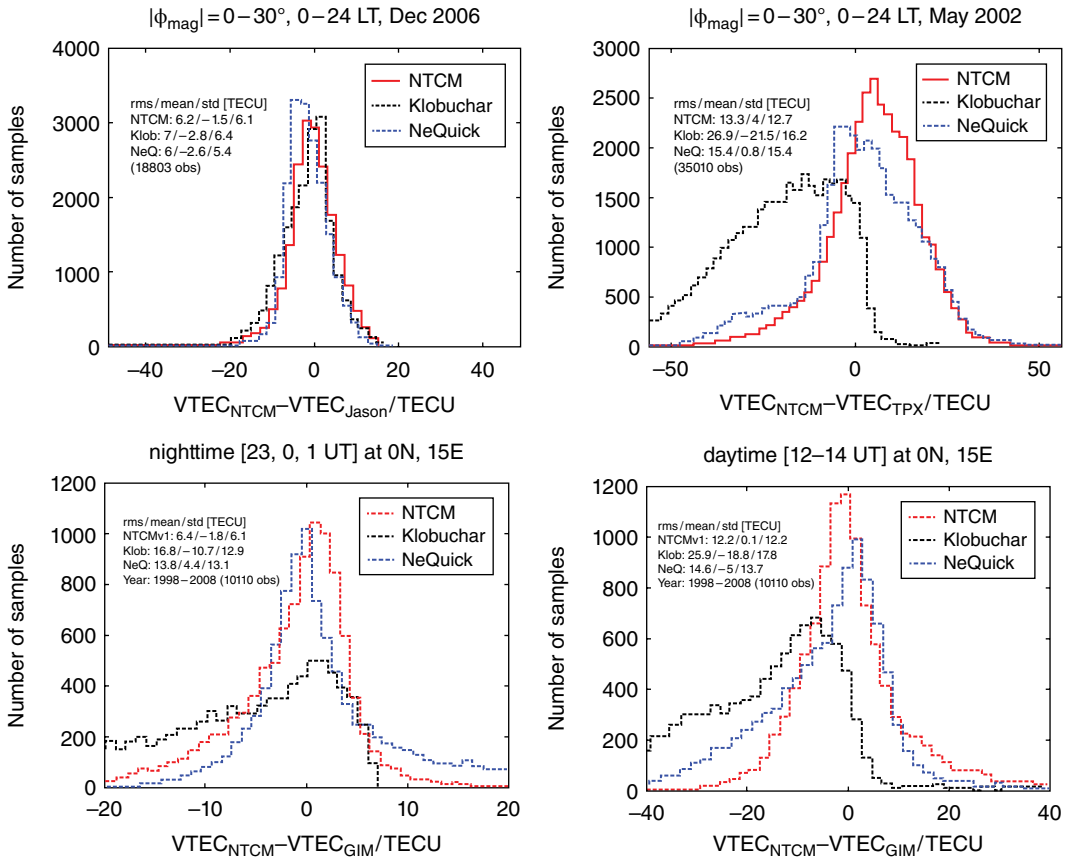


**Figure 7.4** Comparison of VTEC values of the Klobuchar model, NeQuick, and NTCM-GL with TOPEX (2002) and Jason-1 (2006) data at low geomagnetic latitudes (0°–30°) and specifically at the geomagnetic equator at 15°E with JPL derived GIM TEC from year 1998 to 2008.

midnight conditions (23–01 LT) at the geomagnetic equator and 15°E over solar cycle 23 from 1998–2008, RMS ranges from 6.4 to 16.8 TECU. RMS values around noontime (12–14 LT) are worse due to the higher ionization level at daytime (RMS ranges from 12.2 to 25.9 TECU). In all cases, the Klobuchar model deviates considerably from TOPEX. The RMS value is about twice the RMS values of NTCM and NeQuick models. However, NTCM and NeQuick differ considerably also in particular when considering the mean deviations from TOPEX, which are 4.0 and 0.8 TECU, respectively, for the entire low-latitude range over 24 hours. Under more specific equatorial conditions around noon at 15°E the biases for NTCM and NeQuick are 0.1 and −5.0 TECU, respectively.

Apparently, the biases between both models differ considerably from each other (from 1.1 up to 6.2 TECU for analyses shown in Fig. 7.4). Since TOPEX provides VTEC only up to about 1336 km height, the difference (plasmaspheric electron content) should always be positive after correcting TOPEX biases. Since the absolute bias of the satellite altimetry measurements is unknown and may even change in the period considered, here we can refer only to the difference between the models. Indeed, the TOPEX-GPS bias may vary by several TECU as reported by *Orus et al.* [2002]. The biases of the Klobuchar model differ by more than 20 TECU from corresponding biases of NTCM and NeQuick models under high solar activity conditions in 2002 (Fig. 7.4, right upper panel). The big difference can be explained partly by the fixed nighttime level of the Klobuchar model at 5 ns or about 9 TECU. The resulting error is demonstrated in Figure 7.5 where only nighttime values are (00–02 LT) at 50°N; 15°E of all three models are plotted for solar cycle 23 in comparison with corresponding VTEC reconstructions at the German Aerospace Center (DLR). Whereas NTCM and NeQuick follow the solar cycle in an adequate manner, the fixed ionization level of the Klobuchar model overestimates nighttime VTEC at LSA and underestimates nighttime VTEC under HSA conditions by up to 10 TECU as shown in Figure 7.5.

An overall estimation of the HSA performance of the three models considered so far in comparison with related TOPEX measurements and additionally also with

corresponding CODE data, Global Ionosphere Model (GIM) reconstructions at the Jet Propulsion Laboratory (JPL) in the United States (http://iono.jpl.nasa.gov/gim.html) and the International Reference Ionosphere (IRI) is shown in Figure 7.6. The mean deviations or biases from GPS data-based VTEC reconstructions vary from −1.8 to 0.5 TECU indicating that given TOPEX data are overestimated by a few TECU to save reasonable plasmaspheric content [*Orus et al.*, 2002, *Yizengaw et al.*, 2008]. On the other hand, the bias of NTCM (1.0 TECU) is closer to the GPS-derived VTEC data of CODE and GIM as NeQuick (7.1 TECU) indicating a better performance of NTCM-GL than NeQuick. At low solar activity in 2007, all models and map reconstructions are rather similar.

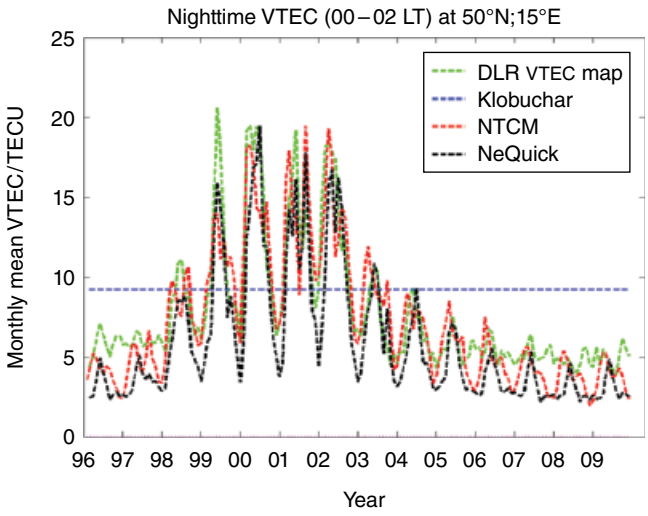


**Figure 7.5** Seasonal variation of the nighttime level of VTEC derived from the Klobuchar model, NTCM-GL and NeQuick over solar cycle 23 in comparison with GPS VTEC reconstructions at DLR at a selected point (50°N; 15°E) in Europe.

## 7.4. CONCLUSIONS

The basic structure and model performance of the NTCM-GL model is discussed in relation to Global Navigation Satellite System (GNSS) single-frequency ionospheric correction models of GPS and Galileo focusing on low latitudes. It has been found that the NeQuick and NTCM-GL models show a similar performance that is better than the Klobuchar model currently used in GPS by a factor of about two. Nevertheless, both these models deviate considerably at low latitudes. The resulting errors are due to mismodeling but might also partly result from erroneous input VTEC data caused by the simplifying mapping function for converting STEC to VTEC as described by Figure 7.2. The strong ionization level in conjunction with strong horizontal gradients and space weather dependence require additional efforts to improve the modeling. This challenging task refers to further densification of the ground-based GNSS network, which is rather sparse over regions like Africa, and to intensify studies of low-latitude ionospheric phenomena in particular under HSA conditions. Since the global NTCM uses only 12 coefficients that are valid for a full solar cycle, this model is much easier to handle than NeQuick. Having the same performance with respect to VTEC, NTCM-GL might also be used as a single-frequency correction model in Global Navigation Satellite Systems.

## ACKNOWLEDGMENTS

The CODE & JPL TEC data and TOPEX/Poseidon & Jason altimeter data used for this chapter are available at NASA's Crustal Dynamics Data Information System (CDDIS) archive (ftp://cddis.gsfc.nasa.gov/pub/gps/products/ionex). The used FORMOSAT-3/COSMIC data are available at UCAR's COSMIC Data Analysis and Archive Center (CDAAC) (ftp://cdaac-ftp.cosmic.ucar.edu/cosmic).

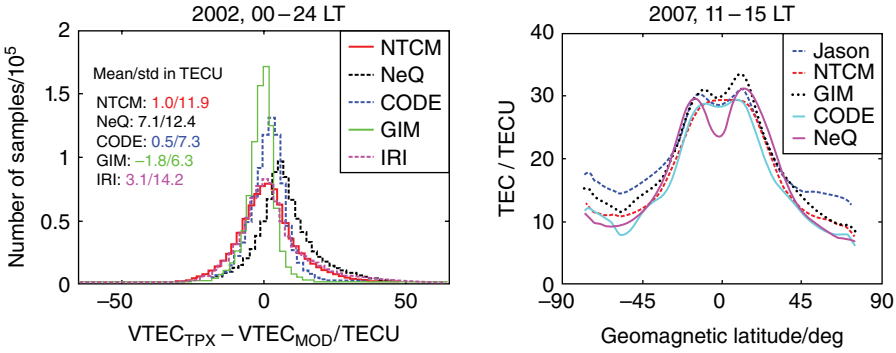


**Figure 7.6** (Left panel) Histogram of VTEC data derived from models NTCM-GL, IRI, and NeQuick and data-based TEC imaging at CODE and JPL (GIM - http://iono.jpl.nasa.gov/gim.html) in comparison with TOPEX-Poseidon measurements at HSA conditions in 2002; (right panel) mean daytime latitudinal variation of these models in comparison with Jason measurements at LSA conditions in 2007.

## REFERENCES


Bilitza, D. (2001), International reference ionosphere (2000), *Radio Sci.*, *36*, 261–275.

Dow, J. J, R. Neilan, and C. Rizos (2009), The international GNSS service in a changing landscape of global navigation satellite systems, *J. Geod.*, *83*(3–4), 191–198; doi:10.1007/s00190-008-0300-3.

Hochegger, G., B. Nava, S. M. Radicella, and R. Leitinger (2000), A family of ionospheric models for different uses, Phys. *Chem. Earth*, *25*(4), 307–310; doi:10.1016/S1464-1917(00)00022-2.

Hoque, M. M., and N. Jakowski (2013), Mitigation of ionospheric mapping function error, ION-GNSS, Nashville, Tennessee, USA.

Hugentobler, U., S. Schaer, T. Springer, G. Beutler, H. Bock, R. Dach, D. Ineichen, L. Mervart, M. Rothacher, U. Wild, A. Wiget, E. Brockmann, G. Weber, H. Habrich, and C. Boucher (2000), CODE IGS Analysis Center Technical Report.

Jakowski, N. (2005), Ionospheric GPS radio occultation measurements on board CHAMP, *GPS Solutions*, *9*, 88–95; doi: 10.1007/s10291-005-0137-7.

Jakowski, N., M. M. Hoque, and C. Mayer (2011a), A new global TEC model for estimating transionospheric radio wave propagation errors, *J. Geod.*; doi:10.1007/s00190-011-0455-1.

Jakowski, N., C. Mayer, M. M. Hoque, and V. Wilken (2011b), TEC models and their use in ionosphere monitoring, *Radio Sci., 46*, RS0D18; doi:10.1029/2010RS004620.

Jones, W. B., and R. M. Gallet (1962), Representation of diurnal and geographic variations of ionospheric data by numerical methods, *ITU Telecom J.*, *29*, 129–149.

Klobuchar, J. A. (1987), Ionospheric time-delay algorithm for single-frequency GPS users, *IEEE Transactions Aerospace and Electronic Systems, AES-23*(3), 325–331; doi:1109/TAES.1987.310829.

Nava, B., P. Coisson, and S. M. Radicella (2008), A new version of the NeQuick ionosphere electron density model, *JASTP*, 1856–1862.

Rawer, K. (1963), *Meteorological and Astronomical Influences on Radio Wave Propagation*, 221–250, edited by B. Landmark, Academic Press, New York.

Schreiner, W., C. Rocken, S. Sokolovskiy, S. Syndergaard, and D. Hunt (2007), Estimates of the precision of GPS radio occultations from the COSMIC/FORMOSAT-3 mission, *Geophys. Res. Lett.*, *34*, L04808; doi:10.1029/2006GL027557.

Wu, X., X. Hu, G. Wang, H. Zhong, and C. Tang (2013), Evaluation of COMPASS ionospheric model in GNSS positioning, *Adv. Space Res.*, *51*(6), 959–968; doi:10.1016/j.asr.2012.09.039.

Yizengaw, E., M. B. Moldwin, D. Galvan, B. A. Iijima, A. Komjathy, and A. J. Mannucci (2008), Global plasmaspheric TEC and its relative contribution to GPS TEC, *J. Atmos. Sol. Terr. Phys.*, *70*, 1541–1548; doi:10.1016/j.jastp.2008.04.022.

# Part III
# Longitude Spatial Structure in Total Electron Content and Electrodynamics

# 8

# Determining the Longitude Dependence of Vertical E × B Drift Velocities Associated with the Four-Cell, Nonmigrating Tidal Structure

**David Anderson and Tzu-Wei Fang**


## ABSTRACT

Previous studies have established the existence of a four-cell, longitude pattern in equatorial *F*-region ionospheric parameters, such as TEC and electron densities and in daytime, equatorial **E** × **B** drift velocities. A recent paper, for the first time, quantified the longitude gradients in **E** × **B** drift velocities at the boundaries of four-cell tidal structures and confirmed that these gradients exist on a day-to-day basis. Using the Ion Velocity Meter (IVM) on the Communication/Navigation Outage Forecast System (C/NOFS) satellite to obtain daytime, vertical **E** × **B** drift velocities, it was found, for example, that for 5, 6, and 7 October 2009 in the Atlantic sector, the **E** × **B** drift velocity gradient was about 1 m/sec/degree. For 23, 24, and 25 March 2009 in the Peruvian sector, it was about −4 m/sec/degree. In this chapter, we briefly review (1) observations and modeling studies of **E** × **B** drift velocities associated with the four-cell longitude patterns, (2) modeling the ionospheric effects produced by the longitude gradients in **E** × **B** drift velocity, and (3) provide indirect evidence that there exists a four-cell pattern in the prereversal enhancement (PRE) in vertical **E** × **B** drift velocity after sunset.


**Key Points:**

- This paper reviews the observations and the theoretical modelling studies related to the **E** × **B** drift velocities associated with the four-cell longitude patterns.
- The paper describes the modeled ionospheric effects produced by the sharp longitude gradients in **E** × **B** drift velocities.
- Provides evidence that there may exist a four-cell pattern in the prereversal enhancement (PRE) in vertical **E** × **B** drift velocity after sunset.

**Key Terms:** equatorial ionosphere, **E** × **B** drift velocities, four-cell longitude patterns, observations and modeling

## 8.1. INTRODUCTION

It is well known that the production of ions and electrons in the Earth's ionosphere comes from solar EUV radiation and the loss of $O^+$ ions in the *F* region is by charge exchange with $N_2$ and $O_2$ followed by recombination

*Cooperative Institute for Research in Environmental Sciences (CIRES), University of Colorado at Boulder, Boulder, Colorado, USA; and Space Weather Prediction Center (SWPC), National Oceanic and Atmospheric Administration (NOAA), Boulder, Colorado, USA*

*Ionospheric Space Weather: Longitude and Hemispheric Dependences and Lower Atmosphere Forcing, Geophysical Monograph 220*, First Edition. Edited by Timothy Fuller-Rowell, Endawoke Yizengaw, Patricia H. Doherty, and Sunanda Basu.

with electrons. The transport of ionization is through plasma ambipolar diffusion parallel to **B**, the component of the neutral wind velocity parallel to **B**, and **E** × **B** drift velocity perpendicular to **B** [*Hanson and Moffett*, 1966; *Anderson*, 1973]. In the equatorial region, **E** × **B** drift velocities are generally upward during the daytime and downward at night. The combined effect of upward **E** × **B** drift perpendicular to **B** and downward diffusion parallel to B by gravity and plasma pressure gradient forces creates crests in ionization at ±15 to ±18 degrees dip latitude known as the equatorial anomaly. To realistically simulate the low latitude ionospheric densities, it is critical to observe and theoretically calculate the vertical **E** × **B** drift velocities as a function of local time, longitude, season, and solar cycle. This paper focuses on our understanding the longitude dependence of vertical **E** × **B** drift velocities associated with the four-cell, nonmigrating tidal structure.

This paper will briefly (1) review observations and modeling studies of **E** × **B** drift velocities related to the four-cell longitude patterns, (2) review modeling of the ionospheric effects produced by the longitude gradients in **E** × **B** drift velocity, and (3) provide indirect evidence that there may exist a four-cell pattern in the prereversal enhancement (PRE) in vertical **E** × **B** drift velocity after sunset. While Section 8.2 very briefly reviews a few already-published studies relating to observations and modeling work of the daytime four-cell longitude patterns in vertical **E** × **B** drift velocities, it is important to provide the reader with a succinct summary of the sets of papers that specifically compare the four-cell **E** × **B** drift observations with theoretical modeling efforts. The purpose of Section 8.3 is to demonstrate the ionospheric effects of incorporating C/NOFS-observed, longitude gradients in **E** × **B** drift velocities into a theoretical ionospheric model. While the gradients are fairly sharp, they are not extreme cases since they are observed at the four-cell boundaries at several different longitudes and exist for 2 or 3 days at a time [*Araujo-Pradere et al.*, 2011]. Section 8.4 addresses the somewhat controversial topic of whether there may be a four-cell longitude pattern in PRE. While there appears to be no direct evidence for such a four-cell pattern in **E** × **B** drift observations, there may be indirect evidence that would suggest a four-cell structure may exist at times.

## 8.2. OBSERVATIONS AND MODELING STUDIES

Several observational studies have identified the existence of a four-cell pattern in longitude structure of ionospheric parameters at low latitudes. *Immel et al.* [2006] presented evidence that a four-cell, longitude pattern existed in FUV (135.6 nm) intensity obtained from the IMAGE satellite during March–April 2001. Since the images were at night, the four-cell pattern represented a four-cell pattern in $N_{max}$ at the crests of the equatorial anomaly. They attributed the four-cell pattern to a four-cell pattern in daytime, vertical **E** × **B** drift velocities associated with the diurnal, eastward propagating, nonmigrating wave number 3 (DE3) tidal mode [*Hagan and Forbes*, 2002]. The authors could not rule out the fact that the four-cell pattern could have been produced by a four-cell pattern in the PRE in **E** × **B** drift velocities after sunset since the IMAGE observations were at night. A subsequent paper by *England et al.* [2006], however, established that the four-cell pattern was observed in CHAMP satellite in-situ electron densities at 1200 LT. Further, the four-cell pattern has also been observed in the Republic of China Satellite (ROCSAT-1) daytime electron densities at 600 km and vertical **E** × **B** drift velocities [*Kil et al.*, 2007; *Kil et al.*, 2008] and occultation observations from Constellation Observing System for Meteorology and Climate (COSMIC) FORMOSAT-3 satellite [*Lin et al.*, 2007b]. Measurements of plasma densities detected by the Planar Langmuir Probe (PLP), zonal plasma drift observed by the Vector Electric Field Investigation (VEFI), and vertical drift observed by the IVM on board the C/NOFS satellite have also shown pronounced four-cell structure [*Huang et al.*, 2011; *Huang et al., 2013*; *Fejer et al.*, 2013].

In order to relate the four-cell **E** × **B** drift observations with theoretical modeling efforts, we describe specific sets of papers that carry out the comparisons: (1) *Kil et al.* [2007] and *Fang et al.* [2009], (2) *Fejer et al.* [2008] and *Maute et al.* [2012], (3) *Anderson et al.* [2009] and *Fang et al.* [2013], and (4) *Pedatella et al.* [2011] includes both observations and modeling.

1. The paper by *Kil et al.* [2007] investigated the longitudinal distribution of vertical **E** × **B** drift velocities obtained from the ROCSAT-1 at roughly 600 km altitude between 1999 and 2004. They found that during the daytime, there exists a four-cell longitude pattern in both **E** × **B** drift velocity and topside plasma density, implying an association with a four-cell pattern in the *E*-region dynamo electric field. An empirical model of vertical drift based on ROCSAT-1 measurements was established by *Kil et al.* [2009]. *Fang et al.* [2009] investigated the annual and local time variations of the four-cell structures in the plasma density through applying the ROCSAT-1 empirical **E** × **B** drifts to the Global Ionosphere and Plasmasphere (GIP) theoretical model. The GIP model physics is based on the ionosphere plasmasphere component of the Coupled Thermosphere Ionosphere Plasmasphere Electrodynamics Model (CTIPe) [*Millward et al.*, 2001]. The global three-dimensional grid in GIP adopts the magnetic apex coordinate system [*Richmond*, 1995] in which magnetic field lines are created by tracing through the full International Geomagnetic Reference Field (IGRF). The GIP model density showed similar annual and local time variation of the four-cell components observed by ROCSAT-1, implying that the vertical drifts are essential in the formation and evolution of the

four-cell longitudinal density structure. The amplitude of the DE3 tide at 110 km shows similar annual and local time variations as the *F*-region parameters, supporting the link between DE3 tide, vertical **E**×**B** drifts, and *F*-region plasma density on a global scale.

2. A more extensive study carried out by *Fejer et al.* [2008] developed a detailed quiet time global empirical model of *F*-region vertical **E**×**B** drift velocities based on ROCSAT-1 drift observations over a 5-yr period. The model results are in excellent agreement with drift observations from the Jicamarca radar. The longitude variation in daytime vertical **E**×**B** drift velocity shows a strong four-cell pattern in the 9–12 LT period, especially during equinox. The morning drifts do not change very much with solar activity. Only the PRE after sunset is affected by solar activity, decreasing as solar activity decreases. In addition, there does not appear to be a four-cell pattern in PRE with longitude. Model simulations of vertical **E**×**B** drift velocities have been carried out by *Maute et al.* [2012] and compared with the Fejer's ROCSAT-1 empirical model. These simulations used the NCAR Thermosphere-Ionosphere-Mesosphere-Electrodynamic General Circulation Model (TIME-GCM) with a lower boundary at 30 km incorporating tidal perturbations from the Global Scale Wave Model (GSWM02) that included both migrating and nonmigrating diurnal and semidiurnal tidal components. They examined the sources of low-latitude ionospheric **E**×**B** drifts and their variability. In particular, when they compared the calculated drifts for March equinox and an $F_{10.7}$ cm flux of 150 with the Fejer's ROCSAT-1 empirical model, they found excellent agreement in the magnitude and longitude of the four peaks in **E**×**B** drift. They found that the main contribution for the production of daytime vertical **E**×**B** drift velocities comes from neutral winds in the *E*-dynamo region and the longitude variability in **E**×**B** drift is due to both migrating and nonmigrating tides.

3. *Scherliess et al.* [2008] also observed the four-cell longitude pattern in TOPEX/TEC observations. The TOPEX/Poseidon satellite incorporates a dual-frequency altimeter operating at 13.6 GHz and 5.3 GHz to observe ocean surface heights. The dual-frequency allows the total electron content (TEC) to be measured from the satellite altitude of 1336 km to the ocean surface. *Scherliess et al.* binned the TEC observations between 1992 and 2005 for quiet days into equinox, June solstice, and December solstice periods by local time. The 12–16 LT period clearly displayed the four-cell pattern that had been observed by other techniques, previously [*England et al.*, 2006; *Kil et al.*, 2007; *Lin et al.*, 2007b]. *Anderson et al.* [2009] quantified the daytime, equatorial **E**×**B** drift velocities presumably associated with the four-cell structures seen in the TOPEX/TEC observations. They investigated the seasonal and longitudinal dependence of the daytime vertical **E**×**B** drift velocities using a recently-developed technique for inferring realistic **E**×**B** drifts from ground-based magnetometer observations [*Anderson et al.,* 2002, 2004, 2006]. They used appropriately placed magnetometers in the Peruvian, Philippine, Indonesian, and Indian longitude sectors to determine the **E**×**B** drift velocities at these four locations. They observed that at the boundary of the TOPEX/TEC four-cell structure between the Philippine and Indonesian sector, the maximum daytime **E**×**B** drift velocity went from 23 m/sec in the Philippine sector to 15 m/sec in the Indonesian sector. This is across 15° longitude or about 0.5 m/sec/degree. Figure 8.1 taken from the paper by *Anderson et al.* [2009] displays the magnetometer-inferred **E**×**B** drift velocities at the four longitude sectors for Equinox and June Solstice periods in 2001 and 2002. These are superimposed on the TOPEX/TEC curves generated by Scherliess.

*Fang et al.* [2013] studied the longitudinal and day-to-day variations in the ionosphere using model simulation. The GIP model with electrodynamic solver was driven by neutral winds from the Whole Atmosphere Model (WAM) to provide global electric fields. WAM is a general circulation model of the neutral atmosphere built from the National Weather Service (NWS) operational weather prediction Global Forecast System (GFS). The height coverage is from the surface to the exobase at the nominal height of about 600 km. WAM is capable of producing realistic representation of lower atmosphere sources of tidal waves important for the *E*-region dynamo. Their simulation produced significant longitudinal variation of the daytime equatorial vertical drifts (Fig. 8.2). The magnitudes of several nonmigrating tides in the paper also showed good agreement with observations. Through analyzing tidal modes from WAM winds, they confirmed that the four-cell longitudinal structure that shows up in the ionosphere is dominated by the DE3 tide.

4. *Pedatella et al.* [2011] carried out an investigation that studied both observations and model simulations of the longitudinal variations in the *F*-region ionosphere and the topside ionosphere-plasmasphere. They analyzed the COSMIC observations of TEC above and below 800 km altitude to study the local time and seasonal variations in the longitude structure. The predominant feature during equinox is a four-cell longitude pattern in TEC below 800 km that persists into the night. The model simulations are based on the coupled GIP and the NCAR Thermosphere-Ionosphere-Electrodynamics General Circulation Model (TIE-GCM). The model simulations replicate the COSMIC observations of TEC below 800 km and further confirm that nonmigrating tides are the primary mechanism for generating longitude variations in the *F*-region ionosphere. The theoretically calculated **E**×**B** drifts show a clear four-cell pattern when tidal forcing is included, and there are very sharp longitude gradients in **E**×**B** drift at the cell boundaries in agreement with the C/NOFS IVM observations discussed by *Araujo-Pradere et al.* [2011].

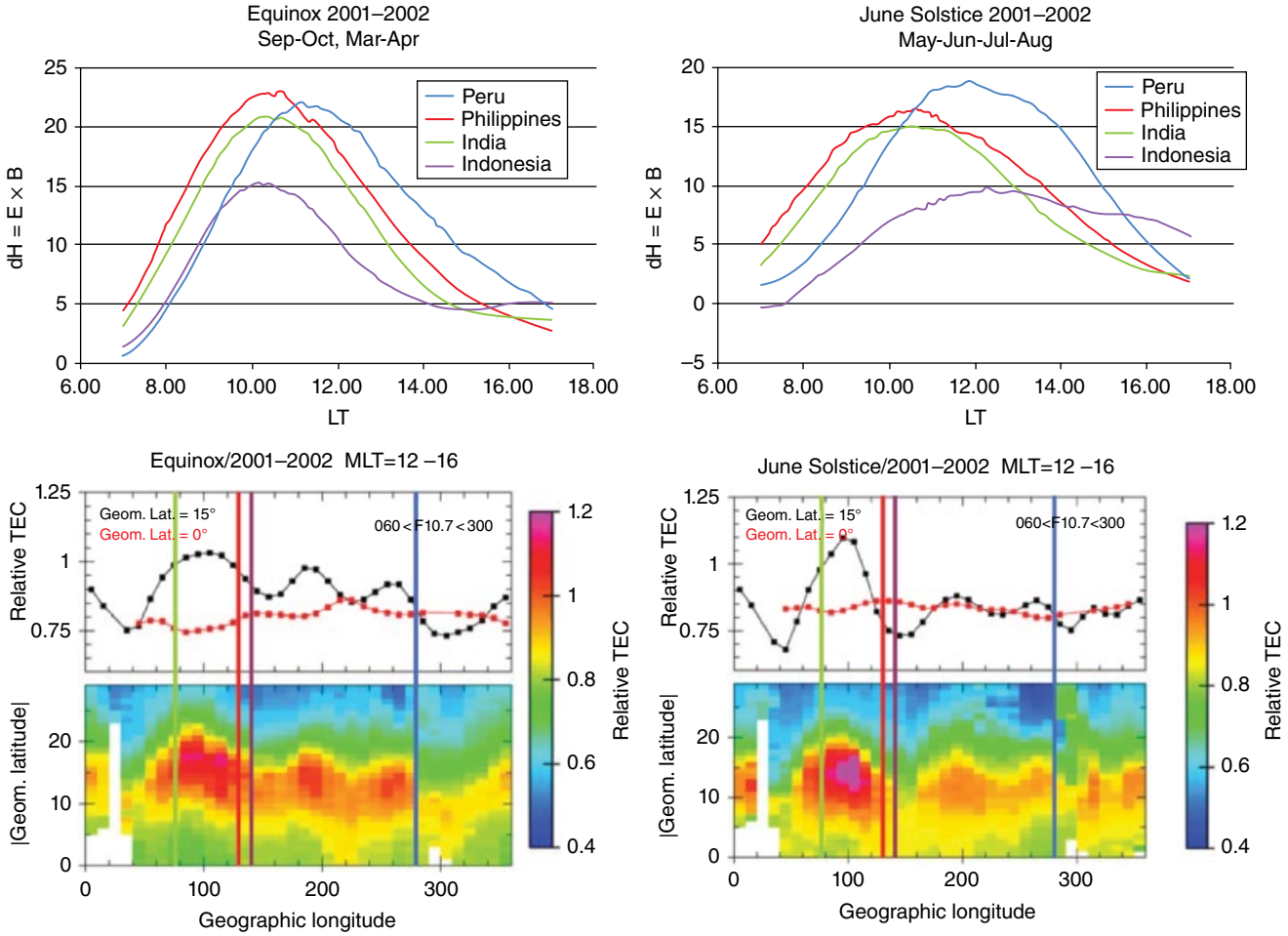


**Figure 8.1** Top curves are the average **E**×**B** drifts for Equinox and June solstice 2001–2002 in the Peruvian, Philippine, Indonesian, and Indian sectors. Bottom plots are TOPEX relative TEC as a function of geographic longitude and magnetic latitude for Equinox and June solstice, 2001–2002 and 12–16 LT (see discussion in text).

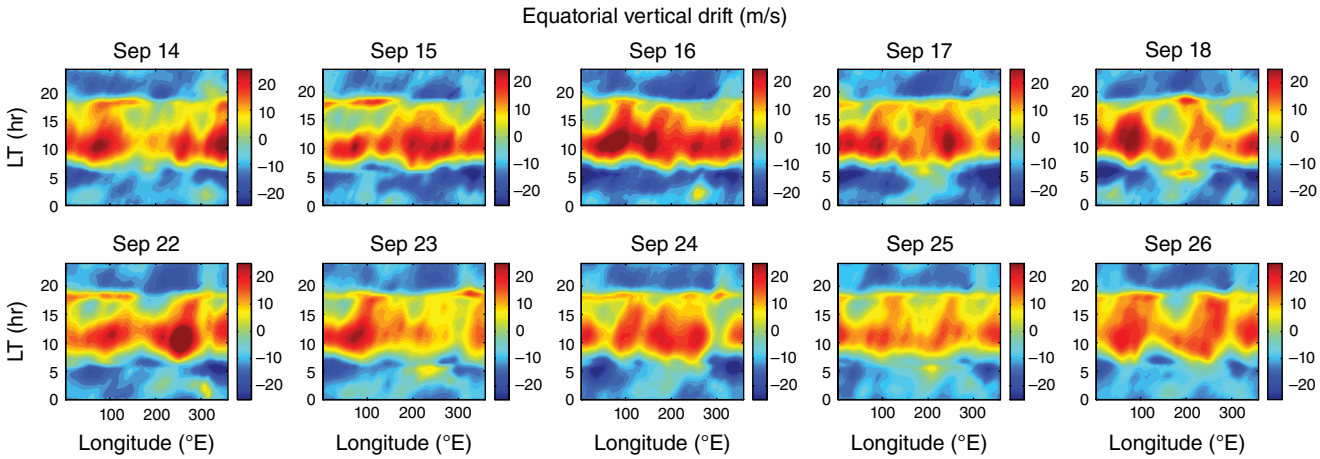


**Figure 8.2** Longitudinal variation of equatorial vertical drifts at all local times from 10 simulation days [*Fang et al.*, 2013] (see discussion in text).

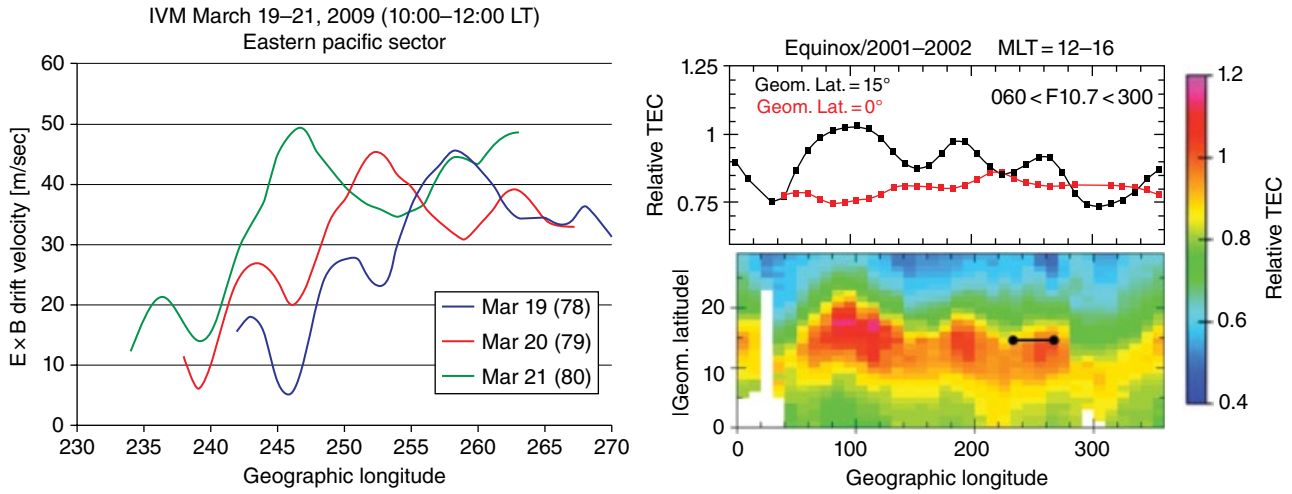


**Figure 8.3** (Left) IVM-observed **E**×**B** drift velocities for 19–21 March 2009 between 10 and 12 LT; (right) relative TEC observed by TOPEX satellite [whole figure from *Araujo-Pradere et al.*, 2011].

## 8.3. MODELING THE IONOSPHERIC EFFECTS OF THE FOUR-CELL LONGITUDE STRUCTURE

In order to study the longitude gradients of the **E**×**B** drift velocities at the boundaries of the TOPEX/TEC four-cell structures, *Araujo-Pradere et al.* [2011] utilized C/NOFS IVM measurements. IVM **E**×**B** drift velocities are meridional ion drifts, perpendicular to **B** and in the plane of the magnetic meridian, measured with an accuracy of 2 m/sec and a sensitivity of 1 m/sec [*de La Beaujardière et al.*, 2004]. The C/NOFS satellite is in a 13° inclination orbit with an apogee of 840 km and a perigee of 400 km. For a more detailed description of C/NOFS and the IVM sensor, the reader is referred to the paper by *de La Beaujardière et al.* [2004]. *Araujo-Pradere et al.* [2011] found that sharp longitude gradients were present at the four-cell boundaries and they existed on a day-to-day basis. For IVM daytime **E**×**B** drift velocities to be useful, a number of constraints had to be imposed related to local time, altitude, and longitude [*Araujo-Pradere et al.*, 2011]. The constraint on local time is to choose C/NOFS IVM **E**×**B** drift observations only between 10 and 13 LT. This insures that the **E**×**B** drifts are near their maximum daytime values so that sharp longitude gradients in **E**×**B** drift velocities are due to longitude effects and not due to local time changes. Since IVM observations are within ±15° magnetic latitude, and there is very little height gradient in daytime **E**×**B** drift velocities up to an apex height of 800 km [*Pingree and Fejer*, 1987], no magnetic latitude constraints had been applied to the data. Because of all the constraints in local time and altitude, it is not possible to measure **E**×**B** drifts at all longitudes every day. The paper by *Araujo-Pradere et al.* [2011] only examined IVM observations in March, October, and December 2009. The cases that were examined all consisted of three consecutive days in a row.

**Table 8.1** The Sharp Longitude Gradients in **E**×**B** Drift Velocities

| Date | E. longitude | **E**×**B** drift velocity gradient |
|---|---|---|
| October 11–13, 2009 | 133° to 145° | −1.3 m/sec/degree |
| March 19–21, 2009 | 240° to 250° | +3 m/sec/degree |
| December 8–9, 2009 | 245° to 260° | −1.7 m/sec/degree |

*Source: Araujo-Pradere et al.* [2011].

Figure 8.3, taken from *Araujo-Pradere et al.* [2011], depicts the IVM-observed **E**×**B** drift velocity gradient in the eastern Pacific sector between ~240°E and 265°E longitude for 3 consecutive days on March 19, 20, and 21, 2009. For these 3 days the slopes in the gradients are roughly +3 m/sec/degree. The altitude and magnetic latitude changes are, respectively, from 405 km to 450 km and 1°S to 11°N. The right-hand side of the figure, from *Scherliess et al.* [2008] presumably indicates that the boundary of the Eastern Pacific sector cell is being observed in going from ~240°E to 250°E longitude. The TEC observations in Figure 8.3 were normalized to a common baseline as described in *Scherliess et al.* [2008]. Table 8.1 demonstrates the velocity gradient observed in other periods at different longitude sectors. As discussed in the paper by *Araujo-Pradere et al.* [2011], in every case, the locations of the sharp gradients coincides with the TOPEX/TEC-observed boundaries. For this reason, we infer that these gradients are associated with the four-cell boundary, and demonstrate from C/NOFS IVM observations that the longitude gradients in **E**×**B** drift velocity at

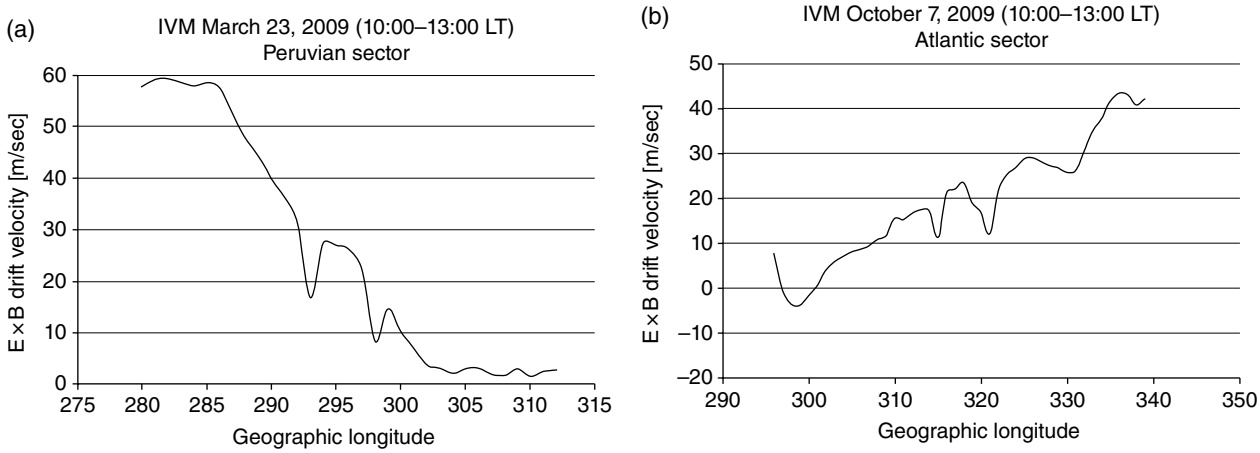


**Figure 8.4** IVM-observed **E**×**B** drifts vs. geographic longitude (a) 23 March 2009 in the Peruvian sector and (b) 7 October 2009 in the Atlantic sector.

the boundaries of the four-cell structures are very strong and exist on a day-to-day basis.

In order to study the effects of sharp longitude gradients in vertical **E**×**B** drift velocities on ionospheric electron and ion densities, we have chosen two specific days, 23 March and 7 October 2009, where IVM **E**×**B** drift velocities were obtained at the boundary between the Peruvian longitude sector and the Atlantic sector. For both days, the local times of the IVM observations run from 10 LT to 13 LT. Figure 8.4a presents IVM observations for March 23 where there is a sharp decrease in **E**×**B** drift velocity between 285°E and 300°E geographic longitude, going from 55 m/sec to 10 m/sec over this 15° segment. This amounts to a −3 m/sec/degree gradient. Figure 8.4b presents IVM observations for October 7 where there is a sharp increase in **E**×**B** drift velocity between 300°E and 337°E geographic longitude. The velocity increases from −10 m/sec to 40 m/sec over this interval for an **E**×**B** drift gradient of +1.3 m/sec/degree. Both of these days are extremely quiet with daily Ap values of 3 and 2, respectively, and an $F_{10.7}$ cm flux value of 69 for both days.

The very sharp longitude gradients in daytime, vertical **E**×**B** drift velocities found by *Araujo-Pradere et al.* [2011] were incorporated into the time-dependent, theoretical ionospheric model GIP to calculate the effects of these gradients on low-latitude ionospheric parameters [*Araujo-Pradere et al.*, 2012]. The stand-alone version of GIP, in which the thermospheric parameters and equatorial vertical drift are externally specified, is used for the study. The horizontal neutral wind from the Horizontal Wind Model [HWM-93; *Hedin et al.*, 1996] and thermospheric parameters (densities and temperature) from the Naval Research Laboratory Mass Spectrometer Incoherent Scatter Radar model [NRLMSISE-00; *Picone et al.*, 2002] are used to drive the model. The equatorial vertical drifts are specified either by the climatological model [*Scherliess and Fejer*, 1999] or by the IVM observations.

The observed vertical drifts are larger than the values derived from the climatological drift model. Therefore, the climatological drifts used in GIP simulations were multiplied by 1.5. Even though the C/NOFS IVM **E**×**B** drift velocities measured on 23 March 2009 near 280°E longitude and on 7 October 2009 near 340°E longitude seem somewhat higher than average, it is not the intent in this paper to go into details of the ongoing IVM validation efforts. We simply accept these values and have adjusted the Scherliess and Fejer climatological model to match the higher daytime **E**×**B** values to avoid discontinuities near 280°E and 340°E longitudes.

The first set of ion density calculations assumed the absence of any sharp longitude gradients in **E**×**B** drift velocity. The **E**×**B** drift velocities times 1.5 is termed the Scherliess and Fejer control run (SF control) and the calculated ion densities at 400 km and 1400 LT are pictured in Figure 8.5a. In the second set of simulation, in order to calculate ion densities as a function of altitude, latitude, longitude, and local time, that reflect the sharp longitude gradients in **E**×**B** drifts pictured in Figures 8.4a and 8.4b, the same conditions of drifts from SF control are chosen to represent the **E**×**B** drift inputs to the GIP model outside of the geographic longitude region between 285°E and 340°E longitude. Between 285°E and 340°E longitude, IVM-observed drifts with sharp gradient are specified in the GIP. The drift velocities are reduced by roughly – 3 m/sec/degree from 55 m/sec to 0 m/sec from 285°E to 300°E longitude and increased from 0 m/sec to 40 m/sec from 300°E to 337°E longitude. These **E**×**B** drift changes are implemented after 8 LT at all longitudes between 285°E and 337°E. This is termed the IVM model and the calculated ion densities at 400 km and 1400 LT

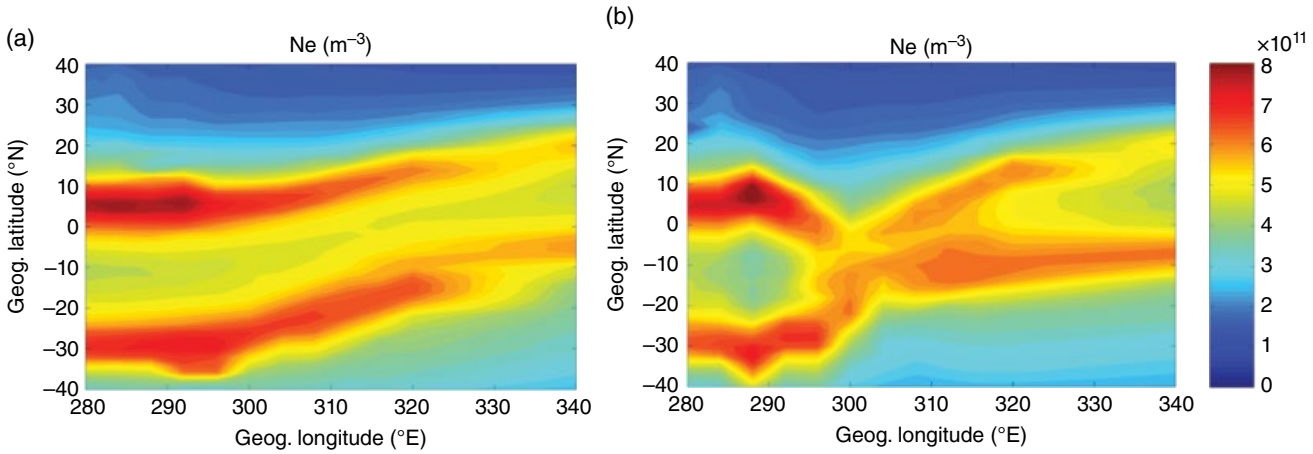


**Figure 8.5** (a) Calculated ion densities at 400 km and 14 LT for the SF control **E**×**B** drift model. (b) Calculated ion densities at 400 km and 14 LT incorporating IVM-observed **E**×**B** drifts (see discussion in text).

are displayed in Figure 8.5b. Both sets of simulations are run for 10 days until model reaches the steady state.

Note that the crests of the equatorial anomaly in Figure 8.5a are roughly symmetric about the geomagnetic equator as the magnetic equator moves northward in going from the Peruvian to the Atlantic longitude sectors. The crests are located at roughly ±15° magnetic longitude and are the result of the daytime, upward **E**×**B** drift velocity that is incorporated into the GIP model. In the absence of upward **E**×**B** drift, the equatorial anomaly crests do not form [*Hanson and Moffett*, 1966]. This dependence of crest formation on the magnitude of upward **E**×**B** drift velocity is clearly demonstrated in Figure 8.5b. At 280°E geographic longitude, the anomaly is well-formed and the crests are located at ±15° magnetic latitude. As the longitude changes from 280°E to 300°E, the crests are located closer and closer to the magnetic equator because the daytime **E**×**B** drift velocity is decreasing dramatically as pictured in Figure 8.4a. Essentially, the equatorial anomaly disappears between 300°E and 305°E longitude. Eastward of 305°E, the crests begin moving away from the magnetic equator because the **E**×**B** drift velocity is increasing as pictured in Figure 8.4b. By 337°E longitude, the crests are located at ±15° magnetic latitude. In essence, the steeper the longitude gradient in **E**×**B** drift, the steeper the longitude gradient in the equatorial anomaly crest location.

## 8.4. EVIDENCE FOR THE EXISTENCE OF A FOUR-CELL STRUCTURE IN PRE

There does not appear to be any direct evidence for a four-cell longitude pattern in prereversal enhancement (PRE) from **E**×**B** drift observations as reported by *Kil et al.* [2007] and *Fejer et al.* [2008] using the ROCSAT-1 satellite. However, there may be indirect evidence that such a pattern exists, at times. We describe, briefly, studies that relate to this indirect evidence.

Probably the strongest evidence that a four-cell pattern in PRE comes from the IMAGE/FUV observations reported by *Sagawa et al.* [2005] and *Immel et al.* [2006] since these were nighttime 135.6 nm images that indicate the $N_{max}$ values at the crests of the equatorial anomaly. A recent paper by *McDonald et al.* [2011] demonstrates a strong linear relationship between the equatorial anomaly and the PRE at solar minimum. Comparing the 135.6 nm radiances measured by the Tiny Ionospheric Photometer (TIP) onboard the COSMIC satellite with the **E**×**B** drift velocities measured at Jicamarca, Peru, they derived a linear relationship between the crest-to-trough ratio of the $N_{max}$ $F_2$ values and the PRE under solar minimum conditions. Previously, *Whalen* [2001, 2003], using an array of ionospheric sounders to determine $N_{max}$ $F_2$, found a linear relationship between $N_{max}$ $F_2$ at the crest of the equatorial anomaly and PRE. Correlating plasma bubbles, evening equatorial ionization anomaly, and the equatorial prereversal enhancement in **E**×**B** drifts at solar maximum from data collected from DMSP, ROCSAT-1, and CHAMP satellites, *Li et al.* [2008] found a four-cell longitude structure in the crest-to-trough ratio during the equinox period from CHAMP observations of electron density between 18 and 20 LT.

*Bankov et al.* [2009] examined the "wavenumber 4" (WN4) longitude distribution of different ion species at low latitudes from DMSP-F13, DMSP-F15, and Demeter satellites. From the Special Sensor-Ion, Electron and Scintillation (SSIES) sensor on DMSP-F13 and 15 and the Instrument Analyser de Plasma (IAP) on Demeter, they found that WN4 is a regular feature in the major ion, $O^+$, longitude distribution. DMSP-F15 is at 840 km and sun-synchronous at 2130 LT while Demeter is at 730 km

and 2230 LT. At these local times, a WN4 feature in the major ion implies a WN4 feature in PRE.

Another indicator that there might exist a four-cell longitude structure in PRE would be to observe if there is a four-cell structure in the *F*-region zonal neutral wind velocities after sunset. *Anderson and Roble* [1974] theoretically demonstrated that if the *F* layer is raised significantly after sunset by the enhanced upward $\mathbf{E}\times\mathbf{B}$ drift velocity, then the eastward zonal neutral wind velocity increases dramatically up to 250 m/sec because of the reduced ion drag on the neutrals. *Häusler and Lühr* [2009], utilizing the accelerometer aboard CHAMP, were able to derive thermospheric zonal wind velocities at the orbit altitude of ~400 km. They studied the zonal wind residuals (deviations from the zonal average) using 4 yr of data (2002–2005) for each month of the year. They observed a wavenumber-4 pattern in the eastward zonal wind residuals before and after sunset. An even more compelling study by *Häusler et al.* [2007], carrying out a statistical analysis of the longitude dependence of thermospheric zonal wind observations from CHAMP, unambiguously determined the presence of a wavenumber-4 pattern in longitude in the 18–21 LT time period with the eastward zonal wind velocity peaks at the same longitude sectors as the IMAGE peaks in 135.6 nm radiances.

*Lin et al.* [2007a] analyzed ionospheric parameters obtained from FORMOSAT-3/COSMIC radio occultation observations. They examined the temporal variations of the four-cell longitudinal structure in integrated (400–450 km altitude) total electron content averaged between ±15° magnetic latitude in 2 hr segments. During the daytime, the four-cell structure emerged in the 1000–1200 LT period and was evident through the 2000–2200 LT period. They also constructed peak altitude maps at various local times. In contrast to the integrated TEC maps, the four-cell structure in peak altitude emerges in the 0800–1000 LT period and disappears after the 1800–2000 LT period. They state that the observed peak altitudes after sunset are much more complicated than the TEC observations and what should be a clear signature if a four-cell structure in PRE existed, does not seem to be present.

In another paper that connects the four-cell pattern in airglow brightness after sunset to daytime four-cell patterns in $\mathbf{E}\times\mathbf{B}$ drift velocities rather than a four-cell pattern in PRE, *England et al.* [2008] demonstrate, using Another Model of the Ionosphere (SAMI2) theoretical model, that calculated brightness intensities using daytime *E*-region dynamo electric fields agree with the observed variations in brightness and latitude of the airglow bands for input conditions to the SAMI2 model. The conditions at the maximum of the wave-4 pattern produce a 40% brightness increase over the conditions for the minimum of the wave-4 pattern. The contributions are most significant for changes close to local noon and in the late afternoon.

Ironically, in a recent paper by *England et al.* [2010] that models and examines possible coupling mechanisms responsible for the longitudinal structure of the equatorial ionosphere, the calculated vertical drift at the geomagnetic equator at 400 km altitude as a function of local time and geographic longitude displays a four-cell pattern of 25 m/sec at the peaks at noontime and also a four-cell structure in PRE of 15 m/sec at 1830 LT. These calculations were carried out using TIME-GCM simulations.

## 8.5. CONCLUSIONS

In this brief chapter, we have attempted to demonstrate that a clear, four-cell signature exists in daytime, vertical $\mathbf{E}\times\mathbf{B}$ drift velocities as a function of longitude as obtained primarily from satellite observations. The longitudes of the peaks agree with the longitudes of the maximum airglow intensities seen after sunset from IMAGE 135.6 nm observations [*Sagawa et al.*, 2005; *Immel et al.*, 2006]. From modeling studies by various authors, the consensus seems to be that the eastward propagating, nonmigrating wave-3 (DE3) diurnal tidal mode is responsible for producing the four-cell structure. This tidal mode is apparently generated in the troposphere by latent heat release in the strong convection zones and propagates upward into the lower thermosphere and *E*-region ionosphere generating zonal electric fields with a characteristic four-cell structure.

We have also demonstrated from C/NOFS IVM observations that the longitude gradients in $\mathbf{E}\times\mathbf{B}$ drift velocity at the boundaries of the four-cell structures are very strong and exist on a day-to-day basis. When these sharp gradients are introduced into time-dependent, theoretical ionospheric models, they produce ion density crests that rapidly converge to the magnetic equator. Essentially, the steeper the longitude gradient in $\mathbf{E}\times\mathbf{B}$ drift, the steeper the longitude gradient in the equatorial anomaly crest location.

Finally, we provide indirect evidence from a number of publications that may suggest the existence of a four-cell pattern in PRE. We also describe some publications that suggest the absence of a four-cell pattern in PRE. It would appear that this is still an open and important question to answer. Clearly, more theoretical modeling work needs to be carried out.

## ACKNOWLEDGMENTS

The research was supported by the NASA Heliophysics Theory Program grant NNX11A061G.

## REFERENCES


Anderson, D., A. Anghel, J. Chau, and K. Yumoto (2006), Global, low-latitude, vertical E × B drift velocities inferred from daytime magnetometer observations, *Space Weather*, *4*, S08003; doi:10.1029/2005SW000193.

Anderson, D, A. Anghel, J. Chau, and O. Veliz (2004), Daytime vertical E × B drift velocities inferred from ground-based magnetometer observations at low latitudes, *Space Weather*, *2*, S11001; doi:10.1029/2004SW000095.

Anderson, D., A. Anghel, K. Yumoto, M. Ishitsuka, and E. Kudeki (2002), Estimating daytime vertical E × B drift velocities in the equatorial *F*-region using ground-based magnetometer observations, *Geophy. Res. Lett.*, *29*(12), 1596; doi:10.1029/2001GL014562.

Anderson, D., E. Araujo-Pradere, and L. Scherliess (2009), Comparing daytime, equatorial E × B drift velocities and TOPEX/TEC observations associated with the 4-cell, non-migrating tidal structure, *Annales Geophysicae*, *27*, 2861–2867; doi:10.5194/angeo-27-2861-2009.

Anderson, D. N. (1973), A theoretical study of the ionospheric, *F*-region equatorial anomaly, I. Theory, *Planet. Space Sci.*, *21*, 409; doi:10.1016/0032-0633(73)90040-8.

Anderson, D. N., and R. G. Roble (1974), The effect of vertical E×B ionospheric drifts on F- region neutral winds in the low-latitude thermosphere, *J. Geophys. Res.*, *79*(34), 5231–5236; doi:10.1029/JA079i034p05231.

Araujo-Pradere, E. A., D. N. Anderson, M. Fedrizzi, and R. Stoneback (2011), C/NOFS Observational Support for the Equatorial E × B Drift Velocities Associated with the 4-Cell Tidal Structures, *Radio Sci.*; doi:10.1029/2010RS004557.

Araujo-Pradere, E. A., T.-W. Fang, D. N. Anderson, M. Fedrizzi, and R. Stoneback (2012), Modeling the daytime, equatorial ionospheric ion densities associated with the observed, four-cell longitude patterns in E × B drift velocities, *Radio Science*, *47*, RS0L12; doi:10.1029/2011RS004930.

Bankov, L., R. Heelis, M. Parrot, J.-J. Berthelier, P. Marinov, and A. Vassileva (2009), WN4 effect on longitudinal distribution of different ion species in the topside ionosphere at low latitudes by means of DEMETER, DMSP-F13, and DMSP-F15 data, *Ann. Geophys.*, *46*, 2893–2902; doi:10.5194/angeo-27-2893-2009.

de La Beaujardière, O. CNOFS Science Definition Team (2004), C/NOFS: A mission to forecast scintillations, *J. Atmos. Solar Terr. Phys.*, *66*(17), 1573–1591; doi:10.1016/j.jastp.2004.07.030.

England, S. L., S. Maus, T. J. Immel, S. B. Mende (2006), Longitudinal variation of the *E*-region electric fields caused by atmospheric tides, *Geophys. Res. Lett.*, *33*, L21105; doi: 10.1029/2006GL027465.

England, S. L., T. J. Immel, and J. D. Huba (2008), Modeling the latitudinal variation ion the post-sunset far-ultraviolet OI airglow using the SAMI2 model, *J. Geophys. Res.*, *113*, A01309; doi:10.1029/2007JA012536.

England, S. L., T. J. Immel, J. D. Huba, M. E. Hagan, A. Maute, and R. DeMajistre (2010), Modeling the multiple effects of atmospheric tides on the ionosphere: An examination of possible coupling mechanisms responsible for the longitudinal structure of the equatorial ionosphere, *J. Geophys. Res.*, *115*, A05308; doi:10.1029/2009JA014894.

Fang, T.-W., H. Kil, G. Millward, A. D. Richmond, J.-Y. Liu, and S.-J. Oh (2009), Causal link of the wave-4 structures in plasma density and vertical plasma drift in the low-latitude ionosphere, *J. Geophys. Res.*, *114*, A10315; doi:10.1029/2009JA014460.

Fang, T.-W., R. Akmaev, T. Fuller-Rowell, F. Wu, N. Maruyama, and G. Millward (2013), Longitudinal and day-to-day variability in the ionosphere from lower atmosphere tidal forcing, *Geophys. Res. Lett.*, *40*, 1–6; doi:10.1029/grl.50550.

Fejer, B. G., B. D. Tracy, and R. F. Pfaff (2013), Equatorial zonal plasma drifts measured by the C/NOFS satellite during the 2008–2011 solar minimum, *J. Geophys. Res. Space Phys.*, *118*, 3891–3897; doi:10.1002/jgra.50382.

Fejer, B. G., J. W. Jensen, and S.-Y. Su (2008), Quiet time equatorial F region vertical plasma drift model derived from ROCSAT-1 observations, *J. Geophys. Res.*, *113*, A05304; doi:10.1029/2007JA012801.

Hagan M. E., and J. M. Forbes (2002), Migrating and nonmigrating diurnal tides in the middle and upper atmosphere excited by tropospheric latent heat release, *J. Geophys. Res.*, *107*(D24), 4754; doi:10.1029/2001JD001236.

Hanson, W. B., and R. J. Moffett (1966), Ionization transport effects in the equatorial F region, *J. Geophys. Res.*, *71*, 5559; doi:10.1029/JZ071i023p05559.

Häusler, K., and H. Lühr (2009), Nonmigrating tidal signals in the upper thermospheric zonal wind at equatorial latitudes as observed by CHAMP, *Ann. Geophys.*, *27*, 2643–2652; doi:10.5194/angeo-27-2643-2009.

Häusler, K., H. Lühr, S. Rentz, and W. Kohler (2007), A statistical analysis of longitudinal dependence of upper thermospheric zonal winds at dip equator latitudes derived from CHAMP, *J. Atmos. Solar Terr. Phys.*, *69*, 1419–1430; doi:10.1016/j.jastp.2007.04.004.

Hedin, A. E., E. L. Fleming, A. H. Munson, F. J. Schmidlin, S. K. Avery, R. R. Clark, S. T. Franke, G. J. Fraser, T. Tsuda, F. Vial and R. A. Vincent (1996), Empirical wind model for the upper, middle and lower atmosphere, *J. Atmos. Terr. Phys.*, *58*, 1421–1447; doi:10.1016/0021-9169(95)00122-0.

Huang, C. Y., P. A. Roddy, E. K. Sutton, R. Stoneback, R. F. Pfaff, L. C. Gentile, and S. H. Delay (2013), Ion-neutral coupling during deep solar minimum, *J. Atmos. Sol. Terr. Phys.*; doi:10.1016/j.jastp.2012.11.009.

Huang, C. Y., S. H. Delay, P. A. Roddy, and E. K. Sutton (2011), Periodic structures in the equatorial ionosphere, *Radio Sci.*, *46*, RS0D14; doi:10.1029/2010RS004569.

Immel, T. J., E. Sagawa, S. L. England, S. B. Henderson, M. E. Hagan, S. B. Mende, H. U. Frey (2006), Control of equatorial ionospheric morphology by atmospheric tides, *Geophys. Res. Lett.*, *33*, L15108; doi: 10.1029/2006GL026161.

Kil, H., E. R. Talaat, S.-J. Oh, L. J. Paxton, S. L. England, and S.-Y. Su (2008), Wave structures of the plasma density and vertical E×B drift in low-latitude F region, *J. Geophys.l Res.*, *113*, A09312; doi:10.1029/2008JA013106.

Kil, H., S.-J. Oh, L. J. Paxton, and T. -W. Fang (2009), High-resolution vertical E × B drift model derived from ROCSAT-1, *J. Geophys. Res.*, *114*, A10314; doi:10.1029/2009JA014324.

Kil, H., S.-J. Oh, M. C. Kelley, L. J. Paxton, S. L. England, E. Talaat, K.-W. Min, and S.-Y. Su (2007), Longitudinal structure of the vertical E × B drift and ion density seen from

ROCSAT-1, *Geophys. Res. Lett.*, *34*, L14110; doi:10.1029/2007GL030018.

Li, G., B. Ning, L. Liu, B. Zhao, X. Yue, S.-Y. Su, and S. Venkatraman (2008), Correlative study of plasma bubbles, evening equatorial ionization anomaly, and equatorial pre-reversal E × B drifts at solar maximum, *Radio Sci.*, *43*, RS4005; doi:10.1029/2007RS003760.

Lin, C. H., C. C. Hsiao, J. Y. Liu, and C. H. Liu (2007a), Longitudinal structure of the equatorial ionosphere: Time evolution of the four-peaked EIA structure, *J. Geophys. Res.*, *112*, A12305; doi:10.1029/2007A012455.

Lin, C. H., W. Wang, M. E. Hagan, C.C. Hsiao, T. J. Immel, M. L. Hsu, J. Y. Liu, L. J. Paxton, T. -W. Fang, and C. H. Liu (2007b), Plausible effect of atmospheric tides on the equatorial ionosphere observed by the FORMOSAT-3/COSMIC: Three-dimensional electron density structures, *Geophys. Res. Lett.s*, *34*, L11112; doi:10.1029/2007GL029265.

Maute, A., A. D. Richmond, and R. G. Roble (2012), Sources of low-latitude ionospheric E × B drifts and their variability, *J. Geophys. Res.*, *117*, A06312; doi:10.1029/2011JA017502.

McDonald, S. E., C. Coker, K. F. Dymond, D. N. Anderson, and E. A. Araujo-Pradere (2011), A study of the strong linear relationship between the equatorial ionization anomaly and the prereversal E × B drift velocity at solar minimum, *Radio Sci.*, *46*, RS6004; doi:10.1029/2011RS004702.

Millward, G. H., I. C. E. Muller-Wodarg, A. D. Aylward, T. J. Fuller-Rowell, A. D. Richmond, and R. J. Moffett (2001), An investigation into the influence of tidal forcing on equatorial F region equatorial vertical ion drift using a global ionosphere-thermosphere model with coupled electrodynamics, *J. Geophys. Res.*, *106*, 24,733–24,744; doi:10.1029/2001JA00034

Pedatella, N. M., J. M. Forbes, A. Maute, A. D. Richmond, T.-W. Fang, K. M. Larson, and G. Millard (2011), Longitudinal variations in the F region ionosphere and the topside ionosphere-plasmasphere: Observations and model simulations, *J. Geophys. Res.*, *116*, A12309; doi:10.1029/2011JA016600.

Picone, J. M., A. E. Hedin, D. P. Drob, and A. C. Aikin (2002), NRLMSISE-00 empirical model of the atmosphere: Statistical comparisons and scientific issues, *J. Geophys. Res.*, *107*(A12), 1468; doi:10.1029/2002JA009430.

Pingree, J. E., and B. G. Fejer (1987), On the height variation of the equatorial F region vertical plasma drifts, *J. Geophys. Res.*, *92*, 4763–4766; doi:10.1029/JA092iA05p04763.

Richmond, A. D. (1995), Ionospheric electrodynamics using magnetic apex coordinates, *J. Geomagn. Geoelectr.*, *47*, 191–212; doi:10.5636/jgg.31.287.

Sagawa, E., T. J. Immel, H. U. Frey, and S. B. Mende (2005), Longitudinal structure of the equatorial anomaly in the nighttime ionosphere observed by IMAGE/FUV, *J. Geophys. Res.*, *110*, A11302; doi:10.1029/2004JA010848.

Scherliess, L. and B. G. Fejer (1999), Radar and satellite global equatorial F region vertical drift model, *J. Geophys. Res.*, *104*, 6829–6842.

Scherliess, L., D. C. Thompson, R. W. Schunk (2008), Longitudinal variability of low-latitude total electron content: Tidal influences, *J. Geophys. Res.*, *113*, A01311; doi: 10.1029/2007JA012480.

Whalen, J. A (2001), The equatorial anomaly: Its quantitative relation to equatorial bubbles, bottomside spread F, and E × B drift velocity during a month at solar maximum, *J. Geophys. Res.*, *106*, A12, 29125–29132.

Whalen, J. A (2003), Dependence of the equatorial anomaly and of the equatorial spread F on the maximum pre-reversal E × B drift velocity measured at solar maximum, *J. Geophys. Res*, *108*(A5); doi:10.1029/2002JA009755.

# 9

# Imaging the Global Vertical Density Structure from the Ground and Space

**Endawoke Yizengaw and Brett A. Carter**

## ABSTRACT

Although satellite observations demonstrate that there are large longitudinal differences in ionospheric density distributions, the availability of uneven distribution of ground-based instruments hinders understanding the physics behind the global ionospheric density distributions. For example, understanding the physics behind the unique equatorial ionospheric irregularities in the African sector is still a problem due to lack of ground-based instruments. The space-based GPS measurements on board Low Earth Orbiting (LEO) satellites are rather good datasets to monitor the ionosphere and plasmasphere on a global scale. In this chapter, we present different capabilities of GPS measurements on board LEO satellites, providing (1) radio occultation (RO) density profiles to routinely monitor the global ionospheric region below the LEO orbiting altitude and (2) topside ionosphere and plasmasphere integrated density values that can be used for space-based tomographic reconstruction techniques to remotely image the vertical structure of the topside ionosphere and plasmasphere density profiles.

**Key Points:**
Tomographically inverted and occultation ionospheric density profiles
Longitudinal variability of *F*-layer peak density ($N_mF_2$) and altitude ($h_mF_2$)
Topside ionospheric and plasmaspheric density profiles

**Key Terms:** Topside ionosphere, radio occultation, tomography

## 9.1. INTRODUCTION

Although much progress has been made in the study of ionospheric density structure and dynamics in the last decade, many gaps still remain in the global understanding of the fundamental formation of equatorial ionospheric density irregularities. This is in part due to the uneven distribution of ground-based instruments. In Africa, there is a significant lack of ground-based space physics instrumentation. To date, much of what is known about the physics of equatorial ionospheric density structures is based on observations of the incoherent scatter radar at Jicamarca, Peru. However, Jicamarca is located in the American sector (outside of Lima, Peru) where there is a fairly large excursion between the geomagnetic and geodetic equator due to the dip of the geomagnetic equator. The inclination and magnitude of the magnetic field at Jicamarca differ considerably from that of African sector. Equatorial ionospheric phenomena, such as equatorial vertical density structure, equatorial electrodynamics, and the tidal behavior of thermospheric winds and tides, are all in some way influenced by the regional geomagnetic field, its declination, and the proximity of the magnetic to the

*Institute for Scientific Research, Boston College, Chestnut Hill, Massachusetts, USA*

*Ionospheric Space Weather: Longitude and Hemispheric Dependences and Lower Atmosphere Forcing, Geophysical Monograph 220*, First Edition. Edited by Timothy Fuller-Rowell, Endawoke Yizengaw, Patricia H. Doherty, and Sunanda Basu.

geographic equator. All these make it impossible to observe the temporal and spatial structures of the small-to-medium scale density irregularities in the region, which becomes the barrier for the ongoing global equatorial ionospheric modeling effort. Satellite observations demonstrate this and often show that there are large differences in the formation of ionospheric irregularities over Africa as compared to other longitudinal sectors [e.g., *Hei et al.*, 2005]. Thus predictions of African-sector equatorial ionospheric phenomenon cannot be made based on Jicamarca radar observations. However, until recently, the equatorial ionospheric density structure in the African sector has been estimated based on model interpolation.

Understanding the physics behind equatorial ionospheric irregularities in the African sector, which has the largest land mass (along the geomagnetic equator) in the world, is becoming critical to our technological systems. In fact, our communication and navigation technologies depend on understanding, modeling, and mitigating the effects of these irregularities [*Doherty et al.*, 2004]. During the past couple of years, a number of small instruments such as magnetometers, ionosondes, and GPS dual frequency receivers, have been deployed in Africa [*Yizengaw et al.*, 2013]. *Yizengaw et al.* [2012] applied tomographic reconstruction technique to the collection of GPS slant TEC (i.e., line integral of the free electron density along individual line of sight) obtained by the newly deployed chain of GPS receivers and reported, for the first time, huge vertical density structure and magnitude difference between African and American longitudinal sectors.

The tomographic reconstruction essentially obtains the vertical structure of electron density from the collections of slant GPS TECs observations in the region. The bottom side ionospheric density structure and dynamics can be imaged using GPS network on the ground (from now onward termed as ground-based tomography in this paper), and has been successfully verified using independently measured density profiles, such as incoherent scatter radar and ionosondes [e.g., *Pryse*, 2003; *Yizengaw et al.*, 2007] as well as using in-situ density observations [e.g, *Yizengaw et al.*, 2012]. The GPS observations on board LEO can be used to obtain the vertical density distribution of the topside ionosphere and plasmasphere by applying tomographic reconstruction on the slant TEC with elevation angle greater than zero (referred to as space-based tomography in the rest of the paper). The advantage of space-based tomography is its ability to image the density structure of the topside ionosphere and plasmasphere, which cannot be done using ground-based tomography due to *F*-region density domination [e.g., *Yizengaw et al.*, 2006]. The reconstruction plane is discretized into pixels, and usually, but not necessarily, for the ground-based tomography the pixels are subdivided equidistantly with height and angular spacing [e.g., *Yizengaw et al.*, 2012]. However, for the space-based tomography, the grid height is not uniform, rather it increases as a function of altitude [e.g., *Heise et al.*, 2002; *Yizengaw et al.*, 2006; *Jakowski et al.*, 2007]. By assuming that the density is uniform in each pixel [*Tsai et al.,* 2002], the TEC along the ray path can then be represented as a finite sum of shorter integrals along segments of the ray path length and is given by:

$$STEC_i = \int n(r)dl \approx \sum_{j=1}^{M} n_j d_{ij}$$

where $STEC_i$ is the integrated density along the line-of-sight of ray $i$, $n(r)$ is the electron density at a point $r$ along the ray path, $d_{ij}$ is the $i^{th}$ raypath length inside pixel $j$, $n_j$ corresponds to the average electron density inside pixel $j$. We use the algebraic reconstruction technique (ART) to invert the slant TEC into vertical density profiles. Detailed description of the ART algorithm and discussion about the potentials and limitations of the technique can be found [e.g., *Na et al.,* 1995; *Raymund*, 1995; Yizengaw et al., 2012 and the reference therein]. *Yizengaw et al.* [2012] also utilized the newly deployed ground-based magnetometers and estimated, using the technique described in [*Anderson et al.*, 2004; *Yizengaw et al.*, 2014], the corresponding equatorial electrodynamics that govern the equatorial density distributions at these longitudinal sectors and found stronger dayside vertical drift in the American sector compared to the African sector.

The Low Earth Orbiting (LEO) satellites, with dual frequency GPS receiver onboard, offer a unique opportunity for remote sensing of the global ionosphere on a continuous basis. By measuring the phase delay of radio waves from GPS satellites as they are occulted by the Earth's atmosphere, the GPS receiver on board LEO satellites provides accurate and precise vertical density profiles of the bending angles of radio-wave trajectories at different locations [e.g., *Hajj and Romans*, 1998]. Since the mid-1960s, the radio occultation technique has been used to study the structure and properties of the atmospheres of not only Earth but also other planets, such as Venus, Mars, some other outer planets, and many of their moons [e.g., *Lindal et al.*, 1983 and the referencess therein]. The success of the GPS/Meteorology (GPS/MET) [*Hajj and Romans*, 1998] mission in 1995 inspired a number of follow-on missions that include radio occultation experiments, including the Gravity Recovery and Climate Experiment (GRACE) [*Chen et al.*, 2005] and Germany's Challenging Minisatellite Payload (CHAMP) [*Jakowski et al.*, 2007], and the joint U.S./Taiwan Constellation Observing System for Meteorology, Ionosphere and Climate (COSMIC) [*Schreiner et al.*, 2007]. The six-satellite COSMIC constellation, which was launched in April 2006, alone has been providing an unprecedented global coverage of density profiles (up to 3000 profiles per day)

with the vertical resolution of nearly 1 km. Therefore, the combined profiles from different LEO satellites provide excellent opportunities to explore the dynamics and structure of the ionosphere of the region, like Africa, that has been devoid of ground-based instruments.

In this chapter, we present the longitudinal variability of the ionospheric vertical structures, primarily the variability of ionospheric peak-density magnitude ($N_mF_2$) and its location in terms of altitudes ($h_mF_2$), and compared it with tomographically inverted density profiles. The tomographically imaged topside ionosphere and plasmasphere density profiles using data from the LEO satellite constellation are also included in this paper.

## 9.2. DATA ANALYSIS

For this study, we used the ground- and space-based GPS receivers' data. The GPS constellation currently consists of 29 satellites orbiting at ~55° inclination in six distinct orbital planes and at ~20, 200 km altitude (~4.2 L). Each satellite broadcasts two L-band signals at frequencies $f1 = 1.57542$ GHz and $f2 = 1.2276$ GHz, and continuously received by GPS receivers on the ground and onboard LEO satellites. Owing to the dispersive nature of the ionosphere, dual-frequency GPS measurements can provide integral information about the ionosphere and plasmasphere by computing the differential phases of the code and carrier phase measurements recorded at the ground- and space-based GPS receivers [*Coster et al.*, 2003]. Details of TEC calculation from GPS observations are described in several papers [e.g., *Yizengaw et al.*, 2004; and references therein]. However, the TEC measurements provide only the line integral of the free electron density along individual line of sight and cannot provide information about the vertical structures of the density distribution. Therefore, to infer the vertical density distributions of the ionosphere and plasmasphere, we applied the tomographic inversion technique on ground-based (ground-based tomography) and space-based (space-based tomography) GPS TECs. A detailed description of the tomographic reconstruction technique we used for this study can be found in *Yizengaw et al.* [2012].

The number of LEO satellites that are equipped with dual-band frequency GPS receivers increases dramatically and provides excellent opportunity to continuously monitor the ionosphere below the LEO satellite orbiting altitude using occultation technique. The LEO satellites are located at different altitudes, which is very important for imaging the topside and plasmasphere density distributions from different altitudes.

Figure 9.1 shows the 2-hr ground tracks (top panel) global coverage of LEO satellites that are used for this study with different colors depicting different satellites. The middle panels in Figure 9.1 indicate the ground tracks of different LEO satellites' descending passes, color coded with the magnitude of topside ionosphere and plasmasphere TEC values. The difference in the orientation of the passes is due to orbital inclination difference for various LEO satellites. Similarly, the density profiles at certain latitudes range (25°S–25°N latitudes) but for all longitudes that are binned into altitude and local time bins is shown in the bottom panel of Figure 9.1. In this figure, the electron density profiles are retrieved from radio occultation measurements on board CHAMP, COSMIC, and GRACE satellites. Such combined data may be useful to get climatological information on the vertical distribution of ionospheric plasma structure as a function of latitudes, local time, and longitudes, especially in the regions that are devoid of ground-based instruments. The data from LEO satellites that we used are obtained from the COSMIC database (http://cosmic-io.cosmic.ucar.edu/cdaac/index.html). The accuracy of the TEC and occultation profiles is believed to be 1–3 TECU and $10^4$–$10^5$ $cm^{-3}$, respectively, and it is a very useful dataset for large-scale ionospheric structure studies.

## 9.3. RESULTS AND DISCUSSION

The vertical motion of the *F*-region ionosphere, which is governed by equatorial electrodynamics or vertical drift velocity, can also be monitored by instruments onboard LEO satellites. The radio occultation profiles are the suitable and valuable dataset to monitor the vertical motion of the *F*-region peak density. Therefore, in order to understand the longitudinal difference in the vertical motion of the ionosphere, we extracted the *F*-region peak altitude ($h_mF_2$) and density ($N_mF_2$) at different longitudes and different local time sectors. This provides good insight of ionospheric vertical motions as a function of local time and longitudes.

Figure 9.2 shows the 3-yr statistical global maps of the $h_mF_2$ (left panels) and $N_mF_2$ (right panels) extracted from occultation profiles estimated from GRACE and COSMIC GPS observations and plotted as a function of latitude and longitudes. The local time and years of observation are shown at the top. Each panel from top to bottom represents different seasons, which are indicated at the top of each panel. Just to make the structure clear, we deliberately used a different color scale for different seasons. As can be seen in the figures, a clear longitudinal variability is evident. The well-known wavenumber 4 structure is clearly visible, especially on the maps of $h_mF_2$ and that creates expanded equatorial anomalies (left panel) at the corresponding longitudes where the peak $h_mF_2$ occurs, which is predominantly visible during fall equinox. The peak $h_mF_2$ at four different longitudes indicates that the vertical drifts magnitudes are stronger at those longitudes, which is consistent with earlier observations [e.g., *England et al.*, 2006; *Yizengaw*, 2012 and the reference therein].

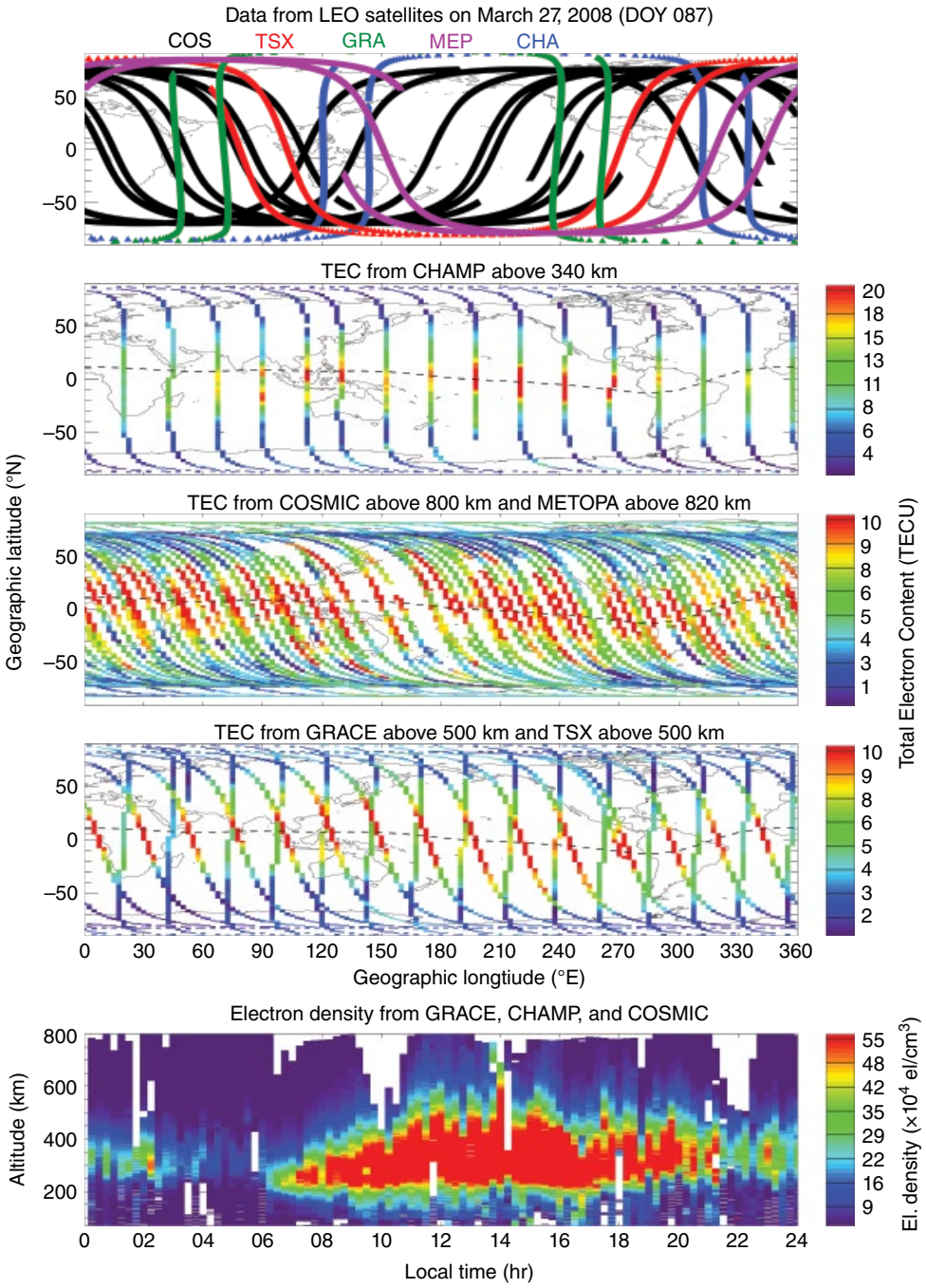


**Figure 9.1** The top panel shows the ground-tracks global coverage of COSMIC, CHAMP, GRACE, METOP, and TerraSAR-X LEO satellites within 2 hr. The second to fourth panels from top, respectively, show the 1 day descending passes, color coded with topside TEC values from CHAMP, COSMIC and METOP, and GRACE and TerraSAR-X satellites. Bottom panel shows occultation density profiles from GRACE, CHAMP, and COSMIC observations over the equatorial region (25°S–25°N latitudes) from all longitudes.

It is well known that the photo ionization of the Earth's ionosphere depends on the incidence angle of solar radiation, which then causes the latitudinal variation of the total ionization. The latitudinal difference can be caused also by transport, which is strongly influenced by magnetic and electric fields that take plasma from one region to another. This creates clear latitudinal density magnitude difference, such as the well-known equatorial ionization anomaly (EIA) with the enhanced ionization crest located at about ±15° from the geomagnetic equator.

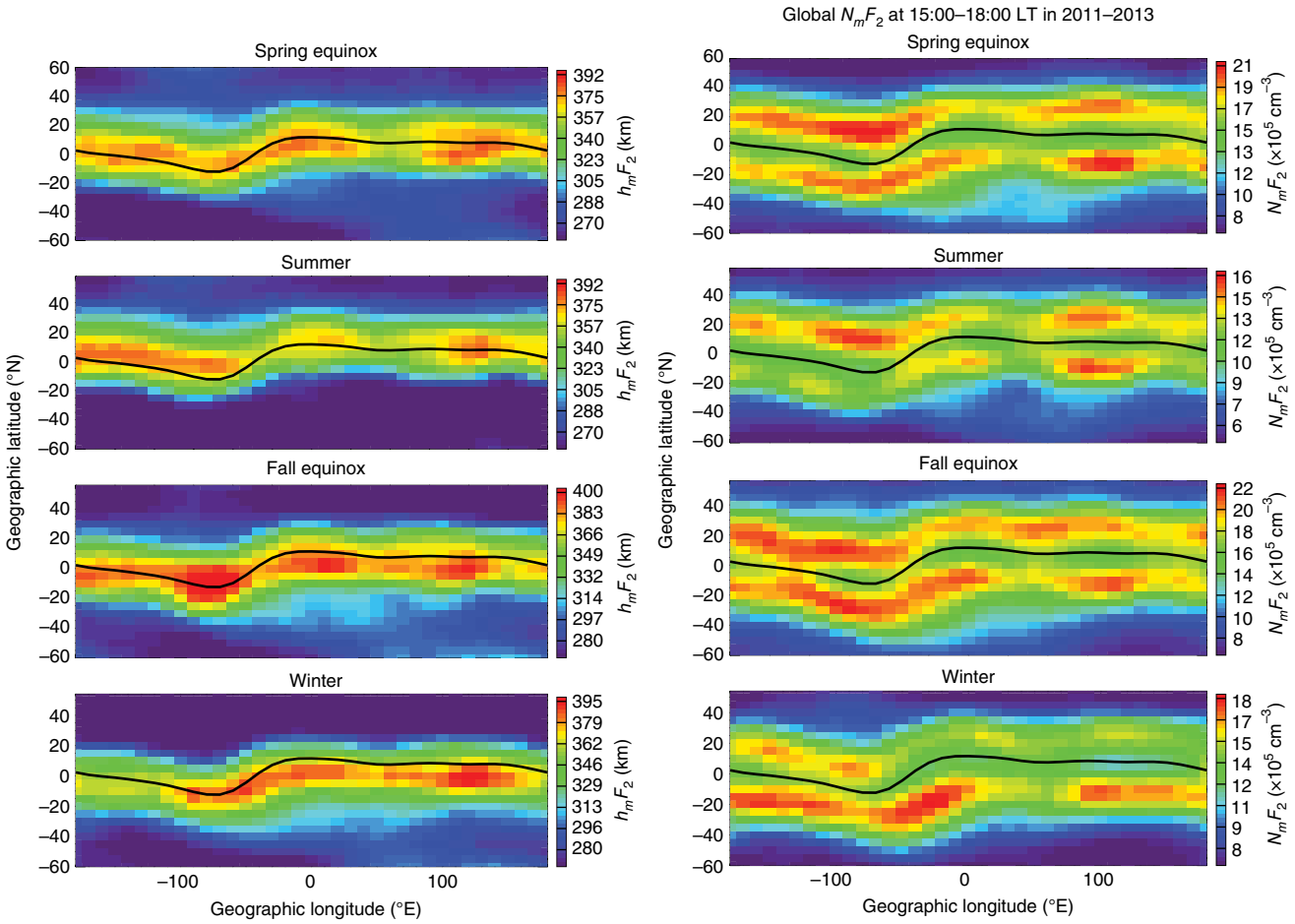


**Figure 9.2** The 3-yr averaged statistical *F*-layer peak density (right panels) and altitude (left panels) extracted from occultation density profiles obtained by COSMIC and GRACE. Different panels from top to bottom represent different seasons as shown at the top of each panel.

The solar cycle variability of ionospheric vertical motion is also investigated using the extended occultation data coverages. Nearly, two solar cycle $h_mF_2$ and $N_mF_2$ structures are shown in Figure 9.3. The figure shows the global maps of $h_mF_2$ (left) and $N_mF_2$ (right) as a function of latitude and longitude. The panels from top to bottom indicate the structure of the two parameters during solar maximum (top), solar minimum (second panel from the top), and solar maximum (third panel from the top) periods. Again the color scale is different for different panels, and the *F*-layer peak daytime ionization has been reduced by nearly 50% during the solar minimum period compared with the solar maximum period. The second panel from the bottom in Figure 9.3 shows the *F*-layer peak density difference between solar maximum (2011–2013) and solar minimum (2006–2008) periods, indicating a clear longitudinal difference in the solar cycle variability of the *F*-layer density. Similarly, the average solar radio flux ($F_{10.7}$cm), which is a proxy for EUV radiation that ionizes the ionosphere, is reduced from ~120 in 2011–2013 down to 80 in 2006–2008 as shown in the bottom panel of Figure 9.3. In the same manner, the *F*-layer peak density altitude ($h_mF_2$) decreases by up to 80 km during solar minimum throughout all latitudes as shown in the second panel from the bottom in Figure 9.3. Since the orbit altitude of the LEO satellites decreases through time, the true value of $h_mF_2$ might be a slightly different, probably higher value, since some of the LEO satellites may orbit underneath the actual $h_mF_2$ altitudes, such as the CHAMP satellite.

The ionospheric *F*-layer peak values ($h_mF_2$ and $N_mF_2$) can also be extracted from the tomographically estimated density profiles using ground-based observations. Recently, a few GPS receivers have been deployed in the African sector, mainly in the East African region. *Yizengaw et al*. [2012], utilizing the GPS observation from

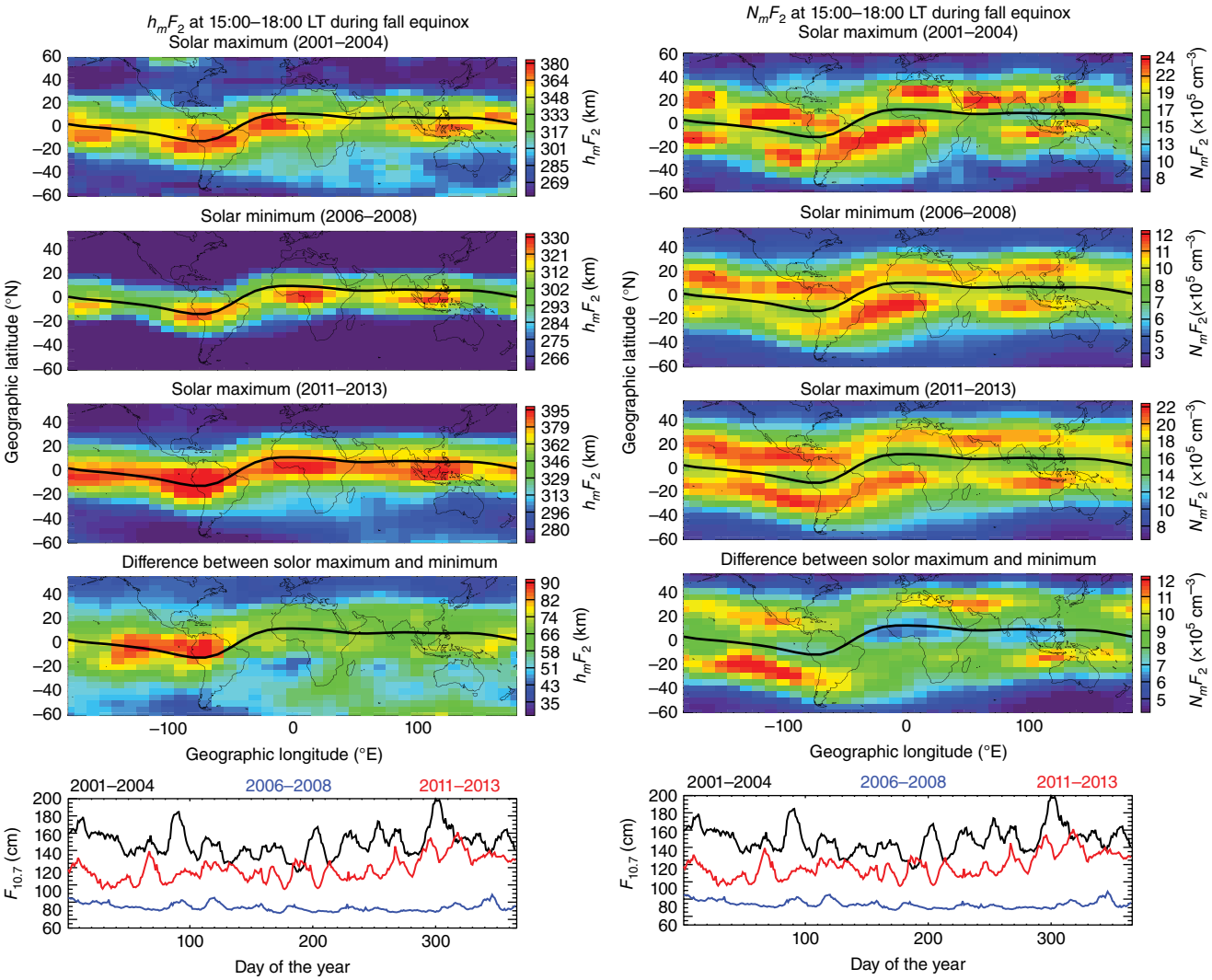


**Figure 9.3** Solar cycle differences in *F*-layer peak density (left panels) and peak altitudes (right panels) during fall equinox. The top three panels show peak values during solar maximum, solar minimum, and solar maximum periods. The second panel from the bottom shows the difference between solar maximum (2011–2013) and minimum (2006–2008) periods. Bottom panels show the average of $F_{10.7}$ values for different solar cycle conditions.

these new instruments, tomographically imaged the ionospheric vertical density structure of the East African sector. From their full-day tomographically reconstructed density profiles, we extracted the *F*-layer peak values. Figure 9.4 shows the *F*-layer peak density (bottom panel) and altitude (top panel) extracted from 1 month (October 2008) of continuous tomographic images.

In this typical example, only the dayside (11:00–18:00 LT) peak values are plotted. These peak values that are extracted from the tomographic profiles are also compared with the peak values extracted from LEO satellites' occultation profiles. The scatter plot comparison of 1 month (1–30 October 2008) of observations, only in the vicinity of East African longitudinal sectors, is shown in Figure 9.5. The comparison is performed deliberately for only the data obtained at low latitudes (30°S–30°N) and only for daytime (11:00–18:00 LT), because occultation profiles perform poorly due to the equatorial electrodynamics that drive the equatorial density structure unstable in these regions and local times.

As shown in Figure 9.5, the tomographically estimated peak altitude ($h_mF_2$) is slightly higher than that of the value estimated from occultation profiles with the correlation coefficient of 0.657. On the other hand, the peak density ($N_mF_2$) extracted from tomography is marginally less than the peak density from occultation profiles, and

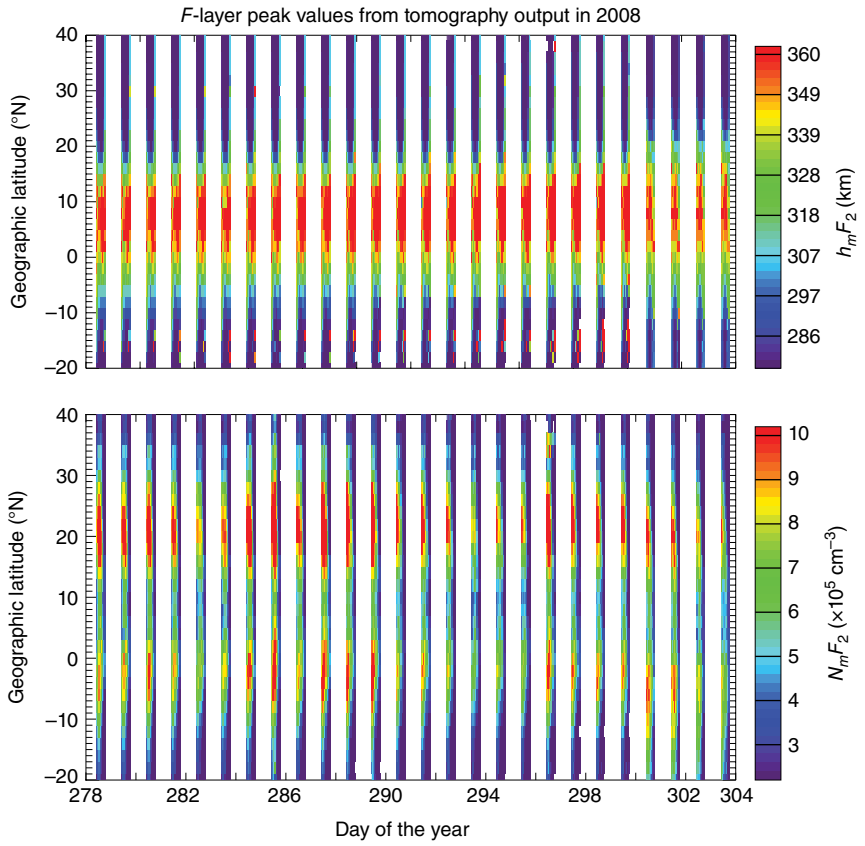


**Figure 9.4** Dayside *F*-layer peak density (bottom panel) and altitude (top panel) values extracted from tomographically imaged density profiles at the East African longitudinal sector.

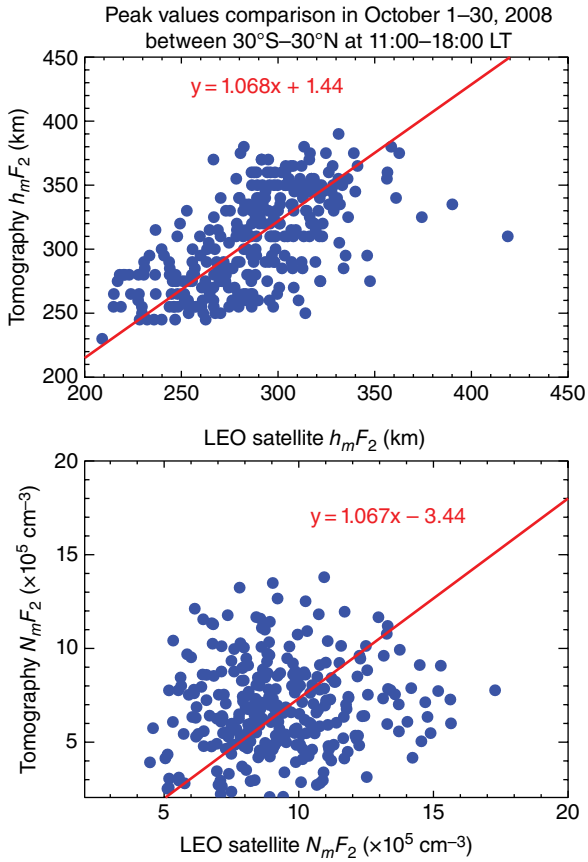


**Figure 9.5** Scatter plot comparison between *F*-layer peak density (bottom panel) and altitude (top panel) extracted from occultation and tomography profiles at the equatorial region at the East African longitude sector.

shows a very low correlation coefficient, 0.322. In general, the comparison between these independently estimated *F*-layer peak values, in the most unstable latitudes, shows very reasonable agreement. This confirms that the occultation profiles from the growing number of LEO satellites are a valuable dataset to monitor the regions that are devoid of ground-based instruments.

Space-weather events also modify the vertical structure of the topside ionosphere and plasmasphere region at significantly different spatial and temporal scales [e.g., *Yizengaw et al.*, 2005]. Obviously, it is impossible to monitor this region with ground-based instruments. The occultation density profiles also provide only density profiles below the orbiting altitude of the satellite and thus most of the profiles do not represent the topside ionosphere. The ground-based tomographic imaging is also unable to show structure of the topside ionosphere and plasmasphere due to the dominance of the *F*-layer density.

A growing number of LEO satellites are equipped with GPS receivers on board. In addition to occultation profiles, a growing number of LEO satellites are equipped with dual frequency GPS receivers and provide integrated value of density distribution between LEO and the GPS satellites orbit altitudes. This allows us to remotely sense and monitor the topside ionosphere and plasmasphere regions. The integrated electron density along the ray path between a LEO and a GPS satellites, usually known as total electron content (TEC), can be derived in the same way that the ground-based GPS TEC is estimated, that is, from the combination of GPS pseudoranges ($P_1$–$P_2$) and carrier phases ($L_1$–$L_2$) [*Yizengaw et al.*, 2005].

However, by themselves, a series of TEC measurements are just a collection of line integrals of the free electron density and not maps of the electron density distribution of topside ionosphere and plasmasphere. Therefore, in order to address the problem of imaging the electron density profiles satisfactorily, we applied a tomographic inversion method on the slant TEC between LEO and GPS satellites [*Yizengaw et al.*, 2005, 2006]. A detailed description of the topside ionosphere and plasmasphere tomographic reconstruction technique can be found in *Yizengaw et al.* [2006]. Therefore, applying the tomographic reconstruction technique to the space-based GPS TEC provides a good opportunity to image the vertical structure of the topside ionospheric and plasmaspheric density effectively up to several thousand kilometers or up to GPS altitudes [e.g., *Jakowski et al.*, 2005; *Yizengaw et al.*, 2006].

The contour map at the top right side of Figure 9.6 shows the tomographically reconstructed electron density distribution of the topside ionosphere and plasmasphere as a function of altitude and latitude. It is obtained by applying tomographic reconstruction technique on the topside TEC observations by three tailgating COSMIC satellites. The ground tracks of these COSMIC satellites are shown in the bottom right panel of Figure 9.6. The time span for the three satellites to cover the given latitudes was about 70 min. By merging the data from these three satellites, we reconstructed a 70-min average topside ionosphere and plasmasphere density profile that shows detailed structures compared with the density structures reconstructed by using data from only one COSMIC satellite (figure not shown here).

Once the density is reconstructed, it is possible to extract the density profile at different latitudes as shown in the top left panel in Figure 9.6 and investigate the latitudinal difference in density structure and magnitude at different altitudes. This may help us understand the physics behind the horizontal and vertical plasma transports both during dayside and nightside at a very high altitude (topside ionosphere and plasmasphere regions). Similarly, the bottom left panel in Figure 9.6 shows the in-situ density extracted from the tomographically imaged density structures at different altitudes. Such in-situ densities at different altitudes provide a clear insight about the latitudinal topside ionosphere and plasmasphere density structures. The troughlike structure at very high altitudes (i.e., in the plasmasphere) could be due to the plasmaspheric near-equatorial manifestations of geomagnetic-field-aligned cavities reported from the Combined Release and Radiation Effects Satellite (CRRES) observations [*Carpenter et al.*, 2000, and the references therein].

In conclusion, the occultation profiles and topside TECs from the growing number of LEO satellites that are equipped with GPS receivers are a valuable asset to monitor the global density distribution of the ionosphere and plasmasphere. This is primarily important for the region, like Africa, that has been devoid of ground-based instruments. Even in the region where there are enough ground-based instruments, the combination of ground- and space-based observations has a high potential for monitoring the vertical structure of ionospheric and plasmaspheric electron density distributions.

The promising space-based tomographic reconstruction techniques is the most valuable means to remotely monitor the topside ionosphere and plasmasphere density structures. The growing number of LEO satellites that provide both occultation profiles and topside ionosphere and plasmasphere TEC values offer great promise to image and model the vertical density distributions of the Earth's ionosphere and plasmasphere, and continuously monitor space-weather impacts on our communication and navigation systems.

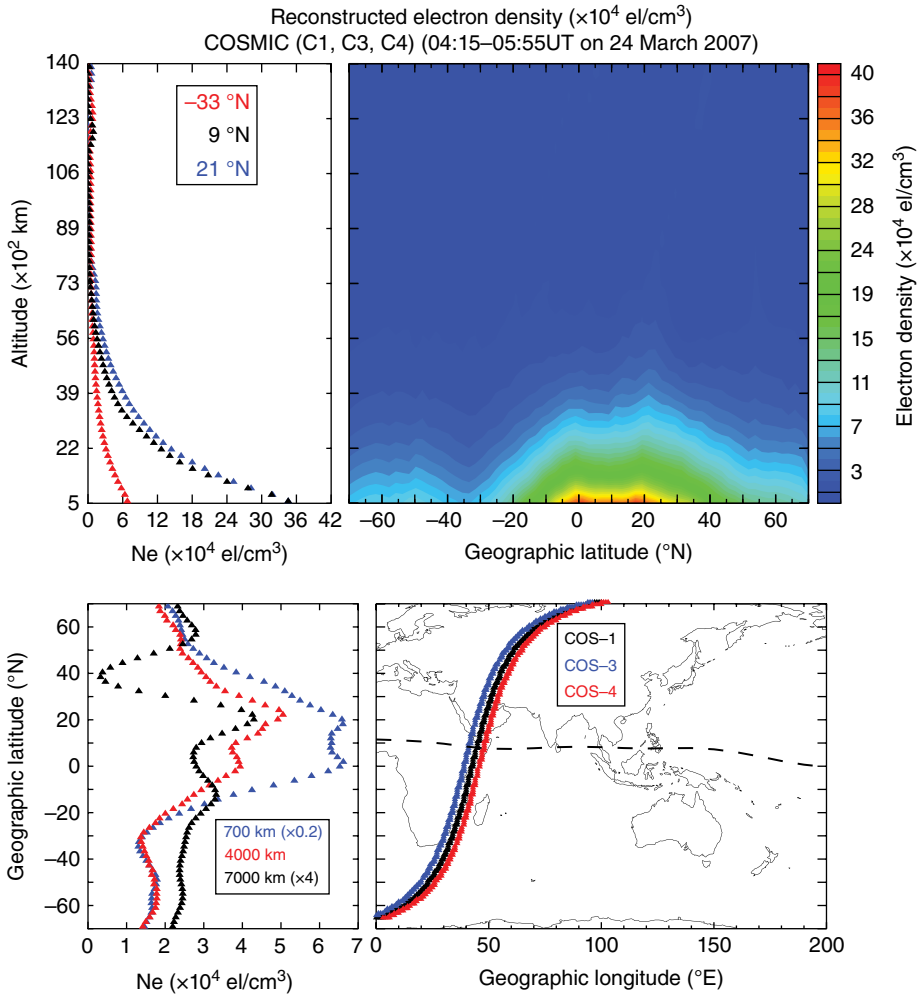


**Figure 9.6** Tomographically reconstructed topside ionosphere and plasmasphere density profiles (top right panel) using TEC data from three tailgating COSMIC satellites along their ground track trajectories (bottom right panel). The vertical (top left panel) and horizontal (bottom left panel) density profiles, obtained at three different latitudes and altitudes, extracted from the reconstructed density profiles.

## ACKNOWLEDGMENTS

This work has been supported by NASA LWS (NNX10AQ53G and NNX11AP02G) and AFOSR (FA9550-12-1-0437) grants. The authors are indebted to the UCAR/COSMIC program team for the LEO satellite data resources they made available to the public.

## REFERENCES

Anderson, D., A. Anghel, J. Chau, and O. Veliz (2004), Daytime vertical E×B drift velocities inferred from ground-based magnetometer observations at low latitudes, *Space Weather*, *2*, S11001; doi:10.1029/2004SW000095.

Carpenter, D. L., R. R. Anderson, W. Calvert, and M. B. Moldwin (2000), CRRES observations of density cavities inside the plasmasphere, *J. Geophys. Res.*, *105*(A10), 23323–23338; doi:10.1029/2000JA000013.

Chen, J. L., M. Rodell, C. R. Wilson, and J. S. Famiglietti (2005), Low degree spherical harmonic influences on Gravity Recovery and Climate Experiment (GRACE) water storage estimates, *Geophys. Res. Lett.*, *32, L14405; doi:*10.1029/2005GL022964.

Coster, A. J., J. C. Foster, and P. J. Erickson (2003), Monitoring the ionosphere with GPS, *GPS World*, *14*, 40.

Doherty, P., A. J. Coster, and W. Murtagh (2004), Space weather effects of October-November 2003, *GPS Solutions*, *8*(3); doi:10.1007/s10291-004-0109-3.

England, S. L., S. Maus, T. J. Immel, and S. B. Mende (2006), Longitudinal variation of the E-region electric fields caused by atmospheric tides, *Geophys. Res. Lett.*, *33*(21), L21105; doi:10.1029/2006GL027465.

Hajj, G. A., and L. J. Romans (1998), Ionospheric electron density profiles obtained with the Global Positioning

System: Results from the GPS/MET experiment, *Radio Sci.*, *33*(1), 175–190; doi:10.1029/97RS03183.

Hei, M. A., R. A. Heelis, and J. P. McClure (2005), Seasonal and longitudinal variation of large-scale topside equatorial plasma depletions, *J. Geophys. Res.*, *110*, A12315; doi:10.1029/2005JA011153.

Heise, S., N. Jakowski, A. Wehrenpfennig, Ch. Reigber, and H. Luhr (2002), Sounding of the topside ionosphere/plasmasphere based on GPS measurements from CHAMP: Initial results, *Geophys. Res. Lett.*, *29*(14), doi:10.1029/2002GL014738.

Jakowski, N., V. Wilken, and C. Mayer (2007), Space weather monitoring by GPS measurements on board CHAMP, *Space Weather*, *5*, S08006; doi:10.1029/2006SW000271.

Jakowski, N., V. Wilken, S. Schluter, S. M. Stankov, and S. Heise (2005), Ionospheric space weather effects monitored by simultaneous ground and space based GNSS signals, *J. Atmos. Sol. Terr. Phys.*, *67*, 1074–1084; doi:10.1016/j.jastp.2005.02.023.

Lindal, G. F., G. E. Wood, H. B. Hotz, D. N. Sweetnam, V. R. Eshleman, and G. L. Tyler (1983), The atmosphere of Titan: An analysis of the Voyager 1 radio occultation measurements, *Icarus*, *53*, 348–363; doi:10.1016/0019-1035(83)90155-0.

Na, H. R., B. Hall, and E. Sutton (1995), Ground station spacing effects in ionospheric tomography, *Ann. Geophys., 13*, 1288–1296.

Pryse, S. E. (2003), Radio tomography: a new experimental technique, *Surv. Geophys.*, *24*, 1–38; doi:10.1023/A:1022272607747.

Schreiner, W., C. Rocken, S. Sokolovskiy, S. Syndergaard, and D. Hunt (2007), Estimates of the precision of GPS radio occultations from the COSMIC/FORMOSAT-3 mission, *Geophys. Res. Lett.*, *34*, L04808; doi:10.1029/2006GL027557.

Raymund, T. D. (1995), Comparisons of several ionospheric tomography algorithms, *Ann. Geophys., 13*, 1254–1262.

Tsai, L. C., C. H. Liu, W. H. Tsai, and C. T. Liu (2002), Tomographic imaging of the ionosphere using the GPS/MET and NNSS data, *J. Atmos. SolarTerr. Phys., 64*, 2003–2011; doi:10.1016/S1364-6826(02)00218-3.

Yizengaw, E. (2012), Global longitudinal dependence observation of the neutral wind and ionospheric density distribution, *Int. J. Geophys.*, *2012*; doi:10.1155/2012/342581.

Yizengaw, E., E. A. Essex, and R. Birsa (2004), The Southern Hemisphere and equatorial region ionization response for September 22, 1999 severe magnetic storm, *Ann. Geophys.*, *22*(8), 2765–2773; doi:10.5194/angeo-22-2765-2004.

Yizengaw, E., E. Zesta, M. B. Moldwin, B. Damtie, A. Mebrahtu, C. E. Valladares, and R. F. Pfaff (2012), Longitudinal differences of ionospheric vertical density distribution and equatorial electrodynamics, *J. Geophys. Res.*, *117*, A07312; doi:10.1029/2011JA017454.

Yizengaw, E., M. B. Moldwin, E. Zesta, C. M. Biouele, B. Damtie, A. Mebrahtu, B. Rabiu, C. E. Valladares, and R. Stoneback (2014), The longitudinal variability of equatorial electrojet and vertical drift velocity in the African and American sectors, *Ann. Geophys.*, *32*, 231–238; doi:10.5194/angeo-32-231-2014.

Yizengaw, E., M. B. Moldwin, P. L. Dyson, and E. A. Essex (2007), Using tomography of GPS TEC to routinely determine ionospheric average electron density profiles, *J. Atmos. Solar Terr. Phys.*, *69*, 314–321; doi:10.1016/j.jastp.2006.07.023.

Yizengaw, E., M. B. Moldwin, P. L. Dyson, B. J. Fraser, and S. K. Morley (2006), First tomographic images of ionospheric outflows, *Geophys. Res. Lett.*, *33, L20102;* doi:10.1029/2006GL027698.

Yizengaw, E., M. Moldwin, P. L. Dyson, and T. J. Immel (2005), The Southern Hemisphere ionosphere and plasmasphere response to the interplanetary shock event of 29–31 October 2003, *J. Geophys. Res., 110*, A09S30; doi:10.1029/2004JA010920.

Yizengaw, E., P. Doherty, and T. Fuller-Rowell (2013), Is space weather different over Africa, and if so, why? AGU Chapman Conference Report, *Space Weather*, *11*; doi:10.1002/swe.20063.

# 10

# On the Longitudinal Dependence of the Equatorial Electrojet

**Vafi Doumbia and Oswald Didier Franck Grodji**


## ABSTRACT

In this study, the longitude dependence of the equatorial electrojet (EEJ) has been reviewed. The most remarkable feature is the "wave-four" structure of the EEJ longitude profile. In order to understand the background physical process of this structure, we have examined the influence of the geomagnetic-field intensity and that of migrating thermospheric tides. The results show a good correlation between the EEJ and the main geomagnetic-field intensity. However, the wave-four structure cannot be explained through this strong correlation. By means of simulation through the National Center for Atmospheric Research (NCAR)'s Thermosphere-Ionosphere Electrodynamics General Circulation Model (TIE-GCM), we have shown that the combination of the longitudinal inequalities of the main geomagnetic-field intensity and the tidal-wave longitudinal structures is necessary to produce the wave-four structure of the EEJ longitude profile. Finally, we have shown the seasonal variability of the EEJ longitude profiles, which may be controlled by the seasonal behaviors of the wind system in the thermosphere.


**Key Points:**
The longitudinal dependence of the equatorial electrojet
The underlying physical processes
The influence of the geomagnetic main field and the wave structure of thermospheric winds.

**Key Terms:** equatorial electrojet, geomagnetic field, thermospheric winds, longitudinal variation

## 10.1. INTRODUCTION

At the dip equator, the horizontal northward geomagnetic and eastward electric fields result in a strong upward vertical polarization electric field between the lower and upper boundary of the *E* region [*Martyn*, 1948]. This vertical polarization field combines also with the horizontal northward geomagnetic field to generate a relatively intense eastward current, known as the equatorial electrojet [EEJ; *Chapman*, 1951]. The "abnormally" enhanced daily regular variation of the geomagnetic field due to the EEJ was first observed at Huancayo in Peru in 1922. This phenomenon has been observed and generalized at all longitudes by *Egedal* [1947], which was lately confirmed by the POGO satellite observations [*Cain and Sweeney*, 1973]. Recent observations have resulted in the discovery of many special features of the equatorial and low-latitude ionosphere, among which is the equatorial ionospheric anomaly (EIA). The EEJ and most of these phenomena vary as

*Laboratoire de Physique de l'Atmosphère, Université Félix Houphouët-Boigny, Abadji Kouté, Abidjan, Côte d'Ivoire*

*Ionospheric Space Weather: Longitude and Hemispheric Dependences and Lower Atmosphere Forcing, Geophysical Monograph 220*, First Edition. Edited by Timothy Fuller-Rowell, Endawoke Yizengaw, Patricia H. Doherty, and Sunanda Basu.

a function of the longitude, in response to the longitudinal dependence of the underlying physical processes.

According to the dynamo theories [*Richmond*, 1979, 1989, 1995], ionospheric currents in general and the EEJ in particular are expected to decrease as the geomagnetic main-field intensity $B$ increases. Thus, variation of the geomagnetic main-field intensity $B$ in longitude is susceptible to cause the longitudinal variation of the EEJ. Based on this idea, *Rastogi* [1962] established an inverse correlation between the EEJ intensity and the main field, by plotting the amplitude ($H$ of the EEJ magnetic signature observed in different longitude sectors as a function of the ambient main-field horizontal component $H$ for December 1957, and March and June 1958. *Gupta* [1973] obtained a similar pattern using the lunar daily variation in the same stations. *Sugiura and Cain* [1966] and *Davis et al.* [1967] proposed models of the EEJ based on the east-west conductivity, which varies with longitude in response to the longitudinal inequality of $B$. *Sugiura and Poros* [1969] demonstrated the longitude dependence of ionospheric currents by setting the total current intensity above 280°E longitude at 100%, at 76% at 0°E, 65% at 40°E, 56% at 80°E, and 77% E at 180°E. *Onwumechili* [1997] made a detailed review of previous studies of the EEJ longitudinal variation.

The studies mentioned above have mainly focused on the geomagnetic main-field influence in the longitude dependence of midlatitude and low-latitude ionospheric currents. In fact, they have not considered the possible impacts of the longitudinal structures of the wind systems in the thermosphere that drive ionospheric currents in low-latitude and midlatitude regions. In the present days, the wave structure of the thermospheric wind fields have been addressed in many recent studies [*England et al.*, 2006; *Häusler et al.*, 2007; *Häusler and Lühr*, 2009]. Furthermore, the influence of the wave structure of the thermospheric wind fields on various low-latitude ionospheric parameters have been investigated [*Immel et al.*, 2006; *Kil et al.*, 2007; *Lühr et al.*, 2007; *Lühr et al.*, 2008].

Recent magnetic measurements performed on board Ørsted, SAC-C, and especially CHAMP satellites have resulted in accurate description of the EEJ longitude profile [*Jadhav et al.*, 2002; *Doumouya and Cohen*, 2004; *Lühr et al.*, 2004; *Alken and Maus*, 2007]. From the analyses of these profiles, the wave-four structure has been set forth as the dominant characteristic of the EEJ longitude profile. However, the underlying physical processes that control this wave-four structure are not completely understood.

In this work, we review (1) the studies on the EEJ longitudinal variation, (2) the influences of the geomagnetic main-field intensity and atmospheric tides on the EEJ current density and its longitude dependence, and (3) the seasonal effects in the longitude profile of the EEJ.

## 10.2. AN OVERVIEW OF THE STUDIES ON THE EQUATORIAL ELECTROJET LONGITUDINAL VARIATION

Using POGO satellite data, *Cain and Sweeney* [1973] established the longitudinal profiles of the EEJ magnetic signature and compared the result with the theoretical result of *Davis et al.* [1967] based on uniform electric field. For satellite observations, two significant peaks were observed at 100°E and 290°E, and a secondary maximum at 195°E. In contrast, the model profile displayed a minimum at 100°E in response to the high intensity of the main field in this longitude sector. *Onwumechili and Agu* [1980] analyzed the longitudinal structures of various EEJ parameters from POGO satellite data. They found three maxima at 100°E, 190°E, and 290°E.

Studies of the longitudinal variation of the EEJ are performed through its magnetic signature along the geomagnetic dip equator. In general, observations at the local noon of different longitude sectors are considered to represent the longitudinal variation of the EEJ. This representation provides an average overall view of how the EEJ intensity varies as a function of longitude. In particular, it gives an idea of how the EEJ behaves in response to the longitude dependence of parameters that control its generating physical process.

The global coverage of satellite observations makes it possible to represent an averaged overall view of the EEJ magnetic effects. Figure 10.1 shows a color map of the EEJ magnetic signatures obtained from CHAMP satellite observations in 2001 and 2002 around local noon. For this figure, the CHAMP satellite vector measurements of the geomagnetic field were used. For the study of the equatorial electrojet, we have considered the X (geographic northward) and Z (vertical downward) components. Note that the satellite observations include various contributions (main field, crustal anomaly fields, ionospheric and magnetospheric current contributions). The main field represents about 99% of the measured magnetic field. To appreciate the other contributions, it is worthwhile to remove an estimate of the main field through a main-field model. For this manuscript, the Gauss coefficients of IGRF (International Geomagnetic Reference Field) 2005 with degree and order 13 have been used. Elements of the geomagnetic field were computed along the satellite orbits. The altitude, latitude, and longitude of each data point are read in the data file. For a given element, for example X and Z, a residual field is determined by subtracting the estimated value from the measured element at the corresponding data point.

To process the residuals, we considered only daytime satellite passes across the dip equator, corresponding to magnetic quiet-time data with the average Kp index along the satellite path weaker than $2^+$. At the dip equator, the

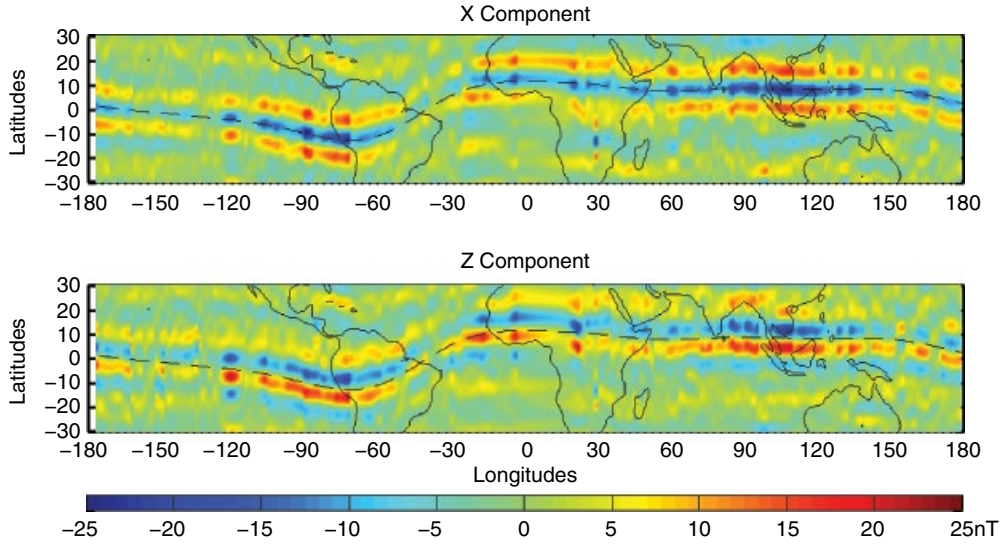


**Figure 10.1** Color map of the EEJ magnetic signatures obtained from CHAMP satellite observations in 2001 and 2002 around local noon, top panel represents the northward (X) and bottom panel, the vertical (Z) components.

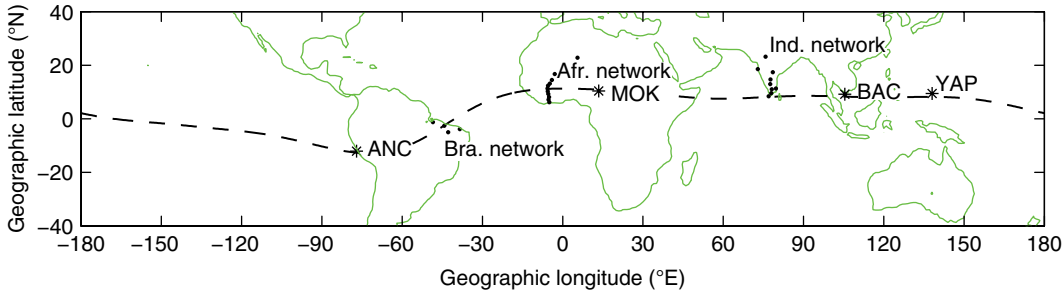


**Figure 10.2** Network of magnetic stations that operated during the International Equatorial Electrojet Year (IEEY) campaign in 1993.

daytime latitude profiles of the residuals exhibit the EEJ signature that superimposes a long wavelength background signal. To isolate the EEJ signature, the background signal was fitted by a polynomial function of degree 12. The choice of this degree was made by trial and error, from 6 to 30. The resulting signals become very stable for $12 \geq$ degrees $\geq 18$. The polynomial function was subtracted from the total residuals of each satellite pass to isolate the EEJ contribution in X and Z. Figure 10.1 results from all the quiet-time passes between 11 and 13 LT in 2001 and 2002.

The shape of X (top) is the typical signature of the EEJ observed on board polar orbiting satellites. For a single latitude profile, this signature exhibits a V-shaped depression at the dip equator that is flanked by what was called "shoulders" in the POGO satellite observations [*Cain and Sweeney*, 1973; *Onwumechili and Agu*, 1980].

The two components clearly show the different phases of the EEJ longitudinal variation. Furthermore, the latitude extents of both components exhibit the reversals on the flanks of the EEJ.

During the international equatorial electrojet year (IEEY), simultaneous records of the EEJ magnetic effects were performed in different longitude sectors [*Amory-Mazaudier et al.*, 1993; Arora *et al.*, 1993]. Figure 10.2 shows the network of magnetic stations that operated during this campaign. Using the IEEY data, *Doumouya et al.* [2003] and *Doumouya and Cohen* [2004] established ground-based longitude profiles of the EEJ magnetic effect.

In Figure 10.3, the noontime IEEY ground-based EEJ magnetic effect and the CHAMP satellite observations in 2001 and 2002 have been plotted together with the inverse of the geomagnetic-field intensity $\left(\frac{1}{B}\right)$ along the dip equator. The black dashed line represents $\left(\frac{1}{B}\right)$; the solid red line represents the horizontal component ($\Delta H$) of the EEJ magnetic effect without including the

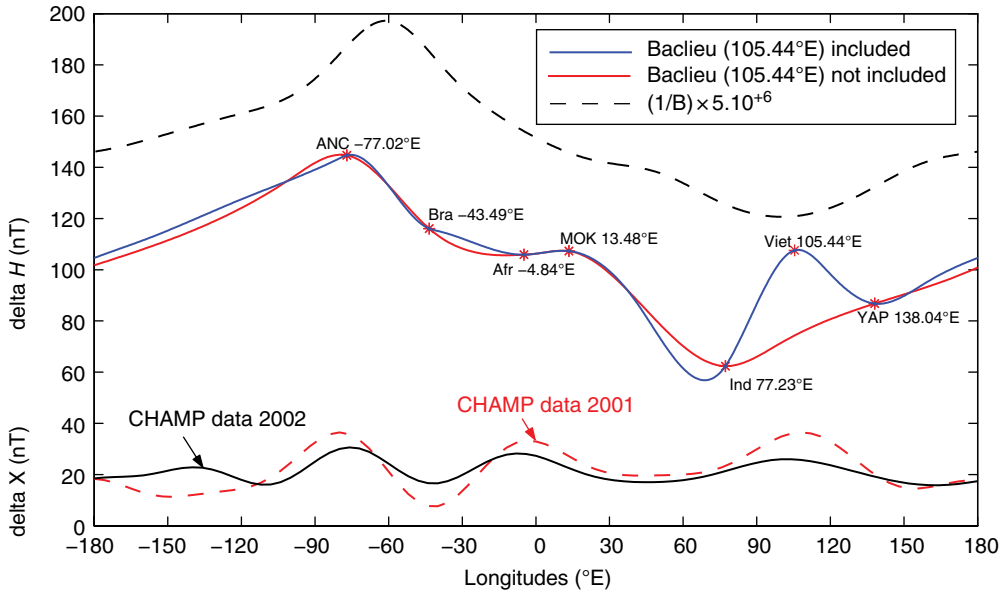


**Figure 10.3** The IEEY ground-based EEJ magnetic effect and the CHAMP satellite observations in 2001 and 2002 compared with the inverse of the geomagnetic field intensity $\left(\frac{1}{B}\right)$ along the dip equator. The black dashed line represents $\left(\frac{1}{B}\right)$; the solid red line represents the horizontal component ($\Delta H$) of the EEJ magnetic effect without including the data from Baclieu (105.44°E); the blue line represents $\Delta H$ with data from Baclieu. The dashed red line and the solid black line at the bottom represent CHAMP satellite noontime observations respectively in 2001 and 2002.

data from Baclieu (105.44°E); the blue line represents $\Delta H$ with data from Baclieu. Note that for the latitude chains of stations shown in Figure 10.2, the EEJ strength is estimated through the maximum amplitude ($\Delta H$) of the latitude profiles of the EEJ magnetic effect at the EEJ center [*Doumouya et al.,* 1998]. In other words, the values of delta *H* in Figure 10.3 (at noon) have been determined from the network shown in Figure 10.2 during the IEEY. This network includes three latitude chains and four individual stations located at different longitude sectors. For latitude chains, delta *H* is obtained by subtracting the average edge values from the maximum of *H* at the center of the latitude profiles [*Doumouya et al.*, 1998], for individual stations to approximately account for the *Sq* effects, $\frac{1}{3}$ was removed from the total amplitude of the daily range at each station.

The dashed red line and the solid black line at the bottom of Figure 10.3 represent the averaged absolute values of delta X obtained from CHAMP satellite observations in 2001 (last 7 months) and 2002 (annual), respectively. The values of delta X were determined from the EEJ signatures that were isolated from the residuals as described above. Delta X was obtained by subtracting the mean edge values from the peak values at the dip equator.

The inverse $\left(\frac{1}{B}\right)$ of the main-field intensity and $\Delta H$ without data at the longitude (105.44°E) of Baclieu (red line) exhibit similar patterns except a slight increase in $\Delta H$ between 0° and 30°E. In contrast, when the data from Baclieu are included, an important maximum appears at the 105.44°E longitude. This maximum matches with the CHAMP satellite observations. The ground-based longitude profile exhibits three maxima around −90°E, 15°E, and 100°E, which roughly coincide with the three maxima exhibited on CHAMP satellite observations. However, none of the fourth maximum shown in the CHAMP satellite observation around −170°E in 2001 and −140°E in 2002 are shown in the ground-based profile. This difference is likely due to the lack of data points in the area of Pacific Ocean.

At present, the so-called wave-four structure of the EEJ longitudinal variation is well established thanks to Ørsted, CHAMP, and SAC-C satellite observations [*Jadhav et al.*, 2002; *Lühr et al.*, 2004; *Doumouya and Cohen*, 2004; *Alken and Maus*, 2007]. It appears that this structure is somewhat consistent with the wave-four pattern of thermospheric tides [*England et al.*, 2006]. *Lühr et al.* [2008] have studied the influence of nonmigrating tides in the EEJ longitudinal wave-four structure through CHAMP satellite observations. However, the underlying physical processes that control this wave-four structure and the roles of different parameters like the geomagnetic field, ionospheric electric field and plasma density, and the thermospheric wind system are not completely understood.

## 10.3. WHAT CONTROLS THE LONGITUDINAL VARIATION OF THE EQUATORIAL ELECTROJET?

The wave-four structure clearly shows that the geomagnetic main-field intensity $B$ is not the unique parameter that controls the EEJ longitudinal variation. On a theoretical basis, the EEJ current density can be expressed as a function of the zonal electric field $\vec{E}_y$ and the Cowling conductivity ($\sigma_c$) as:

$$\vec{J}_{eej} = \sigma_C \vec{E}_y \tag{10.1}$$

where $\sigma_C = \left(\sigma_P + \frac{\sigma_H^2}{\sigma_P}\right)$, $\sigma_P$, and $\sigma_H$ are respectively the Pederson and Hall conductivities.

The expressions $\sigma_P$ and $\sigma_H$ are obtained from the equations of motions of ions and electrons and are given respectively by:

$$\sigma_P = \frac{N_e e}{B}\left(\frac{v_e \Omega_e}{v_e^2 + \Omega_e^2} + \frac{v_i \Omega_i}{v_i^2 + \Omega_i^2}\right) \tag{10.2}$$

$$\sigma_H = \frac{N_e e}{B}\left(\frac{\Omega_e^2}{v_e^2 + \Omega_e^2} - \frac{\sigma_i^2}{v_i^2 + \Omega_i^2}\right) \tag{10.3}$$

where $v_e$ and $v_i$ are effective collision frequencies of electrons and ions, respectively; $\Omega_e$ and $\Omega_i$ are the gyrofrequencies of electrons and ions, respectively, with $\Omega_e = \frac{eB}{m_e}$ and $\Omega_i = \frac{eB}{m_i}$; $m_e$, $m_i$, and $e$ are the masses of electrons and ions, respectively; and the elementary charge, $N_e$, is the electron number density in the plasma.

Writing $\eta_e = \frac{v_e}{\Omega_e}$ and $\eta_i = \frac{v_i}{\Omega_i}$, the ratios of collision frequencies and gyrofrequencies of respective charge species, the expressions of $\sigma_P$ and $\sigma_H$ can be simplified as:

$$\sigma_P = \frac{1}{B^2} \cdot N_e \cdot \left(\frac{m_e v_e}{1+\eta_e^2} + \frac{m_i v_i}{1+\eta_i^2}\right) \tag{10.4}$$

$$\sigma_H = \frac{1}{B} \cdot N_e e \cdot \left(\frac{1}{1+\eta_e^2} - \frac{1}{1+\eta_i^2}\right) \tag{10.5}$$

According to Equations (10.4) and (10.5), the spatiotemporal behaviors of the EEJ current (Equation [10.1]) depend on that of the ambient geomagnetic-field intensity ($B$), of the electron content of the medium ($N_e e$) and of the "momentum balance" of electrons and ions $\left(\frac{m_e v_e}{1+\eta_e^2} + \frac{m_i v_i}{1+\eta_i^2}\right)$. Note that this momentum balance is susceptible to include the effects of local winds. Specifically, the EEJ longitudinal variation should reflect the longitudinal behaviors of these three factors and that of the zonal electric field $\vec{E}_y$ as well.

In order to understand the role of different parameters, the impacts of the geomagnetic main-field intensity $B$ and that of the wave structure of thermospheric tides are examined. We first analyze the dependence of the EEJ strength on the geomagnetic main-field intensity, and after, we use the same approach as *Doumbia et al.* [2007] to examine the influence of the longitudinal patterns of main field and tides. This approach consists of simulating the influences of the longitudinal pattern of both geomagnetic main field and thermospheric tidal winds by using the National Center for Atmospheric Research (NCAR)'s Thermosphere-Ionosphere Electrodynamics General Circulation Model [TIE-GCM; *Richmond et al.*, 1992].

### 10.3.1. Dependence of the EEJ Strength on the Geomagnetic-Field Intensity

In Figure 10.4, geomagnetic quiet-time magnetic data recorded in different longitude sectors during the international equatorial electrojet year (IEEY) are used to examine the dependence of the EEJ strength on the geomagnetic main-field intensity $B$. The average amplitude $\Delta H$ (asterisks) of the EEJ magnetic signature is represented as a function of $B$ along the dip equator, from 09:00 LT to 15:00 LT. The error bars represent the standard deviations from the averaged $\Delta H$. Note that the noontime $\Delta H$ in Figure 10.3 is the same as in Figure 10.4 but for 09:00 LT to 15:00 LT. All the panels show that $\Delta H$ tends to decrease as $B$ increases, with the highest slopes around noon (11LT–13LT).

According to this result, a quasi-linear inverse correlation is observed between $\Delta H$ and $B$ around noon with correlation coefficients that attain 70% at 11:00 LT. This result proves the strong relationship between the EEJ and the geomagnetic-field intensity. Thus, on the basis of this feature, one should expect a longitude profile of the EEJ with a maximum in South America, where the geomagnetic main field has its weakest intensity (about 26,000 nT), and minimum in Asia where $B$ is strongest (about 45,000 nT). In contrast, the observations in section 10.2 show the wave-four structure of the EEJ longitude profile.

To understand the possible roles of the geomagnetic-field longitude distribution in this configuration, the EEJ longitudinal variation was simulated with the NCAR TIE-GCM using separately a realistic model and a non-realistic model of the geomagnetic field. Note that the NCAR TIE-GCM uses by default the International Geomagnetic Reference Field (IGRF) model to calculate electric fields and currents in the ionosphere.

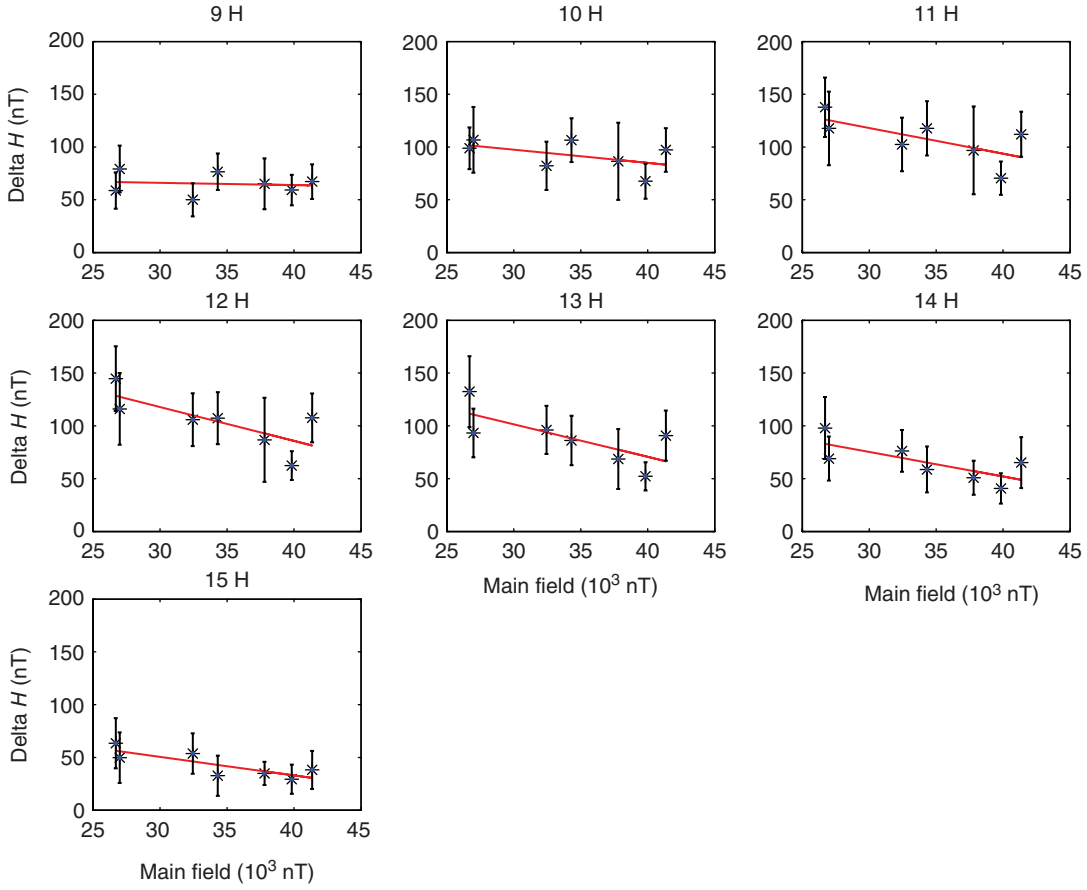


**Figure 10.4** Dependence of the EEJ strength on the geomagnetic main field intensity $B$. The mean values of the amplitude $\Delta H$ of the EEJ magnetic signature are represented as function of $B$ along the dip equator, from 09:00 LT to 15:00 LT. The error bars represent the standard deviations.

Details of the TIE-GCM utilization for this simulation are given by *Doumbia et al.* [2007]. The IGRF model was used as the realistic model, and a tilted ideal dipole model as the nonrealistic model. The simulation results based on the two main-field models are compared and analyzed. Note that both models were used with the migrating diurnal and semidiurnal components of tides.

Figure 10.5 shows the simulated noontime $\Delta H$ longitude profiles of the EEJ magnetic effects in equinox, based on the IGRF model (red line) and the tilted dipole model (dashed blue line). A moderate solar activity for $F_{10.7} = 160\,sfu$ $(1\,sfu = 10^{-22}\,\mathrm{Wm^{-2}Hz^{-1}})$ and geomagnetic quiet-time conditions were considered. Further details on TIE-GCM simulation of the EEJ are given in *Doumbia et al.* [2007]. We notice that the tilted dipole model does not produce any longitude dependence of the EEJ effect ($\Delta H$). $\Delta H$ appears to be constant at all longitudes. On the contrary, the simulation with the IGRF main-field model produced two significant maxima around −90° and 130°E.

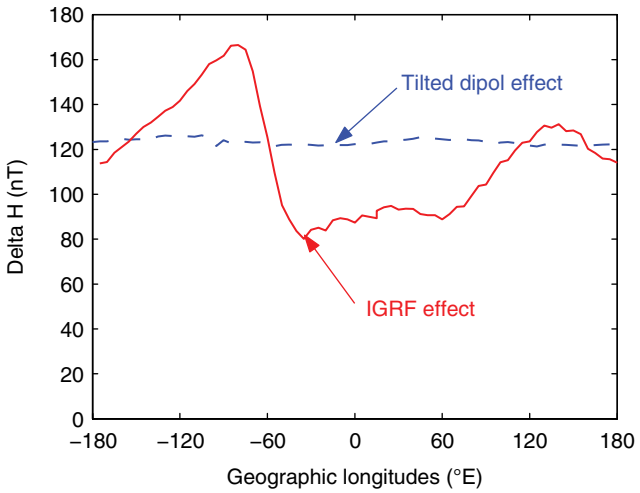


**Figure 10.5** The TIE-GCM simulation of the longitude profiles of the EEJ magnetic effects based on the IGRF model (red line), and the tilted dipole model (dashed blue line) of the geomagnetic main field. This figure is a new version of the top panel of Figure 13 of *Doumbia et al.* [2007].

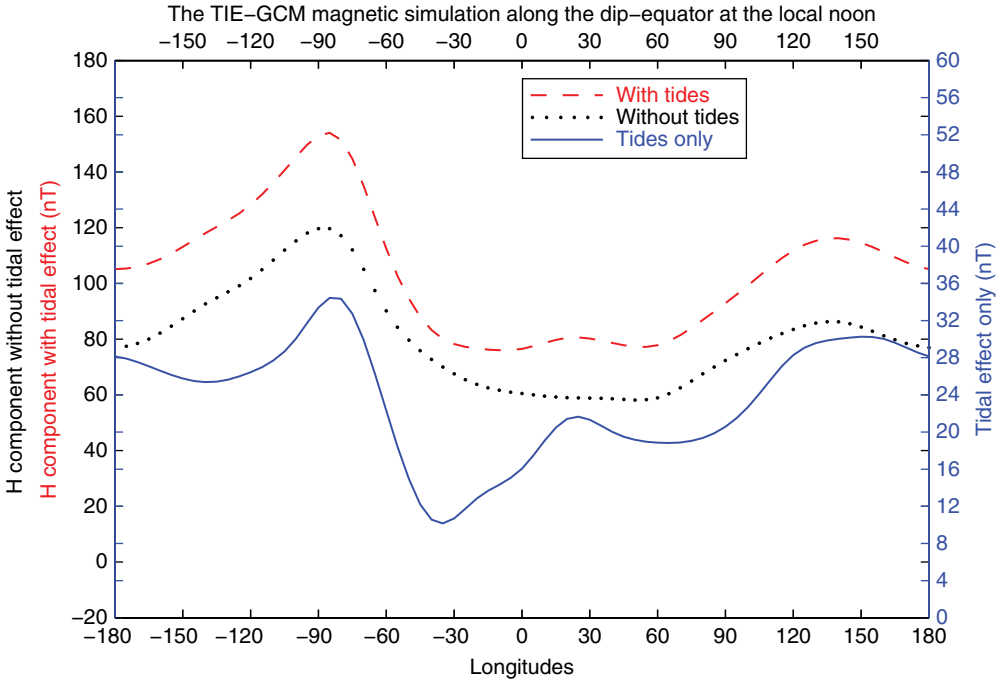


**Figure 10.6** The TIE-GCM simulation of the longitudinal profiles of the EEJ magnetic effects, with tidal forcing (red dashed line) and without tidal forcing (black dotted line). The effect of the migrating diurnal and semidiurnal tides is represented by the blue line. This figure is a new version of Figure 11 of *Doumbia et al.* [2007].

The difference between the results obtained from the two main-field models relies on the fact that, in contrast to the dipole model, the IGRF accounts for the longitudinal inequality of the geomagnetic-field intensity. This difference demonstrates that the longitude distribution of the geomagnetic-field intensity plays a key role in the longitudinal dependence of the EEJ. In other words, the modeling shows that the IGRF field has a large effect, which is due to the magnetic-field intensity and also to the differing magnetic-field direction in the IGRF as compared with the dipole. However, the simulated EEJ longitude profile still does not match the wave-four structure of observations. Thus, in the next subsection, we examine the influence of atmospheric tides in the EEJ longitudinal dependence through the TIE-GCM simulations.

### 10.3.2. Impact of the Thermospheric Tides on the EEJ Longitudinal Variation

In this subsection, we analyze the influence of migrating tide on the basis of the TIE-GCM simulation. The approach for this analysis is based on the flexibility of TIE-GCM to be run with or without lower boundary tidal forcing. Thus, the impact of tidal forcing can be appreciated when the model is alternatively run with and without lower boundary tidal forcing. Note that TIE-GCM accounts for the thermospheric tides through the Global Scale Wave Model (GSWM) proposed by *Hagan and Forbes* [2002, 2003]. *Doumbia et al.* [2007] used the GSWM lower boundary migrating tides to force the TIE-GCM. In a recent work, *Yamazaki et al.* [2014] have replaced the GSWM by the Thermosphere-Ionosphere-Mesosphere Energetic and Dynamics (TIMED) satellite measurements to improve the TIE-GCM simulation of the EEJ magnetic effect. However, in this work, the results obtained by *Doumbia et al.* [2007] with the GSWM tidal forcing are used.

By running TIE-GCM (1) with tidal forcing and (2) without tidal forcing, the impact of the migrating diurnal and semidiurnal tidal forcing is isolated by subtraction. Figure 10.6 presents the simulated EEJ longitudinal profiles, with tidal forcing (red dashed line) and without tidal forcing (black dotted line). The effect of the migrating diurnal and semidiurnal tides is represented by the blue line. As results, it appeared that the tidal effect produces four maxima at about -170°E, -80°E, +30°E, and +140°E longitudes, which better matches with observations. Note that nonmigrating tides have not been accounted for in this simulation [*Doumbia et al.*, 2007]. The important role of nonmigrating tides in modulating the EEJ longitudinal wave-four structure was demonstrated by *Lühr et al.* [2008] on the basis of CHAMP satellite observations.

As shown in the previous subsection (10.3.1), when the migrating diurnal and semidiurnal tides are used with the dipole main-field model, they have no effective impact in the longitudinal variation of the EEJ. On the contrary, when they are used with realistic main-field models, the migrating diurnal and semidiurnal tides effectively contribute to modulate the EEJ longitudinal variation.

According to these analyses, it can be concluded that the longitudinal pattern of the EEJ is the combined effect of the tides and the main geomagnetic-field longitude structures. In such a configuration, one may expect an important seasonal variability in the EEJ longitudinal profiles, in response to the seasonal variability of atmospheric tides.

## 10.4. SEASONAL EFFECTS IN THE EQUATORIAL ELECTROJET LONGITUDINAL VARIATION

In this section, we examine the seasonal effects in the longitudinal variation of the EEJ based on CHAMP satellite magnetic measurements in 2001 and 2002. Figure 10.7 shows the averaged noontime (11–13 LT) longitude profiles of the EEJ magnetic signatures in Lloyd seasons obtained from the CHAMP scalar magnetic data in 2001 and 2002. The top panel shows the longitude profile in equinox, the middle panels shows the longitude profile in June solstice, and the bottom pane shows the December solstice. The dots correspond to the amplitude $\Delta F$ for each single satellite pass across the dip equator, the smoothed solid lines represent the mean longitude profiles of $\Delta F$. This line was drawn on the averaged values of $\Delta F$ in each 10° longitude sector, by a spline interpolation.

In equinox and June solstice, the EEJ longitude profiles exhibit the wave-four structure, while the profile of December solstice shows only three maxima, with a broad maximum on Atlantic Ocean/South American longitude sectors. The profiles of the three seasons are compared in Figure 10.8. The top panels compare, respectively, (left) the December (blue line) and June solstices (green line), and (right) December solstice (blue line) and equinox (red line). In both cases, we notice important phase opposition of December solstice with the June solstice and equinox longitude profiles. In the bottom left panel, the longitude profiles of June solstice (green line) and equinox (red line) are in phase accordance above Africa, Asia, and the eastern Pacific Ocean. Some slight shifts in the phase are observed in the area including the Atlantic Ocean, South America, and Pacific Ocean. The bottom right panel summarizes the variations of phase in the longitude profiles of the EEJ in the courses of seasons, June solstices (green line), December solstice (blue line), and equinox (red line).

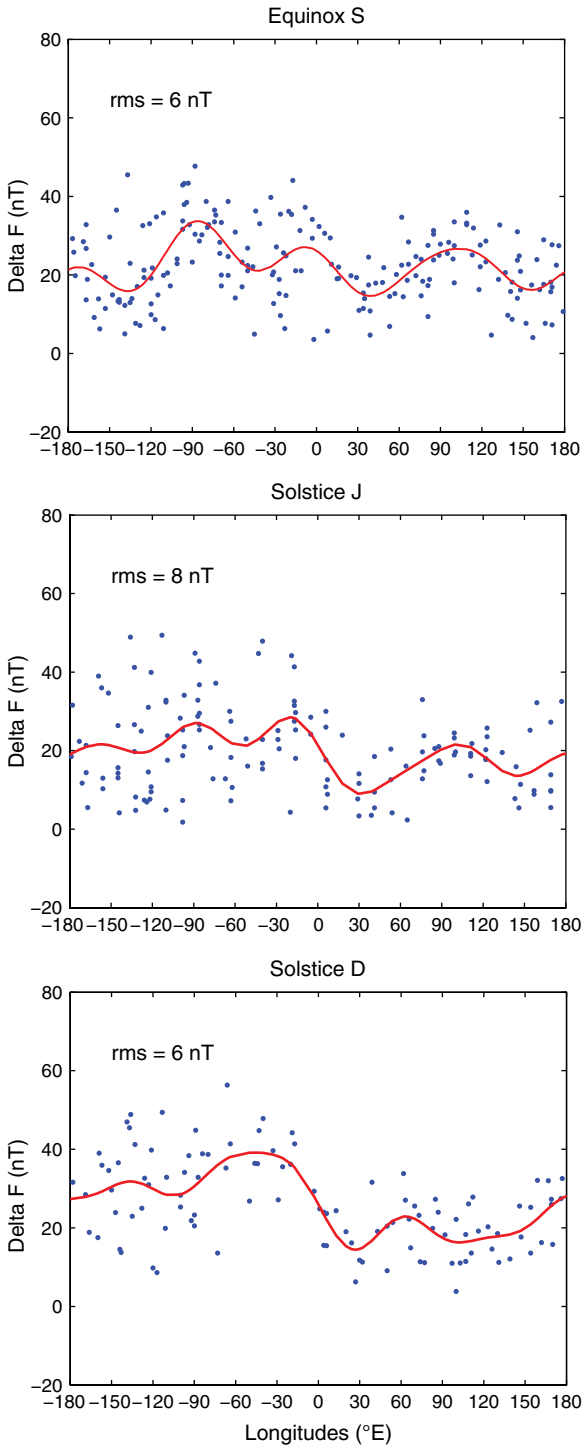


**Figure 10.7** Longitude profiles of the EEJ magnetic signatures in Lloyd seasons obtained from the CHAMP scalar magnetic data in 2001 and 2002. The top panel shows the longitude profile in the equinox, the middle shows the longitude profile for the June solstice, and the bottom shows the December solstice. The dots correspond to the amplitude $\Delta F$ for each single satellite pass across the dip equator, between 1100 LT and 1300 LT, the smoothed solid lines represent the mean longitude profiles of $\Delta F$. This line was drawn on the averaged values of $\Delta F$ in each 10° longitude sector, by a spline interpolation.

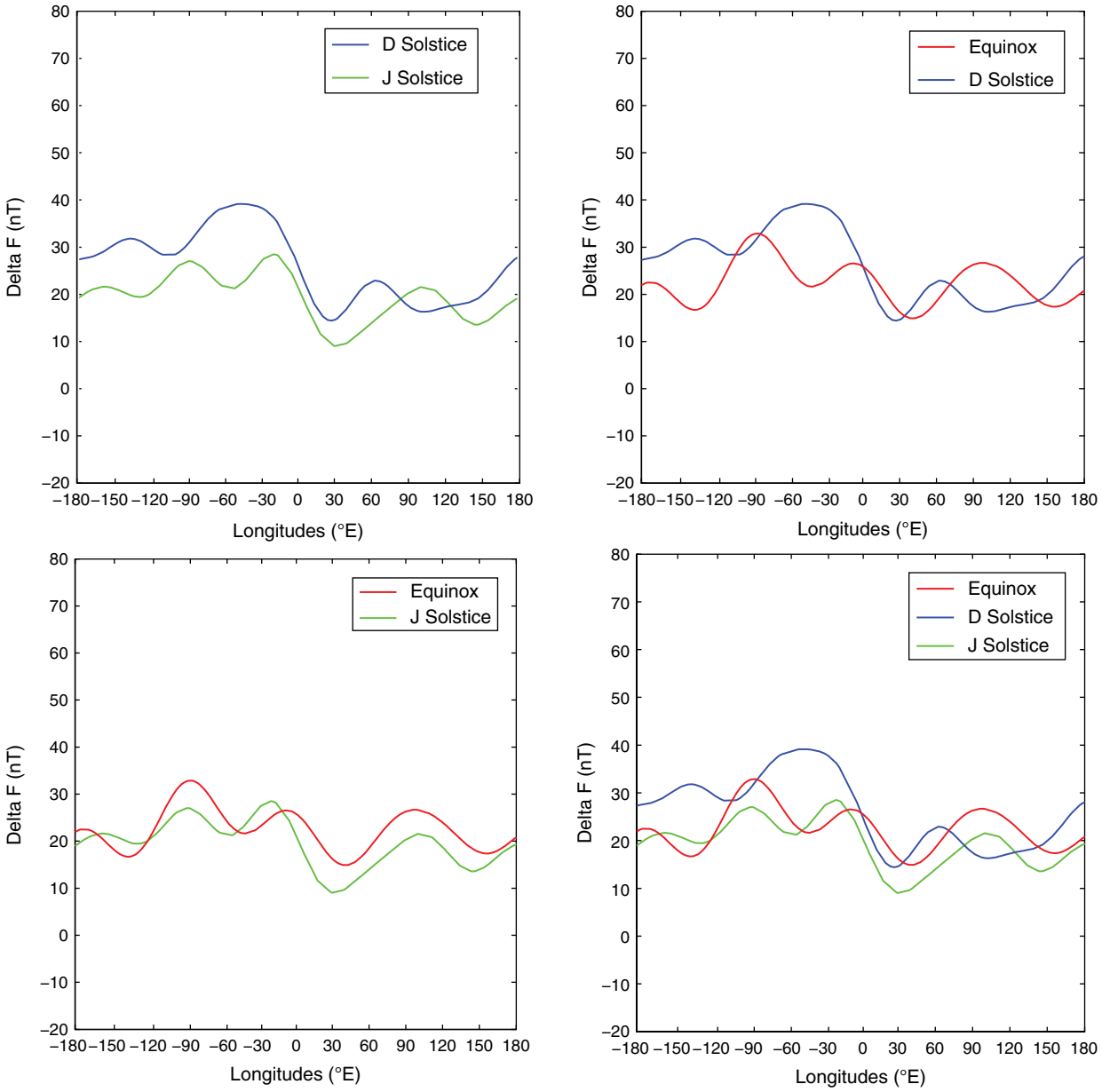


**Figure 10.8** Comparison of the EEJ longitude profiles during the Lloyd seasons. The top panels compare, respectively, (top left) the December solstice (blue line) and June solstices (green line), (top right) December solstice (blue line) and equinox (red line). In the bottom left panel, the longitude profiles of June solstice (green line) and equinox (red line) are compared. The bottom right panel compares the EEJ longitude profiles during the three seasons, June solstices (green line), December solstice (blue line), and equinox (red line).

## 10.5. CONCLUSION

The longitudinal variation of the equatorial electrojet (EEJ) has been addressed through many studies since the early 1960s. Most of the first investigations were focused on the link with the geomagnetic main-field intensity [*Rastogi*, 1962; *Gupta*, 1973; *Sugiura and Cain*, 1966; *Davis et al.*, 1967; *Sugiura and Poros*, 1969]. Although the relationship between the EEJ strength and the main-field intensity is strong, the former studies on the EEJ longitude dependence based on theoretical analyses [*Sugiura and Cain*, 1966; *Davis et al.*; 1967; *Sugiura and Poros*, 1969] and ground-based [*Rastogi*, 1962; *Gupta*, 1973] and POGO satellite magnetic observations [*Cain and Sweeney*, 1973; *Onwumechili and Agu*, 1980] have not been precisely conclusive. The net progress on the topic was brought by

recent observations that were performed during the international equatorial electrojet year (IEEY) and the Ørsted, SAC-C, and especially CHAMP satellites missions. The most remarkable feature that has been highlighted is the wave-four structure of the EEJ longitude profile. In this study, the longitude dependence of the EEJ has been reviewed.

In order to understand the background physical process of this structure, we have examined the influence of the geomagnetic-field intensity and that of thermospheric tides. We have first analyzed the correlation between the EEJ strength and the geomagnetic-field intensity $B$, through its magnetic effect $\Delta H$ observed in the IEEY stations. The results show a good correlation between the EEJ and the inverse $\left(\frac{1}{B}\right)$ of the geomagnetic mean-field intensity. This inverse correlation demonstrates that the EEJ intensity decreases when the $B$ increases. However, the wave-four structure cannot be explained through this strong correlation.

Observations have brought new insight on the wave structure of the thermospheric winds, which exhibit similar patterns as the EEJ longitude profile and numerous other equatorial phenomena [*England et al.*, 2006; *Häusler et al.*, 2007; *Häusler and Lühr*, 2009]. In addition, the influence of the wave structure of the thermospheric wind fields on various low-latitude ionospheric parameters has been demonstrated through many recent studies [*Immel et al.*, 2006; *Hartman and Heelis*, 2007, *Kil et al.*, 2007; *Lühr et al.*, 2007; *Lühr et al.*, 2008].

By means of simulation through the National Center for Atmospheric Research (NCAR)'s Thermosphere-Ionosphere Electrodynamics General Circulation Model (TIE-GCM), we have shown through the migrating diurnal and semidiurnal tidal components that the effectiveness of the thermospheric wind longitude structure depends on the underlying main-field structure. Thus, the combination of the geomagnetic main-field intensity longitudinal inequalities and the tidal-wave longitudinal structures is necessary to produce the wave-four structure of the EEJ longitude profile.

Finally, we have shown the seasonal variability of the longitude profiles. The seasonal effects in the EEJ longitude profile are shown by the change in the wave number in the December solstice and the slight shift in longitude of some maxima. Especially, the maximum at the West African longitude sector (around 0°E longitude) seems to move westward. It finally joins that of South America (around −80° longitude) to form the broad maximum over the Atlantic Ocean and South America in the December solstice. Since the geomagnetic main field does not change with seasons, these seasonal effects may be associated with and controlled by the seasonal behaviors of the wind systems in thermosphere.

## ACKNOWLEDGMENTS

This study was partially carried out at the National Center for Atmospheric Research (NCAR), Boulder Colorado (USA), and at Institut de Physic du Globe de Paris (IPGP). The TIE-GCM simulation was performed in close collaboration with Dr. Art Richmond and Dr. Astrid Maute, at NCAR. The CHAMP satellite data processing and analyses were performed in collaboration with Dr. Yves Cohen at IPGP. I am grateful to CHAMP satellite and the IEEY data providers.

## REFERENCES

Alken, P., and S. Maus (2007), Spatio-temporal characterization of the equatorial electrojet from CHAMP, Ørsted, and SAC-C satellite magnetic measurements, *J. Geophys. Res.*, *112*, A09305; doi:10.1029/2007JA012524.

Amory-Mazaudier, C., P. Vila, J. Achache, A. Achy Seka, Y. Albouy, E. Blanc, K. Boka, J. Bouvet, Y. Cohen, M. Dukhan, V. Doumouya, O. Fambitakoye, R. Gendrin, C. Goutelard, M. Hamoudi, R. Hanbaba, E. Hougninou, C. Huc, K. Kakou, A. Kobea-Toka, P. Lassudrie-Duchesne, E. Mbipom, M. Menvielle, S. O. Ogunade, C. A. Onwumechili, J. A. Oyinloye, D. Rees, A. Richmond, E. Sambou, E. Schmuker, J. L. Tirefort, and J. Vassal (1993), International equatorial electrojet year: the African sector, *Revista Brasileira de Geosica 11*, 303–317 (Especial).

Arora, B. R., M. V. Mahashabde, and R. Kalra (1993), Indian IEEY geomagnetic observational program and some preliminary results, *Brazilian J. Geophys.*, *11*(3), 365–384.

Cain, J. C., and R. E. Sweeney (1973), The POGO data, *J. Atmos. Terr. Phys. 35*, 1231–1247; doi:10.1016/0021-9169(73)90021-4.

Chapman, S. (1951), The equatorial electrojet as detected from the abnormal electric current distribution above Huancayo, Peru, and elsewhere, *Arch. Meteorol. Geophys. Bioklimatol. A*, *4*, 368–390; doi:10.1007/BF02246814.

Davis, T. N., K. Burrows, and J. P. Stolarik (1967), A latitude survey of the equatorial electrojet with rocket-borne magnetometers, *J. Geophys. Res.*, *72*, 1845–1861; doi:10.1029/JZ072i007p01845.

Doumbia, V., A. Maute, and A. D. Richmond (2007), Simulation of equatorial electrojet magnetic effects with the thermosphere-ionosphere-electrodynamics general circulation model, *J. Geophys. Res.*, *112*, A09309; doi:10.1029/2007JA012308.

Doumouya, V., and Y. Cohen (2004), Improving and testing the empirical equatorial electrojet model with CHAMP satellite data, *Ann. Geophysic.*, *22*, 3323–3333; doi:10.5194/angeo-22-3323-2004.

Doumouya, V., Y. Vassal, Y. Cohen, O. Fambitakoye, and M. Menvielle (1998), The equatorial électrojet at African Longitudes: First result from magnetic measurement, *Ann. Geophys.*, *16*, 658–666; doi:10.1007/s00585-998-0658-9.

Doumouya, V., Y. Cohen, B. R. Arora, and K. Yumoto (2003), Local time and longitude dependence of the equatorial electrojet magnetic effects, *J. Atmos. Solar Terr. Phys.*, *65*, 1265–1282; doi:10.1016/j.jastp.2003.08.014.

Egedal, J. (1947), The magnetic diurnal variation of the horizontal force near the magnetic equator, *Terr. Magn. Atmos. Electr.*, *52*, 449–451; doi:10.1029/TE052i004p00449.

England, S. L., S. Maus, T. J. Immel, and S. B. Mende (2006), Longitude variation of the E-region electric fields caused by atmospheric tides, *Geophys. Res. Lett.*, *33*, L21105; doi:10.1029/2006GL027465.

Gupta, J. C. (1973), On the solar and lunar equatorial electrojet, *Ann. Geophys.*, *29*, 49–60.

Hagan, M. E., and J. M. Forbes (2002), Migrating and nonmigrating diurnal tides in the middle and upper atmosphere excited by tropospheric latent heat release, *J. Geophys. Res.*, *107*(D24), 4754; doi:10.1029/2001JD001236.

Hagan, M. E., and J. M. Forbes (2003), Migrating and nonmigrating semidiurnal tides in the upper atmosphere excited by tropospheric latent heat release, *J. Geophys. Res.*, *108*(A2), 1062; doi:10.1029/2002JA009466.

Hartman, W. A., and R. A. Heelis (2007), Longitudinal variations in the equatorial vertical drift in the topside ionosphere, *J. Geophys. Res.*, *112*, A03305; doi:10.1029/2006JA011773.

Häusler, K., and H. Lühr (2009), Nonmigrating tidal signals in the upper thermospheric zonal wind at equatorial latitudes as observed by CHAMP, *Ann. Geophys.*, *27*, 2643–2652; doi:10.5194/angeo-27-2643-2009.

Häusler, K., H. Lühr, S. Rentz, and W. Kohler (2007), A statistical analysis of longitudinal dependences of upper thermospheric zonal winds at dip equator latitudes derived from CHAMP, *J. Atmos. Solar Terr. Phys.*, *69*, 1419–1430; doi:10.1016/j.jastp.2007.04.004.

Immel, T. J., E. Sagawa, S. L. England, S. B. Henderson, M. E. Hagan, S. B. Mende, H. U. Frey, C. M. Swenson, and L. J. Paxton (2006), Control of equatorial ionospheric morphology by atmospheric tides, *Geophys. Res. Lett.*, *33*, L15108; doi:10.1029/2006GL026161.

Jadhav, G., M. Rajaram, and R. Rajaram (2002), A detailed study of the equatorial electrojet phenomenon using Ørsted satellite observations, *J. Geophys. Res.*, *107*(A8), 1175; doi:10.1029/2001JA000183.

Kil, H., S.-J. Oh, M. C. Kelley, L. J. Paxton, S. L. England, E. R. Talaat, K.-W. Min, and S.-Y. Su (2007), Longitudinal structure of the vertical drift and ion density seen from ROCSAT-1, *Geophys. Res. Lett.*, *34*, L14110; doi:10.1029/2007GL030018.

Lühr, H., K. Häusler, and C. Stolle (2007), Longitudinal variation of F region electron density and thermospheric zonal wind caused by atmospheric tides, *Geophys. Res. Lett.*, *34*, L16102; doi:10.1029/2007GL030639.

Lühr, H., M. Rother, K. Häusler, P. Alken, and S. Maus (2008), The influence of nonmigrating tides on the longitudinal variation of the equatorial electrojet, *J. Geophys. Res.*, *113*, A08313; doi:10.1029/2008JA013064.

Lühr, H., S. Maus, and M. Rother (2004), Noon-time equatorial electrojet: Its spatial features as determined by the CHAMP satellite, *J. Geophys. Res.*, *109*, A01306; doi:10.1029/2002JA009656.

Martyn, D. (1948), Electric conductivity of the ionospheric D-region, *Nature*, *162*, 142–143; doi:10.1038/162142a0.

Onwumechili, C. A. (1997), *The Equatorial Electrojet*, Gordon and Breach Science Publishers, The Netherlands, 627 pp.

Onwumechili, C. A., and C. E. Agu (1980), Longitudinal variation of the equatorial electrojet parameters derived from POGO satellite observations, *Planet. Space Sci.*, *29*, 627–634; doi:10.1016/0032-0633(81)90111-2.

Rastogi, R. G. (1962), Longitudinal variation in the equatorial electrojet, *J. Atmos. Terr. Phys.*, *24*, 1031–1040; doi:10.1016/0021-9169(62)90158-7.

Richmond, A. D. (1979), Ionospheric wind dynamo theory: A review, *J. Geomagn. Geoelectr.*, *31*, 287–310; doi:10.5636/jgg.31.287.

Richmond, A. D. (1989), Modeling the ionosphere wind dynamo: A review, *Pure Appl. Geophys.*, *131*, 413–435; doi:10.1007/BF00876837.

Richmond, A. D. (1995), Ionospheric electrodynamics using magnetic apex coordinates, *J. Geomagn. Geoelectr.*, *47*, 191–212.

Richmond, A. D., E. C. Ridley, and R. G. Roble (1992), A thermosphere/ionosphere general circulation model with coupled electrodynamics, *Geophys. Res. Lett.*, *19*, 601–604; doi:10.1029/92GL00401.

Sugiura, M., and D. J. Poros (1969), An improved model equatorial electrojet with meridional current system, *J. Geophys. Res.*, *74*, 4025–4034; doi:10.1029/JA074i016p04025.

Sugiura, M., and J. C. Cain (1966), A model equatorial electrojet, *J. Geophys. Res.*, *71*; doi:10.1029/JZ071i007p01869.

Yamazaki, Y., A. D. Richmond, A. Maute, Q. Wu, D. A. Ortland, A. Yoshikawa, I. A. Adimula, B. Rabiu, M. Kunitake, and T. Tsugawa (2014), Ground magnetic effects of the equatorial electrojet simulated by the TIE-GCM driven by TIMED satellite data, *J. Geophys. Res. Space Physics*, *119*; doi:10.1002/2013JA019487.

# 11

# Tomographic Reconstruction of Ionospheric Electron Density Using Altitude-Dependent Regularization Strength over the Eastern Africa Longitude Sector

**Gizaw Mengistu Tsidu,[1] Gebreab Kidanu,[2] and Gebregiorgis Abraha[3]**

## ABSTRACT

A linear and iterative inversions with second order Tikhonov Regularization for 3-D tomography is employed to reconstruct ionospheric electron density (IED) during the solar minimum 2008 period. However, application of 3-D regularization is not straightforward due to spatial and temporal inhomogeneities in signal and noise along the ray paths that contribute to the observed ionospheric total electron contents (TECs). A regularization scheme is considered that takes into account the inhomogeneity, such that regions with weak signal contributions to TEC measurements are heavily penalized through a weighting factor incorporated with the discrete operator. The a priori IED from the NeQuick model and slant TECs at a chain of GPS stations over Eastern Africa are used in the analysis. The application of the new regularization scheme with iterative inversion on simulated TECs with actual observation geometry has recovered the true IED with lowest reconstruction error of 0.38% and 0.39% from measurement contaminated by 4% and 15% random noise, respectively. In contrast, the reconstruction with commonly used regularization factor has error of 0.79% and 0.85% from the same measurement. Moreover, various diagnostic tools applied to reconstructions from both synthetic and actual observations as well as comparison of vertical TEC (VTEC) from reconstruction and JPL VTEC have shown that the new altitude-dependent regularization performs well. This is reflected in high correlation of 0.87 to 0.91 between VTEC from reconstruction and JPL VTEC under iterative formulation. The tomographic reconstruction results under even bad a priori information show that the algorithm can recover up to 70% of the true IED over dense observations.

**Key Points:**

A new algorithm for 3-D tomographic reconstruction of ionospheric electron density has been developed.

Ionospheric electron density from NeQuick model and slant TECs at a chain of GPS stations over Eastern Africa are used in the tomographic reconstruction and validation of the algorithm.

A new altitude-dependent regularization factor in the framework of Tikhonov regularization based on a Laplace operator is incorporated in the algorithm.

The new regularization scheme outperforms the traditional altitude-independent regularization factor.

[1]*Department of Physics, Addis Ababa University, Addis Ababa, Ethiopia; Karlsruhe Institute of Technology (KIT), Institute for Meteorology and Climate Research (IMK-ASF), Karlsruhe, Germany; and Department of Earth and Environmental Sciences, Botswana International University of Science and Technology (BIUST), Palapye, Botswana*

[2]*Department of Physics, Addis Ababa University, Addis Ababa, Ethiopia; and University of Texas at Dallas, Dallas/Fort Worth, Texas, USA*

[3]*Department of Physics, Addis Ababa University, Addis Ababa, Ethiopia; Department of Physics, Mekele University, Mekele, Ethiopia*

*Ionospheric Space Weather: Longitude and Hemispheric Dependences and Lower Atmosphere Forcing, Geophysical Monograph 220*, First Edition. Edited by Timothy Fuller-Rowell, Endawoke Yizengaw, Patricia H. Doherty, and Sunanda Basu.

**Key Terms:** ionospheric electron density, 3-D tomography, altitude-dependent regularization strength, Eastern Africa, GPS, Global Navigation Satellite Systems (GNSS)

## 11.1. INTRODUCTION

The ionosphere is a weakly ionized atmospheric layer and has several impacts such as propagation delays or advances, and ray-path bending on transionospheric radio-wave propagation. The variability in the electron density of the ionosphere in association with sunspot cycle, season, time of the day, longitude, latitude, and solar disturbances is particularly crucial in this regard. In fact, the peak electron density limits the maximum usable frequency for signal propagation on Earth. The peak electron density also sets the minimum required frequency for transionospheric radio-wave propagation between Earth and space. The regular and irregular variations of the bottom side plasma density can also interrupt a high-frequency signal transmission. Moreover, understanding the variability of the ionosphere is required to mitigate higher-order ionospheric propagation effects such as ray-path bending errors in precise positioning [*Hoque and Jakowski*, 2011] and residual ionospheric errors in bending angles on the accuracy of the atmospheric profiles [*Liu et al.*, 2013] from the Global Navigation Satellite Systems (GNSS).

Therefore, the ability to measure, model, and predict the temporal and spatial variations of the ionospheric electron density is of great use for both ionospheric research and other GNSS applications. A number of efforts have been made over the years to develop global ionospheric models and improve their performance in simulating observations [*Rush et al.*, 1984; *Fox and McNamara*, 1988; *Fuller-Rowell et al.*, 2000; *Bilitza and Reinisch*, 2008; *Nava et al.*, 2008]. However, improvement in the performance of these models has depended on observations with high-density and temporal resolution for better understanding of the physical processes, and then to parameterize certain processes and to empirically constrain certain aspects of the models. A dense network of observations of this kind was not available in the past and it might well be practically difficult to achieve in the future. Nevertheless, with small loss of accuracy, application of tomographic techniques to existing sparse observations from ground and space can alleviate this acute problem to a certain extent.

The tomographic technique pioneered by *Radon* [1917], which is successfully and extensively applied in the field of medical science, is a relatively recent mathematical tool in space and atmospheric research. The typical example of applications of tomography is maps of the electron density in the ionosphere. The total electron contents (TECs) along many intersecting ray paths between a satellite in low Earth orbit (LEO) and a chain of ground-based receivers are considered as the measurements from which ionospheric electron density (IED) is retrieved. In early days, the US Navy Navigational Satellite System (NNSS) and the Russian CICADA satellites were the only satellite systems used for ionospheric tomography [*Austen et al.*, 1986; *Austen et al.*, 1988]. The limited range of orientations from LEO satellite-to-ground receivers is a drawback of the early investigations since the vertical electron-concentration gradient is poorly defined by the TEC measurements [*Yeh and Raymund*, 1991]. Over the years, several investigations were conducted to alleviate the problem and, to this end, many algorithms have been developed [e.g., *Fremouw et al.*, 1992]. Most of these algorithms use orthonormal basis functions and vectors to constrain the solutions. For example, the vertical orthonormal vectors are established from ionospheric models, which themselves are not accurate enough. The improvement in the algorithms and their verifications by independent measurements (e.g., European Incoherent Scatter [EISCAT] radar, ionosondes over the years, recently satellites) extended the use of tomography to various applications [*Andreeva et al.*, 1990; *Pryse and Kersley*, 1992; *Bust et al.*, 1994; *Rogers et al.*, 2001] and to investigate several ionospheric phenomena [*Hajj et al.*, 1994; *Pryse et al.*, 1995; *Cook and Close*, 1995; *Mitchell et al.*, 1995; *Kersley et al.*, 1997; *Leitinger et al.*, 1997; *Walker et al.*, 1998; *Hernández-Pajares et al.*, 1998; *Stolle et al.*, 2003; *Yizengaw et al.*, 2005; *Wen et al.*, 2007].

These advances gained further momentum with data availability from Global Positioning System (GPS) satellites from two L-band radio signals transmitted at 1.575 and 1.228 GHz and received by ground-based receivers, which allow the detection of signals' relative phase shift and delay. The relative phase shift and delay can be related directly to TEC. Unlike LEO satellite signals, GPS signals do not suffer from limited orientations since the satellites are located at higher altitudes. Furthermore, the development of more and more global navigation satellite systems (GNSS) from Europe, China, Russia, and India as well as the increasing number of GPS and multi-GNSS ground-based receivers for diverse applications ranging from navigation to geophysics creates new opportunity to advance the use of tomography for imaging of IED and tropospheric water vapor. The deployment of GPS receivers on LEO satellites has also created the opportunity to scan the topside ionosphere [*Heise et al.*, 2002; *Stankov et al.*, 2003] and triggered the combined use of observations from many different instruments in tomographic reconstruction of IED globally [*Spencer and Mitchell*, 1986; *Bust et al.*, 2004].

Despite enormous observations from different instruments that can be jointly used in ionospheric tomography, ionospheric tomography is still an ill-posed inverse problem. This can arise from either overdetermined or underdetermined situations. In ionospheric tomographic inversion, both problems could coexist in which a certain part of the ionosphere is over sampled and others under sampled. This arises due to a limited field of view that covers only part of the ionosphere. In ionospheric imaging, there are no generally good measurements in directions perpendicular to altitude, leading to altitude resolution worse than the horizontal resolution. As a result, a priori information is usually added to have a well-posed problem [*Yeh and Raymund*, 1991]. The best a priori information should, in principle, be constructed from past climatology based on other observations, including a full covariance matrix of IED over the whole ionosphere. However, such observations do not exist in reality. Therefore, the a priori information often comes from empirical models, such as IRI and NeQuick climatological models. Although the climatological IEDs from these models have improved over the years, their performances are still a function of latitude and seasons.

Satellite-based observations, such as from the recently launched COSMIC satellites, provide additional data that improve global data coverage and reduce the necessity for a priori information. Satellite in-situ measurements of electron density and occultation measurements provide observations that have good altitude information, and help reduce the limited angle limitations. Even under the improved situation, the IEDs determined from tomographic inversion suffer from uncertainty in the limited a priori information and TECs.

In view of these limitations, a large number of theoretical and experimental computer tomography schemes have been developed [*Raymund et al.*, 1990; *Na and Lee*, 1990; *Andreeva et al.*, 1990; *Afraimovitch et al.*, 1992; *Andreeva et al.*, 1992; *Fremouw et al.*, 1992; *Pryse and Kersley*, 1992; *Kunitsyn and Tereshchenko*, 1992; *Na and Lee*, 1994; *Zhou et al.*, 1999; *Andreeva et al.*, 2001; *Tsai et al.*, 2002; *Bhuyan et al.*, 2002, 2004]. As a result of these efforts, the algebraic reconstruction technique (ART), the multiplicative algebraic reconstruction technique (MART), maximum entropy method (MEM), and the decomposed algebraic reconstruction technique (DART) are commonly available but no one of them is better than the other [*Raymund*, 1995].

One of the early attempts to solve such ill-conditioned linear sets of equations in ionospheric tomographic algorithm is the residual correction method (RCM) [*Sutton and Na*, 1996]. An alternative to the iterative approach is based on the truncation of singular values causing larger perturbations in the solution [*Kunitsyn et al.*, 1995]. However, the truncation parameter is arbitrarily chosen. *Zhou et al.* [1999] determined an optimal truncation criterion by incorporating a priori information in the form of a priori and a posteriori covariance for both the observations (TEC) and the model parameters (in this case the electron density).

Recently, a new tomography reconstruction algorithm to solve the set of linear equations optimally in least squares sense by suppressing noise on the basis of the generalized singular value decomposition (GSVD) was also proposed [*Bhuyan et al.*, 2002, 2004]. The amplification of noise can be suppressed using Tikhonov regularization technique where the electron densities at adjacent altitude levels are allowed only to covary during the solution, thereby reducing the degree of freedom. This has the effect of smoothing the solution, which is controlled by the regularization parameter. This parameter can be selected optimally as a trade-off between limiting high-frequency components in the solution and maintaining important information from the measurements. The L-curve and generalized cross validation (GCV) are commonly used for this purpose.

Another variant of ART used in recent times is constrained ART (CART) in which the constraint is imposed according to the two-dimensional multipoint finite difference approximation of the second-order Laplace operator. This algorithm was demonstrated, based on numerical experiments, to have some level of superiority over the conventional ART [*Wen et al.*, 2010].

In all of the above algorithms, a priori information in the form of either ad-hoc constraints, output from empirical models, or in-situ observations are incorporated to force the reconstruction toward a physically sound solution. However, complete characterization of the inversion error arising from the use of a priori information and measurement uncertainty itself is often ignored or the way the inversion algorithm is set up does not allow isolating these error components. For instance, regularization is often considered as a smoothing operator without the effect of biasing the solution toward the a priori. However, such an assumption is not completely true since a regularization parameter is often included along with a smoothing operator to suppress measurement noise. In fact, most of the time, the regularization parameter is selected in an optimal manner to balance the proportion of errors that arise from measurement noise and from smoothing itself. In reality, the regularization imposes a constraint on the vertical profile, only allowing a certain range of possible solutions, which causes deviation from true electron-density distribution [*Fremouw et al.*, 1992; *Bernhardt et al.*, 1998]. But these errors are often not reported.

Therefore, the objective of this paper is to adopt a methodology often used in the atmospheric remote sensing community in which the solution from the inverse problem is characterized by various diagnostics and error budget. Moreover, we propose a regularization approach based on a 3-D Laplace operator that penalizes ionospheric volumes differently depending on the strength of signals contributing to the measured TECs. The proposed method is applied to the Eastern Africa longitude center

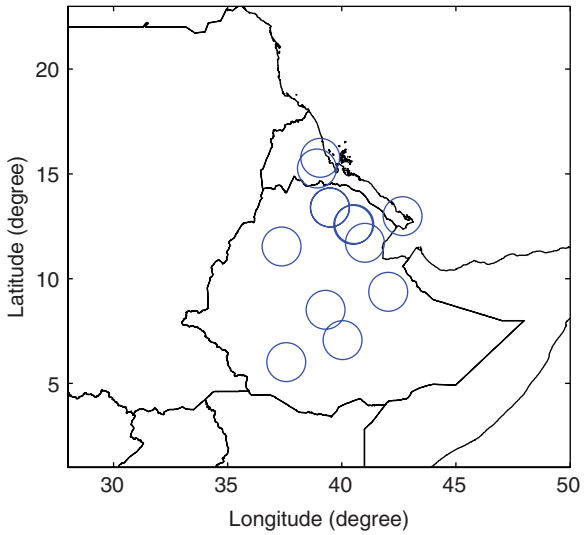


**Figure 11.1** The distribution ground-based GPS receivers located in the domain of ionospheric tomographic reconstruction. The total number of GPS receivers within the domain that are used for the electron density reconstruction is 12. However, not all of them are used in every reconstruction step since some observations are missing.

based on TEC measurements from ground-based GPS receivers located over Ethiopia and Eriteria during the solar minimum 2008 period. The GPS receivers are part of the University NAVstar Consortium (UNAVCO) network in the Great African Rift region (Fig. 11.1).

The paper is organized such that Section 11.2 presents the proposed methodology for ionospheric tomographic reconstruction and various diagnostic tools to understand the retrieved electron density. Section 11.3 gives results of validation of the algorithm based on simulated measurements and characterizes reconstructed IED from measurements in terms of the diagnostic tools described in Section 11.2. Finally, summary and conclusions are presented in Section 11.4.

## 11.2. IONOSPHERIC TOMOGRAPHIC TECHNIQUE

Ionospheric slant TEC (STEC) is defined as the line integral of IED along the ray path from satellite to ground-based receiver, and given as:

$$STEC = \int N_e dl \tag{11.1}$$

where $N_e$ is the IED at a point in the ray path $l$ from satellite to receiver. Equation (11.1) is then discritized such that finite path length along the line of site passes through some small voxels in a selected reference frame. Within each voxel, the electron density is assumed to be constant provided that the voxel volume is reasonably small. The STEC along the ray path can then be represented as a finite sum of the expression in the integrand. This means that we can rewrite Equation (11.1) as

$$STEC_i = \sum A_{i,k} x_k + \epsilon_i \tag{11.2}$$

For TEC measurements along many ray paths, this translates to

$$y_{m\times 1} = A_{m\times n} x_{n\times 1} + \epsilon_{m\times 1} \tag{11.3}$$

where $y$ is column matrix of m TEC measurements, $x$ the electron density in $n$ voxels, $A$ is the coefficient matrix with $A_{ij}$ distance traveled by $i^{\text{th}}$ GPS satellite's ray in the $j^{\text{th}}$ voxel, and $\epsilon_i$ is a column vector associated with the discretization errors and measurement noises. The measured STEC is obtained by calculating the integral of electron density along the line of sight from dual-frequency GPS pseudorange and phase observables. The differential delay between the two frequencies is proportional to electron density along the ray path. The phase and P-code delays between the two GPS frequencies allow for direct measurements of ionospheric TEC:

$$STEC_i = \left( \phi_2 - \frac{f_2}{f1}\phi_1 + f_2\left(t_{IFB} - t_{TGD}\right) + N \right) x \frac{c f_1^2 f_2}{B\left(f_1^2 - f_2^2\right)} \tag{11.4}$$

where $B = 40.3\,\text{m}^3/\text{s}^2$ and $f_1$ and $f_2$ are GPS signal frequencies. $\phi_1$ and $\phi_2$ are phases of the two GPS frequencies, $c$ is speed of light, $N$ is the integer cycle ambiguities, $t_{TGD}$ is the group delay available from the navigation message, and $t_{IFB}$ is the inter-frequency bias that can simultaneously be obtained with STEC from the GPS observations. The software used to determine STEC from the GPS observables is obtained from Purdue University and employed in several other publications [e.g., *Dautermann et al.*, 2009; *Jianyong et al.*, 2015].

The major challenge in 3-D ionospheric tomography is determination of the coefficient matrix as it stands for the distance traveled by each ray from a GPS satellite to a receiver with in each voxel crossed. In this work, the GPS local coordinate system has been used in a selected 3-D reference frame to calculate the distance traveled by the signal with in each voxel accurately. Voxels that are not crossed by a signal are assigned a zero value leading to a sparse coefficient matrix. As a result of the sparsity of matrix $A$, Equation (11.3) can not be inverted to determine the electron density $x$.

As described in Section 11.1, different techniques were developed to overcome the problem. Most of them employ a priori informations to compliment the measurements. Here, we follow a procedure in which the solution is sought by minimizing the cost function given by

$$\chi^2 = \|Ax - y\|_2^2 + \alpha^2 \|L(x - x_0)\|_2^2 \qquad (11.5)$$

in the least squares sense, where the first term on the right-hand side is square of the measurement and discretization errors obtained by solving for $m \times 1$ in Equation (11.3) and the square of error due to constraining the solution to a priori electron density $x_o$. The solution $x_{\alpha,L}$ given by

$$x_{\alpha,L} = \left(A^T A + \alpha^2 L^T L\right)^{-1} \left(A^T y + \alpha^2 L^T L x_o\right) \qquad (11.6a)$$

as a weighted mean of measurements and a priori information assuming linearity. While the linear assumption allows the solution to be readily decomposed into contribution from measurements and a priori electron density, improved solution that minimizes the difference between forward model and measurement is often sought using iterative algorithm. The iterative solution is given by

$$x_f = x_i + \left(A^T A + \alpha^2 L^T L\right)^{-1} \left(A^T (y - A x_i) - \alpha^2 L^T L (x_i - x_o)\right) \qquad (11.6b)$$

Furthermore, the solution is a function of second-order difference operator $L$ and regularization parameter $\alpha$. The difference operator in our case is based on a 3-D Laplace operator. The difference operator has already been applied in a 2-D study [*Wen et al.*, 2010] and found to yield highly improved results compared with ART. The choice of regularization strength is made in a way that damps noise without biasing the solution toward a priori. The regularization parameter is selected in an objective manner using the corner of $L$-curve or generalized cross-validation when Equation (11.6a) is used, and in ad-hoc manner or objective criteria such as Levenberg–Marquardt algorithm when Equation (11.6b) is used. A single value obtained from such procedures penalizes all levels of the electron-density profiles equally irrespective of the strength of contribution to the measured TECs along the GPS-satellite radio-wave paths. This has the effect of suppressing the strong signals such as those from peak electron-density regions equally with the weaker noisy signals below and above these regions.

We propose in this study a scheme in which the regularization operator is scaled down preferentially in favor of stronger signals. A normalized weighting factor is determined from the ratios of the electron density to the maximum electron density during the given epoch such that the region of high electron density is less constrained to the a priori than the extreme bottom and topside of the ionosphere. This kind of approach allows the solution to be determined mainly from the measurement near the peak electron-density regions, whereas the low electron-density regions are strongly constrained toward the a priori. It has the advantage of allowing strong variability, which often happens in the electron peak region and immediate neighborhoods. We demonstrate this aspect later in Section 11.3 in detail. This approach may occasionally fail when the peak of the a priori substantially differs from that of the real electron-density profile. This could be encountered during large perturbations in the ionosphere due to events such as geomagnetic storms. Critical frequencies from ionosonde observation could be used in the NeQuick model to determine appropriate a priori electron-density profiles during the perturbed ionosphere to alleviate the problem.

Full characterization of tomographic reconstruction requires assessment of the magnitude of errors in the solution as a result of the inversion. As indicated in the cost function, the least-squares solution minimizes errors due to TEC measurement noise and discretization on the one hand and errors due to smoothing on the other hand. This implies that the solution vector has corresponding errors given by approximate equations:

$$S_{smoothing} = \left(I - \left(A^T A + \alpha^2 L^T L\right)^{-1}\right)\left(\alpha^2 L^T L\right)\left(I - \left(A^T A + \alpha^2 L^T L\right)^{-1}\right) \qquad (11.7)$$

and

$$S_{measurement} = \left(A^T A + \alpha^2 L^T L\right)^{-1} \left(A^T A\right)\left(A^T A + \alpha^2 L^T L\right)^{-1} \qquad (11.8)$$

which represent the covariance of smoothing error as a result of Tikhonov constraint to the a priori and covariance of inversion noise (measurement noise), respectively. These equations are very much simplified approximations since the $A^T A$ is normally given as $A^T S_y^{-1} A$, where $S_y$ is measurement covariance matrix and $\left(\alpha^2 L^T L\right)^{-1}$ should represent a priori covariance matrix [*Rodgers*, 1990; *Mengistu Tsidu*, 2005]. Both of these are either unavailable or require tremendous efforts to build them from a sufficiently large pool of measurements. Therefore, we use them as the percentage fraction of the total reconstruction error, which is also an approximation for the same reason instead of absolute magnitude.

The error characterization of the solution, the retrieved electron density, is often not reported but it is a very important step toward assessing the quality of the data before using in any scientific studies. These are rather diagnostic quantities along with estimates on the relative contribution of measurements and a priori to the solution.

Moreover, when simulated observations are used to validate tomographic inversion algorithm, the so-called reconstruction error is defined as

$$\sigma = \left( \frac{\left\| x_{simulation} - x_{reconstruction} \right\|^n}{\left\| x_{simulation} \right\|^n} \right)^{\frac{1}{n}} \tag{11.9}$$

where $n$ represents the various norms (e.g., *Bhuyan et al.*, 2004).

In this study, the quadratic norm is used. The various statistics such as correlation, root mean square deviation (RMSD), and bias are also used to assess the algorithm. The tomographic inversion is based on a 3-D spatial domain having 12 voxels along longitude, latitude, and altitude axes, which constitute a total of 1728 voxels. The longitude and latitude grids are spaced at an interval of two degree each from 28°E to 50°E and 1°N to 23°N. However, the altitude grids are spaced nonuniformly to capture strong variability in IED at altitude close to peak electron density. Therefore, the 12 vertical levels consist of 100.0, 150.0, 230.0, 280.0, 330.0, 380.0, 450.0, 550.0, 600.0, 650.0, 700.0, and 800.0 km. This grid setup is chosen to minimize computational costs. However, a test inversion conducted for this study with more grids along the vertical did not reveal any significant improvement on the inversion results over current setup except leading to additional computational burden.

## 11.3. RESULTS AND DISCUSSIONS

### 11.3.1. Assessment of the Performance of Proposed Scheme

The performance of any new tomographic algorithm can be evaluated either through comparison with in-situ observations or using simulated data from known electron density. The former is not easily available. However, if the numerical experiment is designed in a manner that is similar to real observations, such assessment is as good as validation with in-situ observations. To ensure that the tomographic reconstruction is done under realistic observation geometry, the coefficient matrix from true observations is multiplied with assumed electron density. The synthetic TECs are superimposed with values generated from the product of 4% and 15% TECs and a random number in the range of 0 to 1 to represent measurement noise.

The evaluation of the algorithm is based on its skill in reproducing the original electron density used to generate the synthetic measurement and its dependence on the magnitude of measurement noise. Since the algorithm uses a priori information, it is also assessed for its skill in retrieving information from measurement than a priori in particular over the electron peak regions of the ionosphere.

Figure 11.2 shows the spatial distribution of percentage fraction of electron density retrieved from the measurement (panel a), and the a priori (panel b), as well as retrieved (panel c) and a priori (panel d) electron densities at 380 km altitude using Equation (11.6a) from a synthetic TEC measurement with a 4% random error. The a priori electron density is also used to generate the synthetic TECs used as observations in the numerical experiment. The fact that electron densities in Figure 11.2c and d are nearly identical may create the impression that the retrieved electron density is just the a priori. However, as clearly demonstrated in Figure 11.2a and b, the contribution of a priori to the solution is greater than the measurement (in this case synthetic measurement) in the peripheral areas where there are no sufficient rays crossing the voxels (see also Fig. 11.1). In the center of the domain, where most GPS-satellite ray paths pass through the voxels, the contribution of the measurement is far greater than the a priori (in proportion of up to 75%:25%).

Does this mean that a priori does not affect the solution where there are sufficient rays that probe the ionosphere? The answer is obvious even from the formulation of the algorithm as indicated in Equation (11.6a) that the solution is always a weighted mean of the a priori and measurement. What might differ from one case to the other is the proportion of the weighting factor.

To strengthen this argument and to show that the proposed scheme is robust even under bad a priori, another reconstruction using a priori information that is 50% off from the profile used to generate the synthetic measurements is conducted. Figure 11.3 shows the retrieved, a priori, and retrieved electron densities, as well as the percentage departure of the retrieved from the actual electron density. Despite extremely bad a priori used in Equation (11.6a), most of the signal over northern Ethiopia is recovered, as this part of the ionosphere has relatively dense observations (GPS-satellite ray paths). Moreover, the electron-density-dependent regularization parameter introduced in our scheme penalizes the peak electron-density region weakly allowing the solution to be determined more from measurement. As a result, the departure of the solution from truth is about 10% in the center of the study domain. Further, the deviation from the truth increases but it is still under 40% even close to the periphery. This is in fact remarkable given that the measurement contributes only up to a maximum of 30% in these regions (see Fig. 11.2a along the region of maximum electron density) and the a priori used is far from the true profile.

This is just for the sake of demonstration and in a real situation, it is very important to use an appropriate a priori electron-density profile in the reconstruction.

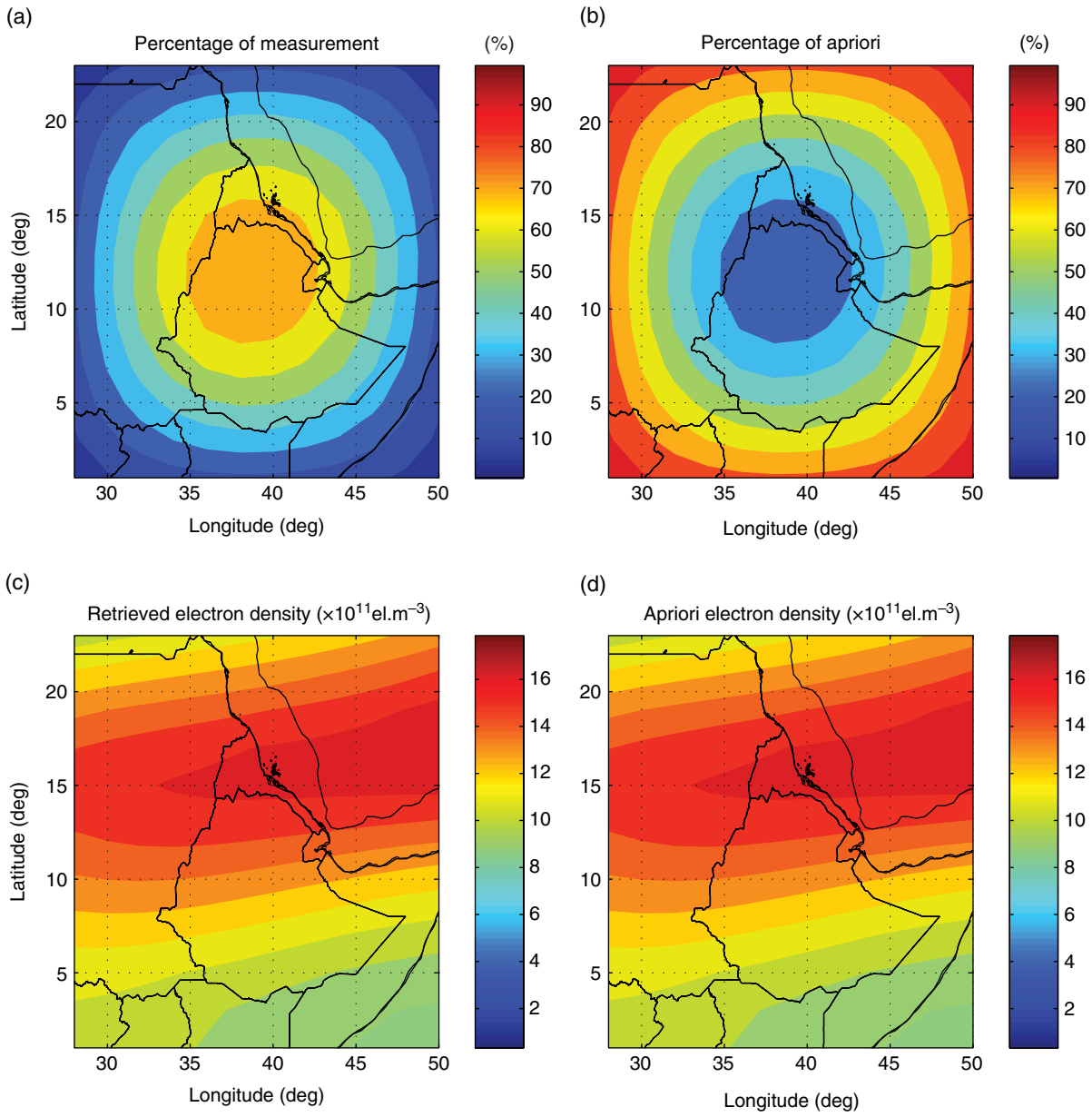


**Figure 11.2** The reconstructed electron density at 380 km is a weighted mean of measurement and a priori. Panels show (a) percentage fraction of measurement, (b) a priori, (c) retrieved electron density, and (d) a priori electron density. Note that the simulated TEC is based on this a priori electron density as described in Section 11.2.

Because even under perfect measurement conditions (which is not the case in the examples above), there is also a contribution from the a priori no matter how small it may be. This shows that the use of the iterative approach given in Equation (11.6b) might be helpful for further improvement of the solution. To demonstrate this, synthetic TECs with random measurement noise of 15% is used to retrieve electron density using Equation (11.6b). The retrieved, a priori, and retrieved electron densities, as well as the percentage departure of the retrieved from the actual electron density under this condition are given in Figure 11.4. The departure of retrieved electron density from the true electron density has significantly reduced as shown in Figure 11.4d within less than 10% over Ethiopia despite an increase in the measurement noise from 4% to 15%. The discrepancies near the boundary of the retrieval domain have remained as high as 40%. Even then, this is an improvement in view of increased measurement noise.

One of the most widely used systems for 3-D/4-D ionospheric tomography in recent times is Multi-Instrument

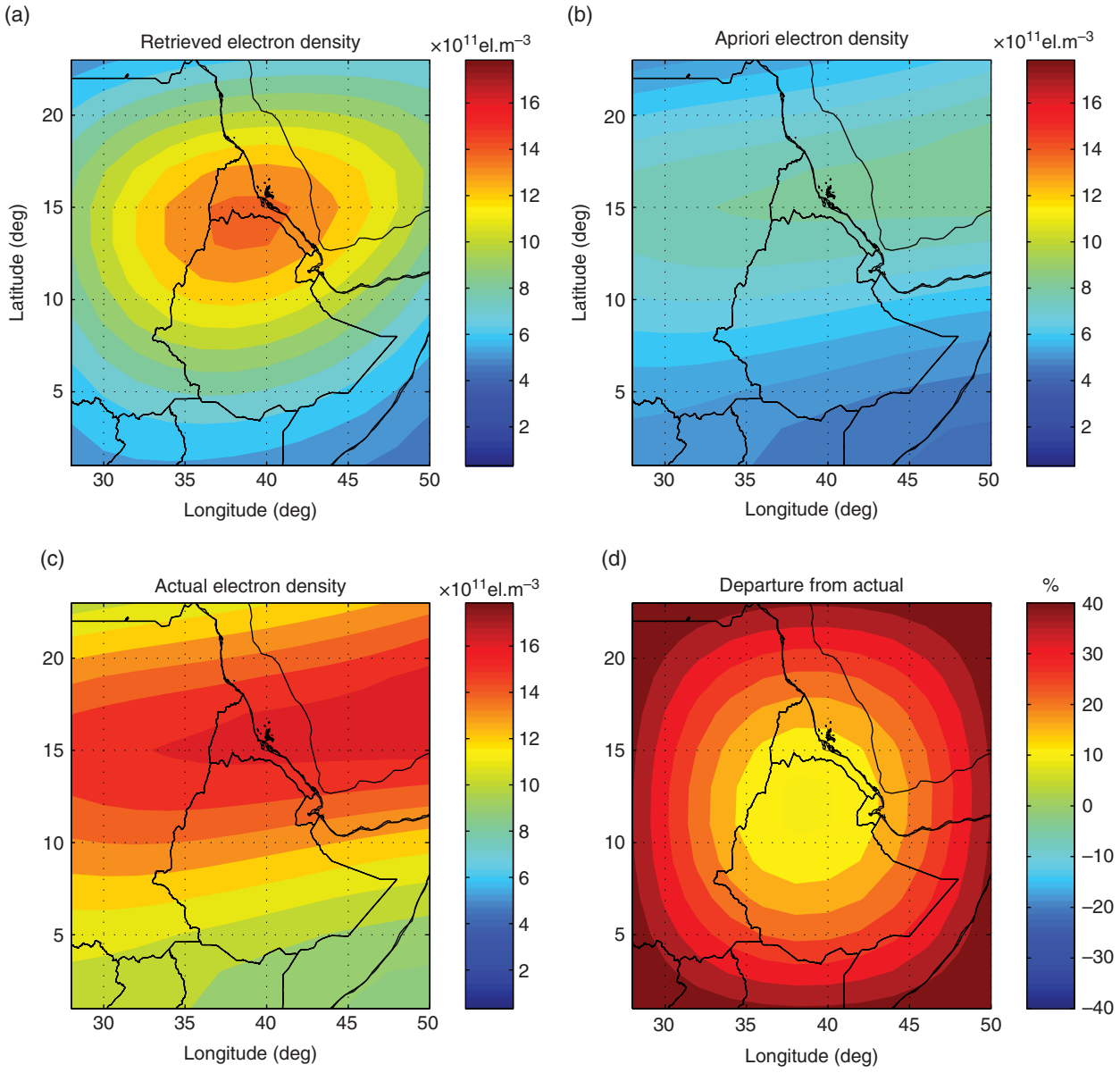


**Figure 11.3** Panels show (a) the tomographic reconstruction of electron density, (b) a priori electron density, (c) actual electron density, and (d) percentage difference between actual and reconstructed electron density at 380 km. The a priori electron density used for reconstruction is off from the actual by 50%.

Data Analysis System (MIDAS). MIDAS limits the impact of regularization by using a weighting factor of $trace(A^T A)/trace(L^T L)$ along with $\alpha$ where $\alpha$ serves as the Lagrangian multiplier. This is also implemented in our algorithm to see the performance of the proposed altitude-based regularization in this work with respect to the widely used approach as shown in Figure 11.5. The departure of the solution from the actual electron density under this approach is larger than the one from the proposed altitude-dependent regularization approach. However, it is apparent that this solution is much better than the linear solution in Figure 11.3 over the interior part of the horizontal spatial domain. This comparison between proposed regularization and the one used by MIDAS can not be fully considered as a complete comparison of the two algorithms but serves to show the relative advantage of the proposed regularization.

Table 11.1 shows the reconstruction error for all voxels for 4% and 15% noise for linear and iterative solutions based on the altitude-dependent regularization and commonly used regularization strength parameter averaged over all voxels. The lower reconstruction error of linear

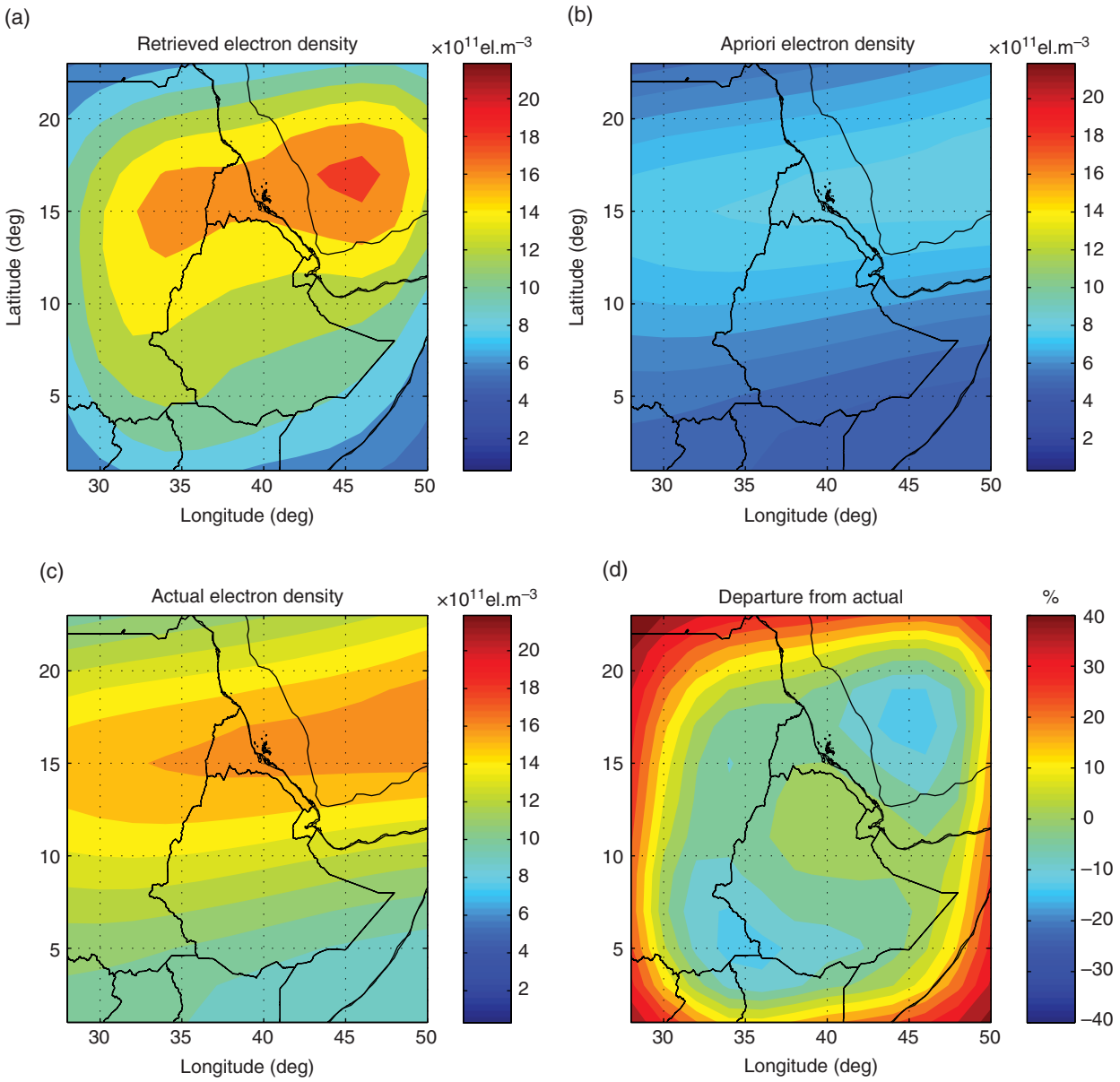


**Figure 11.4** The same as Figure 11.3 but based on iterative approach.

reconstruction (0.66%, averaged over all voxels) than that of MIDAS-type iterative algorithm (0.79% and 0.86%) indicates better performance of the former over most voxels of the reconstruction domain. However, the performance of the MIDAS-type iterative solution is better at individual voxels located in the interior of the domain. The altitude-dependent iterative solution has exhibited better performance with respect to the two methods with weak sensitivity to measurement noise (i.e., 0.38% versus 0.39%). The complete intercomparison of inversion results from different algorithms is not intended within the scope of the current work.

### 11.3.2. Reconstructed Electron Density

The next step is to assess the quality of retrieved electron density from actual GPS observations over Eastern Africa. This can be done by characterizing the tomographic inversion algorithm in terms of its information content and inversion errors. As described in Section 11.2, the smoothing and measurement noise error are two major components of errors of the retrieved electron-density profiles.

Figure 11.6 shows the contribution from the measured TECs and the a priori electron density in percentage

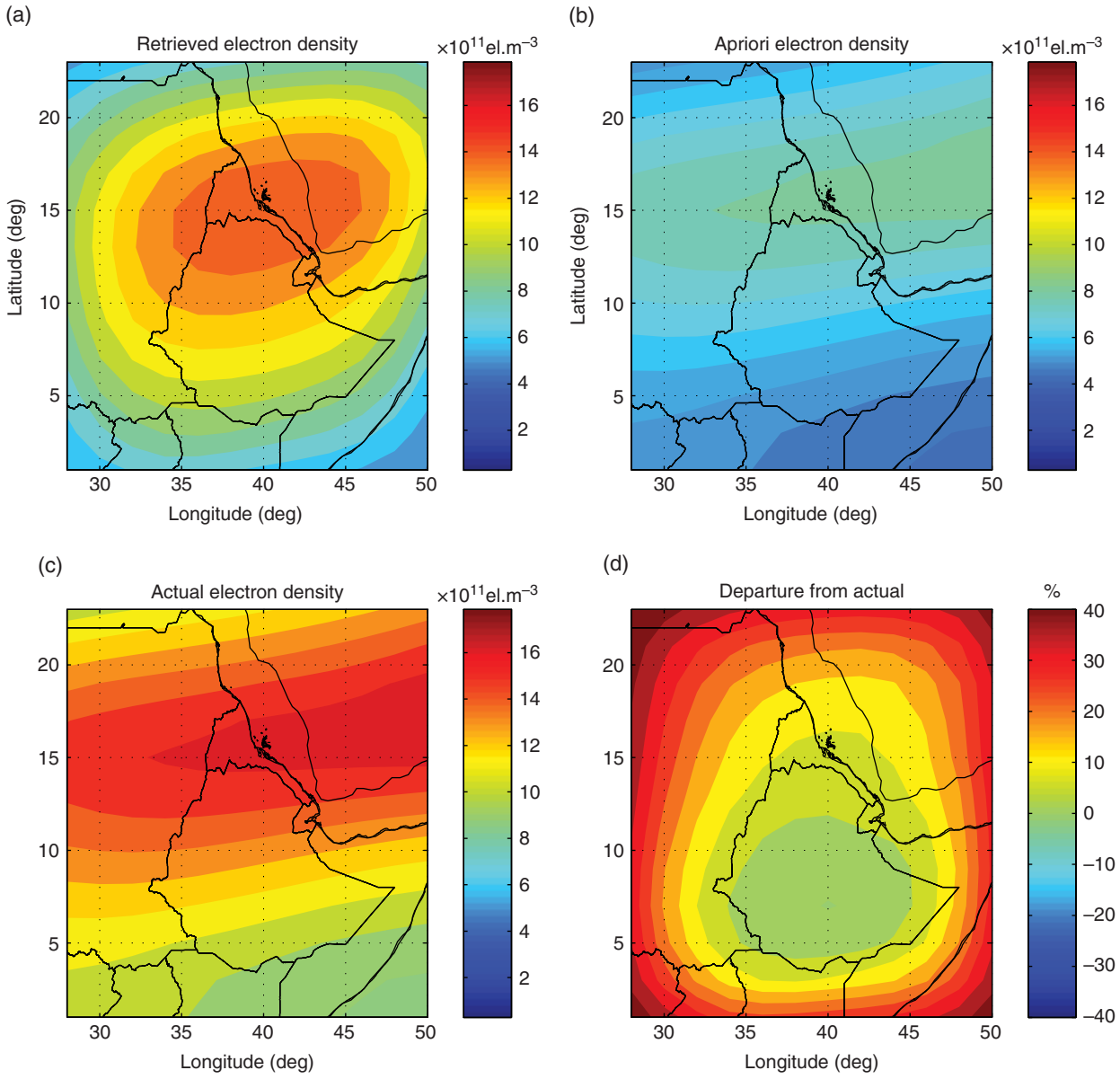


**Figure 11.5** The same as Figure 11.4 but with MIDAS-type regularization factor.

**Table 11.1** Reconstruction Error for Simulated Slant TEC with 4% and 15% Measurement Noise Error under Different Reconstruction Options

| Experiments | Linear solution altitude dependent (4%) | Iterative altitude dependent (4%) | Iterative altitude dependent (15%) | MIDAS-type regularization (4%) | MIDAS-type regularization (15%) |
|---|---|---|---|---|---|
| Reconstruction error ($\sigma$) (%) | 0.66 | 0.38 | 0.39 | 0.79 | 0.85 |

(panels a and b) and corresponding retrieved and a priori electron densities (panels c and d) at 380 km level. As already revealed in the numerical experiments, the contribution of the observed GPS TECs to the solution is dominated over the a priori information over most parts of Ethiopia (this time up to 85% see Fig. 11.6a).

The information provided by the two diagnostics tools, namely the fraction of a priori and measurement,

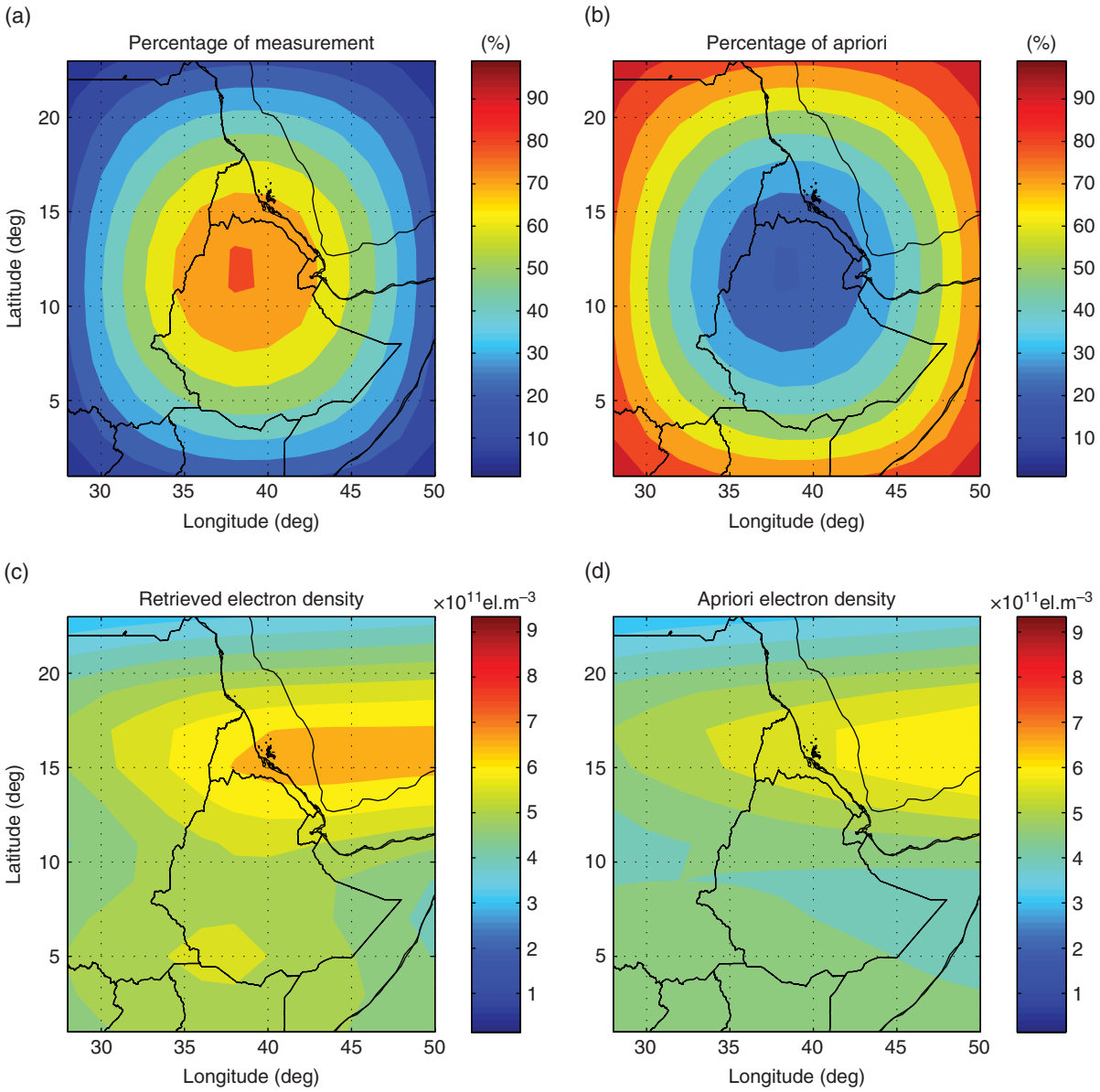


**Figure 11.6** The same as Figure 11.2 but for actual measurements.

can also be appreciated from altitude versus latitude maps shown in Figure 11.7. The altitude-dependent regularization strength has impacted the tomographic reconstruction by increasing the contribution of the measurement to the solution as visibly shown in Figure 11.7a by the vertical extension of the high contour values in contrast along the north-south axis. This is also apparent in Figure 11.7c. As a result, the reconstructed electron density differs from the a priori electron-density profiles by as much as 30% in the altitude regions where the contribution of measurement to the retrieved electron density dominates (compare Fig. 11.7c and d).

In this connection, it is crucial to underline that GPS signals at low elevation can contribute to improve sensitivity of the vertical resolution, provided ray paths with low elevation angles are included in the solution. However, GPS signals at low elevation are prone to multipath effects. In view of this consideration, ray paths with an elevation angle cutoff of 20° are considered in the reconstruction.

Figure 11.8 shows the approximate percentage fraction of smoothing and measurement errors at 380 km. Note that the smoothing error dominates over the measurement errors under the simplified approximation discussed in Section 11.2. This is in contrast to the relative

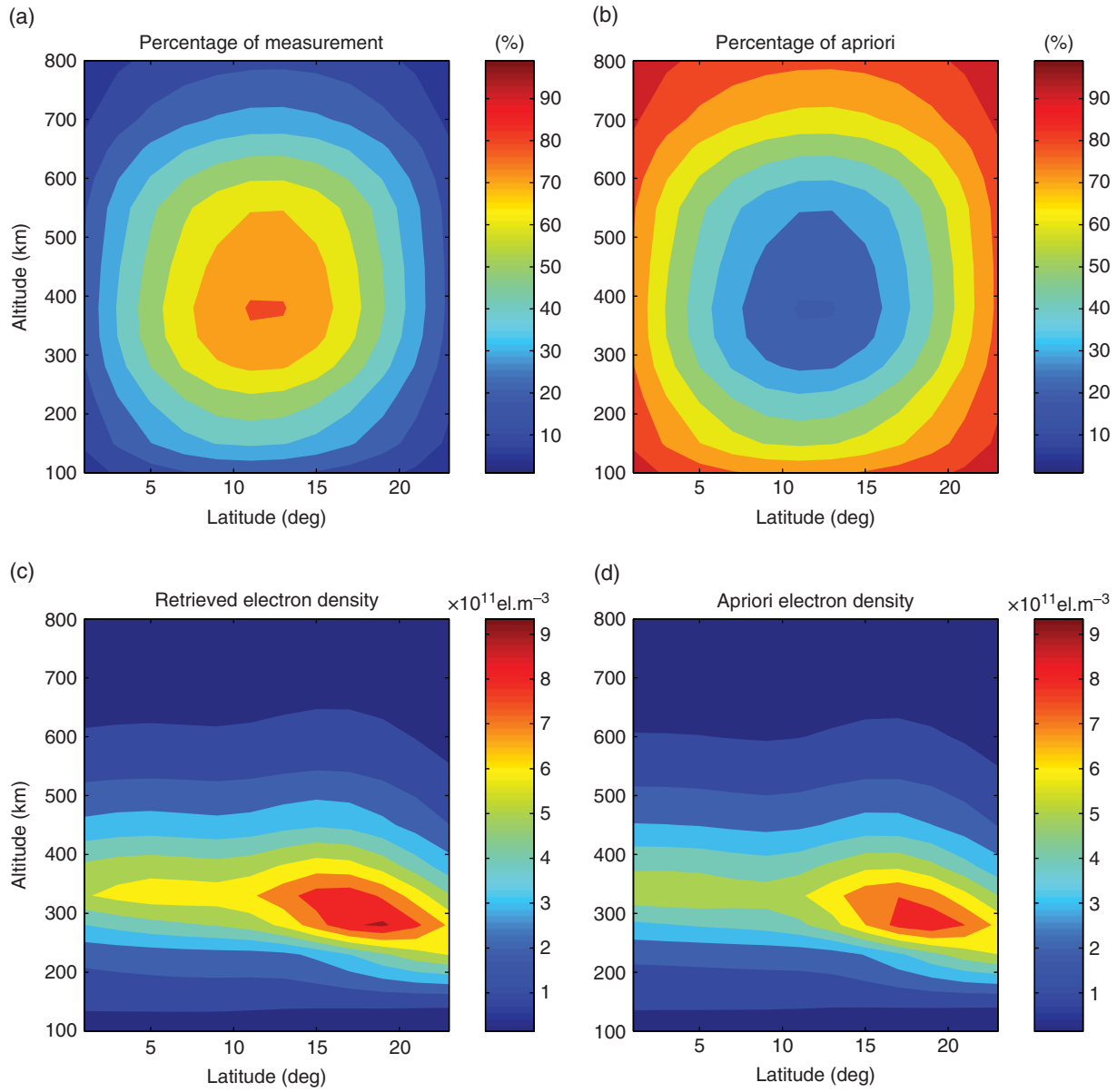


**Figure 11.7** The same as Figure 11.6 but for altitude versus latitude at 38°E.

contribution of a priori and measurement to the solution suggesting that, as the contribution from the a priori to the solution increases, the smoothing error grows steadily. The percentage of the total error of the reconstructed electron density due to measurement noise is also maximum around the center of tomographic grids. This is consistent with the preceding results as the observations are relatively dense in the center of the domain.

Figure 11.9 also shows the relative contributions of the two error sources but for all voxels used in the reconstruction. The smoothing error (solid green line) dominates the error budget everywhere within the volume of the ionosphere considered in the tomographic reconstruction. For some of the voxels, the smoothing error accounts for nearly the whole error budget. The trend is almost the same, even when the regularization parameter is relaxed by a factor of 2.5 as shown by the dotted data points.

It is also interesting to inspect the proportion of contributions from a priori electron-density profiles and measurements to the electron density at all voxels in the domain of the reconstruction. Figure 11.10 shows these contributions for optimal (solid lines) and relaxed (scattered dotted data points) regularization parameters. The decrease in regularization parameter increases the number of voxel volumes whose electron density is predominately determined by measurements at the cost of

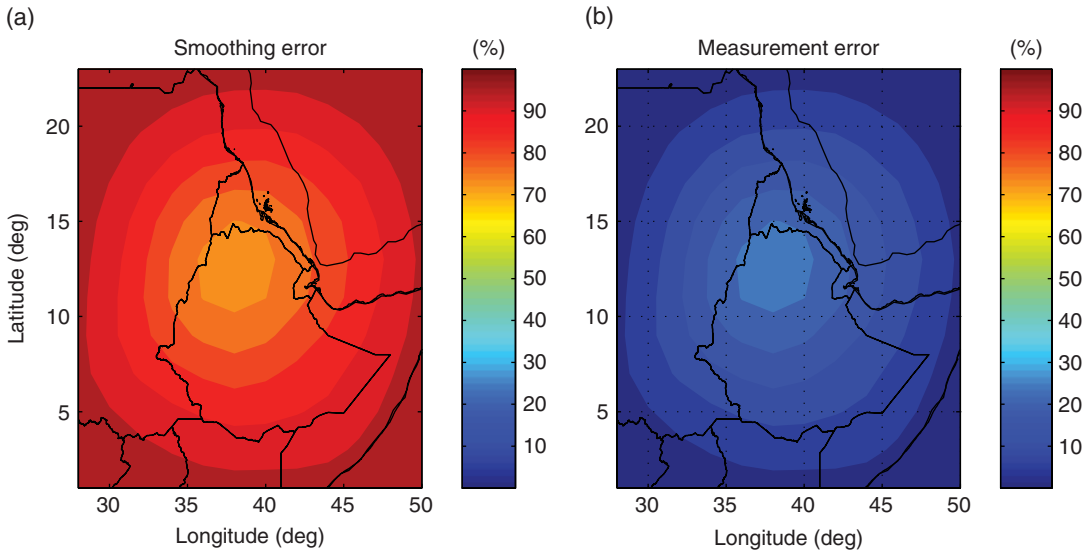


**Figure 11.8** (a) The fraction of smoothing and (b) measurement related error in IED at 380 km.

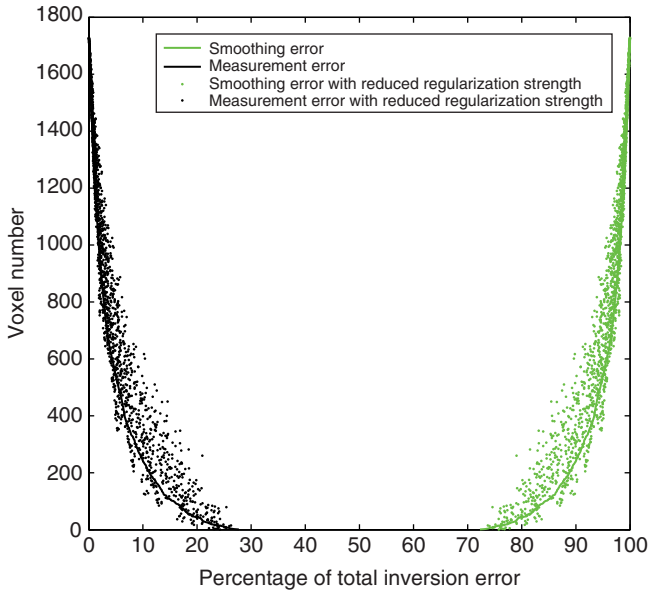


**Figure 11.9** Percentage of total inversion error for all voxel volumes under optimal and relaxed choice of the regularization parameter. The relaxation factor is 2.5 as compared to the optimal regularization parameter.

weakly smoothed electron-density profiles as reflected in the scatter. An interesting aspect of regularization is the appearance of enhanced IEDs over southern Ethiopia (not shown) where one of the GPS receivers is located. The enhancement in IEDs is captured as the measurement is allowed to contribute more to the solution after relaxing smoothing constraint.

We have validated the performance and reliability of the employed ionospheric tomographic reconstruction algorithms using numerical experiments for linear inversion and iterative inversion approaches discussed in Section 11.2 (see Equation [11.6a and b]). The robustness of the proposed regularization over one of common approach has been indicated. Moreover, the performance of the algorithm is also assessed using reconstructed electron density and various diagnostic tools. While it is not the intension of this study to do full validation with in-situ observations, we have compared vertical TEC (VTEC) integrated from the reconstructed electron density with 2-hr JPL VTEC for all coincident observation

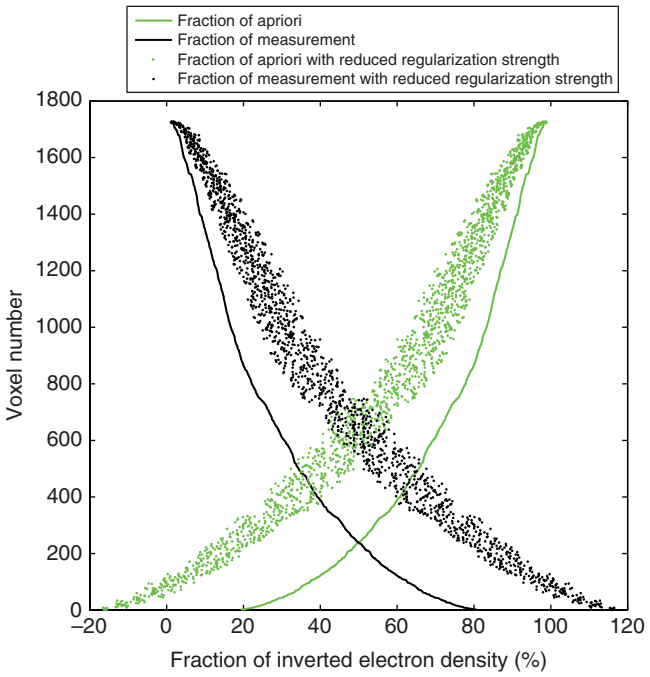


**Figure 11.10** The fraction of inverted IED for all voxel volumes under optimal and relaxed regularization strength.

during the solar minimum period of 2008. Figure 11.11 shows the reconstructed VTEC under linear inversion (left column) and iterative inversion (right column) versus JPL VTEC for four grids along 40°E. The correlation of reconstructed VTEC under both inversions is greater than 0.81 at all grids and is statistically significant. The correlation between reconstructed IED and JPL VTEC is better under iterative inversion than the linear solution (in the range of 0.87 to 0.91 versus 0.82 to 0.84) as shown in Table 11.2. The bias of reconstructed VTEC using the iterative approach with respect to JPL VTEC is lower than that of the linear one except at 20°N. The linear inversion has slightly lower RMSD than the iterative inversion except at 15°N. The comparison of the two inversion methods using the new altitude-dependent regularization parameter shows that the two methods are comparable. Though the iterative procedure improves the phase relationship between reconstructed VTEC and JPL VTEC as compared with the linear solution, there is minor discrepancy in terms of absolute magnitude as noticed from bias and RMSD.

## 11.4. SUMMARY AND CONCLUSIONS

A new regularization scheme in the framework of Tikhonov regularization is developed based on a Laplace operator for 3-D ionospheric imaging. The regularization scheme constrains different parts of the ionosphere preferentially to the a priori IED profiles derived from NeQuick model depending on the strength of signal that contributes to the observed TECs along a given ray-path between satellite and GPS receivers. The normalized weighting factor constructed from the ratio of IED to maximum IED is multiplied by the the regularization operator before the regularization parameter $\alpha$ is selected using *L*-curve. As $\alpha$ is a single parameter, its role under this situation is just to optimally balance the overall smoothing and measurement noise. The robustness of the procedure is evaluated through numerical experiments and various diagnostics adopted from the atmospheric remote sensing discipline. The adopted diagnostics include evaluation of the proportion of measurement and a priori information in the solution and the fraction of errors from these components.

The numerical experiments are performed under realistic observation geometry and for different a priori types. The reconstructed IED from the experiment in which the a priori and the true IED profiles is almost identical to the true IED despite a 4% random noise superimposed on the assumed TEC measurements. This result clearly demonstrates that the algorithm is robust enough when reasonable a priori close to the true profile is used. We would like to underline that this similarity does not suggest that the reconstructed IED is mainly determined from a priori. A proof against this inference is visibly depicted in the stronger contribution from assumed measurement, which is up to 70% –75% over regions well sampled by the ray paths.

To assess whether the performance of the algorithm is trustworthy and robust enough under different extreme conditions, a priori IED, which is off by 50% from the IED used to create the assumed TEC measurements, with measurement noise of 15%, is used. The results of reconstruction even under the extreme scenario are good as reflected in up to 70% agreement over central and northern Ethiopia where there is a dense network of GPS receivers. Even though this is a simulated experiment, the impact of the observation network is easily apparent since the true observation geometry is used in the simulation of assumed TEC measurements. The advantage of the new regularization parameter is also revealed against commonly used regularization factors. The above investigations are applied to actual observed TECs and various diagnostic assessments are also made. The quality of the retrieved IED as judged by more contributions from the measurements and low relative error budget over parts of the ionosphere sounded more by the satellite-GPS ray paths is good. The relaxation of the regularization strength also adds additional information from the measurement on other parts of the ionosphere, in particular over southern Ethiopia. However, such improvement in the measurement signal in the reconstructed IED is at the cost of increasing measurement noise as well in the

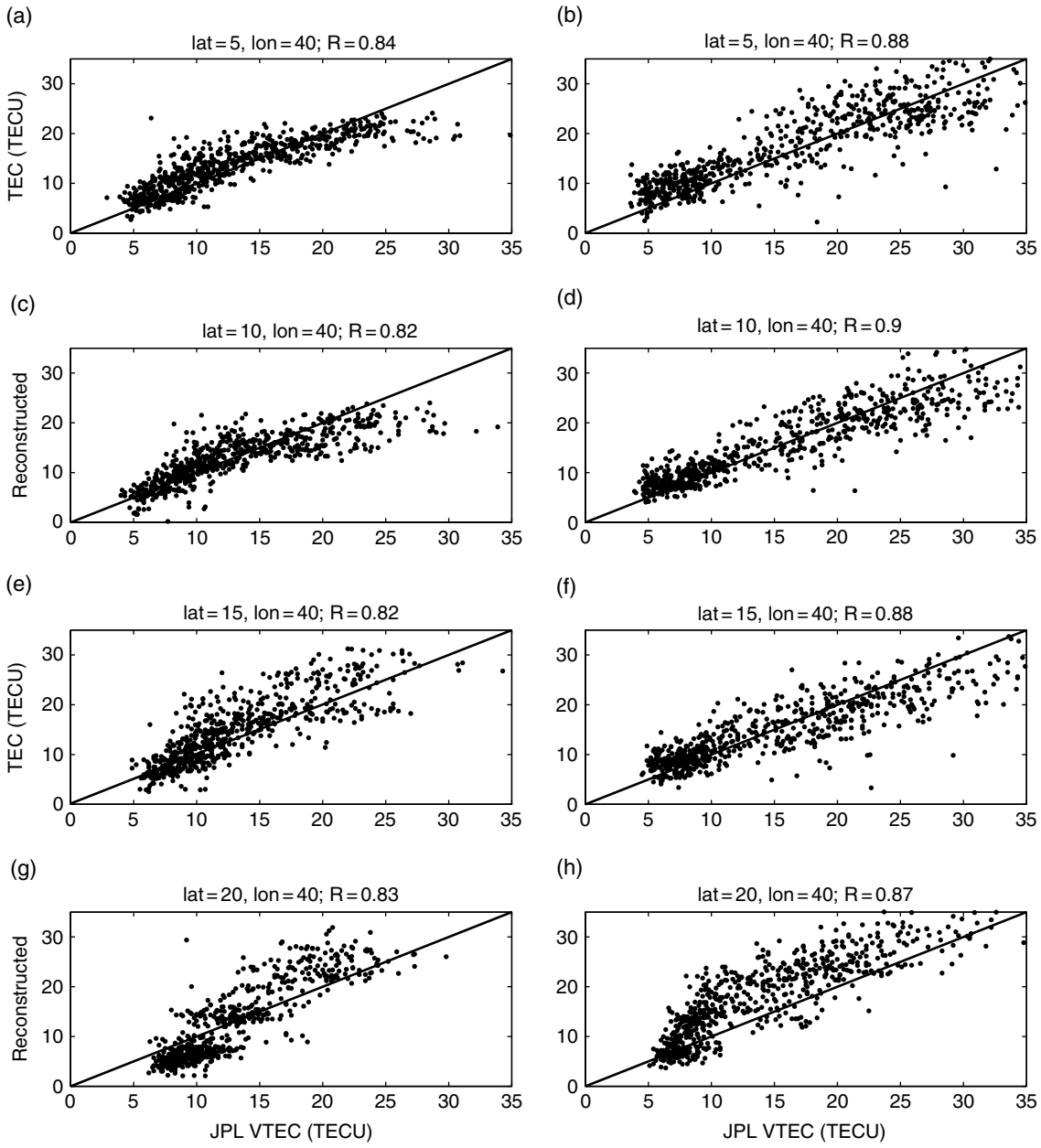


**Figure 11.11** The comparison of VTEC determined from reconstructed IED and JPL VTEC for four grids along 40°E longitude from 5°N to 20°N.

**Table 11.2** Correlation, Bias, and RMSD for the Four Selected Grids over Ethiopia for the Two Inversion Methods

| Method | Longitude (degree East) | Latitude (degree North) | Correlation | Bias (TECU) | RMSD (TECU) |
|---|---|---|---|---|---|
| Linear | 40.0 | 5.0 | 0.84 | –1.27 | 3.45 |
| Iterative | 40.0 | 5.0 | 0.88 | 1.16 | 4.41 |
| Linear | 40.0 | 10.0 | 0.82 | –1.05 | 3.87 |
| Iterative | 40.0 | 10.0 | 0.91 | 0.18 | 3.88 |
| Linear | 40.0 | 15.0 | 0.82 | –2.80 | 5.34 |
| Iterative | 40.0 | 15.0 | 0.88 | 0.61 | 4.37 |
| Linear | 40.0 | 20.0 | 0.83 | –0.05 | 4.87 |
| Iterative | 40.0 | 20.0 | 0.87 | –3.57 | 5.52 |

solution. Comparison of VTEC computed from reconstructed IED with JPL VTEC under two inversion procedures has shown the relative advantage of the iterative approach in capturing the phase relationship (correlation), while there is no significant advantage of one procedure over the other in terms of capturing the absolute magnitude of VTEC.

In summary, the proposed algorithm has been found to be robust under different scenarios and observations over the Eastern Africa longitude sector. Further work involving wider and more dense GPS networks and detailed intercomparison with existing complex models such as MIDAS may be required to see the full capability of the approach.

## ACKNOWLEDGMENTS

The authors acknowledge UNAVCO for installation, maintenance, and free access to GPS data. The first author would also like to acknowledge the financial support of the Humboldt Foundation through the author's Humboldt fellowship grant during which this work was accomplished.

## REFERENCES

Afraimovitch, E., O. Pirog, and T. Terekhov (1992), Diagnostics of large-scale structures of the high-latitude ionosphere based on tomographic treatment of navigation-satellite signals and of data from ionospheric stations, *J. Atmos. Terr. Phys.*, *54*, 1265–1273; doi:10.1016/0021-9169(92)90035-J.

Andreeva, E., A. Galinov, V. Kunitsyn, Y. Melnichenko, E. Tereshchenko, M. Filimonov,, and S. Chernyakov (1990), Radio tomographic reconstruction of ionisation dip in the palsma near the earth, *J. Exp. Theoret. Phys. Lett.*, *52*, 145–148.

Andreeva, E., S. J. Franke, K. Yeh, V. Kunitsyn, and I. Nesterov (2001), On generation of an assembly of images in ionospheric tomography, *Radio Sci.*, *36*(2), 299–309; doi:10.1029/2000RS002437.

Andreeva, E., V. Kunitsyn, and E. Tereshchenko (1992), Phase-difference radio tomography of the ionosphere, *Ann. Geophys.*, *10*, 849–855.

Austen, J., S. Franke, and C. Liu (1988), Ionospheric imaging using computerized tomography, *Radio Sci.*, *23*, 299; doi:10.1029/RS023i003p00299.

Austen, J. R., S. Franke, C. Liu, and K. Yeh (1986), Application of computerized tomography techniques to ionospheric research, 25, in *Proc. International Beacon Satellite Symposium*, Oulu, Finland.

Bernhardt, P., R. McCoy, K. Dymond, J. Picone, R. Meier, F. Kamalabadi, D. Cotton, S. Charkrabarti, T. Cook, J. Vickers, A. Stephan, L. Kersley, S. Pryse, I. Walker, C. Mitchell, P. Straus, H. Na, C. Biswas, G. Bust, G. Kronschnabl, and T. Raymund (1998), Two-dimensional mapping of the plasma density in the upper atmosphere with computerized ionospheric tomography (CIT), *Phys. Plasmas*, *5*, 5; doi:10.1063/1.872872.

Bhuyan, K., S. Singh, and P. Bhuyan (2002), Tomographic reconstruction of the ionosphere using generalized singular value decomposition, *Current Sci.*, *76*(7), 1117–1120.

Bhuyan, K., S. Singh, and P. Bhuyan (2004), Application of generalized singular value decomposition to ionospheric tomography, *Ann. Geophys.*, *22*, 3437–3444; doi:10.5194/angeo-22-3437-2004.

Bilitza, D., and B. W. Reinisch (2008), International reference ionosphere 2007: Improvements and new parameters, *Adv. Space Res.*, *42*(4), 599–609; doi:10.1016/j.asr.2007.07.048.

Bust, G., T. W. Garner, and T. L. G. II (2004), Ionospheric data assimilation three-dimensional (ida3d):a global, multi-sensor, electron density specification algorithm, *J. Geophys. Res.*, *109*, A11312; doi:10.1029/2002JA009570.

Bust, G. S., J. A. Cook, G. R. Kronschnabl, C. J. Vasicek, and S. B. Ward (1994), Application of ionospheric tomography to single-site location range estimation, *J. Img. Sys. Tech.*, *5*, 160–168; doi:10.1002/ima.1850050212.

Cook, J., and S. Close (1995), An investigation of TID evolution observed in MACE '93 data, *Ann. Geophys.*, *13*, 1320–1324.

Dautermann, T., E. Calais, P. Lognonne, and G. S. Mattioli (2009), Lithosphere-atmosphere-ionosphere coupling after the 2003 explosive eruption of the Soufriere Hills Volcano, Montserrat, *Geophys. J. Int.*; doi:10.1111/j.1365-246X.2009.04390.x.

Fox, M., and L. F. McNamara (1988), Improved worldwide maps of monthly median of foF2, *J. Atmos. Terr. Phys.*, *50* (12), 1077–1086; doi:10.1016/0021-9169(88)90096-7.

Fremouw, E., J. Secan, and B. Howe (1992), Application of stochastic inverse theory to ionospheric tomography, *Radio Sci.*, *17*, 721–732; doi:10.1029/92RS00515.

Fuller-Rowell, T., E. Araujo-Pradere, and M. V. Codrescu (2000), An empirical ionospheric storm-time correction model, *Adv. Space Res.*, *25*(4), 139–146; doi:10.1016/S0273-1177(99)00911-4.

Hajj, G., R. Ibañez-Meier, E. Kursinski, and L. Roman (1994), Imaging the ionosphere with the global positioning system, *Int. J. Imag. Syst. Technol.*, *5*(2), 174–184; doi:10.1002/ima.1850050214.

Heise, S., N. Jakowski, A. Wehrenpfennig, C. Reigber, and H. Luhr (2002), Sounding of the topside ionosphere/plasmasphere based on GPS measurements from CHAMP: Initial results, *Geophys. Res. Lett.*, *29*; doi:10.1029/2002GL014738.

Hernández-Pajares, M., J. Juan, and J. Sanz (1998), Global observation of ionospheric electronic response to solar events using ground and LEO GPS data, *J. Geophys. Res.*, *103*(A9), 20789–20796; doi:10.1029/98JA01272.

Hoque, M. M., and N. Jakowski (2011), Ionospheric bending correction for GNSS radio occultation signals, *Radio Sci.*, *46* (RS0D06); doi:10.1029/2010RS004583.

Jianyong, L, M. Guojie, Y. Xinzhao, Z. Rui, S. Hongbo, and H. Yufei (2015), Ionospheric total electron content disturbance associated with May 12, 2008, Wenchuan Earthquake, *Geodesy and Geodynamics*, *6*(2), 126–134; doi:10.1016/j.geog.2015.01.003

Kersley, L., S. Pryse, I. K. Walker, J. Heaton, C. Mitchell, M. Williams, and C. Willson (1997), Imaging of

electron density troughs by tomographic techniques, *Radio Sci*., *32*(4), 1607–1621; 10.1029/97RS00310.

Kunitsyn, E., and E. Tereshchenko (1992), Radio tomography of the ionosphere, *IEEE Antennas Propag. Mag*., *34*, 22–32.

Kunitsyn, V., E. Andreeva, A. Popov, and O. Razinkov (1995), Methods and algorithms of ray radio tomography for ionospheric research, *Ann. Geophys.*, *13*, 1263–1276.

Leitinger, R., H. Ladreiter, and G. Kirchengast (1997), Ionospheric tomography with data from satellite reception of global navigation satellite system signals and ground reception of navy navigation satellite system signals, *Radio Sci.*, *11* (1), 1657–1669.

Liu, C., G. Kirchengast, K. Zhang, R. Norman, Y. Li, S. Zhang, B. Carter, J. Fritzer, M. Schwaerz, S. Choy, S. Wu, and Z. Tan (2013), Characterization of residual ionospheric errors in bending angles using GNSS end-to-end simulations, *Adv. Space Res.*, *52*, 5; doi: 10.1016/j.asr.2013.05.021.

Mengistu Tsidu, G. (2005), On the accuracy of covariance matrix: Hessian versus Gauss Newton methods in atmospheric remote sensing with infrared spectroscopy, *J. Quant. Spectrosc. Radiat. Transf.*, *96*, 103–121; doi:10.1016/j.jqsrt.2004.11.014.

Mitchell, C., D. Jones, L. Kersley, S. Pryse, and I. Walker (1995), Imaging of field-aligned structures in the auroral ionosphere, *Ann. Geophys.*, *13*, 1311–1319.

Na, H., and H. Lee (1990), Resolution analysis of tomographic reconstruction of electron density profiles in the ionosphere, *Int. J. Syst. Technol.*, *2*, 209–218; doi:10.1002/ima.1850020307.

Na, H., and H. Lee (1994), Resolution degradation parameters of ionospheric tomography, *Radio Sci.*, *29*, 115–125; doi:10.1029/93RS02734.

Nava, B., P. Coisson, and S. M. Radicella (2008), A new version of the NeQuick ionosphere electron density model, *J. Atmos. Sol. Terr. Phys.*, *70*(15), 139–146; doi:10.1016/S0273-1177(99)00911-4.

Pryse, S., and L. Kersley (1992), A preliminary experimental test of ionospheric tomography, *J. Atmos. Terr. Phys.*, *54*, 1007–1012; doi:10.1016/0021-9169(92)90067-U.

Pryse, S., C. Mitchell, J. Heaton, and L. Kersley (1995), Travelling ionospheric disturbances imaged by tomographic techniques, *Ann. Geophys.*, *13*, 1325.

Radon, J. (1917), Uber die bestimmung von funktionen durch ihre integralwerte längs gewisser mannigfaltigkeiten, *Saechsische Berichte Akademie der Wissensxhaften 69*, 262.

Raymund, T., J. Austen, S. Franke, C. Liu, J. Klobuchar, and J. Staker (1990), Application of computerized tomography to the investigation of ionospheric studies, *Radio Sci.*, *25*(5), 771–789; doi:10.1029/RS025i005p00771.

Raymund, T. D. (1995), Comparisons of several ionospheric tomography algorithms, *Ann. Geophys.*, *13*, 1254–1262.

Rodgers, C. (1990), Characterization and error analysis of profiles retrieved from remote sounding measurements, *J. Geophys. Res.*, *95*(D5), 5587–5595; doi:10.1029/JD095iD05p05587.

Rogers, N., C. Mitchell, J. Heaton, P. Cannon, and L. Kersley (2001), Application of radio tomographic imaging to hf oblique incidence ray tracing, *Radio Sci.*, *36*(6), 1591–1598; doi:10.1029/2000RS002505.

Rush, C., M. Pokempner, D. N. Anderson, F. G. Stewart, and J. Perry (1984), Maps of foF2 derived from observations and theoretical data, *Radio Sci.*, *19*, 1083–1097; doi:10.1029/RS019i004p01083.

Spencer, P., and C. Mitchell (1986), Multi-instrument data analysis system, in *Proc. Beacon Satellite Symposium*, Boston, Massachusetts, USA.

Stankov, S., N. Jakowski, S. Heise, P. Muhtarov, I. Kutiev, and R. Warnant (2003), A new method for reconstruction of the vertical electron density distribution in the upper ionosphere and plasmasphere,*J. Geophys. Res.*,*108*;doi:10.1029/2002JA009570.

Stolle, C., S. Schlüter, C. Jacobi, and N. Jakowski (2003), 3-dimensional IED reconstruction based on GPS measurements, *Adv. Space Res.*, *31*(8), 1965–1970; doi:10.1016/S0273-1177(03)00168-6.

Sutton, E., and H. Na (1996), Ionospheric tomography using the residual correction method, *Radio Sci.*, *31*(3), 489–496; doi:10.1029/96RS00040.

Tsai, L., C. Liu, W. Tsai, and C. Liu (2002), Tomographic imaging of the ionosphere using the GPS/Met and NNSS data, *J. Atmos. Terr. Phys.*, *64*, 2003–2011.

Walker, I., J. Moen, C. Mitchell, L. Kersley, and P. Sandholt (1998), Ionospheric effects of magnetopause reconnection observed using ionospheric tomography, *Geophys. Res. Lett.*, *25*(3), 293–296; doi:10.1029/97GL53698.

Wen, D., S. Liu, and P. Tang (2010), Tomographic reconstruction of ionospheric electron density based on constrained algebraic reconstruction technique, *GPS Solutions.*, *14*, 375–380; doi 10.1007/s10291-010-0161-0.

Wen, D., Y. Yunbin, and O. Jikun (2007), Monitoring the three-dimensional ionospheric electron density distribution using GPS observations over china, *J. Earth Syst. Sci.*, *116*(3), 235–244; doi:10.1007/s12040-007-0023-5.

Yeh, K., and T. Raymund (1991), Limitations of ionospheric imaging by tomography, *Radio Sci.*, *26*, 1361–1380; doi:10.1029/91RS01873.

Yizengaw, E., P. Dyson, E. Essex, and M. Moldwin (2005), Ionosphere dynamics over the southern hemisphere during the 31 March 2001 severe magnetic storm using multi-instrument measurement data, *Ann. Geophys.*, *23*, 707–721; doi:10.5194/angeo-23-707-2005.

Zhou, C., E. Fremouw, and J. Sahr (1999), Optimal truncation criterion for application of singular value decomposition to ionospheric tomography, *Radio Sci.*, *34*(1), 155–166; doi:10.1029/1998RS900015.

# 12

# Variation of the Total Electron Content with Solar Activity During the Ascending Phase of Solar Cycle 24 Observed at Makerere University, Kampala

**Florence M. D'ujanga, Phillip Opio, and Francis Twinomugisha**

## ABSTRACT

A dual frequency GPS receiver at an equatorial station, Kampala in Uganda (geographic latitude 0.3°N; Lon: 32.5°E), has been used to investigate variation of the total electron content (TEC) during 2010 to 2013, the ascending phase of solar cycle 24. Diurnal and solar activity dependence of GPS-TEC has been investigated. The results show that TEC increases from a minimum at 0600 local time (LT) to a maximum value that starts at about 1300 LT and then decreases to a low value after sunset. However, some months exhibited enhancements in TEC during postsunset hours, particularly the equinoctial months, which exhibited higher TEC values than the solstice months. Variation of TEC was compared with two solar indices, namely, the 10.7 cm solar flux ($F_{10.7}$ cm) and the sunspot numbers (SSN) during the period of study. The solar flux variation indicated that the year 2010 was a relatively quiet year, recording moderate values, but variation increased drastically in 2011, maximizing in November 2011, and later falling off, but keeping moderately high values in 2012 and 2013. The trend in TEC is to follow the solar parameters, while exhibiting more dependence on seasonal variations than on the solar parameters.

**Key Points:**
Solar activity affects total electron content.

**Key Terms:** total electron content (TEC), solar activity, solar flux, solar cycle 24

## 12.1. INTRODUCTION

The total electron content (TEC) is an important parameter in investigating the behavior of the ionosphere. Changes in TEC have become a very serious concern for ionospheric researchers, particularly those studies concerning the equatorial ionosphere. The Global Positioning System (GPS) is a satellite-based navigation radio system that is used to verify the position and time in space and on the Earth. In addition to providing users on a worldwide basis with navigation, positioning, and time information, GPS has great importance in scientific applications. Signals from GPS satellites have been used extensively for monitoring the ionosphere both globally and regionally [e.g., *Valladares et al.*, 2004; *Paznukhov et al.*, 2012; *D'ujanga et al.*, 2012; *Rama Rao et al.*, 2009]. The GPS satellites that are orbiting the Earth, at altitudes of about 20, 200 km, transmit signals that propagate through the ionosphere, which exists at about 60–1500 km above the Earth's surface. The satellites

*Department of Physics, Makerere University, Kampala, Uganda*

*Ionospheric Space Weather: Longitude and Hemispheric Dependences and Lower Atmosphere Forcing, Geophysical Monograph 220*, First Edition. Edited by Timothy Fuller-Rowell, Endawoke Yizengaw, Patricia H. Doherty, and Sunanda Basu.

broadcast at two L-band frequencies, namely, L1 (1575 MHz) and L2 (1228 MHz). A dual-frequency GPS receiver can measure the difference in ionospheric delays between the L1 and L2 of the GPS frequencies, which are generally assumed to travel along the same path through the ionosphere.

Ionospheric plasma density irregularities are an impediment to radio wave communication, since they result in scattering radio waves passing through the ionosphere. This phenomenon, known as ionospheric scintillation, refers to the rapid fluctuations of the phase and amplitude of the radio frequency (RF) signal passing through ionospheric regions embedded with plasma density irregularities. Ionospheric scintillations occur when GPS signals travel through small-scale irregularities in electron density in the ionosphere, typically in the evening and nighttime especially in the equatorial region [*Wong*, 2009].

The plasma density irregularities, which encompass a wide range of scale sizes (from a few cm to a few hundred km), are referred to as the equatorial spread *F* (ESF) [*Paznukhov et al.*, 2012]. Plasma depletions, commonly referred to as equatorial plasma bubbles (EPBs), are the irregularities of the largest scale sizes (up to a hundred km) that are associated with the ESF in which the plasma density can be lowered up to three orders of magnitude compared to the background [*Dashora* and *Pandey*, 2005]. TEC measurements have been used to diagnose the dynamics that drive the formation of plasma depletions. The presence of plasma irregularities within these depletions disrupts satellite communication by scattering radio signals that pass through them.

The origin and variability of the plasma density depletions in relation to the variability of ionospheric total electron content have been well documented [e.g., *Valladares et al.*, 2004; *Dashora and Pandey*, 2005]. Sudden reductions in TEC, observed in the nighttime low-latitude *F* region, have been identified with the plasma density depletions of the equatorial origin [*Valladares et al.*, 2004]. TEC depletions occur when one or more plasma bubbles drift across the line of sight (LOS) between the GPS receiver and the satellite. In addition, rapid changes in electron density resulting from space-weather disturbances may cause severe TEC depletions. During daytime, the *E* region dynamo electric field gives rise to an upward electrodynamic $\mathbf{E} \times \mathbf{B}$ drift that causes the *F*-region plasma to diffuse downward along geomagnetic field lines under the influence of gravity and pressure gradients, resulting in the equatorial ionization anomaly at about 15° magnetic latitude on either side of the equator. After sunset, plasma densities and dynamo electric fields in the *E*-region decrease, and the anomaly begins to fade, and at this local time a dynamo electric field develops in the *F* region [*Rama Rao et al.*, 2006a; *Valladares et al.*, 2004]. Polarization charges, set up by the conductivity gradients at the terminator, enhance the eastward electric field for about an hour after sunset. With the decreased ionization density in the *E* region after sunset, vertical plasma density gradients form in the bottom side of the *F* layer, resulting in the upward density gradients opposite in direction to the gravitational force. Such a configuration is known as the Rayleigh-Taylor (RT) instability, and allows plasma density irregularities to occur [*Rama Rao et al.*, 2006a; *Basu et al.*, 2007; *Paznukhov et al.*, 2012]. These irregularities can grow to become large ionospheric depletions, resulting in EPBs. Ionospheric irregularities may be due to geomagnetic storms, which can affect the ionosphere and hence modify the ionospheric parameters therein [*Rama Rao et al.*, 2009; *Basu et al.*, 2007]. A highly dynamic ionosphere affects both space-based systems and ground-based systems leading to wastage of economic resources.

This paper shows TEC values measured by a dual frequency GPS Scintillation Network and Decision Aid (SCINDA) receiver located at Makerere University, Uganda (Lat: 0.3°N; Lon: 32.5°E) during the ascending phase of solar cycle 24. Makerere is located close to the geographic equator with the following geomagnetic coordinates: Lat. –9.3°; Lon. 104.2°. By analyzing TEC variations with solar activity, we discuss the variability of TEC during the period from 2010 to 2013 observed at this station. We used the $F_{10.7}$ cm solar flux and sunspot numbers as an indication of solar activity.

## 12.2. EXPERIMENTAL DETAILS

In this study, the total electron content (TEC) has been measured using a high data-rate NovAtel GSV400B GPS SCINDA receiver situated at Makerere University, Uganda (Lat. 9.3°; Lon. 104.2°). The GPS SCINDA is a real-time GPS data acquisition and ionospheric analysis system, and computes ionospheric parameters $S_4$ (scintillation index) and TEC using the full temporal resolution of the receiver. The TEC is computed from the combined L1 (1575 MHz) and L2 (1228 MHz) pseudoranges and carrier phase, and is measured in TEC units, where 1 TEC unit is equal to $10^{16}$ electrons per $m^2$. The total electron content is defined as the number of electrons in a column of 1 $m^2$ cross section, from the height of the GPS satellite (~20,000 km) to the receiver on the ground.

The estimation of the absolute TEC using dual frequency GPS receivers has been made possible due to the dispersive nature of the ionosphere. The method of estimation has been described in detail in the literature [*Carrano and Groves*, 2006; *Carrano*, 2007] and uses the satellite interfrequency biases provided by the Center for Orbit Determination in Europe (CODE). In this research, analysis of the TEC data has been carried out using the Gopi GPS-TEC analysis application software [*Seemala*, 2012], which has an algorithm for the estimation of satellite and receiver biases. This

application first calculates the relative values of slant TEC by eliminating the effect of tropospheric water vapor and clock errors using the phase and code values of the L1 and L2 frequencies and then the absolute value of slant TEC after compensating for the satellite and receiver biases [*Sardon and Zarraoa*, 1997]. The vertical TEC is then obtained from the slant TEC by using the single-layer mapping function, $M(\varepsilon, h)$, of the ionosphere given by:

$$M(\varepsilon, h) = \frac{1}{\cos Z} = \left[1 - \left(\frac{R_E \cos \varepsilon}{R_E + h}\right)^2\right]^{\frac{1}{2}} \qquad (12.1)$$

where $Z$ is the solar zenith angle, $R_E$ is the radius of the Earth, $\varepsilon$ is the elevation angle, and $h$ is the height of the ionospheric layer, assumed to be 350 km.

Observations for this research are for a period of 4 yr starting in 2010, when TEC measurements were initiated at this station. During the period of study, lowest solar activity was observed during 2010 (Max. SSN = 77; Max. $F_{10.7}$ cm flux = 96); while 2011 exhibited a sharp rise in solar activity (Max. SSN = 190; Max. $F_{10.7}$ cm flux = 208). The year 2012 exhibited lower values than the previous year (Max. SSN = 188; Max. $F_{10.7}$ cm flux = 178); and 2013 exhibited high fluctuations in solar indices, with some months giving very high values (Max. SSN = 282; Max. $F_{10.7}$ cm flux = 178). The solar indices used in this research are the sunspot number (SSN) and the $F_{10.7}$ cm solar flux index, which is a measure of the noise level generated by the Sun at a wavelength of 10.7 cm at the Earth's orbit (http://www.nwra.com/spawx/f10.html). The solar indices were obtained from http://www.swpc.noaa.gov/ftpmenu/indices/old_indices.html.

## 12.3. RESULTS AND DISCUSSIONS

### 12.3.1. Diurnal Variation of TEC

The diurnal variation of TEC for the years 2010–2013 is depicted in the contour presentation and daily plots of Figure 12.1a and b, respectively. The horizontal axis gives the universal time (UT), and the local time (LT) is given by adding 3 hr (i.e., LT = UT + 3 hr), obtained from the formula: $LT = UT + 32.5^2/15^2$. The figures show TEC rising gradually from minimum at sunrise (0300 UT) to a broad maximum value between 1000 to 1500 UT and then falling steadily until sunset. Several researchers [e.g., *Chauhan et al.*, 2011; *Anderson et al.*, 2004; *Dabas et al.*, 2003] have attributed this rise of TEC to the rapid filling up of the magnetic field tubes at sunrise, leading to the solar extreme ultraviolet (EUV) ionization coupled with the upward vertical $\mathbf{E} \times \mathbf{B}$ drift. These magnetic tubes had initially collapsed after sunset due to the low nighttime temperatures within the thermosphere. It can be seen from the plots that TEC was much higher in 2011, which had maximum values up to 70 TEC units compared with values in 2010, which were less than 50 TEC units. TEC data for 2012 were available for only half the year, showing lower values than in the previous year, but later showing some increase in TEC in 2013.

Figure 12.1 further shows that the equinoctial months of March and April (vernal), and September and October (autumnal) exhibited much higher TEC values than the solstice months during the period of observation. This is in agreement with most of the research carried out within the equatorial regions. The seasonal variations have been attributed to changes in the concentration of atomic oxygen and molecular nitrogen in the *F* region [e.g., *Gupta* and *Singh*, 2001; *Chauhan et al.*, 2011; *Olwendo et al.*, 2013]. It is argued that during equinoctial months, solar radiation is mainly absorbed by atomic oxygen, leading to high values of TEC during these periods. We also note that the equinoxes (around 20 March and 23 September) are the only times when the solar terminator is perpendicular to the equator, thus explaining the high TEC values during equinoxes. In addition, it is a well-known fact that during equinoxes, the Sun is crossing the equator and therefore the period of maximum sunlight would be the same in both the vernal and autumnal equinoxes at equatorial stations.

From the plots of Figure 12.1b, it can be seen that the autumnal months exhibited a little higher TEC values than the vernal equinoxes during 2011, a year that experienced a steep rise in solar activity. The year 2010, on the other hand, exhibited a reverse equinoctial asymmetry, where the vernal equinox TEC was slightly higher than the autumnal one. Similarly, in 2013, though there were no data in April, the trend seems to indicate a slightly higher TEC during the vernal equinox than in the autumnal one.

The equinoctial asymmetry exhibited in 2011 is different from that observed by different researchers who reported the reverse while investigating different parameters. For example, a higher background electron density was observed during vernal equinox than that observed during the autumn period in a low solar activity period [*Sripathi et al.*, 2011]; *Dasgupta et al.* [1983] observed higher values in TEC during the vernal equinox than the autumn one; and a higher scintillation occurrence was observed in the vernal equinox than the autumnal equinox [*Ray and Dasgupta*, 2007; *Rama Rao et al.*, 2006b]. In all these cases, the equinoctial asymmetry was attributed to differences in the meridonal winds, leading to changes in the neutral composition during equinoxes.

The observed difference in the equinoctial asymmetry in our observations could be due to the fact that the autumnal equinox recorded higher solar flux values than those recorded in the vernal equinox of 2011 (as seen in

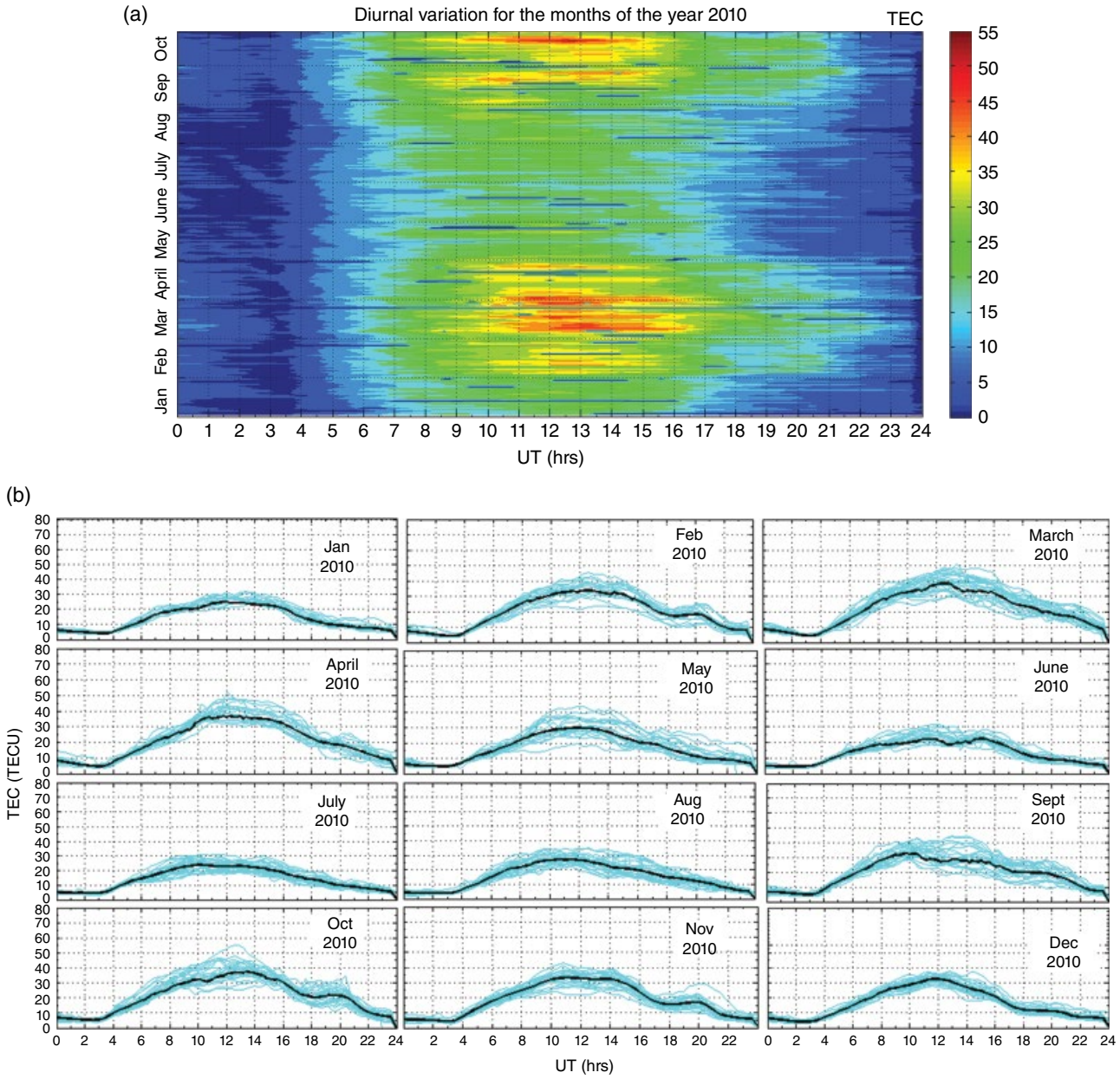


**Figure 12.1** Diurnal variation of TEC for the years 2010 to 2013 depicted as (a) contour presentation with vertical axis depicting months of the year; and (b) daily plots with vertical axis depicting TEC in TEC units. Horizontal axes give time in UT.

Fig. 12.2), leading to higher ambient ionization during this period. There was also an interesting feature observed during the equinoxes: there was a slight shift in the TEC maximum peaks during the vernal equinoctial months so that the diurnal TEC started peaking a little later at about 1100 and ended at about 1600, while the autumnal months started peaking at 1000 and ending at about 1500. This type of peak shifting is normally experienced and is quite pronounced in the polar regions whose dependence has been attributed to the solar zenith angle.

The diurnal plots in Figure 12.1b also showed the existence of nighttime enhancements in TEC during postsunset at around 1800–2000 and these were more pronounced during equinoctial months than in solstice months. The largest enhancements were exhibited during the period 2011–2013. This nighttime enhancement in TEC has been documented by research on the equatorial ionosphere [e.g., *Paznukhov et al.*, 2012; *D'ujanga et al.*, 2012; *Rama Rao et al.*, 2009], and it has been explained in terms of an eastward-directed electric field that produces an upward drift of ionospheric

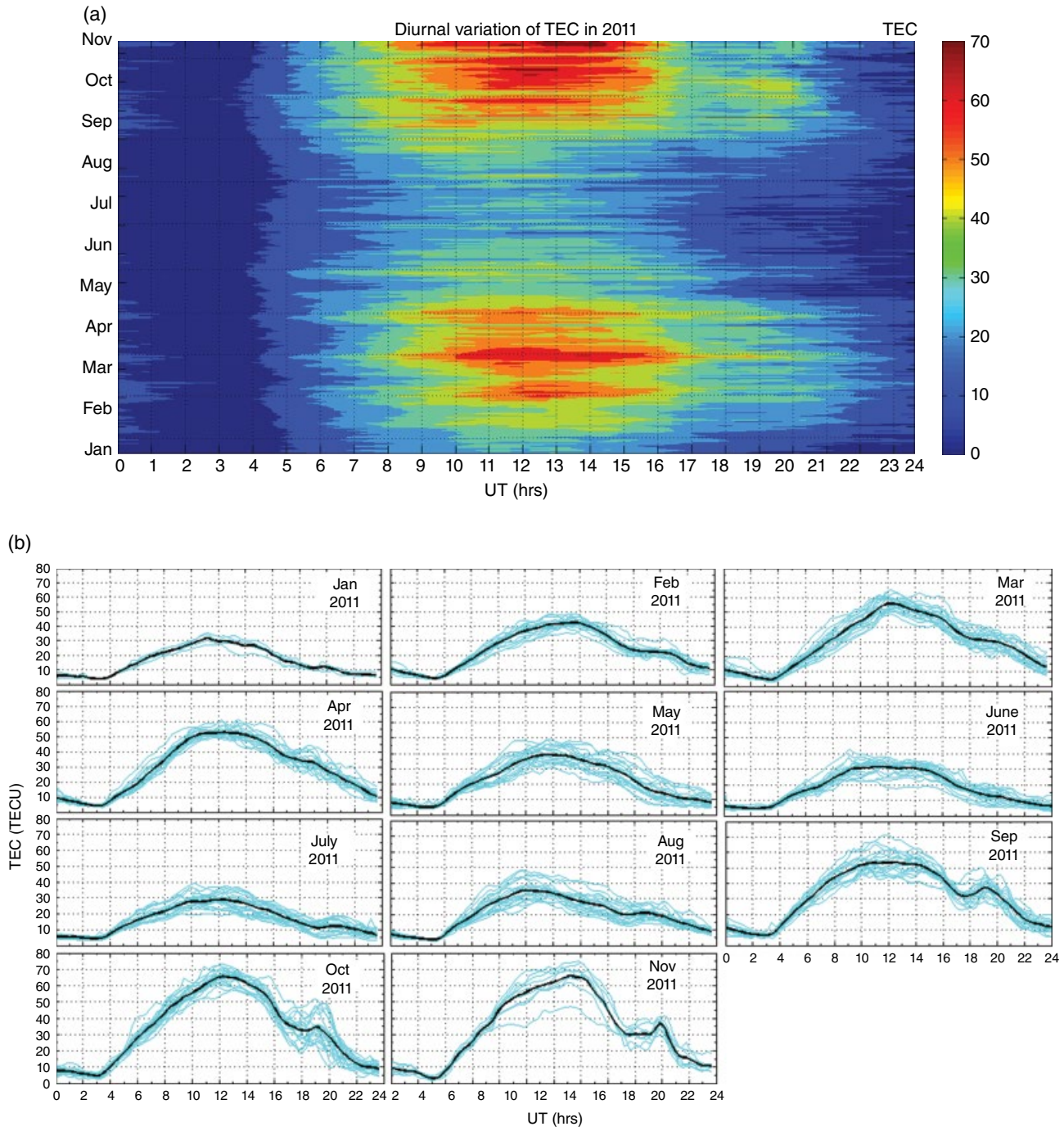


**Figure 12.1** (Continued)

plasma during daytime, while the westward-directed fields during the night cause a downward drift motion [e.g., *Hanson and Moffett*, 1966].

### 12.3.2. Variation of TEC with Solar Parameters

The month-to-month variation of TEC shown in Figure 12.2 is an attempt to investigate the variation of TEC in response to the solar activity by superimposing the solar parameter values in the same plot. The solar parameters indicate that 2010 was relatively a quiet year, recording moderate values, which increased drastically in 2011, maximizing in November 2011, and later falling off, but keeping relatively high values in 2012 and 2013. The $F_{10.7}$ cm solar flux and SSN parameters have a pattern of increasing and decreasing together, though the SSN pattern shows some drastic sharp increases in some months (e.g., the months of March and November 2011, and May

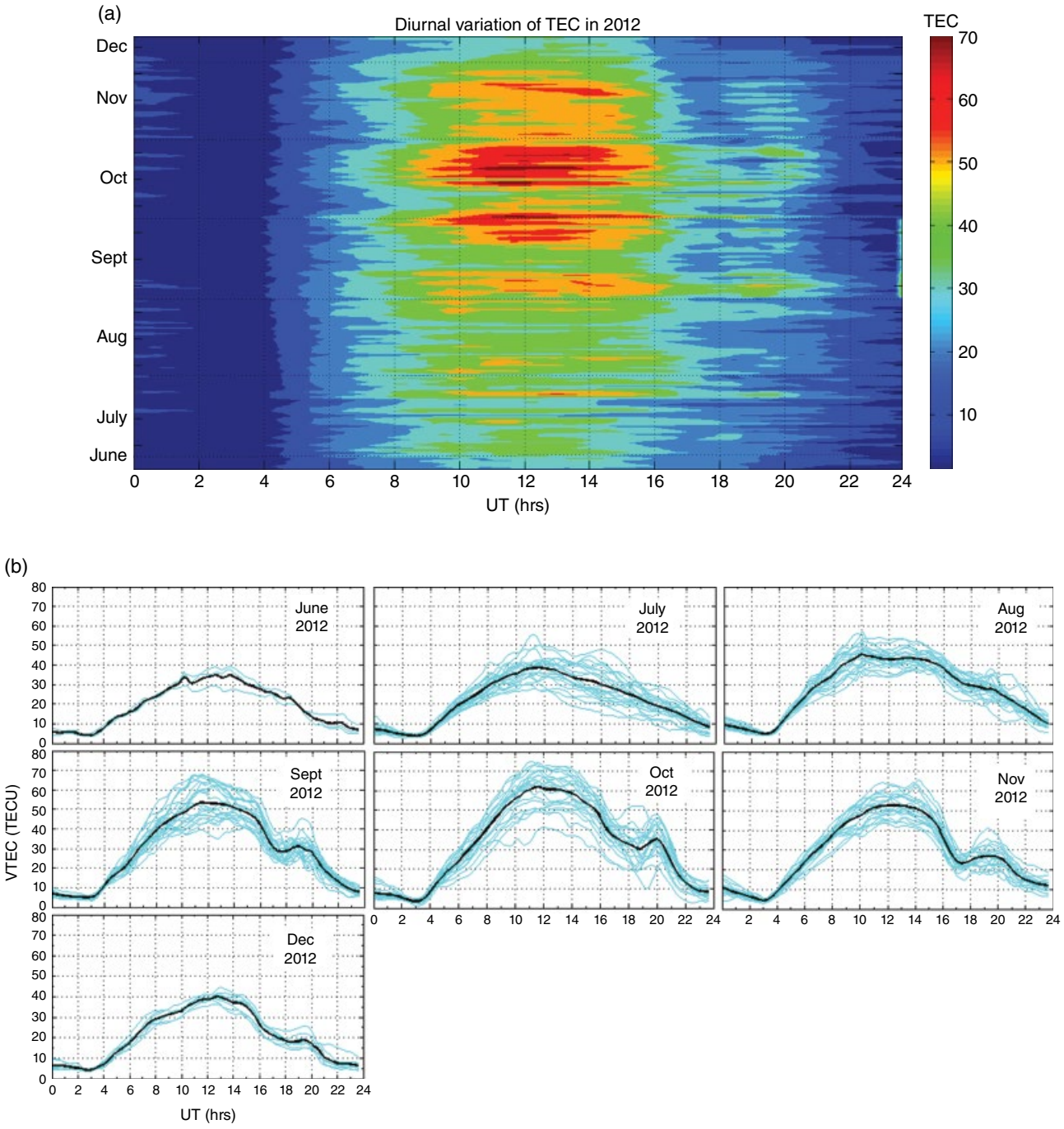


**Figure 12.1** (Continued)

and October 2013), while those for the $F_{10.7}$ cm flux were not as sharp. Such inconsistencies in the variation of the $F_{10.7}$ cm solar flux and the SSN index have been reported by *Chakrabarty et al.* [2012], who observed discrepancies in these parameters over the anomaly crest region and reported a 7-month delay between the onset of enhancement of SSN and that of the solar fluxes. In relation to variation of these parameters with TEC, they reported a direct solar influence on TEC. They also reported that TEC over the anomaly crest region increased more rapidly than the corresponding rate of increase of the $F_{10.7}$ cm flux and attributed this to transport process related to transequatorial and/or chemical processes.

In our findings (Fig. 12.2), we observe that whereas the trend in TEC tends to follow that of the solar parameters, the rate of increase of these solar parameters is much

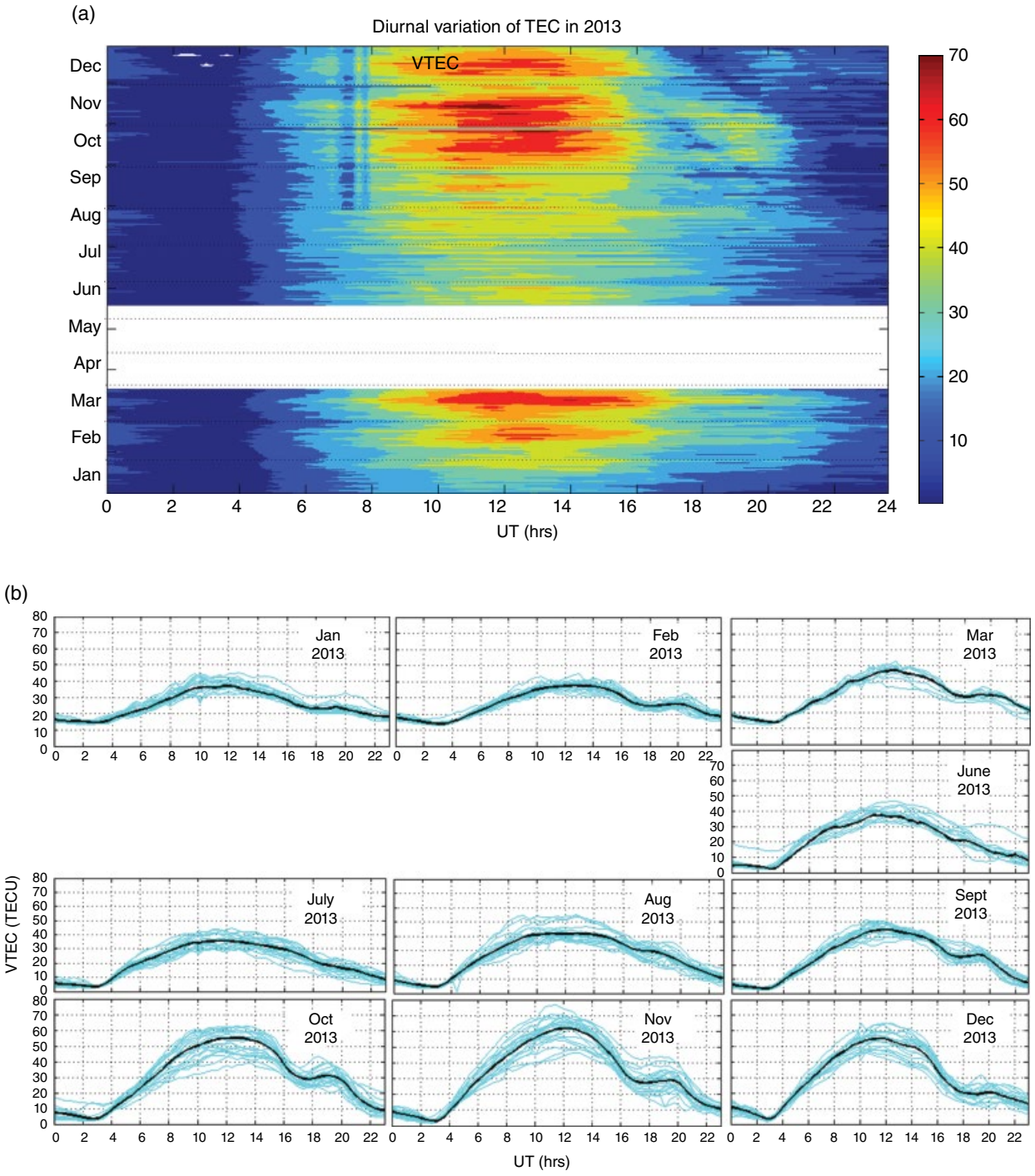


**Figure 12.1** (Continued)

higher than that of the average TEC. In particular, the months of March and April, September and October 2011 had drastic increases in the solar parameters, which did not match the increase in TEC during these months. Related to this, maximum solar flux during 2012 is shown in the month of July, with a corresponding increase in SSN, while the values of these parameters were relatively lower during September and October 2012. TEC values, on the other hand, showed lower values in July and August than in September and October 2012. This scenario is best explained with reference to solstice and equinoctial months, explained in Section 12.3.1, where TEC was much higher in equinoctial than in solstice months. On further scrutiny, still, it can be observed that

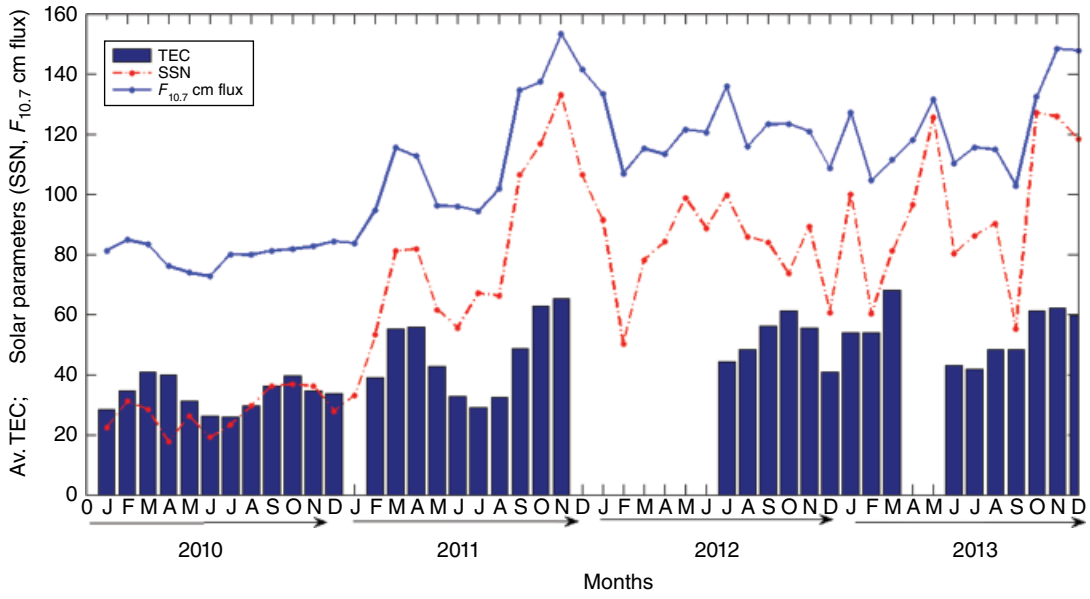


**Figure 12.2** Month-to-month variation of Average TEC from 2010 to 2013 (bar chart), with solar flux ($F_{10.7}$ cm) in blue superimposed as a line plot along with SSN in red.

the TEC in solstice months of July and August 2012 is higher than for the same months in 2010 and 2011, when the solar flux and SSN were relatively lower. This shows the interdependence of seasonal and solar parameters, while noting that TEC responds more to seasonal variations than to the solar-parameter variations.

Very high values in TEC also may be due to geomagnetic storms, which can sometimes affect the ionosphere and modify it in a complex and unpredictable manner. A look at the disturbance storm time ($D_{st}$) and planetary magnetic (Kp) indices for the years 2010–2013 (from the World Data Center catalog: http://www.swpc.noaa.gov/ftpmenu/indices/old_indices.html and http://wdc.kugi.kyoto-u.ac.jp/dst_provisional/index.html) indicate that 2010 had no severe geomagnetic storms throughout the year except for some moderate storms ($D_{st} > -100$) on a few days, while 2011, 2012, and 2013 had some intense geomagnetic storms ($D_{st} < -100$) in September and October of 2011; in March, October, and November of 2012; and in March and June 2013. Magnetic storms have been reported to have effects on TEC within the equatorial region, with some storms showing some increase in TEC, while others show a depression in TEC, with accompanying ionospheric scintillations [*Akala et al.*, 2013; *D'ujanga et al.*, 2013]. For example, the October 2011 geomagnetic storm ($D_{st} = -137$ nT) resulted in severe ionospheric scintillations [*D'ujanga et al.*, 2013]. High values of TEC in our observations could have had some origins in the geomagnetic storms that occurred, particularly in 2011. Such changes in TEC within this region have been attributed to intense disturbances of electric fields origination from the magnetosphere-ionosphere interactions [*Olwendo et al.*, 2013; *D'ujanga et al.*, 2013]. These effects in TEC may cause intense phase and amplitude scintillations of satellite signals and thereby adversely impact satellite communication and navigation systems.

### 12.3.3. Correlation of TEC with Solar Parameters

The Sun, just like the Earth, has seasons and the most notable one is the 11-yr sunspot cycle. The period of this research is during the ascending sunspot cycle phase, which has been shown by the increase in the solar parameters over the period. All these happenings have a source in the variability of the solar magnetic field, which in turn has an influence on the dynamics of the outer layer of the Sun registered in the solar parameters. The variability of these parameters may be responsible for the occurrence pattern of TEC during the ascending phase of solar cycle 24, since the variation of TEC shows an almost similar pattern. This may further indicate similar origins, embedded in the magnetic configuration, which affects all the other parameters simultaneously.

The primary solar indices used normally are the sunspot number (SSN), the $F_{10.7}$cm index, and the solar extreme ultraviolet (EUV) index. These indices are obtained from the global daily values, measured at local noon at the Penticton Radio Observatory in Canada [*Penticton*, 2014]. Nowadays, the $F_{10.7}$cm solar radio flux may be obtained from the GPS-derived $F_{10.7}$cm index inferred from the ionospheric model coefficients transmitted in the GPS navigation signal [*Klobuchar*, 1987]. In

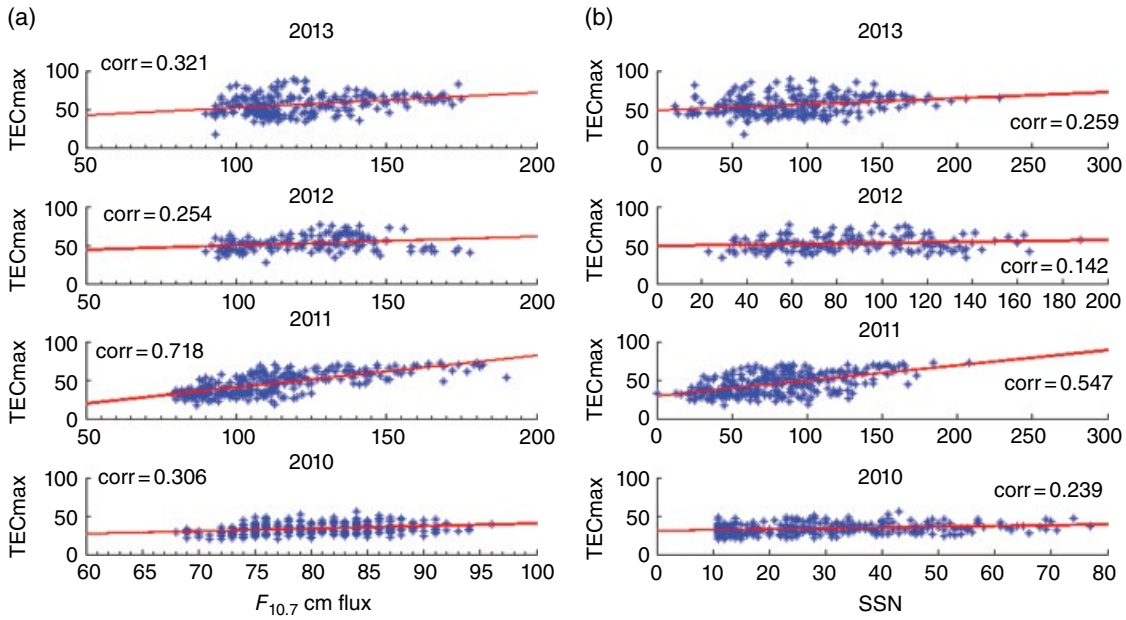


**Figure 12.3** Correlation of daily maximum TEC with (a) solar flux $F_{10.7}$ cm and (b) SSN for the years 2010 (bottom-panel) to 2013 (top-panel).

most researches, when the EUV index is unavailable, the $F_{10.7}$ cm index has been sufficient to measure the effect of the solar flux, though recent research has reported that the approximations of these indices were not so good during the recent solar minimum [*Chakrabarty et al.*, 2012].

In this research, however, we investigate the correlation of TEC with solar parameters using only the SSN and the $F_{10.7}$ cm index. The correlation of these indices with TEC is shown in Figure 12.3, for the years 2010–2013. The figure shows the correlation of maximum TEC with the $F_{10.7}$ cm index in the left panel and with the SSN in the right panel. The correlation coefficient of TEC with the $F_{10.7}$ cm index is 0.306, 0.718, 0.254, and 0.321, while with SSN it is 0.239, 0.549, 0.239, and 0.259 for the years 2010, 2011, 2012, and 2013, respectively. (The correlation coefficient values are indicated on the plots.)

It can be seen that during 2011 both indices show highest correlation with maximum TEC, with the $F_{10.7}$ cm index giving a better correlation than the SSN. In general, the electron population in the ionosphere is controlled by the solar photoionization process, which enhances the background electron density within the ionosphere. The SSN, on the other hand, is an indication of the degree of the sunspot activity. The period of 2011 is when the solar flux exhibited a steep rise from the seemingly quiet period of 2010 (shown in Fig. 12.2). A very good correlation of TEC with the $F_{10.7}$ cm flux has been reported by researchers in the anomaly crest region [e.g., *Chakrabarty et al.*, 2012, and references therein; *Chauhan et al.*, 2011], who reported a higher correlation of TEC with the $F_{10.7}$ cm flux than with SSN.

## 12.4. CONCLUSIONS

An investigation of the correlation between the total electron content and solar activity has been carried out during the ascending phase of solar cycle 24. Results indicated that TEC was much lower in 2010 than the corresponding months of 2011–2013. This was corroborated with solar indices, which were consistently low in 2010, but showed a steep rise in 2011, attaining maximum values, and maintaining relatively high values in 2012. The diurnal variation of TEC over this period showed that the equinoctial months exhibited much higher TEC values than the solstice months during the period of observation, with the equinoctial months exhibiting some asymmetry between the vernal and autumnal equinoxes. The month-to-month variation of TEC shows the interdependence of seasonal and solar parameters on TEC, with TEC exhibiting a more seasonal dependence than the solar-parameter dependence. The correlation coefficient of daily maximum TEC with the solar indices gave the highest correlation during 2011, with the $F_{10.7}$ cm flux giving a better correlation than the SSN.

## ACKNOWLEDGMENTS

Data for solar indices were obtained from World Data Center catalog: http://www.swpc.noaa.gov/ftpmenu/indices/old_indices.html and http://wdc.kugi.kyoto-u.ac.jp/dst_provisional/index.html.

The authors would like to extend their gratitude to Boston College and the Air Force Research Laboratory (AFRL), USA, who supplied the GPS receiver used in this research.

## REFERENCES


Akala, A. O., A. B. Rabiu, E. O. Somoyed, E. O. Oyeyemi, and A. B. Adeloye (2013), The response of African equatorial GPS-TEC to intense geomagnetic storms during the ascending phase of solar cycle 24, *J. Atmos. Solar Terr. Phys.*, *98*, 50–62; doi:10.1016/j.jastp.2013.02.006.

Anderson, D., A. Anghel, J. Chau, and O. Veliz (2004), Daytime vertical E × B drift velocities inferred from ground-based magnetometer observations at low latitudes, *Space Weather*, *2*, S11001; doi:10.1029/2004SW000095.

Basu, S., F. J. Rich, K. M. Groves, E. MacKenzie, C. Coker, Y. Sahai, P. R. Fagundes, and F. B. Guedes (2007), Response of the equatorial ionosphere at dusk to penetration electric fields during intense magnetic storms, *J. Geophys. Res.*, *112*, A08308; doi:10.1029/2006JA012192.

Carrano, C. S. (2007), GPS-SCINDA: A real-time GPS data acquisition and ionospheric analysis system for Scinda, Atmosph. and Environ. Res., Inc., GPS-SCINDA.

Carrano, C. S., and K. Groves (2006), The GPS segment of the AFRL-SCINDA global network and the challenges of real-time TEC in the equatorial ionosphere, ION NTM, Monterey, California, 1036–1047.

Chakrabarty, D., M. S. Bagiya, S. V. Thampi, and K. N. Iyer (2012), Solar EUV flux (0.1–50 nm), F10.7 cm flux, sunspot number and total electron content in the crest region of the ionization anomaly during the deep minimum between solar cycle 23 and 24, *Indian J. Radio and Space Phys.*, *41*, 110–120.

Chauhan, V., O. P. Singh, and B. Singh (2011), Diurnal and seasonal variation of GPS-TEC during a low solar activity period as observed at a low latitude station Agra, *Indian J. Radio and Space Phys.*, *40*, 26–36.

Dabas, R. S., L. Singh, D. R. Lakshmi, P. Subramanyam, P. Chopra, and S. C. Garg (2003), Evolution and dynamics of equatorial plasma bubbles: relationships to ExB drift, post-sunset total electron content enhancements, and equatorial electrojet strength, *Radio Sci.*, *38*; doi:10.1029/2001RS002586.

DasGupta, A., D. N. Anderson, and J. A. Klobuchar (1983), Equatorial F region ionization differences between March and September, 1979, *Adv. Space Res.*, *10*, 199–202; doi:10.1016/0273-1177(82)90390-8.

Dashora, N., and R. Pandey (2005), Observations in equatorial anomaly region of total electron content enhancements and depletions, *Ann. Geophys.*, *23*, 2449–2456; doi:10.5194/angeo-23-2449-2005.

D'ujanga, F. M., J. Mubiru, B. F. Twinamasiko, C. Basalirwa, and T. S. Senyonga (2012), Total electron content variations in equatorial anomaly region, *Adv. Space Res.*, *50*, 441–449; doi:10.1016/j.asr.2012.05.005.

D'ujanga, F. M., P. Baki P, J. O. Olwendo, and B. F. Twinamasiko (2013), Total electron content of the ionosphere at two stations in East Africa during the 24–25 October 2011 geomagnetic storm, *Adv. Space Res.*, *51*, 712–721; doi:10.1016/j.asr.2012.09.040.

Gupta, J. K., and L. Singh (2001), Long term ionospheric electron content variations over Delhi, *Ann. Geophys.*, *18*, 1635–1644; doi:10.1007/s00585-001-1635-8.

Hanson, W. B., and R. J. Moffett (1966), Ionization transport effects in the equatorial *F* region, *J. Geophys. Res.*, *71*(23), 5559–5572; doi:10.1029/JZ071i023p05559.

Klobuchar, J. A. (1987), Ionospheric time-delay algorithm for single-frequency GPS users, *IEEE Trans. Aerospace and Electronic Sys.*, AES-23(3), 325–331; doi:10.1109/TAES.1987.310829.

Olwendo, O. J., P. Baki, P. J. Cilliers, C. Mito, and P. Doherty (2013), Comparison of GPS TEC variations with IRI-2007 TEC prediction at equatorial latitudes during a low solar activity (2009–2011) phase over the Kenyan region, *Adv. Space Res.*, *52*, 1770–1779; doi:10.1016/j.asr.2012.08.001.

Paznukhov, V. V., C. S. Carrano, K. M. Groves, R. G. Caton, C. E. Valladares, G. K. Semaala, C. T. Bridgwood, J. Adeniyi, L. L. N. Amaeshi, B. Damtie, F. M. D'ujanga, J. O. H. Ndeda, P. Baki, O. K. Obrou, B. K. Okere and G. M. Tsidu (2012), Equatorial plasma bubbles and L-band scintillations in Africa, *Ann. Geophys.*, *30*, 675–682; doi:10.5194/angeo-30-675-2012.

Penticton, Canada, Space Environment Center (SEC), Boulder, Colorado: http://www.geomag.bgs.ac.uk/data_service/space_weather/forecast.html.

Rama Rao, P. V. S., S. G. Krishna, J. V. Prasad, S. N. V. S. Prasad, D. S. V. V. D Prasad, and K. Niranjan (2009), Geomagnetic storm effects on GPS based navigation, *Ann. Geophys.*, *27*, 2101–2110.

Rama Rao, P. V. S., S. G. Krishna, K. Niranjan, and D. S. V. V. D. Prasad (2006a), Study of spatial and temporal characteristics of L-band scintillations over the Indian low-latitude region and their possible effects on GPS navigation, *Ann. Geophys.*, *24*, 1567–1580; doi:10.5194/angeo-24-1567-2006.

Rama Rao, P. V. S., S. G. Krishna, K. Niranjan, and D. S. V. V. D. Prasad (2006b), Temporal and spatial variations in TEC using simultaneous measurements from Indian GPS network of receivers during the low solar activity period of 2004–2005, *Ann. Geophys.*, *24*, 3279–3292; doi:10.5194/angeo-24-3279-2006.

Ray, S., and A. DasGupta (2007), Geostationary L-band signal scintillation observations near the crest of equatorial anomaly in the Indian zone, *J. Atmos. Solar Terr. Phys.*, *69*, 500–514; doi:10.1016/j.jastp.2006.09.007.

Sardon, E., and N. Zarraoa (1997), Estimation of total electron content using GPS data: How stable are the differential satellite and receiver instrumental biases? *Radio Sci.*, *32*, 1899–1910; doi:10.1029/97RS01457.

Seemala, G. (2012), Rinex GPS-TEC program, version 2.2, Boston College, http://seemala.blogspot.com/.

Sripathi, S., B. Kakad, and A. Bhattacharyya (2011), Study of equinoctial asymmetry in the Equatorial Spread F (ESF) irregularities over Indian region using multi-instrument observations in the descending phase of solar cycle 23, *J. Geophys. Res.*, *116*, A11302; doi: 10.1029/2011JA016625.

Valladares, C. E., J. Villalobos, R. Sheehan, and M. P. Hagan (2004), Latitudinal extensions of low-latitude scintillations measured with a network of GPS receivers, *Ann. Geophys.*, *22*, 3155–3175; doi:10.5194/angeo-22-3155-2004.

Wong, A. (2009), US space-based PNT international cooperation and support in Africa, paper presented at Satellite & Navig. Sci. and Tech. for Africa Workshop, ICTP, Trieste, Italy, 23 March–9 April, sponsored by Bureau of Oceans & Environ. Sci.

# 13

# Longitudinal Dependence of Day-to-Day Variability of Critical Frequency of Equatorial Type Sporadic *E* ($f_oE_{sq}$)

**Emmanuel O. Somoye,[1] Andrew O. Akala,[2] Aghogho Ogwala,[1] Eugene O. Onori,[1] Rasaq A. Adeniji-Adele,[1] and Enerst E. Iheonu[1]**

## ABSTRACT

The longitudinal effect on the day-to-day variability (VR) of the critical frequency of equatorial type sporadic *E* ($f_oE_{sq}$) is studied. Data from three equatorial stations, one from west of Greenwich Meridian (GM), one in the neighborhood of GM, and one from east of GM, namely Huancayo (12°S, 75.3°W, 3.92° dip [1971]), Ouagadougou (12.4°N, 1.5°W, 2.98° dip [1989]), and Manila (14.7°N, 121.1°E, 14.8° dip [1989]), respectively, were used for the study. The variability of $f_oE_{sq}$ is characterized by sunrise and sunset peaks in the neighborhood of GM during very high solar activity (VHSA; Rz > 120) and high solar activity (HSA; 80 < Rz < 120). During moderate solar activity (MSA; 50 < Rz < 80), no diurnal trend is observed at Ouagadougou. At Huancayo, west of GM, $f_oE_{sq}$ VR is greater during nighttime and sunrise during all three levels of solar activity; while at Manila, east of GM, it is greater during noon and sunset during all three levels of solar activity in general. The $f_oE_{sq}$ VR is found to be greater during the solstices in all the stations and during all three levels of solar activity. Overall, $f_oE_{sq}$ VR is to be greater at Huancayo than at Manila and least at Ouagadougou, while it increases with sunspot number (Rz), in general.

**Key Points:**

At different longitudinal sectors different diurnal trends of $f_oE_{sq}$ relative variability are observed.

Peaks of $f_oE_{sq}$ relative variability occur at sunrise and sunset in the neighbourhood of Greenwich Meridian.

Relative variability of $f_oE_{sq}$ occurs at nighttime and sunrise west of Greenwich Meridian and at noon and sunset east of Greenwich Meridian

Relative variability of $f_oE_{sq}$ is greater west of Greenwich Meridian than at east and in the neighbourhood of Greenwich Meridian.

**Key Terms:** *E* layer, ionosphere, longitudinal effect, Sporadic *E*

## 13.1. INTRODUCTION

The unique role of the ionosphere in the near-Earth environment cannot be overemphasized. The ionosphere is coupled to both the lower atmosphere and to the magnetosphere above it. The effect of the atmosphere from below is regarded as the main source of its day-to-day

[1]*Department of Physics, Lagos State University, Ojo, Lagos, Nigeria*

[2]*Department of Physics, University of Lagos, Akoka, Lagos, Nigeria*

*Ionospheric Space Weather: Longitude and Hemispheric Dependences and Lower Atmosphere Forcing, Geophysical Monograph 220*, First Edition. Edited by Timothy Fuller-Rowell, Endawoke Yizengaw, Patricia H. Doherty, and Sunanda Basu.

variability [*Pulinets et al.*, 2007], while the effect of the magnetosphere is such that solar-wind energy transmitted into the magnetosphere from the Sun may induce influences of different magnitude in the complex morphology of the electric field, temperature, winds, and composition, and affect all ionospheric parameters [*Wang et al.*, 2007].

Between the latitudes with magnetic dip angles in the range –5° to 5°, the geomagnetic field lines are almost horizontal and do not allow electrical charge to leak away to other latitudes, thereby creating vertical polarization fields [*Rajaram and Rastogi*, 1977]. The flow of charge in the east-west direction referred to as equatorial electrojet (EEJ) is thus amplified. The interaction of the EEJ current with the horizontal magnetic field cause $\mathbf{E}\times\mathbf{B}$ uplift of ionization, which subsequently diffuses along the field lines to subtropical latitudes. Thus, ionization is maximum at latitudes ±20° to ±25° instead of at the equator, a phenomenon referred to as the equatorial ionization anomaly (EIA).

While the mechanism and formation of the normal $E$ layer is mainly by photoionization of molecular nitrogen and oxygen, being largely a Chapman layer depending mostly on the activity and zenith angle, $\chi$, of the sun [*Vanzandt*, 1967], that of sporadic $E$ ionization, though situated at the same height of about 100 km as the normal $E$ layer ionization, is different. The mechanism of the formation of sporadic $E$ ionization, $E_s$, differs with latitude. At the aurora and polar cap regions, $E_s$ is due to the precipitation of energetic particles [*Prasad et al.*, 2012] while the occurrence of midlatitude $E_s$ is explained by the wind shear theory of *Whitehead* [1961]. At the equator and low-latitude regions, the large electrojet current gives rise to plasma instabilities causing $E_s$ ionization. The equatorial $E_s$, designated as $E_{sq}$, is thus a plasma irregularity, which is of interest from the standpoint of plasma physics. The $E_{sq}$ is exploitable for radio communication by scattering [*Cohen*, 1967; *Resende and Denardini*, 2012].

The need for more studies of the day-to-day ionospheric variability due to "weather" and not just that of "climatological" or mean behavior of the ionosphere has been pointed out by such researchers as *Bilitza* [2000], *Rishbeth and Mendillo* [2001], and *Forbes et al.* [2000]. One of the ionospheric characteristics whose space-weather effect has not received much attention especially in the equatorial and low-latitude areas is $E_{sq}$. *Pedatella et al.* [2011] mentioned the existence of longitudinal variability in the equatorial electrojet in which the irregularities responsible for $E_{sq}$ is embedded. It is the purpose of this study to investigate the space-weather effect of $f_oE_{sq}$ at some equatorial and low-latitude stations with a view to determining its longitudinal variability and the effect of season on $f_oE_{sq}$ VR at different longitudinal sectors. It is also hoped that the results of this will augment the data used for ionospheric models such as International Reference Ionosphere (IRI).

## 13.2. METHOD

The data used for this study are the $f_oE_{sq}$ hourly values determined from ionosonde data measured at Huancayo (American sector), Ouagadougou (African sector), and Manila (Asian sector) over the period from 1959 to 1993. The data for the three stations were downloaded from Space Physics Interactive Data Research (SPIDR) website (http://spidr.ngdc.noaa.gov/). Data were selected for days on which Kp < 3. Thus, the data used in this study can be regarded as those of quiet days [*Umoh and Adeniyi*, 1995]. The data for each year were grouped into different seasons on a monthly basis: March equinox (February, March, and April), June solstice (May, June, and July), and September equinox (August, September, and October), December solstice (November, December, and January), in order to show seasonal influence. The plots of sunspot number, Rz, and Kp indices for the years considered are shown in Figure 13.1. Table 13.1 shows the coordinates of the stations whose data were used in this study while Table 13.2 shows the selection of epochs for each station based on solar cycle activity.

It is important to mention that by definition $f_oE_{sq}$ is attributed to the maximum frequency observed for the ordinary trace of the $E_s$ layer. However, since the ordinary and extraordinary traces are indistinguishable, a top frequency for $E_s$ is used as a proxy of the $f_oE_{sq}$ [*Bibl et al.*, 1955; *Rishbeth and Garriot*, 1969]. The accuracy of $f_oE_{sq}$ autoscaling at 95% confidence level is ±0.6 MHz.

The relative variability (VR) of ionospheric characteristics is defined as the quotient of standard deviation, $\sigma$ and mean value $\mu$ [*Forbes et al.*, 2000; *Bilitza et al.*, 2004; *Somoye and Akaka*, 2010; *Somoye et al.*, 2011, 2012; *Akala et al.*, 2010]. Thus,

$$VR(\%) = \frac{\sigma}{\mu}\times 100 \tag{13.1}$$

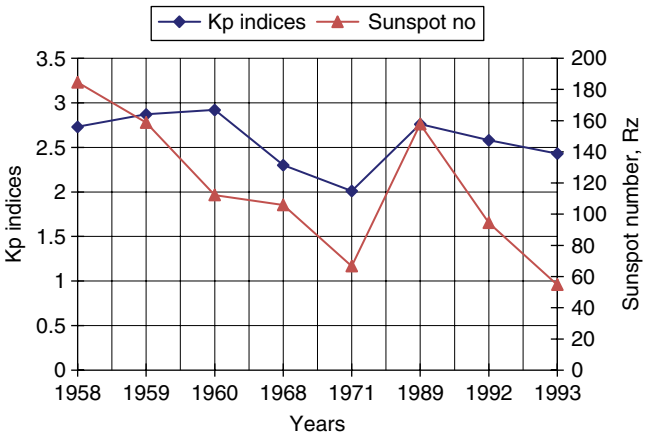


**Figure 13.1** Plots of Kp indices and annual sunspot number, Rz, for the years considered. A yearly average is simply determined from Kp monthly average (following monthly average determination of Ap index by *Rishbeth and Mendillo* [2001]).

**Table 13.1** Coordinates, Magnetic Inclination (Dip), and Magnetic Declination (D) of Stations

| Station | Geographic latitude | Geographic longitude | Dip | D |
|---|---|---|---|---|
| Huancayo | 12°S | 75.3°W | 1959: 5.2° | 1959: 1.98° |
| | | | 1968: 4.24° | 1968: 1.95° |
| | | | 1971: 3.92° | 1971: 1.95° |
| Ouagadougou | 12.4°N | 1.5°W | 1968: 5.7° | 1968: –7.74° |
| | | | 1971: 5.32° | 1971: –7.45° |
| | | | 1989: 2.98° | 1989: –5.29° |
| Manila | 14.70°N | 121.1°E | 1989: 14.8° | 1989: –0.94° |
| | | | 1992: 15.05° | 1992: –1.0° |
| | | | 1993: 15.15° | 1993: –1.02° |

*Source:* http://www.ngdc.noaa.gov/geomag-web/#igrfwmm.

**Table 13.2** Classification of Zurich Sunspot Numbers and Data Years Used for Each Station

| | Years used | | |
|---|---|---|---|
| Station | MSA (50 < Rz < 80) | HSA (80 < Rz < 120) | VHSA (Rz > 120) |
| Huancayo | 1971 (Rz = 68.8) | 1968 (Rz = 105.9) | 1959 (Rz = 159) |
| Ouagadougou | 1971 (Rz = 68.8) | 1968 (Rz = 105.9) | 1989 (Rz = 157.6) |
| Manila | 1993 (Rz = 54.8) | 1992 (Rz = 94.5) | 1989 (Rz = 157.6) |

The VR of ionospheric characteristics is a statistical tool that quantifies the extent of deviation or spread of each data point from the computed mean from the entire dataset. The merit of the formula in Equation (13.1) over other methods used for determining the relative variability is that deviation of all daily values from mean is considered, indicating that the whole dataset is used. The demerit of this method, however, is in the difficulty of its interpretation in terms of probability [*Bilitza et al.*, 2004].

Other methods of determining variability include:

1. VR (%) = Interquartile range/median × 100, that is,

$$VR(\%) = \frac{q_{75} - q_{25}}{median} \times 100 \tag{13.2}$$

The only advantage of this method is that it is easy to interpret in terms of probability while it has the disadvantage of using only 50% of the data. The method has been used by *Zhang et al.* [2004] and *Ezquer et al.* [2004].

2. VR (%) = Interdecile range/median × 100, that is,

$$VR(\%) = \frac{q_{90} - q_{10}}{median} \times 100 \tag{13.3}$$

This method, which was used by *Fotiadis et al.* [2004], covers 80% of the data points and ignores the remaining 20%.

3. VR (%) = Range/median × 100

While this is a possible method of determining variability, it has not been used in literature possibly because of the simplistic nature of range as a measure of dispersion.

4. A method used by *Kouris and Fotiadis* [2002] in determining variability is

$$dx = \frac{x_i - \bar{x}}{\bar{x}} \tag{13.4}$$

$x_i$ being hourly daily values of each parameter and $\bar{x}$, the corresponding hourly monthly median value.

## 13.3. RESULTS AND DISCUSSION

The diurnal plots of the VR of $f_oE_{sq}$ for different seasons for Huancayo (12°S, 75.3°W, 3.92° dip [1971]), Ouagadougou (12.4°N, 1.5°W, 2.98° dip [1989]), and Manila (14.7°N, 121.1°E, 14.8° dip [1989]) are shown in Figures 13.2a–c, 13.3a–c, and 13.4a–c during the three epochs of the solar cycle: very high solar activity (VHSA), high solar activity (HSA), and moderate solar activity (MSA). Low solar activity (LSA) is not considered since $f_oE_{sq}$ VR is not found to show diurnal trend during LSA [*Somoye et al.*, 2013).

The trends in the diurnal plots with solar activity are different in the longitudinal sectors considered in this study. During VHSA, the VR of $f_oE_{sq}$ at Huancayo peaks at nighttime (i.e., 22:00–02:00 [~65%]) and at sunrise (i.e., 05:00–07:00 [~60%]) and generally during the period from midnight to noon in all seasons. During epochs with VHSA, the VR of $f_oE_{sq}$ at Ouagadougou has different diurnal trends in different seasons. While the diurnal trend for the June solstice shows nighttime (~32%) and sunset (i.e., 18:00–20:00 [~30%]) peaks, that of the September

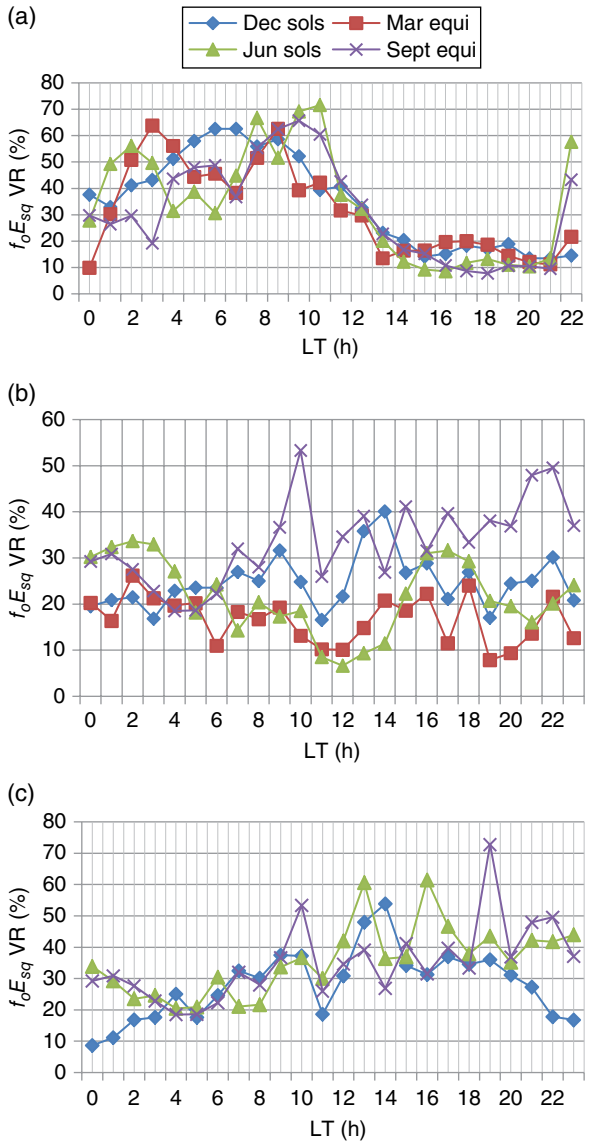


**Figure 13.2** Diurnal variation during VHSA of the VR of $f_oE_{sq}$ for all seasons for (a) Huancayo, (b) Ouagadougou, and (c) Manila.

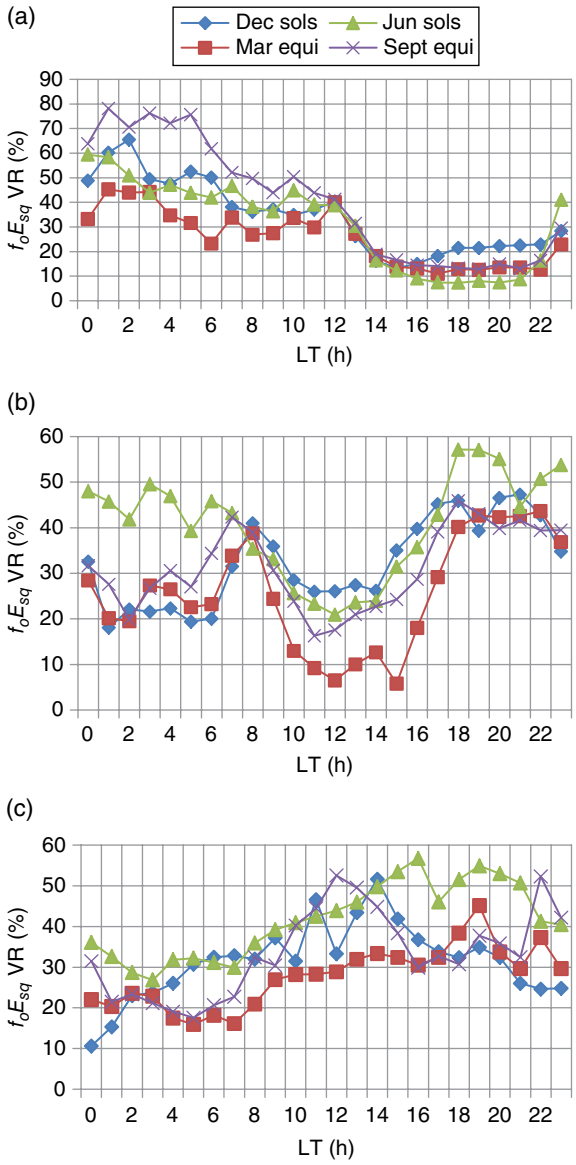


**Figure 13.3** Diurnal variation during HSA of the VR of $f_oE_{sq}$ for all seasons for (a) Huancayo, (b) Ouagadougou, and (c) Manila.

equinox shows noon (~53%) and nighttime (~49%) peaks. The diurnal trends of the March equinox and December solstice are not well defined at Ouagadougou. During VHSA, the VR of $f_oE_{sq}$ at Manila peaks occur from noon (i.e., 10:00–14:00 [~58%]) to sunset (~72%) and generally during the second half of the day during all seasons.

During HSA, the VR of $f_oE_{sq}$ at Huancayo exhibit peaks during nighttime namely ~42%, ~56%, ~76%, ~64%, respectively, for the March equinox, June solstice, September solstice, and December solstice. while the VR of $f_oE_{sq}$ at Ouagadougou is characterized, generally, by postsunrise (~46%) and postsunset (~55%) peaks for all seasons. During HSA, the VR of $f_oE_{sq}$ at Manila is characterized by noon (~52%) and sunset (~54%) peaks for all seasons.

During MSA, the VR of $f_oE_{sq}$ at Huancayo peaks are observed during nighttime (~70%) and before noon (~64%), while at Ouagadougou the VR of $E_{sq}$ is characterized by postsunrise (~48%) and postsunset (~64%) peaks during all seasons. During MSA, the VR of $f_oE_{sq}$ at Manila is characterized by noon (~56%) and postsunset (~47%) peaks, during all seasons. The foregoing indicates longitudinal variation of $f_oE_{sq}$ VR as its maximum value occurs at different times of the day for the three stations.

Longitudinal variation of $f_oE_{sq}$ VR is most likely due to the electrojet current, which has been found to show day-to-day variability [*Oyinloye and Akinrimisi*, 1976] as well as longitudinal variability [*Cohen*, 1967]. The irregularity responsible for $E_{sq}$ is embedded in the electrojet current. *Pedatella et al.* [2011] mentioned the presence of longitudinal variability in the electrojet current. The $E_{sq}$ ionization and the equatorial electrojet current are highly

correlated in their temporal variations [*Matsushita*, 1962a; 1962b] and in their spatial distribution [*Rastogi*, 1973]. *Ren et al.* [2009] pointed out that magnetospheric electric fields, which penetrate from high latitude to the equator even during magnetically quiet times, vary with universal time and may also cause longitudinal variations of equatorial electric fields and therefore that of $f_oE_{sq}$ VR. *Yizengaw et al.* [2012] mentioned that the difference in the behavior of one longitude sector to the other results from the formation of the global wavenumber-four structure due to the different vertical $\mathbf{E}\times\mathbf{B}$ drift magnitudes at different longitudinal sectors.

In order to further investigate variation of $f_oE_{sq}$ VR of the three stations with seasons, the monthly plots of $f_oE_{sq}$ VR of Huancayo in the American sector, Ouagadougou in the African sector, and Manila in the Asian sector are illustrated in Figures 13.5a–c, 13.6a–c, and 13.7a–c during VHSA, HSA, and MSA, respectively. Each plot shows the variation with months for LT bins 22:00–02:00 (nighttime), 05:00–07:00 (sunrise), 10:00–14:00 (noon), and 18:00–20:00 (sunset) based on the recommendation given in the International Reference Ionosphere (IRI) Task Force Activity [*Bilitza*, 2001].

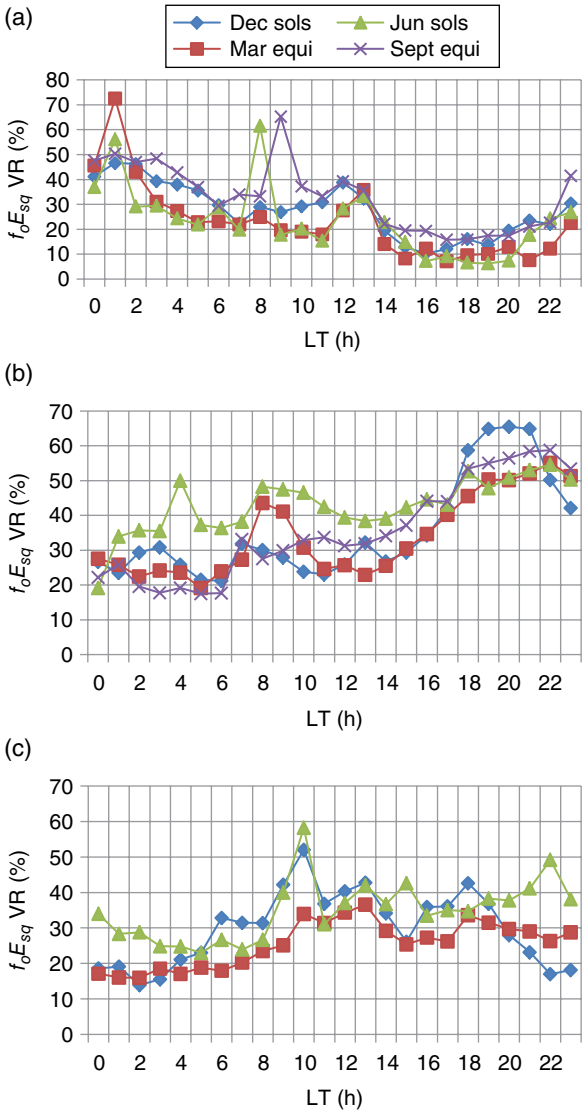


**Figure 13.4** Diurnal variation during MSA of the VR of $f_oE_{sq}$ for all seasons for (a) Huancayo, (b) Ouagadougou, and (c) Manila.

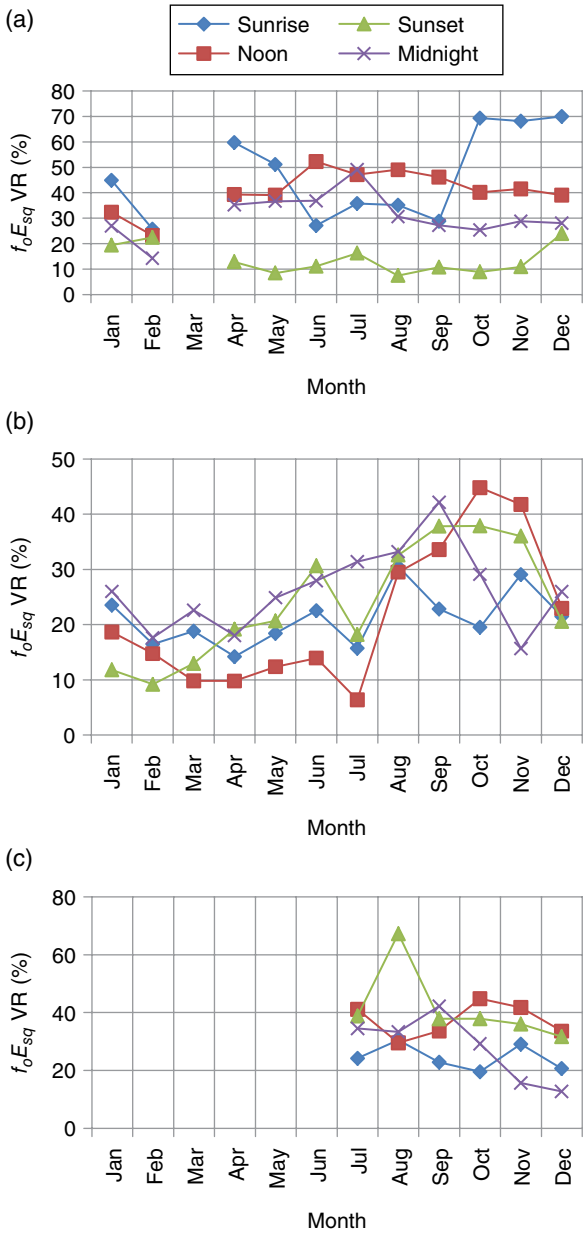


**Figure 13.5** Monthly variation during VHSA of the VR of $f_oE_{sq}$ for all seasons for (a) Huancayo, (b) Ouagadougou, and (c) Manila. No data were available from Manila for the first half of the year during the epochs selected by VHSA, and no data were available from Huancayo during March for VHSA.

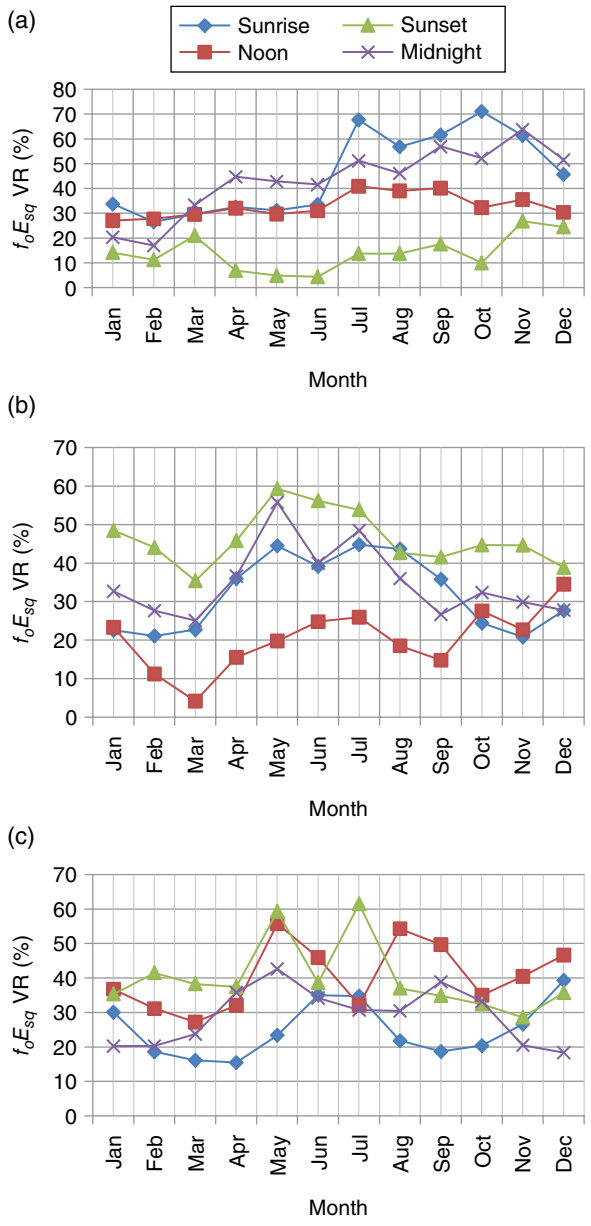


**Figure 13.6** Monthly variation during HSA of the VR of $f_oE_{sq}$ for all seasons for (a) Huancayo, (b) Ouagadougou, and (c) Manila.

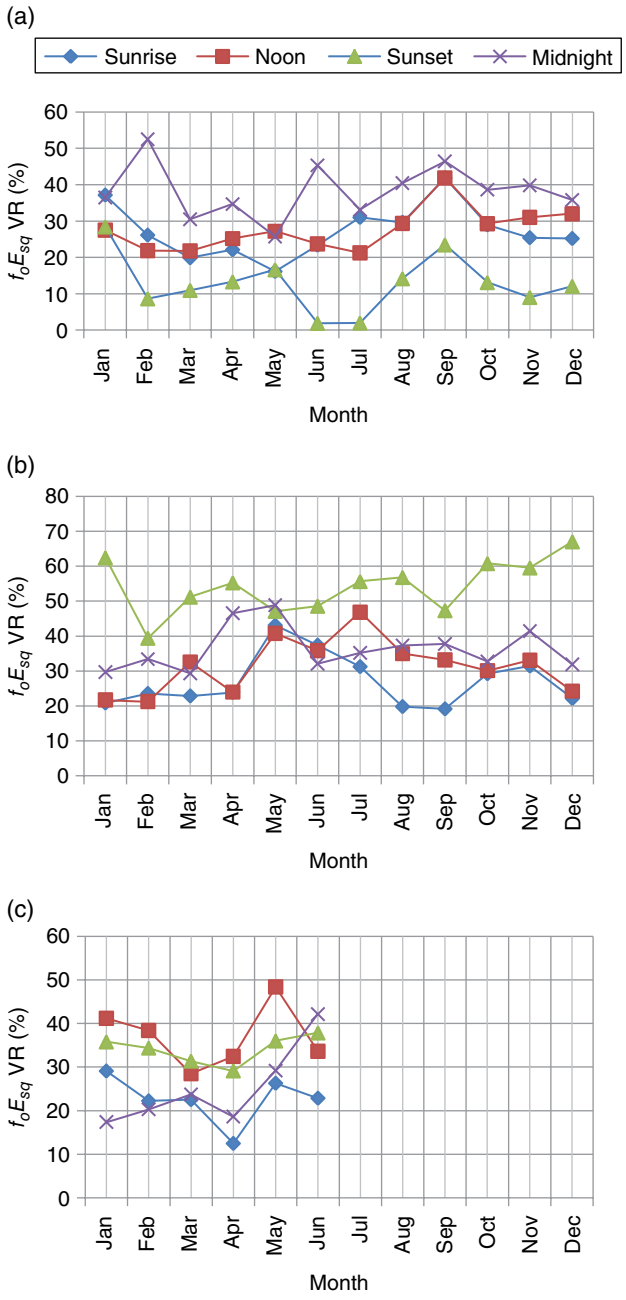


**Figure 13.7** Monthly variation during MSA of the VR of $f_oE_{sq}$ for all seasons for (a) Huancayo, (b) Ouagadougou, and (c) Manila. No data were available from Manila for the second half of the year during the epochs selected for MSA.

During epochs with the same solar activity level, the VR of $f_oE_{sq}$ at Huancayo is maximum in the March equinox (62%) and December solstice (60%), while the VR of $f_oE_{sq}$ at noon is at a maximum during the June solstice (~70%). It is observed that at Ouagadougou, the VR of $f_oE_{sq}$ during VHSA is greater at nighttime and noon during the September equinox (~60% and ~53%). At Manila, the VR of $f_oE_{sq}$ at sunset was found to be greatest during the September equinox (~72%), while the noon VR is at a maximum in October (~48%), (data were available only for July to December at Manila during VHSA).

During HSA, the VR of $f_oE_{sq}$ at Ouagadougou (Fig. 13.6b) is greatest during the June solstice at all times of the day, namely, nighttme (~58%), sunrise (~45%), noon (~28%), and sunset (~60%). The VR of $f_oE_{sq}$ of Manila (Fig. 13.6c) at sunrise has a maximum during June solstice (~70%) and during the September equinox (~72%), while at Manila (Fig. 13.6c), the VR of $f_oE_{sq}$ at sunset has a maximum during the June solstice (~60%).

The VR of $f_oE_{sq}$ is more frequently larger during the solstices, especially the June solstice, than the equinoxes. The peak during the September equinox at Huancayo at sunrise (Fig. 13.6a) is an exception to this general observation. The $E_{sq}$ in the African sector is found to be maximum during the equinox [*Onwumechili*, 1967). It is thus expected that the VR of $f_oE_{sq}$ should be minimum at the equinox and maximum during the solstices, the VR of $f_oE_{sq}$ being inversely proportional to the mean of $f_oE_{sq}$ (see Equation [13.1]).

In general, the VR of $f_oE_{sq}$ is found to be greatest at Huancayo, west of GM, being in the range 10%–74%, 6%–78%, and 5%–71% during VHSA, HSA, and MSA, respectively; followed by Manila, east of GM, with 10%–72%, 10%–56%, and 14%–56% during the three solar activity levels, respectively; and least at Ouagadougou, close to GM with 6%–53%, 6%–58%, and 16%–66% during the three solar activity levels, respectively. The VR of $f_oE_{sq}$ at Huancayo is clearly greater than $f_oE_{sq}$ VR at Manila and Ouagadougou during the three epochs. The peak VR of $f_oE_{sq}$ is greater at Huancayo and Manila than at Ouagadougou during VHSA, while it is greater at Ouagadougou than at other locations during MSA. During HSA, the peak VR of $f_oE_{sq}$ is about the same at all three locations. The greater VR of $f_oE_{sq}$ at Huancayo, west of Ouagadougou and Manila agrees with the result of *Akala et al.* [2011) for VR of $f_oF_2$.

That the VR of $f_oE_{sq}$ is greatest at Huancayo during all solar activity levels is likely due to this location having the largest magnetic declination. The American sector is characterized by larger magnetic declination than other longitudinal sectors. Magnetic declination effects have been invoked to explain the seasonal and longitudinal variations of spread *F* (another irregularity triggered by Gradient Drift Instability [GDI] and Rayleigh-Taylor Instability [RTI]), that is, plasma instability. While equatorial spread *F* is triggered by GDI and RTI, the $E_{sq}$ irregularity is explained by the two-stream instability theory of *Farley* [1963]. *Abdu et al.* [1981] and *Sagawa et al.* [2005] pointed out that the diverse electrodynamic process in the equatorial and low-latitude stations arises from the larger magnetic declinations in the American sector than at other longitudinal sectors.

While the diurnal trend in the VR of $f_oE_{sq}$ at Huancayo seems to be independent of solar activity, the VR of $f_oE_{sq}$ is observed to increase with solar activity at Manila and decrease with solar activity at Ouagadougou. It is necessary to mention that the solar activity of days considered is not extreme, thus high solar-flare activity, which results in ionospheric disturbances due to its effects on thermospheric neutral density [*Ben'kova et al.*, 1983; *Blagoveshchensky et al.*, 2006a; *Blagoveshchensky et al.*, 2006b], is avoided.

## 13.4. CONCLUSION

Diurnal plots of the variability of $f_oE_{sq}$ show longitudinal dependence through different trends occurring at the different longitudes. At Huancayo in the American sector, the VR is characterized by greater values at nighttime and sunrise than during other parts of the day. Sunrise and sunset peaks occur at Ouagadougou in the African sector. At Manila in the Asian sector, the VR values during noon and sunset are greater than at other hours of the day.

Longitudinal differences also occur in the magnitude of the variability of $f_oE_{sq}$. The VR is generally found to be greater at Huancayo, than at the more easterly locations of Manila and Ouagadougou.

The seasonal variation of $f_oE_{sq}$ is characterized by VR generally being greatest during the equinoxes. This is possibly because at the equatorial $E_{sq}$, ionization has its peak during the equinox.

## REFERENCES


Abdu, M. A., J. A. Bittencourt, and I. S. Batista (1981), Magnetic declination control of the equatorial F region dynamo electric field development and spread F, *J. Geophys. Res.*, *86*(A13), 443–446; doi:10.1029/JA086iA13p11443.

Akala, A. O., E. O. Oyeyemi, E. O. Somoye, A. B. Adeloye, and A. O. Adewale (2010), Variability of foF2 in the African equatorial ionosphere, *Adv. Space Res.*, *45*, 1311–1314; doi:10.1016/j.asr.2010.01.003.

Ben'kova, N. P., K. N. Vasilev, V. N. Ishkov, N. S. Kaminer, E. F. Kozlov, N. M. Samorokin, L. A. Kolesnikova, E. V. Lavrova, E. V. Nepmniashchaia, A. M. Novikov, N. K. Pereyaslova, and V. V. Formichev (1983), Helio- and geophysical phenomena in July 1982, *Geomagn. Aeron.*, *23*(5), 579–582.

Bibl, K., R. Busch, K. Rawer, and K. Suchy (1955), La nomenclature Ionospherique et les conventions pour le dépouillement, *J. Atmos. Terr. Phys.*, *6*, 69–87; doi:10.1016/0021-9169(55)90013-1.

Bilitza, D. (2000), Report from 33d COSPAR Scientific Assembly, Warsaw, Poland, 16–23 July 2000, *IRI News Lett.*, *7*(3/4), 1–4.

Bilitza, D. (2001), International Reference Ionosphere 2000, *Radio Sci. 36*, 261–275.

Bilitza, D., O. K. Obrou, J. O. Adeniyi, and O. Oladipo (2004), Variability of foF2 in the equatorial ionosphere, *Adv. Space Res.*, *34*, 1901–1906; doi:10.1016/j.asr.2004.08.004.

Blagoveshchensky, D. V., T. D. Borisova, and J. W. MacDougall (2006a), Irregular HF radio propagation on a subauroral path during magnetospheric substorm, *Ann. Geophys.*, *24*, 1839–1849; doi:10.5194/angeo-24-1839-2006.

Blagoveshchensky, D. V., J. W. MacDougall, and A. V. Pyatkova (2006b), The ionsphere of Europe and North America before the magnetic storm of October 28, 2003, *Geomagn. Aeron.*, *46*(3), 350–360; doi: 10.1134/S001679320603 0091.

Cohen, R. (1967), The equatorial ionosphere, 561–613, in *Physics of Geomagnetic Phenomena*, edited by S. Matsushita and W. H. Campbell, Academic Press, New York.

Ezquer, R. G., M. Mosert, R. Corbella, M. Erazu, S. M. Radicella, M. Cabrera, and L. de la Zerda (2004), Day-to-day variability of ionospheric characteristics in the American sector, *Adv. in Space Res.*, *34*, 1887–1893; doi:10.1016/j.asr.2004.03.016.

Farley, D. T. (1963), A plasma instability resulting in field-aligned irregularities in the ionosphere, *J. Geophys. Res.*, *68*, 6083–6097; doi:10.1029/JZ068i022p06083.

Forbes, J. M., S. E. Palo, and X. Zhang (2000), Variability in the ionosphere, *J. Atmos. Solar Terr. Phys.*, *62*, 685–693; doi: 10.1016/S1364-6826(00)00029-8.

Fotiadis, D. N., G. M. Baziakos, and S. S. Kouris (2004), On the global behaviour of the day- to- day MUF variation, *Adv. Space Res.*, *33*(6), 893–901; doi:10.1016/j.asr.2003.05.005.

Kouris, S. S., and D. N. Fotiadis (2002), Ionospheric variability a comparative statistical study, *Adv. Space Res.*, *29 (6)*, 977–985; doi:10.1016/S0273-1177(02)00045-5.

Matsushita, S. (1962a), Interrelations of sporadic E and ionospheric currents, in *Ionospheric Sporadic E*, 344–375, edited by E. K. Smith, Jr., and S. Matsushita, Macmillan Publishers, New York.

Matsushita, S. (1962b), Lunal tidal variations of sporadic E, in *Ionospheric Sporadic E*, 194–214, edited by E. K. Smith and S. Matsushita, Macmillan Publishers, New York.

Onwumechili, C. A. (1967), Geomagnetic variations in the equatorial zone, 425–507, in *Physics of Geomagnetic Phenomena*, edited by S. Matsushita and W. H. Campbell, Academic Press, New York.

Pedatella, N. M., J. M. Forbes, A. Maute, A. D Richmond, T. W. Fang, K. M. Larson, and G. Milward (2011), Longitudinal variations in the F region ionosphere and topside ionosphere-plasmasphere: Observations and model simulations, *J. Geophys. Res.*, *116*, A12309; doi: 10.1029/2011JA016600.

Prasad, S. N. V. S., D. S. V. V. D. Prasad, K. Venkatesh, K. Niranjan, and P. S. V. Rama Rao (2012), Diurnal and seasonal variation in sporadic E layer (Es layer) occurrences over equatorial, low and mid-latitude stations: A comparative study, *Indian J. Radio Space Phys.*, *41*, 26–38.

Pulinets, S. A., A. N. Kotsarenko, L. Cilaolo, and I. A. Pulinets (2007), Special case of ionospheric day-to-day variability associated with earthquakes preparations, *Adv. Space Res.*, *39*, 970– 977; doi:10.1016/j.asr.2006.04.032.

Rajaram, G., and R. G. Rastogi (1977), Equatorial electron densities- seasonal and solar cycle changes, *J. Atmos. Terrs. Phys.*, *39*, 1175–1182; doi:10.1016/0021-9169(77)90026-5.

Rastogi, R. G. (1973), The effect of polar magnetic substorms on the equatorial sporadic E. *Proc. Ind. Acad. of Sc.*, *A*, *77*(3), 130–138; doi:10.1007/BF03049514.

Ren, Z., W. Wan, L. Liu, R. A. Heelis, B. Zhao, Y. Wei, and X. Yue (2009), Influences of geomagnetic fields on longitudinal variations of vertical plasma drifts in the pre-sunset equatorial topside ionosphere, *J. of Geophys. Res.*, *114*, A03305; doi:10.1029/2008JA013675.

Resende, L. C. A., and C. M. Denardini (2012), Equatorial sporadic E layer abnormal density enhancement during the recovery phase of the December 2006 magnetic storm: A case study, *Earth Planet Space*, *64*, 345–351; doi:10.5047/eps.2011.10.007.

Rishbeth, H., and M. Mendillo (2001), Patterns of F2-layer variability, *J. Atmos. Solar Terr. Phys.*, *63*, 1661–1680; doi:10.1016/S1364-6826(01)00036-0.

Rishbeth, H., and O. K. Garriot (1969), *Introduction to Ionospheric Physics*, Academic Press, New York.

Sagawa, E., T. J. Immel, H. U. Frey, and S. B. Mende (2005), Longitudinal structure of the equatorial anomaly in the nighttime ionosphere observed by IMAGE/FUV, *J. Geophys. Res.*, *110*, A11302; doi:10.1029/2004JA010848.

Somoye, E. O., and A. O. Akala (2010), NmF2 variability at equatorial and low latitude station: a review, *Res. J. Phys.*, *4*, 2, 50–55; doi:10.3923/rjp.2010.50.55.

Somoye, E. O., and A. O. Akala (2011), Comparison of diurnal, seasonal and latitudinal effect of MUF VR and NmF2 VR during some solar cycle effect, *Adv. Space Res.*, *47* (2011) 2182–2187; doi:10.1016/j.asr.2010.11.005.

Somoye, E. O., A. O. Akala, R. A. Adeniji-Adele, E. E. Iheonu, E. O. Onori, and A. Ogwala, (2012), Solar cycle and seasonal variation of F2 layer nighttime/daytime ionization ratio at the equatorial station of Ibadan, Nigerian Union of Radio Science (NURS) 5th Annual Conference Proceedings, 108–111.

Somoye, E. O., A. O. Akala, R. A. Adeniji-Adele, E. O. Onori, and A. Ogwala (2013), Day-to-day variability of $f_oE_s$ in the equatorial ionosphere, *Radio Sci.*, *48*, 513–518; doi:10.1002/rds.20057.

Umoh, A. A., and J. O. Adeniyi (1995), The morphology of the ionospheric F2 layer on quiet days in low latitudes, *Nig. J. Phys*., 57–62.

Vanzandt, T. E. (1967), The neutral atmosphere and the quiet ionosphere, 509–599, in *Physics of Geophysical Phenomena*, edited by S. Matsushita and W. H. Campbell, Academic Press, New York.

Wang, X., J. K. Shi, G. J. Wang, G. A. Zherebtsov, O. M. Pirog. (2007), Responses of ionospheric foF2 to geomagnetic activities in Hainan, *Adv. Space Res.*; doi: 10.1016/j.asr.2007.04.097.

Whitehead, J. D. (1961), The formation of sporadic E in the temperate zones, *J. Atmos. Terr. Phys.*, *20*, 49–58; doi:10.1016/0021-9169(61)90097-6.

Yizengaw, E. (2012), Global longitudinal observation dependence of the neutral wind and ionospheric distribution, *Int. J. Geophys*., Article ID 342581; doi:10.1155/2012/342581.

Zhang, M. L., J. K. Shi, X. Wang, and S. M. Radicella (2004), Ionospheric variability at low latitude station: Hainan, China, *Adv. Space Res.*, *34*, 1860–1868; doi:10.1016/j.asr.2004.04.005.

# Part IV
# Temporal Response to Lower Atmosphere Disturbances

# 14

# Impact of Migrating Tides on Electrodynamics During the January 2009 Sudden Stratospheric Warming

**Timothy J. Fuller-Rowell,[1] Tzu-Wei Fang,[1] Houjun Wang,[1] Vivien Matthias,[2] Peter Hoffmann,[2] Klemens Hocke,[3] and Simone Studer[3]**

## ABSTRACT

A whole atmosphere model (WAM) has been used to determine the physical processes driving the change in electrodynamics during the January 2009 sudden stratospheric warming (SSW). Previously the WAM model was integrated into the National Weather Service Gridpoint Statistical Interpolation (GSI) data assimilation scheme to enable the observed changes in amplitude of planetary wavenumber one and two in the lower atmosphere to be followed. The modeled changes in ozone concentration, which act as a tracer of the middle atmosphere dynamics, agree well with observations from the ground-based station at Bern, Switzerland, which supports the accuracy of the modeled middle atmosphere dynamics. The model showed that the amplitude and phase of both the semidiurnal and terdiurnal migrating tides SW2 and TW3 varied through the period. The change in phase of SW2 and TW3 follows the reversals in direction of the stratospheric longitudinally averaged zonal winds. As the stratospheric zonal winds reverse from eastward to westward, the SW2 and TW3 tidal phases move to earlier local times. Similarly, as the zonal winds slowly recover to the more typical eastward direction expected for the season, the tidal phases gradually move to later local times. The reasonable correlation suggests the tidal phase changes are due to the zonal winds in the stratosphere pushing the tide to earlier or later local times as it propagates from its source at lower altitudes. The phase changes of the SW2 during the SSW recovery period is similar to that expected from the lunar gravitational tide. Since WAM does not explicitly include the lunar tide, the change in phase of the solar-driven SW2 could be mistaken for an increase in the amplitude of the lunar gravitational semidiurnal $M_2$ mode. The apparent signature of the lunar tide in the model simulation is actually due to the gradual change in phase each day of the solar heating-driven semidiurnal tide as it propagates through the slowing changing zonal wind. The WAM winds drove electrodynamics in the dynamo region reasonably consistent with observations from the Jicamarca longitude sector. Near the peak of the SSW, the winds drove a stronger eastward electric field (upward plasma drift) early in the morning, reversing to westward (downward plasma drift) in the afternoon. The peak in upward plasma drift gradually moved back to later local times during the 2- or 3-week recovery from the SSW. The model tidal fields were separated into their components to determine what aspects of the tidal wind changes (i.e., SW2 or TW3 amplitude and phase) caused the shift in phase of the vertical plasma drift at the magnetic equator to earlier local times, and what drove the increases in amplitude. The results show the SW2 tide is the dominant mode producing agreement between observations and modeled electrodynamics,

[1]*Cooperative Institute for Research in Environmental Sciences (CIRES), University of Colorado at Boulder, Boulder, Colorado, USA; and Space Weather Prediction Center (SWPC), National Oceanic and Atmospheric Administration (NOAA), Boulder, Colorado, USA*

[2]*Leibniz Institute of Atmospheric Physics, Rostock University, Kühlungsborn, Germany*

[3]*Institute of Applied Physics, University of Bern, Bern, Switzerland*

*Ionospheric Space Weather: Longitude and Hemispheric Dependences and Lower Atmosphere Forcing, Geophysical Monograph 220*, First Edition. Edited by Timothy Fuller-Rowell, Endawoke Yizengaw, Patricia H. Doherty, and Sunanda Basu.

and that the model changes in TW3 hinder rather than help in the comparison. The model also shows that, although the increase in magnitude of the SW2 drives a stronger upward plasma drift, part of the increase in magnitude at the earlier local times comes from the phase change, from a more efficient dynamo action.

**Key Points:**
Sudden stratospheric warmings (SSW) modulate vertical propagation of migrating tides.
WAM simulated the planetary wave and ozone response to the 2009 SSW.
Phase changes of the migrating semidiurnal tide (SW2) in the lower thermosphere follow the changes in the stratospheric zonal winds.
The phase change of SW2 is similar to that expected from the lunar gravitational tide.
The SW2 tidal winds in the dynamo region drove electrodynamics reasonably consist with Jicamarca incoherent scatter observations.

**Key Terms:** lower atmosphere forcing, planetary waves, sudden stratospheric warming, ozone, semidiurnal tide, terdiurnal tide, lunar tide, electrodynamics, ionosphere

## 14.1. INTRODUCTION

Observations have recently shown compelling evidence of a coherent connection between changes in middle atmosphere dynamics [*Manney et al*., 2009] during the January 2009 sudden stratospheric warming (SSW), and changes in equatorial electrodynamics [*Chau et al*., 2010] and plasma density changes [*Goncharenko et al*., 2010]. A sudden stratospheric warming is a large-scale meteorological process where increase in planetary wave activity causes the winter polar stratospheric vortex to break down allowing for development of meridional circulation and warming of the winter polar region [*Matsuno*, 1971]. The change in circulation during the SSW is expected to alter the propagation of tides into the lower thermosphere dynamo region [*Matthias et al*., 2012; *Sridharan et al*., 2009].

Numerical model simulations can help elucidate the physical processes driving the connection. Several modeling studies of the event have been attempted, which have been reviewed recently by *Pedatella et al*. [2014]. The models include the Ground-to-topside model of Atmosphere and Ionosphere for Aeronomy [GAIA; *Jin et al*., 2012], the Hamburg Model of the Neutral and Ionized Atmosphere [HAMMONIA; *Schmidt et al*., 2006], the whole atmosphere model [WAM; *Akmaev et al*., 2008; *Fuller-Rowell et al*., 2008, 2011], and the Whole Atmosphere Community Climate Model extended version [WACCM-X; *Liu et al*., 2010; *Sassi et al*., 2013]. *Pedatella et al*. [2014] showed the zonal mean winds and planetary waves from the models were in good agreement in the altitude region where dynamics were constrained by observations (up to ~50 km altitude). At higher altitudes, the model results diverged greatly due to the different model physics and gravity-wave parameterization embedded in the models.

Changes in atmospheric tides are thought to be the mechanism for the changes in the electrodynamics in the lower thermosphere and the ionospheric changes. *Fuller-Rowell et al*. [2010, 2011], *Jin et al*. [2012], and *Lin et al*. [2012] suggested the changes are due to solar migrating tides as they propagate through the altered middle atmosphere dynamics; *Pedatella and Forbes* [2010] attributed it to nonmigrating tides; and *Fejer et al*. [2010] and *Forbes and Zhang* [2012] suggested amplification of the lunar semidiurnal tide. In addition, *Goncharenko et al*. [2012] suggested redistribution of ozone in the stratosphere might alter the source of the semidiurnal migrating tide (SW2).

Previously, the WAM model was integrated into a modified version of the US National Weather Service (NWS) Gridpoint Statistical Interpolation (GSI) data assimilation scheme [*Wang et al.*, 2011, 2012, 2014] and was used to simulate the January 2009 SSW [*Fuller-Rowell et al.*, 2011]. The same data used in the US meteorological weather forecast system were used to steer the WAM dynamics and temperature below 60 km altitude. The neutral wind from the model simulation at the peak of the SSW indicated a reduction in the amplitude of the semidiurnal migrating tide (SW2) in the lower thermosphere and an increase in the amplitude of the terdiurnal migrating tide (TW3). The winds from the WAM-GSI analysis were used to drive the Global Ionosphere Plasmasphere (GIP) and electrodynamics model [*Fang et al*., 2009] during the January/February 2009 period. The day-to-day variation of the dayside equatorial zonal electric fields, or vertical plasma drift, showed a similar variation to the observations from the Jicamarca incoherent scatter radar facility in Peru [*Chau et al*., 2010].

The magnitude of the response was weaker in the model simulations, but the change in phase appeared to be in good agreement. The model and data both showed an increase in the zonal electric field (upward plasma drift) earlier in the morning, reversing to westward (downward plasma drift) in the afternoon. The changes in the vertical plasma drift were anticipated to drive the changes seen in dual-frequency GPS observations of total electron content (TEC) over South America [*Goncharenko et al*.,

2010], with increases in plasma density in the morning sector, and decreases in the afternoon sector, compared to the normal diurnal variation. At the time, the reason for the modeled electrodynamic response was not clear.

The present study seeks to attribute the electrodynamic and plasma-density response to specific drivers. *Fuller-Rowell et al.* [2010, 2011] noticed a significant change in the terdiurnal migrating tide TW3 in simulations of the January 2009 SSW and noticed something similar in a whole atmosphere model "free-run" simulation. Based on these results, *Fuller-Rowell et al.* [2011] speculated that the TW3 might be partly responsible for the change in electrodynamics observed by *Chau et al.* [2009] and modeled with WAM-GIP. The numerical simulations presented here strongly suggest that it is the change in phase of the SW2 tidal mode that is the dominant driver, rather than the changes in the TW3, and that if anything, the strong TW3 in the model simulations actually partially degrades the agreement between model and data.

## 14.2. MODEL SIMULATIONS

The numerical simulation of the neutral dynamics presented here is similar to that presented previously by *Wang et al.* [2011, 2012, 2014] and *Fuller-Rowell et al.* [2011]. The objective of the present study is to determine what it is about the changes in tidal amplitude and phase that drives the electrodynamic response. Since the propagation of the spectrum of migrating and nonmigrating tides through the changes in the stratosphere and mesosphere dynamics are expected to be the main drivers of the electrodynamics and changes in the ionosphere during an SSW, it is important to validate the changes in the dynamics of the lower atmosphere during this January 2009 period.

Figure 14.1 shows a comparison of the modeled and observed amplitude of stationary planetary waves SPW1, SPW2, and SPW3 in temperature as a function of latitude and height (0–100 km) in the Northern Hemisphere near the peak of the SSW on 22 January 2009. The observations from the Microwave Limb Sounder [MLS; *Waters et al.*, 2006; *Manney et al.*, 2005] on the Aura spacecraft are shown in the upper panels and the model results are shown in the lower panels. Note that the MLS data were not used in the WAM-GSI data assimilation system, so they are independent of the analysis. The modeled height/latitude structure in the upper panels is generally in good agreement with the data, in both magnitude and latitude structure. Since this was a split vortex event, as expected the amplitude of the stationary planetary wave 2 (SPW2) matches or exceeds the amplitude of the planetary wave 1 (SPW1). The agreement at the lower altitudes is particularly good where the simulation has benefited from being forced by data, but the agreement remains good, particularly for the SPW2 up to 100 km altitude. It is expected, therefore, that the impact on the tidal modes

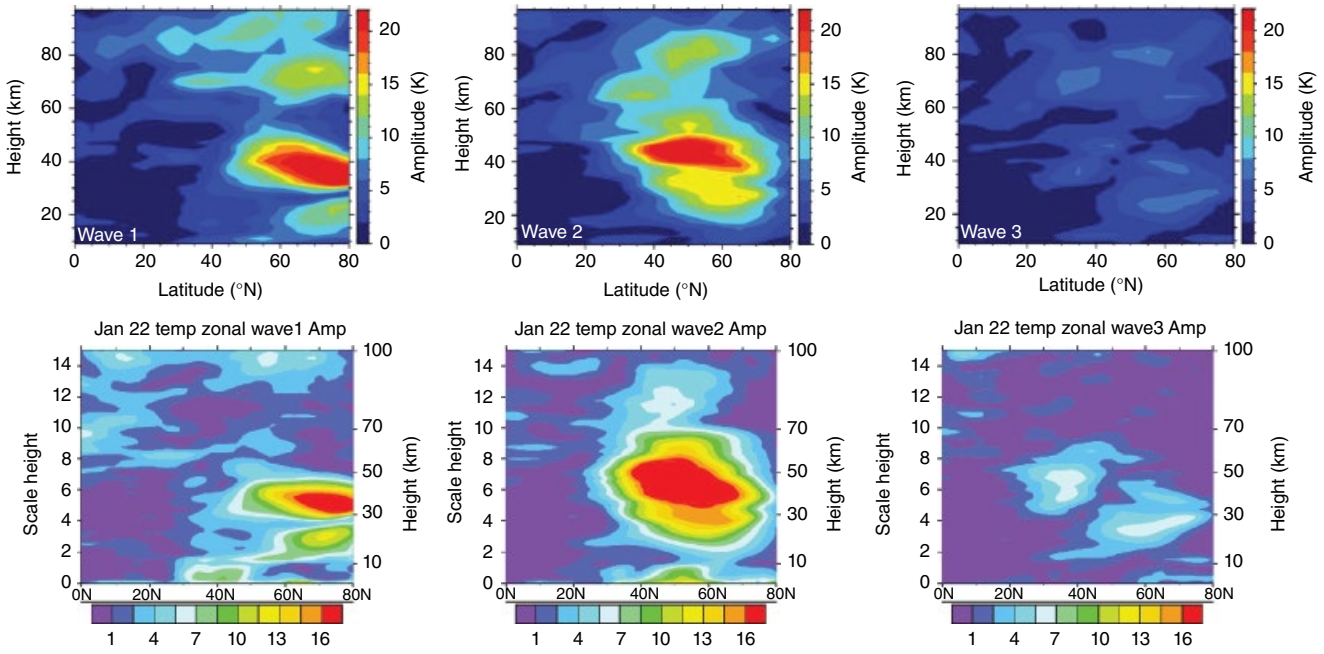


**Figure 14.1** Comparison of the height/latitude structure of stationary planetary waves (SPW) 1 (left), 2, (middle), and 3 (right), on 22 January near the peak of the 2009 sudden stratospheric warming. The upper panels are from the Microwave Limb Sounder on the Aura satellite, and the lower panels are from the WAM simulations including the data assimilation system.

propagating into the lower thermosphere dynamo region should be reasonably realistic.

To further illustrate the realism of the dynamics in the lower atmosphere from the numerical simulation, a model-data comparison of the variation in the ozone profile over Bern is shown in Figure 14.2, from 16 km to 65 km altitude, and from 10 January to 21 February. The observations (upper panel) are from a ground-based 142-GHz microwave radiometer at Bern (46.9°N, 7.4°E), which measured the ozone profile with a vertical resolution of about 10 km and a temporal resolution of about 1 hr [*Dumitru et al.*, 2006]. The observations in Figure 14.2 have a few data gaps, which are related to bad weather when high tropospheric opacity masked the microwave emission from stratospheric ozone. The SSW in January 2009 induces a short-term depletion in stratospheric ozone at Bern, which agrees with a similar observation for the SSW in February 2008 [*Flury et al.*, 2009].

The WAM-modeled ozone in the lower panel of Figure 14.2 uses a simplified ozone chemistry [*McCormack, et al.* 2006], which does not include the full diurnal variation each day that can be seen in the data above about 45 km altitude. The ozone peak values are also a little stronger in the model, possibly due to an overestimate of the solar UV forcing at this time of uncommonly low solar activity at this solar minimum. The temporal variation in the diurnal mean ozone concentration is strongly controlled by the stratospheric dynamics. The agreement is good in terms of the changes in the peak altitude of ozone through the interval. The model also captures much of the long- and shorter-period variations. The breakup of the polar vortex initiates a complex trajectory of parcels of gas and is responsible for much of the temporal change seen in both the model and data. The reason for the ozone changes can be interpreted by the model through transport by the changing wind field.

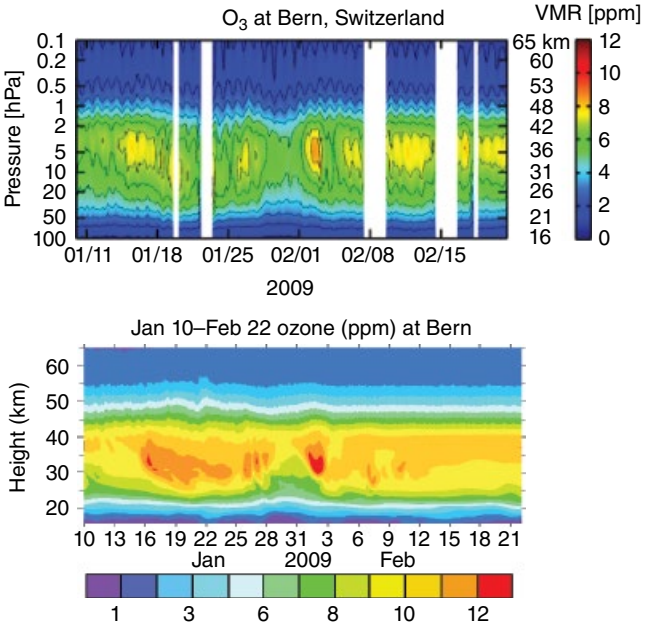


**Figure 14.2** Comparison of the vertical structure of ozone as observed at Bern, Switzerland (upper panel), with the WAM model (lower panel) from 10 January to 21 February 2009.

## 14.3. TIDAL AND ELECTRODYNAMIC RESPONSE

*Fuller-Rowell et al.* [2011] previously suggested that, although many of the tidal modes respond to the change in the stratospheric circulation, the two modes most affected were the semidiurnal and terdiurnal migrating tides, SW2 and TW3, respectively. The tidal wind changes in the lower thermosphere dynamo region were used to drive the electrodynamics and ionosphere in GIP, and the changes and trends in equatorial electric fields agreed reasonably well with the observations by *Chau et al.* [2010] from the Jicamarca incoherent scatter radar facility close to the magnetic equator. What was not clear at the time was which of the tides, SW2 or TW3, was responsible for most of the change in vertical plasma drift, and what was the relative importance of the amplitude or phase changes.

Figure 14.3 shows the amplitude changes of the diurnal, semidiurnal, and terdiurnal migrating tides (DW1, SW2, TW3) tidal modes during the 2009 SSW period, averaged

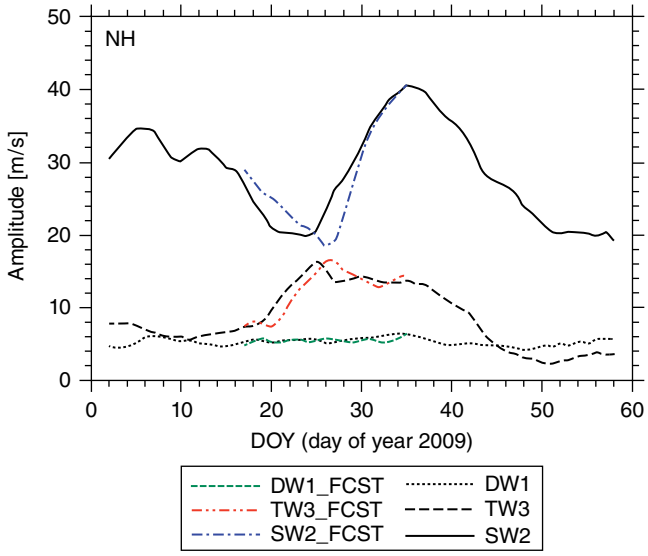


**Figure 14.3** Time series of the Northern Hemisphere zonal wind amplitudes of the diurnal (short-dash), semidiurnal (solid line), and terdiurnal (long-dash) migrating tides for January–February 2009 from the WAM model analysis with data assimilation [from *Wang et al.*, 2011]. The green, red, and blue traces are the results of a WAM forecast initialized on 15 January. The values are averages over 95–155 km altitude and between latitudes 20° and 60°N.

between 95 km and 155 km and between latitude 20° and 60°N, starting from 1 January [from *Wang et al.*, 2011]. The green, red, and blue traces are the results of a WAM forecast initialized on 15 January. The SW2 semidiurnal mode in Figure 14.3 appears to decrease in magnitude as the SSW reaches its peak, when the zonal wind reaches its strongest westward reversal on 23 January (see later in Figure 14.4c), and subsequently sharply increases in magnitude to a peak in early February. The TW3 terdiurnal mode appears to have the opposite trend in Figure 14.3, increasing during buildup of the SSW and decaying after the peak in the wind reversal. The diurnal tide exhibits little change during the interval.

Figures 14.4a and b show the change in phase of SW2 (near 110 km altitude) and TW3 (near 150 km altitude) zonal winds in the Northern Hemisphere midlatitudes taken at the location of peak amplitude (see *Wang et al.* [2011, 2012] for representative latitude/height structure of the tidal modes). The direction and magnitude of the stratospheric longitudinally averaged (or zonal mean) zonal wind near 50 km altitude and 60°N is shown in Figure 14.4c. The correlation between the phases of the SW2 and TW3 and the zonal wind suggests that the tidal phase changes are due to the change in the propagation through the background wind system. *Goncharenko et al.* [2012] and *Jin et al.* [2012] argued that part of the SW2 tidal amplitude changes could be attributed to the changes in the ozone concentration and altitude distribution in the source region between 30 km and 50 km altitude.

Figure 14.5 illustrates the impact on the electrodynamics of the SW2 and TW3 tidal fields. For reference, Figure 14.5a shows the model electrodynamic changes in the vertical plasma drift using the full WAM wind system [from *Fuller-Rowell et al.*, 2011], and Figure 14.5b shows the observations of the change as observed from Jicamarca [*Chau et al.*, 2009] during the period. Figures 14.5c and d show the contribution to the changes in the electrodynamics from the SW2 and TW3 winds, separately. The main features in the observed response, that is, the movement of the peak upward drift to the morning sector, the stronger downward drift in the afternoon, and the gradual recovery after the SSW are all features consistent with the forcing from the SW2 tidal model. If anything, the impact of the WAM TW3 tends to degrade the good correlation between the observations and model, and indicates that perhaps WAM overpredicts the amplitude of the TW3 mode.

Since SW2 appears to be the dominant driver of the electrodynamic changes, Figure 14.6 shows the relative importance of the amplitude and phase changes of the SW2. Figure 14.6a shows the diurnal variation of the vertical plasma drift between 0600 and 2000 hours local time at the magnetic equator using the full WAM windfield changes for each day from 13 January for 18 consecutive days. The electrodynamic response using just the changes in the SW2 are shown in Figure 14.6b, which clearly captures a large fraction of the modeled response.

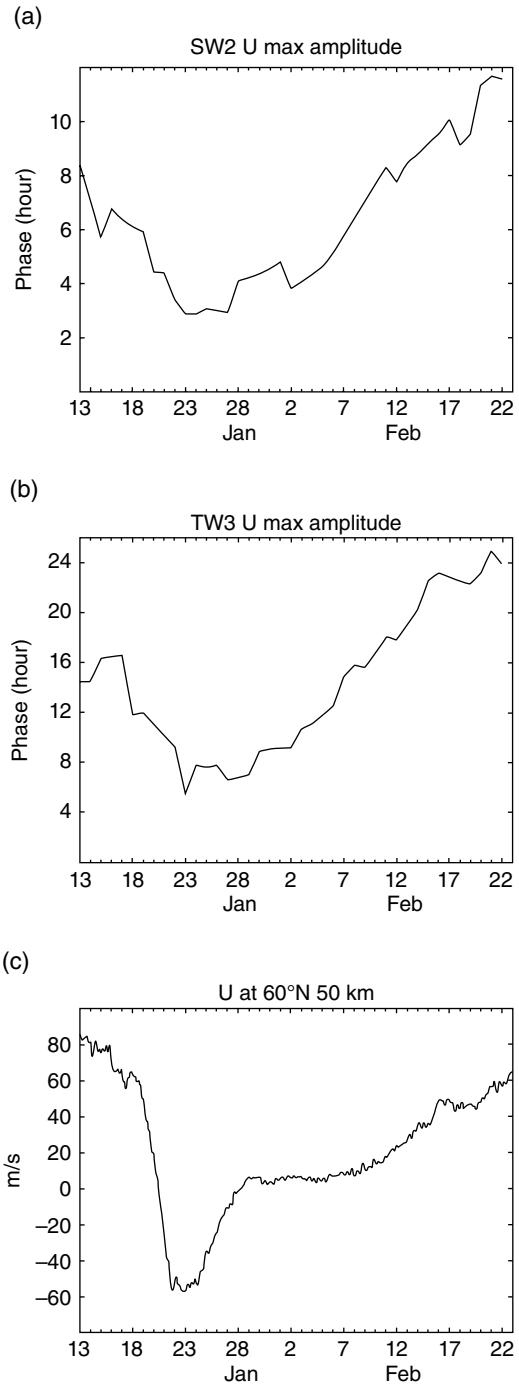


**Figure 14.4** Comparison of the time dependence of the phase of the semidiurnal (a) and terdiurnal (b) migrating tides at their Northern Hemisphere peak with the zonal mean zonal wind (c) at 60°N and 50 km altitude, during the 2009 SSW.

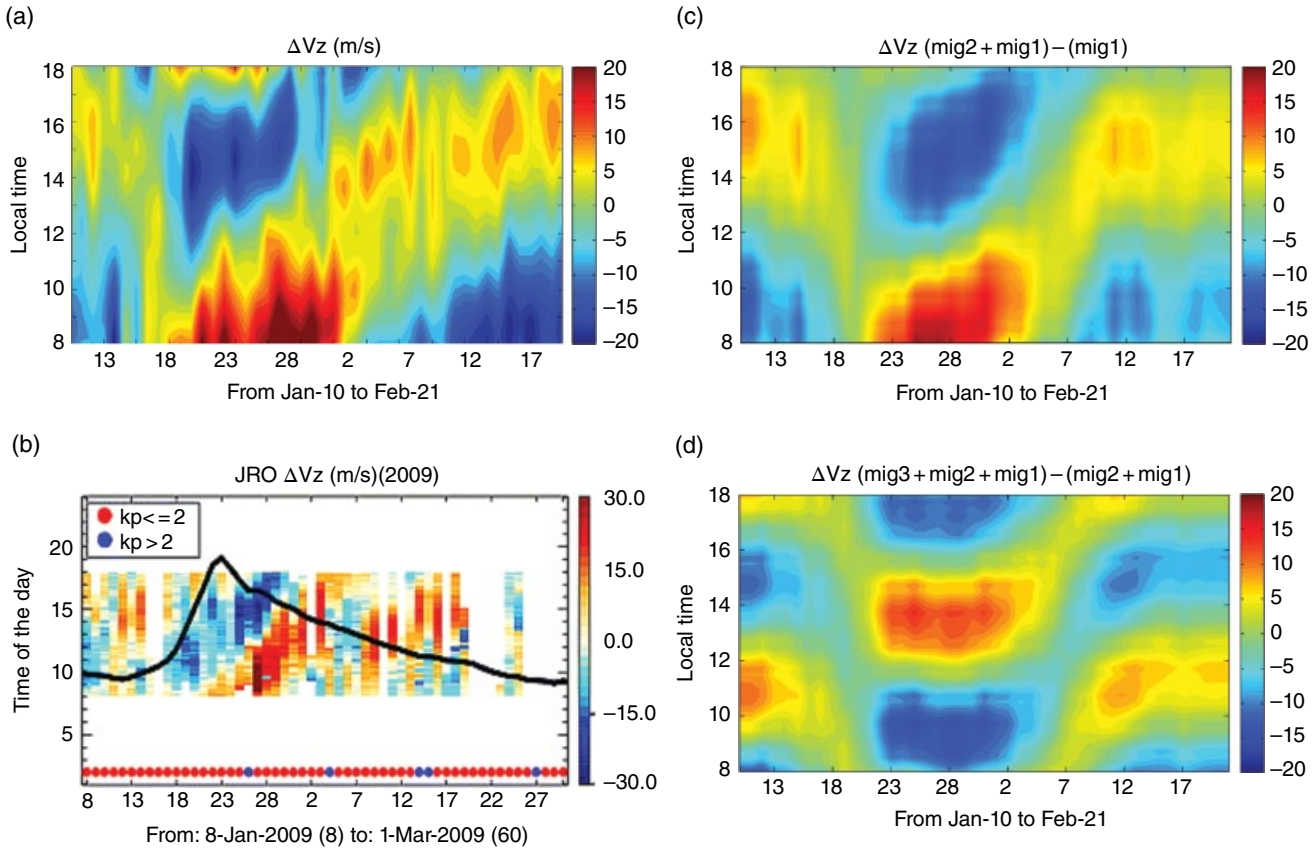


**Figure 14.5** The right side illustrates the impact on changes of the vertical plasma drift during the SSW by the semidiurnal SW2 migrating tidal winds (c, top right) and terdiurnal TW3 migrating tidal winds (d, bottom right), imposed on the electrodynamic solver separately. For reference, on the left are the modeled responses using the full WAM wind field (a, top left), and the observed changes from *Chau et al*. [2009] as seem from Jicamarca (b, bottom left).

Figures 14.6c and d show the impact on the vertical plasma drift of either the changes in SW2 amplitude (14.6c) or phase (14.6d), separately. The changes in the SW2 amplitude clearly capture a significant fraction of the total amplitude changes in the vertical plasma drift, and similarly the SW2 phase changes capture the phase changes in the vertical plasma drift. However, Figure 14.6d also shows that the magnitude of the vertical plasma drift is also sensitive to the phase changes in the tide. When the tidal amplitude moves to earlier local times, the electrodynamic response appears to have a more efficient dynamo.

## 14.4. DISCUSSION

The objective was to determine what it is about the changes in amplitude and phase of the migrating tides that drives the electrodynamic response to the January 2009 SSW. The numerical simulations indicate the most likely driver is the change in amplitude and phase of the SW2 semidiurnal migrating tidal mode. The earlier local times of the upward plasma drift are due to the change in phase of the SW2. The stronger upward drift during the SSW arises from a combination of the amplitude and phase changes of the SW2, since the phase change itself can produce a more efficient dynamo action and drive a stronger upward plasma drift at certain local times.

The phase of the SW2 is strongly correlated with the upper stratosphere zonal mean zonal winds, as the direction changes quite suddenly from eastward to westward, with a slow recovery back to eastward over the 2 or 3 weeks following the peak in the SSW. The indications are that as the tide propagates upward through the westward winds, the phase is shifted to earlier local times, as discussed by *Wang et al.* [2014]. In terms of vertical wavelength, the shift to earlier local times would be interpreted as a shorter vertical wavelength. As the zonal winds gradually return to their seasonally more normal

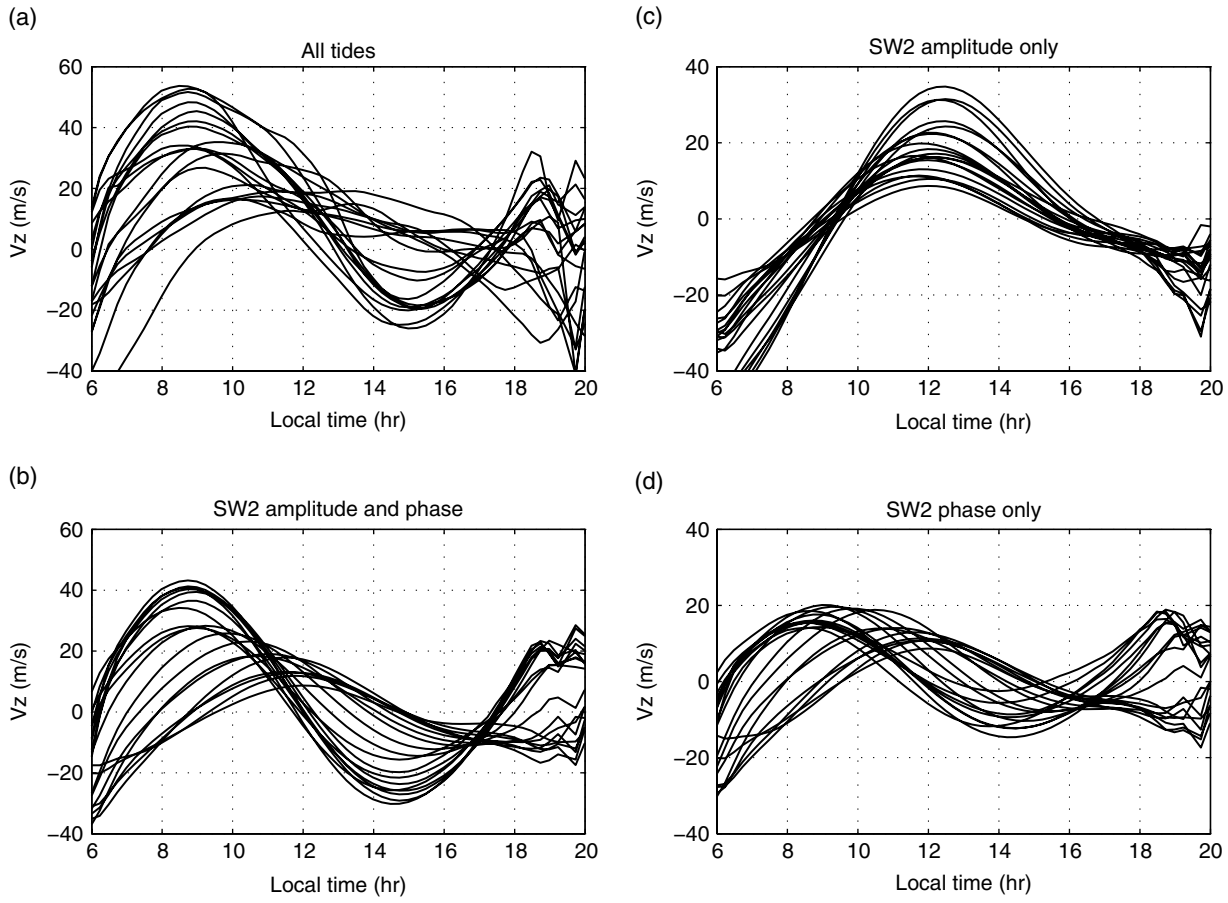


**Figure 14.6** The right side illustrates the impact on the diurnal variation between 06 and 20 hr local time of the vertical plasma drift of either the amplitude changes of the WAM semidiurnal SW2 tidal mode (c, top right) keeping the phase constant, or the phase changes keeping the amplitude fixed (d, bottom right). For reference, (a) the upper left panel shows the diurnal variation using the full WAM wind fields, and (b) the lower left panel using the amplitude and phase variations of the SW2 mode only.

eastward direction in these winter midlatitudes, the phase of the SW2 tide also moves back to later times as it is no longer pushed westward by the prevailing zonal winds. The correlation between the reversal in the zonal winds and the phase of both the semidiurnal and terdiurnal tide (see Figs. 14.4a–c) suggest this interpretation (see also discussion in *Wang et al.* [2014]).

It is also useful to discuss the present result in the context of an alternative interpretation of the cause of the changes in the semidiurnal tide and electrodynamic response. Under normal conditions, the neutral winds in the dynamo region driven by the lunar gravitational semidiurnal tide produce upward vertical plasma drifts of a few m/s [*Eccles et al.*, 2011]. Several authors have suggested that the winds from the lunar tide are somehow amplified during SSW events [*Fejer et al.*, 2010, 2011; *Stening*, 2011]. *Forbes and Zhang* [2012] suggested that the amplification of the lunar tide is a result of a shift in the resonance of the atmosphere closer to the lunar $M_2$ semidiurnal tidal period of 12.42 hr. The 12.42-hr period means that the peak moves about 25 min later each day, through the Moon's orbit.

The results in Figure 14.4 show that after the rapid shift to earlier local times, the phase of the SW2 zonal wind moves to later local times in a similar fashion expected of the lunar tide, that is, moving to later times by an average of about 25 to 30 min each day. In the model simulations, the lunar tide is not explicitly included, so the SW2 signature in Figure 14.4 cannot be due to the lunar tide. We suggest instead, the response is due to a change in phase of the solar heating-driven semidiurnal tide, as it propagates through the slowly changing zonal wind. Since the model has been forced by data in the lower atmosphere below 60 km altitude, we cannot however rule out the possibility that the lunar tidal signature has somehow been

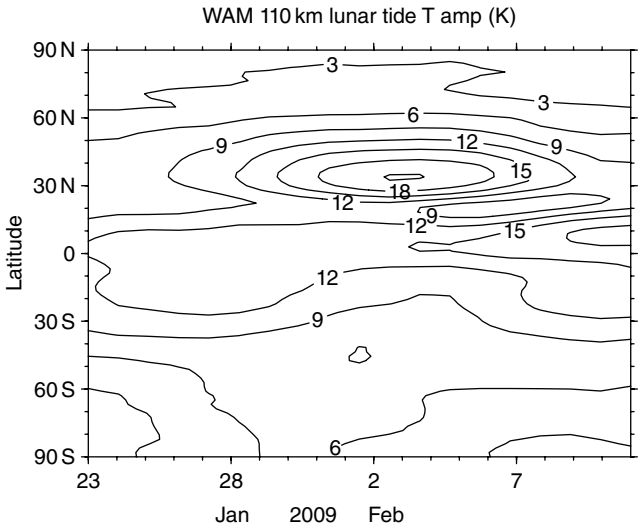


**Figure 14.7** Analysis of the WAM latitude structure of temperature at 110 km altitude during the 2009 SSW. The analysis shows the amplitude of what would appear to be the lunar gravitational $M_2$ mode assuming an expected phase change of 25 min each day.

imparted to the model through the data assimilation system. Including the effects of the lunar tide explicitly in WAM may well increase the amplitude of the SW2. The final Figure 14.7 shows the analysis of the WAM winds extracting out what would be interpreted as a lunar semidiurnal tide at 110 km altitude. As expected, the apparent amplitude of the lunar tide grows at mid-latitudes in the Northern Hemisphere during the recovery period when the solar thermally driven SW2 tidal phase is shifting to later local times from 26 January through mid-February (see Fig. 14.4a).

## 14.5. CONCLUSIONS

Numerical simulation of a whole atmosphere model coupled to an ionosphere and electrodynamic model has been used to interpret the cause of the changes in electrodynamics and the ionosphere during the January 2009 sudden stratospheric warming. The observations from Jicamarca showed that the peak in the vertical plasma drift on the dayside moved to earlier local times and gradually moved back to later local times in the 2 to 3 weeks following the SSW.

The model simulations strongly suggest that the main driver of the electrodynamics is the change in phase of the semidiurnal migrating tidal mode SW2 during the period. Although the model simulations also suggest an increase in the terdiurnal tide during the SSW, this mode does not appear to improve the agreement between the model and observations of the vertical plasma drift at Jicamarca. If anything, the TW3 makes the agreement worse, suggesting the mode may be overestimated in the numerical simulations.

The correlation between the direction of the stratospheric zonal mean zonal wind and the phase of both the SW2 and the equivalent terdiurnal mode TW3, suggests that the changes in phase of the tides in the lower thermosphere are a result of the zonal winds pushing the tide to earlier or later times as it propagates through the background winds. During the recovery to the SSW, the SW2 phase moves to later locals times by about 25 to 30 min each day, which coincidentally matches the phase change expected for the lunar $M_2$ gravitational tidal period of 12.42 hr. Therefore, the solar-driven SW2 change could be mistaken for a change in the amplitude of the lunar tide.

When the phase of the SW2 shifts the peak in the vertical plasma drift to earlier local times, the model indicates the dynamo efficiency is slightly stronger in creating a vertical plasma drift. In addition, the change in the amplitude of the tide also increases the magnitude of the vertical plasma drift. The cause of the change in amplitude of the SW2 is not clear from the WAM-GIP simulations, but *Jin et al.* [2012], *Wang et al.* [2014], and *Goncharenko et al.* [2012] suggest it is driven by some combination of the change in ozone concentration in the source region of the tide around 35 to 40 km altitude and the propagation conditions through the prevailing winds.

## REFERENCES

Akmaev, R. A., T. J. Fuller-Rowell, F. Wu, J. M. Forbes, X. Zhang, A. F. Anghel, M. D. Iredell, S. Moorthi, and H.-M. Juang (2008), Tidal variability in the lower thermosphere: Comparison of Whole Atmosphere Model (WAM) simulations with observations from TIMED, *Geophys. Res. Lett.*, *35*, L03810; doi:10.1029/2007GL032584.

Chau, J. L., B. G. Fejer, and L. P. Goncharenko (2009), Quiet variability of equatorial E × B drifts during a sudden stratospheric warming event, *Geophys. Res. Lett.*, *36*, L05101; doi:10.1029/2008GL036785.

Chau, J. L., N. A. Aponte, E. Cabassa, M. P. Sulzer, L. P. Goncharenko, and S. A. González (2010), Quiet time ionospheric variability over Arecibo during sudden stratospheric warming events, *J. Geophys. Res.*, *115*, A00G06; doi:10.1029/2010JA015378.

Dumitru, M. C., K. Hocke, N. Kämpfer, and Y. Calisesi (2006), Comparison and validation studies related to ground-based microwave observations of ozone in the stratosphere and mesosphere, *J. Atmos. Sol. Terr. Phys.*, *68*, 745–756; doi:10.1016/j.jastp.2005.11.001.

Eccles, V., D. D. Rice, J. J. Sojka, C. E. Valladares, T. Bullett, and J. L. Chau (2011), Lunar atmospheric tidal effects in the plasma drifts observed by the Low-Latitude Ionospheric Sensor Network, *J. Geophys. Res.*, *116*, A07309; doi:10.1029/2010JA016282.

Fang, T.-W., H. Kil, G. Millward, A. D. Richmond, J.-Y. Liu, and S.-J. Oh (2009), Causal link of the wave-4 structures in plasma density and vertical plasma drift in the low-latitude ionosphere, *J. Geophys. Res.*, *114*, A10315; doi:10.1029/2009JA014460.

Fejer, B. G., B. D. Tracy, M. E. Olson, and J. L. Chau (2011), Enhanced lunar semidiurnal equatorial vertical plasma drifts during sudden stratospheric warmings, *Geophys. Res. Lett.*, *38*, L21104; doi:10.1029/2011GL049788.

Fejer, B. G., M. E. Olson, J. L. Chau, C. Stolle, H. Lühr, L. P. Goncharenko, K. Yumoto, and T. Nagatsuma (2010), Lunar dependent equatorial ionospheric electrodynamics effects during sudden stratospheric warmings, *J. Geophys. Res.*, *115*, A00G03; doi:10.1029/2010JA015273.

Flury, T., K. Hocke, A. Haefele, N. Kämpfer, and R. Lehmann (2009), Ozone depletion, water vapor increase, and PSC generation at midlatitudes by the 2008 major stratospheric warming, *J. Geophys. Res.*, *114*, D18302; doi:10.1029/2009JD011940.

Forbes, J. M., and X. Zhang (2012), Lunar tide amplification during the January 2009 stratosphere warming event: Observations and theory, *J. Geophys. Res.*, *117*, A12312; doi:10.1029/2012JA017963.

Fuller-Rowell, T., H. Wang, R. Akmaev, F. Wu, T.-W. Fang, M. Iredell, and A. Richmond (2011), Forecasting the dynamic and electrodynamic response to the January 2009 sudden stratospheric warming, *Geophys. Res. Lett.*, *38*, L13102; doi:10.1029/2011GL047732.

Fuller-Rowell, T. J., F. Wu, R. Akmaev, T.-W. Fang, and E. A. Araujo-Pradere (2010), A whole atmosphere model simulation of the impact of a sudden stratospheric warming on thermosphere dynamics and electrodynamics, *J. Geophys. Res.*, *115*, A00G08; doi:10.1029/2010JA015524.

Fuller-Rowell, T. J., R. A. Akmaev, F. Wu, A. Anghel, N. Maruyama, D. N. Anderson, M. V. Codrescu, M. Iredell, S. Moorthi, H. -M. Juang, Y. -T. Hou, and G. Millward (2008), Impact of terrestrial weather on the upper atmosphere, *Geophys. Res. Lett.*, *35*(9), L09808; doi:10.1029/2007GL032911.

Goncharenko, L. P., A. J. Coster, R. A. Plumb, and D. I. V. Domeisen (2012), The potential role of stratospheric ozone in the stratosphere-ionosphere coupling during stratospheric warmings, *Geophys. Res. Lett.*, *39*, L08101; doi:10.1029/2012GL051261.

Goncharenko, L. P., J. L. Chau, H.-L. Liu, and A. J. Coster (2010), Unexpected connections between the stratosphere and ionosphere, *Geophys. Res. Lett.*, *37*, L10101; doi:10.1029/2010GL043125.

Jin, H., Y. Miyoshi, D. Pancheva, P. Mukhtarov, H. Fujiwara, and H. Shinagawa (2012), Response of migrating tides to the stratospheric sudden warming in 2009 and their effects on the ionosphere studied by a whole atmosphere-ionosphere model GAIA with COSMIC and TIMED/SABER observations, *J. Geophys. Res.*, *117*, A10323; doi:10.1029/2012JA017650.

Lin, J. T., C. H. Lin, L. C. Chang, H. H. Huang, J. Y. Liu, A. B. Chen, C. H. Chen, and C. H. Liu (2012), Observational evidence of ionospheric migrating tide modification during the 2009 stratospheric sudden warming, *Geophys. Res. Lett.*, *39*, L02101; doi:10.1029/2011GL050248 .

Liu, H.-L., B. T. Foster, M. E. Hagan, J. M. McInerney, A. Maute, L. Qian, A. D. Richmond, R. G. Roble, S. C. Solomon, R. R. Garcia, D. Kinnison, D. R. Marsh, A. K. Smith, J. Richter, F. Sassi, and J. Oberheide (2010), Thermosphere extension of the Whole Atmosphere Community Climate Model, *J. Geophys. Res.*, *115*, A12302; doi:10.1029/2010JA015586.

Manney, G. L., M. L. Santee, N. J. Livesey, L. Froidevaux, W. G. Read, H. C. Pumphrey, J. W. Waters, and S. Pawson (2005), EOS Microwave limb sounder observations of the Antarctic polar vortex breakup in 2004, *Geophys. Res. Lett.*, *32*, L12811; doi:10.1029/2005GL022823.

Manney, G. L., M. J. Schwartz, K. Krüger, M. L. Santee, S. Pawson, J. N. Lee, W. H. Daffer, R. A. Fuller, and N. J. Livesey (2009), Aura Microwave Limb Sounder observations of dynamics and transport during the record-breaking 2009 Arctic stratospheric major warming, *Geophys. Res. Lett.*, *36*, L12815; doi:10.1029/2009GL038586.

Matsuno, T. (1971), A dynamical model of the stratospheric sudden warming, *J. Atmos. Sci.*, *28*, 1479–1494; doi:10.1175/1520-046; doi:10.1175/1520-0469(1971)028<1479:ADMOTS>2.0.CO;2.

Matthias, V., P. Hoffmann, M. Rapp, and G. Baumgarten (2012), Composite analysis of the temporal development of waves in the polar MLT region during stratospheric warmings, *J. Atmos. Sol. Terr. Phys.*, *90*, 86–96; doi:10.1016/j.jastp.2012.04.004.

McCormack, J. P., S. D. Eckermann, D. E. Siskind, and T. J. McGee (2006), CHEM2D-OPP: A new linearized gas-phase ozone photochemistry parameterization for high-altitude NWP and climate models, *Atmos. Chem. Phys.*, *6*, 4943–4972; doi:10.5194/acp-6-4943-2006.

Pedatella, N. M., and J. M. Forbes (2010), Evidence for stratosphere sudden warming-ionosphere coupling due to vertically propagating tides, *Geophys. Res. Lett.*, *37*, L11104; doi:10.1029/2010GL043560.

Pedatella, N. M., T. Fuller-Rowell, H. Jin, H. -L. Liu, F. Sassi, H. Schmidt, and L. Goncharenko (2014), The neutral dynamics during the 2009 sudden stratospheric warming stimulated by different whole atmosphere models, *J. Geophys. Res. Space Phys.*, *119*, 1306–1324; doi:10.1002/2013JA019421.

Sassi, F., H. -L. Liu, J. Ma, and R. R. Garcia (2013), The lower thermosphere during the Northern hemisphere winter of 2009: A modeling study using high-altitude data assimilation products in WACCM-X, *J. Geophys. Res. Atmos.*, *118*, 8954–8968; doi:10.1002/jgrd.50632.

Schmidt, H., G. P. Brasseur, M. Charron, E. Manzini, M. A. Giorgetta, T. Diehl, V. I. Fomichev, D. Kinnison, D. Marsh, and S. Walters (2006), The HAMMONIA chemistry climate model: Sensitivity of the mesopause Region to the 11-year solar cycle and CO2 doubling, *J. Clim.*, *19*, 3903–3931; doi:10.1175/JCLI3829.1.

Sridharan, S., S. Sathishkumar, and S. Gurubaran (2009), Variabilities of mesospheric tides and equatorial electrojet strength during major stratospheric warming events, *Ann. Geophys.*, *27*, 4125–4130; doi:10.5194/angeo-27-4125-2009.

Stening, R. J. (2011), The lunar tide in the equatorial electrojet in relation to stratospheric warmings, *J. Geophys. Res.*, *116*, A12315; doi:10.1029/2011JA017047.

Wang, H., R. A. Akmaev, T.-W. Fang, T. J. Fuller-Rowell, F. Wu, N. Maruyama, and M. D. Iredell (2014), First forecast of a sudden stratospheric warming with a coupled whole-atmosphere/ionosphere model IDEA, *J. Geophys. Res. Space Phys.*, *119*, 2079–2089; doi:10.1002/2013JA019481.

Wang, H., T. J. Fuller-Rowell, R. A. Akmaev, M. Hu, D. T. Kleist, and M. D. Iredell (2011), First simulations with a whole atmosphere data assimilation and forecast system: The January 2009 major sudden stratospheric warming, *J. Geophys. Res.*, *116*, A12321; doi:10.1029/2011JA017081.

Wang, H., T. J. Fuller-Rowell, R. A. Akmaev, M. Hu, D. T. Kleist, and M. D. Iredell (2012), Correction to "First simulations with a whole atmosphere data assimilation and forecast system: The January 2009 major sudden stratospheric warming," *J. Geophys. Res.*, *117*, A03326; doi:10.1029/2012JA017630.

Waters, J. W., et al. (2006), The Earth observing system Microwave Limb Sounder (EOS MLS) on the Aura satellite, *IEEE Trans. Geosci. Remote Sens.*, *44*(5), 1075–1092.

# 15

# Simultaneous Measurements and Monthly Climatologies of Thermospheric Winds and Temperatures in the Peruvian and Brazilian Longitudinal Sectors

**John W. Meriwether,[1] Jonathan J. Makela,[2] and Daniel J. Fisher[2]**

## ABSTRACT

The nocturnal variations of the equatorial thermospheric winds and temperatures are studied by comparing the wind and temperature responses for two longitudinal regions separated by ~38°(~4200 km) for selected nights with simultaneous measurements as well as monthly climatologies. The Fabry-Perot observations of thermospheric winds and temperatures were made from Jicamarca (11.96°S, 76.86°W) on the west coast of Peru at the geomagnetic equator and from the northeastern region of Brazil (7.0°S, 36°W) located ~7° south of the geomagnetic equator. Comparisons of the zonal wind data for both sectors on individual nights and monthly climatologies for the September equinoctial months revealed a consistent and similar pattern of behavior characterized by a slow eastward zonal wind, ~40–50 $ms^{-1}$, near evening twilight, then a steady increase to a peak speed near 21–22 LT that was then followed by a slow decay toward dawn when an eastward increase to 40–50 $ms^{-1}$ was seen near 04–05 LT. The maximum peak speeds for Peru and Brazil were 130–140 $ms^{-1}$ and 80–90 $ms^{-1}$, respectively. These results were compared with model nighttime zonal wind variations computed using the empirical Horizontal Wind Model recently updated by the Naval Research Laboratory. Good agreement between the model variations and observations was generally found. The data from both sectors showed the meridional wind behavior to be dominated by a double-peaked structure with the two peaks of equatorward (northward) winds separated by ~6 hr. The Universal Time difference between the Peru and Brazil meridional wind structures was comparable with the solar time difference of 2.5 hr between the two sectors suggesting that the meridional winds were dominated by the migrating tidal wave. The comparison of the Peru and Brazil nighttime temperature variations showed the development of a midnight temperature maximum (MTM) near local midnight. Relative to the Naval Research Laboratory Mass Spectrometer Incoherent Scatter empirical model (NRLMSISE-00) baseline for both sectors, the MTM peak amplitudes were within the range of 50 K to 100 K, with the MTM peak occurring ~1 hr after the time of the first northward peak of the meridional wind structure. This phase offset is interpreted to be the time lag of the tidal-wave temperature fluctuation relative to the meridional wind increase northward as the wind and temperature portions of the tidal wave propagate from below into the thermosphere.

**Key Points:**
Thermospheric zonal neutral winds faster in Peru than in Brazil
Meridional winds for both Peru and Brazil sectors show semi-diurnal tidal signatures
Midnight temperature maximum similar in structure for both Peru and Brazil sectors

**Key Terms:** equatorial thermospheric dynamics, Fabry-Perot measurements of thermospheric winds and temperatures, longitudinal variation of thermospheric winds and temperatures

[1]*Department of Physics and Astronomy, Clemson University, Clemson, South Carolina, USA*

[2]*Department of Electrical and Computer Engineering, University of Illinois at Urbana-Champaign, Urbana, Illinois, USA*

*Ionospheric Space Weather: Longitude and Hemispheric Dependences and Lower Atmosphere Forcing, Geophysical Monograph 220*, First Edition. Edited by Timothy Fuller-Rowell, Endawoke Yizengaw, Patricia H. Doherty, and Sunanda Basu.

## 15.1. INTRODUCTION

Our understanding of the nighttime variations of the thermospheric equatorial winds and temperatures can be improved by comparing the wind and temperature responses for two longitudinal regions. As an example, the longitudinal variations of the dynamic forcing functions such as the day-to-night pressure gradient, ion drag, and tidal-wave forcing may introduce significant differences that can be helpful in improving our understanding of the phenomenon known as the midnight temperature maximum [MTM; *Herrero et al.*, 1982, *Herrero et al.*, 1985; *Faivre et al.*, 2006; *Meriwether et al.*, 2008; *Akmaev et al.*, 2010]. These results would help improve MTM modeling studies because the MTM is a broad-scale phenomenon driven by the upward propagation of the tidal-wave response of the equatorial atmosphere to the solar forcing of the troposphere and stratosphere regions. Measurements for individual nights and monthly averaged climatologies from two widely separated ground-based stations obtained for the same period would help inform our understanding of the longitudinal response of the atmosphere to this tidal-wave source.

Comparisons of the nocturnal variation of meridional wind speed and direction for both longitudinal regions address the question of how different the equatorial thermospheric tidal-wave structure might be as the nonmigrating tidal forcing mode may vary between one longitudinal sector and another. Furthermore, the different plasma density environments within the upper *E*-region for both longitudinal regions would modify the rate of tidal dissipation that occurs as these tidal harmonics propagate into the thermosphere from below. The whole atmosphere model (WAM) calculations of *Akmaev et al.* [2009] and *Akmaev et al.* [2011] and the TIME-GCM modeling by *Ma et al.* [2010] have demonstrated the migrating tidal structure observed during 22–23 LT constitutes a blend of tidal harmonics that include contributions from the diurnal, semidiurnal, and higher order tidal modes. The WAM modeling of the meridional winds for the thermosphere at selected latitudes illustrates how the varying magnitudes of the semidiurnal, terdiurnal, and higher order tidal modes over consecutive days can contribute to the overall day-to-day variability of the composite tidal-wave structure [*Akmaev et al.*, 2010]. The results found by the TIE-GCM modeling of meridional winds at the dip equator at 400 km (from *Miyoshi et al.* [2012]) also illustrated significant day-to-day variability of the thermosphere tidal-wave structure.

Analysis of the the zonal component of the equatorial wind vector for two sectors is also of considerable interest. The eastward speed of the thermospheric neutral wind near the geomagnetic equator depends largely upon how the strength of the day-to-night pressure gradient force across the evening terminator is balanced by ion drag forcing and, possibly, the back pressure generated by the midnight pressure bulge [*Akmaev et al.*, 2010]. The statistical analysis of CHAMP observations from 2002 reported by *Liu et al.* [2006] found a jet of fast zonal winds centered upon the geomagnetic equator with speeds ranging between 100 $ms^{-1}$ to 150 $ms^{-1}$. The CHAMP observations are based upon the analysis of onboard accelerometer data at altitudes of 410 km for an orbital inclination of 87.3°. These results were compared with Dynamics Explorer-2 observations of zonal thermospheric winds with good agreement. This behavior has been modeled by *Miyoshi et al.* [2012] for the equinoctial period of September. Both sets of observations and the modeling results found increased winds over a spatial width of ~10° centered at the geomagnetic equator as compared with latitudes away from the dip equator.

The conclusion from this modeling study was that the zonal speed enhancement observed at the dip equator relative to the Appleton anomaly region may be attributed to the reduced plasma density within the equatorial ionosphere over the geomagnetic equator leading to reduced ion drag and an increased eastward wind speed. This conclusion is supported by the finding of ~25 $ms^{-1}$ reduction in the climatological response of the zonal thermospheric winds observed by two Fabry-Perot interferometers (FPI) located at the latitudes of Arequipa, Peru (−16.2°S) and Carmen Alto, Chile (23.1°S), respectively [*Martinis et al.*, 2001].

Studying the thermal response for these two longitudinal sectors is also of interest to see what difference, if any, there might be in regard to the behavior of the MTM as the MTM phenomenon progresses westward and poleward from the equatorial region toward the polar region. No results pertaining to this have yet been reported in the literature.

A similar study of the thermospheric response at widely separated longitudinal locations was performed by *Wu et al.* [2014], who used results from three Fabry-Perot interferometers (FPI) to compare winds for the American and Asian sectors at midlatitudes. The longitudinal separation between the China FPI observatories (~115°E) and the Boulder FPI observatory (105°W) is ~100°, providing an opportunity to search for a difference in thermospheric wind response. For quiet geomagnetic activity, the zonal and meridional winds for both sectors were found to be similar but with somewhat larger diurnal variation of the zonal wind seen in the American sector as well as an earlier reversal of the zonal wind direction to westward just prior to dawn. Both features were attributed to the higher geomagnetic latitude of the American longitude observations (49°N as compared with 33°N). The meridional wind diurnal behavior was similar for both locations

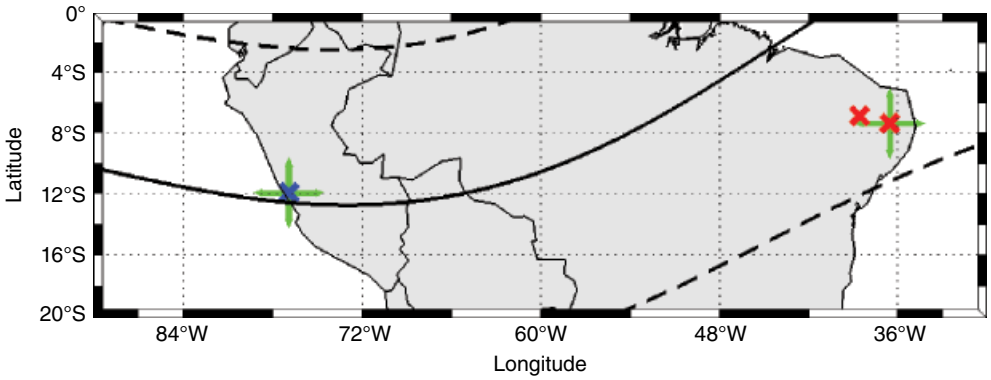


**Figure 15.1** Map of South America illustrating locations of the Peruvian (blue x, MRH) and Brazil (red x, CAJ, and red x, CAR) FPI observatories. The green strips indicate the four cardinal directions for each of the two FPI sites. Also plotted (solid black line) is the geomagnetic equator, and ±10° geomagnetic latitude (dashed black line).

suggesting that there is little difference in the pressure gradient or tidal-wave forcing functions between the two mid-latitude longitudinal sectors.

In this chapter, we report the results of simultaneous and monthly averaged FPI measurements of thermospheric zonal and meridional winds as well as temperatures obtained during the September equinox of the Southern Hemisphere from FPI observatories located at the geomagnetic equator in Peru and in northeastern Brazil, ~7° south of the geomagnetic equator. The FPI instruments observe the 630 nm nightglow emission, allowing estimates of thermospheric winds and temperatures to be made. The Peruvian neutral wind measurements reported in this study were obtained from the FPI instrument deployed at Merihill (geographic: 11.96°S, 76.86°W; geomagnetic: 0.57°N, 5.13°W), which is located on the ridge overlooking the Jicamarca Radio Observatory (see Fig. 15.1). The two Brazil FPI instruments were deployed as a part of the RENOIR project [*Makela et al.*, 2009] in May 2009 at separate sites in northeastern Brazil: Cajazeiras (geographic: 6.87°S, 38.56°W; geomagnetic: 7.11°S, 33.24°E) and Cariri (geographic: 7.38°S, 36.53°W; geomagnetic: 8.34°S, 34.96°E), located as shown in Figure 15.1 near the southern Appleton anomaly, where the optical observation conditions are very good for nightglow measurements [*Buriti et al.*, 2001]. The Peruvian and Brazilian sites are separated in longitude by ~38° (~4200 km), making possible the comparisons of the equatorial thermospheric dynamical response for selected nights and for monthly climatologies for the western and eastern coastal regions of the South American continent. In making these comparisons, we note that the Brazil geomagnetic location is located far enough south of the geomagnetic equator to be out of the fast zonal wind jet zone reported by *Liu et al.* [2006]. The magnetic declinations for the Peru and Brazil locations are 0.8° and ~22.1°, respectively.

Each of these FPI instruments also measures the thermospheric temperature determined from the spectral width of the integrated 630 nm lineshape signal along the line-of-sight through the 630 nm nightglow layer. These temperature results may be used to study the propagation speed, direction of motion, and the amplitude of the MTM phenomenon.

Three nights of simultaneous Peru and Brazil data selected from the 2010 September equinoctial period are compared as well as the monthly climatologies for the three equinoctial months of August, September, and October 2010. For the sake of enabling year to year comparisons, the October climatology for 2011 is also included and compared with results from October 2010.

## 15.2. FPI INSTRUMENTATION AND DATA ANALYSIS PROCEDURES

High-resolution imaging FPI measurements of the atomic oxygen 630 nm line shape are used to determine the Doppler shift and Doppler broadening of the O population within the lower thermosphere (200–275 km), which is assumed to be thermalized. The source of the OI 630 nm nightglow emission is the oxygen atom ($^1$D) metastable state generated in the dissociative recombination reaction of $O_2^+$ to yield $O^+$ and O($^1$D) [*Link and Cogger*, 1988] with a peak emission altitude of ~250 km. The Doppler shift measurements are proportional to the projection of the bulk velocity vector of the [O] population onto the instrument's line of sight, while the broadening is proportional to the temperature within the airglow layer.

The etalon aperture sizes for both RENOIR instruments and for the Peru instrument are 42 mm and 70 mm, respectively. A spacer gap of 1.5 cm and a reflectivity of ~78% are used for each etalon in these FPI instruments. A dual mirror sky-scanning system with a pointing accuracy

of ~0.2° mounted within a dome is used to obtain line-of-sight Doppler shifts in zonal and meridional directions. The exposure time for the CCD camera detector is typically 300 s for each 630.0 nm image. The papers by *Meriwether et al.* [2011], *Makela et al.* [2012], and *Harding et al.* [2014] describe the FPI instrument design and the procedures used for analyzing the multiple orders of the collected FPI images to determine Doppler line centers, Doppler widths, 630.0 nm intensity, and background continuum intensity retrieved for each 630 nm image.

A zero reference for the Doppler shifts must be established to obtain estimates of the line-of-sight neutral wind while allowing for instrumental drifts caused by ambient temperature changes. The approach adopted in the analysis assumes that the measured averaged order offset between zenith observations of the 630 nm emission and a frequency-stabilized HeNe 632.8 nm emission remains constant during the period from 22 LT to 05 LT. This would be the case if the average vertical wind during this period were small. This offset is applied to the laser data to determine the zero-Doppler shift reference for any off-zenith direction. Typical Doppler shift and Doppler width errors for FPI measurements for both Brazil and Peru observatories are 3–5 $ms^{-1}$ and 15–25 K, respectively, but can increase depending on the intensity of the 630 nm emission.

The Brazil observations use two observing strategies called the common volume (CV) and cardinal direction modes. The Peru observations during the study period employed only the cardinal mode. In the CV mode, the zonal and meridional wind speed components in each CV region, defined by the orthogonal intersection of the lines-of-sight of look angles from both FPI observatories, are used for analysis. Although there are two CV positions used in this observing mode, located to the north and south of the two FPI observatories, only the zonal and meridional wind components determined for the northernmost Brazil CV location are used.

In the cardinal mode used for both the Brazil and Peru FPI measurements, a cycle of north, east, south, west, and zenith directions is specified to observe the winds for each line-of-sight direction within the 630 nm nightglow layer. For Peru, data from the west and north directions are used to study the zonal and meridional winds, respectively. For Brazil, data from the east and south directions are used. Almost all of the Brazil FPI data used were from the Cariri site. Isolating these directions in the analysis preserves the information that might be smoothed out due to gradients, if, for example, both the north and south look directions were used from a single site to study the meridional wind.

For the monthly climatologies, individual wind measurements in selected directions were used to calculate weighted-averaged zonal and meridional thermospheric winds for successive 20 min bins. The weights used were the estimated uncertainties for the individual measurements. The vertical bars plotted in the monthly climatology figures represent the range of variability in the wind and temperature values observed within each averaging bin.

The Peru and Brazil temperature averages were determined by using the temperatures measured for all directions for each 20 min averaging bin. The standard deviation error for each averaged data point is ~10 K or less with somewhat larger standard deviations for results obtained just before sunrise when the nightglow intensity is weak. Also included in these temperature plots is the thermal variation of the Naval Research Laboratory Mass Spectrometer Incoherent Scatter Radar model (NRLMSISE-00) [*Picone et al.*, 2002] adjusted to match the observed temperature at the temperature minimum prior to the midnight temperature maximum (MTM) peak near local midnight. The magnitudes of the shift introduced were ~75 K and ~35 K reduction for the Peru and Brazil sectors, respectively. This adjusted NRLMSISE-00 model variation provides a baseline for the determination of the MTM amplitude. Comparative tests involving several FPI instruments have suggested that these offsets relative to the NRLMSISE-00 model may be a result of a weak OH contamination of the 630 nm lineshape that has a slight broadening effect but no effect upon Doppler shifts [*Burnside et al.*, 1977].

Results for the three 2010 months (August, September, October) and the 2011 October month for Peru and Brazil included data for 11, 23, 22, and 14 nights and 8, 21, 10, and 9 nights, respectively. While all instruments made measurements almost continually throughout this period, depending upon the month, cloudy conditions precluded the use of ~18%–54% and ~47%–80% of the Peru and Brazil data, respectively. Only the cardinal mode observing strategy was used in both sectors for the 2 months of August and September 2010, and also for the October months in Peru. About half of the Brazil observations for the October months were also collected in this mode with the remaining observations from Brazil obtained using the CV mode.

## 15.3. RESULTS

Figure 15.2 presents the zonal winds seen for the Brazil and Peru observations for three nights (DOY 246, 247, and 248) selected from September 2010. The geomagnetic activity for the three selected nights was quiet with Kp values within the range of 0 to 3 during the nighttime observing hours (22 to 07 UT for Brazil, 0 to 10 UT for Peru). All results are plotted against Universal Time in contrast to Local Time to make more clear the simultaneous nature of the temporal development of the wind and temperature dynamical response for both longitudinal

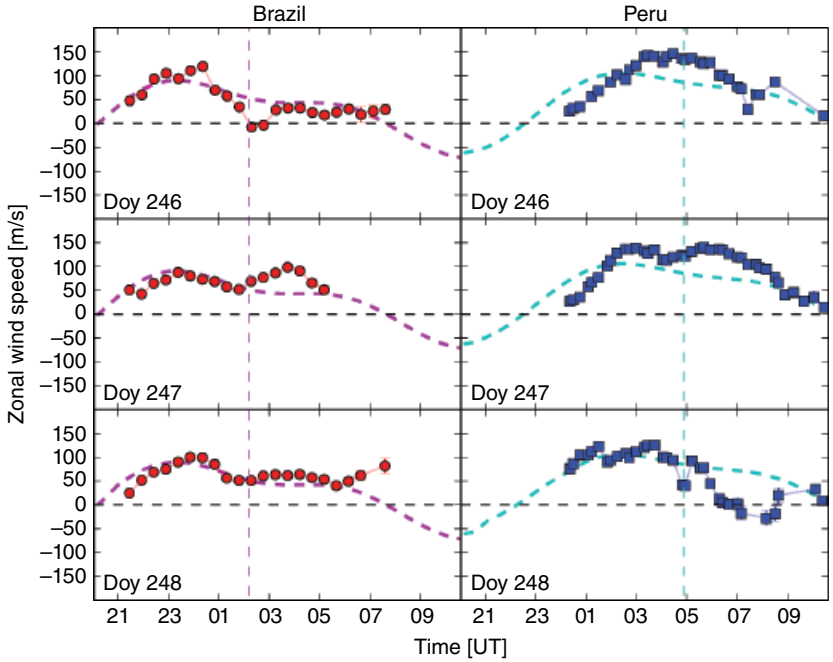


**Figure 15.2** Brazil (circles) and Peru (squares) zonal wind speed variations plotted against Universal Time. Brazil and Peru observations were made in the east and west directions, respectively, for 3–4, 4–5, and 5–6 September 2010 (DOY 246, 247, and 248). The dashed horizontal curve and vertical line plotted in each panel refer to the HWM14 model zonal wind speed variation and Universal Time of solar midnight, respectively. Positive values are eastward.

sectors. The LT-UT difference is −3 hr for Brazil and –5 hr for Peru. Observations typically begin just after twilight near 19 LT, so data collection begins at Brazil first and is followed by Peru 2 hr later. Also included in this figure for each night is the zonal wind variation computed using the 2014 updated version of the Horizontal Wind Model [HWM; *Drob et al.*, 2015; *Drob et al.*, 2008; *Emmert et al.*, 2008].

Figure 15.3 shows the zonal wind monthly climatologies for August, September, and October 2010, which represents the September equinoctial season. Figure 15.3 also includes the monthly climatology for October 2011 to illustrate the year-to-year change in the averaged zonal wind that might be caused by the solar cycle change in the solar flux from ~80 to ~140 flux units between the October months of 2010 and 2011. Averaged HWM14 zonal thermospheric winds are plotted in this figure, with the thickness indicating the range of model variability for each month.

Figures 15.4 and 15.5 show, respectively, the meridional wind results for the three September 2010 nights and for the monthly climatologies for the 3 months of August, September, and October 2010 as well as the 2011 October month. Figures 15.6 and 15.7 present, respectively, the averaged temperature results for the three September 2010 nights and the results for the monthly-averaged temperatures for the 4 months of August, September, and October, 2010, and the 2011 October month. No periods of any major geomagnetic activity appeared during the three 2010 months and the one 2011 month, and the mean monthly ap indices were 8, 5, 6, and 11, respectively.

### 15.3.1. Zonal Winds: Individual and Monthly Climatologies

Figure 15.2 illustrates similar signatures in the nocturnal zonal wind variation for both longitudinal sectors for 3 nights between 3 and 4 September 2010 (day of year [DOY], 246) and 5–6 September 2010 (DOY, 248). Between 00 UT and 02 UT for the Peruvian sector, the zonal wind increases eastward from the initial speed of 25 to 50 $ms^{-1}$, reaching a maximum speed of ~140 $ms^{-1}$ between 02 to 05 UT. The zonal wind then decreases toward zero until just before dawn. The Brazil data tends to behave similarly with one difference. While the initial rate of zonal wind speed increase for Brazil is similar to that of Peru, the peak value of the zonal wind reached for Brazil is only 100 $ms^{-1}$. On 1 night, DOY 248, the Brazil data showed a slight increase of 25 $ms^{-1}$ eastward before dawn. Comparison of the data with the HWM14 model winds shows good agreement for Brazil, but an increase relative to the model of ~40 $ms^{-1}$ for the observed eastward winds near solar midnight for Peru.

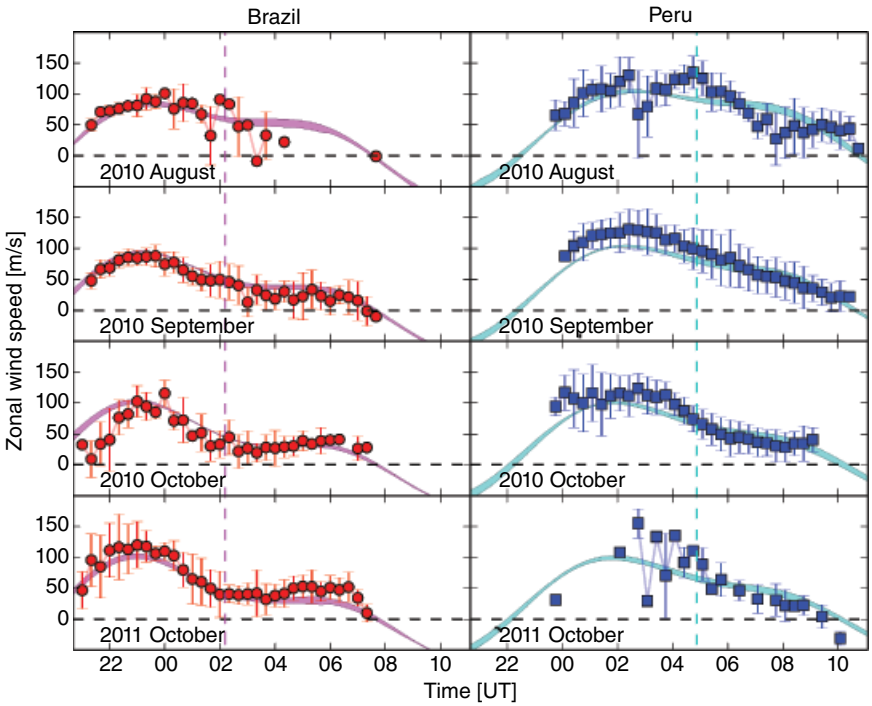


**Figure 15.3** Brazil (circles) and Peru (squares) monthly averaged zonal wind speed variations plotted against Universal Time for three 2010 months (August, September, October) and one 2011 month (October). Each averaging time interval was 20 min. Vertical lines on individual data points indicate the range of variability in the data selected for averaging. Also plotted in each panel is the HWM14 model zonal wind speed variation averaged for the nights selected in each month with the thickness indicating the range of model variability. The dashed vertical line in each panel marks the Universal Time of solar midnight.

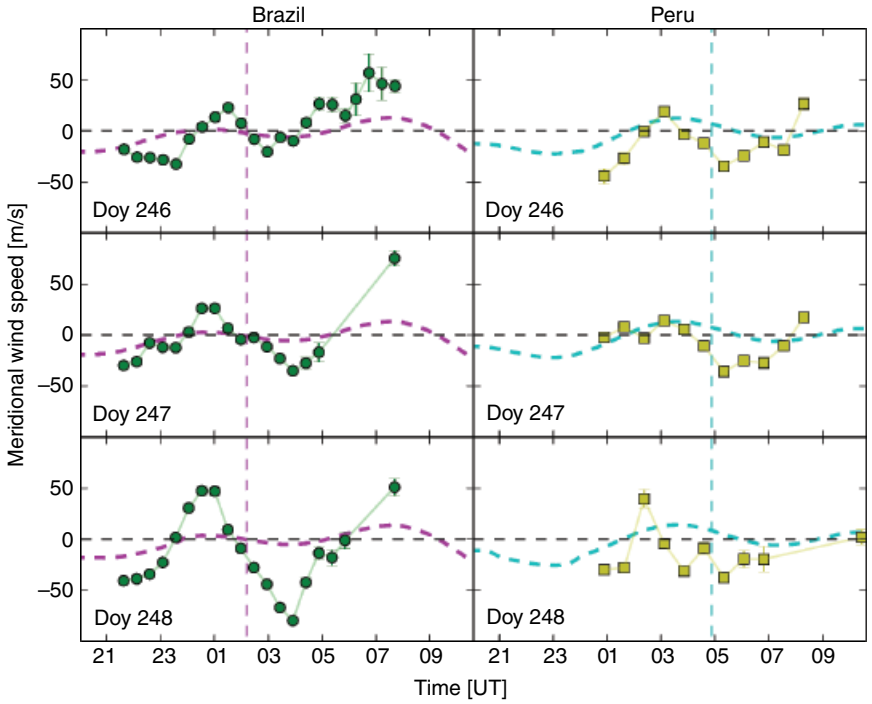


**Figure 15.4** Brazil (circles) and Peru (squares) meridional wind speed variations plotted against Universal Time for 3–4, 4–5, and 5–6 September 2010 (DOY 246, 247, and 248). Brazil and Peru observations were made in the south and north directions, respectively. The dashed horizontal curve and vertical line plotted in each panel refer to HWM14 model meridional wind speed variation and the Universal Time of solar midnight, respectively. Positive values are northward.

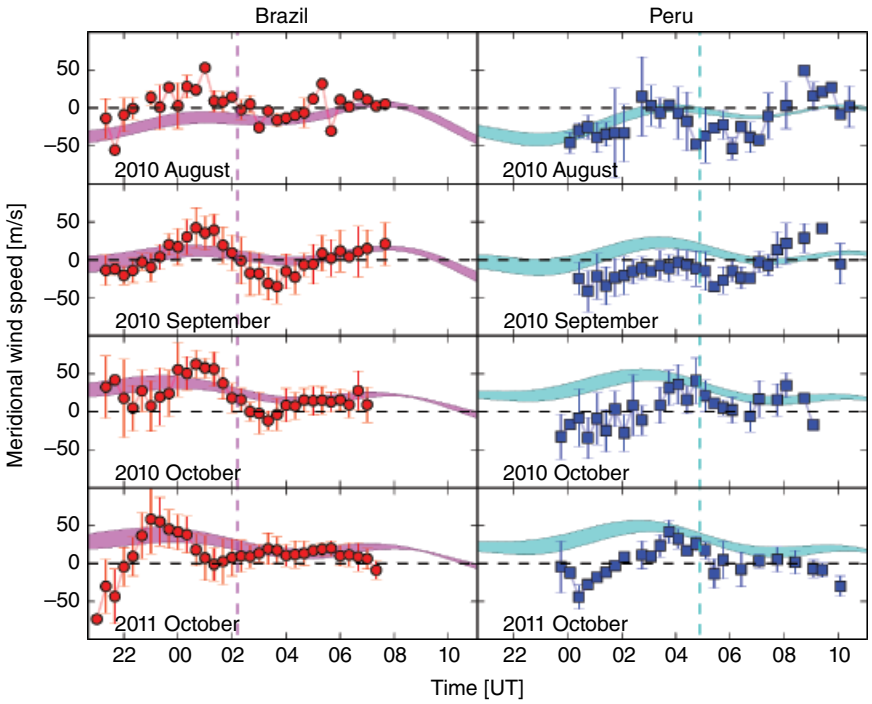


**Figure 15.5** Brazil (circles) and Peru (squares) monthly averaged meridional wind speed variations plotted against Universal Time for three 2010 months (August, September, and October) and one 2011 month (October). The averaging time interval for each data point is 20 min. Vertical lines on individual data points indicate the range of variability in the data selected for averaging. The horizontal curve plotted in each panel refers to the HWM14 model meridional wind speed variation for the nights averaged within each month with the thickness indicating the range of model variability. The dashed vertical line in each panel marks the Universal Time of solar midnight.

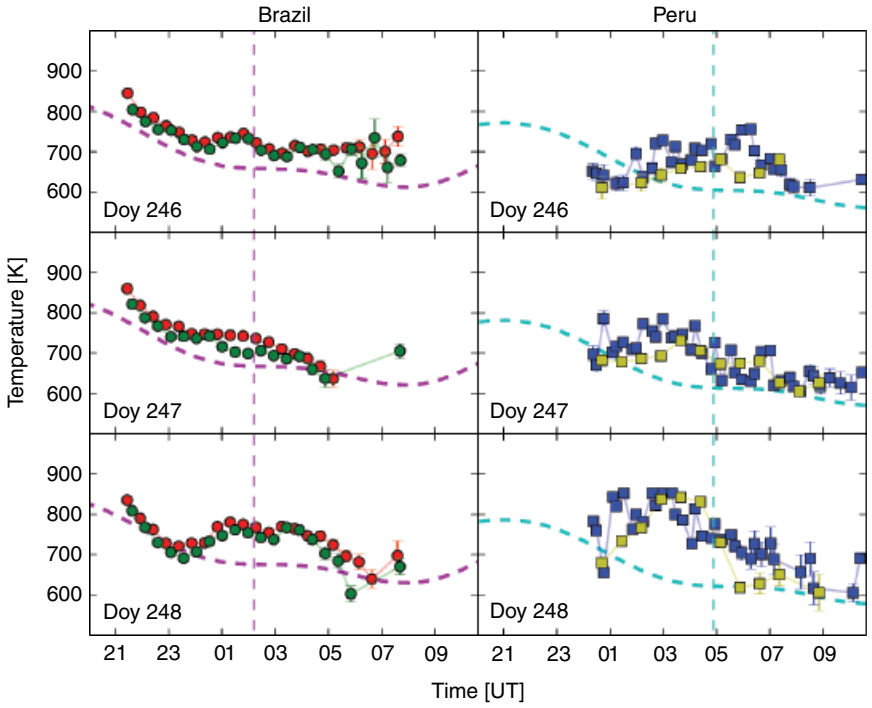


**Figure 15.6** Temperature variations for individual meridional (red, blue) and zonal (green, yellow) data points plotted against Universal Time for 3–4, 4–5, and 5–6, September 2010 (DOY 246, 247, and 248). The dashed vertical line in each panel refers to the Universal Time of solar midnight.

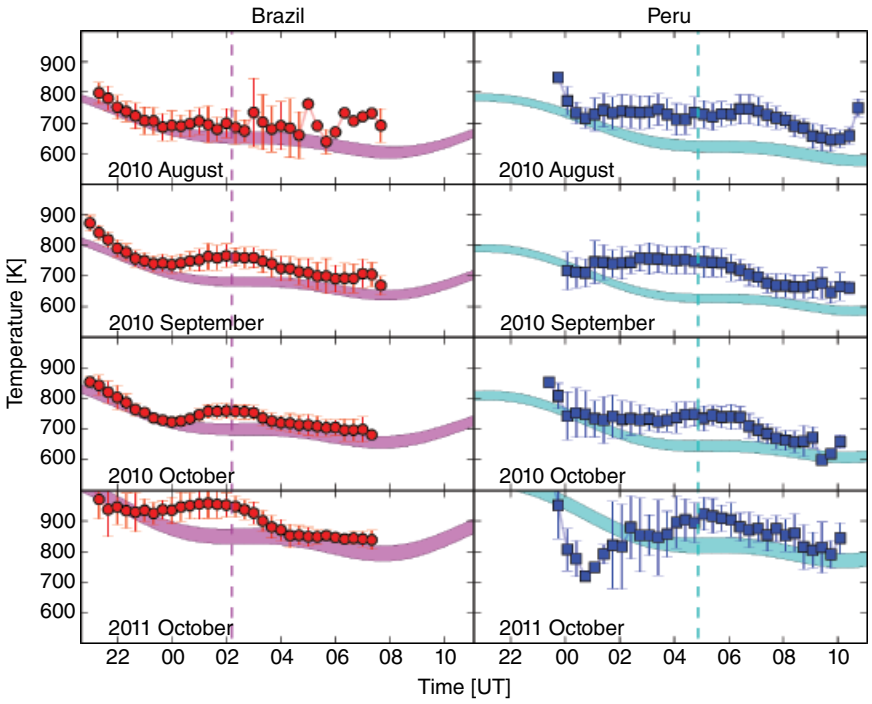


**Figure 15.7** Temperature variations of monthly averaged Brazil (circles) and Peru (squares) observations. Individual data points for all selected directions within each 20 min bin were averaged for each point plotted. Vertical lines on individual data points indicate the range of variability in the data selected for averaging. The horizontal curve plotted in each panel refers to the NRLMSISE-00 model temperature variation for the selected nights averaged within each month with the thickness indicating the range of NRLMSISE-00 model variability.

The zonal wind climatologies plotted in Figure 15.3 for both sectors illustrate the same features seen in Figure 15.2 with rather similar temporal histories for all 4 months. Here again, the zonal wind speed maxima is somewhat stronger for the Peru data, but this enhancement in the averaged winds is only ~15–20 $ms^{-1}$, two times weaker than what was seen for the individual nights plotted in Figure 15.2. The UT time separation between the Brazil and Peru zonal wind maxima is ~3 hr with a possible variation of ±0.5 hr, which is comparable with what is seen in looking at the individual comparisons plotted in Figure 15.2.

While it is attractive to think that the reduction of the zonal wind maximum seen for Brazil is a result of increased ion drag forcing caused by the higher plasma densities off the geomagnetic equator, verification of this hypothesis would require knowledge of the *F*-region plasma density for both sectors. This issue will be studied in more detail in future work using Cariri ionosonde and Jicamarca ISR data.

In comparing the monthly climatologies with the updated HWM model winds, the Peru data for 2 (August and October 2010) of the 4 months plotted show the development of a period of reduced eastward flow relative to the model between 05 and 10 UT following the peak seen near 00 UT. For the Brazil sector, this behavior is captured in the HWM model winds between 00 to 06 UT. For these 2 months of Peru data, the difference relative to the HWM model winds is ~25 $ms^{-1}$. In contrast, no such reduction is evident for the September 2010 month and only a slight weak reduction for October 2011. The Brazil climatologies and the HWM model winds both show the development of this ebb period for 3 of the 4 months with an amplitude of 20–40 $ms^{-1}$ for the extent of speed reduction between the peak near 23 UT and the secondary peak at 06 UT. In general, the application of the HWM14 empirical model found the agreement of the model winds with FPI ground-based data to be markedly improved relative to that of previous comparisons [*Makela et al.*, 2012].

The discussion in the climatology studies by *Meriwether et al.* [2011] and *Makela et al.* [2013] and in the data-modeling comparison study by *Meriwether et al.* [2011] made reference to this ebb period as being a feature of the progression of the MTM pressure bulge through the equatorial region from the geographic equator toward higher latitudes in the south. The MTM tidal winds would be westward on the evening side of the MTM pressure bulge and eastward on the morning side. Thus, the MTM winds tend to first reduce the eastward flow

caused by the evening day-to-night pressure gradient and then enhance the eastward flow subsequent to the MTM passage.

### 15.3.2. Meridional Winds: Individual and Monthly Climatologies

Figure 15.4 shows the Brazil and Peru nocturnal variations of the meridional wind speeds for the same three nights between 3–4 September 2010 and 5–6 September 2010. Southward meridional winds between 25 and 50 $ms^{-1}$ are seen in both Brazil and Peru observations over approximately the first 3 hr of each night. After this period, a northward flow peaking at 01 UT for Brazil and again at 07 UT is seen with a magnitude of ~25–50 $ms^{-1}$ for the first peak and 50–75 $ms^{-1}$ for the second peak. Near 03–04 UT the flow is southward with a speed of about 30 to 75 $ms^{-1}$. Although it is less clear, the Peru data shows a somewhat similar double-peak signature, with the northward flow peaking near 03 UT and again between 09–10 UT. In between these two peaks, the wind is southward with a speed of ~30 $ms^{-1}$ near 05 UT.

In the meridional wind climatologies presented in Figure 15.5, the Brazil meridional wind speed in the early evening for the 2010 months varied from being negative (southward) at speeds of ~25 $ms^{-1}$ in August to zero in September and positive by 20–25 $ms^{-1}$ in October. The 2011 October month showed a stronger variation, switching from southward winds of 50–65 $ms^{-1}$ at 2130 UT to 50 $ms^{-1}$ at 2330 UT. The Brazil meridional winds for the 2010 months then increased from the initial values to a peak of 25 to 40 $ms^{-1}$. The initial behavior of the meridional winds in 2011 October, showing a reversal of magnitude 125 $ms^{-1}$ taking place over an hour, is surprising and suggests a new dynamic feature added to the nominal tidal-wave double-peaked structure. Future research will look at the October monthly averaged climatologies for other years to see if this anomaly seen in the Brazil early evening observations is reproduced.

The Peru meridional wind speeds in Figure 15.5 show a similar double-peaked structure for all 4 months with maxima seen at 03 UT and later at 08–09 UT. For each month, the initial wind speed is southward (negative) at ~25 to 50 $ms^{-1}$.

Figure 15.5 shows monthly climatology plots for the same 4 months as in Figure 15.3, and it can be seen that the same double-peaked structure discussed for Figure 15.4 is evident for both the Brazil and Peru sectors. Again, the phase separation between the two peaks of these two structures is ~6 hours. The difference in the times for the first peak appearance in Brazil and Peru is ~2.5 hr, which suggests that this structure is dominated by the local time dependence of the meridional winds, as this local time difference is equivalent to the ~2.5 hr solar time difference between the two sectors (i.e., 38° longitude difference divided by 15°/1 hr LT).

The observed double-peak behavior for both longitudinal sectors is consistent with the results described by *Meriwether et al.* [2008, 2011] and *Makela et al.* [2013]. The comparison of the observed double-peak structure with the tidal-wave structure behavior predicted by the WAM calculations [*Akmaev et al.*, 2011; *Akmaev et al.*, 2010] that was discussed by *Meriwether et al.* [2013] demonstrated that the combination of the semidiurnal tidal wave with the higher order migrating tidal waves including the terdiurnal tidal wave produced a composite 6 hr nighttime tidal wave that is made up of the contributions from these higher order tidal modes. Thus, the ratio of the amplitudes of the two northward-directed peaks may reflect the day to day variability of the tidal-wave structural contribution to thermosphere winds.

### 15.3.3. Temperatures: Individual and Monthly Averaged

Results for the thermospheric temperatures on the three individual nights plotted in Figure 15.6 and the associated NRLMSISE-00 model data (shifted as described above) show similar temporal behavior from night to night. For Brazil, an initial cooling of 100–125 K over 2–2.5 hr reaching a minimum near 23–24 UT is seen. This initial period of thermal decay is followed by an enhancement relative to the NRLMSISE-00 model of about 30 to 100 K with a peak appearing 2–4 hr after the minimum. This peak is identified to be the midnight temperature maximum (MTM) resulting from the tidal wave propagating into the thermosphere region [*Meriwether et al.*, 2011; *Makela et al.*, 2012; and *Meriwether et al.*, 2013]. The MTM amplitude and the MTM structure defined by the interval between the minimum seen before the MTM peak and the minimum observed just before dawn is variable from one night to the next. The Brazil results for DOY 246 suggest a MTM peak with a base width of ~2 hr. The results for the other two nights suggest a MTM peak profile that is broader, extending over 4 hr. In all cases, the MTM peak is followed by a cooling trend toward dawn.

The behavior seen for the Peru observations shows less of the initial cooling trend than for Brazil, and the increase toward the MTM peak starts almost immediately after the beginning of observations. For Peru, the MTM structure is less clearly defined but has a base width of ~3 to 5 hr. The broad structure of the MTM peak makes the determination of the phase separation between the Brazil and Peru MTM peaks difficult, but 2–3 hr would be representative.

The same extended MTM thermal behavior, as defined by the difference between the times for the two

minima, is seen for the Brazil and Peru monthly climatologies presented in Figure 15.7. The phase difference between the times of the MTM peaks observed for Brazil and Peru is ~3 ± 0.5 hours. The MTM amplitude seen for both Brazil and Peru varied from one month to the next, but was typically within the range of 50 K to 100 K. Relative to the NRLMSISE-00 baseline, the local time base width of the Peru MTM structure was ~6–7 hr for each of the 4 months, which is ~1–3 hr more than the base width observed for the Brazil MTM. Near solar midnight for each sector, an increase of 100 K is evident in the baseline temperature between the October months of 2010 and 2011. This increase is explained by the increase in the solar F10.7 index from nearly solar minimum of 80 flux units in 2010 to the moderate level, 140 flux units, in 2011.

## 15.4. DISCUSSION

These results illustrate the equatorial meridional and zonal wind behavior seen for the September equinox for two longitudinal sectors separated by ~38° longitude, that is, ~2.5 hr solar time. The zonal wind data for both sectors exhibit a similar variation with increased eastward winds seen for 2 hr after sunset. The increase is larger for Peru than for Brazil (i.e., ~40–50 $ms^{-1}$ to 90 $ms^{-1}$ for Brazil and to ~125 $ms^{-1}$ for Peru). This differential behavior may be explained by a modification of the zonal momentum balance in the early evening just after twilight. The reduction of the plasma density over the geomagnetic equator caused by the prereversal enhancement followed by the decreased ion drag resistance to the day-to-night pressure gradient results in increased eastward zonal winds to higher speeds than is seen for the Brazil observatory. The location of the Brazil FPI observatory on the northern border of the southern Appleton anomaly, where the plasma density would be considerably larger, suggests that the resulting increased ion drag resistance to the zonal wind forcing by the pressure gradient would dampen this zonal wind increase [*Martinis et al.*, 2001]. It is unclear how much of a role in this momentum balance is played by the back pressure that would be developed by the passage of the pressure bulge associated with the MTM tidal-wave structure [*Herrero et al.*, 1985; *Akmaev*, 2011], which would be moving southward for both Peru and Brazil sectors near solar midnight.

Another interesting feature indicated by these results at both longitude sectors is the development of a period of reduced eastward winds in the monthly climatologies lasting for 4 to 6 hr. The existence of this feature was discussed by *Meriwether et al.* [2013] as being indicative of the influence of the MTM pressure bulge upon the eastward zonal wind driven by the day-to-night pressure gradient. The development of the MTM peak shows a maximum that occurs midway between the beginning and end times of this ebb period, which is consistent with this interpretation of the zonal winds.

The meridional wind results for both sectors show the development of a double peak structure with amplitude of 30 to 50 $ms^{-1}$. The WAM modeling [*Akmaev*, 2011] showed this feature to be a result of the tidal-wave structure representing a blend of the semidiurnal and higher order tidal modes propagating into the thermosphere region from below. The observed separation of ~6 hr between the times of the two peaks is supported by the results of the WAM analysis [*Akmaev et al.*, 2010, *Akmaev*, 2011].

Analysis of the results for September and October 2010 for both sectors found that the MTM feature appeared with an amplitude of ~50 K to 100 K with the MTM peak following the first northward meridional wind peak by ~1–2 hr. For these monthly climatologies, the amplitude of the Peruvian MTM peak is slightly larger than the Brazil peak by ~25 K. Also interesting is the result that the local time base width of the MTM peak is larger by ~1–2 hr in the Peruvian sector.

To summarize these points and to help illustrate the phase relationships between the zonal wind, meridional wind, and temperature more explicitly, Figure 15.8 shows the monthly climatologies for all three parameters in the September month plotted against UT and also against solar LT. The times of the two northward peaks in the meridional wind structure show a time difference of ~5 hr for Brazil and ~6 hr for Peru, which is comparable with what was reported by *Meriwether et al.* [2013] in the Brazil/WAM comparisons for September. The phase lag between the first northward (equatorward) meridional peak wind speed and the MTM peak for both sectors is ~1.0 hr. This difference is the phase lag expected for the temporal variations of meridional wind and temperature as the change in the meridional winds associated with the upward propagation of the tidal wave reaches the 630 nm airglow layer prior to the arrival of the peak phase of the tidal-wave temperature fluctuation cycle [*Akmaev*, 2011]. In regard to the zonal wind variation when plotted against SLT, inspection of the results in Figure 15.8 shows the phase difference in the zonal winds for the two regions to be close to zero. The time for the progressive increase in the zonal wind for both regions from evening twilight to the peak is expected to be similar as the elevation of the plasma in the prereversal enhancement reduces the ion drag for both regions. What is evident in this figure is the Peru zonal wind enhancement by about 50 $ms^{-1}$, and this is attributed to the lower plasma density at the geomagnetic equator.

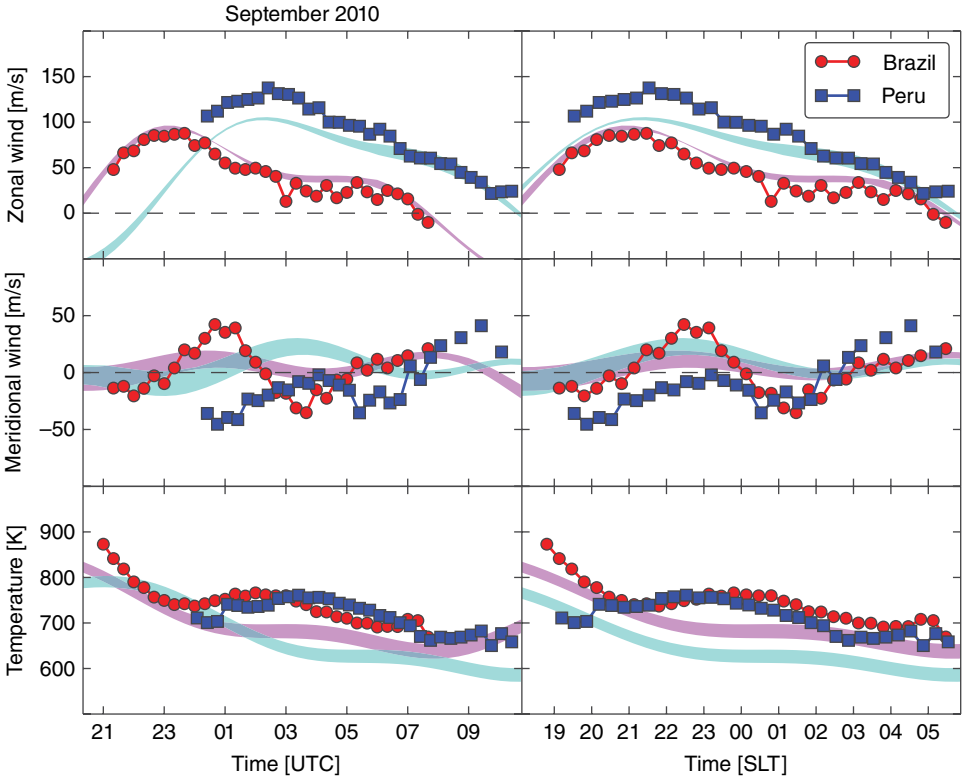


**Figure 15.8** Brazil (red circles) and Peru (blue squares) monthly averaged zonal wind, meridional wind, and temperature variations plotted against Universal Time (left panels) and Solar Local Time (right panels) for September 2010. Also plotted in these panels for Peru (red) and Brazil (blue) are the HWM14 zonal and meridional wind model variations and the NRLMSISE-00 temperature variation. The thickness of the model curves indicates the range of model variability for the winds and temperatures for the nights that FPI data were available.

## 15.5. CONCLUDING REMARKS

These results illustrate the improved insights into the equatorial thermospheric dynamics gained from the study of simultaneous FPI data for two longitudinal sectors. The meridional wind and temperature results from the Peru and Brazil sectors are quite similar, indicating that the migrating tidal-wave structure plays a dominant role in governing the thermospheric meridional wind and temperature responses at low latitudes. Comparisons of the zonal wind monthly climatology results for four different months found the zonal wind in the geomagnetic equator region to be increased by 20 to 40 $ms^{-1}$ relative to the Brazil site located away from the equator by ~7 degrees. As suggested by the CHAMP/DE-2 study [*Liu et al.*, 2006], this zonal wind enhancement at the geomagnetic equator suggests a sensitivity to the change in the local momentum balance that reduction of the *F*-region plasma density near the geomagnetic equator would introduce. Investigating more closely this possible relationship between ion drag reduction and the zonal wind enhancement will be an aim of future work by acquiring *F*-region plasma density measurements simultaneous with FPI wind measurements in both regions. It would be interesting to extend such longitudinal comparisons into the African longitudinal sector with Ethiopian observations, and an effort is underway to achieve this goal.

## ACKNOWLEDGMENTS

Work at the Clemson University and the University of Illinois at Urbana-Champaign was supported by National Science Foundation CEDAR grants ATM-0940217 and ATM-0940253, respectively. The Jicamarca Radio Observatory is a facility of the Instituto Geofisico del Peru operated with support from the NSF AGS-0905448 through Cornell University. We thank the Jicamarca staff, and particularly Luis Navarro and Oscar Veliz, for support provided for the operations of the Jicamarca Fabry-Perot interferometer. We are also grateful to Dr. Ricardo Buriti, Federal University of Campina Grande, Brazil, for his untiring efforts to continue the operations of both FPI instruments at Cariri and Cajazeiras. The NRL-HWM14 model results presented in this paper were calculated using an updated HWM version provided to the University of Illinois by Dr. Douglas Drob, Naval Research Laboratory.

## REFERENCES


Akmaev, R. A. (2011), Whole atmosphere modeling: Connecting terrestrial and space weather, *Rev. Geophys.*, *49*, RG4004; doi:10.1029/2011RG000364.

Akmaev, R. A., F. Wu, T. J. Fuller, Rowell, H. Wang, and M. D. Iredell (2010), Midnight density and temperature maxima, and thermospheric dynamics in Whole Atmosphere Model simulations, *J. Geophys. Res.*, *115*, A08326; doi:10.1029/2010JA015651.

Akmaev, R. A., F. Wu, T. J. Fuller-Rowell, and H. Wang (2009), Midnight temperature maximum (MTM) in Whole Atmosphere Model (WAM) simulations, *Geophys. Res. Lett.*, *36*, L07108; doi:10.1029/2009GL037759.

Buriti, R. A., H. Takahashi, and D. Gobbi (2001), First results from mesospheric airglow observations at 7.5°S, *Rev. Bras. Geofis.*, *19*, 169–176; doi:10.1590/S0102-261X2001000200005.

Burnside, R. G., J. W. Meriwether Jr., and M. R. Torr (1977), Contamination of ground based measurements of OI (6300 Å) and NI (5200 Å) airglow by OH emissions, *Planet. Space Sci.*, *25*, 985–988; doi:10.1016/0032-0633(77)90012-5.

Drob, D. P., et al. (2008), An empirical model of the Earth's horizontal wind fields: HWM07, *J. Geophys. Res.*, *113*, A12304; doi:10.1029/2008JA013668.

Drob, D. P., J. T. Emmert, J. W. Meriwether, J. J. Makela, E. Doornbos, M. Conde, H. Gonzales, J. Noto, S. M. McDonald, J. D. Huba, and J. H. Klenzing (2015), An update to the horizontal wind model: the quiet-time thermosphere, *Earth and Space Sci.*, *2*, 301–319; doi:10.1002/2014EA000089.

Emmert, J. T., D. P. Drob, G. G. Shepherd, G. Hernandez, M. J. Jarvis, J. W. Meriwether, R. J. Niciejewski, D. P. Sipler, and C. A. Tepley (2008), DWM07 global empirical model of upper thermospheric storm-induced disturbance winds, *J. Geophys. Res.*, *113*, A11319; doi:10.1029/2008JA013541.

Faivre, M., J. Meriwether, C. Fesen, and M. Biondi (2006), Climatology of the midnight temperature maximum at Arequipa, Peru, *J. Geophys. Res.*, *111*, A06302; doi:10.1029/2005JA011321.

Harding, B. J., T. W. Gehrels, and J. J. Makela (2014), A nonlinear regression method for estimating neutral wind and temperature from Fabry-Perot interferometer data, *Appl. Optics*, *53*, 666–673; doi:10.1364/AO.53.000666.

Herrero, F. A., and N. W. Spencer (1982), On the horizontal distribution of the equatorial thermospheric midnight temperature maximum and its seasonal variation, *Geophys. Res. Lett.*, *9*, 1179–1182; doi:10.1029/GL009i010p01179.

Herrero, F. A., H. G. Mayr, N. W. Spencer, and A. E. Hedin (1985), Interaction of zonal winds with the equatorial midnight pressure bulge in the Earth's thermosphere: Empirical check of momentum balance, *Geophys. Res. Lett.*, *12*(8), 491–494; doi:10.1029/GL012i008p00491.

Link, R., and L. L. Cogger (1988), A reexamination of the O I 6300 nightglow, *J. Geophys. Res.*, *93*, 98839892; doi:10.1029/JA093iA09p09883.

Liu, H., H. Lühr, S. Watanabe, W. Koehler, V. Henize, and P. Visser (2006), Zonal winds in the equatorial upper thermosphere: Decomposing the solar flux, geomagnetic activity, and seasonal dependencies, *J. Geophys. Res.*, *111*, A07307; doi:10.1029/2005JA011415.

Ma, R., J. Xu, W. Wang, J. Lei, H. L. Liu, A. Maute, and M. E. Hagan (2010), Variations of the nighttime thermospheric mass density at low and middle latitudes, *J. Geophys. Res.*, *115*, A12301; doi:10.1029/2010JA015784.

Makela, J. J., J. W. Meriwether, J. P. Lima, E. S. Miller, and S. J. Armstrong (2009), The remote equatorial nighttime observatory of ionospheric regions project and the International Heliospherical Year, *Earth Moon Planet*, *104*, 211–226; doi:10.1007/s11038-008-9289-0.

Makela, J. J., J. W. Meriwether, A. J. Ridley, M. Ciocca, and M. Castellez (2012), Large-scale measurements of thermospheric dynamics with a multisite Fabry-Perot interferometer network: Overview of plans and results from midlatitude measurements, *Int. J. Geophys.*, *103*, 94–102; doi:10.1155/2012/872140

Makela, J. J., D. J. Fisher, J. W. Meriwether, R. A. Buriti, and A. F. Medeiros (2013), Near-continual ground-based nighttime observations of thermospheric neutral winds and temperatures over equatorial Brazil from 2009 to 2012, *J. Atmos. Solar-Terr. Phys.*; doi:10.1016/j.

Martinis, C., J. Meriwether, R. Niciejewski, M. Biondi, C. Fesen, and M. Mendillo (2001), Zonal neutral winds at equatorial and low latitudes, *J. Atmos. Solar-Terr. Phys.*, *63*, 1559–1569; doi:10.1016/S1364-6826(01)00022-0.

Meriwether, J., M. Faivre, C. Fesen, P. Sherwood, and O. C. Veliz (2008), New results on equatorial thermospheric winds and the midnight temperature maximum, *Ann. Geophys.*, *26*, 447–466; doi:10.5194/angeo-26-447-2008.

Meriwether, J. W., J. J. Makela, D. J. Fisher, R. A. Buriti, A. F. Medeiros, R. A. Akmaev, T. J. Fuller-Rowell, and F. Wu (2013), Comparisons of thermospheric wind and temperature measurements in equatorial Brazil to Whole Atmosphere Model Predictions, *J. Atmos. Solar-Terr. Phys.*, http://dx; doi.org/10.1016/j.jastp.2013.04.002.

Meriwether, J. W., J. J. Makela, Y. Huang, D. J. Fisher, R. A. Buriti, A. F. Medeiros, and H. Takahashi (2011), Climatology of the nighttime equatorial thermospheric winds and temperatures over Brazil near solar minimum, *J. Geophys. Res.*, *116*, A04322; doi:10.1029/2011JA016477.

Miyoshi, Y., H. Fujiwara, H. Jin, H. Shinagawa, and H. Liu (2012), Numerical simulation of the equatorial wind jet in the thermosphere, *J. Geophys. Res.*, *117*, A03309; doi:10.1029/2011JA017373.

Picone, J. M., A. E. Hedin, D. P. Drob, and A. C. Aikin (2002), NRL-MSISE-00 empirical model of the atmosphere: Statistical comparisons and scientific Issues, *J. Geophys. Res.*, *107*, 1468; doi:10.1029/2002JA009430.

Wu, Q., W. Yuan, J. Xu, C. Huang, X. Zhang, J.-S. Wang, and T. Li (2014), First U.S.-China joint ground-based Fabry-Perot interferometer observations of longitudinal variations in the thermospheric winds, *J. Geophys. Res.*, *119*, 5755–5763; doi:10.1002/2014JA020089.

# 16

# Observations of TIDs over South and Central America

**Cesar E. Valladares,[1] Robert Sheehan,[1] and Edgardo E. Pacheco[2]**

## ABSTRACT

TEC values measured by GPS receivers that belong to the low-latitude ionosphere sensor network (LISN) and several other networks that operate in South and Central America were used to study the characteristics and origin of traveling ionospheric disturbances (TID) in these regions. The TEC perturbations associated with these TIDs show a high degree of spatial coherence over distances > 1000 km allowing us to use measurements from receivers spaced by hundreds of km to calculate the TIDs' travel velocities, propagation direction, and scale size. We first applied the TID analysis to TEC measurements corresponding to 4 July 2011. This processing method is then used to study the characteristics of TIDs for 20 and 21 August 2011, a period when a tropical storm was active in the Caribbean region. A pronounced increase in TID activity was observed in South and Central America at 16 UT on 20 August 2011 lasting until the end of 21 August 2011. The TID velocities show a very variable pattern that depends upon their local time and location. Counter-streaming TIDs were observed over the western part of South America on 21 August 2011. Regional maps of tropospheric temperature brightness, measured by the GOES-12 satellite, are used to identify and follow the development of the tropical storm (TS) Irene and several deep convective plumes. TIDs were observed propagating away from TS Irene. This storm moved into the Caribbean region and intensified earlier on 20 August spawning a train of atmospheric gravity waves (AGW). The small scale size, the velocity less than 150 m/s, and the close location of several TIDs with respect to TS Irene indicate that these TIDs may be the result of primary AGWs that reached the *F*-region bottomside. These results open the possibility of using TEC values measured by networks of GPS receivers to construct regional, and probably global, maps of TIDs, identify their origin, and study in detail the characteristics of TIDs corresponding to primary and secondary AGWs.

**Key Points:**
Regional maps of traveling ionospheric disturbances
Primary and secondary gravity waves
Networks of GPS receivers

**Key Terms:** atmospheric gravity waves, distributed observatory, traveling ionospheric disturbances

## 16.1. INTRODUCTION

Atmospheric gravity waves (AGW) are buoyancy waves that have a dynamic characterized by the interplay between gravity, pressure gradient, and inertial force [*Hocke and Schlegel*, 1996]. Traveling ionospheric disturbances (TID) are the ionospheric response to the passage of AGWs [*Hines*, 1960].

[1]*Institute for Scientific Research, Boston College, Newton, Massachusetts, USA*
[2]*Instituto Geofísico del Perú, Jicamarca Radio Observatory, Lima, Lima, Peru*

*Ionospheric Space Weather: Longitude and Hemispheric Dependences and Lower Atmosphere Forcing, Geophysical Monograph 220*, First Edition. Edited by Timothy Fuller-Rowell, Endawoke Yizengaw, Patricia H. Doherty, and Sunanda Basu.

Gravity waves (GW) produce perturbations in the plasma density, ion velocity, and ion and electron temperatures. TIDs are often classified as large scale and medium scale, according to their wave velocity and period. Typical scales size for TIDs (medium and large scales) vary between hundreds and thousands of kms, and periods between 15 min and 3 hr. The terminology of medium-scale TIDs (MSTID) also includes buoyancy waves that have been electrified, following the Perkins instability [*Perkins*, 1973]. They mainly occur at mid-latitude regions where the magnetic field lines are tilted.

Several measuring techniques have been used to study the characteristics and morphology of TIDs. Airglow imagers placed at opposite hemispheres have shown the conjugate characteristics of nighttime MSTIDs in the opposite hemisphere [*Otsuka et al.*, 2004; *Shiokawa, et al.*, 2005, *Martinis et al.*, 2011]. Radio beacon receivers in the VHF band have shown that daytime and nighttime TIDs have different seasonal variations of their occurrence and propagation direction [*Jacobson et al.*, 1995]. Similarly, dense networks of GPS receivers have provided 2-D maps of TEC perturbations caused by TIDs [*Saito et al.*, 1998; *Afraimovich et al.*, 2001]. The radio beacon technique [*Mercier*, 1986; *Jacobson, and Erickson*, 1992; *Jacobson, et al.*, 1995] overcomes many limitations of other observation methods, enabling continuous characterization of key TID parameters. Although radio beacon TEC measurements are integrated over the whole altitude range of the ionosphere, the vertical localization of GW-induced TEC fluctuations makes this technique a powerful tool for studying TIDs that propagate through the *F*-region bottomside. In addition, observations [*Kirkland, and Jacobson*, 1998] and model results [*Vadas*, 2007] have shown that most TIDs do not commonly rise above 400 km. Thus, the bulk of the TEC perturbations become highly localized to the bottomside region.

The modeling study of *Vadas and Liu* [2009] has shown that the dissipation of "primary" GWs can create localized thermospheric body forces able to excite "secondary" large-scale TIDs with a wavelength close to 2100 km, velocity near 500 m/s, and a period of ~80 min. *Vadas and Crowley* [2010] have presented evidence that multiple convective plumes can create thermospheric body forces containing smaller scales due to constructive and destructive wave interference. Such body forces are able to excite secondary GWs with smaller horizontal scale sizes. These authors were able to relate TID observations conducted with the TIDDBIT sounder [*Crowley and Rodrigues*, 2012] and the development of a tropical storm and several convective plumes that appeared in the Caribbean region. *Vadas and Crowley* [2010] found TIDs having large phase speeds, which were too large to have originated from convective overshoot. Therefore, they postulated that these waves were originated in the upper mesosphere and thermosphere.

In the radio beacon technique, also known as radio interferometry, phase differences measured at the various stations can be used to determine TID velocity, propagation azimuth, and amplitude. Recently, this radio-interferometry technique has been adapted for use with GPS satellites [*Afraimovich et al.*, 1998, 2000, 2003]. This new innovation makes it possible to utilize inexpensive, easily deployed GPS receivers to study gravity waves at a wide variety of locations. The large number of GPS satellites in orbit makes it possible for a single receiver to continuously monitor the bottomside region at multiple ionospheric locations simultaneously. Recently, *Valladares and Hei* [2012] used a GPS-radio interferometer to measure the phase velocity and propagation direction of gravity waves that were propagating near Huancayo (12.042°S, 75.321°W) in Peru. The phase velocity and direction of propagation were extracted by using two algorithms: the Statistical Angle of Arrival and Doppler Method for GPS interferometry (SADM-GPS) and the cross-correlation method (CCM). Both methods agreed that on 20 July 2008 between 22 and 24 UT, several TIDs moved across the small array of GPS receivers with a velocity near 130 m/s, were directed northward and had wavelengths close to 450 km. The CCM method was later applied to TEC values collected by other GPS receivers that were operating hundreds of kilometers away from Huancayo providing phase velocities close to 150 m/s [*Valladares and Chau*, 2012]. This new method offers the possibility of exploiting measurements from adjacent GPS receivers to study the characteristics of TID within a much larger region.

The main goal of this chapter is to describe the results of a method that produces regional maps of TEC perturbations associated with TIDs within the South and Central America regions and to relate these observations to maps of tropospheric brightness temperature measured by the GOES-12 satellite. GOES-12 satellite images are used to pinpoint the locations of deep convective plumes across South and Central America and the existence of tropical storms that move throughout the Caribbean region on 20 and 21 August 2011. The chapter is organized in the following order: In Section 16.2, we introduce the general characteristics of the cross-correlation analysis that was applied in a regional context to extract the characteristics (e.g., occurrence, velocity, scale size) of the TIDs of 4 July 2011. Results of the regional analysis of the TEC observations recorded by hundreds of GPS receivers on 20 and 21 August 2011 are presented in Section 16.3. The association of TIDs with tropical storms and convective plumes imaged with the GOES-12 satellite are presented in Section 16.4. The discussion section and the main conclusions of the chapter are presented in Sections 16.5 and 16.6.

## 16.2. ANALYSIS OF TEC OBSERVATIONS FOR 4 JULY 2011

The low-latitude Ionospheric Sensor Network (LISN) is a distributed observatory designed to monitor and specify the condition of the ionosphere over South America in a regional context. LISN provides near real-time observables

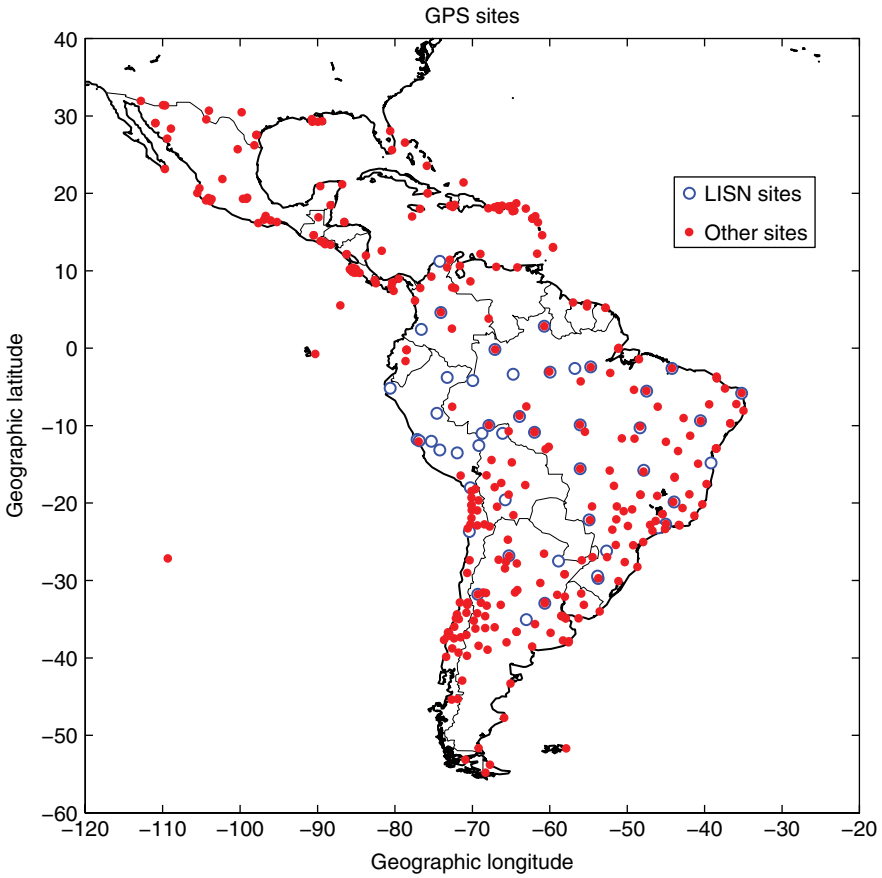


**Figure 16.1** Locations of GPS receiver stations installed by the LISN project (blue) and several other networks (red) in South and Central America and the Caribbean region.

(nowcast) from 47 dual-frequency GPS receivers [*Valladares and Chau*, 2012]. Figure 16.1 shows the locations of the LISN GPS receivers (blue circles) together with a much larger number of GPSs (red dots) that belong to several networks currently operating in South and Central America and the Caribbean region. In 2011, a total of 324 GPS receivers operated in South and Central America for ionospheric, plate tectonic, and seismology research, studies of river-land interactions, tropospheric weather, and land surveying. As part of the LISN project, we are processing the RINEX files corresponding to all of these GPS receivers stored in the LISN server. These files are stored in the LISN website for display and dissemination. This section presents the results of an investigation of the regional characteristics of TIDs that were observed on 4 July 2011.

### 16.2.1. Regional Maps of TEC Perturbations

The TEC perturbations (TECP) of Figure 16.2 were obtained using all the GPS receivers that operated in South and Central America on 4 July 2011. The TECP traces are plotted in red, centered along the satellite subionospheric intersection (short black segments). Note that most of the GPSs did not record any TEC perturbation or their peak values were below the threshold level (0.4 TEC units) leaving blank areas in all three frames. The algorithm to detect TECP removes the 24-hr solar-produced daily TEC variability and excludes other perturbations not directly associated with TIDs (e.g., plasma bubbles). The first step of our TID identification algorithm consists of estimating the background TEC values by fitting a fourth-order polynomial to every 3-hr segment of TEC values and then subtracts these values from the measured TEC. The second step excludes TEC depletions originated by equatorial plasma bubbles or midlatitude depletions by comparing the magnitude of the positive and negative excursions of TEC perturbations. As depletions only produce TEC decreases and TIDs create both positive and negative variations, a positive-to-negative perturbation ratio between 0.66 and 1.3 was selected for a valid detection of a TID. The third step consists of a wavelet-type analysis using quasi-sinusoidal functions to extract the amplitude and scale size of the TIDs. The last step involves a low-pass filter to eliminate noise signals containing periods smaller than 5 min. In addition, the automatic identification of TIDs is restricted to wave periods between 90 and 15 min. On many occasions, we observed TEC perturbations with two or more spectral peaks produced by the transit of

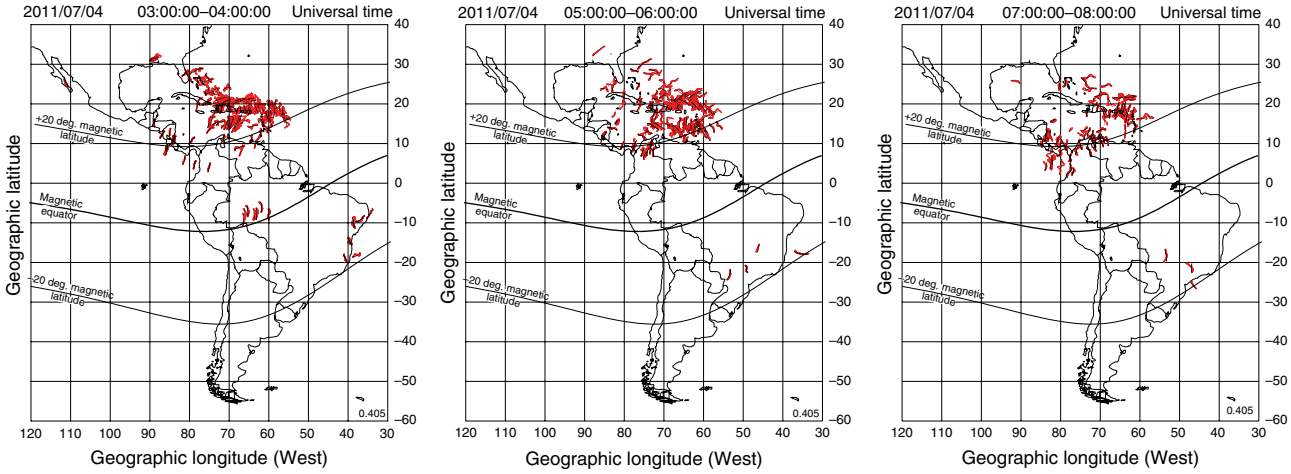


**Figure 16.2** TEC perturbation (TECP) values measured with all the GPS receivers that operated on 4 July 2011 during three time intervals (03–04, 05–06 and 07–08 UT). The red traces correspond to the TECP values after subtracting the daily variability. The thin black traces indicate the locations of the ionospheric piercing points at 350 km altitude.

multiple TIDs propagating simultaneously through the same volume. During these cases, we band-pass filtered the dTEC perturbation and only considered the TID that contained the largest amplitude.

Figure 16.2 shows the hour-to-hour variability of the TIDs corresponding to 4 July 2011 observed in South and Central America between 03 and 08 UT and detected automatically using the software described above. This figure depicts TEC perturbations at the latitude and longitude of the subionospheric intersection for each GPS satellite pass and for each station that reported a valid TID detection. The left frame shows TIDs placed mainly at the center of the Caribbean region. Two hours later (center frame), TIDs have expanded southward covering a larger area and populating the northern boundary of South America. The right frame of Figure 16.2 indicates that the TIDs have propagated southward toward lower latitudes; they are sparse and are likely in a decay process. TIDs decayed completely after 08 UT, not only in the Caribbean and Central America region, but also in the South America continent. This behavior of intense TIDs in the Caribbean and Central America regions near midnight and the early hours of the day is quite typical during the June solstice season.

### 16.2.2. Cross-Correlation Analysis Applied to Regional Network of GPS Receivers

To derive the motion of the TIDs across a continent-size region (regional context), we divide the receivers of Figure 16.1 into small clusters of receivers, varying in number between 3 and 18 GPSs. Only the receivers that have simultaneously observed TIDs with similar amplitudes and periodicities are considered part of the cluster. The TIDs' drift velocity is then calculated employing the software presented by *Valladares and Hei* [2012], in which dTEC values measured by three adjacent receivers are cross-correlated between them to derive the phase drift velocity. Consequently, each cluster is further subdivided in several subgroups of three adjacent receivers and analyzed independently. One receiver acts as the reference point and its location defines the center of the coordinate system. TECP values of this receiver are correlated with the values corresponding to the other two receivers, providing the time offset along two different directions that do not need to be perpendicular. Both time offsets and Equations (16.1) and (16.2) are used to resolve the magnitude of the phase velocity ($V_h[t]$) and the propagation angle of the TID ($\alpha[t]$).

$$\alpha(t) = arctan\left(\left(Y_A T_{B-C} - Y_C T_{B-A}\right) / \left(X_C T_{B-A} - X_A T_{B-C}\right)\right) \tag{16.1}$$

$$V_h(t) = \left(Y_C cos\left(\alpha(t)\right) + X_C sin\left(\alpha(t)\right)\right) / T_{B-C} + w_x(t)\sin\alpha(t) + w_y(t)\cos\alpha(t) \tag{16.2}$$

Where $T_{B-A}$ and $T_{B-C}$ are the time delays between the TECP traces. The symbols $X_A$, $Y_A$, $X_C$, and $Y_C$ refer to Cartesian distances between the satellite-receiver pierce points for the reference receiver and the pierce points for both additional receivers (named A and C). The satellite velocity is removed by subtracting the component of the motion of the pierce points ($w_x(t)$ and $w_y(t)$) in the propagation direction of the TIDs. The receiver placed further southwest is commonly designated as the reference receiver (also called B).

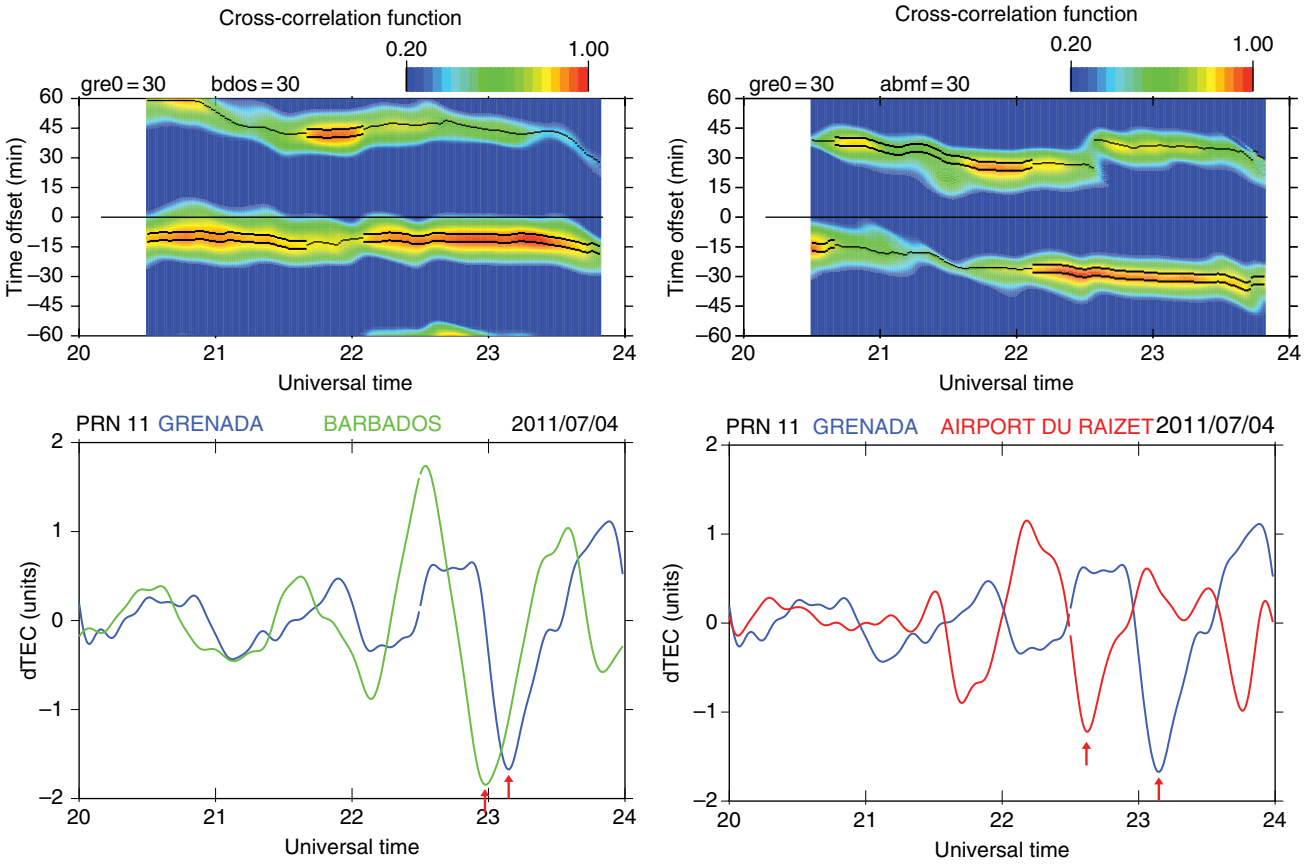


**Figure 16.3** Cross-correlation functions (top panels) and TECP curves (lower frames) for GPS satellite 11. The left frames show the CCFs for TECP signals from Grenada and Barbados. The right panels correspond to Grenada and Airport du Raizet. The cross-correlation functions are plotted using a color scale that varies between 0.2 and 1.0. The double black line that crosses through the middle in the top frames correspond to the correlation maximum and it is considered to be the time delay ($T_{B-A}$ or $T_{B-C}$).

The lower panels of Figure 16.3 show dTEC values from three GPS receivers placed in the Caribbean region. These receivers detected a train of TIDs on 4 July 2011 that lasted for 4 hr. Note that the blue trace, corresponding to Grenada, acts as receiver B and it is displayed in both panels. The dTEC increases after 22 UT attaining peak-to-peak values near 4 TECu. It is also evident that a second TID with much shorter periodicity (10–20 min) and smaller amplitude is superimposed on the near 60 min period of the primary TID. To extract the velocity information of both TIDs (primary and secondary), it is necessary to use a cross-spectrum analysis [*Crowley and Rodrigues*, 2012]. However, we opted for filtering and then analyzing only the period (~60 min) that contains the largest amplitude. All three traces (blue, green, and red) show a high degree of similarity that is reflected in the high correlation factor (~1) displayed in the upper panels. Only positive values of the correlation factor, between 0.2 and 1.0 are color coded in the top panels. The correlation time series show two prominent peaks that are produced by the periodic nature of the dTEC signal associated with a quasi-periodic train of TIDs. However, the time of the first large negative peak of the TID, indicated by the red arrows, is used to discern the correct delay between the dTEC traces. It is evident that a large minimum was observed at Barbados (green trace) just before 23 UT. This was observed at Grenada (blue) a few minutes after 23 UT. A larger delay between the minimum peaks is seen in the right lower panel where the first large minimum at Airport du Raizet (red) occurs at 2240 UT and ~30 min ahead of minimum at Grenada. In summary, this simple analysis helps us to conclude that the TID passed first through Airport du Raizet (abmf), then Barbados (bdos), and at the end through Grenada (gre0). Due to the locations of these three receivers, as seen in the top frame of Figure 16.4, it is concluded that the TIDs' velocity was close to southward.

Figure 16.4 displays a map of the geographic locations of the three GPS receivers (top panel) and the magnitude

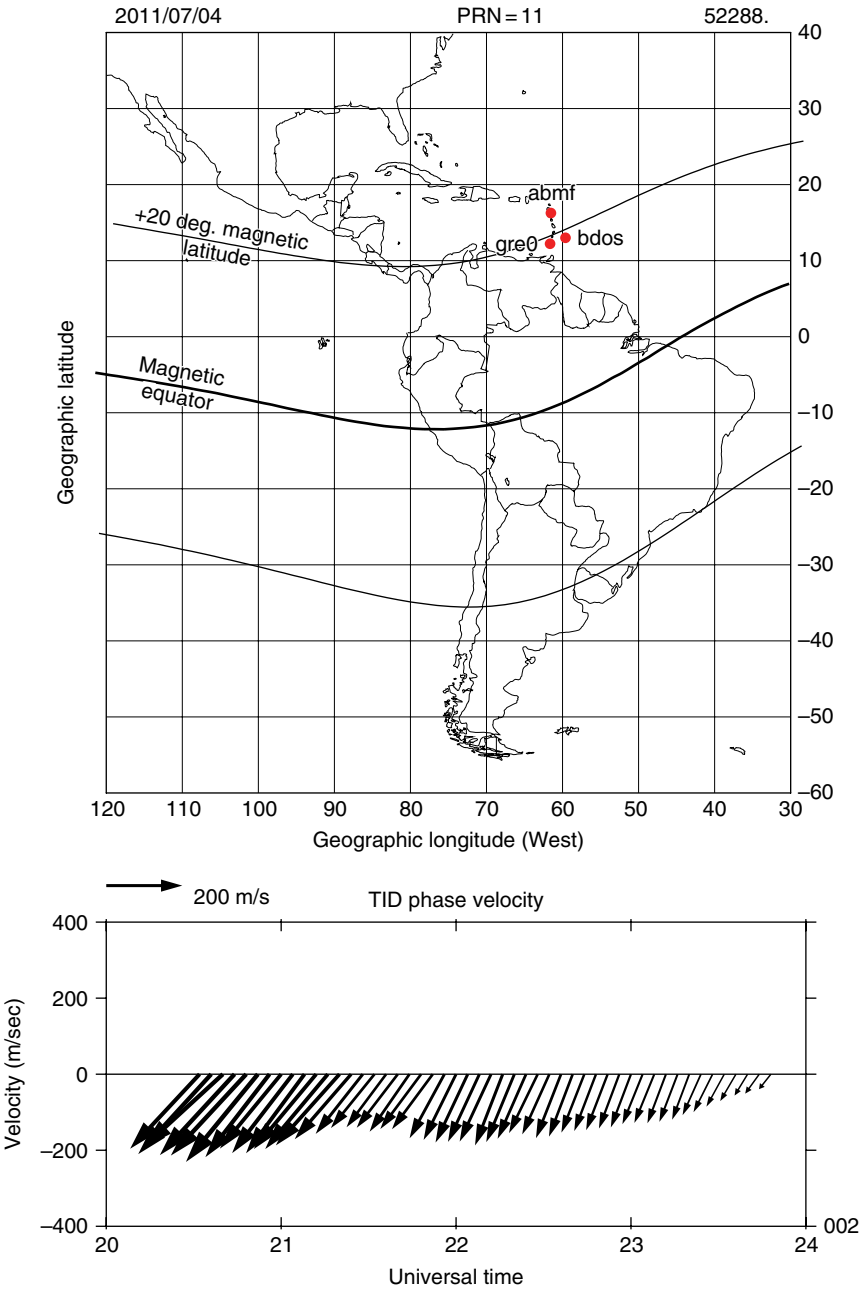


**Figure 16.4** The top panel shows the locations of the three stations used in the velocity analysis: Grenada, Barbados, and Airport du Raizet. The lower panel shows the phase velocities of the TIDs calculated using the CCM method and TEC perturbation from all three stations for 4 July 2011.

and direction of the phase velocity derived between 20 and 24 UT (lower panel). The velocity is directed southwest and the magnitude decreases from 250 m/s near 20 UT until it reaches 50 m/s at 24 UT. The more refined and precise calculation of the TID velocity corroborates the intuitive motion of the dTEC perturbation described earlier.

## 16.3. ANALYSIS OF TEC OBSERVATIONS FOR 20–21 AUGUST 2011

This section describes the analysis of the TIDs that were observed on 20 and 21 August 2011 across South and Central America and the Caribbean region. First, we divided the receivers in clusters of adjacent GPSs that

observed TIDs with similar characteristics and during equal time intervals. Then, each cluster was analyzed independently providing a time series of the TIDs' velocity. Finally, all these time series were arranged in time and space to build regional maps of TIDs' velocity over South and Central America. These results allow us to relate regional maps of the occurrence, location, and velocity of the TIDs over the continent and regional maps of tropospheric deep convective cells observed by the GOES-12 satellite. The goal of this section is to relate the dynamics of the TIDs observed on 20–21 August 2011 to the existence of a tropical storm in the Caribbean region and deep convective cells that originated within the central and southern parts of South America.

### 16.3.1. Regional Maps of TIDs Occurrence for 20–21 August 2011

The regional maps of Figure 16.5 show TEC perturbations associated with the TIDs that developed over South and Central America on 20 and 21 August 2011. Each frame corresponds to a 4-hr interval in which we have plotted all the TIDs detected by the GPS receivers presented in Figure 16.1. The four frames in the top row of Figure 16.5 indicate an absence of TIDs between 00 and 16 UT on 20 August 2011. After this period, TIDs' population increases across the South American continent in a sector limited between −10° and −20° geographic latitude. The middle row, second frame, corresponding to the period 20–24 UT, displays dTEC perturbations persisting in South America, across the same latitudinal sector observed 4 hr earlier. This frame also shows TIDs extending between the Caribbean Sea and the eastern part of Central America. These newly developed TIDs remain active until 08 UT on the following day. The South American TIDs decay before the start of day 21 August 2011. However, they reappear after 15 UT on 21 August 2011. In summary, it was observed that on these two days, TIDs developed over South America at latitudes slightly south of the magnetic equator between 16 and 24 UT. In fact, during the following 10 days, TIDs occur very systematically and almost every day between 16 and 24 UT. In Central America, the Caribbean region, and the northern part of South America, TIDs occur at different time epochs and extend through different areas.

### 16.3.2. Analysis of TIDs Using a Cluster of GPS Receivers

Figure 16.6 displays dTEC perturbations associated with a train of TIDs that were detected by one cluster of 11 GPS receivers between 19 and 24 UT on 20 August 2011. These receivers are located in northern Colombia as shown in the small panel placed in the upper right side. The dTEC values were derived using signals from the GPS satellite PRN = 17. The station's four-letter name, the latitude, and the longitude are indicated in the right margin. Note also that the amplitude of the dTEC is printed at the middle right side and it is equal to 5 TEC units. From top to bottom, the stations are organized following their geographic latitude, starting at the top with the station placed farther north, Santa Marta (lsam), and ending with Bogota (lbo_). These two stations belong to the LISN network. This display arrangement helps us to discern the propagation direction of the TID. We select a conspicuous feature within the dTEC traces, such as the largest minimum or maximum, and determine how this feature time shifts at different sites. Red arrows indicate the time when the largest minimum occurs for each of the 11 traces of Figure 16.6. As this feature appears at earlier times at sites that are placed farther south, it is concluded that the TIDs observed on 20 August 2011 in northern Colombia are propagating northward. We also calculate the average period of the TIDs equal to 63 min and the spectral width 44 min. We also indicate that some of the stations present rapid dTEC fluctuations, as seen at Dorada (dora) and Aguachica (agua) at 22 UT. This effect is likely produced by the transit of additional TIDs containing shorter spatial scales.

Figure 16.7 shows the velocity analysis for three stations (Corozal, Cucuta, and Maracaibo) that are part of the cluster of GPS receivers presented in Figure 16.6. To avoid contamination produced by TIDs that have periods different than 63 min and are transiting across the stations with different velocities and scale sizes, we apply a band-pass filter to the dTEC traces and filtered out these unwanted TIDs. The middle frames display the dTEC traces after they have been filtered using a band-pass filter centered at 63 min (0.2 mHz). The top panels display the cross-correlation functions (CCF) in which two peaks separated by ~60 min are evident produced by the periodicity of the TIDs. To determine the peak associated with the true motion of the TIDs, we use the information provided by Figure 16.6 in which it was realized that the TIDs were moving northward. Note that a negative (positive) offset is an indication that Corozal's TEC perturbation lags (leads) Cucuta's. As Corozal is located north of Cucuta and south of Maracaibo, to calculate the TIDs' velocity we considered the CCF peak with a negative delay for the first pair of stations (Corozal and Cucuta) and the positive delay for the second pair (Corozal and Maracaibo). Similar analysis was performed for every set of three different receivers of the cluster of GPSs depicted in Figure 16.6.

The velocity of the train of TIDs is shown in the lower panel of Figure 16.7. This velocity is equal to 250 m/s and directed northward at 20 UT, and becomes northwestward

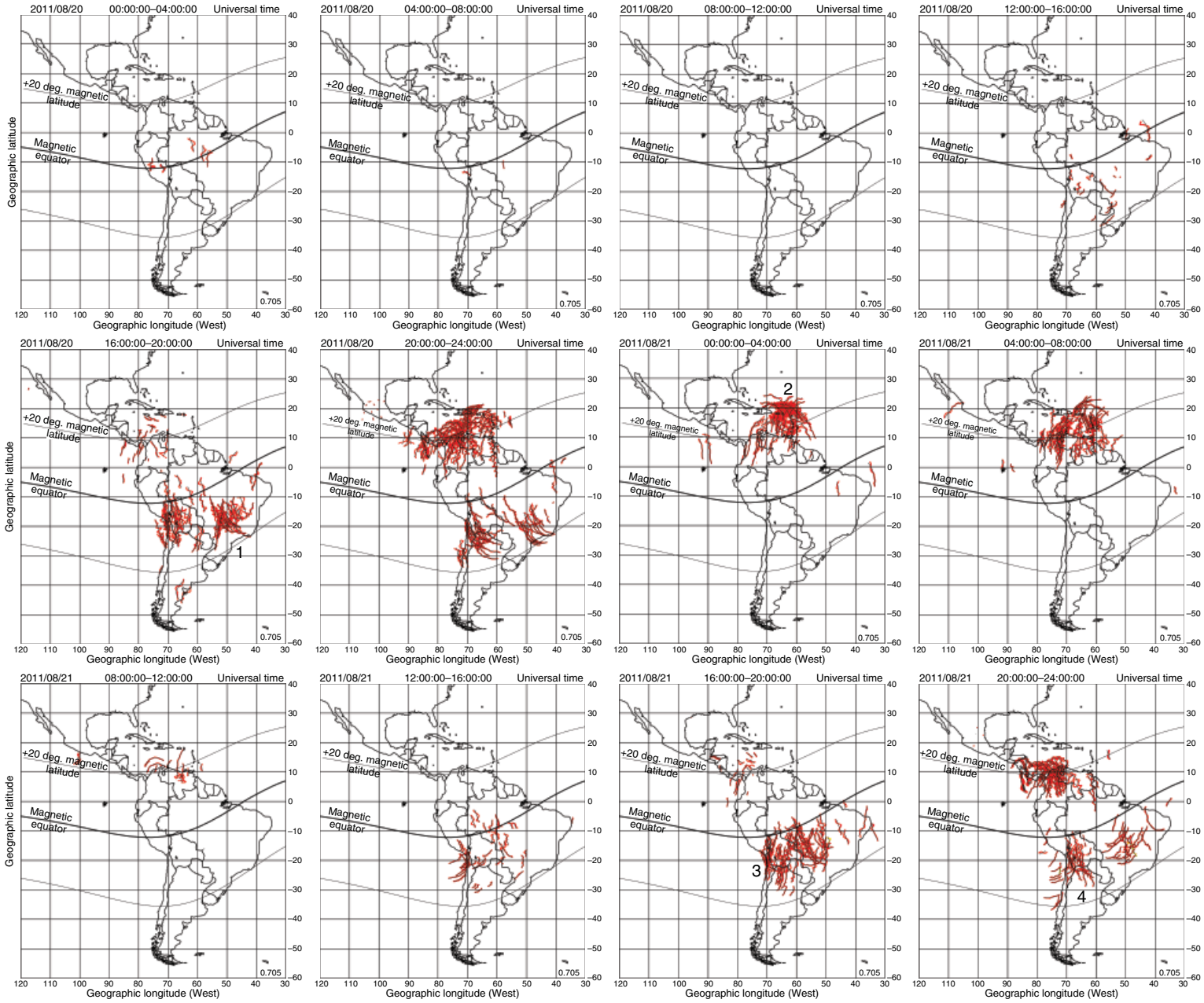


**Figure 16.5** Same as Figure 16.2, but for TIDs measured on 20 and 21 August 2011. Each panel displays the amount of TIDs observed during a 4-hr segment. Each red segment indicates the location of a TID detected by our analysis package. Large spaces without red traces are the result of the absence of TIDs in those regions.

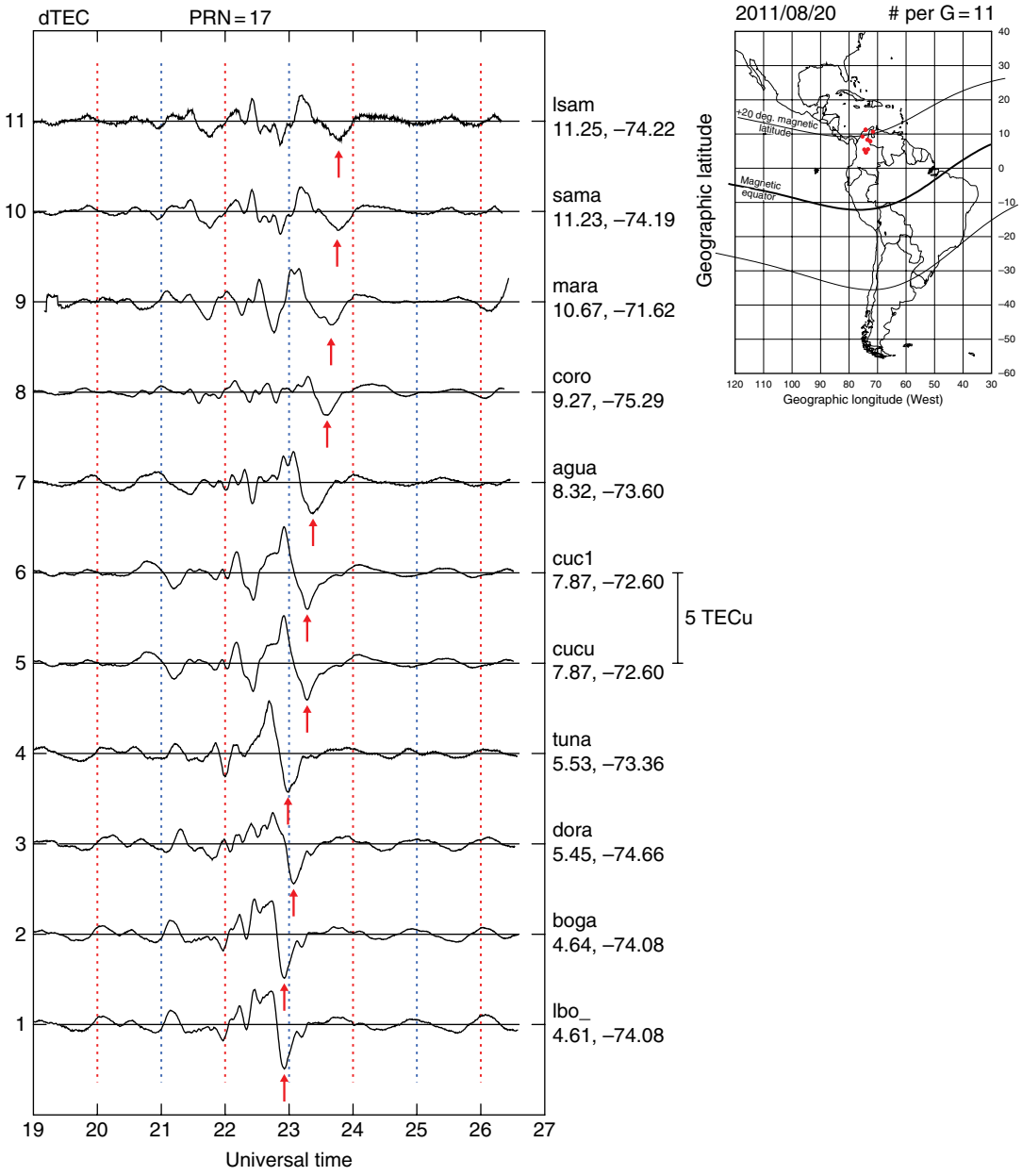


**Figure 16.6** TEC perturbation (dTEC) values measured by 11 stations located in northern Colombia and Venezuela. The red arrows indicate the time when the minimum dTEC value was found in each trace. The four-letter GPS station code and the latitude and longitude for each station are printed on the right margin. The red dots in the upper-right frame indicate the geographic location of the 11 stations.

at 24 UT. These values confirm the direction of motion that was determined based on the time shift of the largest minimum of Figure 16.6. At the same time, they provide a more precise estimate of the TID transit motion. It is indicated that similar phase velocities were determined when our analysis procedure was performed using other receivers that belong to the GPS cluster of Figure 16.6.

### 16.3.3. Regional Maps of TIDs Velocity for 20–21 August 2011

Figure 16.8 compiles the TIDs' velocity information from the majority of the GPS clusters. Red vectors indicate northward velocities and blue vectors depict velocities with a southward component. The velocity field was decimated a factor of 8 to avoid cluttering the figure. The

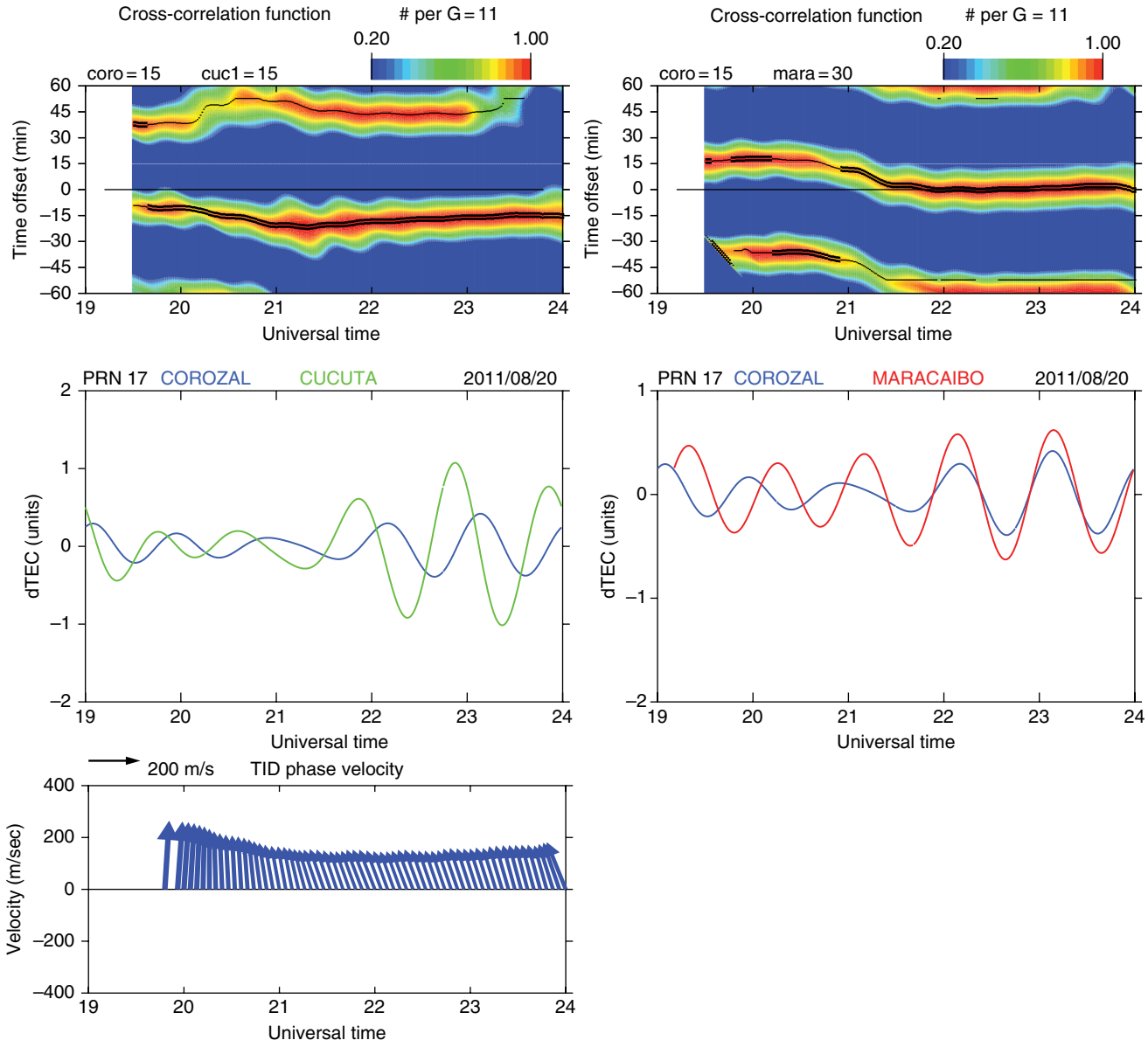


**Figure 16.7** Same as Figure 16.3, but for GPS satellite 17 and stations Corozal and Cucuta in the left frames and Corozal and Maracaibo in the right frames. The unfiltered dTEC values for these three stations are displayed in Figure 16.6. The lower panel shows the phase velocities of the TIDs calculated using the time delays provided by the CCM algorithm (upper frames).

main characteristic of the plots is the general trend of the velocities: they are principally directed northward or southward. However, there exist some exceptions and the TID velocity can have a small westward or eastward component during the early evening and early hours of the day. On 20 August 2011 at 16 UT, the velocities over South America vary between 200 and 500 m/s (first frame, middle row). At this time, the TIDs' velocities are mainly directed northward with a ±20° directional variability. The following frame corresponding to 20–24 UT shows the velocities directed northwestward in the northern part of South America. These velocities intrude into Central America reaching values as high as 400 m/s. There also exists a region near Puerto Rico where velocities are directed southeastward reaching 420 m/s.

The next frame, corresponding to 21 August 2011 at 00–04 UT, displays velocities over the eastern side of the Caribbean region, where the flow is ~200 m/s, and it is directed southwestward. Downstream in eastern Colombia, the TIDs' velocities were also pointing southwestward, but the velocity magnitude was ~300 m/s. On the same day and between 12 and 16 UT, TID activity

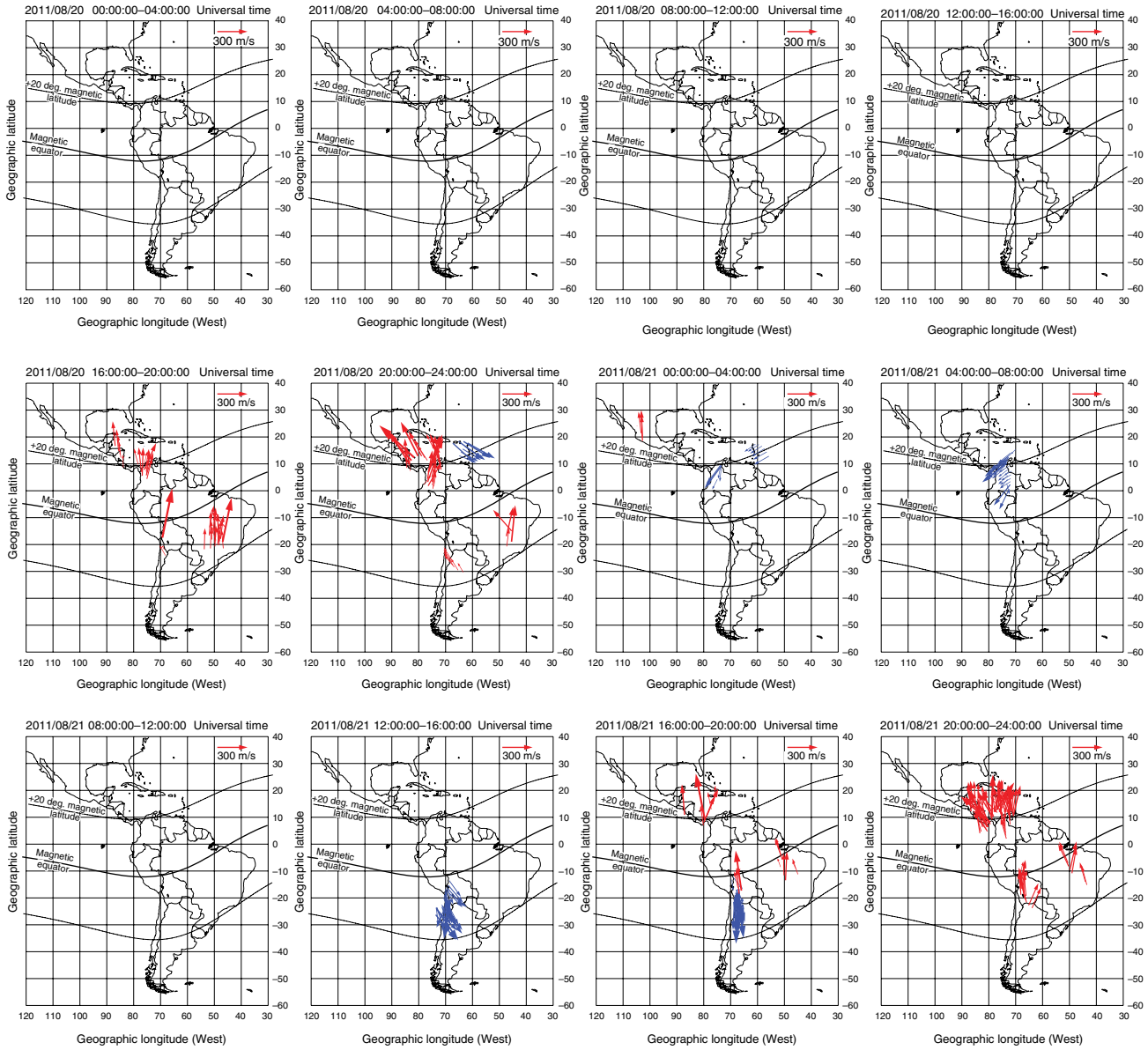


**Figure 16.8** TIDs' phase velocities calculated using the CCM algorithm. See text for further details of the method employed to calculate the velocities. Red arrows are used for velocities having a northward component. Blue arrows correspond to velocities that have a southward component.

develops near the border between Peru, Bolivia, and Chile with velocities in the range of 300–400 m/s. Between 16 and 20 UT, there exists a region over central Bolivia where counter-streaming TIDs' velocities are found. We interpret this event as the superposition of two different trains of TIDs that are transiting in opposite directions, but propagating across two very close or overlapping volumes. The last frame indicates that the flow of TIDs is mainly northward over two regions separated by thousands of kilometers. One is located in the central part of South America and the other in Central America.

### 16.3.4. GOES-12 Infrared Images

The Geostationary Satellite system (GOES) mission provides weather monitoring, and aids research to understand land, atmosphere, ocean, and climate interactions. GOES-12 was launched in 2001, and has been in standby orbit most of its lifetime. However, during a few months in 2011, GOES-12 operated in the GOES-EAST position (parked in geostationary orbit at 60°W), providing coverage of the east coast of the United States and South America. The spacecraft was designed to "stare" at the Earth and image clouds, monitor Earth's surface temperature and water vapor fields, and sound the atmosphere for its vertical thermal and vapor structures. Therefore, the evolution of atmospheric phenomena can be followed, ensuring real-time coverage of short-lived dynamic events, especially severe local storms and tropical cyclones.

The imager on board GOES-12 is a multichannel instrument that senses infrared radiant energy and visible reflected solar energy from the Earth's surface and atmosphere. The satellite also measures the temperature of the clouds and the surface of the Earth with an infrared sensor. This allows for the detection of changes in the temperature of clouds during the day and at night. The temperature of the clouds also indicates how tall clouds are since temperature is usually inversely proportional to height in the troposphere. Red color indicates the appearance of temperatures as cold as −80°C and clouds extending up to 11,000–12,000 m. *Vadas and Crowley* [2010] pointed out that the type of clouds that prevail in Central and South America consist of convective plumes able to trigger gravity waves that propagate through the troposphere and mesosphere, which dissipate in the thermosphere (or mesosphere) and create body forces that are able to generate secondary gravity waves that can reach *F*-region altitudes.

Figure 16.9 shows four images taken with the infrared sensor on board GOES-12 between (1) 20 August 2011 at 11:45 UT, (2) 20 August 2011 at 20:45 UT, (3) 21 August 2011 at 05:45 UT, and (4) 21 August 2011 at 17:45 UT. Images with a 3 hr cadence time can be found at the GOES website. Several series of convective plumes were seen within Central and South America during two days when tropical storm Irene developed in the Caribbean region (see storm indicated with a yellow arrow in Fig. 16.9a). The first frame, corresponding to 11:45 UT on 20 August 2011, shows the remnants of a tropical depression that originated over the Pacific Ocean, drifted northeast, and was located over Central America at the time of the GOES-12 image. Figure 16.9a also displays the formation of a tropical depression moving north of the northern coast of South America (yellow arrow). A few hours later this tropical depression became organized enough to be classified as tropical storm Irene.

Figure 16.9b shows Irene transiting through the Caribbean region before it became a category 1 hurricane. This frame displays a cluster of convective plumes that extended through the southern part of Peru and western Brazil (see yellow ellipse). This frame also provides evidence for the presence of another region of very cold temperatures located to the east of the southern tip of South America and close to Antarctica. This region persists for many hours until 14:45 UT on 21 August 2011. Figure 16.9c shows the northward expansion of this region of cold temperatures seen close to Antarctica (enclosed by a yellow ellipse). Figure 16.9d shows the continuing energization of Hurricane Irene that displays a cluster of convective cells with temperatures below −80 °C. Figure 16.9d indicates the decay of the majority of convective cells seen in previous frames. This frame also displays the initiation of a new cluster of convective plumes near northern Peru and extending into Brazil in the western side of South America (yellow line).

## 16.4. PROPAGATION ANALYSIS OF THE TIDS MOVING ACROSS CENTRAL AND SOUTH AMERICA

This section presents an origin finding analysis aiming to associate the characteristics of the TIDs observed by several networks of GPS receivers in South and Central America, with corresponding regional images of tropical storms and tropospheric convective cells detected by the GOES-12 satellite. The cause-effect relationship is investigated using recent results from several experimental and modeling studies of AGWs conducted by *Fritts and Vadas* [2008], *Vadas and Liu* [2009], and *Vadas and Crowley* [2010]. It is known that atmospheric gravity waves (AGW) can be initiated at polar regions due to extreme Joule heating that is deposited during magnetic storms [*Saito et al.*, 1998; *Shiokawa et al.*, 2002; *Valladares et al.*, 2009]. Similarly, AGWs can also be triggered by earthquakes [*Galvan et al.*, 2011], tsunamis [*Makela et al.*, 2011], nuclear explosions, tropospheric deep convective cells [*Hocke and Tsuda*, 2001; *Bishop et al.*, 2006], and thermosphere body forces [*Fritts and Luo*, 1992; *Vadas and Fritts*, 2001]. This study introduces observations of 20 and 21 August 2011 in which neither earthquakes nor

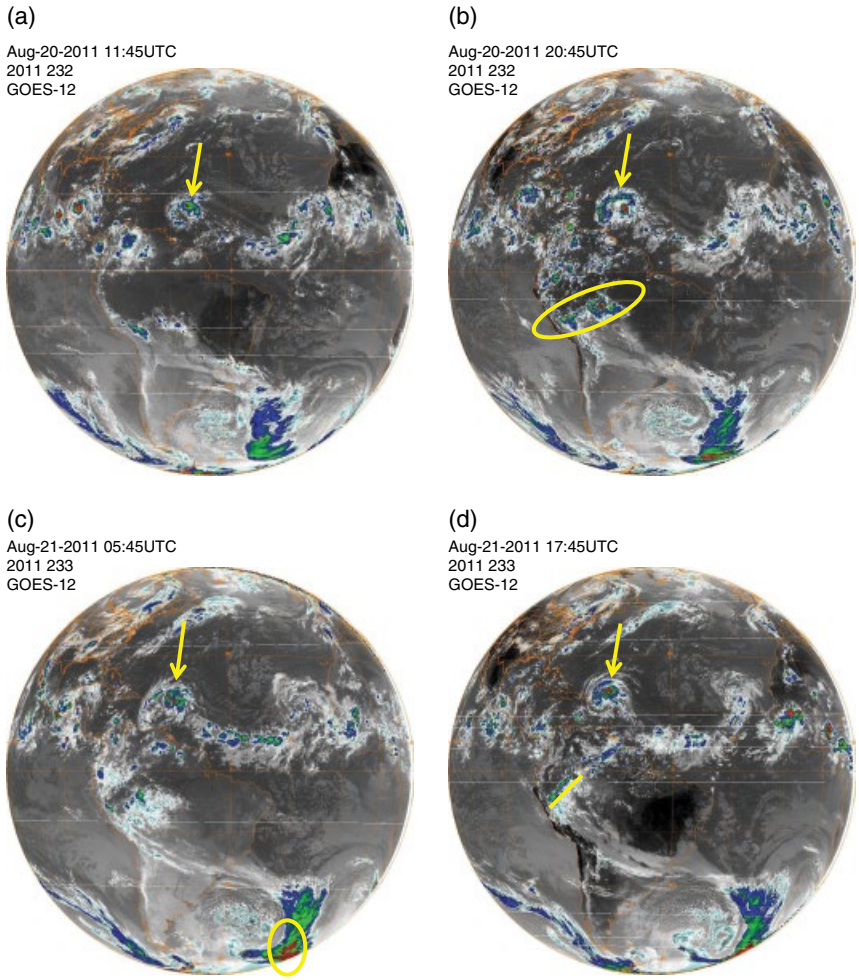


**Figure 16.9** Four images observed with the GOES 12 satellite corresponding to (a) 20 August 2011, 12:00 UT; (b) 20 August 2011, 21:00 UT; (c) 21 August 2011, 06:00 UT; and (d) 21 August 2011, 18:00 UT. Yellow symbols indicate important features in the images such as the tropical storm Irene (arrows) and deep convective cells (ellipses).

tsunamis nor nuclear explosions occurred. In addition, during these 2 days magnetic activity was quiet. We discuss below the association of TIDs observed on 20–21 August 2011 in the American sector, and primary and secondary AGWs triggered by the tropical storm Irene that developed in the Caribbean region, and/or deep convective plumes that developed over or near South America.

When primary AGWs are created near the tropopause, they travel outward from the origin in all directions forming at mesospheric altitudes an almost circular pattern of perturbed densities. At higher altitudes, the variable thermospheric wind filters the AGWs in some directions leaving a segmented pattern of AGWs propagating only at selected directions. Saturation, wind filtering, and wave breaking make the primary waves dissipate and transfer momentum to the atmosphere creating horizontal body forces [*Vadas and Fritts*, 2004]. AGWs containing large-scale sizes might be able to propagate to the *F*-region bottomside. Smaller-scale AGWs (20–30 km) dissipate at 90 km and others with larger sizes (50–150 km) at 140 km, creating mesospheric and thermospheric body forces, respectively [*Vadas and Crowley*, 2010]. These body forces excite large-scale, upward and downward propagating secondary AGWs and then TIDs with scale sizes between 1000 and 2000 km, horizontal velocity ~500 m/s, and periods ~80 min, which propagate away from the body forces, traveling up to altitudes as high as 400 km [*Vadas and Liu*, 2009]. AGWs propagating against the neutral wind can reach the *F*-region bottomside and produce TIDs by moving plasma along the magnetic field lines [*Hines and Reddy*, 1967; *Fritts and Vadas*, 2008]. However, AGWs propagating in the same direction of the neutral wind dissipate due to the wind-filtering effect.

We have used GPS receivers (279) belonging to several networks that operated across the South American continent and the Caribbean region in 2011 to observe and

characterize TIDs in these regions. If the velocity of the AGWs is constant, then their signatures will reach the different stations at different instants depending on the separation between the stations and the place of the AGWs' origin. Therefore, any feature of the TIDs (e.g., valleys, peaks) will align linearly in a travel distance versus universal time diagram. We have used this property of the TIDs to find their propagation velocity, and also to search for the locations where the body forces excited secondary waves and the places where deep convective plumes generated primary waves. Thus, this method can be used to define the inception point of the TIDs.

The four frames of Figure 16.10 show the TEC perturbations in a distance versus universal time format. These diagrams are similar to the travel time versus universal time plots presented by *Galvan et al.* [2012]. These authors calculated the travel velocity of Rayleigh, acoustic, and gravity waves associated with the Tohoku tsunami as these different waves were sequentially observed by GPS receivers located farther distant from the epicenter. Figure 16.10 shows the TEC perturbations corresponding to four events of TIDs associated with primary and secondary AGWs that developed on 20 and 21 August 2011. These diagrams display perturbation troughs and crests traveling at a constant velocity that are aligned with straight lines. Because we do not have a priori information about the geographic location where the thermospheric body forces excited secondary AGWs, we searched for the geographic latitude and longitude that made the troughs and crests align along parallel lines. This method provides

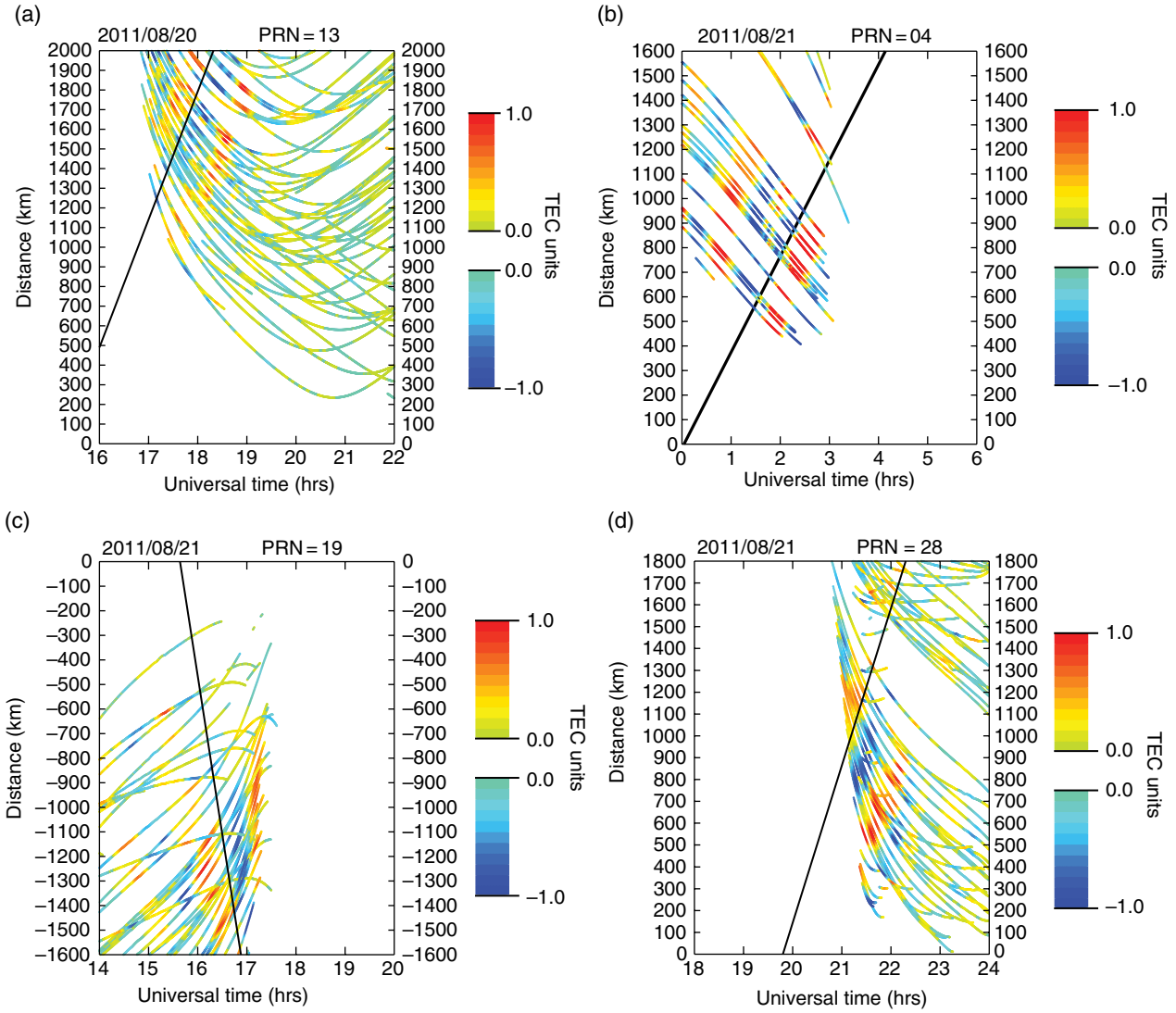


**Figure 16.10** Travel time (distance) as a function of Universal Time plots corresponding to the following four events: (a) 20 August 2011, 16–22 UT. (b) 21 August 2011, 0–6 UT. (c) 21 August 2011, 14–20 UT. (d) 21 August 2011, 18–24 UT. Note that we have used negative distances in panel (c) since the TIDs were moving southward.

a good estimate of the geographic location of the body forces and/or the deep convective plumes.

Figure 16.10a displays the TEC perturbations from PRN 13 measured between 16 and 22 UT on 20 August 2011. These TEC perturbations were also displayed in Figure 16.5 (see number 1 in the middle row, first frame, corresponding to 16–20 UT). They are observed south of the magnetic equator, over the eastern part of Brazil. We found that an origin placed at Lat = 34°S and Long = 50°W produced TECP peaks (red) and valleys (blue) forming parallel lines. This origin or center place is about 2° off the southern coast of Brazil and near the border with Uruguay. The slope of the line delineated in this figure gives a velocity equal to 208 m/s. However, a more precise calculation of the TID velocity, as shown in Figure 16.8, provided a value of 250 m/s. The peak-to-peak amplitude of the TEC perturbations presented in this frame and the following is close to ±1 TEC unit.

Figure 16.10b shows a trail of TEC perturbations from PRN 04 measured between 00 and 06 UT on 21 August 2011. During this event, the TIDs' velocity was equal to 135 m/s. This value is close to the TIDs' phase velocity calculated in Section 16.3.3 that indicated a velocity equal to 140 m/s directed westward. This velocity is in the range of primary AGWs that are able to propagate up to the *F*-region bottomside. The period and scale size of the TIDs of Figure 16.10b are about 30 min and 250 km, respectively. We also determined that the origin of the TIDs was at 18°N, 54°W. This location is within the broad extension of tropical storm Irene (see Fig. 16.9a), which was centered near 15°N and 59°W on 21 August 2011 at 00 UT. Images of the GOES-12 satellite indicated a region of low temperature (−80°) observed near 16°N, 54°W (see Fig. 16.9b) and within the reach of TS Irene. Figure 16.10b also indicates that the average distance between the TID observations and the point of origin varied between 400 and 1400 km. As some of the TIDs were observed 1400 km away, it is possible to infer that these waves were likely generated ~2.5 hr before 00 UT and, as stated before, within the vicinity of tropical storm Irene.

Figure 16.11 shows precipitation rainfall measured by the Tropical Rainfall Measuring Mission (TRMM) satellite on 21 August 2011 at 00 UT. TRMM is a joint

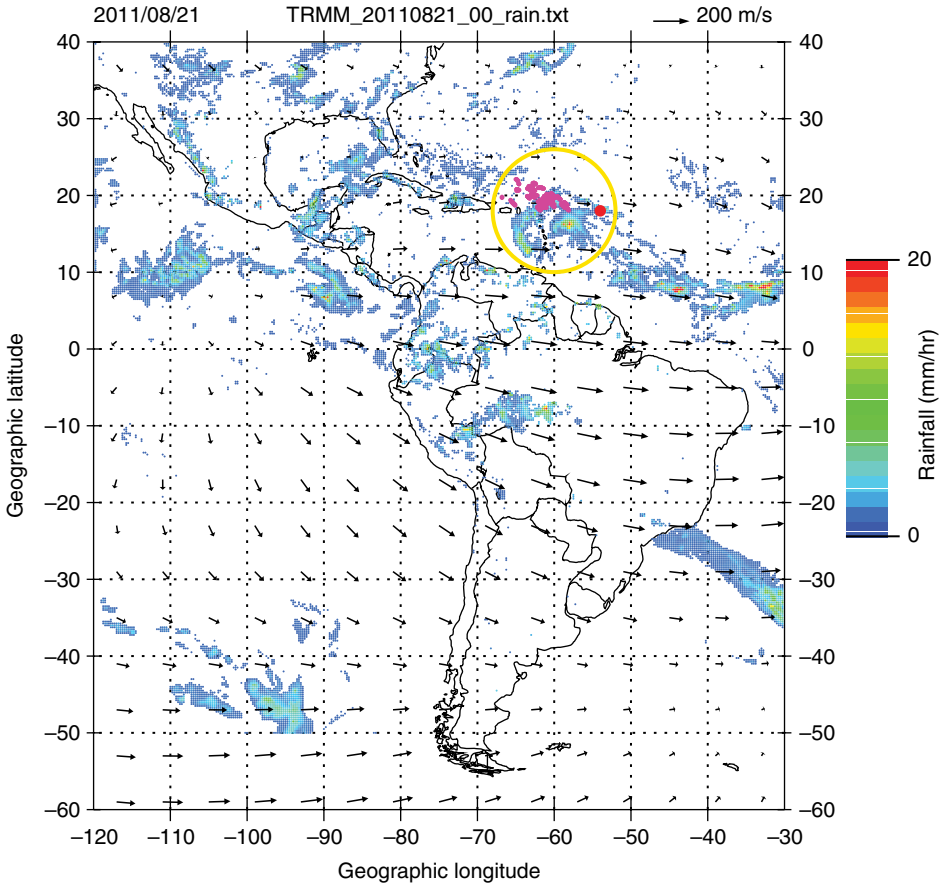


**Figure 16.11** Rainfall measured by the TRMM satellite over South and Central America and the Caribbean region on 21 August 2011 at 00 UT. Note the region of heavy rain at the location of the tropical storm Irene. The large red dot indicates the location of the origin of the dTEC perturbations displayed in Figure 16.10b. The positive values of dTEC, displayed in Figure 16.10b, are displayed in purple.

US-Japan satellite mission to monitor tropical and subtropical precipitation and to estimate its associated latent heat. Figure 16.11 displays (1) the amount of rainfall in mm/hour in the American sector, (2) black arrows representing neutral wind vectors from the Horizontal Wind model (HWM) at 200 km altitude [*Hedin et al.*, 1988], and (3) TEC perturbations (in purple). Note that the TECPs and the rain associated with TS Irene are contained inside a yellow circle. Figure 16.11 points out that the neutral wind velocity over the Caribbean region, where TS Irene developed, is ~100 m/s directed eastward. This magnitude and direction of the wind make waves propagating eastward dissipate. However, it favors the propagation of AGWs in the opposite direction as seen in Figure 16.8.

Figure 16.10c displays the signature of TIDs from PRN 19 measured on 21 August 2011 between 14 and 20 UT. Note that the axis of the travel distance is labeled using negative distances due to the southward propagation of the TIDs. The negative slope in this plot indicates TIDs moving southward from the origin located at 6°S, 72°W. The TID velocity is equal to 420 m/s, in agreement with the phase velocity displayed in Figure 16.8. The scale sizes and periods of the TIDs are equal to 1750 km and 65 min. We suggest that these TIDs are associated with secondary AGWs excited by body forces in the mesosphere or thermosphere. It is worth mentioning that Section 16.3.4 introduced a region of deep convective cells that developed over northern Peru and the western part of Brazil (see yellow line in Fig. 16.9d). This region was active between 12 and 21 UT on 21 August 2011 and decayed shortly after 21 UT.

Figure 16.10d depicts TEC perturbations from PRN 28 measured between 18 and 24 UT on 21 August 2011. The origin of these TIDs was found to be located at 22°S, 68°W. This location is in the northern part of Chile close to the border with Bolivia. The slope in the boundary between positive and negative TECP excursions indicates a velocity equal to 250 m/s and directed northward. The phase velocity of the TIDs was also calculated in Section 16.3.3 using the CCM delay method and Equations (16.1) and (16.2) resulting in a value equal to 300 m/s. This large velocity and the fact that the scale size of the TID was of order 1000 km indicate an association with secondary AGWs and not with primary waves that usually have small scale sizes and velocities less than 180 m/s. Therefore, we suggest that the TIDs in Figure 16.10d were excited by mesosphere or thermosphere body forces centered at 22°S, 68°W. We have shown in Figure 16.8 that the TIDs were moving northward on 21 August 2011, between 20 and 24 UT. Based on these arguments, we conclude that these waves might have originated in the southern part of South America or probably farther south near Antarctica (see yellow ellipse in Fig. 16.9c for an extended region of red indicating low temperatures). This region near Antarctica seems a likely place to excite AGWs that could be propagating northward to the South American continent.

## 16.5. DISCUSSION

This chapter presents the results of an analysis program built to calculate the characteristics of TIDs propagating across South and Central America and the Caribbean region. This method uses TEC values measured by the LISN GPS receivers and several other networks of GPS receivers that are presently operating in these regions. This type of analysis can be extended to include other regions of the globe or applied to other low- and/or midlatitude regions, such as the African, European, or Asian continents, to investigate the dynamics of TIDs in a larger regional or global context. In essence, the analysis provides regional maps of the population, the phase velocity, and the scale size of the TID waves. When this analysis is combined with theoretical and modeling results of the generation and propagation of AGWs, it is possible to derive information of the place of origin of the TIDs and the nature of AGWs responsible for the TIDs (e.g., primary versus secondary).

We found that on 20 and 21 August 2011, the TIDs' phase velocity was highly variable. We obtained phase velocities between 140 and 500 m/s. This velocity variability was too large to conclude that all TIDs corresponded to secondary waves excited only by thermospheric or mesospheric body forces. It is proposed that at least one event corresponded to primary AGWs produced by tropospheric convective overshoot that occurred in the proximity of tropical storm Irene. We also found that the TIDs, observed on these 2 days, contained scale sizes between 250 and 1800 kms, and periods between 30 and 70 min. Waves with smaller periods (20 min) were detected but not fully analyzed.

To find the locations where the TIDs originated, we searched for the geographic location that made crests and valleys of TECP to align along parallel lines in a distance versus time plot (Fig. 16.10). This method was based on the notion that AGWs propagate as concentric rings away from a central focal point. This center point could be the geographic location of a cluster of convective cells in the tropopause (for the generation of primary AGWs) or the region of body forces on the thermosphere-mesosphere system (for the generation of secondary AGWs). Our principal objective was to investigate the possibility if any of these origins coinciding with regions of tropospheric deep convective plumes that were detected by the GOES-12 satellite (Fig. 16.9). We suggest that one out of the four cases analyzed in this publication is likely associated with primary AGWs triggered within TS Irene.

Figure 16.10a introduced a cluster of TIDs observed between 16 and 22 UT over Brazil that were propagating northward with velocities between 200 and 300 m/s. These TIDs are displayed in Figure 16.5 and indicated with a

number 1. Figure 16.10d introduced another cluster of TIDs located at the same geographic latitude as the TIDs in Figure 16.10a. They contained similar velocities and occurred at similar universal times. These TIDs are indicated with a number 4 in Figure 16.5. Due to their similarity, we suggest that these two sets of TIDs were produced by thermospheric body forces responding to almost similar inputs that operate on a daily basis. The common source could be a region of cold temperatures near Antarctica (yellow circle in Fig. 16.9c) or very high wave/tide activity near the southern tip of South America. The latter region is considered a steady source of tropospheric and mesospheric waves (D. Janches, personal communication). This source of AGWs was probably active almost every day between 16 and 24 UT, for the following 10 days. More analysis is needed to determine the seasonal and day-to-day variability of the TIDs in this region.

Figure 16.10b (number 2 in Fig. 16.5) seems to be closely related to the presence of TS Irene. However, TIDs are only observed between 20 and 08 UT on the following day. This temporal constraint is likely due to the wind-filtering effect that dissipates waves when their velocity becomes almost parallel with the neutral wind motion. Figure 16.11 indicates that at 00 UT on 21 August 2011, the wind is directed eastward favoring the propagation of westward-directed AGWs. Figure 16.10c (number 3 in Fig. 16.5) and Figure 16.8 displayed the existence of a channel of TIDs propagating southward in the opposite direction to the majority of TIDs that prevailed after 17 UT on 21 August 2011. Based on the magnitude and direction of the phase velocity, the scale size, and period of the TIDs, it is suggested that these southward propagating TIDs were excited by thermospheric sources produced by the dissipation of primary AGWs that originated within TS Irene or in the region of several convective plumes that occurred in the northern part of Peru (see yellow line in Fig. 16.9d).

On 20 and 21 August 2011, TIDs in the America sector propagated mainly in the geographic northward and southward directions. TID velocities larger than 300 m/s directed northward were observed across South America. These velocities seem to correspond to secondary AGWs that were probably generated thousands of kilometers away, and quite likely between the continent and Antarctica. However, an important deviation from the strictly north-south velocity existed. Near TS Irene, westward velocities were observed between 01 and 03 UT on 21 August 2011. Eastward velocities were also seen near TS Irene a few hours prior to the event presented in Figure 16.10b. As the TIDs were detected very close to TS Irene, it was suggested that they may correspond to primary AGWs excited by tropospheric sources. We also found a region of counter-streaming TIDs separated by less than 100 km.

The regional plots presented in Figures 16.5 and 16.8 show the variability of the TID activity during 2 days: 20 and 21 August 2011. These 2 days are magnetically quiet periods and point out an absence of large-scale TIDs (>2000 km) that are commonly observed during large magnetic storms. It has been reported by *Valladares et al.* [2009] that during times of magnetic activity, large-scale TIDs move toward the equator from the poles. However, the TIDs reported here were likely generated in the midlatitude or low-latitude troposphere, mesosphere, or thermosphere.

## 16.6. CONCLUSIONS

This study has led to the following:

1. This analysis has provided regional maps of TEC perturbations associated with the TIDs that circulated throughout South and Central America and the Caribbean region on 20 and 21 August 2011. Similar plots can be constructed for other continents such as Africa and Asia to further our understanding on the longitudinal differences that exist in different regions of the globe.
2. Calculations of the phase velocity and the scale size of TIDs and regional images of tropospheric temperature brightness recorded by the GOES-12 satellite were used to assess the role of a tropical storm and clusters of tropospheric convective cells on the initiation of TIDs in the South American continent.
3. A group of TIDs, observed in the Caribbean region between 0 and 06 UT on 21 August 2011, were likely associated with primary AGWs. These waves were triggered within the region of TS Irene. These TIDs were moving eastward at 140 m/s and had a scales size of 250 km.
4. TIDs associated with primary and secondary AGWs were identified and an estimation of their place and time of origin was calculated using plots of the TEC perturbations in a travel-distance versus universal time format.

## ACKNOWLEDGMENTS

The authors thank Dr. Claudio Brunini and Mauricio Gende of the Geocentric Reference System for the Americas (SIRGAS) and Dr. Michael Bevis from Ohio State University-Central and Southern Andes GPS Project (OSU-CAP) for providing GPS data. Dr. Hector Mora from the Colombian Institute of Geology and Mining (INGEOMINAS) provided RINEX files from several stations in Colombia. One of the authors, Dr. Valladares, was partially supported by Air Force Research Laboratory contract FA8718-09-C-0041, NSF Grants ATM-1135675, and ATM-1242476 and NASA LWS Grant NNX11AP02G. The Low-Latitude Ionospheric Sensor Network (LISN) is a project led by Boston College in collaboration with the Geophysical Institute of Peru, and other institutions that provide information in benefit of the scientific community. We thank all organizations and persons that are supporting and operating receivers in LISN. The TEC values presented in this publication are stored in the LISN web page (http://lisn.igp.gob.pe).

## REFERENCES


Afraimovich, E. L., K. S. Palamartchouk, and N. P. Perevalova (1998), GPS radio interferometry of travelling ionospheric disturbances, *J. Atmos. Sol. Terr. Phys.*, *60*, 1205–1223; doi:10.1016/S1364-6826(98)00074-1.

Afraimovich, E. L., E. A. Kosogorov, L. A. Leonovich, K. S. Palamartchouk, N. P. Perevalova, and O. M. Pirog (2000), Determining parameters of large-scale traveling ionospheric disturbances of auroral origin using GPS-arrays, *J. Atmos. Sol. Terr. Phys.*, *62*, 553–565; doi:10.1016/S1364-6826(00)00011-0.

Afraimovich, E. L., E. A. Kosogorov, N. P. Perevalova, and A. V. Plotnikov (2001), The use of GPS arrays in detecting shock-acoustic waves generated during rocket launchings, *J. Atmos. Sol. Terr. Phys.*, *63*(18), 1941–1957; doi:10.1016/S1364-6826(01)00071-2.

Afraimovich, E. L., N. P. Perevalova, and S. V. Voyeikov (2003), Traveling wave packets of total electron content disturbances as deduced from global GPS network data, *J. Atmos. Sol. Terr. Phys.*, *65*(11–13), 1245–1262; doi:10.1016/j.jastp.2003.08.007.

Bishop, R., N. Aponte, G. D. Earle, M. Sulzer, M. Larsen, and G. Peng (2006), Arecibo observations of ionospheric perturbations associated with the passage of tropical storm Odette, *J. Geophys. Res.*, *111* (A11), A11320; doi:10.1029/2006JA011668.

Crowley, G., and F. S. Rodrigues (2012), Characteristics of traveling ionospheric disturbances observed by the TIDDBIT sounder, *Radio Sci.*, *47*, RS0L22; doi:10.1029/2011RS004959.

Fritts, D. C., and S. L. Vadas (2008), Gravity wave penetration in to the thermosphere: Sensitivity to solar cycle variations and mean winds, *Ann. Geophys.*, *26*, 3841–3861; doi:10.5194/angeo-26-3841-2008.

Fritts, D. C., and Z. Luo (1992), Gravity wave excitation by geostrophic adjustment of the jet stream, Part1: Two-dimensional forcing, *J. Atmos. Sci.*, *49*, 681–697; 10.1175/1520-0469(1992)049<0681:GWEBGA>2.0.CO;2.

Galvan, D. A., A. Komjathy, M. P. Hickey, and A. J. Mannucci (2011), The 2009 Samoa and 2010 Chile tsunamis as observed in the ionosphere using GPS total electron content, *J. Geophys. Res.*, *116*, A06318; doi:10.1029/2010JA016204.

Galvan, D. A., A. Komjathy, M. P. Hickey, P. Stephens, J. Snively, Y. Tony Song, M. D. Butala, and A. J. Mannucci (2012), Ionospheric signatures of Tohoku-Oki tsunami of March 11, 2011: Model comparisons near the epicenter, *Radio Sci.*, *47*, RS4003; doi:10.1029/2012RS005023.

Hedin, A. E., N. W. Spencer, and T. L. Killeen (1988), Empirical global model of upper thermosphere winds based on Atmosphere and Dynamics Explorer satellite data, *J. Geophys. Res.*, *93*(A9), 9959–9978; doi:10.1029/JA093iA09p09959.

Hines, C. O. (1960), Internal atmospheric gravity waves at ionospheric heights, *Can. J. Phys.*, *38*, 1441–1481; doi:10.1139/p60-150.

Hines, C. O., and C. A. Reddy (1967), On the propagation of atmospheric gravity waves through regions of wind shear, *J. Geophys. Res.*, *72*, 1015–1034; doi:10.1029/JZ072i003p01015.

Hocke, K., and K. Schlegel (1996), A review of atmospheric gravity waves and travelling ionospheric disturbances: 1982–1995, *Ann. Geophys.*, *14*, 917; doi:10.1007/s00585-996-0917-6.

Hocke, K., and T. Tsuda (2001), Gravity waves and ionospheric irregularities over tropical convection zones observed by GPS/MET radio occultation, *Geophys. Res. Lett.*, *28*, 2815–2818; doi:10.1029/2001GL013076.

Jacobson, A. R., and W. C. Erickson (1992), A method for characterizing transient ionospheric disturbances using a large radiotelescope array, *Astron. Astrophys.*, *257*, 401–409.

Jacobson, A. R., R. C. Carlos, R. S. Massey, and G. Wu (1995), Observations of traveling ionospheric disturbances with a satellite-beacon radio interferometer: Seasonal and local time behavior, *J. Geophys. Res.*, *100*(A2), 1653–1665; doi:10.1029/94JA02663.

Kirkland M. W., and A. R. Jacobson (1998), Drift-parallax determination of the altitude of traveling ionospheric disturbances observed with the Los Alamos radio-beacon interferometer, *Radio Sci.*, *33*(6), 1807–1825; doi:10.1029/98RS02033.

Makela, J. J., P. Lognonné, H. Hébert, T. Gehrels, L. Rolland, S. Allgeyer, A. Kherani, G. Occhipinti, E. Astafyeva, P. Coïsson, A. Loevenbruck, E. Clévédé, M. C. Kelley, and J. Lamouroux (2011), Imaging and modeling the ionospheric airglow response over Hawaii to the tsunami generated by the Tohoku earthquake of 11 March 2011, *Geophys. Res. Lett.*, *38*, L00G02; doi:10.1029/2011GL047860.

Martinis, C., J. Baumgardner, J. Wroten, and M. Mendillo (2011), All-sky imaging observations of conjugate medium-scale traveling ionospheric disturbances in the American sector, *J. Geophys. Res.*, *116*, A05326; doi:10.1029/2010JA016264.

Mercier, C. (1986) Observations of atmospheric gravity waves by radio- interferometry, *J. Atmos. Terr. Phys.*, *48*, 605–624; doi:10.1016/0021-9169(86)90010-3.

Otsuka, Y., K. Shiokawa, T. Ogawa, and P. Wilkinson (2004), Geomagnetic conjugate observations of medium-scale traveling ionospheric disturbances at midlatitude using all-sky airglow imagers, *Geophys. Res. Lett.*, *31*, L15803; doi:10.1029/2004GL020262.

Perkins, F. (1973), Spread *F* and ionospheric currents, *J. Geophys. Res.*, *78*(1), 218–226; doi:10.1029/JA078i001p00218.

Saito, A., T. Iyemori, and M. Takeda (1998), Evolutionary process of 10 kilometer scale irregularities in the nighttime midlatitude ionosphere, *J. Geophys. Res.*, *103*(A3), 3993–4000; doi:10.1029/97JA02517.

Shiokawa, K., Y. Otsuka, T. Tsugawa, T. Ogawa, A. Saito, K. Ohshima, M. Kubota, T. Maruyama, T. Nakamura, M. Yamamoto, and P. Wilkinson (2005), Geomagnetic conjugate observation of nighttime medium-scale and large-scale traveling ionospheric disturbances: FRONT3 campaign, *J. Geophys. Res.*, *110*, A05303; doi:10.1029/2004JA010845.

Shiokawa, K., Y. Otsuka, T. Ogawa, N. Balan, K. Igarashi, A. J. Ridley, D. J. Knipp, A. Saito, and K. Yumoto (2002), A large-scale traveling ionospheric disturbance during the magnetic storm of 15 September 1999, *J. Geophys. Res.*, *107*, 1088; doi:10.1029/2001JA000245.

Vadas, S. L. (2007), Horizontal and vertical propagation and dissipation of gravity waves in the thermosphere from lower atmospheric and thermospheric sources, *J. Geophys. Res.*, *112*, A06305; doi:10.1029/2006JA011845.

Vadas, S. L., and D. C. Fritts (2001), Gravity wave radiation and mean responses to local body forces in the atmosphere, *J. Atmos. Sci.*, *58*, 2249–2279; doi:10.1175/1520-0469(2001)058<2249:GWRAMR>2.0.CO;2.

Vadas, S. L., and D. C. Fritts (2004), Thermospheric responses to gravity waves arising from mesoscale convective complexes, *J. Atmos. Sol. Terr. Phys.*, *66*, 781–804; doi:10.1016/j.jastp.2004.01.025.

Vadas, S. L., and G. Crowley (2010), Sources of the traveling ionospheric disturbances observed by the ionospheric TIDDBIT sounder near Wallops Island on October 30, 2007, *J. Geophys. Res.*, *115*, A07324; doi:10.1029/2009JA015053.

Vadas, S. L., and H. Liu (2009), Generation of large-scale gravity waves and neutral winds in the thermosphere from the dissipation of convectively generated gravity waves, *J. Geophys. Res.*, *114*, A10310; doi:10.1029/2009JA014108.

Valladares, C. E., and J. L. Chau (2012), The Low-latitude Ionosphere Sensor Network (LISN) initial results, *Radio Sci.*; doi:10.1029/2011RS004978.

Valladares, C. E., and M. A. Hei (2012), Measurement of the characteristics of TIDs using small and regional networks of GPS receivers during the campaign of 17–30 July of 2008, *Int. J. Geophys.*, Article ID 548784; doi:10.1155/2012/548784.

Valladares C. E., J. Villalobos, M. A. Hei, R. Sheehan, S. Basu, E. MacKenzie, P. H. Doherty, and V. H. Rios (2009), Simultaneous Observation of traveling ionospheric disturbances in the northern and southern hemispheres, *Annales Geophys.*, *27*, 1501; doi:10.5194/angeo-27-1501-2009.

# 17

# Modeling the East African Ionosphere

**Melessew Nigussie,[1] Baylie Damtie,[1] Endawoke Yizengaw,[2] and Sandro M. Radicella[3]**

## ABSTRACT

Modeling the Earth's ionosphere is vital for mitigating the effect of the ionosphere on radio waves. In this study, a nontomographic technique has been developed to estimate near-real-time total electron content (TEC) and electron density maps from slant TEC (sTEC) measurements. The technique has been demonstrated using data simultaneously collected by 16 GPS receivers installed in the East African sector. Effective ionization level Az, which is the driver of NeQuick model, is computed by minimizing the magnitude of the absolute difference between experimental and NeQuick modeled sTEC corresponding to each GPS signal ray path. To estimate Az at the locations where no GPS data are available, Az values are represented by Universal Kriging algorithm. An Az map, which is estimated using Universal Kriging, has been utilized to drive the model to reproduce three-dimensional electron density and two-dimensional TEC maps. It is shown that the modeling technique reproduces in situ ion density observations of C/NOFS satellite and GPS TEC better than NeQuick in its regular application. In addition, the new approach provides clear features of the equatorial ionosphere such as the effects of prereversal enhancement of $\mathbf{E}\times\mathbf{B}$ on equatorial ionization anomaly. Moreover, maps of the variance of TEC can be estimated through this approach.

**Key Points:**

- TEC ingestion into NeQuick combined with Universal Kriging is very helpful to describe the equatorial ionospheric dynamics.
- TEC ingestion into NeQuick combined with Universal Kriging provides near-real-time maps of TEC and electron density.
- TEC ingestion into NeQuick combined with Universal Kriging is an excellent proxy for ionospheric tomography.
- TEC ingestion into NeQuick combined with Universal Kriging provides maps of variance of TEC and electron density.

**Key Terms:** Universal Kriging, TEC ingestion, NeQuick, TEC and electron density maps, C/NOFS, equatorial ionosphere

[1]*Department of Physics, Washera Geospace and Radar Science Laboratory, Bahir Dar University, Bahir Dar, Ethiopia*

[2]*Institute for Scientific Research, Boston College, Chestnut Hill, Massachusetts, USA*

[3]*Telecommunication/ICT for Development Laboratory, Abdu Salam International Center for Theoretical Physics (ICTP), Trieste, Italy*

*Ionospheric Space Weather: Longitude and Hemispheric Dependences and Lower Atmosphere Forcing, Geophysical Monograph 220*, First Edition. Edited by Timothy Fuller-Rowell, Endawoke Yizengaw, Patricia H. Doherty, and Sunanda Basu.

## 17.1. INTRODUCTION

The ionosphere affects transionospheric radio propagation [*Davies*, 1990]. For example, the ionosphere reflects radio waves, with frequencies comparable to its plasma frequency by which signals are propagated over long distances. In the case of the radio wave with a frequency higher than plasma frequency, the ionosphere delays the signal (group delay) and creates a phase shift (phase advance) [*Hartmann and Leitinger*, 1984]. Since the group delay and phase advance of a signal (e.g., Global Positioning System, GPS, signals) is directly proportional to TEC along the ray path (slant TEC), the variability of the ionosphere severely degrades the usability of the given signals in communication and navigation. The ionosphere is the largest error source in single frequency GPS receivers, which cannot correct the ionospheric error by itself. This means that applications related to transionospheric radio waves depend on an ionospheric TEC (or electron density) model, which is also useful for ionospheric study.

Different approaches have been developed to estimate ionospheric parameters at the location where there are no measurements. The numerical model of Global Ionospheric Map (GIM) of vertical TEC (vTEC), for example, has been developed by combining experimental vTEC and spherical harmonics to estimate vTEC for every 2 hr at the geographic spatial resolution of 2.5° latitude and 5° longitude [*Hernàndez-Pajares et al.*, 2010]. *Jakowski et al.* [2011] have also developed a global TEC model by combining TEC measurements and polynomial function consisting of 12 coefficients by applying the least-squares estimation technique. The vTEC used in this approach is estimated by converting the slant TEC (sTEC) to vTEC by using ionospheric thin shell mapping function. But, the mapping function by itself produces errors during sTEC to vTEC conversion or vice versa, especially for the low-latitude ionosphere, which usually exhibits TEC gradient [*Sparks et al.*, 2004].

Recent modeling effort by considering a multilayer mapping function has provided the technique to reduce ionospheric mapping function error during vTEC to sTEC conversion [*Horque and Jakowski*, 2013]. Similarly, empirical models such as NeQuick are used to estimate electron-density distribution and TEC everywhere in the Earth's ionosphere. It is developed based on the long-collected ground-based and space-based ionospheric data obtained mostly from the midlatitude of the Northern Hemisphere [*Nava et al.*, 2008; *Jones and Gallet*, 1962]. In addition, it is designed to estimate the hourly monthly median ionospheric characteristics. This implies that the model in its regular usage could not produce near-real-time characteristics of the ionosphere especially for the African sector where very few measurements were used for the model development. For example, *Nigussie et al.* [2013] have investigated its performance in reproducing the East African region ionosphere and they indicated when and why the model is unable to describe the median characteristics of the regional ionosphere.

On the other hand, electron-density distributions have been estimated by inverting the sTEC obtained from GPS receiver measurements. Ionospheric tomography is one of the techniques used to estimate the vertical electron-density structure from sTEC measurements collected by a chain of GPS receivers [*Austen et al.*, 1988]. Usually, it produces 20 to 30 min an average electron-density map since the algorithm requires many sTEC measurements as input. This implies that a technique is required to approximate an instantaneous variation of the ionosphere, especially for the equatorial region, which always exhibits dynamic and complex characteristics.

The state-of-the-art techniques have been developed to improve the performances of the preexisting empirical models by assisting them with ionospheric measurements [*Komjathy et al.*, 1998; *Hernàndez-Pajares et al.*, 2002; *Nava et al.*, 2006; *Jakowski et al.*, 2011]. Moreover, *Jakowski et al.* [2011] have developed the technique to forecast TEC maps up to 1 hr in advance by assisting the model with GPS measurements. The performance of NeQuick in reproducing the experimental sTEC can be improved by assisting the model with ionospheric measurements, which can be done by means of sTEC data ingestion using single or multistation measurements [*Nava et al.*, 2006]. The basic idea of the data assimilation is to determine the local effective solar radio flux (Az) or effective ionization level, which minimizes the difference between the modeled and experimental sTEC values. This has been demonstrated for one day of data obtained for the North America region during a high solar activity period using NeQuick 1, and the results have shown significant improvements. Similarly, *Memarzadeh* [2009] adapted the model to CODE (Center for Orbit Determination in Europe) vTEC GIM to develop a vTEC map using NeQuick 1 after adaption. But the Az that are estimated from the vTEC map might be contaminated by mapping function error, which has very high value for the low-latitudes ionosphere [*Kersely*, 2005; *Sparks et al.*, 2004]. *Nigussie et al.* [2012] also demonstrated that adapting NeQuick 2 with sTEC obtained during geomagnetic quiet conditions from one reference station can significantly improve its performance to reproduce TEC even at wider spatial distance up to about 620 km from the reference station located in the East African region. This result indicates that good estimates of TEC and electron-density maps can be obtained by adapting NeQuick 2 to sTEC, which is obtained from multiple GPS receivers.

Recently, ionospheric monitoring devices were installed at regions around the globe, especially in regions, such as

Africa, which were devoid of ground-based ionospheric monitoring instruments. For example, the IGS (International Global Navigation Satellite System, GNSS service) and Scintillation Network Decision Aid (SCINDA) receivers were installed recently in the East African region for ionospheric study [*Amory-Mazaudier et al.*, 2009]. Also, 16 GPS receivers are being deployed by seismologists (and others) to study the Earth's plate movement in and around the East African region (www.unavco.org).

The measurements taken by these receivers are very useful to extract sTEC, which is an excellent resource to get near-real-time representation of the East African ionosphere. Therefore, to estimate the true state of the equatorial ionosphere, adaptation of NeQuick 2 model to multistation measurements collected by the GPS receivers installed recently in the East African region has been applied in this study. Adjusting the input of the model (modeled sTEC) to match with the experimental sTEC is done in the adaptation procedure. The adjusted input of the model (effective ionization level, Az), derived from the sTEC measurement, approximates the true state of the ionosphere.

The main objective of this study is to develop strategies to model the small-scale spatiotemporal variability of TEC and three-dimensional electron-density maps by combining NeQuick 2 and GPS receivers' sTEC measurements taken at an epoch. This has been done first by mapping the Az using Universal Kriging interpolation technique. Universal Kriging is the robust approach that can take the correlation of data into account to estimate parameters at the locations where no measurements are available. An Az map, in turn, drives the model to reconstruct time-dependent three-dimensional electron-density and two-dimensional vTEC maps. Moreover, the technique has been applied to estimate the variance of the vTEC maps, which indicates that adaptation of NeQuick 2 to sTEC combined with Universal Kriging enables NeQuick 2 (climatological model) to be utilized as a stochastic model. The technique applied in this work has been verified using independent in situ ion density observations from the C/NOFS (Communication/Navigation Outage Forecast System) satellite and GPS receiver TEC measurements that not used for Az estimation.

## 17.2. DATA AND MODELING TECHNIQUE

The dual-frequency GPS receivers, which have been deployed mostly by seismologists to measure the Earth's plate movement in the East African region, provide TEC data. Figure 17.1 shows the locations of GPS receivers

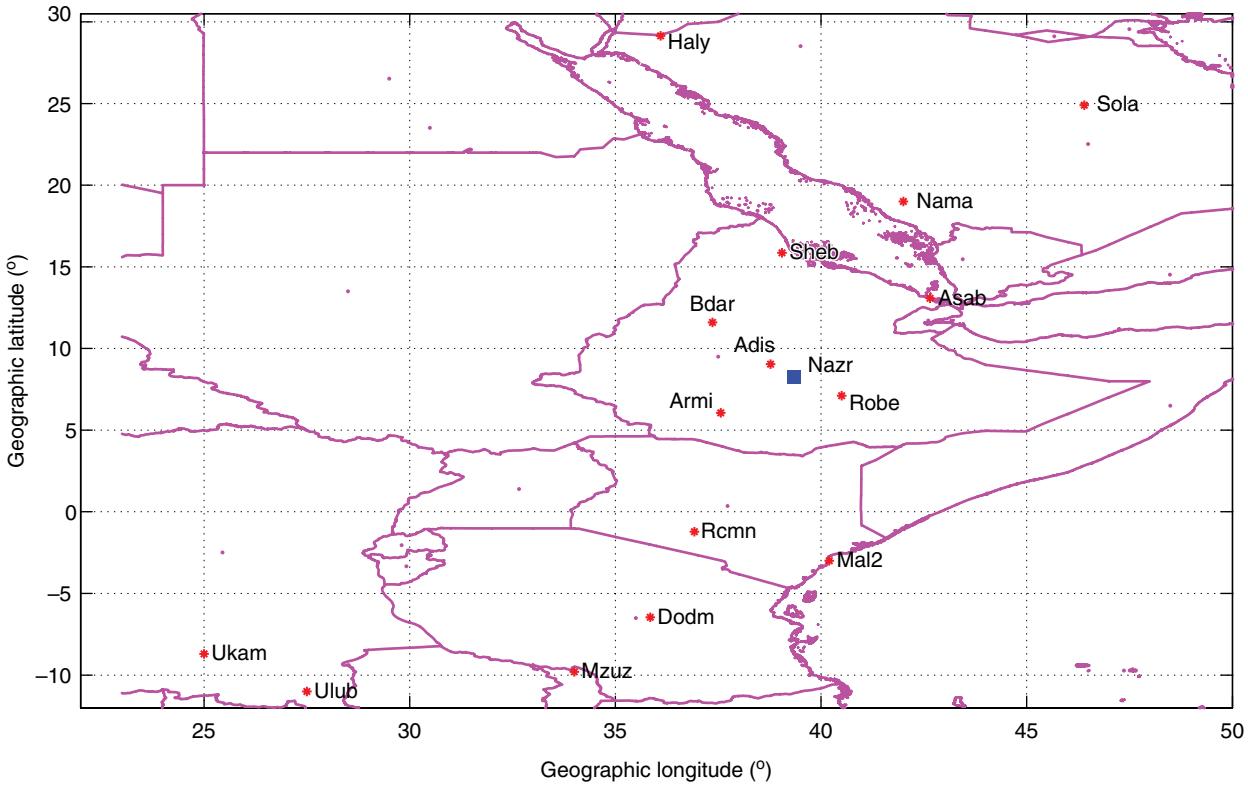


**Figure 17.1** Locations of the 16 GPS receivers in the East Africa region used for vTEC and electron density maps development (red asterisk) and validation of mapping methods (blue square).

(i.e., 16) available in the region and used for this study. The sTEC from 15 GPS receivers (red asterisk) have been used for the adaptation process. The remaining receiver (blue square) with station name Nazr has been used for the internal consistency test of the modeling strategy. For this study, 11 March 2011 has been selected since all 16 GPS receivers and the C/NOFS satellite have been nearly simultaneously operational and provided data. On 11 March 2011, a moderate storm (Ap = 37) was reported. It is also very useful to test the performance of the model after adaptation in reproducing the ionospheric parameters during disturbed conditions. Since there are a limited number of ground-based GPS receivers in the region, the study area is bounded by the geographic latitudes of −10° to 30°N and longitudes of 30° to 50°E.

The sTEC observed at those 15 GPS receivers have been used for NeQuick 2 adaptation. Each sTEC in an epoch has been ingested into NeQuick 2 to compute Az. Az is different from the daily solar radio flux index ($F_{10.7}$), but it has the same unit as solar radio flux (i.e., solar flux unit, sfu). The local effective ionization level Az that produces the minimum magnitude of the absolute difference between the experimental and the modeled sTEC corresponding to each GPS ray path is then estimated. This means that Az is calculated by minimizing

$$dsTEC(Az) = \left| sTECm(Az) - sTECo \right|, \qquad (17.1)$$

where, sTECm and sTECo represent the modeled and experimental sTEC, respectively, and dsTEC denotes the magnitude of their absolute difference. If each receiver observes eight GPS signals at an epoch, 120 Az values are estimated using Equation (17.1).

### 17.2.1. Universal Kriging

Kriging is the geostatistical technique applicable for interpolation (prediction) of spatial scattered data by computing the weighted mean value of measurements [*Cressie*, 1993]. Kriging weights are essential for estimation of parameters using Kriging algorithm and they are estimated by taking into account the spatial correlation among measurements. Kriging interpolation has two main approaches, Ordinary Kriging and Universal Kriging. Ordinary Kriging considers a constant unknown mean of data in the region, whereas Universal Kriging considers a variable unknown mean of data in the region [*Cressie*, 1993].

These methods have been widely applied by geostatistics for different applications such as mining, hydrology, and so on [*Cressie*, 1993]. Nowadays, the method is being adopted for ionospheric study and related applications. *Sparks et al.* [2011] have applied the method to estimate the slant delay of the GPS signal in the ionosphere to improve the GPS application. Similarly, *Orús et al.* [2005] have applied the Ordinary Kriging technique to estimate the vTEC from its residuals regarding to a previous model at the locations where no vTEC measurements and developed a respective vTEC map. In this study, Universal Kriging interpolation technique has been applied to estimate an Az map, which in turn drives the NeQuick model to estimate TEC and electron-density maps. The same technique has been applied to estimate vTEC maps using experimental vTEC from GPS measurements (i.e., without using NeQuick 2).

TEC measurements at 1400 UT on 11 March 2011, which are depicted in the left top panel of Figure 17.2, have been considered to describe the mapping technique used for this study. The left bottom panel of this figure shows the Az values estimated (using Equation [17.1]) from the sTEC corresponding to the vTEC shown in this figure. The right top and bottom panels show the plots of quantiles of standard normal distribution (theoretical) against the corresponding quantiles of vTEC and Az (i.e., QQ plot) depicted in the left panels, respectively. As can be seen in both panels, the QQ plots deviate from the straight line, which indicates that the vTEC and Az do not approximate the normal distribution [*Lee et al.*, 1998].

This means both vTEC and Az have a trend [*Crujeiras and Keilegom*, 2010]. The trend of these data may be due to equatorial ionosphere physical process, for example, the equatorial electrojet (EEJ). As described in *Cressie* [1993], data with trend (like vTEC and Az) can be modeled as a sum of deterministic (trend) and stochastic variability components, which is given by

$$z(\theta, \phi, t) = m(\theta, \phi, t) + \varepsilon(\theta, \phi, t). \qquad (17.2)$$

Here, $z$, $m$, and ε represent the experimental, deterministic, and stochastic components of vTEC (or Az), respectively, and $\theta$, $\phi$, and $t$ are the geographic latitude, longitude, and time, respectively. The deterministic and stochastic components of spatial data can be modeled separately.

#### *17.2.1.1. Deterministic Component Modeling*

In Equation (17.2), the deterministic component mimics the large-scale variability, whereas the stochastic component represents the small-scale variability of the processes [*Cressie,* 1993]. The deterministic component can be modeled by a deterministic model (example, polynomial) assuming the stochastic component has zero mean [*Crujeiras and Keilegom*, 2010].

A deterministic mathematical model of vTEC and Az has been selected based on their scatter plot as a function of the independent variables ($\theta$, $\phi$). The panels in Figure 17.3 show the latitudinal and longitudinal variations of the vTEC and Az.

As can be seen in Figure 17.3, vTEC and Az have shown insignificant longitudinal variations (bottom panels);

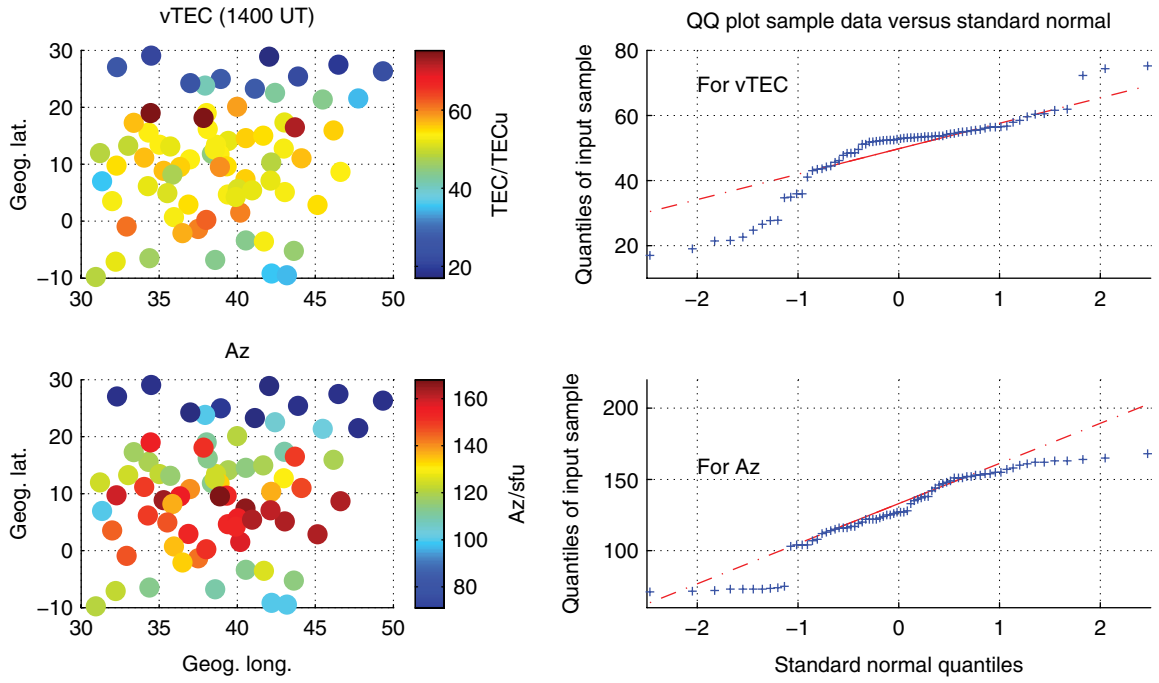


**Figure 17.2** Scatter plot of vTEC (left top) and Az (left bottom) and their corresponding qq-plots (right top) and (right bottom) estimated at 1400 UT on 11 March 2011.

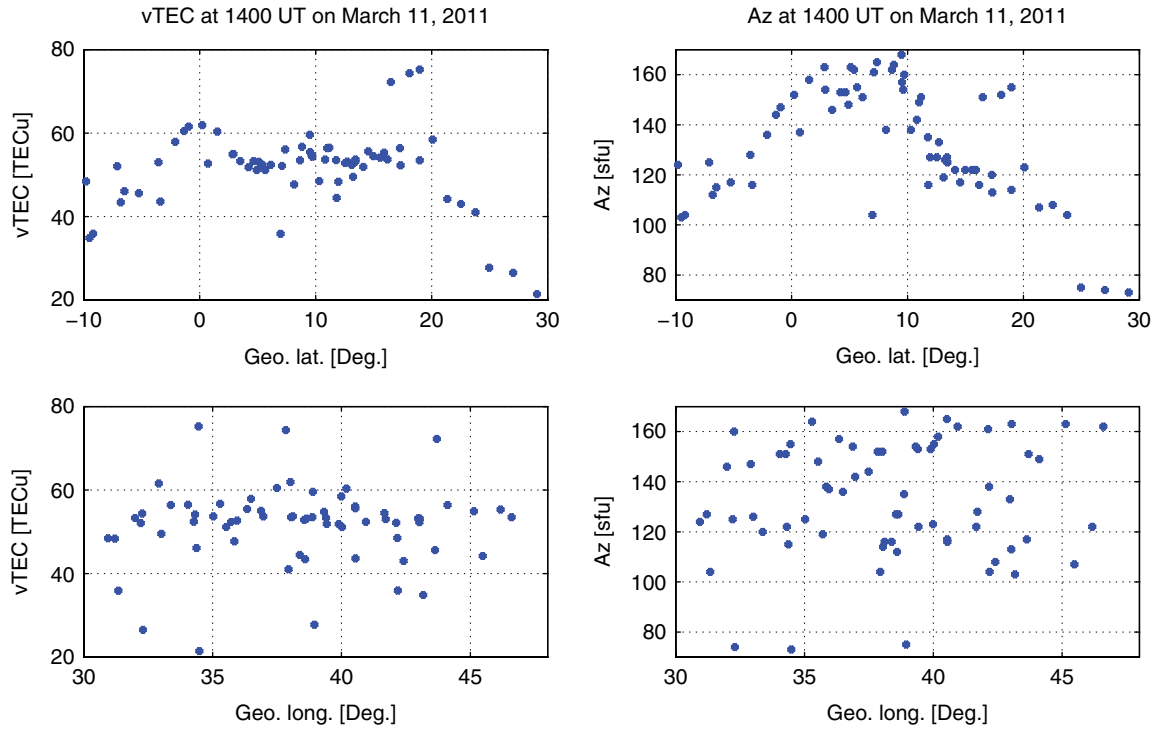


**Figure 17.3** Latitudinal variations of vTEC (top left) and Az (top right) and longitudinal variations of vTEC (left bottom) and Az (right bottom) estimated at 1400 UT on 11 March 2011.

however, they have shown significant variations with respect to geographic latitude (top panels). The latitudinal variations of vTEC show peak values at about 0°N and 19°N and decreased values in between and beyond these latitudes. The peaks of vTEC and small values in between are due to the transportation of charged particles from the equatorial region to higher latitude due to $\mathbf{E}\times\mathbf{B}$ drift forces [*Yizengaw and Moldwin*, 2008]. Hence, the function of second order in latitude and first order in longitude used to model the deterministic components of vTEC and Az is given by

$$m(\theta,\phi,t)=\beta_1(t)+\beta_2(t)\theta+\beta_3(t)\phi+\beta_4(t)\theta^2 \qquad (17.3)$$

where, the $\beta_i(t)(\mathrm{I}=1,\ldots,4)$ are time dependent coefficients of the polynomial. Let n denote the number of vTEC (or Az), then the combination of Equations (17.2) and (17.3) can be rewritten in matrix form as

$$\mathrm{Z}=\mathrm{A}\,\beta+\varepsilon \qquad (17.4)$$

where, **A** is n × p (p is the number of coefficients) theory matrix of coordinates of vTEC (or Az), **β** is a p dimensional vector that contains coefficients of polynomial, and **Z** is the measurement (vTEC or Az) matrix. The **ε** is the stochastic component column vector, which has zero mean ($\mathrm{E}[\boldsymbol{\varepsilon}]=0$) and n × n covariance matrix ($\Sigma=\mathrm{E}[\boldsymbol{\varepsilon}\boldsymbol{\varepsilon}^t]$) [*Haining*, 1987]. The parameter **β**, which represents the deterministic trend of vTEC or Az, is estimated following the procedures suggested by *Haining* [1987] and *Crujeiras and Keilegom* [2010]. First, assuming the stochastic components are independent, the ordinary least square (OLS) solution can be estimated by minimizing the logarithm of the likelihood function and the solution is given by

$$\hat{\beta}_{ols}=\left(A^tA\right)^{-1}A^tZ \qquad (17.5)$$

where, $A^t$ stands for transpose of matrix A. To reduce the ill-conditioned of the matrix A, spatial coordinates are transformed into intervals of [−1,1] [*Ligas and Banasik*, 2012]. Second, the stochastic components are approximated by the OLS residuals ($\hat{\varepsilon}_{ols}=\mathbf{Z}-\mathbf{A}\,\beta_{ols}$) from which the covariance matrix is constructed. Then, the generalized least squares (GLS) solution of $\beta$-parameter is estimated by

$$\hat{\beta}_{gls}=\left(\mathbf{A}^t\Sigma^{-1}\mathbf{A}\right)^{-1}\mathbf{A}^t\Sigma^{-1}\mathbf{Z} \qquad (17.6)$$

where, **Σ** is the covariance matrix. The procedures on how to estimate this matrix and the roles of GLS residuals for Kriging weight estimation are described in the next subsection (17.2.1.2).

#### 17.2.1.2. Stochastic Component Modeling

Stochastic component estimation requires determination of the spatial dependence structure of residuals [*Crujeiras and Keilegom*, 2010]. For data, which have trend, the stochastic component is approximated by the residuals. As suggested by *Crujeiras and Keilegom* [2010] and *Haining* [1987], the OLS residuals are useful to estimate the spatial dependence structure of the small-scale variability, which in turn is useful to construct the variance covariance matrix. The spatial variability of the small-scale component is characterized by the semivariogram. If $\hat{\varepsilon}_{ols}$ denotes n number of residuals, then the semivariogram (hereafter "variogram") is defined [*Cressie,* 1993] as

$$\hat{\gamma}(h)=\frac{1}{2\left|N(h)\right|}\sum_{N(h)}\left[\hat{\varepsilon}_{ols}(x_i)-\hat{\varepsilon}_{ols}(x_j)\right]^2, \qquad (17.7)$$

where, $N(h)=\{(x_i,x_j)\ :x_i-x_j=h\}$, and $|N(h)|$ denotes the number of pairs and $\hat{\varepsilon}_{ols}$ is the experimental data. The data locations are given in geographic latitude and longitude and hence the distance between two data points is computed by the great circle formula. In this work, for simplicity, the isotropic variogram is used.

To apply Universal Kriging, a variogram model that mimics the spatial dependence structure of data is fitted to the empirical variogram. Different authors [*Parado-Igúzquiza*, 1999; *Zhang et al.*, 1995] suggested the weighted least-squares (WLS) technique to fit the model to the empirical variogram by minimizing

$$R(\Phi)=\sum_{k=1}^{Np}N(h_k)\left[\frac{\hat{\gamma}(h_k)}{\gamma(\Phi,h_k)}-1\right]^2 \qquad (17.8)$$

where, Φ is the vector of parameters such as $c_o$, $c_1$, and a. $\gamma(\Phi,h_k)$ is the variogram model and Np is the number of data points of empirical variogram. The most common variogram models are spherical, exponential, and Gaussian [*Lloyd*, 2011]. For example, the exponential variogram is given by

$$\gamma(h)=c_o+c_1\left[1-\exp\left(-\left(\frac{h}{a}\right)^2\right)\right] \qquad (17.9)$$

where, $c_o$ (nugget), $c_1$ (sill), and a (range) are parameters to be estimated from the experimental variogram. The nugget and sill represent the minimum and maximum variance, respectively. The range is the distance where the dissimilarity of data starts to be flat. Minimizing Equation (17.8) yields these parameters.

The variance ($\sigma^2$), variogram ($\gamma[h]$), and the covariance ($c[h]$) are related [*Crujeiras and Keilegom*, 2010] as

$$c(h) = \sigma^2 - \gamma(h) = \mathrm{cov}\left(\hat{\varepsilon}_{ols}(x), \hat{\varepsilon}_{ols}(x+h)\right), \quad (17.10)$$

where $\sigma^2 < \infty$ is the variance of the spatial process. The variance covariance matrix, which is useful for spatial dependence structure of data, can be estimated from Equation (17.10).

The weighted mean of the GLS residuals [*Cressie*, 1993] carries out prediction of the stochastic component. Mathematically, it is given by

$$\hat{\varepsilon}(x_o) = \sum_{i=1}^{n} \lambda_i \hat{\varepsilon}_{gls}(x_i), \quad (17.11)$$

where, $\hat{\varepsilon}(x_o)$ is the stochastic component to be predicted at a location $\chi_o$ given its coordinates $(\theta_o, \phi_o)$, $\hat{\varepsilon}_{gls}(x_i)$ are the residuals estimated from GLS solution at the locations where there are vTEC or Az, and $\lambda_i$ are Kriging weights determined by spatial dependence structure of GLS residuals.

A Kriging weight is estimated by minimizing the prediction error [*Lloyd*, 2011], which provides Kriging weight that relies on spatial dependence structure of the residuals. Kriging weights are estimated from

$$\lambda\Gamma = \mu_o, \quad (17.12)$$

where,

$$\lambda = \begin{pmatrix} \lambda_1 \\ \lambda_2 \\ \cdot \\ \cdot \\ \cdot \\ \lambda_n \\ \psi_o \\ \cdot \\ \cdot \\ \psi_{p-1} \end{pmatrix}, \Gamma = \begin{pmatrix} \gamma(x_1 - x_1) & \cdots & \gamma(x_1 - x_n) & 1 & m_1(x_1) & \cdots & m_{p-1}(x_1) \\ \cdot & \cdots & \cdot & \cdot & \cdot & \cdots & \cdot \\ \cdot & \cdots & \cdot & \cdot & \cdot & \cdots & \cdot \\ \cdot & \cdots & \cdot & \cdot & \cdot & \cdots & \cdot \\ \gamma(x_n - x_1) & \cdots & \gamma(x_n - x_n) & 1 & m_1(x_n) & \cdots & m_{p-1}(x_n) \\ 1 & \cdots & 1 & 0 & 0 & \cdots & 0 \\ m_1(x_1) & \cdots & m_1(x_n) & \cdot & \cdot & \cdots & \cdot \\ \cdot & \cdots & \cdot & \cdot & \cdot & \cdots & \cdot \\ \cdot & \cdots & \cdot & \cdot & \cdot & \cdots & \cdot \\ \cdot & \cdots & \cdot & \cdot & \cdot & \cdots & \cdot \\ m_{p-1}(x_1) & \cdots & m_{p-1}(x_n) & 0 & \cdot & \cdots & 0 \end{pmatrix}, \quad \mu_o = \begin{pmatrix} \gamma(x_1 - x_o) \\ \cdot \\ \cdot \\ \cdot \\ \gamma(x_n - x_o) \\ 1 \\ m_1(x_o) \\ \cdot \\ \cdot \\ \cdot \\ m_{p-1}(x_o) \end{pmatrix}$$

and $\lambda_i$ (I = 1,…,n) in $\lambda$ are the Kriging weights, whereas as the $\Psi_{p-1}$ ($p$ = 1,…,4) are the Lagrangian multipliers. The values of $m_{p-1}(p = 2,\ldots,4)$ in $\mathbf{\Gamma}$ are the coordinates of the locations [*Lloyd*, 2011] of data, for example, $m_1(x_1)$ to $m_1(x_n) = \theta$, $m_2(x_1)$ to $m_2(x_n) = \phi$, and $m_3(x_1)$ to $m_3(x_n) = \theta^2$, and $x_1$ to $x_n$ are the locations of experimental vTEC (or Az). The variogram in $\mathbf{\Gamma}$ should be the one estimated from the GLS residuals. In $\mu_o$, $\chi_o$ and $m_1(\chi_o)$ to $m_{p-1}(\chi_o)$ are the locations where the parameters (vTEC and Az) are going to be estimated using the Universal Kriging algorithm. A detailed description about determination of these matrices is available in *Lloyd* [2011] and *Cressie* [1993].

To illustrate the above algorithms, variogram and Kriging weights are estimated corresponding to vTEC and Az shown in Figure 17.2 (left panels). The results are depicted in Figure 17.4 (top for vTEC and bottom for Az).

As can be seen in these panels, the nugget for both vTEC and Az is different from zero. However, as the distance between the data points increases, the variance also increases until it reaches some distance (range). For example, beyond about 600 km (left bottom panel of Figure 17.4), the spatial variation of residuals saturates. Exponential variogram is used for this variogram modeling since it provides minimum root-mean-square-error over the other models. The right-hand side panels show the Kriging weights, which are estimated using Equation (17.12), to predict vTEC (top right) and Az (bottom right) at the geographic latitude of 9°N and longitude of 39°E. Evidently, the Kriging weights have larger values for the observations found closer to the location where vTEC and Az are going to be estimated. As distance increases, the weighting values become almost zero, which means the data that are far from the location where we want to estimate are given insignificant weights.

As discussed previously, the deterministic and stochastic components are modeled separately. Hence, the Universal Kriging (UK) solution of vTEC or Az is determined by combining the two approaches as

$$\hat{z}(x_o) = \hat{m}(x_o) + \hat{\varepsilon}(x_o), \quad (17.13)$$

where, $\hat{m}(x_o)$ and $\hat{\varepsilon}(x_o)$ are the modeled deterministic and stochastic components, respectively, of vTEC (or Az) and $\chi_o$ is the location with coordinates $(\theta_o, \phi_o)$ where we want to

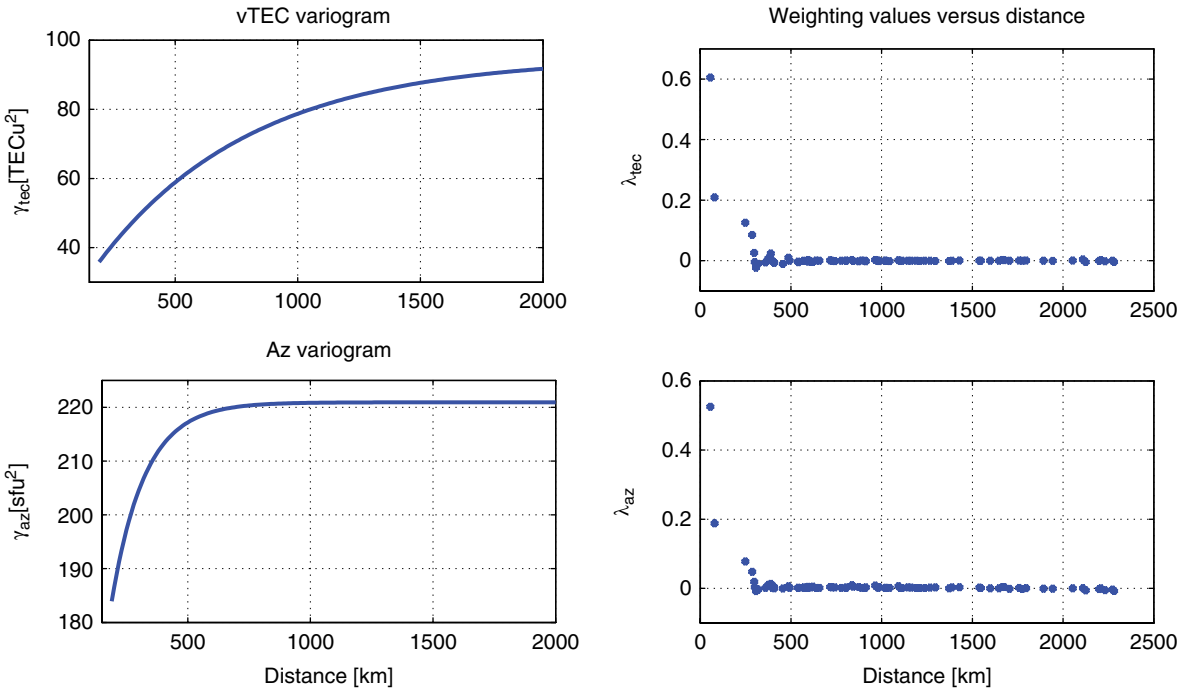


**Figure 17.4** Variogram of vTEC (left top) and Az (left bottom) and Kriging weights estimated to estimate vTEC (right top) and Az (right bottom) at geographic latitude of 9°N and longitude of 39°E at 1400 UT on 11 March 2011.

estimate parameters. In addition, the UK provides the Kriging estimate of variance [*Lloyd*, 2011], which is given by

$$\sigma^2 = \mu_o^t \lambda, \tag{17.14}$$

The variance of UK estimate of Az, from this equation can drive the NeQuick 2 model. This means the climatological model (NeQuick 2) can behave as a stochastic electron-density model and, hence, NeQuick 2 can be used to estimate vTEC or electron density with possible error estimates.

## 17.3. RESULTS AND DISCUSSION

Figure 17.5 shows experimental vTEC estimated from the data recorded by the 15 ground-based GPS receivers (red asterisks in Figure 17.1) on 11 March 2011. The Az values (driver of NeQuick) are computed by combining the NeQuick model and sTEC corresponding to the vTEC shown in Figure 17.5. For example, interpolating experimental vTEC shown in Figure 17.5 at 1400 UT and the corresponding Az using Universal Kriging (UK) technique results in the vTEC and Az maps displayed in Figures 17.6 and 17.7. As it is discussed in Section 17.2, the vTEC and Az are modeled as random variables in which each parameter has large- and small-scale variability components. The large-scale component (or trend) is modeled by a quadratic surface function that varies linearly with geographic longitude and quadratically with geographic latitude (Equation [17.3]). Assuming, the small-scale variability components are independent, the large-scale variability component of vTEC (or Az) is modeled applying the generalized least squares (GLS) solution technique. The large-scale components of vTEC and Az at 1400 UT, for example, are modeled as

$$vTEC(\theta,\phi) = 56.20 - 9.73\theta - 3.70\phi - 27.02\theta^2 \tag{17.15}$$

and

$$Az(\theta,\phi) = 140.05 - 21.60\theta - 0.64\phi - 48.00\theta^2 \tag{17.16}$$

These equations are used to compute the large-scale variability component (trend) of vTEC and Az at 1400 UT. The outputs of these models in one-degree intervals in latitude and longitude are displayed in Figures 17.6a (for vTEC) and 17.6b (for Az). Thereafter, the residuals between the experimental vTEC (or Az) and the outputs of the trend models (Equations [17.15] and [17.16]) are considered as the small-scale variability components, which are also modeled by the stochastic approaches. Similarly, the corresponding small-scale models are also used to estimate the small-scale components of vTEC and Az at 1400 UT, which are displayed in the 17.6c and 17.6d, respectively.

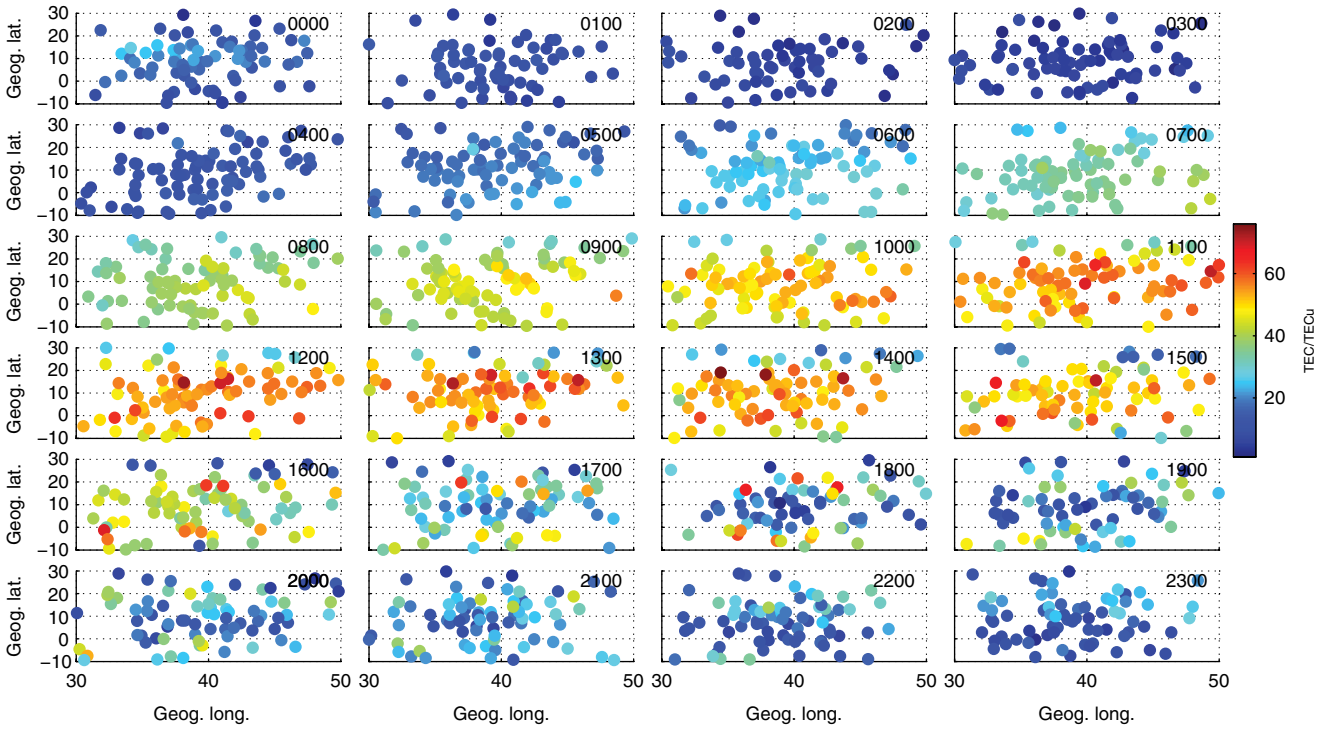


**Figure 17.5** Diurnal variations of scatter plots of experimental vTEC obtained on 11 March 2011 in East African ionosphere.

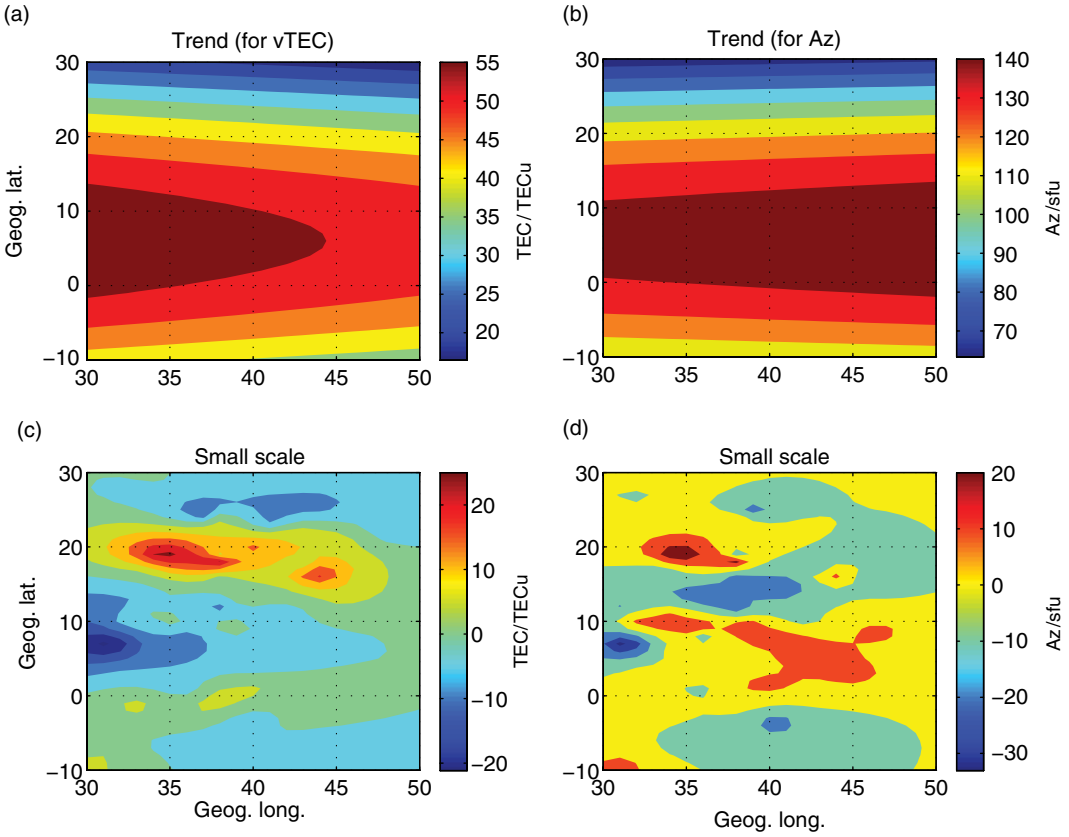


**Figure 17.6** Maps of large-scale (a) vTEC and (b) Az and small-scale (c) vTEC and (d) Az at 1400 UT on 11 March 2011.

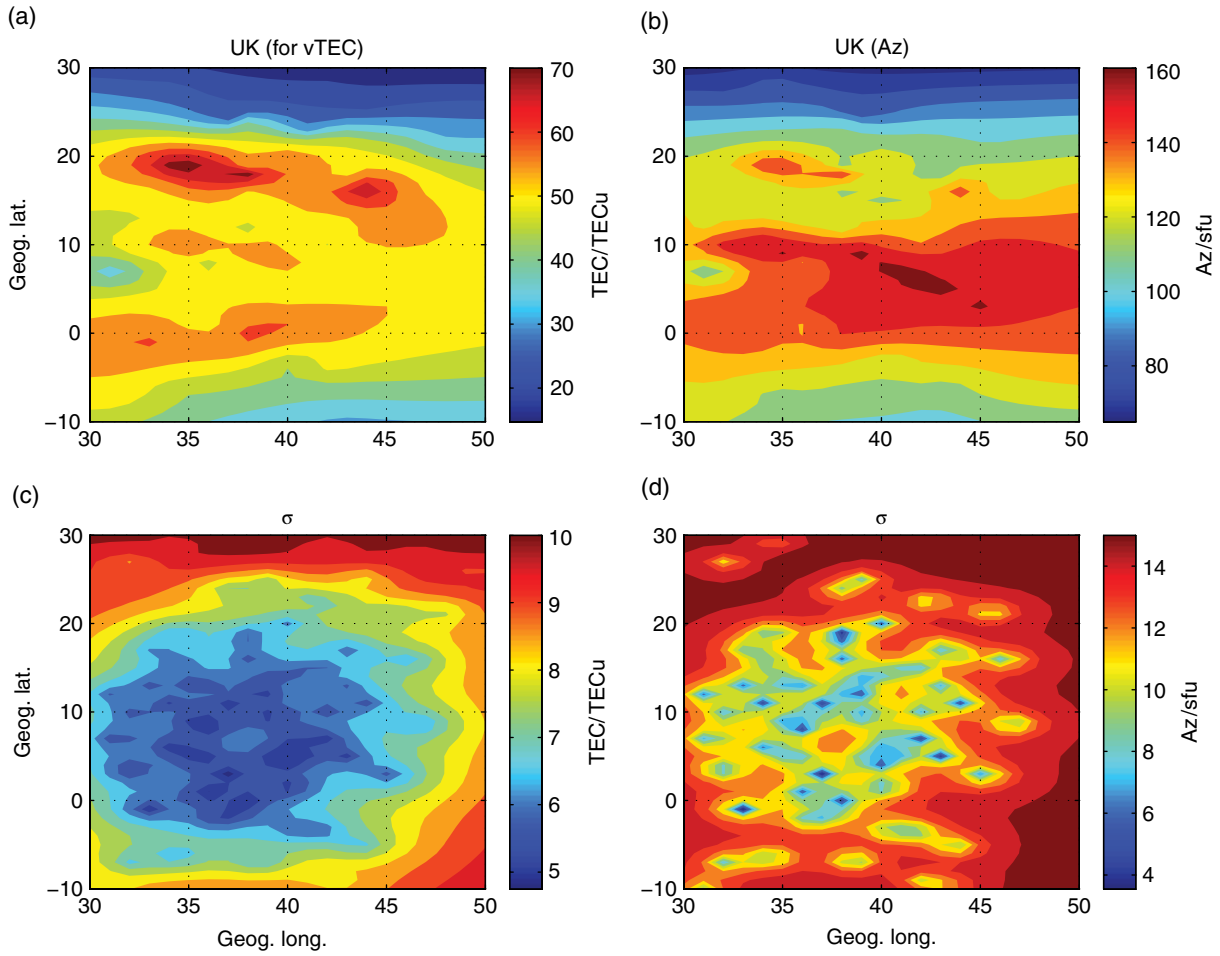


**Figure 17.7** Maps of Universal Kriging solutions of (a) vTEC and (b) Az and estimate of standard deviations for (c) vTEC and (d) Az at 1400 UT on 11 March 2011.

The sum of trend and stochastic models provide the UK maps of vTEC and Az. The UK maps of vTEC and Az at 1400 UT are depicted in Figures 17.7a and 17.7b, respectively. The standard deviations for UK maps and Az are estimated and shown in Figures 17.7c and 17.7d, respectively. Therefore, vTEC can be estimated together with its possible error bars and moreover the monthly median empirical model (NeQuick) can be used as a stochastic model. For example, the vTEC and the standard deviation (in TECu) maps, which are estimated from NeQuick driven by Az (Figure 17.7b) and the standard deviation (Figure 17.7d) maps of Az, are depicted by the left and right panels of Figure 17.8, respectively.

### 17.3.1. The vTEC Maps

In this section, 1 day hourly vTEC maps are presented. The maps are developed by interpolating the experimental vTEC using the UK technique (hereafter this map is called "UK vTEC map") and the results are displayed in Figure 17.9. Also, vTEC maps are estimated before and after adapting the NeQuick 2 model to sTEC observation. The vTEC map after adaptation is computed by driving the model with the Az maps estimated by UK technique (hereafter it is called "vTEC map after adaptation") and the results are shown in Figure 17.10. The corresponding vTEC maps before adaption are obtained using $F_{10.7}$ as a driver of the model and the results are shown in Figure 17.11.

As can be seen by Figure 17.9, the maps of the vTEC have shown clear spatial and temporal variations. The general features of the diurnal variations of these maps show minimum values around 0300 UT. Starting from 0500 UT, the vTEC values increase and reach maximum values at 1100 UT before starting to decrease. These temporal variations are similar to the temporal variations of experimental vTEC shown in Figure 17.5. These results are in agreement with observations at other longitudinal sectors [*Akala et al.*, 2013]. The peak vTEC around 1100 UT (see both Figures 17.9 and 17.10) might

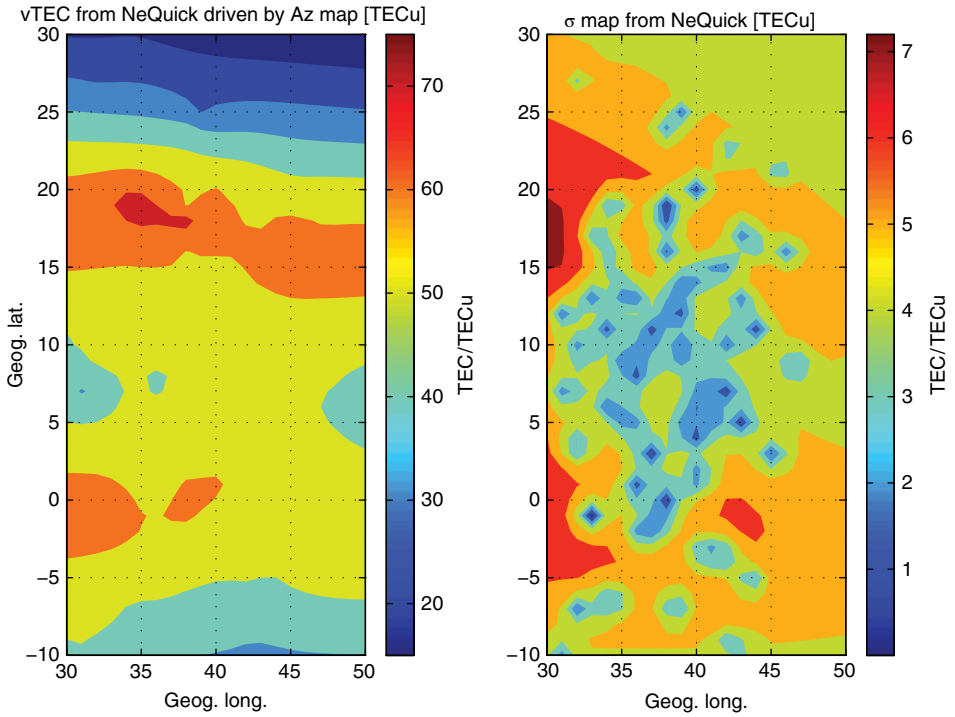


**Figure 17.8** The vTEC maps from NeQuick driven by Az maps (left) and standard deviation estimates (in TECu) from NeQuick driven by standard deviation estimates of Az (right) at 1400 UT on 11 March 2011.

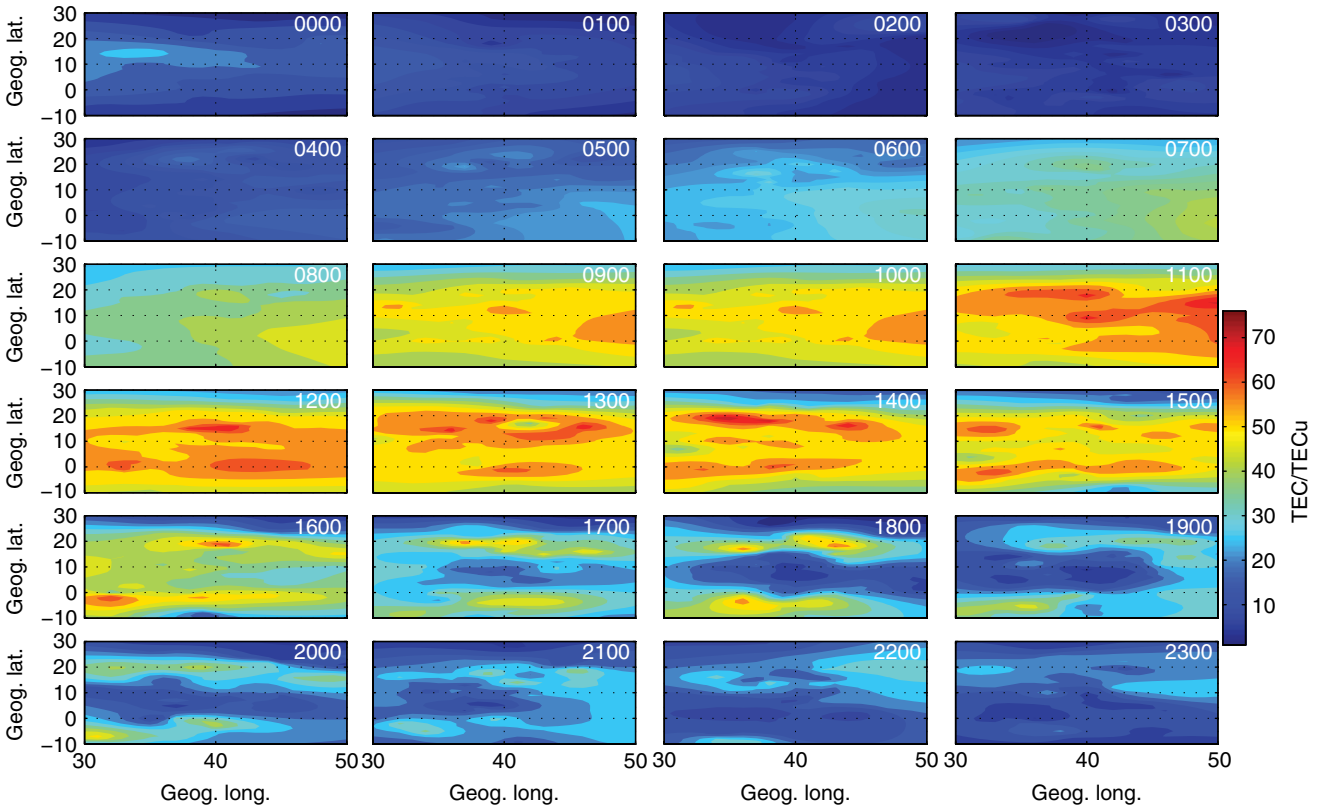


**Figure 17.9** Diurnal variations of vTEC maps estimated by interpolating experimental vTEC using Universal Kriging, on 11 March 2011.

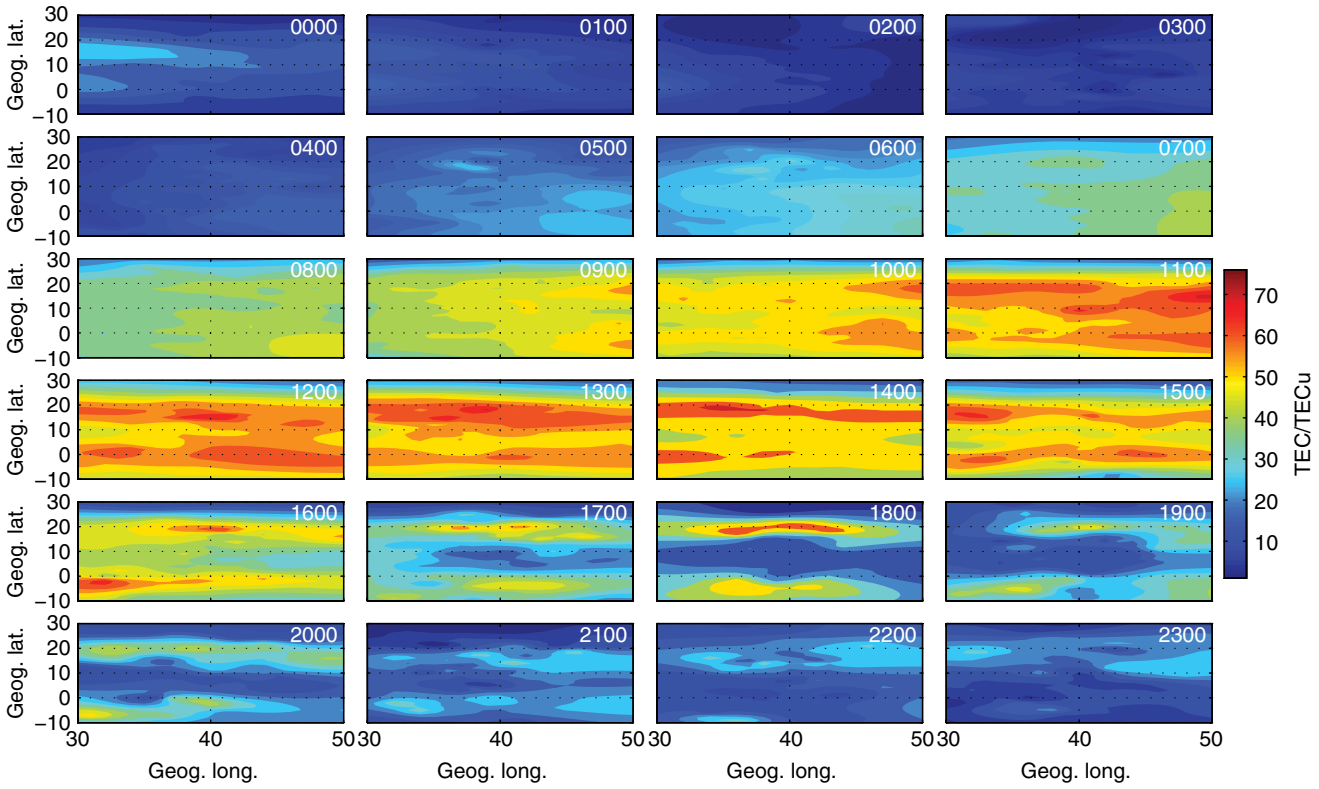


**Figure 17.10** Diurnal variations of vTEC maps estimated using Az maps as driver of NeQuick on 11 March 2011.

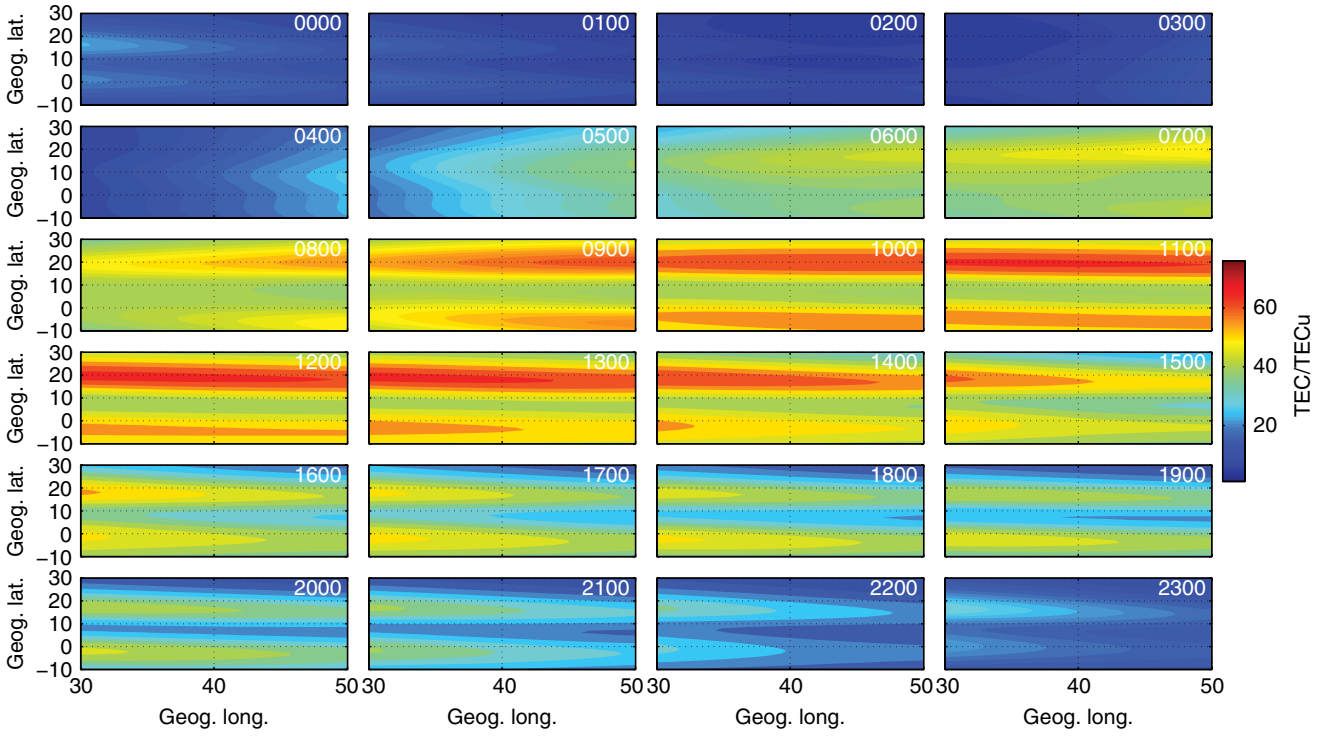


**Figure 17.11** Diurnal variations of vTEC maps estimated using $F_{10.7}$ as driver of NeQuick on 11 March 2011.

be due to equatorial **E**×**B** drift that usually has its maximum earlier than the vTEC [*Scherliess and Fejer*, 1999]. However, in between 1000 and 1500 UT, there is no clear equatorial ionization anomaly (EIA) indicating that the equatorial fountain effect is not strong enough to transport ionization from the magnetic equator regions to the North and South of the magnetic equator. But, in between 1600 and 2100 UT, the clear depletion of vTEC at geographic latitude of about 10° N and concentration of vTEC at around −2° and 20° N of geographic latitudes (see both Figures 17.9 and 17.10) indicate that the presence of prereversal strong **E**×**B** drift creating a clear EIA [*Fejer et al.*, 1991; *Heelis*, 2004; *Yizengaw et al.*, 2012]. The vTEC maps after adaptation (Figure 17.10) have shown almost identical features to UK vTEC maps (Figure 17.9). However, the corresponding vTEC maps before adaptation (Figure 17.11) have shown significant variations with the vTEC maps displayed in Figures 17.9 and 17.10.

The vTEC from the GPS station Nazr (see Figure 17.1) has been reserved only for verifying vTEC mapping methods. First, vTEC have been estimated at the location of this station using UK (vTEC_UK), NeQuick driven by Az (vTEC_Az), and NeQuick driven by daily solar flux (vTEC_$F_{10.7}$) for each hour. The driver Az has been estimated using UK at the location of Nazr for each hour. Comparing the diurnal variations of the modeled and experimental (vTEC_exp) vTEC values were used for the verification of the methods (see the left panel of Figure 17.12). The right panel of this figure shows the absolute difference between the modeled and experimental vTEC.

As can be seen in both panels of this figure, the experimental, interpolated, and NeQuick modeled (after adaption) vTEC values have shown excellent agreement. More interesting, the interpolated and NeQuick (after adaptation) modeled vTEC, unlike that of NeQuick (before adaption) modeled vTEC, mimics the presunset and postsunset patterns of experimental vTEC (see results between 0400 and 0800 UT and between 1700 and 2100 UT). This indicates that sTEC ingestion into NeQuick 2 corrects the problem of NeQuick 2 in estimating ionospheric slab thickness, which is mainly mentioned as the source of the discrepancy between experimental and modeled (without adaptation) vTEC [*Nigussie et al.*, 2013].

### 17.3.2. Nontomographic Map of Electron Density

In the previous section, it is shown that NeQuick driven by Az maps provide an excellent estimate of vTEC. NeQuick driven by Az map, in addition, provides an unprecedented advantage to estimate the time-dependent two- or three-dimensional electron density, which may not be easily obtained by other tomographic methods.

In order to estimate the vertical profile of the electron density, first we estimate the Az values across the

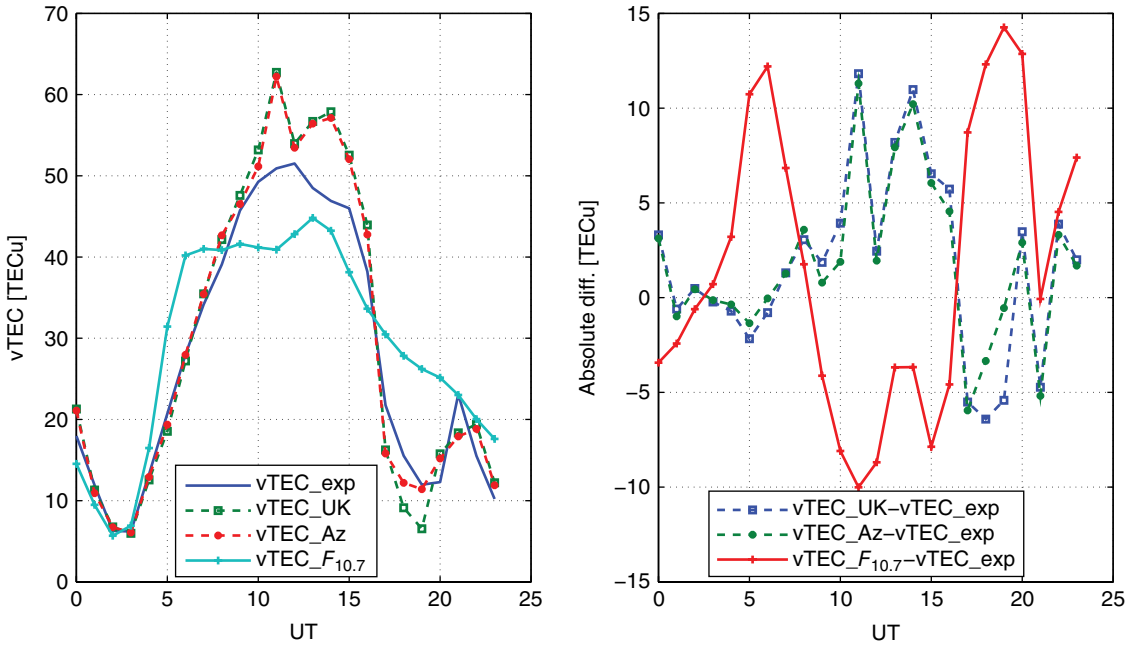


**Figure 17.12** Diurnal variations of experimental (vTEC_exp.), interpolated (vTEC_UK), NeQuick after adaptation (vTEC_Az), and before adaptation (vTEC_$F_{10.7}$) modeled vTEC (left panels) and the corresponding absolute difference between modeled and experimental vTEC (right).

geographic latitude of −10° to 30°N at any meridian. The Az values are estimated at each latitude and at 39°E meridian, i.e., used to drive the NeQuick model and generate vertical electron-density distribution at the same meridian. The top panels in Figure 17.13 show the density profiles at 39°E meridian generated at 1700 (top left) and 1800 (top right) UT. The corresponding electron-density distributions estimated without NeQuick adaptation are shown in the middle panels. As can be seen in the top panels, the equatorial ionization anomaly crests are symmetric with respect to the magnetic equator (which corresponds to about 9.04°N). However, the peak values at 1800 UT are greater and their locations are shifted slightly to higher latitudes, which may be due to the variation of the prereversal enhancement of the vertical drift velocity [*Fejer et al.*, 1991]. Such an anomaly peak magnitude difference and location shift are not shown in the middle panels. The bottom panels also show the experimental vTEC estimated at the geographic latitude of −10° to 30° N and longitudes of 37° to 41°E. The vertical axes in these panels are altitudes and their purpose is simply to handle the axes for visualizing vTEC against latitude.

These vTEC plots are displayed to show the advantage of the model adaptation to GPS measurements to drive the model for realistic electron-density estimation. For example, the vTEC around the crests at 1800 UT are greater in magnitude than the vTEC obtained around the crests at 1700 UT. Also, the trough vTEC values at 1800 UT are less than the trough vTEC values at 1700 UT. The reconstructed electron-density profiles at 1700 UT and 1800 UT have shown similar features to the vTEC obtained at these hours. The vTEC differences at these hours are not reflected in the electron-density distribution obtained by the model with $F_{10.7}$. The diurnal variations of the vertical electron-density distribution estimated in the same way as Figure 17.13 are displayed in Figures 17.14 and 17.15.

Evidently, in the presunset and postsunset hours (1600 to 2100 UT), symmetric and clear EIA anomalies are depicted unlike that of the results obtained between 1000 and 1500 UT. This indicates that the plasma fountain effect in between 1600 and 2100 UT is much stronger than the plasma fountain effect between 1000 and 1500 UT, which could be due to strong prereversal enhancement of $\mathbf{E}\times\mathbf{B}$. Panels in Figure 17.15 have shown the diurnal variations of vertical profile of electron-density distribution maps estimated at the same time and location as the results shown in Figure 17.14, but without adapting the model to the observations. In general, the results in Figures 17.14 and 17.15 have shown significant variations.

The other advantage of data-driven modeling is that it is useful to compute three-dimensional electron-density profiles by assimilating the data collected at nearby GPS receivers epoch by epoch. Figure 17.16 shows the three-dimensional electron-density maps estimated at 1700 UT. This plot shows the latitudinal, longitudinal, and

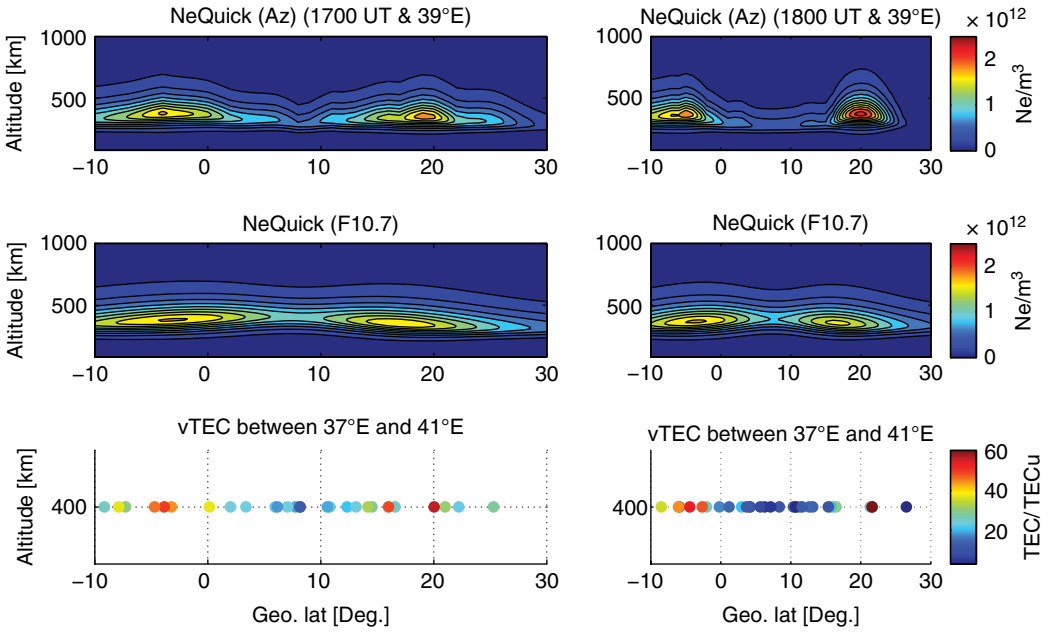


**Figure 17.13** Two-dimensional maps of electron density estimated at 1700 UT after and before adaptation (left top and left middle) and at 1800 UT after and before adaptation (right top and right middle) and the corresponding experimental vTEC between geographic longitudes of 37°E and 41°E (bottom panels).

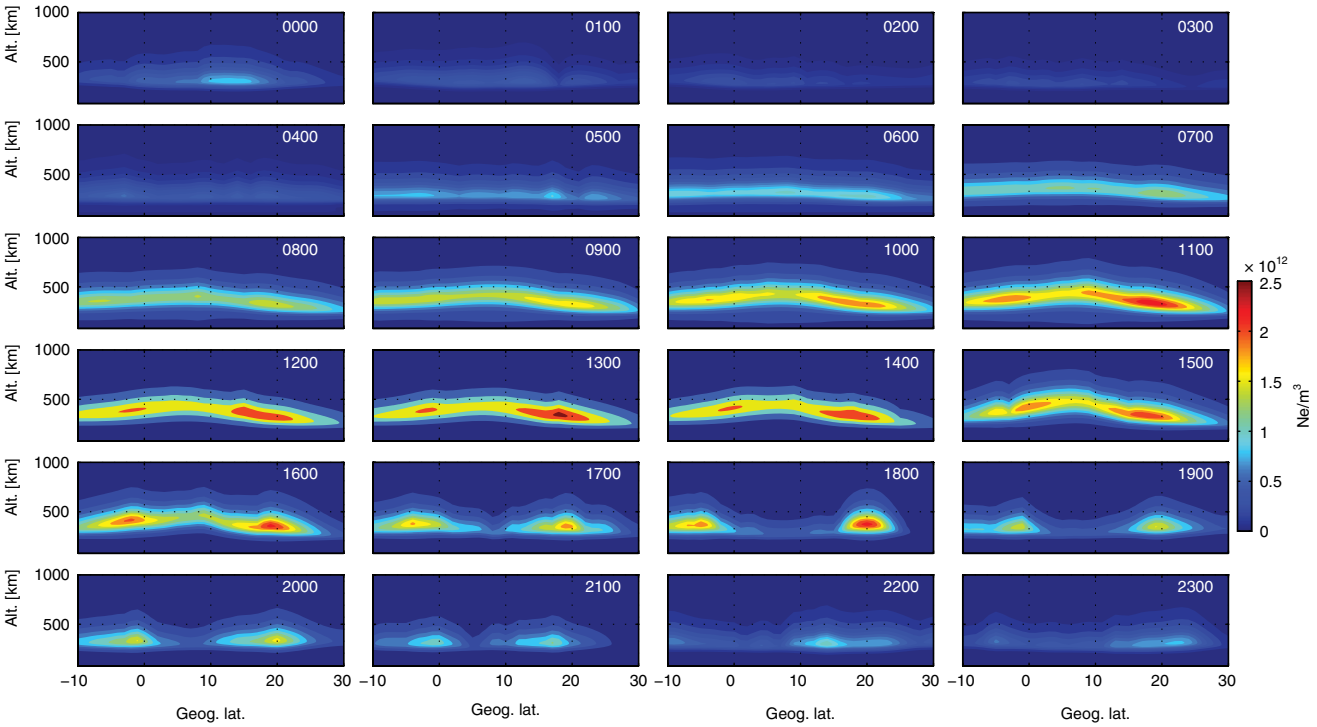


**Figure 17.14** Diurnal variations of the contour plot of electron density profile estimated using NeQuick driven by Az maps at 39°E on 11 March 2011.

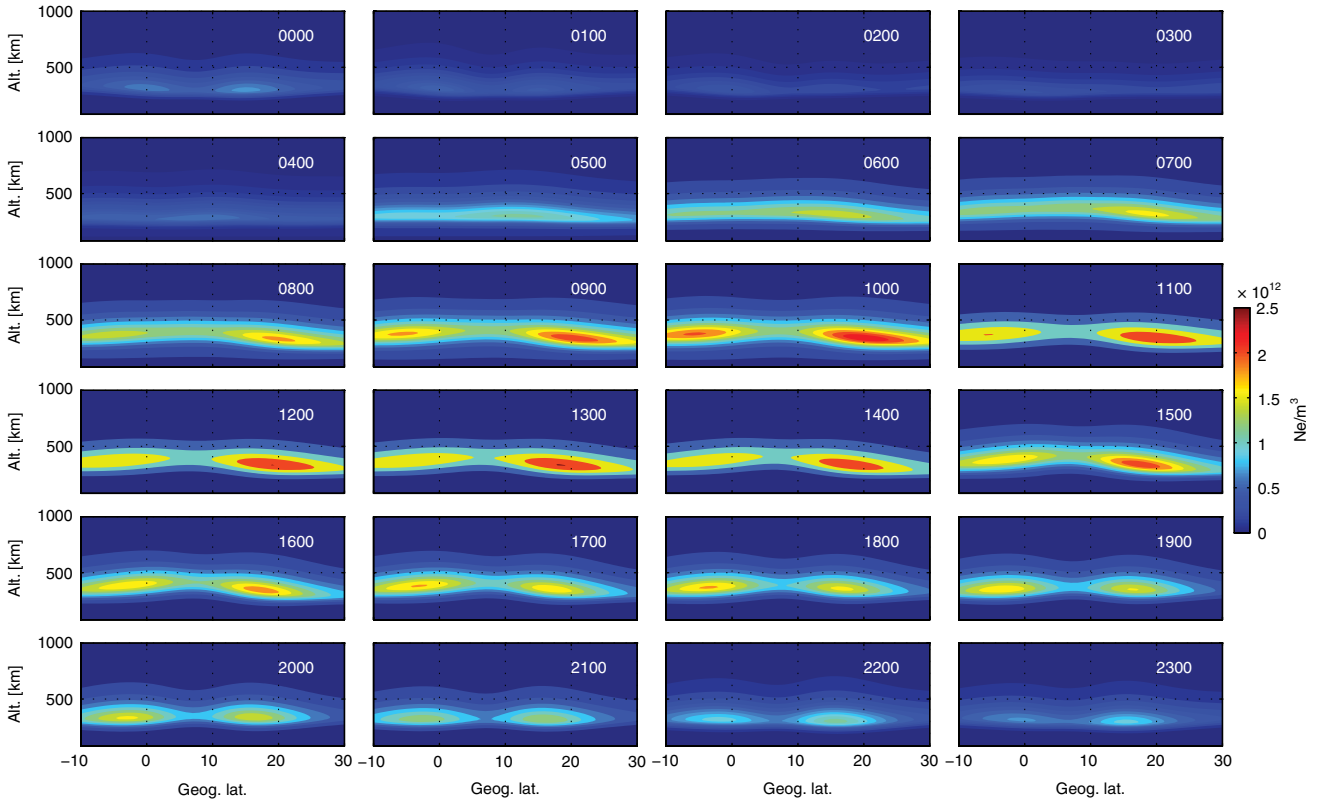


**Figure 17.15** Diurnal variations of the contour plot of electron density profile estimated using NeQuick driven by $F_{10.7}$ at 39°E on 11 March 2011.

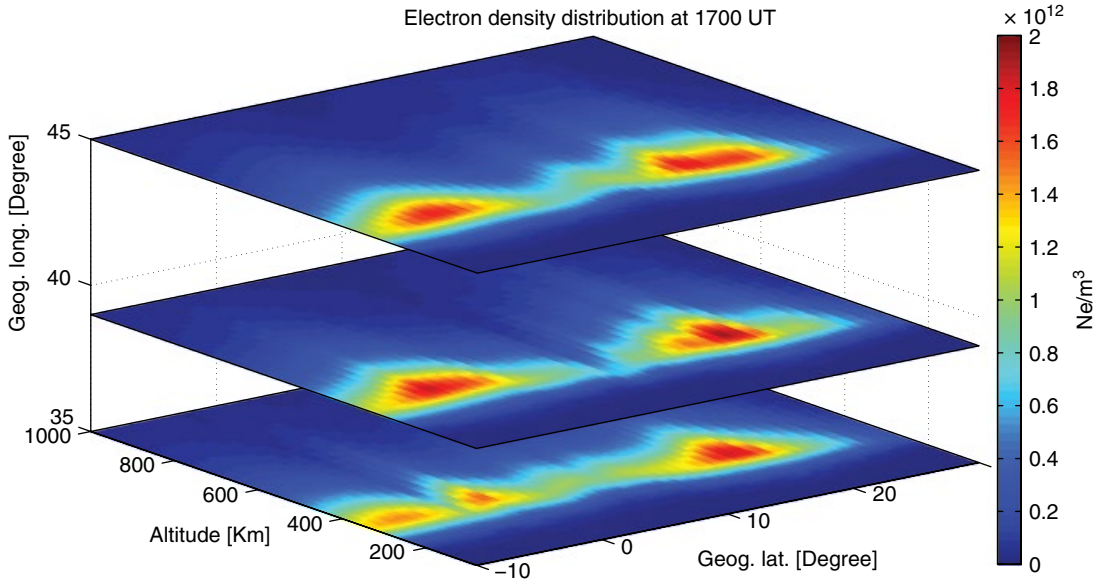


**Figure 17.16** Three-dimensional electron density maps estimated by nontomographic technique at 1700 UT on 11 March 2011.

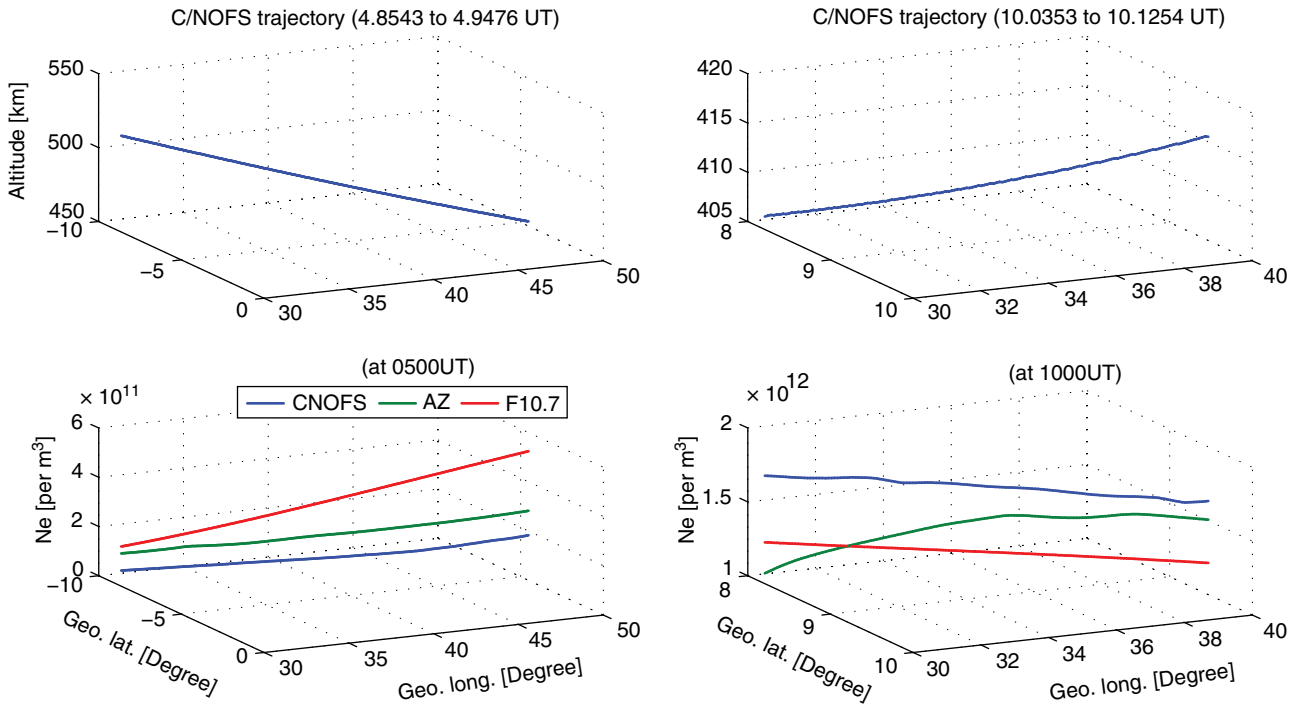


**Figure 17.17** Trajectories of C/NOFS satellite (top panels) and modeled (marked by Az and $F_{10.7}$) and experimental (C/NOFS) electron densities.

altitude variations of the electron density estimated after model adaptation. While Figure 17.16 shows clear latitudinal and altitude variability, no significant longitudinal variation is visible in the electron distribution, indicating the ionospheric density varies less as a function of longitude.

In order to validate the effectiveness of the nontomographically produced density maps, conjunction C/NOFS trajectories have been identified. Figure 17.17 (top panels) shows the trajectories of the C/NOFS satellite (top panels) at different local times. The corresponding experimental (from the Planar Langmuir Probe (PLP) instrument

on board C/NOFS) and modeled (before and after data adaptation) electron densities are shown in the bottom panels in Figure 17.17. As expected, the in situ density estimated after the model adaptation agrees very well with the C/NOFS observations, except when the satellite was around $F_2$-peak altitudes (~400 km) as shown in the right bottom panel in Figure 17.17. This discrepancy might be due to the slight time difference of the ionospheric information used for model adaptation (at 1000 UT) and obtained by the C/NOFS satellite (between 10.0353 and 10.1254 UT).

## 17.4. CONCLUSIONS

To understand the type of modeling approach that has been utilized to represent the true state of the East African ionosphere, investigations focused on developing time-dependent two- and three-dimensional electron-density maps and two-dimensional TEC maps. This has been done first by computing Az that minimizes the magnitude of the absolute difference between modeled (NeQuick 2) and experimental sTEC for each GPS ray path from 15 GPS receivers. This has been carried out simultaneously epoch-by-epoch. Az values at the locations where no GPS measurements are available were obtained using Universal Kriging interpolation algorithm. The maps of Az values have been developed using this algorithm for each hour. The Az maps in turn were then used to drive NeQuick to produce instantaneous maps of electron density and TEC for East African ionosphere. This mapping technique has been applied to estimate vTEC at the locations where there were no experimental vTEC. In addition, the interpolation technique has been applied to estimate the variance of Az, which allows the NeQuick model to produce the variance of TEC and electron-density estimates.

The vTEC maps have been for the first time assessed by comparing the diurnal variations of NeQuick (driven by interpolated Az and daily $F_{10.7}$) modeled with interpolated and experimental vTEC. Similarly, the electron-density estimation technique, which is known as nontomographic imaging, has been validated by comparing the model-estimated electron density with the in situ ion density observations taken by the C/NOFS satellite.

From the results we conclude the following points. In comparison to in situ ion density observation, nontomographic imaging provides a better electron density than the NeQuick model in its regular application (i.e., NeQuick driven by daily solar flux). Similarly, the vTEC from the nontomographic and interpolation techniques do agree better with experimental vTEC than the vTEC from the NeQuick model in its regular application. Moreover, the diurnal variations of vTEC values from the nontomographic and interpolated (through Universal Kriging interpolation techniques) are almost identical, indicating that the estimation of the Az as a driver of the NeQuick model is very useful and valuable to estimate the true state of the ionosphere.

The nontomographic imaging results show clearly the time and spatial evolution of the equatorial ionosphere features, for example, equatorial ionization anomaly. The monthly median ionospheric model, NeQuick driven by variance (standard deviation) of Az maps provides variance (standard deviation) of TEC (electron density), which indicates that the method applied leads the NeQuick climatological model to behave as a stochastic ionospheric model.

## ACKNOWLEDGMENTS

M. Nigussie is grateful to the Abdu Salam International Center for Theoretical Physics (ICTP), TWAS, Trieste, Italy, for its support and hospitality through the ICTP STEP program. In addition, M. Nigussie's work is supported by AFOSR grant (FA8655-13-1-3052). Also, the authors would like to thank the University of NAVSTAR Consortium (UNAVCO) and IGSSA for GPS data available.

## REFERENCES

Akala, A. O., G. K. Seemala, P. D. Doherty, C. E. Valladares, C. S. Carrano, J. Espinoza, and S. Olvyo (2013), Comparison of the equatorial GPS-TEC observations over an African station and an American station during the minimum and ascending phases of solar cycle 24, *Ann. Geophys.*, *31*, 2085–2096; doi:10.5194/angeo-31-2085-2013.

Amory-Mazaudier, C., S. Basu, O. Bock, A. Combrink, K. Groves, T. F. Rowell, P. Lassudrie-Duchesne, M. Petitdidier, and E. Yizengaw (2009), International Heliophysical Year: GPS Network in Africa, *Earth, Moon, Planet*, *104*, 263–270; doi:10.1007/s11038-008-9273-8.

Austen, J. R., S. J. Franke, and C. H. Liu (1988), Ionospheric imaging using computerized tomography, *Radio Sci.*, *23*, 299–307; doi:10.1029/RS023i003p00299.

Cressie, N. A. C. (2010), *Statistics for Spatial Data*, rev. ed. Wiley, New York, EUA, 1993.

Crujeiras, R. M., and I. V. Keilegom (2010), Least squares estimation of nonlinear spatial trends, *Computational Stat. Data Anal.*, *54*, 452–465; doi:10.1016/j.csda.2009.09.014.

Davies, K. (1990), *Ionosphere Radio*, Peter Peregrinus Ltd., London; doi:10.1049/PBEW031E.

Fejer, B. G., E. R. de Paula, S. A. González, and R. F. Woodman (1991), Average vertical and zonal F region plasma drifts over Jicamarca, *J. Geophy. Res.*, *96*(A8), 13, 901; doi:10.1029/91JA01171.

Haining, R. (1987), Trend-Surface models with regional and local scales of variation with an application to aerial survey data, *Technometrics*, *29*(4), 461–469; doi:10.2307/1269458.

Hartmann, G. K., and R. Leitinger (1984), Range errors to ionospheric and tropospheric effects for signal frequencies above 100MHz, *Bull. Géod.*, *58*, 109–136; doi:10.1007/BF02520897.

Heelis, R. A. (2004), Electrodynamics in the low and middle latitude ionosphere: A tutorial, *J. Atmos. Sol. Terr. Phys.*, *66*, 825–838; doi:10.1016/j.jastp.2004.01.034.

Hernàndez-Pajares, M., J. M. Juan, J. Sanz, and D. Bilitza (2002), Combining GPS measurements and IRI model values for space weather specification, *Adv. Space Res*. *29*(6), 949–958; doi:10.1016/S0273-1177(02)00051-0.

Hernàndez-Pajares, M., J. M. Juan, J. Sanz, R. Orús, A. Garcia-Rigo, J. Feltens, A. Komjathy, S. C. Schaer, and A. Krankowski (2010), The IGS VTEC maps: A reliable source of ionosphere information since 1998, *J. Geod*, *83*, 263–275; doi:10.1007/s00190-008-0266-1.

Hoque, M. M., and N. Jakowski (2013), Mitigation of ionospheric mapping function error, *Proceedings of the 26th International Technological Meeting of the Satellite Division of the Institute of Navigation* (ION GNSS+2013), Nashville, TN, 1848–1855, September.

Jakowski, N., C. Mayer, M. M. Hoque, and V. Wilken (2011), Total electron content models and their use in ionosphere monitoring, *Radio Sci*., *46*, RS0D18; dio:10.1029/2010RS004620.

Jones, W. B., and R. M. Gallet (1962), The representation of diurnal and geographical ionospheric data by numerical methods, *Telecommun. J.*, *29*, 129–149.

Kersely, L. (2005), Ionospheric tomography and its applications in radio science and geographical investigations, *Ann. Geophys.*, *48*, 3; doi:10.4401/ag-3218.

Komjathy, A., R. B. Langley, and D. Bilitza(1998), Ingesting GPS-derived TEC data into the International Reference Ionosphere for single frequency radar altimeter ionosphere delay corrections, *Adv. Space Res.*, *22*, 793–801; doi:10.1016/S0273-1177(98)00100-8.

Lee, J. Y., J. S. Woo, and S. W. Rhee (1998), A transformed quantile-quantile plot for normal and binormal distributions, *J. Info. Optimiza. Sci.*, *19*, 3.

Ligas, M., and P. Banasik (2012), Local height transformation through polynomial regression, *Geodesy and Cartography*, *61*, 1, 3–17; doi:10.2478/v10277-012-0018-5.

Lloyd, C. D. (2011), *Local Models for Spatial Analysis*, 2nd ed., Taylor and Francis Group, LLC.

Memarzadeh, Y. (2009), Ionospheric modeling for precise GNSS applications, PhD thesis.

Nava, B., P. Coïsson, and S. M. Radicella (2008), A new version of the NeQuick ionosphere electron density model, *J. Atmos. Sol. Terr. Phys.*, *70*, 1856–1862; doi:10.1016/j.jastp.2008.01.015.

Nava, B., S. M. Radicella, R. Leitinger, and P. Coïsson (2006), A near-real-time model assisted ionospheric electron density retrieval method, *Radio Sci*., *41*, RS6S16; dio:10.1029/2005RS003386.

Nigussie, M., S. M. Radicella, B. Damtie, B. Nava, E. Yizengaw, and K. Groves (2013), Validation of the NeQuick 2 and IRI-2007 models in East-African equatorial ionosphere, *J. Atmos. Sol. Terr. Phys. 102*, 26–33; doi:10.1016/j.jastp.2013.04.016.

Nigussie, M., S. M. Radicella, B. Damtie, B. Nava, E. Yizengaw, and L. Ciraolo (2012), TEC ingestion into NeQuick 2 to model the East African equatorial ionosphere *Radio Sci*., *47*, RS5002; doi:10.1029/2012RS004981.

Pardo-Igúzquiza, E. (1999), VARFIT: A fortran-77 program for fitting variogram models by weighted least squares, *Comput. Geosci.*, *25*, 251–261; doi:10.1016/S0098-3004(98)00128-9.

Orús, R., M. Hernández-Pajares, J. M. Juan, and J. Sanz (2005), Improvement of global ionosphere vTEC maps by using kringing interpolation technique, *J. Atmos. Sol. Terr. Phys.*, *67*, 1598–1609; doi:10.1016/j.jastp.2005.07.017.

Scherliess, L., and B. G. Fejer (1999), Radar and satellite global equatorial F region vertical drift model, *J. Geophys. Res. 104*(A4), 6829–6842; doi:10.1029/1999JA900025.

Sparks, L., A. Komjathy, and A. J. Mannucci (2004), Estimating SABAS ionospheric delays without Grides: The conical domain approach, *Proceedings of the 2004 National Technology Meeting of the Institute of Navigation*, San Diego, CA, 530–541, January.

Sparks, L., J. Blanch, and N. Pandya (2011), Estimating ionospheric delay using Kriging: Impact on satellite-based augmentation system availability, *Radio Sci*., *46*, RS0D22; doi:10.1029/2011RS004781.

Yizengaw, E., and M. B. Moldwin (2008), African Medidian B-Filed Education and Research (AMBER) Array, *Earth Moon Planet*; doi:10.1007/s11038-008-9287-2.

Yizengaw, E., E. Zesta, M. B. Moldwin, B. Damtie, A. Mebrahtu, C. E. Valadares, and R. F. Pfaff (2012), Longitudinal differences of the ionospheric vertical density distribution and equatorial electrodynamics, *J. Geophys. Res.*, *117*, A07312; doi:10.1029/2011JA017454.

Zhang, X. F., J. C. H. Van Eijkeren, and A. W. Heemink (1995), On the weighted least squares method for fitting a semi-variogram model, *Comput. Geosci. 21*, 4, 605–608; doi:10.1016/0098-3004(94)00099-G.

# Part V
# Response of the Thermosphere and Ionosphere to Variability in Solar Radiation

# 18

# Ionospheric Response to X-Ray and EUV Flux Changes During Solar Flares: A Review

**Ludger Scherliess**

## ABSTRACT

Solar extreme ultraviolet (EUV) radiation heats the Earth's dayside upper atmosphere and ionizes the neutral gas to create the ionosphere. Consequently, during solar flares, when in a matter of minutes the relative changes in the emissions of X-ray and EUV radiation can become greatly enhanced, the Earth's atmosphere and ionosphere can be strongly affected. However, different components of the solar irradiance spectrum affect the ionospheric layers differently and the ionospheric response depends strongly on the specific spectrum of the flare. Enhancements in the X-rays penetrate to lower heights to ionize the *D* and *E* regions while enhancements in the EUV more strongly affect the ionospheric *F* region. Over the past decade, the availability of Global Positioning System/Total Electron Content (GPS/TEC) observations in concert with new and improved irradiance observations and proxy models have lead to a renaissance in studies to evaluate the solar irradiance variability as a driver of ionospheric variability during solar flares. These studies have investigated the complex altitude dependence of the response of the ionosphere to the detailed characteristics of solar flares and have established the need for high spectral and temporal resolution irradiance observations to understand the ionospheric variability observed during solar flares. This chapter will provide a brief review of the current understanding of the complex ionospheric response to solar flares.

**Key Points:**
Solar flares lead to a complex altitude dependence of the response of the ionosphere.
High spectral and temporal resolution irradiance observations are needed to understand the ionospheric response to flares.

**Key Terms:** solar flares, solar extreme ultraviolet radiation, solar X-ray radiation, ionosphere, total electron content, space weather

## 18.1. INTRODUCTION

Solar vacuum ultraviolet (VUV; 0.1–200 nm) radiation is the major source of energy input into the Earth's thermosphere and ionosphere, and heats, excites, dissociates, and ionizes the neutral constituents in the Earth's upper atmosphere. Photons with wavelength above about 90 nm generally cause dissociation, while shorter wavelength photons cause ionization with the exact distribution depending on the relevant cross sections and atmospheric species [*Schunk and Nagy*, 2009].

Changes in the solar radiation can greatly affect the Earth's atmosphere and ionosphere. The most rapid

*Center for Atmospheric and Space Sciences, Utah State University, Logan, Utah, USA*

*Ionospheric Space Weather: Longitude and Hemispheric Dependences and Lower Atmosphere Forcing, Geophysical Monograph 220*, First Edition. Edited by Timothy Fuller-Rowell, Endawoke Yizengaw, Patricia H. Doherty, and Sunanda Basu.

variations in the Sun's ionizing radiation occur during times of solar flares when the relative changes in the solar irradiance for some wavelengths can exceed those of the solar cycle variation in a matter of minutes [*Chamberlin et al.*, 2008]. Solar flares predominantly take place in active regions of the Sun as they are rapidly growing and changing complexity resulting in sudden energy releases over a wide range of the electromagnetic spectrum.

Solar flares are typically classified as A-, B-, C-, M-, X-, and Z-class flares based on the magnitude of their peak intensity in the 0.1–0.8 nm band, as observed by the X-ray instrument on board the Geostationary Environmental Operational Satellite [GOES; *Davies*, 1990]. A solar flare can also be classified as an optical flare based on the sudden brightening of the H-alpha line (656.28 nm) in an active region. The optical flares are classified based on the area of maximum brightness (0 to 4) and its brightness (faint "F," normal "N," and bright "B") [*Davies*, 1990]. Furthermore, observations of two EUV bands, namely, 0.1–50 nm and 26–34 nm obtained from the solar EUV monitor (SEM) onboard the Solar Heliospheric Observatory (SOHO) are often used to further specify the characteristics of a solar flare and its effect on the ionosphere.

Large flares significantly increase the solar output in the X-ray, UV, and radio range, but variations in the infrared and visible spectrum is less than 0.01% [*Foukal*, 2004]. The larger flares can cause the solar irradiance to increase by three to four orders of magnitude in the X-ray range (0.1–10 nm), by up to 10-fold in the extreme ultraviolet (EUV; 10–120 nm) and the far ultraviolet (FUV; 122–200 nm) ranges, and by about 20% for Lyman-alpha (121.6 nm) [*Woods et al.*, 2004, 2006]. To date, the physical mechanisms that generate these spectral differences are still under investigation.

For the ionosphere, changes in the solar irradiance in the XUV [0.1–10 nm] and EUV [10–120 nm] ranges are of particular importance since these wavelengths not only deposit their energy in the Earth's thermosphere but also ionize the neutrals in the sunlit hemisphere causing a significant ionization of the *D*, *E*, and *F* regions of the Earth's ionosphere at short intervals of time. While X-rays penetrate deep into the ionosphere and could cause enhanced *D*-region ionization during solar flares, EUV flux enhances the ionization in the *E* and *F* regions of the ionosphere. One of the main peculiarities of the ionospheric response to solar flares is that the maximum relative increase in the electron density concentration typically occurs in the *D* region (by an order of magnitude and more), while in the *E* and *F* regions the increase ranges from 50% to 200% and from 10% to 30%, respectively. The increased ionization in the various ionospheric regions can result in sudden increases of total electron content (SITEC), changes in the altitude dependent plasma composition and density, increases in the electron and ion temperatures, changes in the field-aligned and the cross-**B** (**E** × **B**) motion of the plasma, as well as changes in the ionospheric current system.

Over the past decades, the rapid increase of the electron density during solar flares has been extensively studied and its effects have been reviewed by *Mitra* [1974] and *Davies* [1990]. Initial studies were based on ground-based observations and focused on the increased ionization in the *D* region, associated with enhanced X-ray radiation with wavelengths below 1.0 nm. These increases of the electron density enhancements were identified as sudden radio signal fadeouts, sudden *D*-region absorption, and geomagnetic solar flare effects (SFEs) also often known as geomagnetic crochets [*Dodson and Hedeman*, 1958; *Donnelly*, 1971; *Mitra*, 1974; *Davies*, 1990].

In the upper ionosphere, the effects of solar flares on the ionization have been observed by ground-based observations as an increase in the critical frequency in the $F_2$ region by ionosondes [e.g., *Dieminger and Geisweid*, 1950; *Knecht and Davies*, 1961], as an increase in electron density in the *E* and $F_1$ regions by incoherent scatter radars (ISR) [e.g., *Thome and Wagner*, 1971; *Mendillo and Evans*, 1974], and by sudden frequency variations (SFD) associated with a sudden change in the frequency of a high-frequency (HF) wave that propagates through the ionosphere [e.g., *Davies*, 1962; *Baker and Davies*, 1966; *Davies and Donnelly*, 1966]. The first two ground-based techniques, ionosonde and ISR, are, however, limited in their time resolution making it difficult to capture the temporal evolution of the ionospheric response to solar flares while the third technique only provides limited information about the location and altitude structure of the ionospheric response.

With the arrival of space-based observations, and in particular the availability of total electron content (TEC) observations, it became possible to investigate the detailed temporal and spatial effects of solar flares on the ionosphere. The first study to identify a sudden increase in TEC was reported by *Garriott et al.* [1967] using observations of the plane of polarization of VHF signals received from the geostationary ATS-1 satellite. *Mendillo et al.* [1974] used TEC observations obtained from Faraday rotation measurements made at 17 stations in North America, Europe, and Africa during the large solar flare that occurred on 7 August 1972. The observations spanned more than 10 hr and covered more than 70° in latitude, which provided the first global morphology of the effects of solar flares on the ionosphere. They reported increases in TEC that ranged from 15 to about 30% with the larger increases occurring at the lower latitudes. *Mendillo et al.* [1974], however, did not find any significant correlation between the changes observed in TEC and the solar zenith angle.

More recently, the use of Global Navigation Satellite System (GNSS) ground-based TEC observations have resulted in a "renaissance" [*Tsurutani et al.*, 2009] of studies of the effects of solar flares on the ionosphere. Currently, thousands of GNSS ground receivers can be

used to observe the ionosphere with high temporal (~30 seconds) and high spatial resolution.

*Afraimovich* [2000] and *Afraimovich et al.* [2000, 2001] used GPS/TEC observations to detect the global response of the ionosphere to solar flares. They presented the first GPS measurements of the global response of the ionosphere to the powerful 29 July 1999 and 28 December 1999 solar flares. They found that fluctuations of TEC, obtained by removing the linear trend of TEC with a time window of about 5 min, are coherent for all stations on the dayside of the Earth. *Afraimovich et al.* [2002] extended their earlier studies to investigate the ionosphere response to faint C-class solar flares. In order to extract the ionospheric response for these small solar flares, they coherently processed the TEC variations over the entire sunlit ionosphere. This technique was later also used by *Yasyukevich et al.* [2013] to analyze TEC variation for small C- and M-class solar flares that occurred in February 2010.

*Wan et al.* [2005] investigated the correlation between the observed SITEC and the observation locations based on the GPS/TEC data obtained for the large X5 solar flare, which occurred on 14 July 2000. They reported a decrease in the TEC enhancement as well as a decrease in the rate of change of TEC with increasing solar zenith angle. *Liu et al.* [2004] used TEC and its time rate of change (rTEC) derived from the worldwide network of ground-based GPS receivers and found that the ionospheric effects following the solar flare of 14 July 2000 could be observed from predawn to postdusk with the most pronounced effects occurring in the middle of the day. *Zhang and Xiao* [2005] used TEC from 114 GPS ground stations to analyze the morphological features of the TEC changes in the sunlit hemisphere during the 28 October 2003 flare and also reported a dependence of the magnitude of SITEC on the local solar zenith angle (SZA) in the Northern Hemisphere in contrast to *Mendillo et al.* [1974], who reported no relationship between SZA and an increase in TEC.

A new technique to estimate the contributions from different ionospheric regions to the response of TEC variations was presented by *Leonovich et al.* [2002] using ground-based GPS/TEC observations obtained during the powerful flare of class X5.7/3B on 14 July 2000. Using the effect of partial shadowing, they estimated that about 75% of the observed TEC increase corresponded to an electron-density increase in the ionospheric region below 300 km and about 25% to regions above 300 km, consistent with the findings of *Mendillo and Evans* [1974] and *Mendillo et al.* [1974] who reported that about 40% of the TEC increase during the powerful 7 August 1972 flare occurred at altitudes above 300 km but in contrast to the results of *Thome and Wagner* [1971].

*Tsurutani et al.* [2005] used approximately 100 ground-based GPS receivers to obtain high time resolution (~30 sec) and high spatial resolution global changes in the dayside TEC for the 2003 Halloween and the 14 July 2000 Bastille Day solar flare events. They reported a dramatic response of the dayside ionosphere for the 28 October 2003 flare with an increase of the order of 25 TECU and an approximately 2.5 min rise time. The TEC response for the 28 October 2003 flare was found to be significantly larger than the TEC increase of only about 5–7 TECU during the much more intense 4 November 2003 X-ray flare. They explained that part of this observed difference could be due to the fact that the 4 November flare occurred near the limb of the Sun and that the EUV emissions generated in the lower corona may have been absorbed by the solar atmosphere.

This limb effect invited significant attraction and was further investigated by *Leonovich et al.* [2010] who studied the response of TEC to flare distance from the central solar meridian and found a decrease in the TEC response with increasing distance. *Mahajan et al.* [2010] used 10 X-class flares that occurred during the maximum phase of solar cycle 23 to investigate the correlation between the peak intensities in the X-ray and the EUV fluxes and found that they are generally only poorly correlated, but vastly improve when the central meridian distance (CMD) of the flare location was taken into account. They also reported that the midday peak TEC enhancement is highly correlated with the peak enhancement in the EUV flux. *Liu et al.* [2006] examined the ionospheric effect of 11 solar flares by using TEC and rTEC derived from ground-based GPS receivers in the midday regions and compared these with the 0.1–0.8 nm X-ray flux as well as its time rate of change (rX-ray). After correcting the rX-ray for the location of active region on the solar disc, that is, the central meridian distance (CMD), they found reasonably good correlation between the CMD modified X-ray flux and SITEC and pointed out that the solar disc location of the flare has a significant effect on the ionospheric response. *Zhang et al.* [2011] used observations of TEC changes over the subsolar region for all X-class flares that occurred from 1998 to 2006 to statistically analyze their correlation with observations of the peak X-ray and EUV fluxes as well as the flare location on the solar disc. They found a generally poor correlation between ionospheric TEC enhancement and the soft X-ray peak flux in the 0.1–0.8 nm region, but a noticeable dependence on the flare location on the solar disc. Their study indicated that for the same X-ray class, the flares near the solar disc center have much larger effects on the ionospheric TEC than those near the solar limb region. For the EUV band, they reported that although TEC enhancements and EUV flux increases in both the 0.1–50 and 26–34 nm regions have a positive relation, the flux increase in the 26–34 nm region during flares is more correlated with the TEC enhancements.

The improved observation capabilities provided by the GNSS networks as well as the availability of new and improved observations of the solar irradiances [e.g., *Woods et al.*, 2005, 2012] and their empirical representation during flares [e.g., *Warren et al.*, 2001; *Chamberlin et al.*, 2008]

have also spurred an extensive modeling efforts over the past decade to better understand the many aspects of the ionospheric response to solar flare [e.g., *Meier et al.*, 2002; *Huba et al.*, 2005; *Smithtro et al.*, 2006; *Le et al.*, 2007; *Smithtro and Solomon*, 2008; *Leonovich et al.*, 2010; *Qian et al.*, 2010, 2011, 2012; *Sojka et al.*, 2013].

*Meier et al.* [2002] estimated the EUV spectral irradiance enhancement for the Bastille Day flare using a new techniques developed by *Warren et al.* [1998, 2001] and modeled the ionospheric response associated with the flare using the two-dimensional SAMI2 ionospheric model [*Huba et al.*, 2000]. Their study was extended by *Huba et al.* [2005], who presented the first global simulation study of the ionospheric effects due to the enhanced EUV irradiance during the Bastille Day flare.

A one-dimensional ionosphere model was used by *Le et al.* [2007] to investigate the seasonal and local time dependence of the ionospheric response to an X-class flare. In their study, the SOHO/SEM 26–34 nm observations with a time resolution of 15 s and the GOES X-ray (0.1–0.8 nm) data with 1 min resolution for the 28 October 2003 flare were used to scale the empirical HEUVAC model. Simulations were performed for spring, summer, autumn, and winter conditions and for different local times. They found, for this particular flare spectrum, that during the daytime most of the relative increases in electron density occur at an altitude lower than 300 km, with a peak at about 115 km, whereas around sunrise and sunset, the strongest ionospheric responses occur at much higher altitudes (e.g., 210 km for a summer flare).

*Smithtro et al.* [2006] observed an anomalous reduction in peak density $N_mF_2$ in the $F_2$ region during flares and were able to explain the observed reduction in $N_mF_2$ in terms of a thermal expansion and an upward diffusion of the plasma to the topside caused by enhanced electron temperatures that resulted from the heating by fast photoelectrons produced in the $F_1$ region.

*Sojka et al.* [2013] further investigated the altitude response of the ionosphere to solar flares with an emphasize on the details of the solar spectrum and noted that the specific time evolution of the electron-density response depends not only on the ionosphere but also on the specific spectrum of the flare irradiance.

*Qian et al.* [2010] revisited the limb effect and modeled the thermosphere and ionosphere response by assuming two X17 flares that were identical except that one occurs near disc center and the other near the limb. For their study, solar irradiances were obtained from the flare irradiance spectral model (FISM) as input to the National Center for Atmospheric Research (NCAR) thermosphere-ionosphere-mesosphere electrodynamics general circulation model (TIME-GCM).

Their simulations showed that in the *E*-region ionosphere, where XUV dominates ionization, flare location does not affect the ionosphere/thermosphere (I/T) response. However, flare-driven changes in the *F*-region ionosphere, TEC, and neutral density in the upper thermosphere are two to three times stronger for a disc-center flare than for a limb flare, due to the importance of EUV enhancement.

*Qian et al.* [2011] evaluated the effect of different rise and decay rates of solar flares using again FISM and the NCAR TIME-GCM model and reported that for idealized flares with the same magnitude and location on the solar disc the thermosphere and ionosphere response changed significantly as a function of the rise and decay rates. The differences were explained as a result of the "Neupert Effect," which predicts that a faster flare rise rate leads to a larger EUV enhancement during the impulsive phase and consequently a larger maximum ion production enhancement. In addition, their simulations showed that increased $\mathbf{E}\times\mathbf{B}$ plasma transport due to conductivity increases during the flares caused a significant equatorial anomaly feature in the electron-density enhancement in the *F* region but a relatively weaker equatorial anomaly feature in TEC enhancement, owing to dominant contributions by photochemical production and loss processes. The effects of solar flares on the ionospheric electrodynamics was further investigated by *Qian et al.* [2012], who found that the vertical $\mathbf{E}\times\mathbf{B}$ plasma transport near the magnetic equator plays a significant role in the response of the ionosphere to solar flares.

In the following, a brief overview of the general principles of the upper-atmosphere ionization due to solar radiation is presented followed by an overview of solar-irradiance observations and their empirical representations. This is followed by an overview of more recent studies of the effects of solar flares on the ionosphere with a particular emphasis on the large flares that occurred during solar cycle 23 followed by a brief review of recent investigations of the altitude response of the ionosphere to solar flares.

## 18.2. VUV IONIZATION

The major source of atmospheric ionization is solar EUV and X-ray radiation, which ionizes the thermosphere in different altitude regions [e.g., *Schunk and Nagy*, 2009]. Over most of the globe, the daytime *E* and $F_1$ regions is produced by solar soft X-ray ultraviolet (XUV) radiation with a wavelength of about 1–30 nm. These photons ionize $O_2$, $N_2$, O, and to a lesser degree NO. In addition, photoelectrons produced by this radiation have enough energy to create secondary ionization. Photons with wavelength between 90–103 nm are an additional source that ionizes $O_2$ in the *E* region. However, the photoelectrons produced by these longer wavelength photons are not energetic enough to create secondary ionization. In the *F* region, EUV emissions in the range from about 10–90 nm are effective to ionize atomic oxygen, which constitutes the main source of ionization in this altitude range.

Figure 18.1, taken from *Heroux et al.* [1974], shows an example of the altitude dependence of the total production rates of $O^+$, $O_2^+$, and $N_2^+$ produced by several wavelength regions of the solar EUV spectrum from about 5 to 103 nm. The total production rates, which are a product of the solar spectrum, the wavelength-dependent atmospheric absorption, and the ionization cross sections, were calculated by using the EUV intensities observed on 23 August 1972 and correspond to a solar zenith angle of 27°. Clearly seen in Figure 18.1 is the strong altitude dependence of the ion production rate for the different wavelength bands. In the *D* region, at altitudes below about 90 km, solar Lyman-alpha (121.6 nm) and cosmic rays are a steady source of ionizing NO. Solar X-rays are not a principle source of ionization below an altitude of about 90 km during quiet solar conditions. However, during solar flares, ionization due to solar X-rays gives rise to an ionization enhancement in the *D* region that can exceed that of solar Lyman-alpha. As a result of this solar flare effect, the fadeout of radio waves can occur due to the enhanced attenuation.

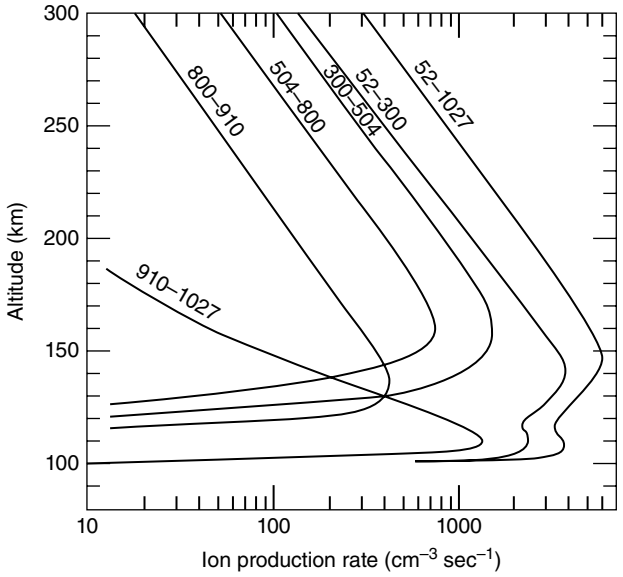


**Figure 18.1** Total production rates of $O^+$, $O_2^+$, and $N_2^+$ produced by several wavelength regions of the solar EUV spectrum. The rates were calculated using the solar EUV intensities of 23 August 1972 and solar zenith angle of 27° [from *Heroux et al.*, 1974].

### 18.2.1. VUV Observations and Proxy Models

Observations of the solar irradiance in the XUV range requires space-based measurements due to the atmospheric absorption of these wavelengths, which eliminates the ability for ground-based observations. Consequently, the first observations of the VUV irradiance became possible when the first VUV spectrum from a sounding rocket was obtained in 1946 [*Baum et al.*, 1946]. Since then, both rocket- and satellite-based instruments have sporadically observed different parts of the X-ray ultraviolet, the extreme ultraviolet, and the far ultraviolet regions.

Figure 18.2 shows a survey of the time/wavelength coverage of solar irradiance measurements on board satellites [*Schmidtke et al.*, 2006]. Starting with Atmospheric Explorer C, the satellite missions provided good temporal coverage in the 100–200 nm spectral region. Below about 100 nm, however, substantial gaps, marked a "EUV holes," can be seen until about the end of the century. The Solar EUV Experiment [SEE; *Woods et al.*, 2005] on the Thermosphere Ionosphere Mesosphere Energetics and

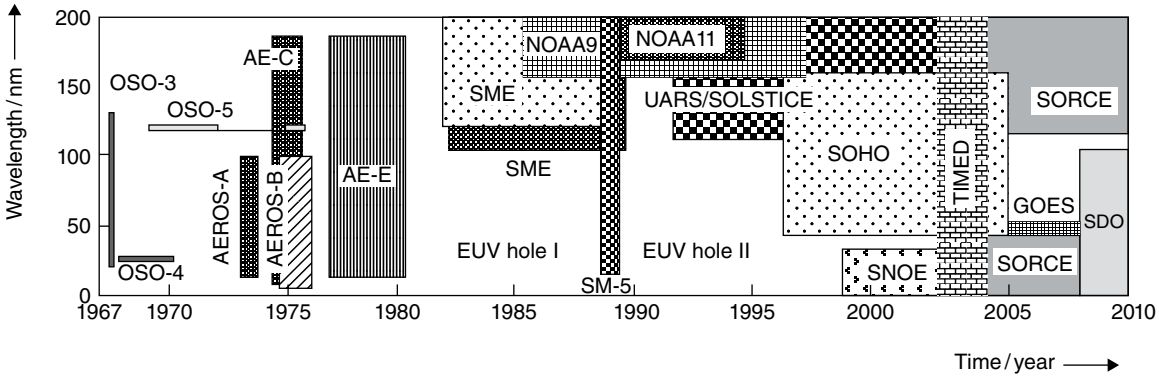


**Figure 18.2** Time/wavelength coverage of solar flux measurements from satellites: OSO, Orbiting Solar Observatory; AEROS, aeronomy satellite; AE, atmospheric explorer; SME, solar mesospheric explorer; NOAA, National Oceanic and Atmospheric Administration; satellites, SM, San Marco satellite; UARS, upper atmospheric research satellite; SOHO, Solar and Heliospheric Observatory; SNOE, students nitric oxide explorer; TIMED, thermospheric-ionospheric-mesospheric energetics and dynamics; SORCE, solar radiation and climate experiment; GOES, geostationary satellite server; SDO, Solar Dynamics Observatory [from *Schmidtke et al.*, 2006].

Dynamics (TIMED) satellite is the first instrument since the Atmospheric Explorer-E (AE-E) satellite measurements in the late 1970s [*Hinteregger et al.*, 1981] to make subdaily solar irradiance measurements over the full EUV range from 0.1 to 195 nm, but with only broadbands below 27 nm. However, during each 97 min orbit, the SEE instrument observes the solar spectrum for roughly only a 3 min interval [*Woods et al.*, 2003] making the instrument not ideally suited for solar-flare observations. Note that SEE nevertheless was able to capture a number of solar flares [*Woods et al.*, 2003]. The Solar and Heliospheric Observatory (SOHO) Solar Extreme Ultraviolet Monitor (SEM) instrument measures the 26–34 nm and the 0.1–50 nm irradiances with a time cadence of 1 min [*Judge et al.*, 1998] and has provided nearly continuous observations since its launch in 1998. The SOHO Coronal Diagnostic Spectrometer (CDS) instrument measures the solar EUV irradiance with a time cadence of only about once per month [*Thompson and Brekke*, 2000]. The first recent XUV measurements were done with the Solar X-ray Photometer (SXP) on the Student Nitric Oxide Explorer (SNOE) from 1997 until 2003 [*Bailey et al.*, 1999, 2000]. Subsequent measurement of the XUV have been, and continue to be, made from two versions of the XUV Photometer System (XPS), one on the TIMED satellite [*Woods et al.*, 2005] and another on SORCE. The SOHO SEM also contains XUV measurements in its broadband central channel from 0.1 to 50 nm, but this channel is dominated by wavelengths from the EUV.

The Extreme ultraviolet Variability Experiment [EVE; *Woods et al.*, 2012] on board the NASA Solar Dynamics Observatory (SDO) observes the solar EUV irradiance from 0.1 to 105 nm with unprecedented spectral resolution (0.1 nm), temporal cadence (10 s), and accuracy (20%). The instrument provides improvements of up to 70% in spectral resolution measurements in the wavelengths below 30 nm, and a 30% improvement in "time cadence" by taking measurements every 10 s over a 100% duty cycle [*Woods et al.*, 2012]. SDO EVE was launched on 11 February 2010 and includes several irradiance instruments, including the Multiple EUV Grating Spectrographs (MEGS)-A that measures the solar EUV irradiance in the 5–37 nm range with 0.1 nm resolution, and the MEGS-B that measures the solar EUV irradiance in the 35–105 nm range also with 0.1 nm resolution. SDO EVE also includes the EUV SpectroPhotometer (ESP), which measures the solar XUV irradiance in broadbands between 0.1 and 39 nm, and a Photometer, which measures the Sun's bright hydrogen emission at 121.6 nm. An example EVE spectrum from the peak of the X1.7 flare that occurred on 27 January 2012 between approximately 17 and 22 UT is shown in Figure 18.3 [*Warren et al.*, 2013]. Shown is the spectrum obtained from the MEGS-A and both the observed and preflare subtracted spectra are shown. The flare occurred on the northwest limb of the Sun and was associated with sunspot 1402. Clearly seen in the observations are the strong enhancements in the irradiance between about 9 and 15 nm while other parts of the spectrum remain only slightly changed or unchanged.

While these instruments have provided many solar EUV measurements over the past 50 years, there are still large data gaps in the observations, and large uncertainties in some of these existing data [*Schmidtke et al.*, 2006]. Despite the few current and historical measurements of the solar VUV irradiance, several challenges remain to fully understand the VUV irradiance from only having broadband measurements in the 0–5 nm range and historically many data gaps, both in wavelength coverage and in time coverage. In an effort to overcome these shortcomings,

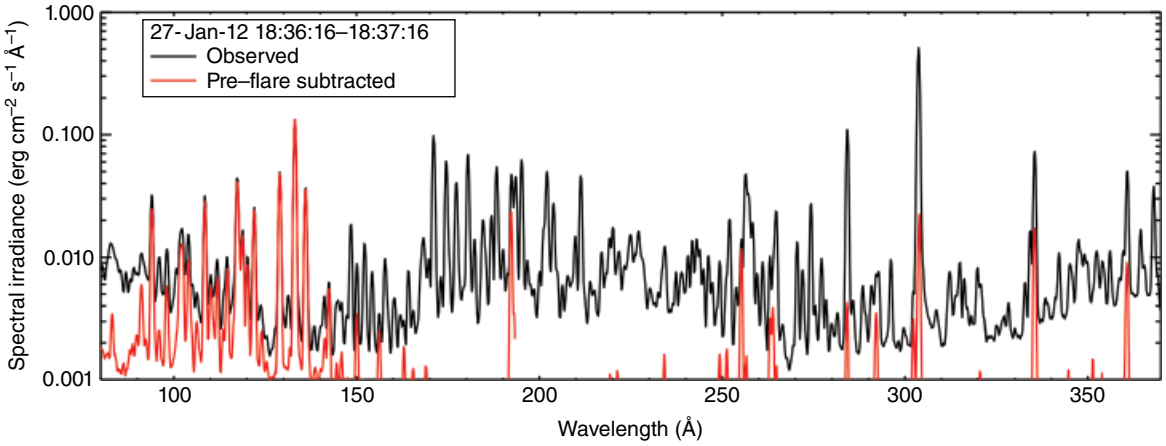


**Figure 18.3** EVE MEGS_A observations of the solar spectral irradiance near the peak of an X1.7 flare that occurred on 27 January 2012. Both the observed (black) and preflare subtracted spectra (red) are shown [from *Warren et al.*, 2013; copyright AAS, reproduced with permission].

several empirical irradiance proxy models have been developed over the past decades and these models have helped to fill the gaps between the measurements and provide a convenient input to ionospheric and thermospheric models.

Commonly used solar irradiance proxy models that are used for ionospheric modeling studies are the HFG model [*Hinteregger et al.*, 1981], the EUVAC/HEUVAC model [*Richards et al.*, 1994, 2006], the SOLAR2000 model [*Tobiska et al.*, 2000; *Tobiska*, 2004], and the NRLEUV model [*Warren et al.*, 1998, 2001; *Lean et al.*, 2003]. These models, with the exception for SOLAR2000, are daily average models and do not estimate the increased spectral irradiances from solar flares. SOLAR2000 has recently been updated to produce the historical irradiances at a 3 hr temporal resolution and also includes a new component, SOLARFLARE, that can now cast (7 min latency) the solar VUV irradiance with a 2-min cadence [*Tobiska*, 2007].

The most recent model that is capable to represent the solar flare spectral variations is the Flare Irradiance Spectral Model [FISM; *Chamberlin et al.*, 2007, 2008], which estimates the solar irradiance at wavelengths from 0.1 to 190 nm at 1 nm resolution with a time cadence of 60 s. The temporal and spectral resolution of FISM is well-suited to model variations due to solar flares including irradiance variability from both the impulsive and gradual phases of solar flares. FISM is based on data from the Solar EUV Experiment (SEE) on the Thermosphere Ionosphere Mesosphere Energetics and Dynamics (TIMED) satellite and the Solar Stellar Irradiance Comparison Experiment (SOLSTICE) on the Upper Atmospheric Research Satellite (UARS). Recently, FISM has been used extensively in modeling studies to investigate the ionospheric response to solar flares [e.g., *Qian et al.*, 2010, 2011, 2012; *Sojka et al.*, 2013].

### 18.2.2. The Large Solar Flares of Solar Cycle 23

Some of the most intense solar flares in recent history in the X-ray range (0.1–0.8 nm) occurred during the last solar cycle (solar cycle 23). On 14 July 2000, a X5.7 solar flare was observed, which together with its coronal mass ejection (CME) is known as the Bastille Day event. On 2 April 2001, another very large X20 solar flare occurred, which was the second most powerful ever recorded. In late October 2003, a series of large solar flares occurred. A X17.2-class flare was observed on 28 October 2003 followed a few days later by the largest solar flare ever measured, on 4 November 2003. This latter flare was classified based on the GOES 0.1–0.8 nm X-ray observations as an X28 flare. The GOES instrument, however, saturated for about 13 min during the peak of the flare from about 1943 to 1956 UT, and NOAA's estimate of the peak at X28 thus had to be made by extrapolation. This large flare was later upgraded by *Thomson et al.* [2004] to an X45 ± 5-class flare using the large observed phase changes recorded at Dunedin, New Zealand, on long VLF radio paths across the Pacific from transmitters in the continental United States and Hawaii. The whole sequence of events occurring from 28 October to 4 November is known as the Halloween Solar Storm. Other very large solar flares occurred on 7 September 2005 (X17), 15 April 2001 (X14.4), and 29 October 2003 (X10). Many of these storms were associated with CMEs and energetic particles, and their effects on the Earth's space environment have been subject to many studies [e.g., *Mannucci et al*, 2005; *Tsurutani et al.*, 2009].

The occurrence of these large flares together with the wide spatial coverage of ground-based GPS stations provided a great opportunity to study the global ionospheric response to solar flares. *Wan et al.* [2005] investigated the GPS/TEC response to the large X5 solar flare, which occurred on 14 July 2000 and was the most intense flare that happened in the preceding decade. To investigate the correlation between the observed sudden increase in TEC and the observation locations, they calculated the geographical distribution of the largest peak values of the flare-induced TEC variation rate, dTECf/dt, at UT 10:24, as well as the flare-induced TEC increment, dTECf. These values are shown in Figure 18.4 as solid lines. Figure 18.4 also shows as dashed lines the solar zenith angle $\chi$ of the corresponding observations. Clearly seen

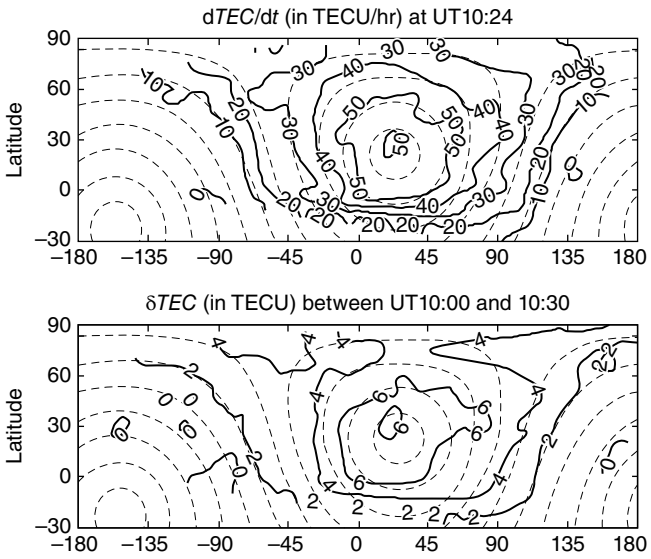


**Figure 18.4** Contours of the flare-induced time rate of change of the TEC, $dTEC_f/dt$, at UT 10:24 (top panel) and the flare-induced TEC increment, $\Delta TEC_f$ (bottom panel). For comparison, contours of the solar zenith angle are also given as the dashed lines [from *Wan et al.*, 2005].

is the good agreement between the flare-induced TEC variation rate and the flare-induced TEC increment, and their close relationship with $\chi$.

The X17.2-class flare that was observed on 28 October 2003 is probably the most widely studied solar flare in terms of its effects on the ionosphere. *Zhang and Xiao* [2005] used TEC from 114 GPS ground stations to analyze the morphological features of the TEC changes in the sunlit hemisphere during the 28 October 2003 flare, which was located near the Sun's central meridian (16°S, 08°E). They found that that the strongest SITEC happened during the flare, and the magnitudes of SITEC vary at regions with different local solar zenith angle (SZA). In the Northern Hemisphere, the TEC enhancement is approximately symmetrical to the local noon, and its value is usually greater than 14 TECU (1 TECU = $10^{16}$/m$^2$) if the SZA is less than 60°. On the whole, as the SZA increases, the value of TEC enhancement in the Northern Hemisphere decreases. It is interesting that they reported that even in the regions of SZA between 90° and 100°, the SITEC was still seen from the temporal TEC curves.

*Sahai et al.* [2006] studied the 28 October 2003 solar flare event over the Brazilian sector using a GPS receiver and ionosonde and found increase of TEC up to 25 TECU and lack of reflected echoes in the ionograms for a 1 hr period during the flare onset. They suggested that the reason for complete or partial radio signal fadeout could be intense absorption. The response of the presunset low- to middle latitude ionosphere in the Indian sector to the same flare has been examined by *Manju et al.* [2009] using magnetometer data, ionosonde data, and GPS TEC. They noticed large and prolonged Ne enhancements observed from the ionosonde just after the flare-related peak enhancement in EUV flux, a significant enhancement in TEC (~10 TECU) near the equatorial anomaly region and positive and negative variations in the equatorial electrojet (EEJ) currents.

*Tsurutani et al.* [2005] also used ground-based TEC from approximately 100 GPS receivers to obtain high time resolution (~30 sec) and high spatial resolution global changes in the dayside TEC. Figure 18.5 shows the SOHO SEM EUV 26.0–34.0 nm count rate together with the GOES 0.1–0.8 nm and 0.5–4.0 nm X-ray flux and the ground-based GPS/TEC (mapped to the vertical) observed at Libreville, Gabon, during the 28 October 2003 flare. Figure 18.5 clearly shows the simultaneous onset of the flare, as detected by SOHO and GOES, and the TEC enhancement in the ionosphere. The TEC increased most rapidly from about 1100 UT to ~1105 UT followed by a less steep increase up to 1118 UT to a peak value of about 25 TECU causing an increase in TEC of about 30% above the prior background level. Figure 18.5 also shows that after about 3 hr the TEC relaxed back to their background values.

*Tsurutani et al.* [2005, 2006] compared the 28 October 2003 flare event with other Halloween 2003 and the Bastille Day solar flare events and surprisingly found that the TEC increase during the 28 October 2003 was significantly larger than the TEC increase of about 5–7 TECU during the much more intense 4 November 2003 X-ray flare. As a possible explanation for this, they pointed out the large spectral differences between the individual flares. Figure 18.6 shows the 26.0–34.0 nm SOHO SEM count rates for the 28 and 29 October and 4 November 2003 (Halloween events) and the 14 July 2001 (Bastille Day) solar flares. The count rates in Figure 18.6 have been adjusted to their preflare baselines. In this EUV wavelength range, the 28 October 2003 event is the largest event with a peak count rate greater than twice that of the other three events, which are roughly comparable in peak intensity. This is in sharp contrast to the peak intensities observed in the 0.1–0.8 nm X-ray range where the November flare is by far the largest event. *Zhang and Xiao* [2003] found a similar behavior when investigating the ionospheric response to a X14.4/2B solar flare that occurred on the solar disc at 20°S 85°W. They found that the largest TEC enhancement during this flare was only about 2.6 TECU, which is much smaller than that for the 28 October 2003 flare, even though the levels of the soft X-ray fluxes for these two flares were similar.

It is reasonably to think that the large difference of the TEC enhancements associated with these flares is due to the difference of EUV fluxes reaching to the Earth. It is generally accepted that the main part of the TEC enhancement is attributed to the enhanced EUV radiation during the flare, which increases the electron density in the *F* region [*Donnelly*, 1969, 1976; *Taylor and Watkins*, 1970; *Mendillo et al.*, 1974; *Matsoukas et al.*, 1972]. Consequently it can be estimated that the main part of the observed 25 TECU increase in TEC is caused by the enhanced solar EUV. The fact that the October 28 flare was very close to the solar central meridian and its active region is very large (4B) may have been the main factors to cause such a strong ionospheric response. Part of this difference could be due to the fact that the 4 November flare occurred near the limb of the Sun and that the EUV emissions generated in the lower corona may have been absorbed by the solar atmosphere [*Donnelly and Puga*, 1990]. *Tsurutani et al.* [2005], however, noted that although the 28 October 2003 flare peak EUV irradiance was much greater (more than double) that of the other three events, a TEC enhancement ratio of approximately 5:1 is not easy to understand and might require detailed modeling including ionospheric dynamics.

The "limb effect" was nevertheless further investigated and statistically analyzed. *Mahajan et al.* [2010] used 10 X-class flares that occurred during the maximum phase of solar cycle 23 and found only a weak correlation between

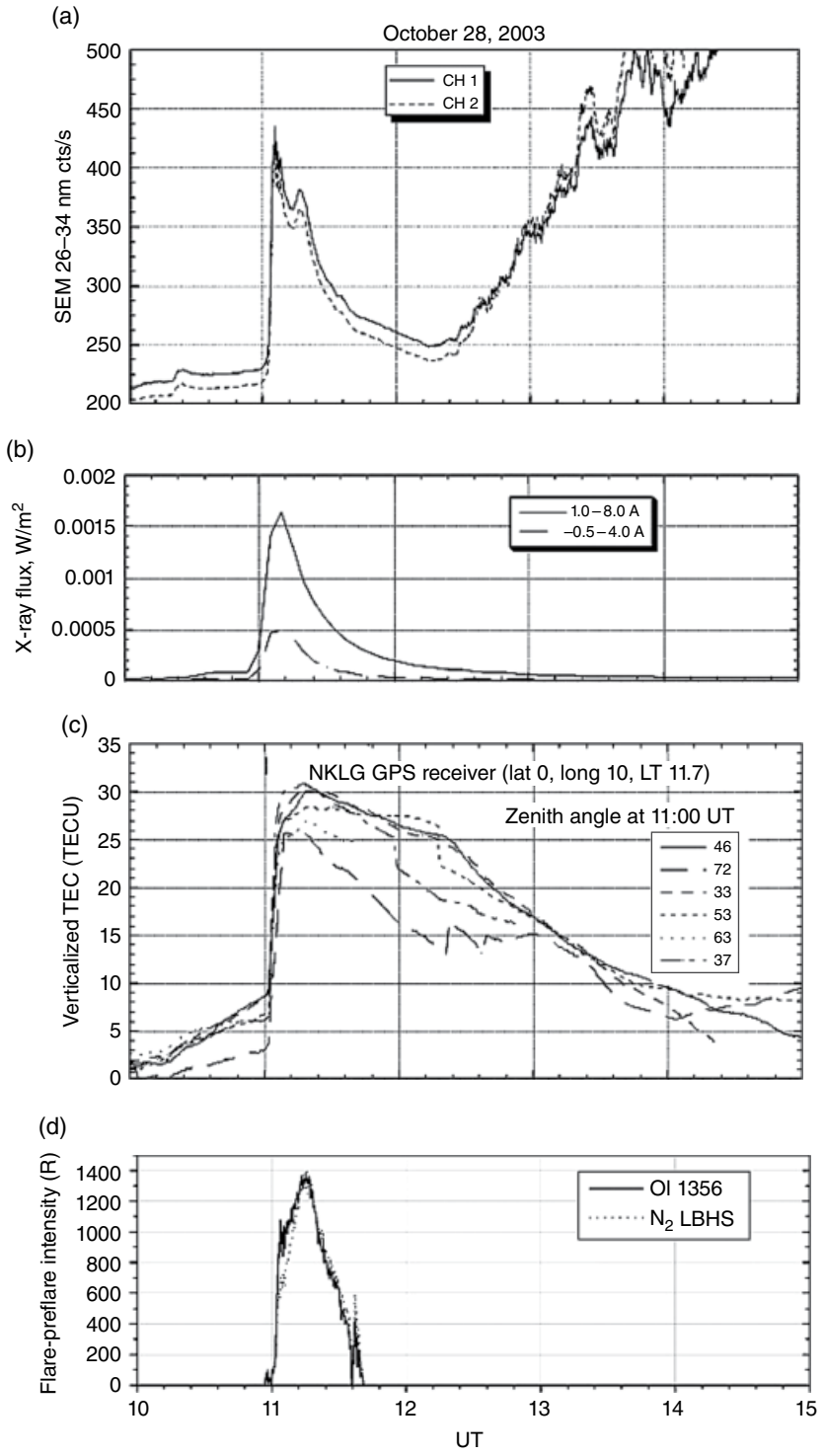


**Figure 18.5** (a) The SOHO SEM EUV count rate, (b) the GOES x-ray flux, (c) the Libreville, Gabon TEC data, and (d) the GUVI FUV O and $N_2$ dayglow data [from *Tsurutani et al.*, 2005].

the peak intensities in the X-ray and the EUV fluxes. The correlation, however, vastly improved when the central meridian distance (CMD) of the flare location was taken into account. *Mahajan et al.* [2010] also reported that the midday peak TEC enhancement was highly correlated with the peak enhancement in the EUV flux. A similar result was found by *Leonovich et al.* [2010], who reported that the average amplitude of the TEC response depends

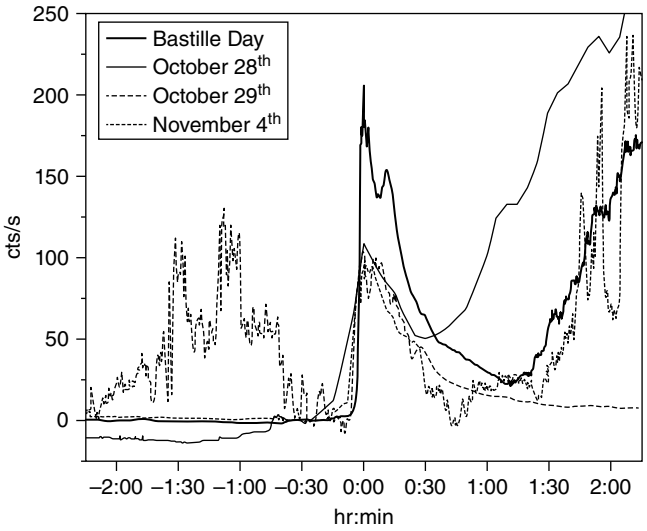


**Figure 18.6** The 26–34 nm SOHO SEM (EUV) count rates for the 28 and 29 October and 4 November 2003 (Halloween events) and 14 July 2001 (Bastille Day) solar flares. The 28 October 2003 flare is the largest event by more than a factor of 2 [from *Tsurutani et al.*, 2006].

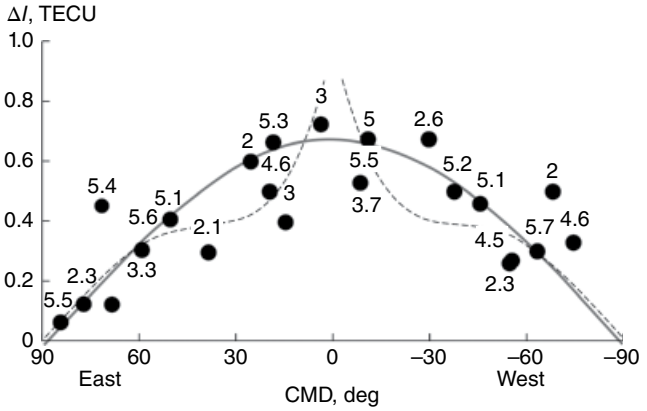


**Figure 18.7** Dependence of the TEC response ΔI of the M2.0–M5.7 solar X-ray flares to the flare distance to the central solar meridian (CMD). The gray line indicates the approximation of the dependence by *cos(CMD)*. The numerals mark the class of the corresponding flare in the X-ray range [from *Leonovich et al.*, 2010].

on the CMD. Figure 18.7 illustrates the dependence (marked by dots) of the ionospheric TEC response amplitude to solar flares from CMD, obtained for the M2.0–M5.7 solar flares in the X-ray range used in their study. Numerals mark the class of the corresponding flare in the X-ray range. This dependence was approximated by a *cos(CMD)* variation (gray line). The obtained dependence indicates that the ionospheric TEC response amplitude decreases with increasing distance from the CMD.

*Donnelly and Puga* [1990] analyzed the dependences of the radiation intensities of active solar sources for different wavelengths from CMD. These dependences were obtained based on the measurements of intensities of the emission from long-living sources of soft X rays [*Mosher*, 1979], radio emission with a wavelength of 10 cm [*Riddle*, 1969], and UV radiation [*Saiman*, 1979] during several solar rotations. The measurement results indicated that the UV radiation intensity decreases when a UV source moves from the central solar meridian to the limb, whereas the intensity of soft X-rays remains almost unchanged. This is related to the fact that the UV radiation path length increases with increasing distance of a source from the central solar meridian to the limb, which results in additional absorption of UV in the solar atmosphere.

### 18.2.3. Altitude-Dependent Response to Solar Flares

The altitude response of the upper ionosphere to solar flares is a complicated interplay between production by the solar irradiance, loss due to chemical reactions, and transport processes. Incoherent scatter radar (ISR) measurements are the obvious preferred choice to simultaneously observe the ionospheric response of the various ionospheric parameters and their altitude variations to a solar flare. However, ISRs are sparsely distributed around the globe and generally operate on low duty cycles. Thus, the chance of observing a flare are low, and opportunities to investigate the ionospheric response as a function of latitude for a given flare or between different flares at a given site are rare.

The availability of ISR data at Millstone Hill for the important 3B flare, which occurred on 7 August 1972, provided a unique opportunity to investigate the altitude variation of various ionospheric parameters and was used by *Mendillo and Evans* [1974] to investigate the ionospheric response to the flare. They reported electron density enhancements of nearly 100% at 125 km altitude and 60% at 200 km altitude. Using TEC data from Faraday rotation experiments, *Mendillo et al.* [1974] reported for the same flare that about 40% of the TEC increase corresponded to altitudes above 300 km. The ISR data also revealed substantial electron temperature increases at all altitudes in concert with a dramatic upward surge in which the drifts increased nearly linearly with height over the height range from 300 to 750 km. *Thome and Wagner* [1971] used Arecibo incoherent scatter radar observations during four 2B solar flares to investigate the electron density response of the ionospheric *E* and *F* regions. They found that, in contrast to the *Mendillo et al.* [1974] results, an increase in the electron density associated with the flare was observed only to about 300 km altitude.

The altitude response of the ionosphere was further investigated by *Leonovich et al.* [2002] using the effect of partial shadowing of the atmosphere by the terrestrial globe on ground-based GPS/TEC observations. They reported that for the powerful 14 July 2000 X5.7/3B solar

flare, about 75% of the observed TEC increase could be attributed to an increase in the electron density below 300 km altitude and about 25% to an increase in the electron density above 300 km altitude. This estimate was found to be consistent with the results of *Mendillo and Evans* [1974] and *Mendillo et al.* [1974] but in contrast with those of *Thome and Wagner* [1971], who noted that an increase in the electron density associated with the flare was observed only to about 300 km altitude. *Leonovich et al.* [2002] pointed out that this apparent difference underlines the fact that each solar flare is a unique event, which is characterized by its own spectrum and dynamics.

*Xiong et al.* [2011] used IS radar data from Millstone Hill, Sondrestrom, and Tromsø, as well as occultation data from the CHAMP satellite to investigate the altitude variation of the ionospheric response due to the 7 September 2005 X17 flare, which occurred near the limb on the Sun (CMD of 77°). They found that the observations from both Millstone Hill and Sondrestrom show the average percentage enhancements of electron density during 17:40–18:10 UT are more than 200% near the *E*-region peak height but only about 10% near the *F*-region peak height, which resulted in larger electron densities in the *E* region than those observed in the *F* region. They speculated that this unusual response was the result of only a weak enhancement in the EUV flux and a strong enhancement in the X-ray flux during this flare.

*Leonovich et al.* [2010] theoretically examined the earlier conflicting results of *Mendillo et al.* [1974] and *Thome and Wagner* [1971] using a theoretical model of the ionosphere and plasmasphere. The altitude-time variations in the charged particle density in the ionosphere from 100 to 1000 km were modeled depending on the solar flare spectrum. An analysis of the modeling results indicated that an intensification of the flare UV emission in the 55–65 and 85–95 nm spectral ranges resulted in a pronounced increase in the electron density in the topside ionosphere (above 300 km). These results pointed out the importance to correctly represent the flare spectrum and its dynamics when modeling the ionospheric response to solar flares.

The dependence of the ionospheric altitude response on the details of the solar spectrum was also recently studied by *Sojka et al.* [2013]. They used the Utah State University time-dependent ionosphere model (TDIM) to access the sensitivity of the ionospheric response to SDO EVE-type observations. Their study covered quiet solar conditions as well as X-class flares and mainly focused on the characteristic responses of the ionospheric *E* and $F_1$ regions to specific regions in the solar spectrum but the $F_2$-region response was also investigated. Figure 18.8 shows the evolution of the altitude response of the electron density at midlatitudes as determined by TDIM for an X28 flare. The simulation corresponds to the solar flare that occurred on 9 March 2011 on the limb of the Sun and was shifted in the onset time so that the flare initiated at noon at the Bear Lake Observatory (BLO) in Utah (42°N, 111°W). Shown is the electron density response near noon as the logarithm of the percentage increase relative to the TDIM simulation for quiet conditions. Also shown in Figure 18.8 is the time evolution of the 2–5 nm binned solar irradiances. Clearly seen are large differences in the response of the ionosphere at different altitudes. Figure 18.8 shows that in the *E* region the electron densities respond nearly instantaneous to the change in the solar irradiance and increase by about 350% corresponding to $\log_{10}$ difference of about 2.54.

With increasing altitude, a delay in the ionospheric response to the flare builds up with the time delay increasing with altitude. In the $F_2$ region, above about 200 km altitude, the ionospheric response is no longer in step with the XUV irradiance but is delayed by several minutes. As the solar flare irradiances pass their peak, the $F_2$ electron density is still increasing due to the effects of diffusion. At about 250 km altitude, near the peak of the $F_2$ region, the peak in the response of the electron density occurs about 15 min after the onset of the flare. This time delay is longer

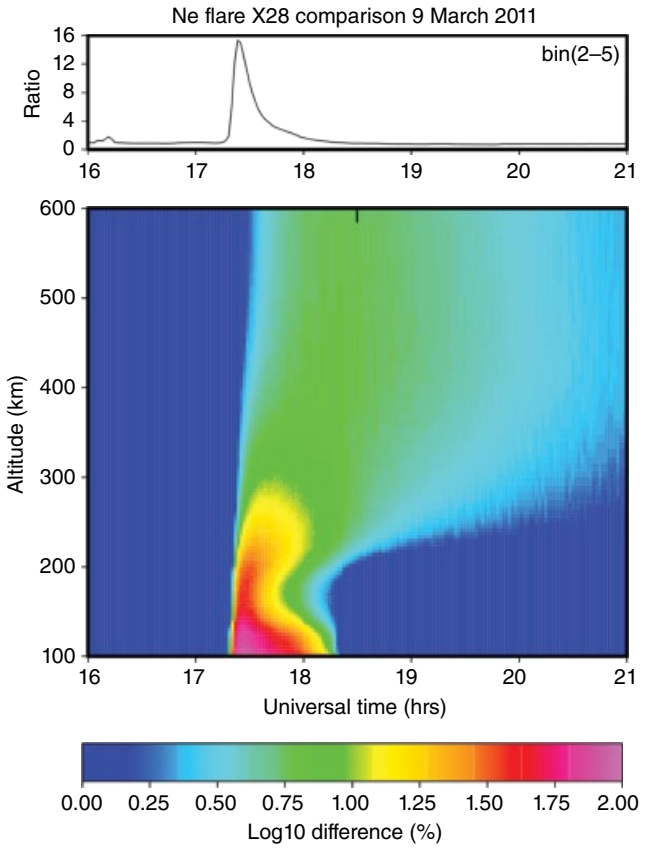


**Figure 18.8** Simulated response of the ionospheric electron density to the X28 flare. The electron density response is shown as the logarithm of the percentage difference between the flare and the quiet Sun electron densities. Red is the highest percentage, where 1.75 corresponds to a 56% increase. The top panel shows the time evolution of the 2–5 nm irradiance bin [from *Sojka et al.*, 2013].

than the flare rise-time as well as the *E*-region response time. At 450 km altitude the electron density increase reaches its peak about 1 hr after the flare onset.

In addition to the increase in the time to reach the peak in the ionospheric response, an increase in the recovery time can be seen. In the *E* region, the effect of the flare is sudden and short-lived, but in the *F* region it lasts long after the flare subsides. As a result of this, the plasma dynamics is changed and leads to time constants of the electron density increase above the $F_2$ peak of more than 1 hr and even after several hours the effects of the flare can clearly be seen at higher altitudes whereas the electron densities have relaxed back to their quiet values at lower altitudes. *Sojka et al.* [2013] noted that the specific time evolution of the electron density response depends not only on the ionosphere but also on the specific spectrum of the flare irradiance.

*Smithtro et al.* [2006] used dynasonde observations from the Bear Lake Observatory to investigate the altitude variation of the ionosphere during solar flares. For their investigation, ionospheric flare events were identified by searching the dynasonde database for *D*-region absorption events. However, their flare events needed to be strong enough to induce a *D*-region cutout, but not so strong as to cause absorption of the entire signal. This criterion eliminated most flares larger than X1 class and smaller than M1, and, as a result, 10 events were selected during the period from 1999 to 2001. An investigation of these events revealed that all of them exhibited a characteristic increase in the *E* and $F_1$ regions, but also showed an anomalous reduction in peak density $N_mF_2$ in the $F_2$ region, which recovered after the end of the flare.

Using the TDIM, *Smithtro et al.* [2006] were able to explain the observed reduction in $N_mF_2$ in terms of a thermal expansion and an upward diffusion of the plasma to the topside caused by enhanced electron temperatures that resulted from the heating by fast photoelectrons produced in the $F_1$ region. The rapid increase in temperature alters the plasma scale height, expanding the $F_2$ region and forcing diffusion to higher altitudes. On the example of the 22 June 1999 M1 flare, *Smithtro et al.* [2006] explained that the irradiance increases do not significantly increase production at the $F_2$ peak but that continuity requires $N_mF_2$ to decrease as the plasma shifts to higher altitudes, leading to a depression of $N_mF_2$. Figure 18.9 shows the model results for the 22 June 1999 flare. The upper panel clearly shows the large *F*-region enhancement

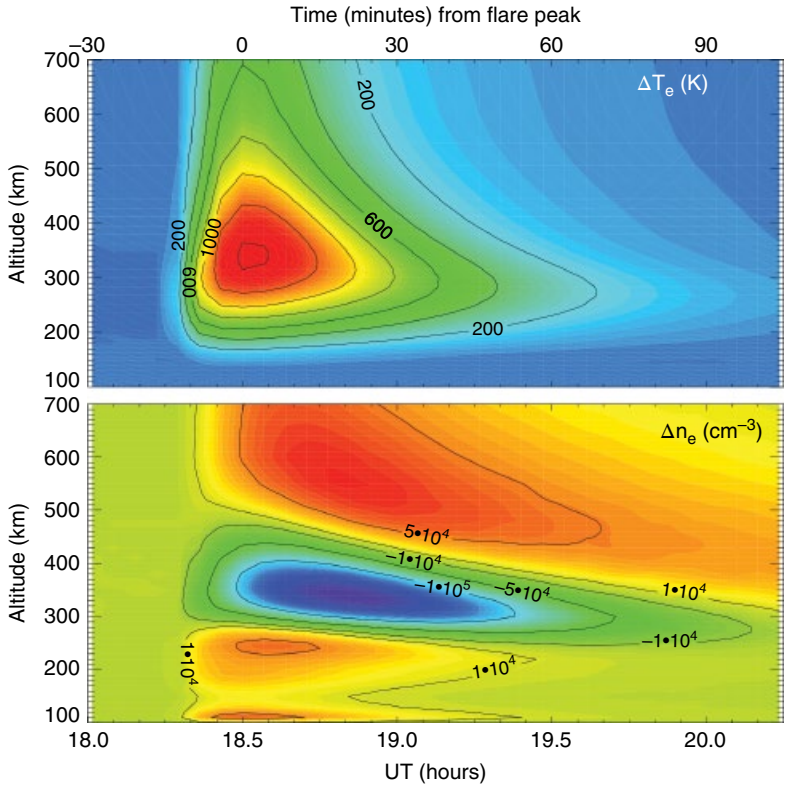


**Figure 18.9** Differences in (top) the electron temperature and (bottom) density computed by two simulations; one included flare effects and the other did not, valid 22 June 1999 over the Bear Lake Observatory. The differences are plotted as a function of altitude and time in UT hours along the bottom x axis and minutes from the flare peak across the top; x axis ticks are spaced in 5 min increments [from *Smithro et al.*, 2006].

in the electron temperature while the lower panel shows the corresponding reduction of the electron density from about 300–400 km altitude and an increase in the electron density in the topside ionosphere.

The *Smithtro et al.* [2006] study, however, was limited in a number of ways by only using a single X1 solar X-ray flare measured by the SEE instrument on 21 April 2002. This flare exhibited variations from more than a factor of 10 for the X-ray emissions to less than 10% at the longer EUV wavelengths. It is not clear, however, whether the flare events investigated by *Smithtro* [2006] exhibited similar spectral characteristics or differed significantly. Furthermore, their study used a parameterization for the photoelectrons created by the flare and did not self-consistently treat the photoelectrons to accurately account for the increase in the thermal electron volume heating rate, and secondary ionization by photoelectrons. This is a common limitation for global ionospheric models, which typically rely on parameterizations to account for heating of the plasma by photoelectrons and an important limitation of these models to investigate flare effects on the ionosphere [*Sojka et al.*, 2013].

*Smithtro and Solomon* [2008] evaluated the impact of photoelectrons on the flare response. They compared the most commonly used parameterization to a rigorous photoelectron model and found that the parameterization underpredicts the thermal electron volume heating rate by 20–30% under nominal solar conditions. When applied to a large solar flare, the parameterized heating rate was found to be more than an order of magnitude smaller than the peak rate calculated with the rigorous photoelectron model. They incorporated these results into a 1-D Global Average Ionosphere/Thermosphere (GAIT) model and found that the electron temperature response for the X17 flare of 28 October 2003 is up to 10% higher prior to the flare, and 15% higher at the flare peak when compared with the commonly used parameterizations.

## 18.3. SUMMARY

During solar flares, the relative changes in the solar X-ray and EUV irradiance can become greatly enhanced, which in turn can strongly affect the Earth's upper atmosphere and ionosphere. It was found that the effect of this enhanced radiation on the ionosphere largely depends on the details of the flare spectrum. Enhanced X-ray radiation penetrates to lower altitudes to ionize the *D* and *E* regions while enhancements in the solar EUV radiation mostly affects the ionospheric *F* region. During the past decade, new and improved solar irradiance observations together with global observations of the ionospheric response to solar flares and theoretical modeling studies have led to a much improved understanding of the observed ionospheric variability during solar flares and have shown the importance of high temporal and spectral resolution irradiance observations to unravel the complex altitudinal response of the ionosphere to solar flares.

## ACKNOWLEDGMENTS

This work was supported in part by NSF grant AGS-1329544 to Utah State University.

## REFERENCES

Afraimovich, E. L. (2000), GPS global detection of the ionospheric response to solar flares, *Radio Sci.*, *35*(6), 1417–1424; doi:10.1029/2000RS002340.

Afraimovich, E. L., E. A. Kosogorov, and L. A. Leonovich (2000), The use of the international GPS network as the global detector (GLOBDET) simultaneously observing sudden ionospheric disturbances, *Earth Planet Space*, *52*, 1077–1082; doi:10.1186/BF03352334.

Afraimovich, E. L., A. T. Altyntsev, E. A. Kosogorov, N. S. Larina, and L. A. Leonovich (2001), Ionospheric effects of the solar flares of September 23, 1998 and July 29, 1999 as deduced from global GPS network data, *J. Atmos. Sol. Terr. Phys.*, *63*, 1841–1849; doi:10.1016/S1364-6826(01)00060-8.

Afraimovich, E. L., A. T. Altyntsev, V. V. Grechnev, and L. A. Leonovich (2002), The response of the ionosphere to faint and bright solar flares deduced from global GPS network data, *Ann. Geophys.*, *45*(1), 3; doi:10.4401/ag-3480.

Bailey, S. M., T. N. Woods, C. A. Barth, and S. C. Solomon (1999), Measurements of the Solar Soft X-ray Irradiance from the Student Nitric Oxide Explorer, *Geophys. Res. Lett.*, *26*, 1255–1258; doi:10.1029/1999GL900236.

Bailey, S. M., T. N. Woods, C. A. Barth, S. C. Solomon, L. R. Canfield, and R. Korde (2000), Measurements of the solar soft X-ray irradiance by the Student Nitric Oxide Explorer: First analysis and underflight calibrations, *J. Geophys. Res*, *105*, 27179–27193; doi:10.1029/2000JA000188.

Baker, D. M., and K. Davies (1966), Solar flare effects and the relaxation time of the ionosphere, *J. Geophys. Res.*, *71*(11), 2840–2842; doi:10.1029/JZ071i011p02840.

Baum, W. A., F. S. Johnson, J. J. Oberly, C. C. Rockwood, C. V. Strain, and R. Tousey (1946), Solar ultraviolet spectrum to 88 kilometers, *Phys. Rev.*, *70*, 781; doi:10.1103/PhysRev.70.781.

Chamberlin, P. C., T. N. Woods, and F. G. Eparvier (2007), Flare Irradiance Spectral Model (FISM): Daily component algorithms and results, *Space Weather*, *5*, S07005; doi:10.1029/2007SW000316.

Chamberlin, P. C., T. N. Woods, and F. G. Eparvier (2008), Flare Irradiance Spectral Model (FISM): Flare component algorithms and results, *Space Weather*, *6*, S05001; doi:10.1029/2007SW000372.

Davies, K. (1962), Ionospheric effects associated with the solar flare of September 28, 1961, *Nature*, *193*, 763–764; doi:10.1038/193763a0.

Davies, K. (1990), *Ionospheric Radio*, Peter Peregrinus, London.

Davies, K., and R. F. Donnelly (1966), An ionospheric phenomenon associated with explosive solar flares, *J. Geophys. Res.*, *71*, 2843–2845; doi:10.1029/JZ071i011p02843.

Dieminger, W., and K. H. Geisweid (1950), Der Zustand der Ionosphäre während des Mögel-Dellinger Effektes am 19 November 1949, *J. Atmos. Terr. Phys.*, *1*, 42–47.

Dodson, H. W. and Hedeman, E. R. (1958), Crochet-associated flares, *Astrophys. J.*, *128*, 636; doi:10.1086/146577.

Donnelly, R. F. (1969), Contribution of X-ray and EUV bursts of solar flares to sudden frequency deviations, *J. Geophys. Res.*, *74*, 1873–1877; doi:10.1029/JA074i007p01873.

Donnelly R. F. (1971), Extreme ultraviolet flashes of solar flares observed via sudden frequency deviations: experimental results, *Sol. Phys.*, *20*, 188–203; doi:10.1007/BF00146110.

Donnelly, R. F. (1976), Empirical models of solar flare X-ray and EUV emission for use in studying their E and F region effects, *J. Geophys. Res.*, *81*, 4745–4753; doi:10.1029/JA081i025p04745.

Donnelly, R. F., and L. C. Puga (1990), Thirteen day periodicity and the center-to-limb dependence of UV, EUV and X-ray emission of Solar activity, *Sol. Phys.*, *130*, 369–390; doi:10.1007/BF00156800.

Foukal, P. V. (2004), *Solar Astrophysics*, 2nd ed., Wiley-VCH, Chichester, U.K.

Garriott, O. K., A. V. da Rosa, M. J. Davies, and O. G. Villard Jr. (1967), Solar flare effects in the ionosphere, *J. Geophys. Res.*, *72*, 6099–6103; doi:10.1029/JZ072i023p06099.

Heroux, L., M. Cohen, and J. E. Higgins (1974), Electron density between 110 and 300 km derived from solar EUV fluxes of August 23, 1972, *J. Geophys. Res.*, *79*, 5237–5244; doi:10.1029/JA079i034p05237.

Hinteregger, H. E., K. Fukui, and B. R. Gilson (1981), Observational, reference, and model data on solar EUV, from measurements on AE-E, *Geophys. Res. Lett.*, *8*, 1147–1150; doi:10.1029/GL008i011p01147.

Huba, J. D., G. Joyce, and J. A. Fedder (2000), Sami2 is Another Model of the Ionosphere (SAMI2): A new low-latitude ionosphere model, *J. Geophys. Res.*, *105*(A10), 23035–23053; doi:10.1029/2000JA000035.

Huba, J. D., H. P. Warren, G. Joyce, X. Pi, B. Iijima, and C. Coker (2005), Global response of the low-latitude to mid-latitude ionosphere due to the Bastille Day flare, *Geophys. Res. Lett.*, *32*, L15103; doi:10.1029/2005GL023291.

Judge, D. L., et al. (1998), First solar EUV irradiances obtained from SOHO by the CELIAS/SEM, *Sol. Phys.*, *177*, 161, 10.1007/978-94-011-5000-2_12.

Knecht, R. W., and K. Davies (1961), Solar flare effects in the F-region of the ionospheric, *Nature*, *190*, 797–798; doi:10.1038/190797a0.

Le, H., L. Liu, B. Chen, J. Lei, X. Yue, and W. Wan (2007), Modeling the responses of the middle latitude ionosphere to solar flares, *J. Atmos. Sol. Terr. Phys.*, *69*, 1587–1598; doi:10.1016/j.jastp.2007.06.005.

Lean, J. L., H. P. Warren, J. T. Mariska, and J. Bishop (2003), A new model of solar EUV irradiance variability: 2. Comparisions with empirical models and observations and implications for space weather, *J. Geophys. Res.*, *108*(A2), 1059; doi:10.1029/2001JA009238.

Leonovich, L. A., A. V. Taschilin, and O. Y. Portnyagina (2010), Dependence of the ionospheric response on the solar flare parameters based on the theoretical modeling and GPS data, *Geomagn. Aeron.*, *50*, 201–210; doi:10.1134/S0016793210020076.

Leonovich, L. A., E. L. Afraimovich, E. B. Romanova, and A. V. Taschilin (2002), Estimating the contribution from different ionospheric regions to the TEC response to the solar flares using data from the international GPS network, *Ann. Geophys.*, *20*, 1935–1941; doi:10.5194/angeo-20-1935-2002.

Liu, J. Y., C. H. Lin, H. F. Tsai, and Y. A. Liou (2004), Ionospheric solar flare effects monitored by the ground-based GPS receivers: Theory and observation, *J. Geophys. Res.*, *109*, A01307; doi:10.1029/2003JA009931.

Liu, J. Y., C. H. Lin, Y. I. Chen, Y. C. Lin, T. W. Fang, C. H. Chen, Y. C. Chen, and J. J. Hwang (2006), Solar flare signatures of the ionospheric GPS total electron content, *J. Geophys. Res.*, *111*, A05308; doi:10.1029/2005JA011306.

Mahajan, K. K., N. K. Lodhi, and A. K. Upadhayaya (2010), Observations of X-ray and EUV fluxes during X-class solar flares and response of upper ionosphere, *J. Geophys. Res.*, *115*, A12330; doi:10.1029/2010JA015576.

Manju, G., T. K. Pant, C. V. Devasia, S. Ravindran, and R. Sridharan (2009), Electrodynamical response of the Indian low-mid latitude ionosphere to the very large solar flare of 28 October 2003—A case study, *Ann. Geophys.*, *27*, 3853–3860; doi:10.5194/angeo-27-3853-2009.

Mannucci, A. J., B. T. Tsurutani, B. A. Iijima, A. Komjathy, A. Saito, W. D. Gonzalez, F. L. Guarnieri, J. U. Kozyra, and R. Skoug (2005), Dayside global ionospheric response to the major interplanetary events of October 29–30, 2003 "Halloween Storms", *Geophys. Res. Lett.*, *32*, L12S02; doi:10.1029/2004GL021467.

Matsoukas, D. A., M. D. Papagiannis, J. Aarons, and J. A. Klobuchar (1972), Correlation of solar radio bursts and sudden increases of the total electron content (SITEC) of the ionosphere, *J. Atmos. Terr. Phys.*, *34*, 1275–1283; doi:10.1016/0021-9169(72)90137-7.

Meier, R. R., H. P. Warren, A. C. Nicholas, J. Bishop, J. D. Huba, D. P. Drob, J. L. Lean, J. M. Picone, J. T. Mariska, G. Joyce, D. L. Judge, S. E. Thonnard, K. F. Dymond, and S. A. Budzien (2002), Ionospheric and dayglow responses to the radiative phase of the Bastille Day flare, *Geophys. Res. Lett.*, *29*(10), 1461; doi:10.1029/2001GL013956.

Mendillo, M. and J. V. Evans (1974), Incoherent scatter observations of the ionosphere with respect to a large solar flare, *Radio Sci.*, *9*, 197–210; doi:10.1029/RS009i002p00197.

Mendillo, M., J. A. Klobuchar, R. B. Fritz, A. V. da Rosa, L. Kersley, K. C. Yeh, B. J. Flaherty, S. Rangaswamy, P. E. Schmid, J. V. Evans, J. P. Schödel, D. A. Matsoukas, J. R. Koster, A. R. Webster, and P. Chin (1974), Behavior of the ionospheric F region during the great solar flare of August 7, 1972, *J. Geophys. Res.*, *79*, 665–672 doi:10.1029/JA079i004p00665.

Mitra, A. P. (1974), *Ionospheric Effect of Solar Flares*, Springer, New York.

Mosher, J. M. (1979), The height structure of solar active regions at X-ray wavelengths as deduced from OSO-8 limb crossing observations, *Sol. Phys.*, *64*, 109–115; doi:10.1007/BF00151119.

Qian, L., A. G. Burns, P. C. Chamberlin, and S. C. Solomon (2010), Flare location on the solar disk: Modeling the thermosphere and ionosphere response, *J. Geophys. Res.*, *115*, A09311; doi:10.1029/2009JA015225.

Qian, L., A. G. Burns, P. C. Chamberlin, and S. C. Solomon (2011), Variability of thermosphere and ionosphere responses to solar flares, *J. Geophys. Res.*, *116*, A10309; doi:10.1029/2011JA016777.

Qian, L., A. G. Burns, S. C. Solomon, and P. C. Chamberlin (2012), Solar flare impacts on ionospheric electrodyamics, *Geophys. Res. Lett.*, *39*, L06101; doi:10.1029/2012GL051102.

Richards, P. G., J. A. Fennelly, and D. G. Torr (1994), EUVAC: A Solar EUV Flux Model for Aeronomic Calculations, *J. Geophys. Res.*, *99*, 8981–8992; doi:10.1029/94JA00518.

Richards, P. G., T. N. Woods, and W. K. Peterson (2006), HEUVAC: A new high resolution solar EUV proxy model, *Adv. Space Res.*, *37*(2), 315; doi:10.1016/j.asr.2005.06.031.

Riddle, A. C. (1969), The quiet and slowly varying components of 9.1 cm radio emission during sunspot minimum, *Sol. Phys.*, *7*(3), 434–447; doi:10.1007/BF00146146.

Sahai, Y., F. Becker-Guedes, P. R. Fagundes, W. L. C. Lima, A. J. de Abreu, F. L. Guarnieri, C. M. N. Candido, and V. G. Pillat (2007), Unusual ionospheric effects observed during the intense 28 October 2003 solar flare in the Brazilian sector, *Ann. Geophys.*, *25*, 2497–2502; doi:10.5194/angeo-25-2497-2007.

Samain, D. (1979), Solar continuum data on, absolute intensities, center to limb variations and laplace inversion between 1400 and 2100 Å, *Astron. Astrophys.*, *74*, 225–228.

Schmidtke, G., F. G. Eparvier, S. C. Solomon, W. K. Tobiska, and T. N. Woods (2006), The TIGER program: Introduction, *Adv. Space Res.*, *37*, 194–198; doi:10.1016/j.asr.2005.02.088.

Schunk, R.W., and A.F. Nagy (2009), *Ionospheres*, 2nd ed., Cambridge Univ. Press, Cambridge, U.K.

Smithtro, C. G., and S. C. Solomon (2008), An improved parameterization of thermal electron heating by photoelectrons, with application to an X17 flare, *J. Geophys. Res.*, *113*, A08307; doi:10.1029/2008JA013077.

Smithtro, C. G., J. J. Sojka, T. Berkey, D. Thompson, and R. W. Schunk (2006), Anomalous F region response to moderate solar flares, *Radio Sci.*, *41*, RS5S03; doi:10.1029/2005RS003350.

Sojka, J. J., J. Jensen, M. David, R. W. Schunk, T. Woods, and F. Eparvier (2013), Modeling the ionospheric *E* and *F1* regions: Using SDO-EVE observations as the solar irradiance driver, *J. Geophys. Res. Space Physics*, *118*, 5379–5391; doi:10.1002/jgra.50480.

Taylor, G. N., and C. O. Watkins (1970), Ionospheric electron concentration enhancement during a flare, *Nature*, *228*, 653–654; doi:10.1038/228653a0.

Thome, G. D., and L. S. Wagner (1971), Electron density enhancement in the E and F regions of the ionosphere during solar flares, *J. Geophys. Res.*, *76*, 6883–6894; doi:10.1029/JA076i028p06883.

Thompson, W.T., and P. Brekke (2000), EUV irradiance variations measured with the SOHO Coronal Diagnostic Spectrometer, *The Solar Cycle and Terrestrial Climate*, ESA SP-463, 435.

Thomson, N. R., C. J. Rodger, and R. L. Dowden (2004), Ionosphere gives the size of greatest solar flare, *Geophys. Res. Lett.*, *31*, L06803; doi:10.1029/2003GL019345.

Tobiska, W. K. (2004), SOLAR2000 irradiances for climate change research, aeronomy, and space system engineering, *Adv. Space Res.*, *34*, 1736; doi:10.1016/j.asr.2003.06.032.

Tobiska, W. K. (2007), Solar2000 v2.30 and SOLARFLARE v1.01: New Capabilities for Space System Operations, Am. Inst. of Aeron. and Astron., Reston, Va.

Tobiska, W. K., T. N. Woods, F. G. Eparvier, R. Viereck, L. Floyd, D. Bower, G. J. Rottman, and O. R. White (2000), The SOLAR2000 empirical solar irradiance model and forcast tool, *J. Atmos. Sol. Terr. Phys.*, *62*, 1233; doi:10.1016/S1364-6826(00)00070-5.

Tsurutani, B. T., et al. (2005), The October 28, 2003 extreme EUV solar flare and resultant extreme ionospheric effects: Comparison to other Halloween events and the Bastille Day event, *Geophys. Res. Lett.*, *32*, L03S09; doi:10.1029/2004GL021475.

Tsurutani, B. T., et al. (2006), Extreme solar EUV flares and ICMEs and resultant extreme ionospheric effects: Comparison of the Halloween 2003 and the Bastille day events, *Radio Sci.*, *41*, RS5S07; doi:10.1029/2005RS003331.

Tsurutani, B. T., O. P. Verkhoglyadova, A. J. Mannucci, G. S. Lakhina, G. Li, and G. P. Zank (2009), A brief review of "solar flare effects" on the ionosphere, *Radio Sci.*, *44*, RS0A17; doi:10.1029/2008RS004029.

Wan, W., L. Liu, H. Yuan, B. Ning, and S. Zhang (2005), The GPS measured SITEC caused by the very intense solar flare on July 14, 2000, *Adv. Space Res.*, *36*, 2465–2469; doi:10.1016/j.asr.2004.01.027.

Warren, H. P., J. T. Mariska, and G. A. Doschek (2013), Observations of thermal flare plasma with the EUV variability experiment, *Ap. J.*, *770*, 116; doi:10.1088/0004-637X/770/2/116.

Warren, H. P., J. T. Mariska, and J. Lean (1998), A new reference spectrum for the EUV irradiance of the quiet Sun: 1. Emission measure formulation, *J. Geophys. Res.*, *103*, 12, 077; doi:10.1029/98JA00810.

Warren, H. P., J. T. Mariska, and J. Lean (2001), A new model of solar EUV irradiance variability: 1. Model formulation, *J. Geophys. Res.*, *106*, 15, 745; doi:10.1029/2000JA000282.

Woods, T. N., et al. (2012), Extreme Ultraviolet Variability Experiment (EVE) on the Solar Dynamics Observatory (SDO): Overview of science objectives, instrument design, data products, and model developments, *Sol. Phys.*, *275*, 115–143; doi:10.1007/s11207-009-9487-6.

Woods, T. N., F. G. Eparvier, J. Fontenla, J. Harder, G. Kopp, W. E. McClintock, G. Rottman, B. Smiley, and M. Snow (2004), Solar irradiance variability during the October 2003 solar storm period, *Geophys. Res. Lett.*, *31*, L10802; doi:10.1029/2004GL019571.

Woods, T. N., F. G. Eparvier, S. M. Bailey, P. C. Chamberlin, J. Lean, G. J. Rottman, S. C. Solomon,W. K.Tobiska, and D. L.Woodraska (2005), Solar EUV Experiment (SEE): Mission overview and first results, *J. Geophys. Res.*, *110*, A01312; doi:10.1029/2004JA010765.

Woods, T. N., G. Kopp, and P. C. Chamberlin (2006), Contributions of the solar ultraviolet irradiance to the total solar irradiance during large flares, *J. Geophys. Res.*, *111*, A10S14; doi:10.1029/2005JA011507.

Woods, T. N., S. M. Bailey, W. K. Peterson, H. P. Warren, S. C. Solomon, F. G. Eparvier, H. Garcia, C. W. Carlson, and J. P. McFadden (2003), Solar extreme ultraviolet variability of the

X-class flare on 21 April 2002 and the terrestrial photoelectron response, *Space Weather*, *1*(1), 1001; doi:10.1029/2003SW000010.

Xiong, B., et al. (2011), Ionospheric response to the X-class solar flare on 7 September 2005, *J. Geophys. Res.*, *116*, A11317; doi:10.1029/2011JA016961.

Yasyukevich, Y. V., S. V. Voeykov, I. V. Zhivetiev, and E. A. Kosogorov (2013), Ionospheric response to solar flares of C and M classes in January–February 2010, *Cosmic Research*, *51*(2), 114–123; doi:10.1134/S0010952513010097; Original Russian Text: Y. V. Yasyukevich, S. V. Voeykov, I. V. Zhivetiev, and E. A. Kosogorov (2013), in *Kosmicheskie Issledovaniya*, *51*(2), 125–135.

Zhang, D. H., and Z. Xiao (2003), Study of the ionospheric total electron content response to the great flare on 15 April 2001 using International GPS Service network for the whole sunlit hemisphere, *J. Geophys. Res.*, *108*(A8), 1330; doi:10.1029/2002JA009822.

Zhang, D. H., and Z. Xiao (2005), Study of ionospheric response to the 4B flare on 28 October 2003 using international GPS service network data, *J. Geophys. Res.*, *110*, A03307; doi:10.1029/2004JA010738.

Zhang, D. H., X. H. Mo, L. Cai, W. Zhang, M. Feng, Y. Q. Hao, and Z. Xiao (2011), Impact factor for the ionospheric total electron content response to solar flare irradiation, *J. Geophys. Res.*, *116*, A04311; doi:10.1029/2010JA016089.

# 19

# Spectrally Resolved X-Ray and Extreme Ultraviolet Irradiance Variations During Solar Flares

**Thomas N. Woods, Francis G. Eparvier, and James P. Mason**

## ABSTRACT

New X-ray and extreme ultraviolet (EUV) irradiance observations from the Solar Dynamics Observatory (SDO) EUV Variability Experiment (EVE) provide full coverage from 0.1 to 106 nm at 0.1 nm resolution and with a cadence of 10 sec. These observations during flares can usually be decomposed into four distinct characteristics. First, the emissions that dominate during the flare's impulsive phase are the transition region emissions, such as the He II 30.4 nm. Second, the hot coronal emissions above 5 MK dominate during the gradual phase and are highly correlated with the X-ray measurements. A third flare characteristic is coronal dimming, seen best in the cool coronal emissions such as the Fe IX 17.1 nm. The coronal dimming appears to be related to coronal mass ejections (CMEs), thus representing a new way to possibly estimate CME parameters from SDO observations. As the postflare loops reconnect and cool, warm coronal emissions (e.g., Fe XVI 33.5 nm) peak a few minutes after the X-ray peak and sometimes exhibit a second large peak by many minutes to hours later. We refer to this second peak as the EUV late phase (ELP), which is the fourth flare characteristic. The characterization of many flares during the SDO mission is provided, noting that only some flares have all four phases.

**Key Points:**
SDO EVE is providing new solar EUV spectral irradiance results for ionosphere / thermosphere studies
EVE observations reveal four key flare phases: impulsive phase, gradual phase, EUV late phase, coronal dimming
The EUV Late Phase (ELP) is new discovery for flare variations in having EUV enhancements without X-ray increases

**Key Terms:** solar irradiance, flares, chromosphere, corona, transition region, ultraviolet emissions, solar radiation and cosmic ray effects, thermosphere - energy deposition, solar effects

## 19.1. INTRODUCTION

The NASA Solar Dynamics Observatory (SDO) has three solar instruments on board to study the radiative output, magnetic field, and variability of the solar plasma with high time cadence. The extreme ultraviolet (EUV) irradiance instrument, named the EUV Variability Experiment (EVE), measures the solar spectral irradiance (full-disc radiation). The solar irradiance is the major energy driver of the Earth's upper atmosphere and is a key variable in understanding a variety of planetary and heliophysical phenomena. Solar EUV irradiance measurements also show the variability of the solar radiation over all time scales ranging from minutes to decades and can provide calibration for some solar physics

*Laboratory for Atmospheric and Space Physics, University of Colorado at Boulder, Boulder, Colorado, USA*

*Ionospheric Space Weather: Longitude and Hemispheric Dependences and Lower Atmosphere Forcing, Geophysical Monograph 220*, First Edition. Edited by Timothy Fuller-Rowell, Endawoke Yizengaw, Patricia H. Doherty, and Sunanda Basu.

spectrographs and imagers. The high cadence (10 sec) and modest spectral resolution (0.1 nm) for SDO EVE is also valuable for examining the spectral variations during flare events. While EVE observations provide full-disc spectra, the irradiance variations during many of the flare events have corresponded to flaring in a single active region as confirmed by examining the SDO Atmospheric Imaging Assembly [AIA; *Lemen et al.*, 2012] solar EUV images. Therefore, an EVE spectrum minus the preflare spectrum provides a good approximation of the flare spectrum over the full EUV range when only one dominant flare event is in progress at a time. The EVE spectra over the full EUV range, EUV images from AIA, and magnetic fields from SDO Helioseismic and Magnetic Imager [HMI; *Scherrer et al.*, 2012] provide a powerful combination to study flare processes.

Solar flares have long been of interest for sudden ionosphere disturbances and their effect on radio communication [e.g., *Dellinger*, 1937], and flare observations have been made for decades in the visible, primarily in Hα [e.g., *Ellison*, 1946], and also in the soft X-ray (SXR) and EUV ranges from sounding rocket and satellite experiments [e.g., *Friedman*, 1963]. *Hudson* [2010, 2011], *Doschek and Feldman* [2010], *Lang* [2009], and *Aschwanden et al.* [2009a] provide reviews of recent progress in understanding flares from observations that involve the Solar and Heliospheric Observatory (SOHO), Transition Region and Coronal Explorer (TRACE), Reuven Ramaty High Energy Solar Spectroscopic Imager (RHESSI), Hinode (Solar-B), and Solar Terrestrial Relations Observatory (STEREO) missions. These satellites include imagers in X-ray and EUV broadbands and imaging spectrographs with high spectral resolution but limited EUV range.

The new and exciting aspects of the SDO EVE observations for flare studies are the spectral coverage over the full EUV range from 0.1 to 106 nm with 0.1 nm resolution and the continuous monitoring of the solar activity with high cadence of 10 sec. The EVE flare observations have revealed that many EUV emissions do not behave like the X-ray variations that are often used for classifying the flare magnitude and as a proxy for EUV emissions in models such as the Flare Irradiance Spectral Model [FISM; *Chamberlin et al.*, 2008]. The EVE flare observations are being used to improve the understanding of flare energetics and their impacts on Earth's space environment.

The new irradiance observations by EVE are significantly improved over the previous solar EUV irradiance instruments flying on SOHO, Thermosphere Ionosphere Mesosphere Energetics Dynamics (TIMED), and Geostationary Operational Environmental Satellite (GOES) spacecraft. The EVE suite includes the Multiple EUV Grating Spectrograph (MEGS) that provides EUV spectral observations with spectral resolution of 0.1 nm from 6 to 106 nm, cadence of 10 sec, and accuracy to better than 20%. The EUV SpectroPhotometer (ESP) provides broadband observations between 0.1 and 39 nm with even higher cadence of 0.25 sec and with improved accuracy of better than 10%. *Woods et al.* [2012] provide an overview of EVE's science plans, instrument design, and data products. *Didkovsky et al.* [2012] provide an overview of the ESP instrument and its calibration, and *Hock et al.* [2012] provide an overview of the MEGS instrument and its calibration. SDO was launched on 11 February 2010, and EVE began normal operations on 1 May 2010.

The flare data from EVE shown here are primarily from the MEGS-A channel measuring the spectrum from 7 to 37 nm and the ESP zeroth-order channel (0.1–7 nm band) as the flare variations are most evident in these wavelengths. The EVE spectral resolution of 0.1 nm is especially significant for the wavelength range from 7 to 27 nm because previously there have only been broadband (~10 nm wide) EUV irradiance measurements at these wavelengths. With EVE's improved spectral resolution and continuous observations with 10 sec cadence and in conjunction with AIA EUV images and HMI magnetic fields, we now have a much more accurate knowledge of how the solar EUV irradiance varies during flare events. While not discussed here, the EVE spectra have better than anticipated wavelength stability and Doppler shifts are evident in the EVE spectra, both for the ±3 km/sec drift over its 24-hr orbit period and during some flare events [*Hudson et al.*, 2011].

Flares are often decomposed into an impulsive phase with significant nonthermal signatures and a gradual (slow) mostly thermal phase that follows the impulsive phase [*Donnelly*, 1976; *Hudson*, 2010, 2011]. The rapid release of energy from magnetic reconnection in the corona accelerates electrons and ions during the impulsive phase, which is often dominated by intense bremsstrahlung radiation in hard X-ray (HXR) from the energetic electrons as they interact with the dense, cool plasma in the solar chromosphere and transition region. These energetic particles heat the chromosphere, and the evaporated plasma rises into the corona during the gradual phase while emitting much of its radiation in the SXR and EUV ranges. This is part of an overall process of cooling the hot plasma in progressively higher postflare loops that are an indication of magnetic reconnection as part of the standard flare model [e.g., *Kopp and Pneuman*, 1976; *Švestka*, 1989; *Švestka and Cliver*, 1992; *Raftery et al.*, 2009]. The gradual component normally peaks a few minutes after the impulsive phase, and its intensity rise can often be approximated as the time integral of the impulsive component, referred to as the Neupert effect [*Neupert*, 1968]. The magnetic reconnection process can be fast, so some flare models have many flaring loops, or strands within such coronal loops, heated at slightly different times to form a continuous source [*Warren and Doschek*, 2005].

Flare events can be studied in detail only when isolated in time and space. So only one major flare can happen at a time to study flares with EVE's full-disc irradiance measurements. Fortunately, this happens frequently. *Woods et al*. [2011] provide examples of the four major phases seen during flares with the EVE data. These phases include (1) the impulsive phase best seen in transition region emissions such as He II 304 Å, (2) gradual phase seen in hot coronal emissions such as the Fe XX/Fe XXIII 133 Å, (3) coronal dimming seen in cool corona emissions such as Fe IX 171 Å and often associated with a CME, and (4) EUV late phase (ELP), which has a second, broad peak 1–5 hr after the main flare phases and is seen best in the Fe XVI 335 Å emission [*Woods et al*., 2011]. The X-ray flare classification by the GOES X-Ray Sensor (XRS) is identification of the gradual phase, and the derivative of its 1–8 Å SXR emission can be a proxy for the impulsive phase, as related to the Neupert effect [*Neupert*, 1968]. The coronal dimming and EUV late-phase effects are only observable in the EUV emissions.

Each flare can have its own unique behavior; some flares have all four of these phases, and some flares only have the gradual phase (by definition from the X-ray flare identification by GOES/XRS). For more detailed information, *Hudson* [2011] reviews flare processes and phases, and *Hock et al.* [2012] identifies different categories of flares based on the new SDO/EVE and SDO/AIA observations of hundreds of flares. Notably, the eruptive flares tend to have impulsive phase, gradual phase, and coronal dimming; and some eruptive flares also have the EUV late phase as explained in Section 19.5.

The C8.8 flare on 5 May 2010 is a good example when all four components clearly exist as shown in Figure 19.1. The various EUV emissions have one or more of these aspects in their time series, and the four emissions that best highlight each component are included in this figure. The EUV spectral variations during this C8.8 flare are shown in Figure 19.2.

There are dozens of other emission lines in the EUV spectra with several being blends at EVE's 0.1 nm spectral resolution, but the four emission lines selected for Figure 19.1, which are discussed more in Sections 19.2–19.5, represent reasonably well how the other EUV emission lines behave. In particular, the cool coronal Fe IX, Fe

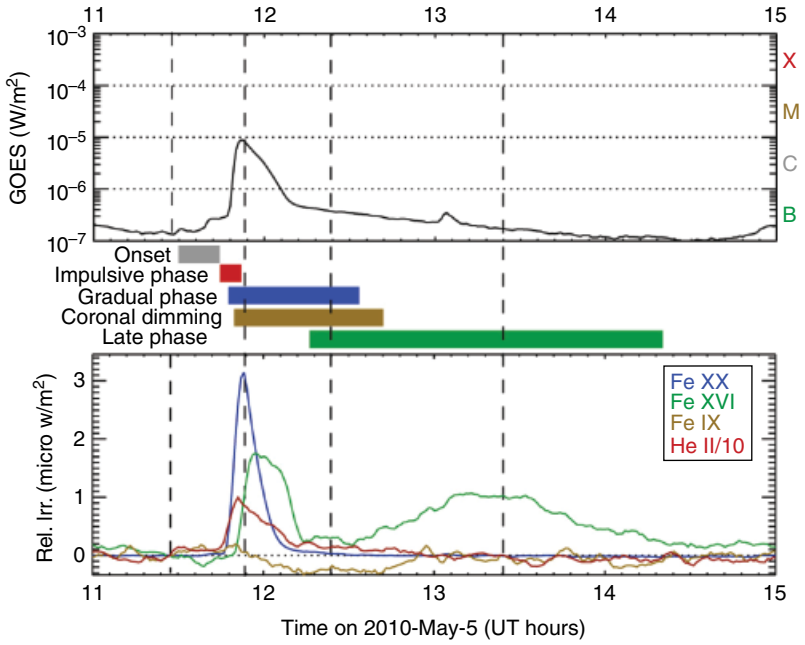


**Figure 19.1** Flare variations for the C8.8 flare on 5 May 2010 as adapted from *Woods et al.* [2011]. The relative irradiance (Rel. Irr.), being the solar irradiance spectrum minus the preflare spectrum, represents well the flare variations over its different phases. The transition region He II 30.4 nm emission highlights the impulsive phase. We assume that GOES X-ray defines the gradual phase, and the hot corona Fe XX/Fe XXIII 13.3 nm emission behaves almost identically to the X-ray. The cool corona Fe IX 17.1 nm emission is the EUV emission with the largest amount of coronal dimming after the impulsive phase. The warm corona Fe XVI 33.5 nm emission has its first peak a few minutes after the X-ray gradual phase peak and then has a second peak many minutes later. The change in decay slope of the GOES X-ray during the gradual phase is indicative of the late-phase contribution (second Fe XVI peak). The four vertical dashed lines, left to right, are for spectra in Figure 19.2 of the preflare, main phase, coronal dimming, and EUV late phase.

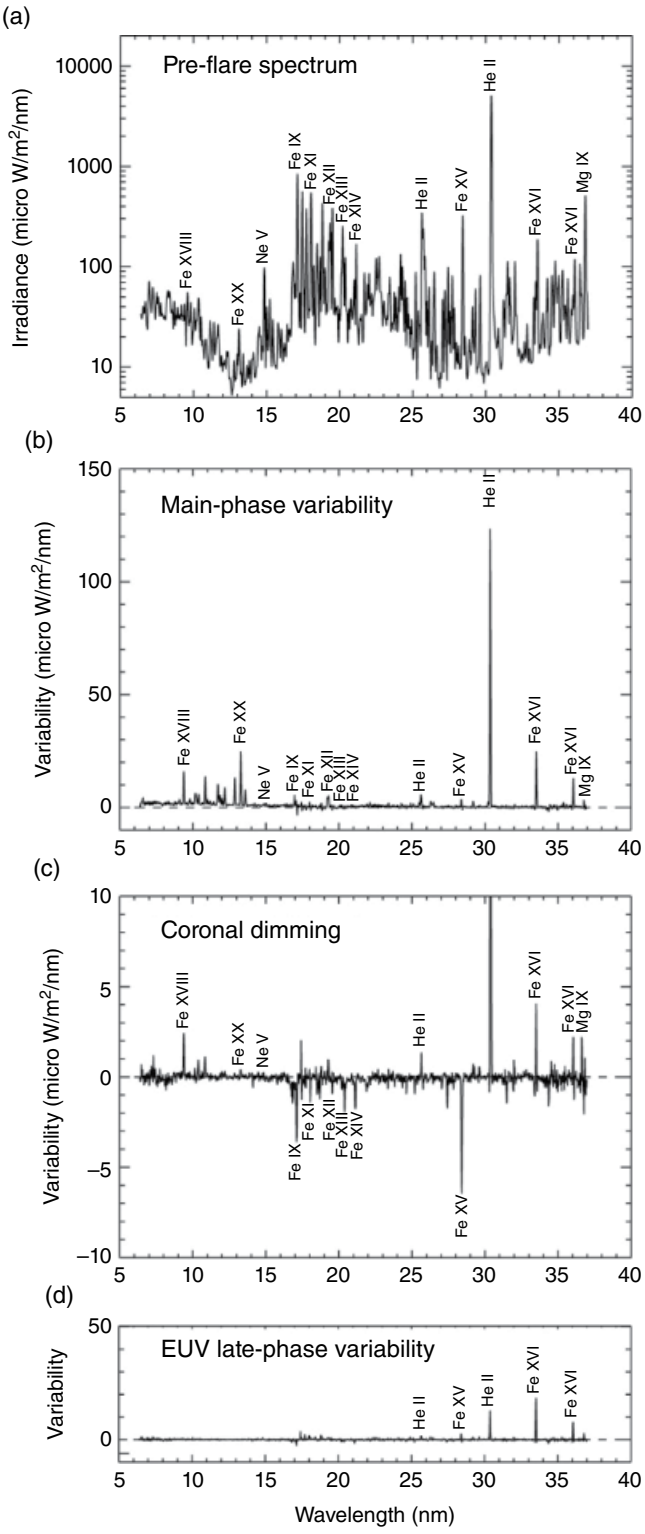


**Figure 19.2** Flare spectral variations from the EVE MEGS A channel (6–37 nm) for the C8.8 flare on 5 May 2010 as adapted from *Woods et al.* [2011]. Panel (a) shows the preflare spectrum. Panels (b–d) show the variability between the preflare irradiance and the main phase, coronal dimming, and EUV late phase, respectively. These results used 5 min averages taken at the times indicated in Figure 19.1 as vertical dashed lines.

X, and Fe XI emissions vary similarly, and the warm coronal Fe XV and Fe XVI emissions have similar variations. The moderately warm coronal Fe XII, Fe XIII, and Fe XIV emissions vary about the same as each other and sometimes have the character of coronal dimming similar to the Fe IX emission but with less dimming depth. Both the much cooler transition region emissions such as the He II 30.4 nm (~0.08 MK) and hot coronal emissions Fe XX/Fe XXIII 13.3 nm (10–16 MK) emissions, shown in Figure 19.1, exhibit their largest increases during the flare's main phase, as do the X-ray measurements, but no significant variations after the flare's main phase.

The GOES X-ray emission is also included in Figure 19.1 because it has been used as a proxy for the short-term variations of the solar EUV irradiance [e.g., *Chamberlin et al.*, 2008]. We note that the GOES X-ray emission correlates well with the very hot coronal emissions and that the time derivative of the GOES X-rays (Neupert effect) correlates reasonably well with the transition region emissions. But the GOES X-ray emission in either form does not correlate well with the variations seen in the other coronal emission lines (~0.7–5 MK), so additional studies for how to best model these coronal emissions during flares are needed for space weather applications.

The next four sections briefly discuss the four different flare phases. *Woods et al.* [2011] provide an overview of about 200 flares observed during the first year of the SDO mission (May 2010–April 2011). Of those flares, 88.5%, 11%, and 0.5% of them were C-, M-, and X-class flares, respectively. All of them had a gradual phase (as expected since flare identification starts with finding GOES X-ray peaks), 55% had an impulsive phase, 22% had coronal dimming, and 14% had an EUV late phase. In general, there is higher probability for having impulsive phase, coronal dimming (eruptive), and EUV late phase for the larger flares.

### 19.1.1. Impulsive Flare Phase

The He II 30.4 nm emission is from the transition region, and it contributes more energy than any other single emission in the EUV range during a flare (see Fig. 19.2b). If the flare has a strong impulsive phase, then the He II emission has a peak a few minutes before the X-ray peak and sometimes a second peak soon after the X-ray peak corresponding to postflare loop reconnections. This emission sometimes does not exhibit an impulsive phase contribution and just has enhancements during the postflare loop reconnections. Based on the timing of the He II peak, 55% of the flares during the first year of SDO mission (May 2010–April 2011) had a strong impulsive phase [*Woods et al.*, 2011]. The impulsive phase is also seen clearly in hard X-ray (HXR) observations, such as by

Reuven Ramaty High Energy Solar Spectroscopic Imager (RHESSI). *Chamberlin et al.* [2012] provides a more detailed examination of impulsive phase flares with EVE observations.

The impulsive phase is important for a myriad of space weather applications because of its indication of the start of the flare event and the possibility of highly energetic radiation and particles that can be created during the impulsive phase. The energetic radiation can include the nonthermal bremsstrahlung radiation (HXR) and sometimes gamma rays that reach the Earth in 8 min. Furthermore, the brighter flares are sometimes associated with eruptive events that create solar energetic particles (SEP) that reach the Earth in minutes to hours and CMEs that reach Earth in 1–3 days.

### 19.1.2. Gradual Flare Phase

The Fe XX/Fe XXIII 13.3 nm emission represents the hot corona at 10–16 MK, and this emission behaves very similar to the GOES X-ray time series and represents well the flare's gradual phase. This emission is an excellent proxy for the SXR and vice versa. The gradual phase is characterized as the chromospheric evaporation resulting from the initial heating caused during the impulsive phase. The intense increase in SXR and EUV radiation in the 0.1–15 nm range during the gradual phase, as shown in Figure 19.2b, is important for space weather applications as this wavelength range is energetic enough to quickly enhance the ionization in Earth's upper atmosphere (80–300 km). Furthermore, the gradual phase typically lasts for many minutes to even hours and thus impacts Earth's atmosphere for a longer period of time than the impulsive phase.

There are several other hot coronal emissions that also agree with the GOES X-ray time series (gradual phase), such as Fe XXIV at 19.2 nm. For example, *Nitta et al.* [2013] and *Aschwanden and Shimizu* [2013] compare EUV image results from the AIA 19.3 nm band to GOES X-ray time series during flares. While there is good correlation to the GOES X-ray gradual phase for several flares, these AIA bands do have blends, such as from Fe XII and Fe VIII emissions, that can complicate the comparisons.

### 19.1.3. EUV Dimming Phase

A third EUV emission included in Figure 19.1 is the Fe IX 17.1 nm emission that represents the cool corona at 0.7 MK. If there is coronal dimming, then the Fe IX through Fe XII emissions usually show coronal dimming. For this example flare in Figure 19.1, the Fe IX emission has a large decrease as shown in Figure 19.2c. The decrease of the Fe IX coronal emission starts near the peak of the impulsive phase, and this emission usually reaches its minimum after the peak of the Fe XX/Fe XXIII emission and sometimes not until after the first peak of the Fe XVI 33.5 nm emission, as is the case in Figure 19.1. The duration of the coronal dimming can be a few hours to a day or so [*Rust*, 1983; *Sterling and Hudson*, 1997; *Reinard and Biesecker*, 2008]. The Fe IX emission showed coronal dimming for 22% of the flares analyzed.

The importance of the coronal dimming to space weather is that it is highly correlated with CME events [e.g., *Rust*, 1983; *McIntosh et al.*, 2007]. This is indeed the case for these Fe IX coronal dimmings as compared to CMEs detected by coronagraphs aboard SOHO and STEREO (CME lists at http://sidc.oma.be/cactus/). *Aschwanden et al.* [2009b] have shown that the amount of coronal dimming can be used to derive CME characteristics such as its mass, so the near real-time EVE Fe IX 17.1 nm data have potential application for providing alerts of CME events. A brief summary about coronal dimming is first presented, and then a comparison of EVE EUV dimming to AIA coronal dimming is provided.

EVE flare data clearly show coronal dimming (decrease in irradiance during flares) for the cooler coronal emission lines for many flares. Coronal dimming has been known from solar SXR and EUV images since the 1970s [e.g., *Rust and Hildner*, 1976; *Rust*, 1983], but it has not been seen in solar EUV irradiance records until the EVE observations. Studies using the SOHO Extreme-ultraviolet Imaging Telescope [EIT; *Delaboudinière et al.*, 1995] made clear associations to the source of coronal mass ejections and have established that EUV dimmings are a good indicator of the apparent base of the white light CME [*Thompson et al.*, 2000; *Harrison et al.*, 2003; *Zhukov and Auchère*, 2004] and with 55% of the CMEs having detectable EUV dimmings [*Bewsher et al.*, 2008; *Reinhard and Biesecker*, 2009]. Dimmings are usually interpreted as mass depletions due to the loss or rapid expansion of the overlying corona [*Hudson et al.*, 1998; *Harrison and Lyons*, 2000; *Zhukov and Auchère*, 2004]. This interpretation is supported by observations of simultaneous and cospatial dimmings in solar EUV images taken at multiple wavelengths [e.g., *Zarro et al.*, 1999; *Sterling et al.*, 2000; *Harra and Sterling*, 2001].

Coronal dimming is of particular interest for the space weather community because CMEs, when directed toward Earth, can cause geomagnetic storms. The negative consequences of these storms on our space-based and even ground-based technology are well established [*National Research Council*, 2008]; therefore, understanding CMEs and improving predictions for CME properties are important for space weather. We aim to establish parameterizations of coronal dimming and correlate them with CME velocity and mass, two key components of CME geoeffectiveness. These coronal dimming analyses hold little promise, however, of predicting the southward

component of the CME's magnetic field, the third important indicator of CME geoeffectiveness.

Extended studies of coronal dimmings have begun to develop a statistical understanding of these events. *Reinard and Biesecker* [2008] found that coronal dimmings in the SOHO 19.5 nm images are more likely to occur near active regions, and typically have a rapid decrease in emission followed by a more gradual recovery, lasting from 3 to 12 hr and rarely persisting longer than 1 day (whereas true coronal holes tend to persist for many days). Although CMEs are also observed to occur without dimmings, *Reinard and Biesecker* [2009] found that nondimming CMEs all have speeds of less than 800 km/sec, suggesting a more intimate connection between the CME and dimming properties. *Krista and Reinard* [2013] found further correlations between dimming magnitudes, flares, and CME mass by studying variations between recurring eruptions and dimmings.

Similar solar EUV observations, and detection of coronal dimming regions during flares, are now routine with SDO/AIA [SDO, *Pesnell et al.*, 2012; AIA, *Lemen et al.*, 2012]. The AIA obtains seven EUV images every 12 sec, including similar EUV bands as measured by SOHO. Additionally, dimming has been observed numerous times in SDO/EVE irradiance measurements during hundreds of flares.

Various physical processes can lead to similar observational signals, particularly if one is focused on only a single emission line. This is particularly true in the case of SDO/EVE data being used independently because EVE full-disc observations (with no spatial information) can not identify the source of an observed dimming. This shortcoming can be solved by examining multiple emission lines in the EVE spectra and by examining SDO/AIA images for dimming regions. *Mason et al.* [2014] have identified six processes that can cause dimming: mass-loss dimming (CME event), thermal evolution, obscuration, wave dimming, Doppler dimming, and bandpass shift. *Mason et al.* [2014] explains each of these processes in more detail and provides a case study for the 7 August 2010 coronal dimming event. For this specific event and several other events, the mass-loss dimming is the dominant process that causes dimming in the EVE data.

The expectation for mass-loss dimming is that the amount of dimming is proportional to the mass loss and that all corona Fe emissions originating in the CME initiation region (i.e., not the confined, flaring loops) would have the same level of dimming. While this expectation is seen with EUV images at multiple wavelengths, the EVE irradiance time series for this 2010 event (and many other events) indicates that the EUV dimming amount decreases with the hotter Fe emissions. While thermal dimming could play a role in such behavior, it is known from the SDO/AIA analysis that thermal dimming is not a major contribution for this 7 August 2010 event. *Mason et al.* [2014] identified the difference between EVE and AIA dimming results as related to main (impulsive/gradual) phase effects modifying the full-disc irradiance measurement by EVE, and they developed an analysis technique for the EVE coronal dimming data that effectively corrects for the main-phase peak effects in the irradiance time series to isolate better the mass-loss dimming contribution in order to be consistent with AIA coronal dimming. The goal for this correction to EVE EUV dimming data is to eventually use EVE space weather data products to forecast CME properties near real-time without the need for more complicated analysis of EUV images. This correction to EVE time series adjusts the EVE full-disc measurement to agree with the spatially resolved coronal dimming region identified in the AIA images. Without such a correction, the EVE EUV dimming depth would underestimate the true amount of coronal dimming (CME mass).

As an example, the results from this correction are shown in Figure 19.3 for the 7 August 2010 dimming event [*Mason et al.*, 2014]. The corrected dimming amount from the EVE data is about 3% for the Fe IX 17.1 nm and Fe XII 19.5 nm and is consistent with the AIA results that are also included in this figure for the core dimming region found in the AIA solar EUV images. As expected (intended), the EVE-corrected dimming depths are much more self-consistent for all of the cool coronal emissions (Fe IX to Fe XII) than the uncorrected results.

Our expectation is that the dimming slope could represent the CME velocity, and the depth could represent the CME mass loss. The coronal dimming amount (depth) has been studied more and appears to be related well to CME mass [e.g., *Aschwanden et al.*, 2009b], but the dimming slope interpretation is not yet established. The dimming slope tracks the depth variation well; that is, the slope is less when the depth is less. Therefore, the slope result may not be providing any useful (unique) information beyond the depth result. Our analysis of more flare events with large dimmings is in progress to address this assumption.

### 19.1.4. EUV Late Phase

The warm corona emission in Figure 19.1 is the Fe XVI 33.5 nm emission that represents a coronal temperature of about 3 MK. Being cooler than the Fe XX, the Fe XVI emission peaks, on average, 6 min after the Fe XX and GOES X-ray peak, and this time delay indicates the cooling rate of the postflare coronal loops in the volume involved in the impulsive and gradual phases. For long duration event (LDE) flares, the delay for the Fe XVI gradual phase peak is even longer, ranging up to 2 hr for the C3.4 flare on 3 November 2010 (X-ray peak at 13:08

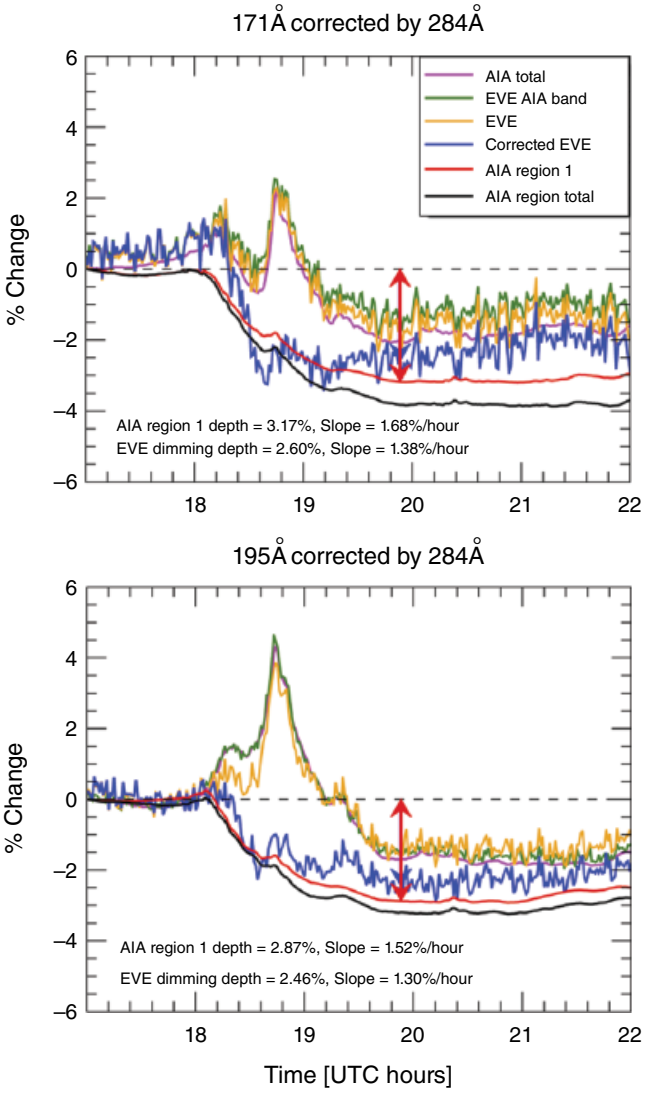


**Figure 19.3** Comparisons of SDO EVE and AIA light curves for coronal dimming as adapted from *Mason et al.* [2014]. The EVE raw data show the main-phase contributions and less dimming than the AIA dimming results (AIA Region 1 and AIA Region Total). The AIA Total is the AIA signal integrated over the full disk and is in agreement with the EVE raw data (EVE and EVE AIA Band, the latter being the convolution of the AIA bandpass with the EVE spectrum). The Corrected EVE data, as corrected for the main-phase contribution using the Fe XV 28.4 nm emission time series, indicates a very similar level of dimming as the AIA mass-loss dimming component (labeled as AIA Region 1).

UT). For the 1 August 2010 LDE (C3.2 flare), the delay for the Fe XVI gradual phase peak was 101 min. The Fe XV and Fe XVI emissions are also interesting as it sometimes has a second peak, and their irradiances during the second peak are often similar in magnitude to the first peak. This second peak of the Fe XVI (and also Fe XV) emissions occurred about 20% of the time. When there is a second peak, the second peak occurred between 16 and 295 min after the first peak during the gradual phase, with an average delay of 75 min. In addition, the ratio of the second peak to the first peak ranges from 0.2 to 4.1; the average ratio is 1.2. The importance of these second peaks to space weather is just now being studied in ionosphere-thermosphere models, but it is clear that they contribute to ionization in Earth's atmosphere for even longer than its first peak during the gradual phase. The following discusses the importance of this second peak that we refer to as the EUV late phase.

As defined by *Woods et al.* [2011], the identification of EUV late phase includes:

1. a second peak of the warm coronal emissions (Fe XV and Fe XVI) several minutes to a few hours after the GOES X-ray peak,
2. no significant enhancements of the GOES X-ray or hot coronal emissions (e.g., Fe XX/Fe XXIII 133 Å) during this second peak,
3. an eruptive event as seen in the AIA images and also seen as coronal dimming in the Fe IX 171 Å emission, and
4. a second set of longer loops being reconnected higher than the original flaring loops and at a much later time than the first set of postflare loops formed just minutes after the flare, as observed in AIA images.

It is important to note that the EUV late phase is distinct from a long-duration flare. The physics of plasma cooling in higher loops is important for both EUV late phase and long-duration events, but the EUV late phase has two peaks of the warm coronal emissions while the long-duration event has only a single gradual phase peak. For the EUV late-phase flares, the disturbance of the coronal loops by the eruption is at about the same time, but the relaxation and cooling down of the heated coronal loops during the postflare reconnections have different time scales with the longer, upper loops being significantly delayed from the lower loops [*Woods et al.*, 2011]. The difference in these cooling time scales is related to the difference between the two peak times of the warm coronal emission and is also apparent in the decay profile of the X-ray emissions having two distinct decays, with the first decay slope being steeper (faster) and the delayed decay slope being smaller (slower) during the time of the warm coronal emission second peak.

Figure 19.4 shows an example of this dual-decay characteristic for the X-ray time series on 1 day during the SDO mission and 1 day during the previous solar cycle. The frequency and relationship of the EUV late-phase decay times between the Fe XVI 335 Å two flare peaks and X-ray decay slopes are examined by *Woods* [2014] for all of the EUV late-phase flares during the first 3 yr of the SDO mission, and the X-ray dual decay character is

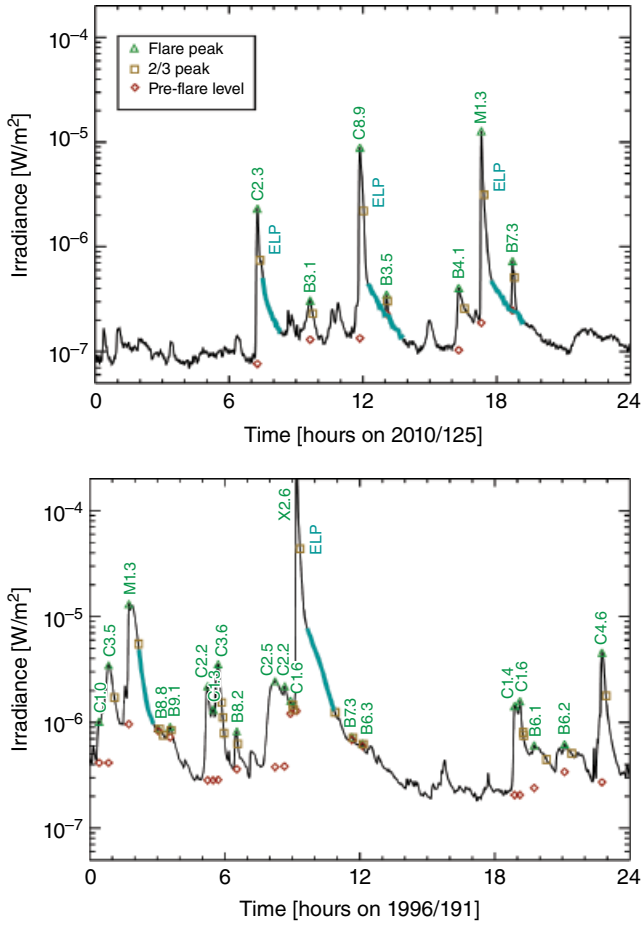


**Figure 19.4** Examples of identifying possible EUV late-phase (ELP) flares with the GOES X-ray data as adapted from *Woods* [2014]. The dual-decay algorithm for the GOES X-ray time series identifies and labels the second, slower decay slope in the GOES X-ray data with blue symbols, and these are also labeled as potential ELP events. The top panel shows a day during the SDO mission (4 May 2010), and three ELP flares are identified and are found to be consistent with ELP flares identified by *Woods et al.* [2011]. The bottom panel shows a day during the previous solar cycle (8 July 1996), and the dual-decay algorithm identified two likely ELP flare events. For each flare considered in the algorithm, the flare peak is labeled in green text, the preflare level is labeled as a red diamond, and the main-flare end time is labeled as an gold square.

exploited to estimate the frequency of EUV late-phase flares during the past four solar cycles as discussed in Section 19.2.

## 19.2. SOLAR CYCLE VARIATIONS

The *Woods* [2014] results indicate that the frequency of EUV late-phase flares peaks before and after each solar cycle minimum as highlighted in Figure 19.5. The total number of flares found in the GOES X-ray record per year is shown in the top panel of Figure 19.5. This result is from searching the GOES record for flare peaks and thus is regardless of whether a dual-decay X-ray flare is found or not. This plot clearly shows that more flares appear during solar cycle maximum than during minimum, as expected. However, the long-term trend from maximum to maximum is interesting in showing a decrease in the number of flares since 1990. That is, the number of flares during solar cycle 23 maximum in 2000 to 2003 is lower than the flares during cycle 22 maximum in 1989–1992. This decrease is seen for all levels (C, M, and X) and the decrease for X-class flares is larger than the M-class flares, which in turn has a decrease larger than the C-class flares. Furthermore, the number of flares during cycle 24 maximum in 2011–2013 is even more reduced as compared to cycle 23 maximum. Of course, the solar cycle 24 maximum period is not necessarily over yet, but many of the solar proxies, such as sunspot number and 10.7 cm radio flux ($F_{10.7}$), appear to have already had their peak for this cycle in late 2011. This downward trend for flares during cycle maximum is also seen in the cycle-minimum trend, although the minimum trend is less clear with the number of M and X flares sometimes being close to zero near cycle minimum. The wider than usual cycle minimum in 2007–2010 may also contribute to the trend for the flares during cycle minimum.

One concern with any long-term solar trend is if the performance and calibration of the instruments could be changing enough to influence the observed trend. The series of GOES/XRS instruments have been cross-calibrated with concurrent measurements from multiple GOES satellites, and their calibrations are thought to have an accuracy of at least 30% [private communication, *R. Viereck and W. Neupert*, 2013]. Furthermore, we have flown calibration rockets for Thermosphere Ionosphere Mesosphere Energetics and Dynamics/Solar EUV Experiment (TIMED/SEE) and SDO/EVE for the past 10 yr, and these comparisons to GOES/XRS irradiances have consistently shown differences of less than 30%. The downward trend in the number of flares is almost a factor of two for M and X flares from one maximum to the next, so instrumental effects at the 30% level cannot be a major concern for these trend results. Then the logical conclusion is that the downward trend is due to a long-term decrease in solar activity (e.g., fewer number of active regions, decrease in magnetic field). *Russell et al.* [2010] and *Fröhlich* [2011] have reported that solar activity has been decreasing since the 1990s, and these results also support this conclusion.

The results for the dual-decay X-ray (proxy for EUV late phase) flares are shown in the middle and bottom panels of Figure 19.5. The middle panel shows the number per year, and the bottom panel shows the relative number (percent) relative to the total number of flares

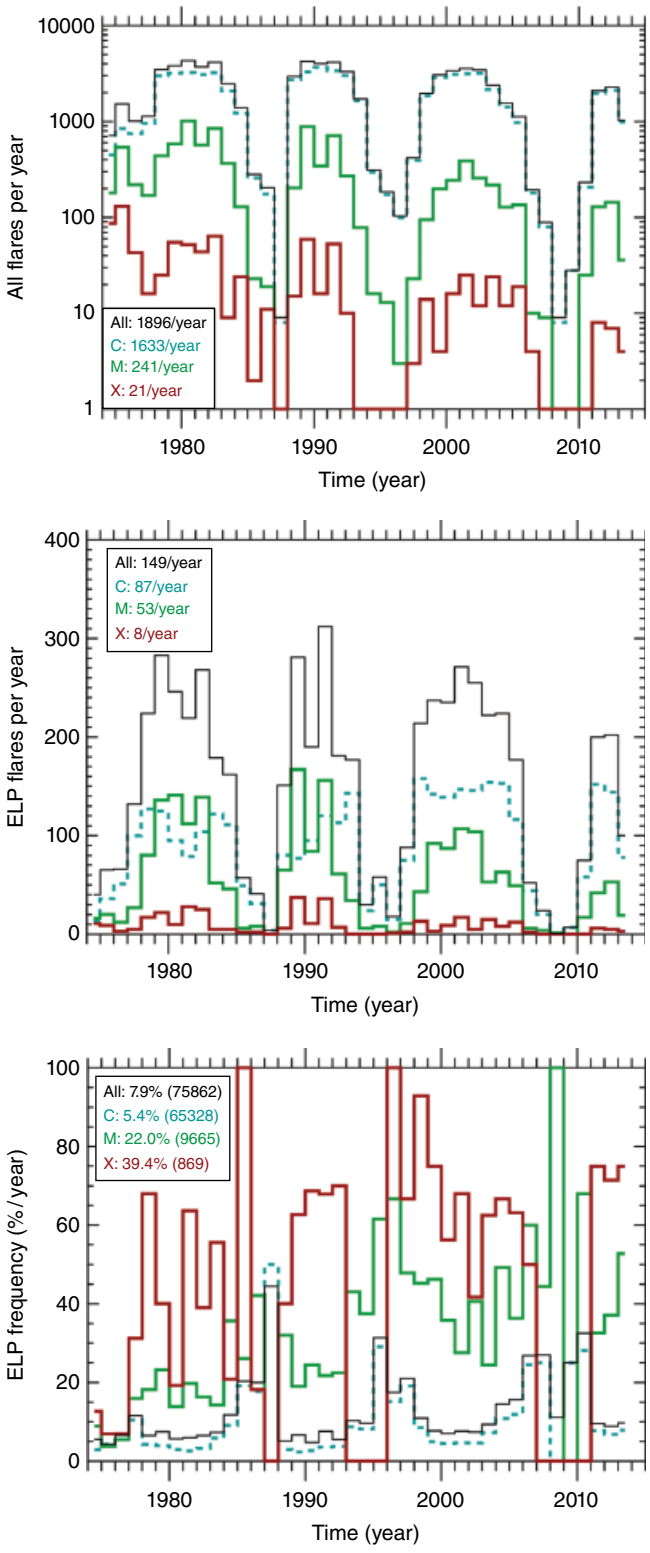


**Figure 19.5** Annual variations of potential EUV Late Phase (ELP) flares as adapted from *Woods* [2014]. The dual-decay algorithm results are compiled into annual averages for C-, M-, and X-class flares separately. The top panel shows the number of all flares identified per year in the GOES X-ray data. The middle panel shows the number of potential ELP flares identified per year. The solar cycle trend is clear in both the top and middle panels, and there is an interesting trend that there are fewer flares in sequential cycle maxima since the 1990s. The bottom panel shows the ratio of the number of ELP flares to all flares, and this ratio represents the frequency that flares might be ELP flares. The ELP frequency for all flares and C-class flares has peaks right before and right after solar cycle minimum and is lower during solar cycle maximum. The ELP frequency for M- and X-class flares can be more confusing because there are very few, or no, large flares for years during and nearby solar cycle minimum.

per year. These results are considered to be a proxy for ELP flares, but with the understanding that there is about 50% uncertainty in these values and also larger uncertainty during cycle maximum. The middle panel of number of potential ELP flares follows a similar pattern as the total number of flares in having more events during cycle maximum than during minimum. The bottom panel may be more enlightening because it represents the frequency that flares might be ELP flares. As the Figure 19.5 panels have four traces each, one may want to focus on the total flare trace (black line) to understand these results. The ELP frequency for all flares and C-class flares has peaks before and after solar cycle minimum of about 20% to 30% and is lower during solar cycle maximum at about 10%. The cycle minima were in 1985, 1995, and 2008. This result of solar-cycle dependence for ELP flare frequency is at least a three-$\sigma$ result. Furthermore, this behavior is consistently seen for all four solar cycles.

The ELP flare frequency for M and X flares can be more confusing because there are very few, or no, large flares for years during cycle minimum. Ignoring the periods near cycle minima when there are often no X-class flares, the frequency for ELP flares for larger flares is about 50% and is significantly higher than the results for the C-class flares. Many X-class flares are two-ribbon flares or long duration events (LDEs) and are associated with larger and more complex active regions. The confirmed ELP flares during the SDO mission are associated with the more complex active regions that have multiple sets of coronal loops, so perhaps it is reasonable that M- and X-class flares could have more ELP flares than the C-class flares, which often are associated with simpler active-region configurations.

## 19.3. CONCLUSIONS

Prior to the SDO mission, the flare irradiance models were using the GOES X-ray signal as a proxy for the gradual phase and the derivative of the X-ray signal as a proxy for the impulsive phase emissions. It is clear now

from the SDO EVE and AIA measurements that at least two additional flare components, (1) coronal dimming for cool coronal emissions and (2) an EUV late phase for warm coronal emissions, are required for modeling the EUV irradiance. While coronal dimming and long duration events like postflare giant arches have been known for some time, their impact on EUV irradiance is now being clarified with the new SDO observations.

The new EVE results are also very important for many space weather applications as deposition of the solar EUV irradiance into Earth's atmosphere depends on the spectral variability, that is which wavelengths are varying, and on the timing that determines the local (regional) effects on Earth. For example, the ionospheric *F* layer is expected to have an additional increase 1–5 hr after the GOES X-ray peaks for EUV late-phase flares. These late-phase flares are also significant because they can enhance the total EUV irradiance flare variation by a factor of 40% or more when the EUV late-phase contribution is included.

The study of the EUV late-phase flares indicates that the frequency of EUV late-phase flares peaks before and after each solar-cycle minimum and has a minimum frequency of occurrence during cycle maximum. This behavior is consistently seen over four cycles. Many EUV late-phase (ELP) flares were seen in the early part of the SDO mission during the initial rise of cycle 24, and not as many ELP flares were observed during cycle 24 maximum. This study suggests that this behavior of ELP flares during the SDO mission is normal behavior over the solar cycle. Another important result from this study is that the number of flares has been decreasing since the 1990s. The downward trend is notably greater for the larger M- and X-class flares, being almost a factor of two decrease per cycle.

Obviously, the new EUV irradiance observations from SDO EVE have huge potential for expanding our understanding of how different EUV emissions vary during flares and how these variations can cause changes in Earth's ionosphere and thermosphere over many different time scales. While we have made some progress in understanding the EUV late-phase solar process and coronal dimming relationship to CME mass loss, the wealth of new data from SDO and other solar observatories over the next several years is expected to lead to even more insightful knowledge of the solar processes throughout the flare time series.

## ACKNOWLEDGMENTS

This research is supported by NASA contract NAS5-02140 to the University of Colorado. The authors thank the SDO/EVE team for providing the high-quality data used in this study. We also thank Vanessa George for her assistance with this manuscript.

## REFERENCES

Aschwanden, M. J., J. P. Wuelser, N. V. Nitta, and J. R. Lemen (2009a), Solar flare and CME observations with STEREO/EUVI, *Sol. Phys.*, *256*, 3–40; doi:10.1007/s11207-009-9347-4.

Aschwanden, M. J., N. V. Nitta, J.-P. Wuelser, J. R. Lemen, A. Sandman, A. Vourlidas, and R. C. Colaninno (2009b), First measurements of the mass of coronal mass ejections from the EUV dimming observed with STEREO EUVI A + B spacecraft, *Astrophys. J.*, *706*, 376–392; doi:10.1088/0004-637X/706/1/376.

Aschwanden, M. J., and T. Shimizu (2013), Multi-wavelength observations of the spatio-temporal evolution of solar flares with AIA/SDO. II. Hydrodynamic Scaling Laws and Thermal Energies, *Astrophys. J.*, *776*, 132; doi:10.1088/0004-637X/776/2/132.

Bewsher, D., R. A. Harrison, and D. S. Brown (2008), The relationship between EUV dimming and corona mass ejections, *Astron. Astrophys.*, *478*, 897; doi: 10.1051/0004-6361:20078615.

Chamberlin, P. C., R. O. Milligan, and T. N. Woods (2012), Thermal evolution and radiative output of solar flares observed by the EUV Variability Experiment (EVE), *Solar Phys.*, *279*, 23; doi 10.1007/s11207-012-9975-y.

Chamberlin, P. C., T. N. Woods, and F. G. Eparvier (2008), Flare Irradiance Spectral Model (FISM): Flare component algorithms and results, *Space Weather J.*, *6*, S05001; doi: 10.1029/2007SW000372.

Delaboudinière, J.-P., G. E. Artzner, J. Brunaud, A. H. Gabriel, J. F. Hochedez, F. Millier, X. Y. Song, B. Au, K. P. Dere, R. A. Howard, R. Kreplin, D. J. Michels, J. D. Moses, J. M. Defise, C. Jamar, P. Rochus, J. P. Chauvineau, J. P. Marioge, R. C. Catura, J. R. Lemen, L. Shing, R. A. Stern, J. B. Gurman, W. M. Neupert, A. Maucherat, F. Clette, P. Cugnon, and E. L. Van Dessel (1995), EIT: Extreme-Ultraviolet Imaging Telescope for the SOHO mission, *Sol. Phys. 162*, 291–312; doi:10.1007/BF00733432.

Dellinger, J. H. (1937), Sudden disturbances of the ionosphere, *J. Appl. Phys.*, *8*(11), 732–751; doi:10.1063/1.1710251.

Didkovsky, L., D. Judge, S. Wieman, and T. Woods (2012), EUV SpectroPhotometer (ESP) in Extreme Ultraviolet Variability Experiment (EVE): Algorithms and calibrations, *Sol. Phys.*, *275*; doi:10.1007/s11207-009-9485-8.

Donnelly, R. F. (1976), Empirical models of solar flare X ray and EUV emission for use in studying their E and F region effects, *J. Geophys. Res.*, *81*, 4745–4753; doi:10.1029/JA081i025p04745.

Doschek, G. A., and U. Feldman (2010), Topical review: The solar UV-x-ray spectrum from 1.5 to 2000 Å, *J. Phys. B: At. Mol. Opt. Phys.*, *43*(23), 232001; doi:10.1088/0953-4075/43/23/232001.

Ellison, M. A. (1946), Visual and spectrographic observations of a great solar flare, 1946 July 25, *Mon. Not. Roy. Astron. Soc.*, *106*, 500–508; doi: 10.1093/mnras/106.6.500.

Friedman, H. (1963), Ultraviolet and X Rays from the Sun, *Ann. Rev. Astron. Astrophys.*, *1*, 59.

Fröhlich, C. (2011), A four-component proxy model for total solar irradiance calibrated during solar cycles 21–23, *Contrib. Astron. Obs. Skalnaté Pleso*, *41*(2), 113–132.

Harra, L. K., and A. C. Sterling (2001), Material outflows from coronal intensity "dimming regions" during coronal mass ejection onset, *Astrophys. J. Lett.*, *561*, 215; doi:10.1086/324767.

Harrison, R. A., and M. Lyons (2000), A spectroscopic study of coronal dimming associated with a coronal mass ejection, *Astron. Astrophys.*, *358*, 1097–1083; doi:10.1051/0004-6361:20030088.

Harrison, R. A., P. Bryans, G. M. Simnett, and M. Lyons (2003), Coronal dimming and the coronal mass ejection onset, *Astron. Astrophys.*, *400*, 1071.

Hock, R. A., P. C. Chamberlin, T. N. Woods, D. Crotser, F. G. Eparvier, M. Furst, D. L. Woodraska, and E. C. Woods (2012), Extreme Ultraviolet Variability Experiment (EVE) Multiple EUV Grating Spectrographs (MEGS): Radiometric calibrations and result, *Sol. Phys.*, *275*; doi: 10.1007/s11207-010-9520-9.

Hudson, H. (2010), Observations of solar and stellar eruptions, flares, and jets, 123–158, in *Heliophysics Space Storms and Radiation: Causes and Effects*, edited by C. J. Schrijver & G. L. Siscoe, Cambridge University Press, Cambridge.

Hudson, H. (2011), Global properties of solar flares, *Sp. Sci. Rev.*, *158*, 5; doi: 10.1007/s11214-010-9721-4.

Hudson, H. S., J. R. Lemen, O. C. St. Cyr, A. C. Sterling, and D. F. Webb (1998), X-ray coronal changes during halo CMEs, *Geophys. Res. Lett.*, *25*, 2481; doi: 10.1029/98GL01303.

Hudson, H. S., T. N. Woods, P. C. Chamberlin, *et al.* (2011), The EVE Doppler sensitivity and flare observations, *Sol. Phys. 273*, 69; doi: 10.1007/s11207-011-9862-y.

Kopp, R. A., and G. W. Pneuman (1976), Magnetic reconnection in the corona and the loop prominence phenomenon, *Sol. Phys.*, *50*, 85–98; doi:10.1007/BF00206193.

Krista, L. D., and A. Reinard (2013), Study of the recurring dimming region detected at AR 11305 using the Coronal Dimming Tracker (CoDiT), *Astrophys. J.*, *762*, 91; doi:10.1088/0004-637X/762/2/91.

Lang, K. R. (2009), *The Sun from Space*, Astronomy and Astrophysics Library, Springer-Verlag Berlin Heidelberg.

Lemen, J. R., *et al.* (2012), The Atmospheric Imaging Assembly (AIA) on the Solar Dynamics Observatory (SDO), *Sol. Phys.*, *275*, 17; doi:10.1007/s11207-011-9776-8.

Mason, J. P., T. N. Woods, A. Caspi, B. J. Thompson, and R. A. Hock (2014), Mechanisms and observations of coronal dimming for the 2010 August 7 event, *Astrophys. J.*, *789*, 61; doi:10.1088/0004-637X/789/1/61.

McIntosh, S. W., R. J. Leamon, A. R. Davey, and M. J. Wills-Davey (2007), The Posteruptive evolution of a coronal dimming, *Astrophys. J.*, *660*, 1653–1659; doi:10.1086/512665.

National Research Council (2008), *Severe Space Weather Events: Understanding Societal and Economic Impacts*, D. N. Baker, The National Academies Press, Washington, DC.

Neupert, W. M. (1968), Comparison of solar X-Ray line emission with microwave emission during flares, *Astrophys. J.*, *153*, L59; doi:10.1086/180220.

Nitta, N. V., M. J. Aschwanden, P. F. Boerner, S. L. Freeland, J. R. Lemen, and J.-P. Wuelser (2013), Soft X-ray fluxes of major flares far behind the limb as estimated using STEREO EUV images, *Solar Phys.*, *288*, 241; doi: 10.1007/s11207-013-0307-7.

Pesnell, W. D., B. J. Thompson, and P. C. Chamberlin (2012), The Solar Dynamics Observatory (SDO), *Sol. Phys.*, *275*, 3; doi:10.1007/s11207-011-9841-3.

Raftery, C. L., P. T. Gallagher, R. O. Milligan, and J. A. Klimchuk (2009), Multi-wavelength observations and modelling of a canonical solar flare, *Astron. Astrophys.*, *494*, 1127; doi:10.1051/0004-6361:200810437.

Reinard, A. A., and D. A. Biesecker (2008), Coronal mass ejection-associated coronal dimmings, *Astrophys. J.*, *674*, 576; doi:10.1086/525269.

Reinard, A. A., and D. A. Biesecker (2009), The relationship between coronal dimming and coronal mass ejection properties, *Astrophys. J. 705*, 914–919; doi:10.1088/0004-637X/705/1/914.

Russell, C. T., J. G. Luhmann, and L. K. Jian (2010), How unprecedented a solar minimum?, *Rev. Geophys.*, *48*, RG2004; doi:10.1029/2009RG000316.

Rust, D. M. (1983), Coronal disturbances and their terrestrial effects/Tutorial Lecture, *Space Sci. Rev*., *34*, 21; doi:10.1007/BF00221193.

Rust, D. M., and E. Hildner (1976), Expansion of an X-ray coronal arch into the outer corona, *Sol. Phys. 48*, 381; doi:10.1007/BF00152003.

Scherrer, P. H., J. Schou, R. I. Bush, A. G. Kosovichev, R. S. Bogart, J. T. Hoeksema, Y. Liu, T. L. Duvall Jr., J. Zhao, A. M. Title, C. J. Schrijver, T. D. Tarbell, and S. Tomczyk (2012), The Helioseismic and Magnetic Imager (HMI) Investigation for the Solar Dynamics Observatory, *Sol. Phys. 275*, 207; doi:10.1007/s11207-011-9834-2.

Sterling, A. C., and H. S. Hudson (1997), Yohkoh SXT observations of X-ray "dimming" associated with a halo coronal mass ejection, *Astrophys. J.*, *491*, L55; doi:10.1086/311043.

Sterling, A. C., H. S. Hudson, B. J. Thompson, and D. M. Zarro (2000), Yohkoh SXT and SOHO EIT observations of sigmoid-to-arcade evolution of structures associated with halo coronal mass ejections, *Astrophys. J.*, *532*; doi:10.1086/311043.

Švestka, Z. (1989), Solar flares, the gradual phase, *Sol. Phys.*, *121*, 399; doi:10.1007/BF00161709.

Švestka, Z., and E. W. Cliver (1992), History and basic characteristics of eruptive flares, in *Eruptive Solar Flares*, Proceedings of Colloquium no. 133 of the IAU held at Iguaz, Argentina, 2–6 August 1991, edited by Z. Şvestka, B. V. Jackson, M. E. Machado, 399 of *Lecture Notes in Physics*, 1, Springer, Berlin; New York.

Thompson, B. J., E. W. Cliver, N. V. Nitta, C. Delannée, and J.-P. Delaboudinière (2000), Coronal dimmings and energetic CMEs in April–May 1998, *Geophys. Res. Lett.*, *27*, 1431; doi:10.1029/1999GL003668.

Warren, H. P., and G. A. Doschek (2005), Reconciling hydrodynamic simulations with spectroscopic observations of solar flares, *Astrophys. J.*, *618*, L157; doi:10.1086/427749.

Woods, T. N. (2014), Extreme ultraviolet late-phase flares: Before and During the Solar Dynamics Observatory Mission, *Sol. Phys.*; doi:10.1007/s11207-014-0483-0.

Woods, T. N., *et al.* (2012), Extreme Ultraviolet Experiment (EVE) on the Solar Dynamics Observatory (SDO): Overview of science objectives, instrument design, data products, and model developments, *Sol. Phys.*, *275*, 115; doi:10.1007/s11207-0009-9487-6.

Woods, T. N., R. Hock, F. Eparvier, A. R. Jones, P. C. Chamberlin, J. A. Klimchuk, L. Didkovsky, D. Judge, J. Mariska, H. Warren, C. J. Schrijver, D. F. Webb, S. Bailey, and W. K. Tobiska (2011), New solar extreme ultraviolet irradiance observations during flares, *Astrophys. J.*, *739*, 59; doi:10.1088/0004-637X/739/2/59.

Zarro, D. M., A. C. Sterling, B. J. Thompson, H. S. Hudson, and N. V. Nitta (1999), SOHO EIT observations of extreme-ultraviolet "dimming" associated with a halo coronal mass ejection, *Astrophys. J. Lett.*, *520*, 139; doi:10.1086/312150.

Zhukov, A. N., and F. Auchère (2004), On the nature of EIT waves, EUV dimmings and their link to CMEs, *Astron. Astrophys.*, *427*, 705–716; doi:10.1051/0004-6361:20040351.

# Part VI
# Ionospheric Irregularities and Scintillation

# 20

# Effect of Magnetic Declination on Equatorial Spread *F* Bubble Development

**Joseph D. Huba**


## ABSTRACT

The NRL SAMI3/ESF three-dimensional ionosphere model is used to study the effect of magnetic declination on the development of large-scale plasma bubbles in the postsunset equatorial *F* region. The study focuses on the role of conductance gradients in the development of equatorial plasma bubbles; their role in the development of the background ionosphere (e.g., prereversal electric-field enhancement) is not considered. We find that plasma bubbles develop faster when the magnetic declination angle is zero (i.e., the magnetic field points to true north) because the flux-tube integrated Pedersen conductivity is smaller for this situation than when the magnetic declination angle is finite. However, for the cases studied, the reduction in the growth rate for situations, where the magnetic declination angle is nonzero, is $\lesssim$20%.

**Key Points:**
The magnetic declination angle affects the growth rate of equatorial plasma bubbles because of conductance gradients
Plasma bubbles develop fastest when the magnetic declination angle is zero
When the magnetic declination angle is non-zero the growth rate is reduced by up to 20%


**Key Terms:** equatorial spread *F*, ionospheric irregularites, equatorial plasma bubbles, SAMI3/ESF model, generalized Rayleigh-Taylor instability

## 20.1. INTRODUCTION

Equatorial spread *F* (ESF) is a postsunset phenomenon [*Booker and Wells*, 1938] in which large-scale (10s km) electron-density "bubbles" can develop and rise to high altitudes (at times over 1000 km) in the equatorial *F* region. Associated with the large-scale electron density structures are smaller-scale irregularities that generate turbulence down to length scales as small as 10 cm [*Huba et al.*,1978]. The basic understanding of this phenomenon is that the bubbles are generated by a generalized Rayleigh-Taylor instability [*Haerendel*, 1974; *Ossakow*, 1981; *Hysell*, 2000; *Sultan*, 1996]. ESF is an important space weather concern because it scintillates radio signals that can degrade and disrupt communications and navigation systems.

One of the issues concerning the onset of equatorial spread *F* has been the longitudinal variability of ESF

*Plasma Physics Division, Naval Research Laboratory, Washington, D.C., USA*

*Ionospheric Space Weather: Longitude and Hemispheric Dependences and Lower Atmosphere Forcing, Geophysical Monograph 220*, First Edition. Edited by Timothy Fuller-Rowell, Endawoke Yizengaw, Patricia H. Doherty, and Sunanda Basu.

bubble development. *Tsunoda* [1985] found that scintillation activity was correlated with the Sun setting at the same time in conjugate *E* layers. Longitudinal variations in the vertical electron density profile and equatorial electrodynamics have been reported by *Yizengaw et al.* [2012].

In this chapter, we focus on the role of magnetic declination in affecting the development of equatorial plasma bubbles via the generalized Rayleigh-Taylor instability and not on global electrodynamics. We find that plasma bubbles develop faster when the magnetic declination angle is zero (i.e., the magnetic field points to true north) because the flux-tube integrated Pedersen conductivity is smaller for this situation than when the magnetic declination angle is finite. However, for the cases studied, the reduction in the growth rate for situations where the magnetic declination angle is nonzero is $\lesssim$20%.

## 20.2. MODEL

The NRL 3-D equatorial spread *F* code SAMI3/ESF [*Huba et al.*, 2008; *Krall et al.*, 2009] is used in this study. The plasma is modeled from hemisphere to hemisphere up to ±31° magnetic latitude in a longitudinal band 4°; the peak altitude at the magnetic equator is ~2400 km. The geophysical parameters used are $F_{10.7}$ = 125, $F_{10.7}$ A = 125, Ap = 4, and day-of-year 80. The grid resolution is *nf* = 200, *nz* = 200, and *nl* = 192, where *nf* is the number of field lines in each longitude plane, *nz* is the number of points along each field line, and *nl* is the number of longitude planes. This grid has a resolution of ~6 km × 2 km in altitude and longitude in the magnetic equatorial plane. The grid is periodic in longitude. However, the background thermosphere composition and wind are not periodic and the small differences between the boundaries introduces a large-scale wave structure on the grid width. The simulation is initialized using ionospheric conditions specified by SAMI2 [*Huba et al.*, 2000] at time 19:14 LT. A random seed perturbation of the electron density is imposed along a flux tube with a peak altitude of 380 km. There is a half-width of this perturbation in altitude of ~60 km. The perturbation is in the range ±10% . In this study, the full SAMI3 ionosphere equations are included, providing ion dynamics both along and across the magnetic field lines. The thermosphere composition and temperature is provided by NRLMSISE-00 [*Picone et al.*, 2002] and the neutral wind is provided by HWM14 [*Drob et al.*, 2014].

We note that the original version of SAMI3/ESF used the donor cell method to transport plasma by the **E** × **B** drift. This method is very stable but numerically diffusive. Thus, previous studies of equatorial spread *F* reported relatively smooth and unstructured plasma bubbles. The **E** × **B** transport scheme has been improved in SAMI3/ESF: a fourth-order partial donor cell algorithm has been implemented [*Hain*, 1987; *Huba*, 2003]. This algorithm substantially reduces numerical diffusion and allows plasma bubbles to bifurcate and structure, consistent with observations [*Makela*, 2006].

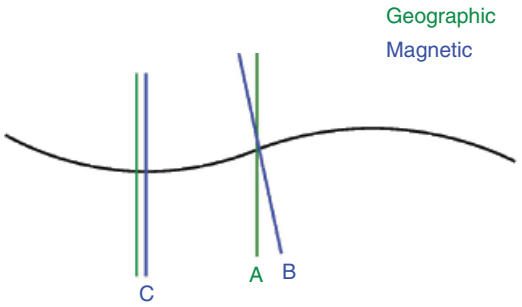


**Figure 20.1** Schematic of the magnetic field and geographic alignment used in the simulation study for a tilted dipole.

Three simulations are performed (A, B, C) for different magnetic declination angles and longitudes as shown in Figure 20.1. In case A, we assume that the dipole axis is aligned with the Earth's spin axis so the magnetic and geographic coordinates are the same (the magnetic declination angle is 0°). In case B, we assume that the dipole axis is tilted and not aligned with the Earth's spin axis so the magnetic declination angle is nonzero. The magnetic North Pole is at 78.8°N latitude and 269.9°E longitude. The geographic longitude for these cases is $\phi = 0°$. In case C, we assume that the dipole axis is tilted and not aligned with the Earth's spin axis but choose a longitude where the magnetic declination angle is zero ($\phi = 270°$). The dipole model assumes that the magnitude of *B* is constant in longitude.

In all cases we use the same initial plasma conditions; however, the background neutral composition, temperature, and winds are different between case C and cases A and B (which are the same). We note that the model does not calculate the background ionospheric electric field associated with the vertical **E** × **B** drift, nor is a background electric field imposed. The vertical **E** × **B** drifts are associated with bubble onset and evolution.

## 20.3. RESULTS

In Figure 20.2, we plot the maximum upward **E** × **B** drift as a function of local time for case A (black), case B (blue), and case C (red). The maximum upward drift velocity is a proxy for assessing the time development of equatorial bubbles. We find that case B, which has a finite magnetic declination angle, has the slowest growing plasma bubbles. Case A, which is at the same geographic longitude as case B but has zero magnetic declination angle, grows faster than case B and saturates at a somewhat larger velocity. The growth time for case A is ~16.3 min while the growth time for case B is ~19.5 min. On the other hand, case C, which has zero declination angle but is at a different geographic longitude,

grows the fastest and reaches a maximum upward velocity roughly twice as large as cases A and B.

In Figure 20.3, we show color-coded contour plots on the electron density as a function of longitude and altitude at time 21:08 LT for cases A, B, and C. The results are consistent with Figure 20.2 in that case C has developed plasma depletions that are "deeper" and at a higher altitude than cases A and B. Similarly, case B has the least-developed plasma bubbles at this time. Although case B (nonzero magnetic declination angle) grows slower than the other cases, it still develops significant plasma depletions.

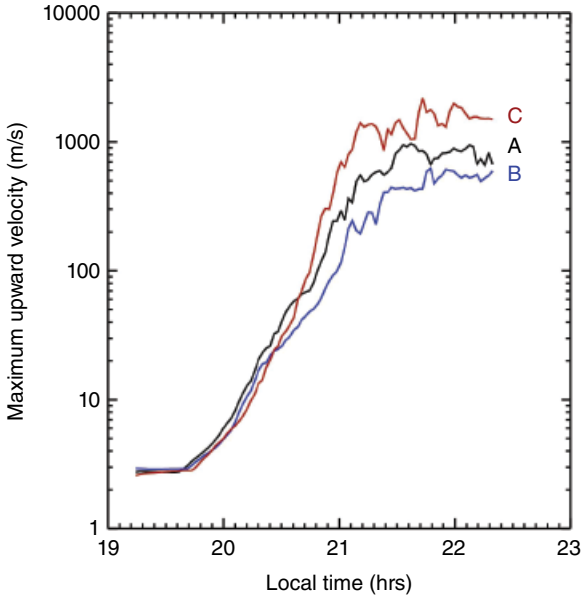


**Figure 20.2** Maximum upward $\mathbf{E}\times\mathbf{B}$ drift as a function of local time for case A (black), case B (blue), and case C (red).

We attribute the differences in the development of equatorial plasma bubbles between cases A, B, and C to differences in the Pedersen conductance. The Pedersen conductance $\Sigma_P$ affects bubble development in two ways. First, to lowest order, the growth rate of the generalized Rayleigh-Taylor instability in the equatorial ionosphere is given by [*Sultan*, 1996; *Krall et al.*, 2009]

$$\gamma_g = -\frac{\int \sigma_{Hc}\left(g_p / L_n\right) ds}{\int \sigma_P \, ds} \tag{20.1}$$

with $L_n^{-1} = \partial \ln n_0 / \partial p$, and

$$\sigma_P \simeq \sum_i \frac{nec}{B}\frac{\nu_{in}}{\Omega_i} \quad \sigma_{Hc} \simeq \sum_i \frac{nec}{B}\frac{1}{\Omega_i}.$$

Here, $p$ is the dipole coordinate orthogonal to the geomagnetic field in the radial direction. Gravity being directed downward, $g_p < 0$ and $\gamma_g$ is always positive (destabilizing) in the bottomside $F$ layer. We note that $\gamma_g$ is inversely proportional to the Pedersen conductance $\Sigma_p = \int \sigma_P \, ds$. Thus, by increasing $\Sigma_p$, the growth rate

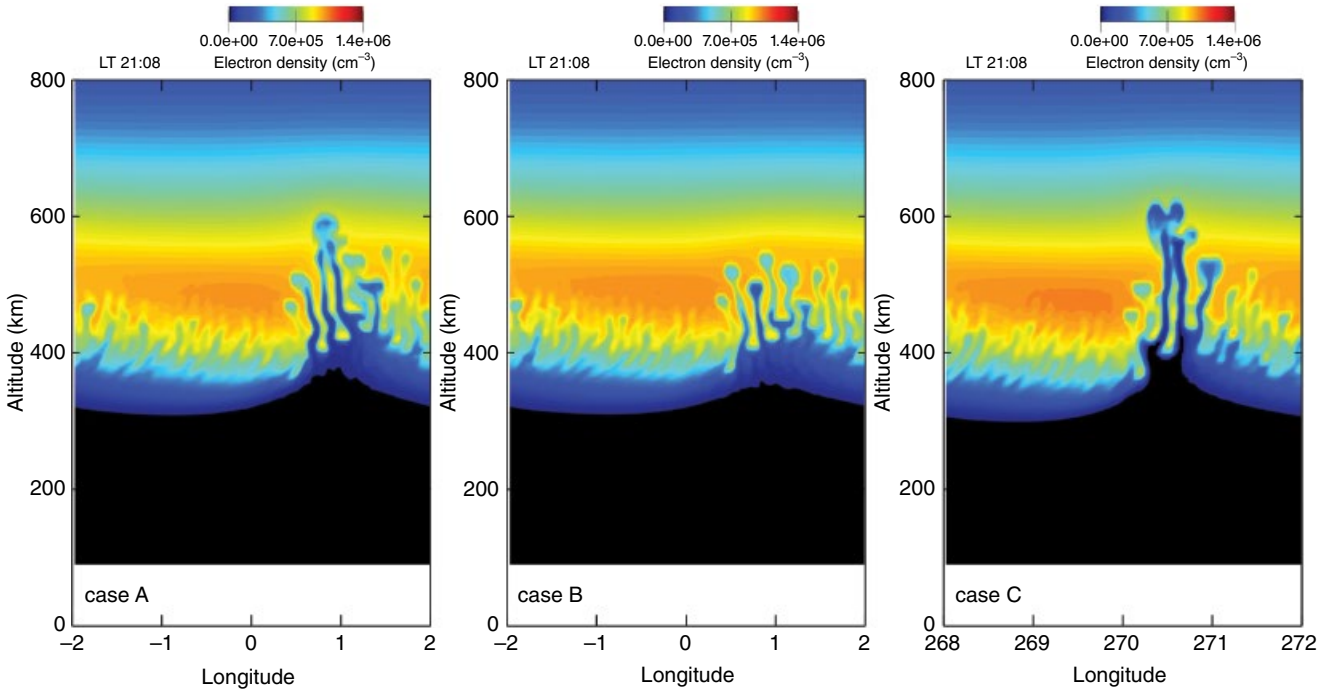


**Figure 20.3** Color-coded contour plots on the electron density as a function of longitude and altitude at time 21:08 LT for cases A, B, and C.

of the instability is reduced [*Maruyama et al.*, 2009; *Krall et al.*, 2009]. Second, the Pedersen conductance enters the potential equation in determining the electric field associated with the instability, that is, $\nabla \cdot \Sigma_P \nabla \Phi = S(g, V_n)$. Thus, other factors being the same, a reduction in the Pedersen conductance leads to a larger electric field.

In Figure 20.4, we plot the percentage differences in the Pedersen conductance between cases B and A, and between cases B and C at times 19:14 LT and 20:00 LT in the center of the grid ($\phi = 0°$). Specifically, we plot

$$\frac{\left(\Sigma_P^B - \Sigma_P^A\right)}{\Sigma_P^B} \text{(BA)} \tag{20.2}$$

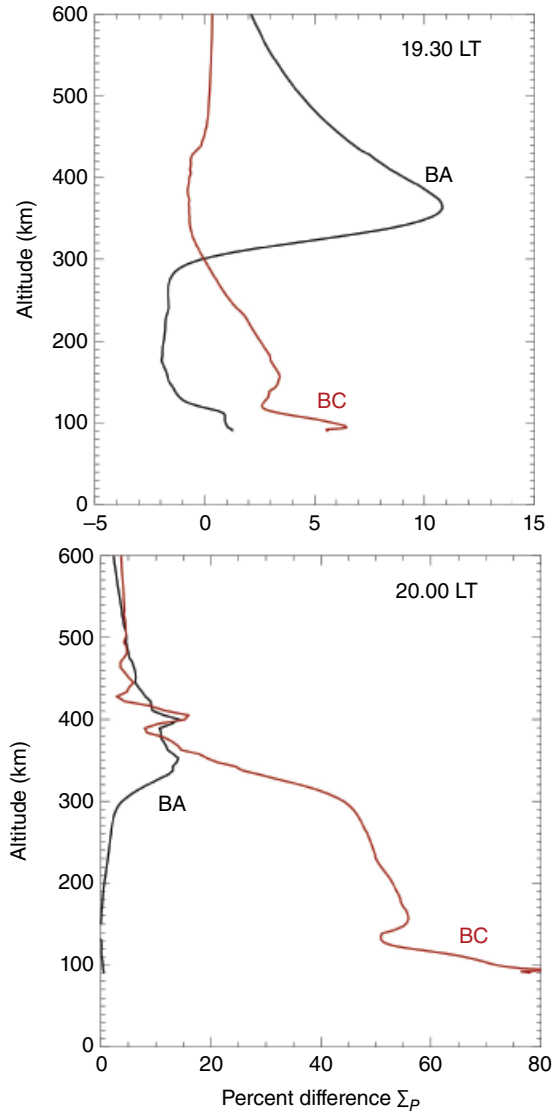


**Figure 20.4** Percent difference of the Pedersen conductance as a function of altitude at times 19:14 LT and 20:00 LT.

and

$$\frac{\left(\Sigma_P^B - \Sigma_P^C\right)}{\Sigma_P^B} \text{(BC)} \tag{20.3}$$

The top plot in Figure 20.4 is near the start of the simulation and shows that $\Sigma_P^B > \Sigma_P^A$ by roughly 10% in the *F* region (~350 km) but that $\Sigma_P^B \simeq \Sigma_P^C$. This suggests that the initial growth rate for case A should be greater than case B, and that the initial growth rates for cases B and C should be about the same. This is consistent with the results shown in Figure 20.3. The bottom panel is later in time and shows that the BA curve is similar to that in the top panel but that the BC curve has increased dramatically. Again, this is consistent with Figure 20.3, which shows that case C eventually dominates in the growth of the plasma bubbles.

The reason that $\Sigma_P^B > \Sigma_P^A$ initially is because the northern footpoint, the magnetic field of case B, is at an earlier local time in the evening than that of case A. The electron density is higher in this region for case B than case A which leads to a longitudinal conductance gradient that affects the development of plasma bubbles in these two cases. Although the opposite is true in the Southern Hemisphere, it seems that the Northern Hemisphere dominates. The difference in the behavior of case C relative to cases A and B is primarily associated with a longitudinal difference in thermospheric conditions (neutral composition), which affects the integrated Pedersen conductivity.

## 20.4. SUMMARY

The NRL SAMI3/ESF three-dimensional ionosphere model is used to study the effect of magnetic declination on the development of large-scale plasma bubbles in the postsunset equatorial *F* region. The study focuses on the role of conductance gradients as opposed to the development of the background ionosphere (e.g., prereversal electric-field enhancement). We find that plasma bubbles develop faster when the magnetic declination angle is zero (i.e., the magnetic field points to true north) because the flux-tube integrated Pedersen conductivity is minimized for this situation. However, the reduction in the growth rate for situations where the magnetic declination angle is nonzero is ≲20% for the cases studied. Thus, the declination angle does not appear to be a major effect in explaining the longitudinal dependence of equatorial plasma-bubble development for similar ionospheric conditions. This suggests that the longitudinal variations in equatorial spread *F* are related to global thermospheric/ionospheric conditions (e.g., ionospheric electric field [*Yizengaw et al.*, 2012], meridional winds [*Huba and Krall*, 2013]).

## ACKNOWLEDGMENTS

This research has been supported by NRL 6.1 Base Funds.

## REFERENCES

Booker, H. G., and H. G. Wells (1938), Scattering of radio waves by the *F*-region of the ionosphere, *Terr. Mag. Atmos. Elec. 43*, 249; doi:10.1029/TE043i003p00249.

Drob, D. P., J. T. Emmert, J. W. Meriwether, J. J. Makela, E. Doornbos, M. Conde, G. Hernandez, J. Noto, K. A. Zawdie, S. E. McDonald, J. D. Huba, and J. F. Klenzing (2015), An update to the Horizontal Wind Model (HWM): The quiet time thermosphere, *Earth and Space Sci., 2*, 301–319; doi:10.1002/2014EA000089.

Haerendel, G. (1974), Theory of equatorial spread *F*, preprint, Max-Planck Inst. für Extraterr. Phys., Munich, Germany.

Hain, K. (1987), The partial donor cell method, *J. Comput. Phys.*, *73*, 131.

Huba, J. D. (2003), A tutorial on Hall magnetohydrodynamics, 170, in *Space Plasma Simulation*, ed. J. Büchner, C.T. Dum, and M. Scholer, Springer, New York.

Huba, J. D., and J. Krall (2013), Impact of meridional winds on equatorial spread *F*: Revisited, *Geophys. Res. Lett. 40*; doi:10.1002/grl.50292.

Huba, J. D., G. Joyce, and J. A. Fedder (2000), SAMI2 (Sami2 is Another Model of the Ionosphere): A new low-latitude ionosphere model, *J. Geophys. Res.*, *105*, 23,035–23,053; doi:10.1029/2000JA000035.

Huba, J. D., G. Joyce and J. Krall (2008), Three-dimensional equatorial spread *F* modeling, *Geophys. Res. Lett. 35*, L10102; doi:10.1029/2008GL033509.

Huba, J. D., P. K. Chaturvedi, S. L. Ossakow, and D. M. Towle (1978), High frequency drift waves and wavelengths below the ion gyroradius in equatorial spread *F, Geophys. Res. Lett*. *5*, 695; doi:10.1029/GL005i008p00695.

Hysell, D. L. (2000), An overview and synthesis of plasma irregularities in equatorial spread *F*, *J. Atmos. Sol. Terr. Phys.*, *62*, 1037; doi:10.1016/S1364-6826(00)00095-X.

Krall, J., J. D. Huba, G. Joyce, and S. Zalesak (2009), Three-dimensional simulation of equatorial spread-*F* with meridional wind effects, *Ann. Geophys. 27*, 1821–1830; doi:10.5194/angeo-27-1821-2009.

Makela, J. J. (2006), A review of imaging low-latitude ionon-spheric irregularity processes, *J. Atmos. Solar-Terr. Phys.*, *68*, 1441–1458; doi:10.1016/j.jastp.2005.04.014.

Maruyama,T., S. Saito, M. Kawamura, K. Nozaki, J. Krall, and J. D. Huba (2009), Equinoctial asymmetry of a low-latitude ionosphere-thermosphere system and equatorial irregularities: Evidence for meridional wind control, *Ann. Geophys. 27*, 2027–2034; doi:10.5194/angeo-27-2027-2009.

Ossakow, S. L. (1981), Spread *F* theories: A review, *J. Atmos. Terr. Phys.*, *43*, 437–452; doi:10.1016/0021-9169(81)90107-0.

Picone, J. M., A. E. Hedin, D. P. Drob, and A. C. Aikin (2002), NRLMSISE-00 empirical model of the atmosphere: Statistical comparisons and scientific issues, *J. Geophys. Res. 107*; doi: 10.1029/2002JA009430.

Sultan, P. J. (1996), Linear theory and modeling of the Rayleigh-Taylor instability leading to the occurrence of equatorial spread *F*, *J. Geophys. Res.*, *101*, 26,875–26,891; doi:10.1029/96JA00682.

Tsunoda, R. T. (1985), Control of the seasonal and longitudinal occurrence of equatorial scintillations by the longitudinal gradient in the integrate *E* region Pedersen conductivity, *J. Geophys. Res.*, *90*, 447–456; doi:10.1029/JA090iA01p00447.

Yizengaw, E., E. Zesta, M. B. Moldwin, B. Damtie, A. Mebrahtu, C. E. Valladares, and R. F. Pfaff (2012), Longitudinal differences of ionospheric vertical density distribution and equatorial electrodynamics, *J. Geophys. Res.*, *117*, A07312; doi:10.1029/2011JA017454.

# 21

# Global Ionospheric Electron Density Disturbances During the Initial Phase of a Geomagnetic Storm on 5 April 2010

**Chigomezyo M. Ngwira[1] and Anthea J. Coster[2]**


## ABSTRACT

Ionospheric storms are a manifestation of solar wind interaction with the Earth's magnetosphere, and in one of their forms appear as modification of the electron density in the ionosphere. The major focus of this case study is on global ionospheric response characteristics during the initial phase (first 12 hr after storm commencement) of a geomagnetic storm that started on 5 April 2010, when minimum $D_{st}$ reached ~–60 nT. We use a synergy between in situ satellite measurements and ground-based observations in combination with numerical modeling to examine the dayside ionospheric response during this initial phase. Total electron content (TEC) differences between the observed TEC on the storm-day and the preceding quiet-day TEC are presented. Results show that both strong and persistent storm-enhanced density features, and deep TEC depletions were present during the storm. We propose electric field-driven ion vertical drifts as the major controlling process in the development of positive ionospheric disturbances with likely contribution from other mechanisms such as neutral winds and composition changes. Disturbance dynamo electric fields are the likely candidate for the development of strong TEC depletions.

**Key Points:**
We examine the dayside global ionospheric response characteristics during the initial phase of a storm.
Both strong long-lasting enhanced TEC and deep TEC depletions were present.
Propose electric field-driven ion vertical drifts as the major controlling process, with contribution from other mechanisms.


**Key Terms:** ionospheric storms, total electron content, storm enhanced density, electric fields, neutral winds, and composition changes.

## 21.1. INTRODUCTION

Ionospheric storms are a manifestation of solar wind interaction with the Earth's magnetosphere. Storm-time energy dissipation in the polar regions can lead to profound large-scale changes of the quiet-time upper atmosphere. Global upper-atmospheric changes can in turn enhance (positive) or reduce (negative) the large-scale electron density [see, e.g., *Fuller-Rowell et al.*, 1994; *Buonsanto*,

[1]*Department of Physics, Catholic University of America, Washington, D.C., USA; and Space Weather Laboratory, NASA Goddard Space Flight Center, Greenbelt, Maryland, USA*
[2]*Haystack Observatory, Massachusetts Institute of Technology, Westford, Massachusetts, USA*

*Ionospheric Space Weather: Longitude and Hemispheric Dependences and Lower Atmosphere Forcing, Geophysical Monograph 220*, First Edition. Edited by Timothy Fuller-Rowell, Endawoke Yizengaw, Patricia H. Doherty, and Sunanda Basu.

1999; *Mendillo*, 2006]. Ionospheric storms are important because they lead to changes in the electron density that can adversely affect transionospheric radio signals such as those used by Global Navigation Satellite System (GNSS) applications. Inland marine navigation and airborne navigation are good examples of critical GNSS applications affected by ionospheric storms.

The appearance of positive and negative storm effects is dependent on the latitude, local time, and phase of the storm. The primary control mechanisms that are responsible for the different storm effects have been broadly investigated using observational and modeling techniques and are well documented [e.g., *Buonsanto*, 1999; *Coster et al.*, 2003; *Burns et al.*, 2007; *Crowley et al.*, 2010; *Zou et al.*, 2013]. There is general agreement within the science community that negative storms are caused by neutral composition changes [see, e.g., *Mendillo*, 2006]. In contrast, origins of positive storms are still largely a subject of debate. Therefore, several physical mechanisms have been proposed to explain their generation [see, e.g., *Foster*, 1993; *Werner et al.*, 1999; *Huang et al.*, 2005; *Ngwira et al.*, 2012b; *Li et al.*, 2012].

Storm-time electron density enhancements, also known as storm enhanced density (SED), can be grouped into several classes depending on the duration, local time, and latitude. One frequently observed class of SED is characterized by a short-duration dayside enhancement of the midlatitude ionospheric electron density. This is usually attributed to middle and upper atmospheric dynamics induced by atmospheric gravity waves that are launched in the high latitudes and travel to midlatitudes during storms or substorms [see, e.g., *Prölss and Jung* 1978; *Werner et al.*, 1999]. The equatorward disturbance winds act by pushing plasma up along magnetic field lines to higher altitudes where the plasma loss rate is low, and subsequently results in an increase of plasma density at *F*-region heights. Furthermore, large enhancements in *F*-region electron density are usually observed in the local dusk sector during geomagnetic storms and are termed the "dusk effect."

The dusk effect is suggested to be associated with sunward convection of high-density plasma from the low latitudes [see, e.g., *Foster*, 1993]. SED features can also manifest as spatially narrow, distinct, regions of enhanced TEC, commonly referred to as SED plumes, that are observed in the postnoon and premidnight sectors extending from the equatorward edge of the main ionospheric trough to the noontime cusp [e.g., *Foster*, 1993; *Yizengaw et al.*, 2008; *Coster and Skone*, 2009]. SED/TEC plumes are related to the erosion of the midlatitude ionosphere and outer plasmasphere by the subauroral polarization stream electric field [e.g., *Foster et al.*, 2002; *Yizengaw et al.*, 2006].

Major changes in ionospheric electron density can also be produced by intensified storm-time electric fields emanating from the solar wind and magnetosphere-ionosphere interaction. The storm-time electric fields have been classified as the direct prompt penetration electric field associated with magnetospheric convection [e.g., *Kelley et al.*, 2003; *Tsurutani et al.*, 2004], and/or the ionospheric disturbance dynamo electric field, with a characteristic delayed development, driven by Joule heating at auroral latitudes, which changes the global circulation pattern in the thermosphere and the ionosphere [e.g., *Blanc and Richmond*, 1980; *Fejer and Scherliess*, 1997].

Generally many previous ionospheric storm studies have focused on understanding the morphological, electrodynamic and chemical processes that accompany intense or severe geomagnetic disturbances with $D_{st}$ index less then −100 nT [e.g., *Mannucci et al.*, 2005; *Pedatella et al.*, 2009; *Ngwira et al.*, 2012a; *Katamzi and Habarulema*, 2013, and references therin]. However, other studies show that in some instances the ionosphere-thermosphere system responds dramatically to minor and moderate ($D_{st}$ between −30 and −70 nT) geomagnetic storm disturbances [e.g., *Pi et al.*, 2000; *Goncharenko et al.*, 2006, and references therin]. Consequently, there has been a renewed interest in the science community that has fueled recent increase in the number of studies investigating the ionospheric response during minor geomagnetic disturbances [e.g., *Goncharenko et al.*, 2007; *Lu et al.*, 2008; *Lei et al.*, 2008; *Li et al.*, 2012; *Ngwira et al.*, 2013, and references therein].

The geomagnetically active period of 5–10 April 2010 is widely studied since it produced the largest geomagnetic activity in the recent solar minimum period [see, e.g., *Wilder et al.*, 2012; *Clilverd et al.*, 2012; *Shimeis et al.*, 2012; *Wilder et al.*, 2013; *Fathy et al.*, 2014]. For instance, *Shimeis et al.* [2012], analyzed the low-latitude ionospheric and geomagnetic signatures of the storm event for stations in Egypt. Their analysis showed that the large storm-time electron density increase observed at the early phase of the storm was driven by prompt penetration of magnetospheric electric fields, while signatures of ionospheric disturbance dynamo due to wind generated by Joule heating in the auroral zone dominated in the recovery phase. Using AMPERE (Active Magnetosphere and Planetary Electrodynamics Response Experiment) data as an input to the Assimilative Mapping of Ionospheric Electrodynamics (AMIE) algorithm, *Wilder et al.* [2012] investigated the deposition of energy in the dayside ionosphere. They demonstrated the presence of intense ionospheric Joule heating in the dayside polar regions during the recovery phase of the storm on 5 April. More recently, a case study by *Fathy et al.* [2014] examined the magnetic disturbance associated with the ionospheric disturbance dynamo in the European-African, Asian, and American longitude sectors and reported that the strongest effects were observed during the daytime in the European-African sector on 5 April.

While many of the studies highlighted above are focused on specific regional sectors of the Earth, the purpose

of the present paper is to provide a global picture of ionospheric characteristics in the initial phase of a geomagnetic storm that commenced on 5 April 2010, and reached a minimum $D_{st}$ of ~−60 nT. It is important to note that the main phase of this geomagnetically active period of 5–10 April occurred on 6 April with a $D_{st}$ minimum around −100 nT. However, for the present study,we consider only the first 12 hr after onset of this storm when the largest solar wind energy injection was experienced.

In this study, we employ a multiinstrument approach comprising in situ satellite measurements, ground-based observations, and numerical modeling. We first present the interplanetary conditions before closely examining the global ionospheric features and their evolution. Then to understand the underlying physical processes responsible for the observed storm-time disturbances, we examine solar wind [*Akasofu*, 1981] and high-latitude energy dissipation characteristics [*Ostgaard et al.*, 2002; *Knipp et al.*, 2004], direct observations of the thermosphere extracted from the Global Ultraviolet Imager (GUVI) instrument [*Christensen et al.*, 2003], and model results from the Thermosphere-Ionosphere Electrodynamics General Circulation Model (TIE-GCM) [e.g., *Richmond et al.*, 1992].

## 21.2. DATA SOURCES

There are approximately 29 operational GPS (Global Positioning System) satellites transmitting radio signals in the L-band on two coherent carrier frequencies at f1 = 1.575 GHz and f2 = 1.228 GHz. GPS satellite signals offer unprecedented opportunities for ionospheric research. The phase delay in the dual frequency radio-wave signals from the GPS satellites to ground receivers allow for the estimation of total electron content (TEC) by difference techniques. The global availability of GPS signals creates an opportunity for the ionospheric community to monitor the TEC at any dual frequency GPS ground station on the globe. To get a clear picture of the global evolution of the storm, we make use of global GPS TEC maps readily provided by the MIT Haystack Observatory through the Madrigal database. Detailed information of the data-processing methods utilized to derive the observations of ground-based GPS TEC is given by *Rideout and Coster* [2006]. The variations in the ionospheric electron density as inferred from the vertical TEC values determined from the global network of ground-based GPS receivers using the standard ionospheric mapping function are discussed by *Coster et al.* [2003].

For this study, direct observations of the thermospheric drivers needed to explain the ionospheric behavior have been extracted from the GUVI instrument on board the NASA TIMED satellite. The NASA TIMED mission's primary purpose is to investigate the energetics and dynamics of the mesosphere and lower thermosphere region. GUVI provides remote sensing observations of the column-integrated $O/N_2$ ratio [*Christensen et al.*, 2003]. The $O/N_2$ ratio can be determined from GUVI dayglow measurements in the OI (135.6 nm) and N2 LBHs channels (135.6/LBHs) [*Strickland et al.*, 2004]. GUVI measures a narrow belt beneath the satellite track, thus does not provide a global snapshot. However, a global picture is acquired after about 15 orbits that are typically completed over a day. The TIMED orbit precesses slowly, thus, over a few days, the data are all gathered within a small range of local times.

The TIE-GCM is a global 3-D numerical model developed and maintained by the National Center for Atmospheric Research. The model self-consistently solves the fully coupled, nonlinear, hydrodynamic, thermodynamic, and continuity equations of the neutral gas, the ion and electron energy and momentum equations, the ion continuity equation, and neutral wind dynamo [e.g., *Richmond et al.*, 1992]. The model simulates the coupled thermosphere/ionosphere system from ~97 to ~600 km altitude, and calculates global distributions of the neutral gas temperature and winds, the height of the constant pressure surface, and the number densities of the major constituents $O_2$, $N_2$, and O, and of some minor neutral constituents. A full description of the TIE-GCM is available in reports by, for example, *Richmond et al.* [1992] and *Qian et al.* [2013].

For the present study, the TIE-GCM open-source community model was run using high-latitude ionospheric electric fields provided by the empirical Weimer 2005 model [*Weimer*, 2005]. A description of how this empirical model is implemented in the TIE-GCM is documented by *Solomon et al.* [2012], while the open-source TIE-GCM model is available through the runs-on-request system at the Community Coordinated Modeling Center (CCMC) resident at NASA Goddard Space Flight Center.

## 21.3. OBSERVATIONS AND RESULTS

Following a coronal mass ejection that was first observed to leave the Sun on 3 April 2010 [*Möstl et al.*, 2010], a geomagnetic storm occurred on 5 April 2010 after a sudden storm commencement (SSC) around 0827 UT signaling the shock arrival as indicated by the vertical dashed line in Figure 21.1. This figure displays OMNI time-shifted solar-wind interplanetary conditions and ground-based geomagnetic indices for 4–6 April 2010. The interplanetary magnetic field (IMF) $B_z$ southward component rapidly intensified from ~−2.5 nT to −15 nT, while the IMF $B_y$ suddenly turned positive. The solar wind speed jumped from around 575 km/s to about 740 km/s, and remained relatively highly for ~2.5 hours, then further increased to about 800 km/s. At the time of the SSC, the solar-wind particle density increased from around 2 to 9 particles/cc.

At the Earth's surface, the SSC manifested as a sudden increase in the $D_{st}$ index, represented by its high resolution 1-min equivalent SYM-H index. Soon after the SSC, the $D_{st}$ steadily decreased to a peak negative value of about

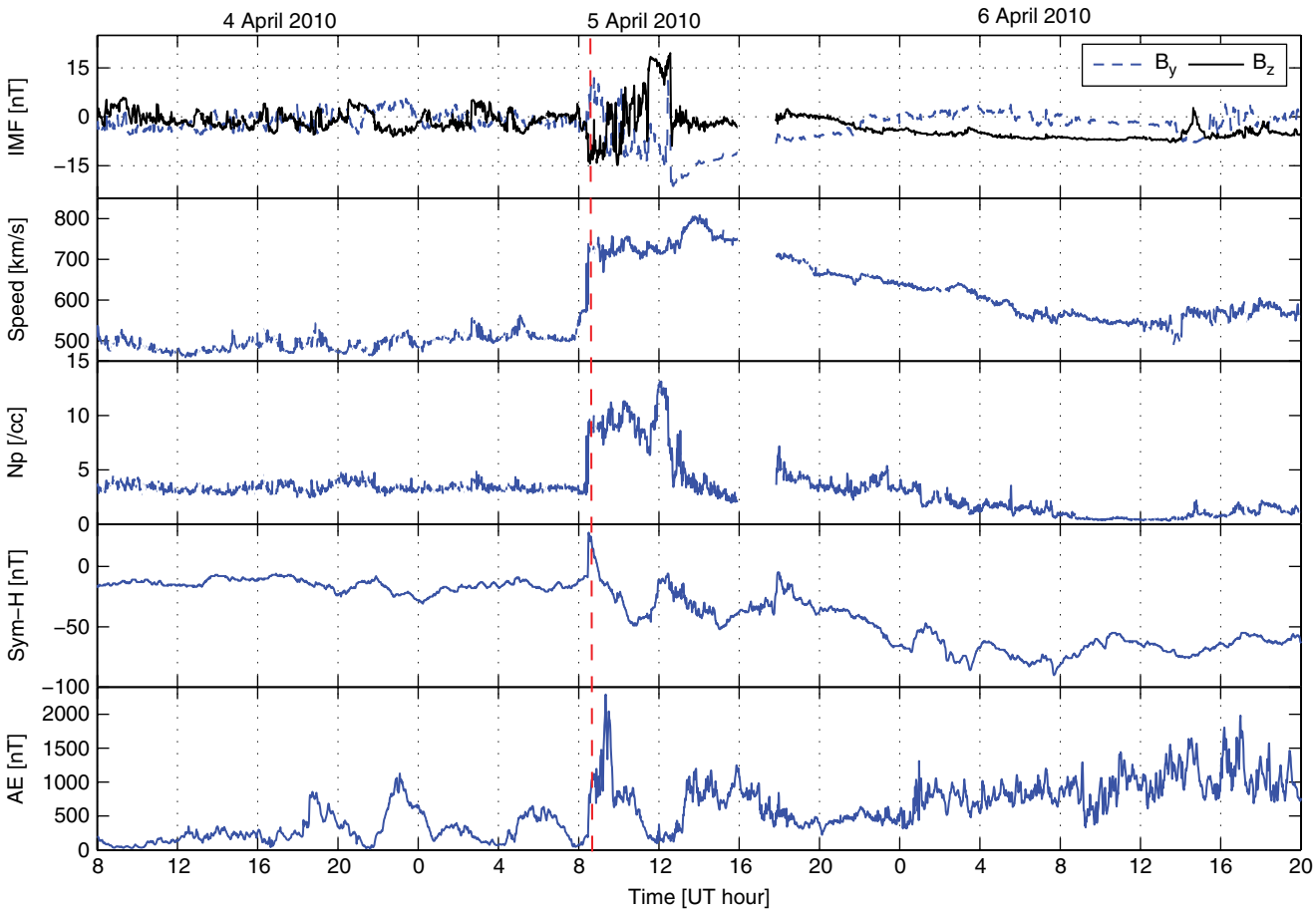


**Figure 21.1** Interplanetary solar wind and ground-based geomagnetic conditions for 4–6 April 2010. From top to bottom are IMF $B_y$ (blue dashed trace) and IMF $B_z$ (black trace), solar wind bulk speed, density (Np), geomagnetic SYM-H index, and AE index. The shock arrival time is represented by the vertical red line.

–48 nT at around 1100 UT followed by a recovery to the prestorm levels. This recovery is consistent with the variations of the IMF $B_z$, which suddenly turned from southward to northward as shown in Figure 21.1. About 2 hr after the recovery, a second storm phase developed where a minimum value of –51 nT was reached. The storm main-phase peak occurred on 6 April at about 0740 UT with a minimum $D_{st}$ near –100 nT. At high latitudes, the auroral electroject (AE) index was enhanced soon after the SSC on 5 April for about 3 hr reaching a peak value over 2000 nT after 0900 UT. After the peak, the AE sharply decreased to around 1000 nT where it fluctuated for about an hour before returning to prestorm levels for 2 hr. Then AE increased again on 5 April at about 1300 UT to a value around 1000 nT and gradually reduced after 1700 UT. AE was mostly enhanced on 6 April when $B_z$ was dominantly southward for an extend period of the day.

To analyze temporal and spatial distribution of electron density, we use ground-based GPS TEC data. The TEC maps displayed in the present study use TEC data derived according to the method described in the previous section. To examine the TEC variations during the storm, we determine the deviation of storm-time TEC by taking the difference for 5 April with respect to quiet-time TEC on 4 April 2010, that is., $\Delta\text{TEC} = \text{TEC}_{stormday} - \text{TEC}_{quietday}$. The resulting TEC deviations are shown in Figure 21.2 for the period 0800 UT to 1300 UT. Both negative and positive TEC response features are present. The negative TEC regions are mainly observed on the nightside in the American sector, while strong (i.e., $\Delta\text{TEC} > 15$ TECU) SED features manifest in African/Europe and Asian/Australian sectors with low-level patches of SED observed over North America. For these specific TEC observations, we consider only features lying in longitudes from 0° to 180° that correspond to the dayside ionosphere at the time of the SSC. There are large areas without data on the dayside, however, large SED regions are observed mainly over Africa/Europe longitudes in both hemispheres. The strongest enhancements appear between 1200 UT and 1300 UT in the Southern Hemisphere.

Figure 21.3 displays the TEC deviations for the time period from 1400 UT to 2000 UT. For these examples, we consider the response in the longitudes from −180 to 0 representing the dayside ionosphere covering the

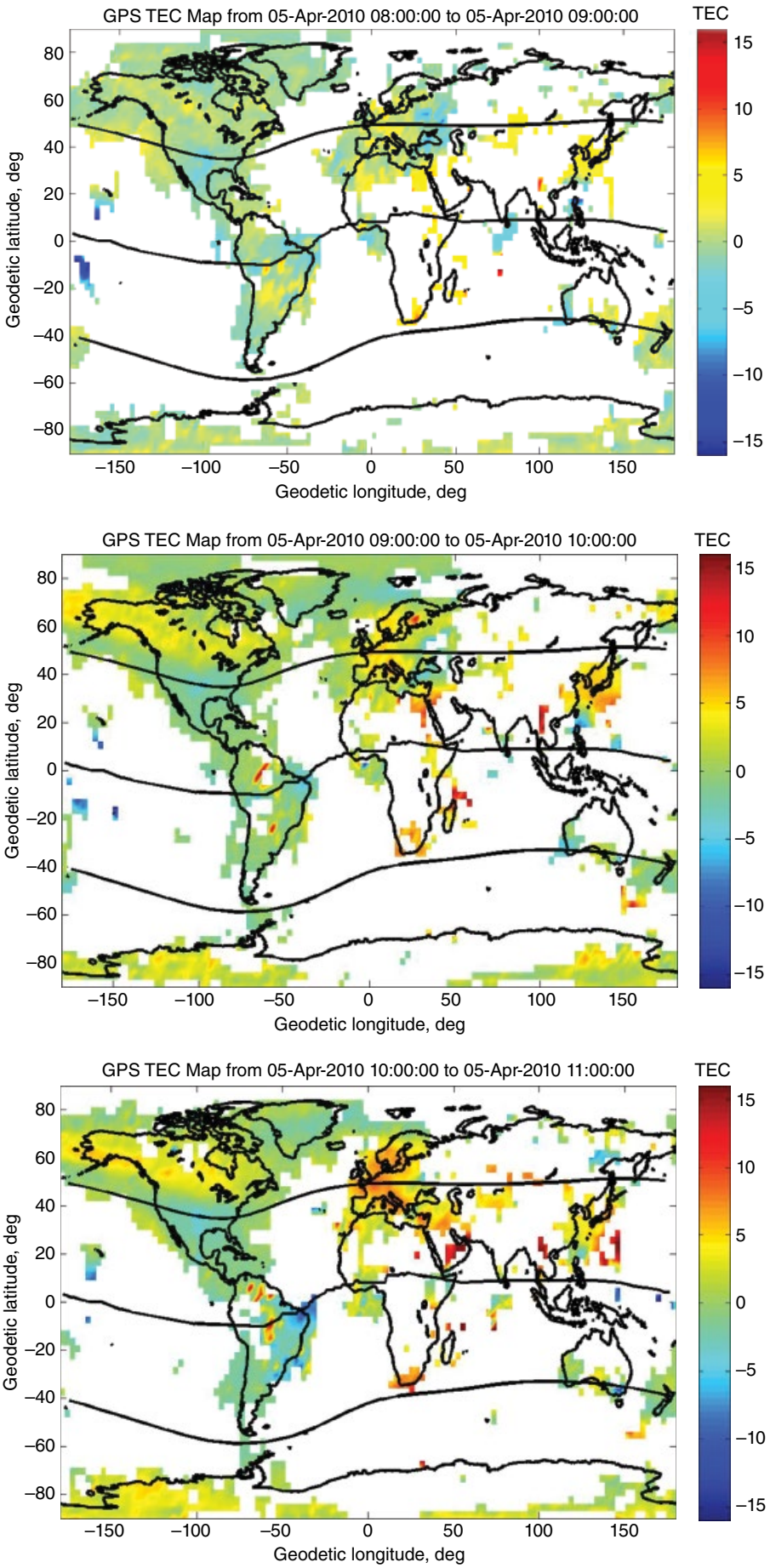


**Figure 21.2** Global differential GPS TEC on 5 April (storm day) relative to 4 April (quiet day) for the period 08:00 UT to 14:00 UT. Peak TEC values exceeded 30 TECU during this period, while the color code saturates at 15 TECU in order to better capture the storm response.

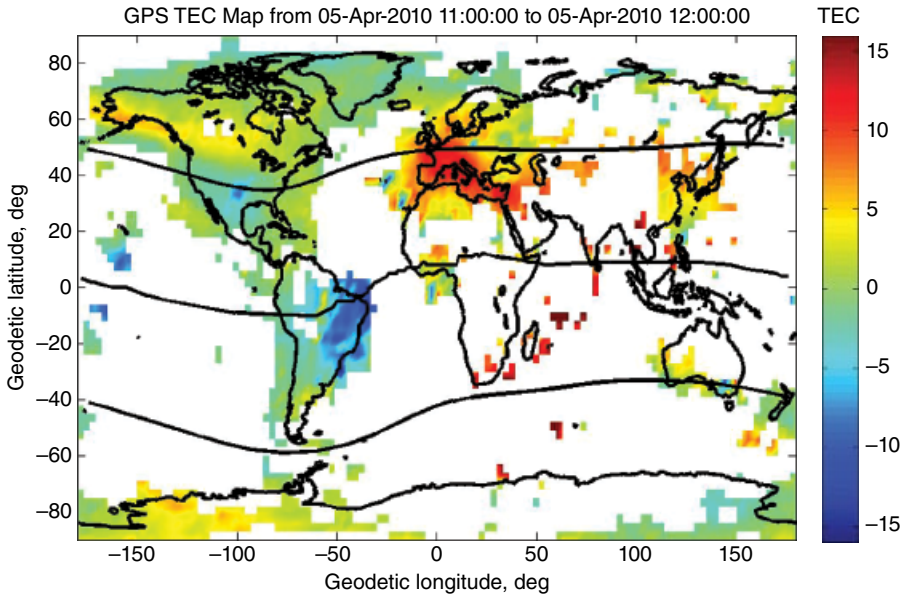


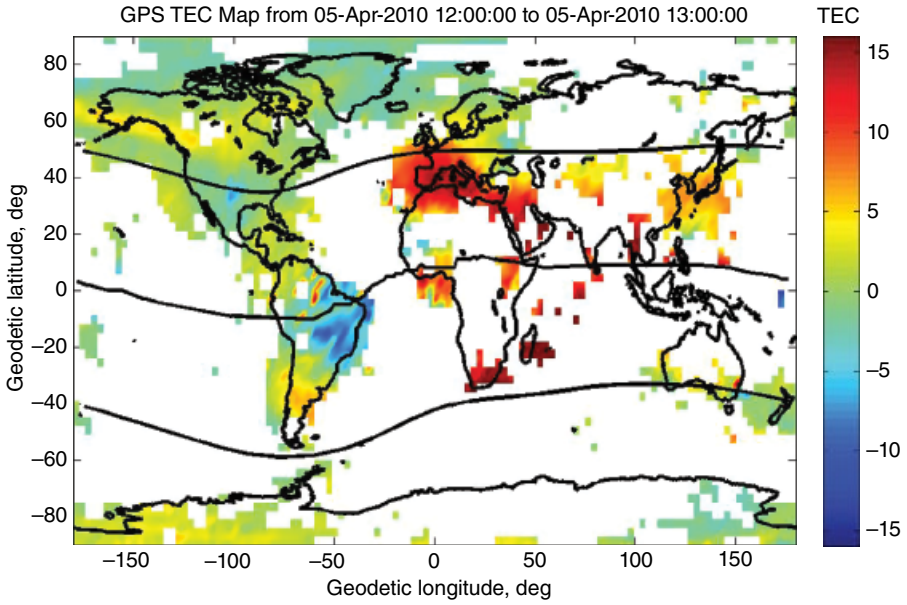


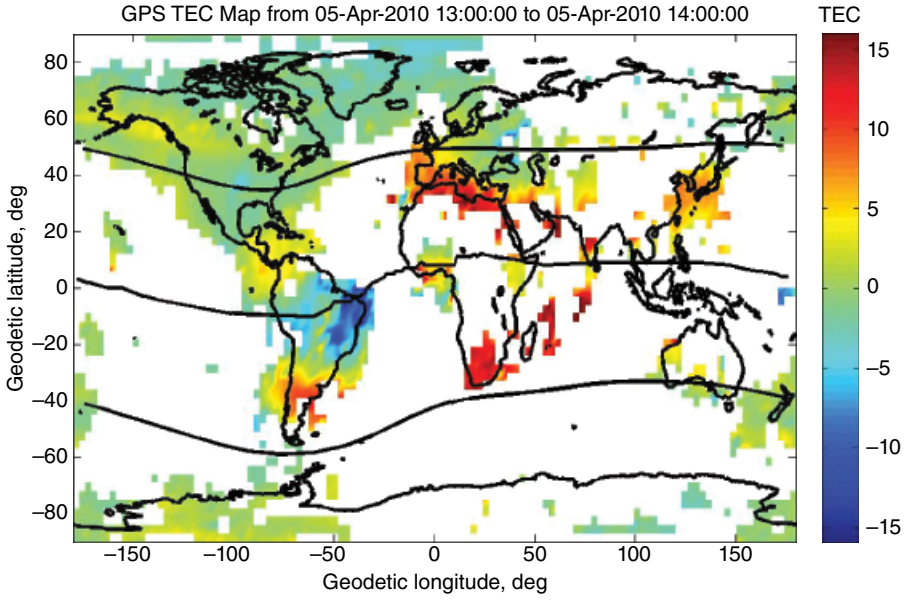


**Figure 21.2** (Continued)

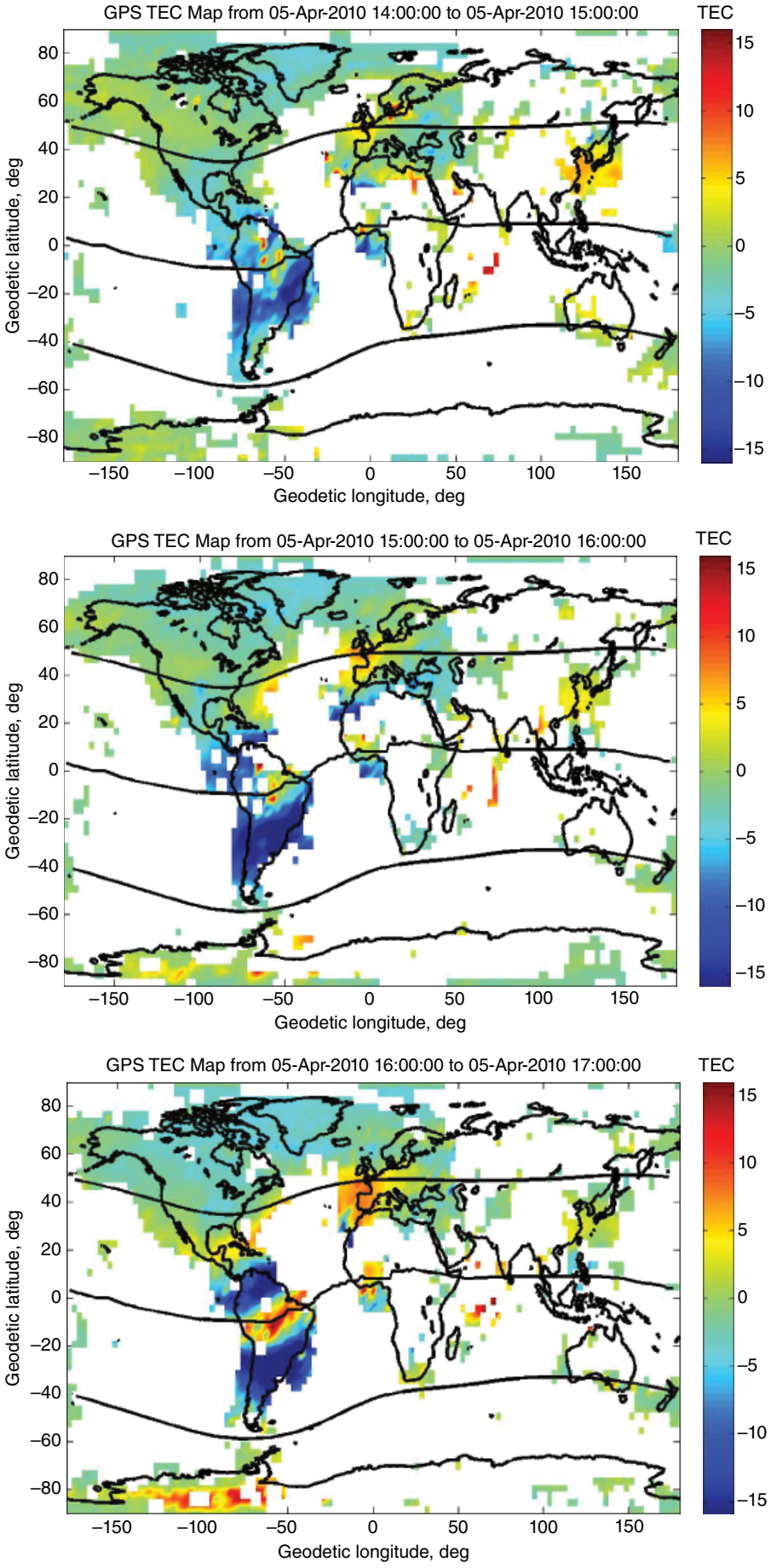


**Figure 21.3** Same as Figure 21.2, but for the time interval from 14:00 UT to 20:00 UT.

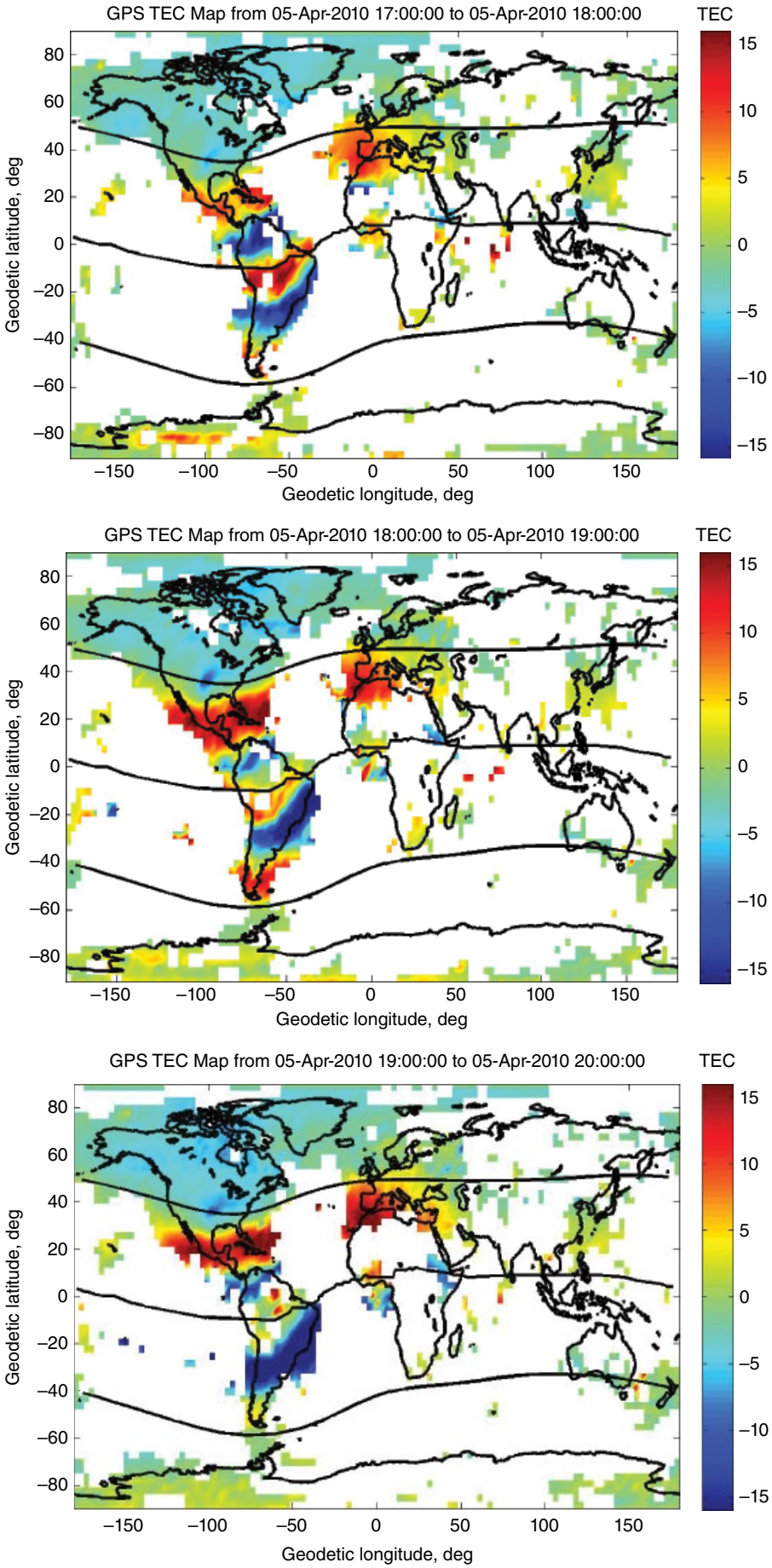


**Figure 21.3** (Continued)

American sector and western regions of Africa/Europe. In the selected longitudes, it is immediately noted that there are SED structures over the geomagnetic equator. In all cases, we see evidence of marked hemispherical differences with very deep plasma depletions in the Southern Hemisphere, while the Northern Hemisphere has strong enhancements. A negative TEC phase is prevalent over most of the high latitudes in North America, but a persistent enhanced TEC region appears over northern Africa and southern Europe. Then around 1900–2000 UT enhanced TEC regions have disappeared in southern low latitudes to midlatitudes of the American sector. Both Figures 21.2 and 21.3 show what looks like a SED plume in the Antarctic region, while density depletion exists in the Arctic, most notably during the period from 1300 UT to 2000 UT.

By using digital interplanetary solar wind data (IMF, speed and density) in conjunction with ground geomagnetic field measurements, we derive and examine the solar wind energy-coupling efficiencies, and the corresponding magnetosphere-ionosphere energy dissipation characteristics on 4–6 April. Figure 21.4 depicts the Akasofu (top) solar wind coupling function [*Akasofu*, 1981], and estimates of the Joule heating (middle) and auroral precipitation (bottom) energy deposition. The Joule heating is derived from the polar cap (PC) index using the method of *Knipp et al.* [2004], while the auroral precipitation is calculated from the auroral electrojet (AE) index using formulation described by *Ostgaard et al.* [2002].

Evidently, all parameters in Figure 21.4 illustrate that there was a significant increase of energy activity after 0800 UT that lasted to 1100 UT on 5 April. The start

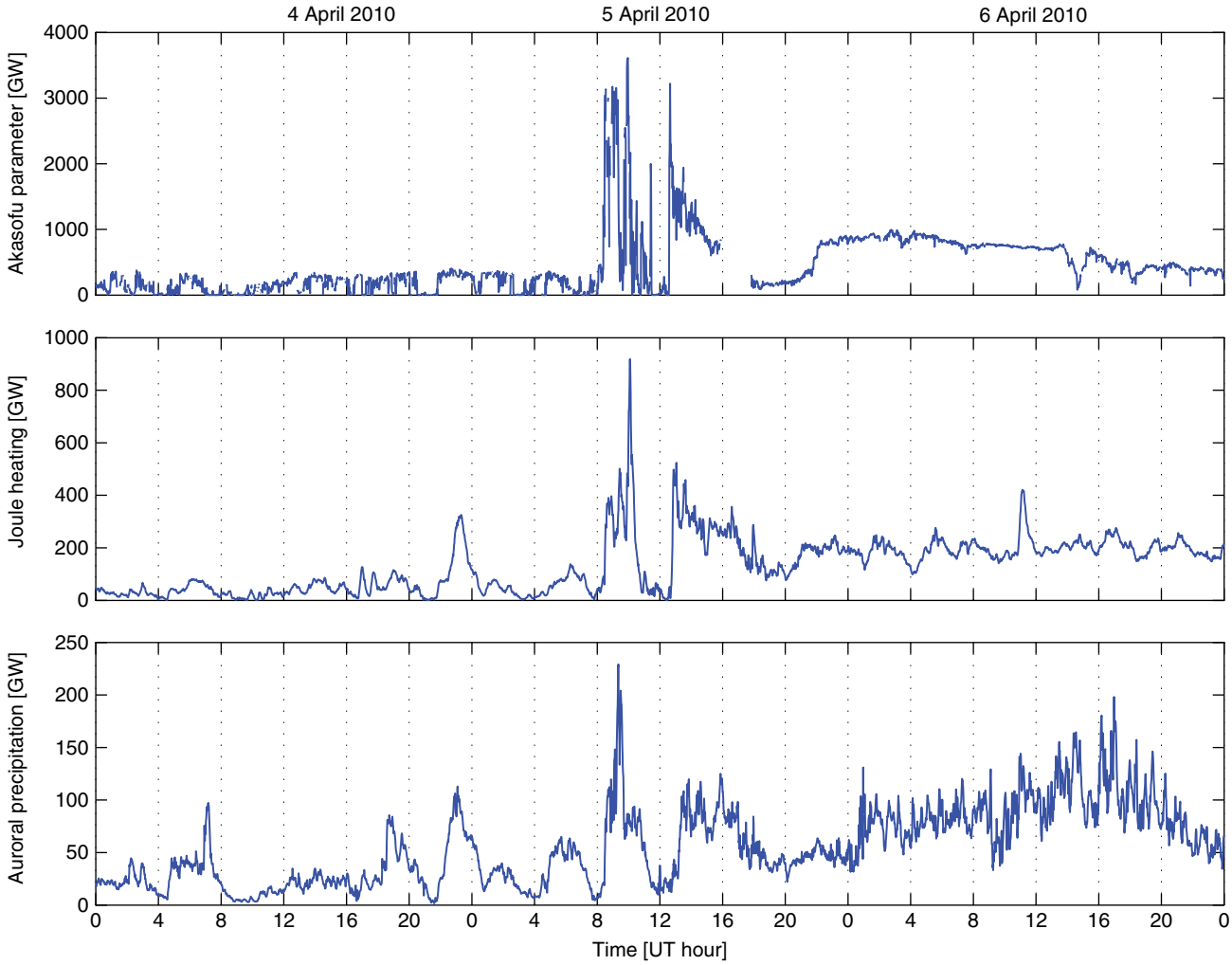


**Figure 21.4** Solar wind Akasofu coupling function (top), and estimates of Joule heating (middle) and auroral precipitation energy dissipation at high latitudes (bottom) for the geomagnetic conditions on 4–6 April 2010.

time is consistent with the time of the SSC identified in Figure 21.1. A second energy dissipation surge is also seen after 1300 UT and lasts for the remainder of the day. The commencement of this second surge is consistent with changes in the solar wind that show that the IMF $B_z$ and $B_y$ both sharply reversed from positive to negative. Energy levels were relatively high on 6 April (most notably the auroral precipitation) but were more than 30% lower than peak levels observed on 5 April.

The electric field plays a major role on the density distribution of the low-latitude ionosphere and largely controls the equatorial ionization anomaly (EIA). To examine the contribution of electric fields in generating the ionospheric disturbances, we turn to TIE-GCM simulations. Figure 21.5 depicts the distribution of TIE-GCM model vertical ion drifts associated with electric fields determined in the simulations for 4 April (left) and 5 April (right). Clearly, significant vertical ion drift differences can be seen by comparing each panel on the left (quiet day) to the corresponding panel on the right (storm day). For example, at 0700 UT, vertical drift patterns on both days look similar, except in the North American sector where there appears to be a prereversal enhancement on the storm day. However, there is a dramatic change at 0900 UT when large drifts in excess of 80 m/s appear mostly at high latitudes on the storm day (right) and in the Australia/Japan sector.

Results in Figure 21.6 show the distribution of TIE-GCM model vertical ion drifts related to the TEC variability in Figure 21.3 that corresponds to the second phase of the storm, which occurred around 1500 UT. As before, the right panels depict the drifts on the storm day, which show notable upward vertical drifts existing across the mid to low latitudes in comparison with the quiet day in the left panels.

To investigate meridional wind effects on TEC variation, we examine the distribution of neutral gas meridional drifts using TIE-GCM as displayed in Figure 21.7. The

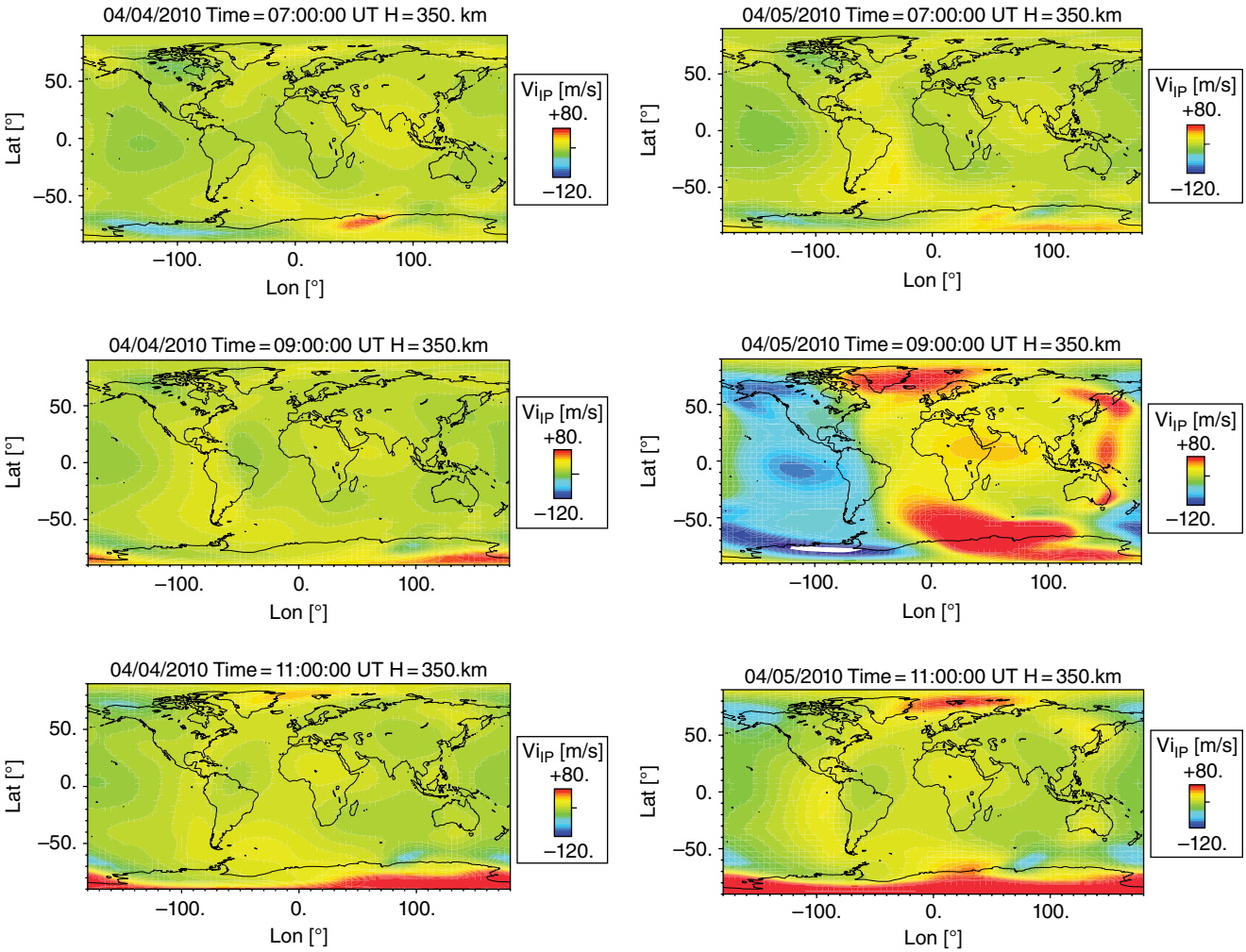


**Figure 21.5** Global distributions of the TIE-GCM-modeled ion plasma vertical drifts ($V_i$ in m/s) on 4 April (left) and 5 April (right).

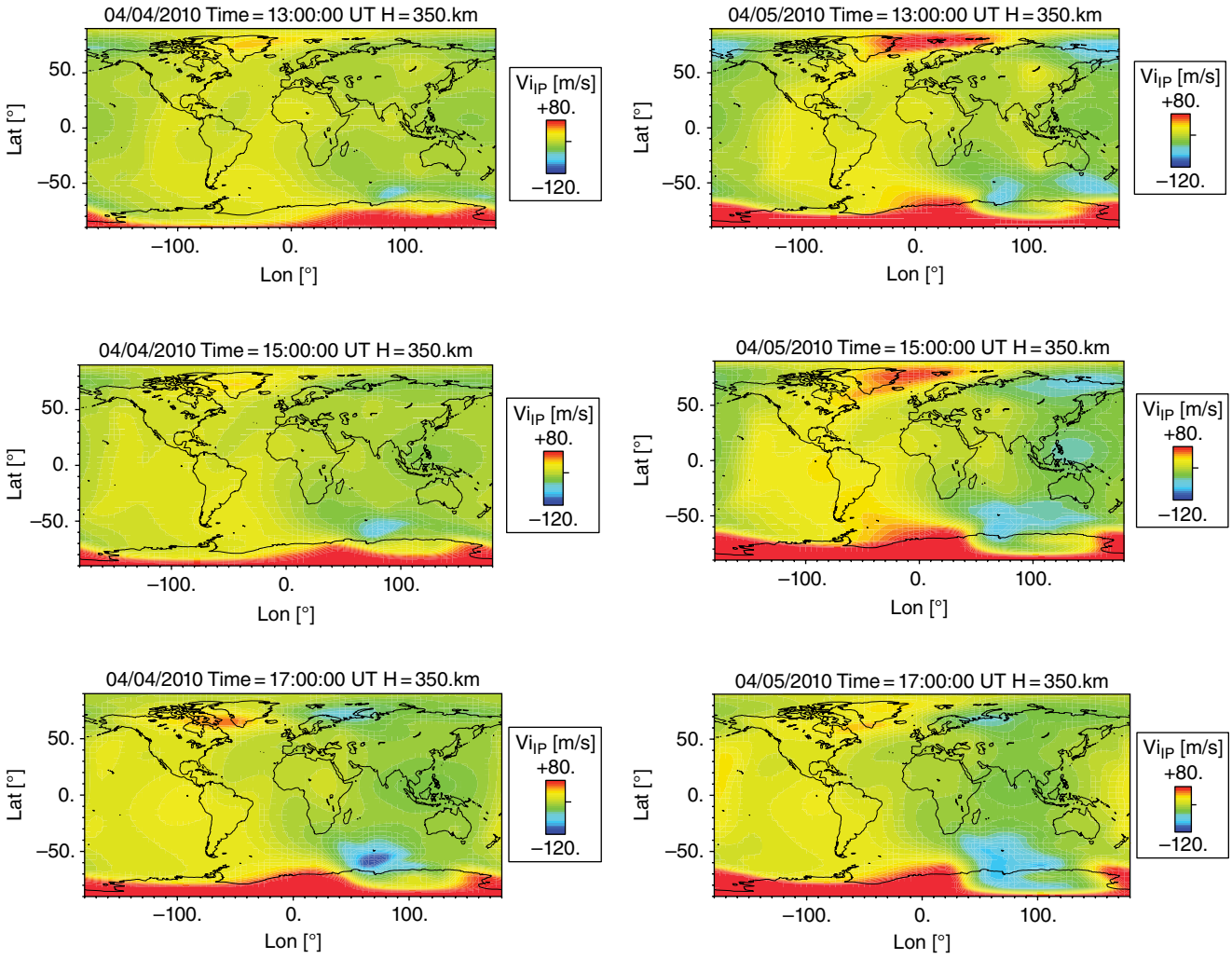


**Figure 21.6** Same as Figure 21.5 but for the time interval from 13:00 to 17:00 UT.

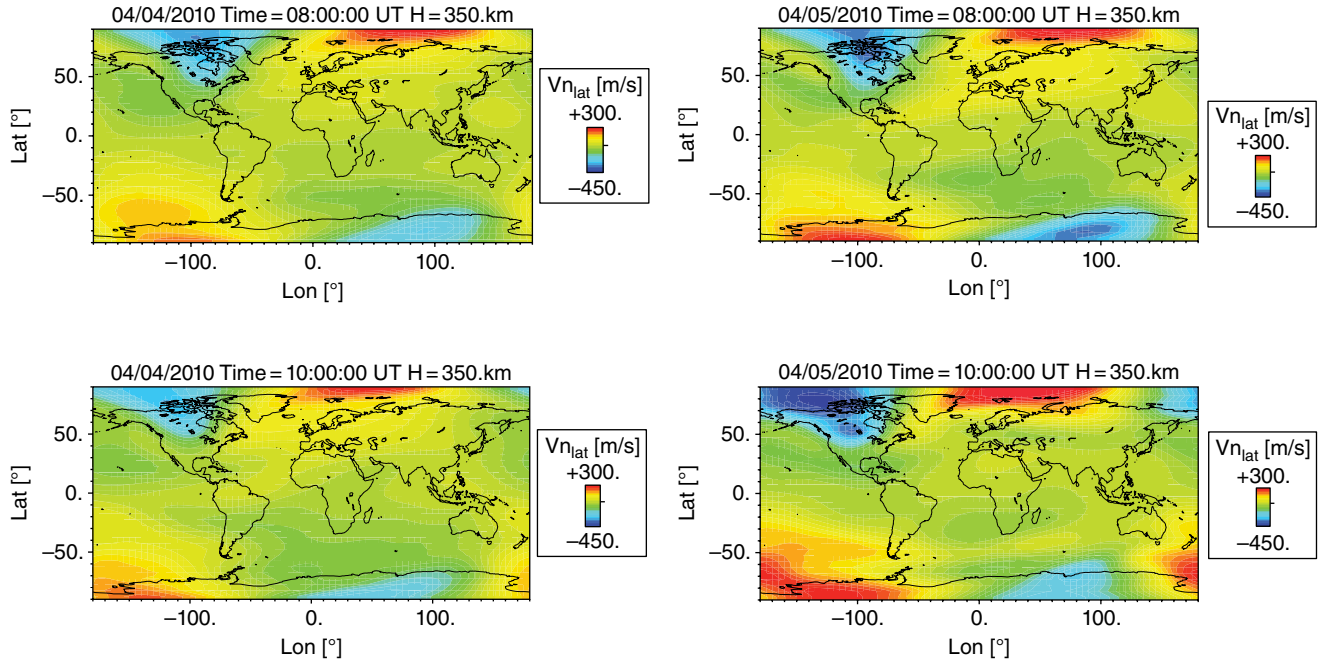


**Figure 21.7** Global distribution of the TIE-GCM-modeled neutral gas meridional velocity component, $V_n$, in m/s. The plots cover the time interval from 08:00 to 12:00 UT. The velocity is positive northward.

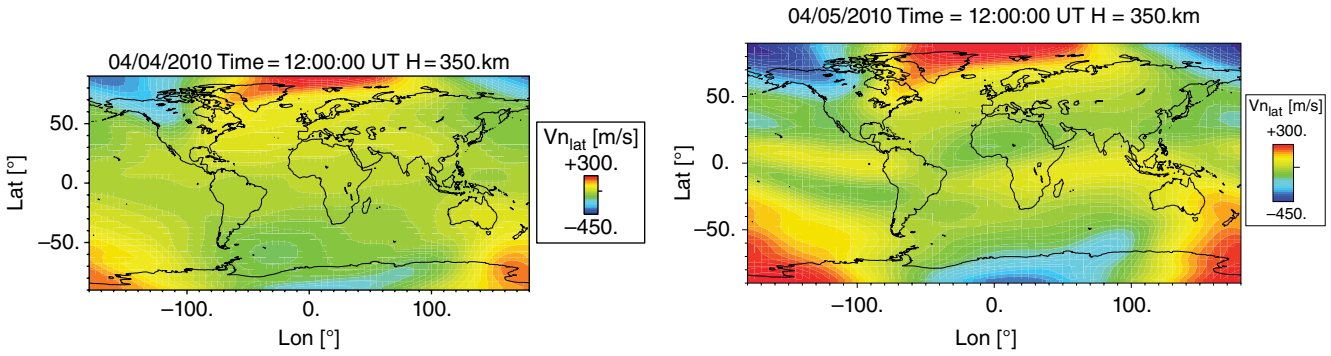


**Figure 21.7** (Continued)

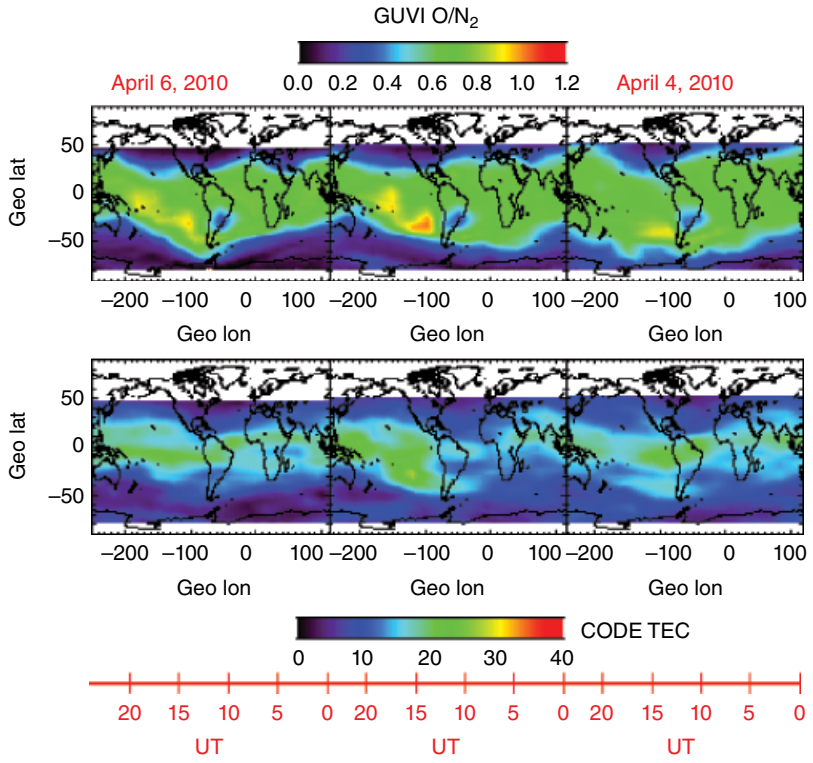


**Figure 21.8** (Top) An overlay of successive dayside orbits on 4–6 April 2010, displaying the column integrated $O/N_2$ ratio obtained from GUVI radiance measurements; (middle) global code TEC for the same period. The bottom panel shows the local solar time related to each TIMED spacecraft equatorial crossing. These data are made available through the JHUAPL webpage at *http://guvi.jhuapl.edu*.

figure (right panels) shows a presence of medium-scale structures (between ±100° longitude) that can be associated with traveling ionospheric disturbances (TIDs). Medium-scale TIDs propagate in the lower atmosphere and have horizontal velocities between 100 and 250 m/s, with wavelengths of several hundred kilometers [e.g., *Hocke and Schlegel*, 1996].

Many studies have demonstrated that a positive storm phase is also commonly associated with a large increase in the $O/N_2$ ratio [e.g., *Prölss*, 1995; *Rishbeth and Barron*, 1960]. To verify whether the composition changes are a controlling factor in producing observed positive storm structure in this event, we examine the GUVI radiance measurements to illustrate the global behavior of $O/N_2$ column density ratio, which is exhibited in Figure 21.8. Top panel shows GUVI global maps of the $O/N_2$ ratio for 4–6 April 2010. The data span a full 24 hr for each day at a fixed local time as the Earth moves under the TIMED

orbit. The local solar time for each equatorial crossing is around 1200 noon (number line in bottom panel). The middle panel displays global GPS-derived code TEC. The $O/N_2$ ratio in Figure 21.8 shows strong enhancement west of South America centered around 1500 UT on 5 April in comparison to 4 April, while a deep depletion centered around 1100 UT exists over Argentina. Both the enhanced $O/N_2$ ratio and deep depletion zones are consistent with code TEC measurements in the same regions.

## 21.4. DISCUSSION

Ionospheric and thermospheric structures are regulated by several externally and internally driven dynamic and electrodynamic mechanisms, such as magnetospheric penetration electric fields, disturbance dynamo electric fields, and gravity waves. Because of the complex interplay among the different drivers, it is often very difficult to separate the effects of one forcing from another.

It is evident from Figure 21.5 that the electric field-driven vertical ion drift is mostly confined to the high-latitude regions on 4 April (left) with no major changes in the mid to low latitudes. On the other hand, ion drifts on 5 April show marked variability. There are also demonstrated hemispherical differences showing regions of much larger drifts in the Southern than Northern, particularly south of the African sector. Perhaps this could explain why we see much larger SED levels in the Southern Hemisphere as noted earlier concerning observations in Figure 21.2. On the dayside, the eastward electric field and the associated positive or upward plasma drifts will uplift the ionospheric plasma to higher altitudes where chemical recombination is less prevalent. At the same time, increased solar radiation intensity will aid the formation of new electron-ion plasma at lower altitudes, thus leading to an overall increase in dayside ionospheric plasma and formation of SED regions [e.g., *Mannucci et al.*, 2005; *Huang et al.*, 2005; *Goncharenko et al.*, 2007; *Lu et al.*, 2012, and references therein].

Across the Asia/Australia sector, an intense ion drift pattern appears over the high to low latitudes at 0900 UT in Figure 21.5 and 1000 UT (not shown). This latitudinal attenuation of the vertical ion drift could be an indication to eastward prompt penetration electric fields during the initial storm phase, however it is out of the scope of the present study to separate the effects of penetration and dynamo electric fields. Similar observations with the TIE-GCM were reported by *Lu et al.* [2008]. *Shimeis et al.* [2012] report on observations of increased interplanetary electric fields on 5 April, which they considered as the cause of the prompt penetration electric fields that they in turn associated with enhanced TEC. The penetration electric fields may be driven by sudden changes in the IMF $B_z$ seen around 0900 and 1000 UT in Figure 21.1. It is well known that sudden rapid reversal of the IMF $B_z$ leads to changes in the strength of the region 1 and region 2 field-aligned current systems [*Kikuchi et al.*, 2000a; *Maruyama and Nakamura*, 2007], and a leak of the interplanetary electric field to midlatitudes and low latitudes. However, it should be noted that the calculation of electric-field penetration from the auroral region to lower latitudes in the TIE-GCM does not account for the electrodynamic interaction with hot plasma in the inner magnetosphere [*Lu et al.*, 2008], as was shown in simulations by, for example, *Maruyama et al.* [2005].

In the upper atmosphere, transport processes due to wind-induced drifts along B-field lines also play an important role in regulating the peak height and density of the *F*-region ionosphere [*Rishbeth*, 1991], especially in the midlatitude ionosphere. During the day, the conventionally poleward winds at midlatitudes direct plasma down along magnetic field lines into regions of greater neutral density, where it is rapidly lost via recombination. At night, the opposite holds true. However, storm-induced equatorward neutral wind will uplift plasma along field lines to higher altitudes where recombination rates are lower, thereby leading to increase of electron density.

For the present study, we consider storm-time Joule heating as the primary candidate for TID development. Figure 21.4 shows that the Joule heating was significantly enhanced immediately following the storm commencement and later in the recovery phase. This is consistent with findings by *Wilder et al.* [2012] and *Shimeis et al.* [2012] that reported intense ionospheric Joule heating in the dayside polar regions, as earlier mentioned. It should be pointed out that for the level of geomagnetic perturbation ($D_{st}$ > s − 60 nT) presented here, the amount of energy deposition into the high latitudes is considered to be unusually high [see, e.g., *Goncharenko et al.*, 2007; *Wilder et al.*, 2012; *Li et al.*, 2012]. According to *Wilder et al.* [2012], the intense ionospheric Joule heating on 5 April was associated with an intense field-aligned current pair near the noon meridian that was in turn related to northward IMF and strong IMF $B_y$. Generally during geomagnetic storms, enhanced Joule heating dissipation in the high-latitude regions produces large pressure gradients that drive equatorward neutral winds to midlatitudes and low latitudes, which can even penetrate into the opposite hemisphere [e.g., *Yizengaw et al.*, 2005]. The altered thermospheric neutral winds can thus affect the dynamic structures of the midlatitude and low-latitude ionosphere causing the formation of SED [see, e.g., *Werner et al.*, 1999; *Nicolls et al.*, 2004; *Lynn et al.*, 2008; *Ngwira et al.*, 2012b, and references therein].

We now consider the time interval in Figure 21.3. For this case, we find that electric field-driven vertical ion

drifts again play an important role in the formation of SED in the Western Hemisphere, as exhibited in Figure 21.6. At low latitudes, within ±15° of dip latitude, the **E × B** vertical drift primarily controls the redistribution of the ionospheric plasma density [e.g., *Abdu et al.*, 1995; *Kikuchi et al.*, 2000b; *Maruyama et al.*, 2005, and references therein]. The observed TEC increase at the dip equator in the American sector is therefore probably related to a storm-enhanced vertical drift component.

A closer examination of TEC perturbations in Figure 21.3 and the TIE-GCM results in Figure 21.6 reveals features that appear to be related to the disturbance dynamo effect. During geomagnetic storm conditions, excess high-latitude Joule heating energy leads to changes in the global thermospheric circulation pattern. The dynamo action of these winds then controls the development of disturbance dynamo electric fields [e.g., *Blanc and Richmond*, 1980], which have a characteristic delay ranging from about 2 hr to several hours after storm commencement [e.g., *Fejer and Scherliess*, 1997; *Fuller-Rowell et al.*, 2002]. The dynamo effect of the modified wind circulation opposes the normal diurnal variation, with downward (or westward) ion drift on the dayside and upward (eastward) drift on the nightside [e.g., *Fuller-Rowell et al.*, 2002; *Galav et al.*, 2014]. In the observed TEC data (Fig. 21.3), there appears to be a TEC depletion between 1600 and 1800 UT in the local nighttime around the southeast Asian sector on 5 April compared with 4 April, except for the region around Japan where a local TEC enhancement is present. The TEC depletion is consistent with TIE-GCM results, which show a decreased (negative) plasma drift at 1500 UT on 5 April.

In addition to the dynamic and electrodynamic processes, neutral composition changes also play a major role in generating ionospheric disturbances during geomagnetic storms. On 5 April (Fig. 21.8), the $O/N_2$ ratio was enhanced at low latitudes to midlatitudes with stronger enhancements centered around 1500 UT on the western coast of South America. It is well known that peak electron density is proportional to the $O/N_2$ ratio, as seen here for 5 April. Therefore we can conclude that composition changes could have contributed to the observed SED features during the period between 1400 and 1800 UT, although such contribution might be minor. On the other hand, a depletion region is seen also over Argentina that could be related to the South Atlantic anomaly. This depleted region shows good agreement with TEC data presented in Figure 21.3 that show decreased TEC around the same time period. The $O/N_2$ ratio was mostly depleted at higher midlatitudes on 5 April indicating that the composition disturbance zone was formed at high latitudes and carried to lower latitudes by equatorward wind surges, which can change the global circulation [e.g., *Fuller-Rowell et al.*, 1994].

Under suitable conditions, minor geomagnetic storms can also cause intense disturbances in the ionosphere. *Li et al.* [2012] investigated the variations in the ionosphere during a small geomagnetic storm on 23 June 2000. By analyzing the coupling functions, Joule heating and auroral precipitation, they suggested that the large ionospheric variations were driven by long-lasting enhanced energy input from the disturbed solar wind. *Li et al.* [2012] then concluded that the sustained energy input led to enhanced equatorward meridional winds that uplifted the ionosphere causing TEC enhancements, and also led to areas of reduced $O/N_2$ that were responsible for negative storms that followed the TEC enhancements.

For the present case study, we find that the energy input was not long-lasting, but had two bursts of enhanced energy periods separated by about 2 hr of low activity. These periods are consistent with the variations in the solar wind IMF $B_z$ component. However, results show that electric field-driven ion drifts were predominantly present during the storm and could be the major driver of the ionospheric disturbances reported in this study with smaller contribution from neutral winds, and composition changes manifested by increased $O/N_2$.

It is well established that SED formation can be a combination of different driving mechanisms [e.g., *Foster*, 1993; *Lei et al.*, 2008; *Li et al.*, 2012; *Zou et al.*, 2013]. For example, *Lei et al.* [2008] investigated the thermospheric and ionospheric response during the initial phase of the 14–15 December 2006 geomagnetic storm using GPS observations and the Coupled Magnetosphere Ionosphere Thermosphere model simulations. They showed that changes of electric fields were the primary cause of the SED in the initial phase of the December 2006 event, whereas neutral winds and composition played a secondary role.

Additionally, *Wang et al.* [2010] examined the common features associated with the initial phase of three geomagnetic storms. Their analysis identified daytime-enhanced penetration eastward electric field as the primary cause of the observed positive storm effects at low and middle latitudes, whereas the negative response around the geomagnetic equator in the daytime was attributed to plasma transport processes. More recently, *Zou et al.* [2013] used a multi-instrument approach to study SED formation processes during the 24–25 October 2011 storm. They found that mechanisms responsible for the formation of SED can be different at different phases of a storm. *Zou et al.* [2013] further showed evidence suggesting that in addition to the major driving processes identified in their study, other mechanisms were present. All these studies are to a large extent in agreement with the results in the present case study.

Clearly, results in the present study show that the initial phase of the storm on 5 April generated both increased and decreased TEC regions. The SED formation mechanisms

have largely been discussed above. As for the deep negative TEC deviations seen in the American sector, we suspect that these could be due to the suppression of the EIA by disturbance dynamo electric fields. Similar results using TIE-GCM were recently reported by *Carter et al.* [2014]. These authors discuss the effect of downward plasma drifts on the formation of equatorial plasma bubbles during geomagnetic activity, which is also related to the suppression of the EIA. In addition, composition changes could be related to these TEC depletions. In Figure 21.8, a comparison of GUVI observations in the American sector for 4 and 5 April shows some differences at equatorial and low latitudes. At the time of writing this paper, the primary cause of these deep negative TEC deviations was not clear. Therefore, more investigations need to be carried out in order to determine their source.

## 21.5. SUMMARY

In the present case study, we investigate the dayside ionospheric response to a minor geomagnetic storm that occurred on 5 April 2010, which can be considered as equinox. We use a synergy between in situ satellite measurements and ground-based observations in combination with numerical modeling to examine the storm-response drivers. Observed TEC data show both significantly enhanced and depleted TEC structures on the day of the storm relative to the quiet day.

The dayside ionospheric SED response was characterized by longitude and hemispheric dependence. During the first main phase that occurred around 1100 UT about two and a half hours after the SSC, strong positive TEC changes where largely confined in the longitudes from 0% to 180°. The strongest SED deviations were seen over the Southern Hemisphere. The second main phase was reached around 1500 UT covering dayside longitudes from –180 to 0 degrees. Both positive and negative TEC deviations where observed in the American sector. The geomagnetic equator region was characterized by enhanced TEC structures, while strong SED deviations appeared mainly in the midlatitudes of North America, North Africa, and southern Europe.

Model TIE-GCM simulations results indicate that electric field-driven ion vertical drifts were the major controlling process in the development of ionospheric disturbances. Notable dayside upward electric field-driven drifts appeared across the high to low latitudes during the initial phase of the storm relative to the quiet day. There is likely a contribution from other mechanisms such as neutral winds and composition changes. We also suggest disturbance dynamo electric fields as the likely candidate for the development of TEC depletions reported in this study.

## ACKNOWLEDGMENTS

Simulation results have been provided by the Community Coordinated Modeling Center at Goddard Space Flight Center through its public runs-on-request system (*http://ccmc.gsfc.nasa.gov*). The CCMC is a multiagency partnership between NASA, AFMC, AFOSR, AFRL, AFWA, NOAA, NSF, and ONR. The TIE-GCM Model was developed by R. G. Roble et al., at the High Altitude Observatory, National Center for Atmospheric Research. GUVI data used here are provided through support from the NASA MO&DA program. The GUVI instrument was designed and built by the Aerospace Corporation and The Johns Hopkins University. The principal investigator is Andrew B. Christensen and the chief scientist and co-PI is Larry J. Paxton. Authors would like to thank the reviewers for their invaluable comments and suggestions.

## REFERENCES

Abdu, M. A., I. S. Batista, G. Walker, J. H. A. Sobral, N. B. Trivedi, and E. R. de Paula (1995), Equatorial ionospheric electric fields during magnetospheric disturbances: local time/longitude dependences from recent EITS campaigns, *J. Atmos. Solar Terr. Phys.*, *57*(10), 1065–1083; doi:10.1016/0021-9169(94)00123-6.

Akasofu, S.-I. (1981), Energy coupling between the solar wind and magnetosphere, *Space Sci. Rev.*, *28*, 121–190; doi:10.1007/BF00218810.

Blanc, M., and A. D. Richmond (1980), The ionospheric disturbance dynamo, *J. Geophys. Res.*, *85*(A4), 1669–1686.

Buonsanto, M. J. (1999), Ionospheric storms, A review, *Space Sci. Rev.*, *88*, 563–601; doi:10.1023/A:1005107532631.

Burns, A. G., S. C. Solomon, W. Wang, and T. L. Kileen (2007), The ionospheric and thermospheric response to CMEs: Challenges and successes, *J. Atmos. Solar Terr. Phys.*, *69*, 77–85; doi:10.1016/j.jastp.2006.06.010.

Carter, B. A., J. M. Retterer, E. Yizengaw, K. Groves, R. Caton, L. McNamara, C. Bridgwood, M. Francis, M. Terkildsen, R. Norman, and K. Zhang (2014), Geomagnetic control of equatorial plasma bubble activity modeled by the TIEGCM with Kp, *Geophys. Res. Lett.*, *41*, 15; doi:10.1002/2014GL060953.

Christensen, A. B., et al. (2003), Initial observations with the Global Ultraviolet Imager (GUVI) in the NASA TIMED satellite mission, *J. Geophys. Res.*, *108*, A12, 1451; doi:10.1029/2003JA009918.

Clilverd, M. A., C. J. Rodger, D. Danskin, M. E. Usanova, T. Raita, T. Ulich, and E. L. Spanswick (2012), Energetic particle injection, acceleration, and loss during the geomagnetic disturbances which upset Galaxy 15, *J. Geophys. Res.*, *117*, A12; doi:10.1029/2012JA018175.

Coster, A. J., and S. Skone (2009), Monitoring storm-enhanced density using IGS reference station data, *J. Geod.*, *83*, 345–351; doi:10.1007/s00190-008-0272-3.

Coster, A. J., J. C. Foster, and P. Erickson (2003), Monitoring the ionosphere with GPS: Space weather, *GPS World*, (14), 42–49.

Crowley, G., D. J. Knipp, K. A. Drake, J. Lei, E. Sutton, and H. Lühr (2010), Thermospheric density enhancements in the dayside cusp region during strong $B_y$ conditions, *Geophys. Res. Lett.*, *37*, L07110; doi:10.1029/2009GL042143.

Fathy, I., C. Amory-Mazaudier, A. Fathy, A. M. Mahrous, K. Yumoto, and E. Ghamry (2014), Ionospheric disturbance dynamo associated to a coronal hole: Case study of 5–10 April 2010, *J. Geophys. Res.*, *119*, 4120–4133; doi:10.1002/2013JA019510.

Fejer, B. G., and L. Scherliess (1997), Empirical models of storm time equatorial zonal electric fields, *Geophys. Res. Lett.*, *102*, A11, 24,047–24,056; doi:10.1029/97JA02164.

Foster, J. C. (1993), Storm time plasma transport at middle and high latitude, *J. Geophys. Res.*, *98*(A2), 1675–1689; doi:10.1029/92JA02032.

Foster, J. C., P. J. Erickson, A. J. Coster, J. Goldstein, and F. J. Rich (2002), Ionospheric signatures of plasmaspheric tails, *Geophys. Res. Lett.*, *29*, 13; doi:10.1029/2002GL015067.

Fuller-Rowell, T. J., M. V. Codrescu, R. J. Moffett, and S. Quegan (1994), Response of the thermosphere and ionosphere to geomagnetic storms, *J. Geophys. Res.*, *99*, 3893–3914; doi:10.1029/93JA02015.

Fuller-Rowell, T. M., G. H. Millward, A. D. Richmond, and M. V. Codrescu (2002), Storm-time changes in the upper atmosphere at low latitudes, *J. Atmos. Solar Terr. Phys.*, *64*, 1383–1391; doi:10.1016/S1364-6826(02)00101-3.

Galav, P., S. Sharma, S. S. Rao, B. Veenadhari, T. Nagatsuma, and R. Pandey (2014), Study of simultaneous presence of DD and PP electric fields during the geomagnetic storm of November 7–8, 2004 and resultant TEC variation over the Indian Region, *Astrophys. Space Sci.*, *350*, 459–469; doi:10.1007/s10509-014-1792-3.

Goncharenko, L., et al. (2006), Large variations in the thermosphere and ionosphere during minor geomagnetic disturbances in April 2002 and their association with IMF By, *J. Geophys. Res.*, *111*, A03303; doi:10.1029/2004JA010683.

Goncharenko, L. P., J. C. Foster, A. Coster, C. Huang, N. Aponte, and L. J. Paxton (2007), Observations of a positive storm phase on September 10, 2005, *J. Atmos. Solar Terr. Phys.*,, *69*, 1253–1272; doi:10.1016/j.jastp.2006.09.011.

Hocke, K., and K. Schlegel (1996), A review of atmospheric gravity waves and traveling ionospheric disturbances, *Ann. Geophys.*, *14*, 917–940; doi:10.1007/s00585-996-0917-6.

Huang, C.-S., J. C. Foster, and M. C. Kelley (2005), Long-duration penetration of the interplanetary electric field to the low-latitude ionosphere during the main phase of magnetic storms, *J. Geophys. Res.*, *110*, A11309; doi:10.1029/2005JA011202.

Katamzi, Z. T., and J. B. Habarulema (2013), Traveling ionospheric disturbances observed at South African midlatitudes during the 29–31 October 2003 geomagnetically disturbed period, *Adv. Space Res.*, *53*, 48–62; doi:10.1016/j.asr.2013.10.019.

Kelley, M. C., J. J. Makela, J. L. Chau, and M. J. Nicolls (2003), Penetration of the solar wind electric field into the magnetosphere/ionosphere system, *Geophys. Res. Lett.*, *30*, 4, 1158; doi:10.1029/2002GL016321.

Kikuchi, T., H. Lühr, K. Schlegel, H. Tachihara, M. Shinohara, and T.-I. Kitamura (2000a), Penetration of auroral electric fields to the equator during a substorm, *J. Geophys. Res.*, *105*, A10, 23,251–23,261; doi:10.1029/2000JA900016.

Kikuchi, T., M. Pinnock, A. Rodger, H. Lüher, T. Kitamura, H. Tachihara, M. Watanabe, N. Sato, and M. Ruohoniemi (2000b), Global evolution of a substorm-associated DP2 current system observed by SuperDARN and magnetometers, *Adv. Space Res.*, *26*(1), 121–124; doi:10.1016/S0273-1177(99)01037-6.

Knipp, D. J., W. K. Tobiska, and B. A. Emery (2004), Direct and indirect thermospheric heating sources for solar cycles 21–23, *Solar Phys.*, *224*, 495–505; doi:10.1007/s11207-005-6393-4.

Lei, J., W. Wang, A. G. Burns, S. C. Solomon, A. D. Richmond, M. Wiltberger, L. P. Goncharenko, A. Coster, and B. W. Reinisch (2008), Observations and simulations of the ionospheric and thermospheric response to the december 2006 geomagnetic storm: Initial phase, *J. Geophys. Res.*, *113*, A01314; doi:10.1029/2007JA012807.

Li, Z., F. Wei, X. Feng, J. Guo, B. A. Emery, and X. Zhao (2012), Large ionospheric disturbances during a minor geomagnetic storm on June 23, 2000, *Ann. Geophys.*, *55*(2); doi:10.4401/ag-5409.

Lu, G., L. P. Goncharenko, A. D. Richmond, R. G. Roble, and N. Aponte (2008), A dayside ionospheric positive storm phase driven by neutral winds, *J. Geophys. Res.*, *113*, A08304; doi:10.1029/2007JA012895.

Lu, G., L. P. Goncharenko, M. J. Nicolls, A. Maute, A. Coster, and L. J. Paxton (2012), Ionospheric and thermospheric variations associated with prompt penetration electric fields, *J. Geophys. Res.*, *117*, A08312; doi:10.1029/2012JA017769.

Lynn, K. J. W., R. Gardiner-Garden, M. Sjarifudin, M. Terkildsen, J. Shi, and T. J. Harris (2008), Large-scale travelling atmospheric disturbances in the night ionosphere during the solar-terrestrial event of 23 May 2002, *J. Atmos. Solar Terr. Phys.*, *70*, 2184–2195; doi:10.1016/j.jastp.2008.05.016.

Mannucci, A. J., B. T. Tsurutani, B. A. Iijima, A. Komjathy, A. Saito, W. D. Gonzalez, F. L. Guarnieri, J. U. Kozyra, and R. Skoug (2005), Dayside global ionospheric response to the major interplanetary events of October 29–30, 2003 "Halloween Storms," *Geophys. Res. Lett.*, *32*, L12S02; doi:10.1029/2004GL021467.

Maruyama, N., A. D. Richmond, T. J. Fuller-Rowell, M. V. Codrescu, S. Sazykin, F. R. Toffoletto, R. W. Spiro,, and G. H. Millward (2005), Interaction between direct penetration and disturbance dynamo electric fields in the storm-time equatorial ionosphere, *Geophys. Res. Lett.*, *32*, L17105; doi:10.1029/2005GL023763.

Maruyama, T., and M. Nakamura (2007), Conditions for intense ionospheric storms expanding to lower midlatitudes, *J. Geophys. Res.*, *112*, A05310; doi:10.1029/2006JA012226.

Mendillo, M. (2006), Storms in the ionosphere: Patterns and processes for total electron content, *Rev. Geophys.*, *44*, RG4001, 2005RG000193.

Möstl, C., M. Temmer, T. Rollett, C. J. Farrugia, Y. Liu, A. M. Veronig, M. Leitner, A. B. Galvin, and H. K. Biernat

(2010), STEREO and Wind observations of a fast ICME flank triggering a prolonged geomagnetic storm on 5–7 April 2010, *Geophys. Res. Lett*., *37*, L24103; doi:10.1029/2010GL045175.

Ngwira, C. M., G. K. Seemala, and J. B. Habarulema (2013), Simultaneous observations of ionospheric irregularities in the African low-latitude region, *J. Atmos. Solar Terr. Phys.*, *97*, 50–57; doi:10.1016/j.jastp.2013.02.014.

Ngwira, C. M., L. A. McKinnell, P. J. Cilliers, and A. J. Coster (2012a), Ionospheric observations during the geomagnetic storm events on 24–27 July 2004: Long-duration positive storm effects, *J. Geophys. Res.*, *117*; doi:10.1029/2011JA016990.

Ngwira, C. M., L. A. McKinnell, P. J. Cilliers, and E. Yizengaw (2012b), An investigation of ionospheric disturbances over South Africa during the magnetic storm on 15 May 2005, *Adv. Space Res*., *49*, 327–335; doi:10.1016/j.asr.2011.09.035.

Nicolls, M., M. C. Kelley, A. J. Coster, S. A. González, and J. J. Makela (2004), Imaging the structure of a large-scale TID using ISR and TEC data, *Geophys. Res. Lett.*, *31*, L09812; doi:10.1029/2004GL019797.

Ostgaard, N., G. Germany, J. Stadnes, and R. R. Vondrak (2002), Energy analysis of substorms based on remote sensing techniques, solar wind measurements, and geomagnetic indices, *J. Geophys. Res.*, *107*, A9, 1233; doi:10.1029/2001JA002002.

Pedatella, N. M., J. Lei, K. M. Larson, and J. M. Forbes (2009), Observations of the ionospheric response to the 15 December 2006 geomagnetic storm: Long-duration positive storm effect, *Geophys. Res. Lett.*, *114*, A12313; doi:10.1029/2009JA014568.

Pi, X., M. Mendillo, W. J. Hughes, M. J. Buonsanto, D. P. Sipler, J. Kelly, Q. Zhou, G. Lu, and T. J. Hughes (2000), Dynamical effects of geomagnetic storms and substorms in the middle-latitude ionosphere: An observational campaign, *J. Geophys. Res.*, *105*, A4, 7403–7417; doi:10.1029/1999JA900460.

Prölss, G. W. (1995), Ionospheric F region storms, 195, in *Handbook of Atmospheric Electrodynamics*, edited by H. Volland, CRC press Boca Raton, Florida.

Prölss, G. W., and M. J. Jung (1978), Travelling atmospheric disturbances as a possible explanation of the daytime positive storm effects of moderate duration at middle latitudes, *J.Atmos. Terr. Phys*., *40*, 1351–1354; doi:10.1016/0021-9169(78)90088-0.

Qian, L., et al. (2013), The NCAR TIE-GCM: A community model of the coupled thermosphere/ionosphere system, in *Modeling the Ionosphere-Thermosphere*, edited by J. D. Huba et al., Geophysical Monograph 201, American Geophysical Union, Washington, D. C.; doi:10.1029/2012GM001297.

Richmond, A. D., E. C. Ridley, and R. G. Roble (1992), A thermosphere/ionosphere general circulation model with coupled electrodynamics, *Geophys. Res. Lett.*, *19*(6), 601–604; doi:10.1029/92GL00401.

Rideout, W., and A. Coster (2006), Automated GPS processing for global total electron content data, *GPS Solutions*, *10*(3), 219–228; doi:10.1007/s10291-006-0029-5.

Rishbeth, H. (1991), F-Region Storms and Thermospheric Dynamics, *J. Geomag. Geoelectr.*, *43, Suppl.*, 513–524; doi:10.5636/jgg.43.Supplement1_513.

Rishbeth, H., and D. W. Barron (1960), Equilibrium electron distributions in the ionospheric F2-layer, *J. Atmos. Terr. Phys.*, *18*, 234–252; doi:10.1016/0021-9169(60)90095-7.

Shimeis, A., I. Fathy, C. Amory-Mazaudier, R. Fleury, A. M. Mahrous, K. Yumoto, and K. Groves (2012), Signature of the coronal hole near the north crest equatorial anomaly over Egypt during the strong geomagnetic storm 5 April 2010, *J. Geophys. Res.*, *117*, A07309; doi:10.1029/2012JA017753.

Solomon, S. C., A. G. Burns, B. A. Emery, M. G. Mlynczak, L. Qian, W. Wang, D. R. Weimer, and M. Wiltberger (2012), Modeling studies of the impact of high-speed streams and corotating interaction regions on the thermosphere-ionosphere, *J. Geophys. Res*., *117*, A00L11; doi:10.1029/2011JA017417.

Strickland, D. J., et al. (2004), Solar EUV irradiance variability derived from terrestrial far ultraviolet dayglow observations, *Geophys. Res. Lett.*, *31*, L03801; doi:10.1029/2003GL018415.

Tsurutani, B., et al. (2004), Global dayside ionospheric uplift and enhancement associated with interplanetary electric fields, *J. Geophys. Res.*, *109*, A08302; doi:10.1029/2003JA010342.

Wang, W., J. Lei, A. G. Burns, S. C. Solomon, M. Wiltberger, J. Xu, Y. Zhang, L. Paxton, and A. Coster (2010), Ionospheric response to the initial phase of geomagnetic storms: Common features, *J. Geophys. Res.*, *115*, A07321; doi:10.1029/2009JA014461.

Weimer, D. R. (2005), Improved ionospheric electrodynamic models and application to calculating Joule heating rates, *J. Geophys. Res.*, *110*, A05306; doi:10.1029/2005JA011270.

Werner, S., R. Bauske, and G. W. Prölss (1999), On the origins of positive ionospheric storms, *Adv. Space Res.*, *24*(11), 1485–1489; doi:10.1016/S0273-1177(99)00711-5.

Wilder, F. D., G. Crowley, B. J. Anderson, and A. Richmond (2012), Intense dayside Joule heating during the 5 April 2010 geomagnetic storm recovery phase observed by AMIE and AMPERE, *J. Geophys. Res.*, *117*, A05207; doi:10.1029/2011JA017262.

Wilder, F. D., S. Eriksson, H. Korth, J. B. H. Baker, M. R. Hairston, C. Heinselman, and B. J. Anderson (2013), Field-aligned current reconfiguration and magnetospheric response to an impulse in the interplanetary magnetic field BY component, *Geophys. Res. Lett.*, *40*, 11, 2489–2494; doi:10.1002/grl.50505.

Yizengaw, E., M. B. Moldwin, and D. A. Galvan (2006), Ionospheric signatures of a plasmaspheric plume over Europe, *Geophys. Res. Lett.*, *33*, L17103; doi:10.1029/2006GL026597.

Yizengaw, E., M. B. Moldwin, P. L. Dyson, and T. J. Immel (2005), Southern Hemisphere ionosphere and plasmasphere response to the interplanetary shock event of 29–31 October 2003, *J. Geophysl Res*., *110*, A09S30; doi:10.1029/2004JA010920.

Yizengaw, E., J. Dewar, J. MacNeil, M. B. Moldwin, D. Galvan, J. Sanny, D. Berube, and B. Sandel (2008), The occurrence of Ionospheric Signatures of Plasmaspheric Plumes over different longitudinal sectors, *J. Geophys. Res.*, *113*, A08318; doi:10.1029/2007JA012925.

Zou, S., A. J. Ridley, M. B. Moldwin, M. J. Nicolls, A. J. Coster, E. G. Thomas, and J. M. Ruohoniemi (2013), Multi-instrument observations of sed during 24–25 October 2011 storm: Implications for sed formation processes, *J. Geophys. Res.*, *118*, 12, 7798–7809; doi:10.1002/2013JA018860.

# INDEX




*Ionospheric Space Weather: Longitude and Hemispheric Dependences and Lower Atmosphere Forcing, Geophysical Monograph 220*, First Edition. Edited by Timothy Fuller-Rowell, Endawoke Yizengaw, Patricia H. Doherty, and Sunanda Basu.